

# International Journal of Engineering Works (IJEW)



OPEN  ACCESS

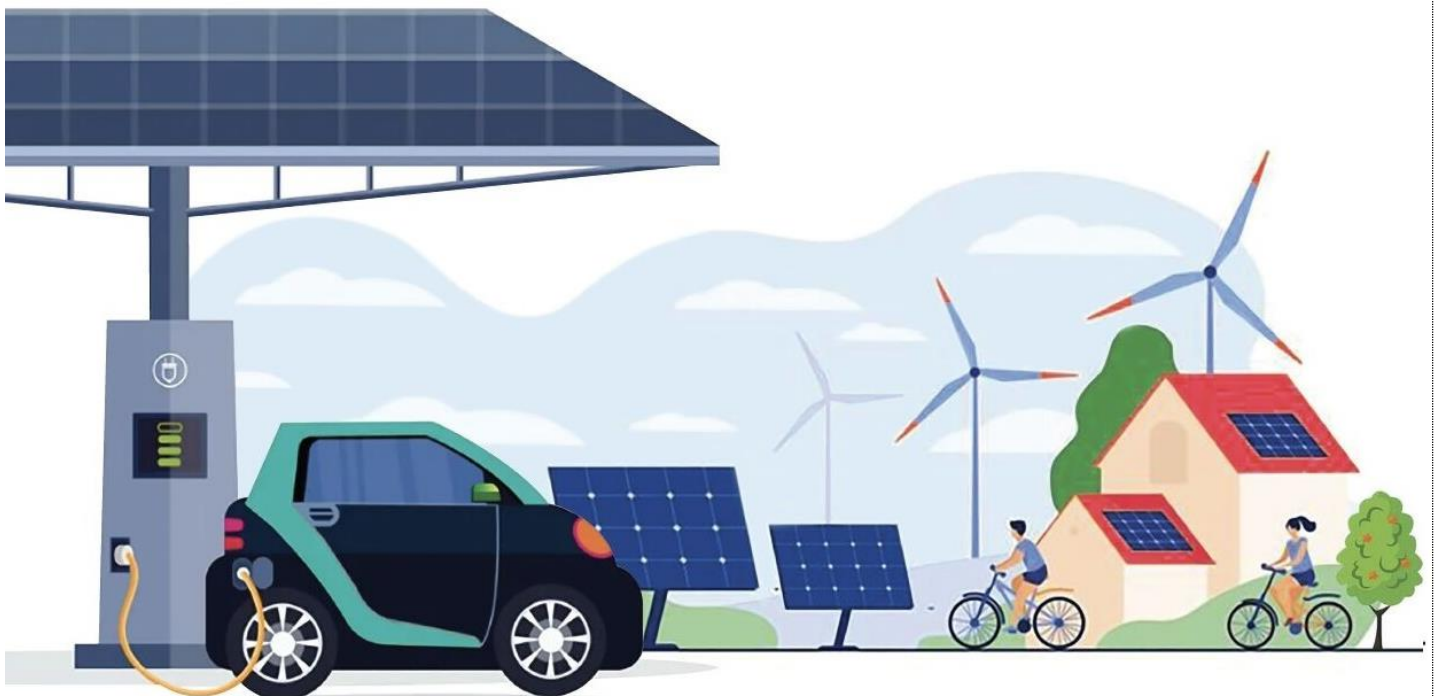
ISSN E 2409-2770  
ISSN P 2521-2419





**VOL. 5-2018**

Printable Version Vol. 5 Issue 01-12, Page: 01-259



Managing Editor: Dr. Irfan Jamil  
Chief-In-Editor: Prof. Isak Karabegovic

**[www.ijew.io/](http://www.ijew.io/)**

**<https://www.ijew.io/rss/2018>**

# Editorial Board

Prof. Isak Karabegovic, University of Bihać, Bosnia and Herzegovina  
Prof. Jinquan Zhao, Hohai University, Nanjing, China  
Prof. Ahmed Kovačević, City University London, UK  
Prof. Cristian SUVAGAU, BC Hydro, Canada  
Prof. Lejla, University Tuzla, Bosnia and Herzegovina  
Prof. Elsayed Ahmed Elnashar, Kaferelsheikh University, Egypt  
Prof. Liisa HALONEN, Aalto University, Finland  
Prof. Axel STOCKMAR, Technische Fachhochschule Hanover, Germany  
Prof. Alam Mangle, CASVAB University of Balochistan, Pakistan  
Prof. Sermin ONAYGIL, Istanbul Technical University, Turkey  
Prof. Jean Luc CAPRON, Institut Supérieur d'Architecture Saint-Luc, Bruxelles, Belgium  
Prof. Arturo COVITTI, Polytechnic of Bari, Italy  
Associate Prof. Abdus Samee, PIEAS Islamabad, Pakistan  
Associate Prof. Urmila Shrawankar, G H Rasoni College of Engineering, India  
Associate Prof. Muhammad Kamran Taj, CASVAB university of Balochistan, Pakistan  
Assistant Prof. Reda Hassanien Eman Hassanien, Cairo University, Egypt  
Assistant Prof. Sajad Hussain, Majmaah University, Kingdom of Saudi Arabia  
Assistant Prof. Imran Taj, CASVAB University of Balochistan, Pakistan  
Assistant Prof. B.Thangagiri, MEPCO Schlenk Engineering College, India  
Assistant Prof. Abdullah, Mohammad Ali Jinnah University, Karachi, Pakistan  
Assistant Prof. Ahmed Kadhim Hussein, babylon University, Iraq  
Assistant Prof. Kaveh Ostad Ali Askari, Islamic Azad University, Iran  
Assistant Prof. Shahzad Ashraf, NFC Institute of Engineering & Technology, Pakistan  
Lecturer S.M Hasan Mahmud. Daffodil International University, Bangladesh  
Dr. Raja Muhammad Ishtiaq Khan, Majmaah University, Kingdom of Saudi Arabia  
Dr. Sajid Ali, Govt. College of Science, Multan, Pakistan  
Dr. Nik Mohd Izual Nik Ibrahim, DRB-Hicom University of Automotive Malaysia  
Dr. Chrito Ananth, Department of ECE, Francis Xavier Engineering College, India  
Dr. Sandeep Gupta, Department of Electrical Engineering, JECRC University, India  
Dr. Marwa Elbany, Civil Engineering Department, Port Said University, Egypt  
Dr. Kader Ali Ibrahim, School of Internet Things Engineering, Jiangnan University, China  
Dr. Muhammad Abubakar, School of Electrical Engineering, Tianjin University, China  
Mr. Rehan Jamil, TBEA Xinjiang SunOasis Co., Ltd.

# Table of Content

**Intelligent Control Algorithm for Distributed Battery Energy Storage Systems**  
Vol. 5, Issue 12, PP. 252-259, December 2018

**Reducing Energy Consumption of Light Rail Train by using CO<sub>2</sub>-Controlled Ventilation for Air Condition**  
Vol. 5, Issue 12, PP. 248-251, December 2018

**An Innovative Automation of Production Processes in the Automotive Industry**  
Vol. 5, Issue 11, PP. 240-247, November 2018

**A Qualitative Overview of Fuzzy Logic in ECG Arrhythmia Classification**  
Vol. 5, Issue 11, PP. 232-239, November 2018

**Control of Optimal Operation with a Hybrid Energy System**  
Vol. 5, Issue 11, PP. 224-231, November 2018

**APU Gas Turbine Performance Monitoring and Fault Diagnosis in Aircraft System based on QAR**  
Vol. 5, Issue 10, PP. 216-223, October 2018

**Formation Control of Unmanned Vehicles via Extended Feedback Consensus**  
Vol. 5, Issue 10, PP. 211-215, October 2018

**Homer based Techno-Economic Comparison of Solar PV, Micro Hydro and Biomass Renewable Energy System with and without Battery Storage**  
Vol. 5, Issue 10, PP. 203-210, October 2018

**Heliostats Automation System for a Solar Power Tower Plant's Efficiency Increment**  
Vol. 5, Issue 10, PP. 183-187, October 2018

**Voltage Control for DC-DC Converters**  
Vol. 5, Issue 10, PP. 198-202, October 2018

**Signal Path Loss Measurement for Future Terahertz Wireless Propagation Links**  
Vol. 5, Issue 10, PP. 193-197, October 2018

**Synthesis of Ni Nanotubes for Enhanced Oxygen Reduction Reaction at Cathode Side of PEM Fuel Cell**  
Vol. 5, Issue 10, PP. 188-192, October 2018

**Modelling a Standalone Hybrid Micro Grid and Analyzing its Voltage Control Capabilities**  
Vol. 5, Issue 10, PP. 176-182, October 2018

**Analysis of Flow Rate and Humidity Effect on Polymer Electrolyte Membrane Fuel Cell Performance using MATLAB/SIMULINK**  
Vol. 5, Issue 10, PP. 172-175, October 2018

**Effect of Fly Ash on Mechanical Properties of Aluminum Alloy**  
Vol. 5, Issue 9, PP. 167-171, September 2018

**Study the Effect of Transient Load on Pipeline Supported by Concrete Blocks**  
Vol. 5, Issue 9, PP. 163-166, September 2018

**An Improvement In Load Forecasting Model Using Parametric Tuned Support Vector Machine (SVM) Kernel Based Functions**

**Vol. 5, Issue 9, PP. 154-162, September 2018**

**A Socio-Technical Survey of Micro Hydro Power Projects in District Shangla, Pakistan**  
**Vol. 5, Issue 9, PP. 147-153, September 2018**

**An investigation on the Flow Behavior in the Airfoil of a Flapping Wing**  
**Vol. 5, Issue 9, PP. 138-146, September 2018**

**In-situ Combustion: Reservoir Candidacy/Project Selection Criteria(s) For Niger Delta Heavy Oil Reservoirs**  
**Vol. 5, Issue 9, PP. 130-137, September 2018**

**Waterflooding: A key Option for Stratified Oil Reservoirs in the Niger Delta**  
**Vol. 5, Issue 9, PP. 124-129, September 2018**

**An Efficient Plasmonic Back Reflector for Thin-film Silicon Solar Cell Application**  
**Vol. 5, Issue 6, PP. 120-123, June 2018**

**Published online An Efficient Plasmonic Back Reflector for Thin-film Silicon Solar Cell Application**  
**PDF read more**

**To Study the Effects of Heat Treatment on the Welded Joints**  
**Vol. 5, Issue 5, PP. 116-119, May 2018**

**A Review on Properties Amelioration of Wearable Antennas**  
**Vol. 5, Issue 5, PP. 111-115, May 2018**

**Design and Implementation of MPPT for a PV System using Variance Inductance Method**  
**Vol. 5, Issue 5, PP. 105-110, May 2018**

**Voltage Profile and Stability Analysis for High Penetration Solar Photovoltaics**  
**Vol. 5, Issue 5, PP. 109-104, May 2018**

**The Behaviour of an Enhanced Earthing System of Transmission Voltage**  
**Vol. 5, Issue 5, PP. 103-108, May 2018**

**Impact of Solar PV Integration on Short Circuit Current and Protection of Distribution System**  
**Vol. 5, Issue 5, PP. 96-102, May 2018**

**A Case Study of Bio-char Production from Biomass using Microwave Assisted Pyrolysis and its Utilization**  
**Vol. 5, Issue 5, PP. 87-95, May 2018**

**Existence Criteria and Hyers-Ulam Theorem for a Coupled P-Laplacian System of Fractional Differential Equations**  
**Vol. 5, Issue 5, PP. 76-86, May 2018**

**Geomechanical Principles of Hydraulic Fracturing Method in Unconventional Gas Reservoirs**  
**Vol. 5, Issue 5, PP. 68-75, May 2018**

**Novel Approach to Develop an Efficient Boost Converter by Using Coupled Inductors**  
**Vol. 5, Issue 4, PP. 61-67, April 2018**

**Classification Performance of Linear Binary Pattern and Histogram Oriented Features for Arabic Characters Images: A Review**  
**Vol. 5, Issue 4, PP. 56-60, April 2018**

**Optimizing Computations in Intermittently Powered Wireless Sensor Nodes**  
**Vol. 5, Issue 3, PP. 50-55, March 2018**



**Design of Optimal Linear Quadratic Gaussian (LQG) Controller for Load Frequency Control (LFC) using Genetic Algorithm (G.A) in Power System**  
Vol. 5, Issue 3, PP. 40-49, March 2018

**Effect of Sandstone on Concrete Procedure With Plastic Synthetic Aggregate**  
Vol. 5, Issue 2, PP. 37-39, February 2018

**A Novel Method for Insulation Testing of High Voltage Electrical Equipment**  
Vol. 5, Issue 2, PP. 32-36, February 2018

**Research in Sensorless Vector Control of Induction Motor based on MRAS Technique**  
Vol. 5, Issue 2, PP. 21-31, February 2018

**Grid Integration of Multistring Photovoltaic Plants with Modular Multilevel Converter**  
Vol. 5, Issue 2, PP. 16-20, February 2018

**Static VAR Compensator for Weak Grid Systems**  
Vol. 5, Issue 1, PP. 10-15, January 2018

**Optimum Sizing and Siting for DG Units using Hybrid 2/3 Rule and Harmony Search Algorithm**  
Vol. 5, Issue 1, PP. 1-9, January 2018

## Welcome to

### Online Manuscript Submission

If you are a first time users, please visit the submission home ([www.ijew.io](http://www.ijew.io)) and read the information before registering for an account. If you are an experienced user, please log in and proceed the steps. If you experience any problems, please send email [info@ijew.io](mailto:info@ijew.io).

### About the IJEW:

International Journal of Engineering Works (IJEW) is the official, monthly peer-reviewed journal affiliated Kambohwel Publisher. IJEW serves as an international forum for sharing ideas and deliver information between all engineering studies and reflecting common challenges in engineering and technology professional academic sectors including industries.

### Bibliographic Information:

ISSN: 2409-2770 (Online)

ISSN: 2521-2419 (Print)

[Int.j.eng.works](http://Int.j.eng.works)

DOI Prefix: 10.34259

Journal DOI: 10.34259/ijew



**Managing Editor: Dr. Irfan Jamil**  
**Cheif-In-Editor: Prof. IsK karabegovic**

[www.ijew.io](http://www.ijew.io)



## Optimum Sizing and Siting for DG Units using Hybrid 2/3 Rule and Harmony Search Algorithm

Abdulsalam A. Aloukili, Metwally A. El-Sharkawy, Mahmoud A. Attia

**Abstract**—The electrical energy one of most important basics of modern life and the demand on this energy increase consciously. Which make some challenges to operators to increase the generation to feed the growing demand. This growth lead to extend the centralized plant to provide distribution network by required energy also lead them to develop transmission system. This method is so costly where it is required money to extend the power system. An appearance of distributed generation DG is considered a solution for these problems and can reduce the cost where it provides the load by electricity in customer side without passing through transmission system. While the aim target from DG is supporting the grid and improve power quality, voltage profile, reduction of power losses and reliability. In this paper will discuss sizing and siting the distributed generation in the grid. In this work introduced hybrid method where it is used 2/3 rule and harmony search algorithm to find optimum location and sizing respectively. This work is done under several loading cases up to 250 % from normal load also compared with other researches in this filed used the same model (IEEE 33 bus radial distribution system) that used in this paper. MATLAB software used to complete this research.

**Keywords**— harmony search algorithm, distributed generation and 2/3 rule.

### I. INTRODUCTION

Last decades DG becomes more important due to meet the growth demand without needing to upgrade the transmission system (overhead, cables and transformers). Also the centralized power station should be extended to produce enough power meet the demand of load. Recently, using DG as power source in customer side is to feed those increasing demand. Where many researches studied the impact of DG units on distributed system where has positive and negative

impact on system performance as voltage profile, losses (active and reactive power) and protective devices. [1,2]

The impact of DG on the system performance is depending on position and size of DG units. Where Authors of [3] speak about that the installation of small DG-PV units near the customer is very attractive to utilities and consumers due to the energy produced close the loads. The distributed generation (DG) always installed at sub transmission network. Where the main aims are to:

- ✓ Reduce transmission lines losses
- ✓ Improve voltage profile on system
- ✓ Reduce the emission from centralized plant
- ✓ Low operating cost due to peak shaving
- ✓ Reduced or deferred investment in generation, transmission, transformers and distribution infrastructure upgrades due to relieve T&D congestion

To get best performance to distributed generation on power system many researchers proposed several studied include a lot of methods to get the optimum place and size of DG to improve the voltage profile and power losses. Some researches assumed the location of DG depend on availability of renewable source (sun, wind seas and Ocean or etc.) in media and it's space [3], also other researchers in by H.L. willis [4]. used simple analytical approach techniques as 2/3 rule which is based on installing the DG on 2/3 of feeder by sizing of DG's estimated as 2/3 the value of loads but this techniques not use in uniformly distributive load due to this techniques follow the method of exact loss formula where the size of DG determine by calculate direct equation prevail from the generalized reduced gradient (GRG) method..

In [5], PSO algorithm is used to find the optimum size of DG and the location of DG is limited by Loss Sensitivity Factor LSF and WK bus. Also Zhu and others in [6] are suggested method called Ordinal Optimization to find optimal location and size of DG with keep the balance between loss minimization and capacity maximization. A. Keane et al [7] used linear programming to DG problem.

In [8], A. M. El. Zonkely proposed Sequential quadratic programming (SQP) to find placement of DG without consideration fault restraints suggested. Also in [9] the authors

Abdulsalam A. Aloukili: Electrical Power and Machines Department, Faculty of Engineering, Ain Shams University, Cairo, Egypt, Email: a\_alaokali@yahoo.com.

Metwally A. El-Sharkawy: Electrical Power and Machines Department, Faculty of Engineering, Ain Shams University, Cairo, Egypt, Email: metwallyalsharkawy@yahoo.com.

Mahmoud A. Attia: Electrical Power and Machines Department, Faculty of Engineering, Ain Shams University, Cairo, Egypt, Email: Mahmoud.Abdullah@eng.asu.edu.eg.

used multi objective function to reduce losses by insertion DG units in optimum allocated. In [10], M. Shaaban and Petinrin proposed method to minimize losses and improve power voltage profile via using combination of sensitivity index, exact loss formula and voltage sensitivity coefficient.

Genetic Algorithm one of oldest search method where based on natural is chosen to get optimum sizing and siting of DG units to minimize losses [11,12]. L. Wang et al. in [13] used Ant Colony optimization to get the optimum location and size of DG units where this search method based on ant behavior to find shortest way from den to food please also search for food.

R.S. Rao et al. [14] used Harmony search to find the optimum site of DG which was depend on the loss sensitivity factor to reduce losses and improve voltage profile in a system. In [15], N.G.A. Hemdan et al. used Particle Heuristic Algorithm to find optimum place of DG where based on the resumption of flow power presented. This technique contains two methods which are clustering techniques and exhaustive search.

#### Impact of distributed generation in voltage regulation

One of the troubles occurs to far-end of radial distribution system or in the rural is dip on voltage. This made some problem to loads and protective device. The voltage profile can be supported and improved by using tap change transformer, shunt capacitor switched on feeder and shifting transformer towards the load center. According for several researches the previous techniques can keep the voltage in the required limit. According to [16] the place and size of DG has important effect in voltage profile. Also when using improved analytical (IA-method) the minimum voltage increase to more acceptable limit. According to American National Standards in voltage fluctuation on distribution systems is within range (+7% to -13%) but in practical many companies keep voltage fluctuation within  $\pm 6\%$  which should be considered in any solution suggested to enhance voltage profile. One of the methods used to control on voltage profile in customer side as in [17]. The concept is insertion DG in distribution system as capacitor bank with the DG units inject real power or both active and reactive power where most distributed generation work at between ranges 0.85 lagging to unity power factor. Also the inverter connected to photovoltaic, wind turbine or any DC source to provide the system via leading power factor. All previous cases lead to improve voltage profile when select optimum places and size especially in rural and far-end of distribution system. Also reduce all substation capacities from distribution system. Other researches talk about the bad position of DG can be lead to worst system performance [18,19].

#### Impact of distributed generation in power losses

One of the important solution can DG introduce in distribution network is to reduce power losses in distribution system. Where several researches appear ability of reduce both

active and reactive power losses by inject DG units also increase reliability of system [20].

As appear in [21], the both active and reactive losses in distribution system can be reducing by inserting DG in optimum location and sizing. Several researches apply this concept by injecting both active and reactive power in distribution system which reduce losses and improve ability of system [16,19]. But the most important rule to insert DG units to improve system performance is selection optimum location and sizing to the DG units in distribution system. Authors of [21] considered concept of DG units exactly as capacitor bank but a capacitor bank produce the grid just by reactive power. In [16] Authors used two different methods to select the placement and size of DG units. The active power losses in the system without DG was around 202.677 kW and after use Improved analytical IM-method to find site and size of DG units the losses reduction to 110.1537 kW and by use PSO the losses reduce decrease to 92.4365 kW [16].

In this paper hybrid method is proposed by using both 2/3 rule and harmony search algorithm to find optimum placement and sizing of DG units. 2/3 rule is used to find the location of DGs and harmony search is used to find the optimal sizing of DGs at several loading conditions.

## II. METHODOLOGY

This part of paper will introduce the mechanism to select the location of DGs and DGs sizing. This operation is important to minimize the losses and improve voltage profile to the selection system. In this research the sizing for DG is studied in many cases 100%, 150% 200% and 250% from normal load and the siting will be fixed for all cases. IEEE 33 bus radial distribution system was selected. The total load of system is (3581KW& 1745KVar). Fig.1 shows IEEE 33 bus.

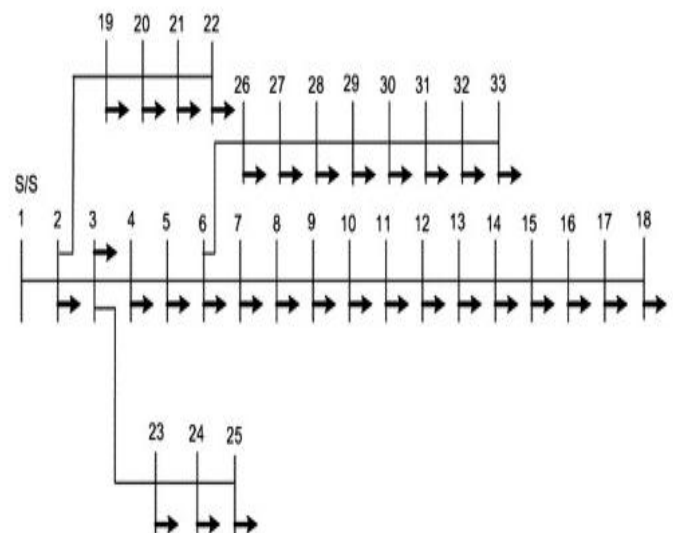


Figure 1. IEEE 33 bus radial distribution system

Backward/Forward Sweep Method of power flow is used in this paper to obtain the voltage at each bus and the active & reactive power losses in each branch of the system [24]. Table.1 shows the voltage at each bus and power losses at each branch by using Backward/ Forward Sweep Method.

TABLE I. IEEE 33 BUS DATA WITHOUT DG UNIT

Branch	Power Loss (KW)	Reactive loss (KVar)	Bus	Voltage (p.u)
1	13.6400	6.9531	1	1.0000
2	56.4646	28.7592	2	0.9964
3	20.6039	10.4934	3	0.9794
4	19.1936	9.7756	4	0.9705
5	39.0578	33.7165	5	0.9618
6	2.1213	7.0121	6	0.9411
7	5.3191	1.7578	7	0.9374
8	4.5562	3.2734	8	0.9315
9	3.8563	2.7334	9	0.9242
10	0.5958	0.1970	10	0.9175
11	0.9502	0.3142	11	0.9164
12	2.8786	2.2648	12	0.9146
13	0.7903	1.0403	13	0.9076
14	0.3964	0.3528	14	0.9051
15	0.3083	0.2252	15	0.9035
16	0.2738	0.3656	16	0.9019
17	0.0571	0.0448	17	0.8997
18	0.2088	0.1992	18	0.8991
19	1.0760	0.9696	19	0.9957
20	0.1302	0.1521	20	0.9910
21	0.0563	0.0745	21	0.9901
22	3.8420	2.6252	22	0.9893
23	6.1978	4.8941	23	0.9749
24	1.5431	1.2074	24	0.9665
25	2.3500	1.1970	25	0.9623
26	2.9464	1.5002	26	0.9388
27	9.7751	8.6185	27	0.9359
28	6.5969	5.7471	28	0.9237
29	3.1339	1.5963	29	0.9149
30	1.8333	1.8119	30	0.9109
31	0.2430	0.2833	31	0.9062
32	0.0140	0.0217	32	0.9052
33	zero	zero	33	0.9049
Total Losses	211.0103	140.1770	Min VOLT	0.8991

#### A. Location of DG

The location of DG is not less important than sizing of DG where the wrong location for distributed generation lead to increase losses to the system and not support the grid also sometimes caused increasing in the voltage more that demand which produced over voltage. In this paper 2/3 rule is used to find location of DG where this method widely used in several application of power system especially in FACTS where this method so easy to apply in any feeder which based on install DG at 2/3 of feeder by 2/3 of capacity of load but in this research using this method just to location of DG. And by looking to Fig.1 the IEEE 33 BUS and by referring to 2/3 rule the buses selected as location to the distributed generation are (13, 21, 24 and 31) where those sites will be fixed to all cases

of loading (100%, 150% 200% and 250% from normal load) and the change will be just in sizing of distributed generation.

#### B. Sizing of DG

To find optimum size for distributed generation Harmony search algorithm is used in this work. This technique run the power flow program several times and at each process the harmony memory used new data and save the best solution. In this research processed the sizing operation four times at each case use new sizing to the new develop in the grid (100%, 150% 200% and 250% from normal load). The distributed generation produces only active power (unity power factor).

**Harmony Search algorithm (HS):** Recently proposed a new heuristic optimization technique inspired from music phenomenon. The procedures of solution. by HS algorithm are to. Initialize the design parameters at first, then harmony. memory (HM) is initialized. After that a New Harmony improvisation is created from the HM, then. Harmony memory is. Updated. Finally, the procedure is repeated starting from harmony memory improvisation until the criteria. of termination is satisfied [25, 26]. The flowchart of the HS algorithm is shown in Fig. 2

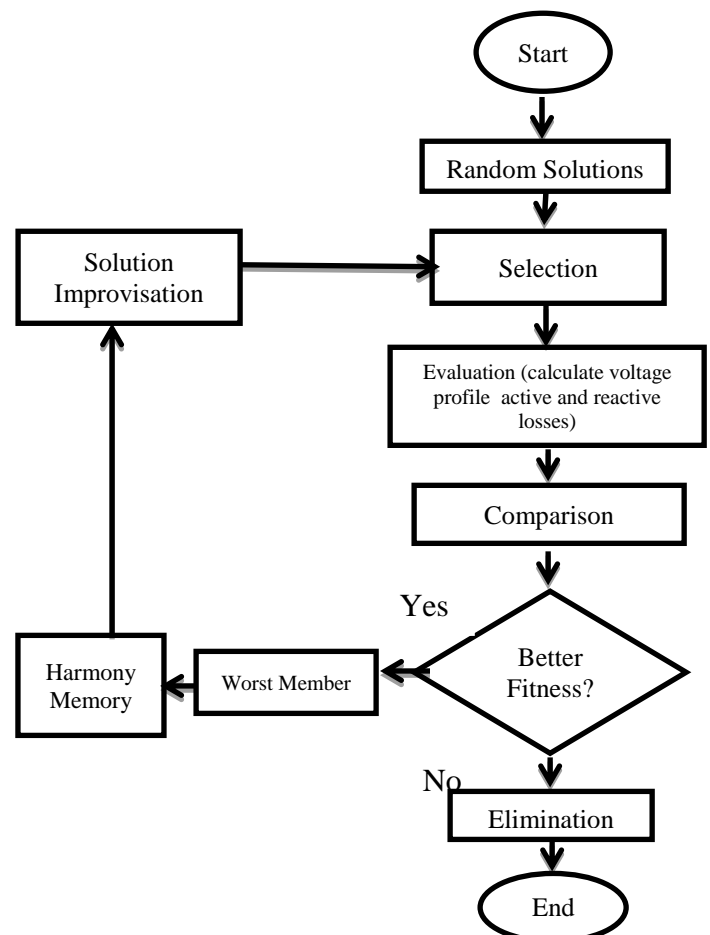


Figure 2. Flow Chart of Harmony Search algorithm

### III. RESULT

In first case at 100% loading the DG installed at (13, 21, 24 and 31) where the harmony search select rating for each bus around (595, 200, 285 and 599) KW present around % 45 from load. The voltage in system is reached to 0.9526 pu from 0.8991 and the losses are reduced to 72.27KW which present 2.01% from load and the reactive losses are reduced to 47.71KVAR that present around 2.73%. Where the losses

before insert the DG were 211KW (5.89%) and 140.17KVAR present 8.03%. Also can see clear different on voltage at each bus as shown in Fig.3.

TABLE II. SYSTEM AT 100% LOADING

Case of system	Minimum voltage pu	Maximum voltage pu	Active power losses		Reactive power losses	
Without DG	0.8991	1	211.013 kW	5.89%	140.1770 KVAR	8.03%
With DG (1680 kW) 45% of loading	0.9526	1	72.273 kW	2.01%	47.7134 KVAR	2.73%

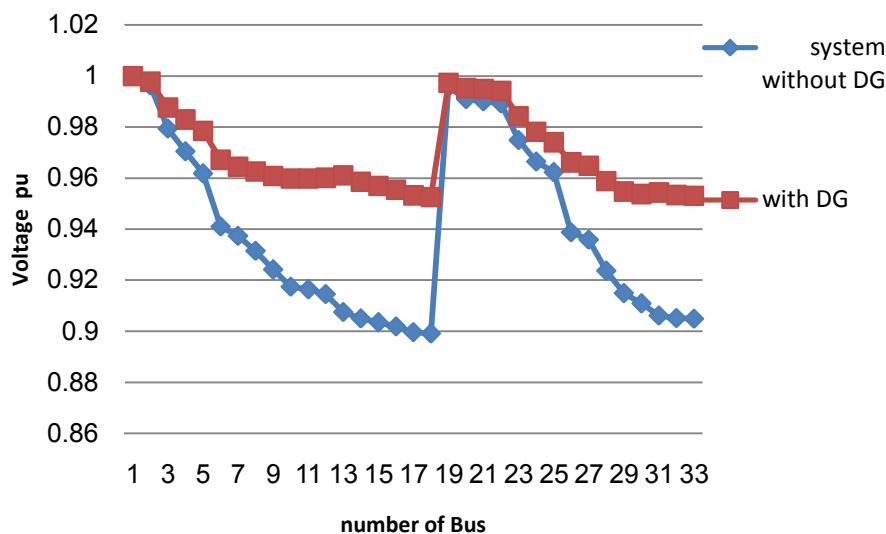


Figure 3. voltages at each bus case 100% from normal load

In second case at 150% loading where the system load is (5371KW & 2617.5KVAR) where the value of DG selected by HS are (1000, 500 500 and 1000) KW present around 55 % of loading. And by looking to Table 3 it can be seen that the minimum voltage is increased to 0.9378 pu and the losses in system are reduced to 2.8% & 3.8% of loading for both active and reactive losses. And by increasing the DG rating to (4579KW) 85% the losses are reduced to 2.06 % & 2.9% of loading for active and reactive power and the voltage is reached to 0.9637pu. System result described in Table.3 .Fig.4 show the voltage at each bus at 150% loading.



TABLE III. SYSTEM AT 150% LOADING

Case of system	Minimum voltage pu	Maximum voltage pu	Active power losses		Reactive power losses	
Without DG	0.8412	1	522.9711 KW	9.73%	348.0025 KVar	13.2%
With DG (3000 kW) 55% of loading	0.9378	1	150.4276 KW	2.8%	100.0809 KVar	3.8%
With DG (4579 kW) 85% of loading	0.9637	1	110.7010 KW	2.06%	77.6112 KVar	2.9 %

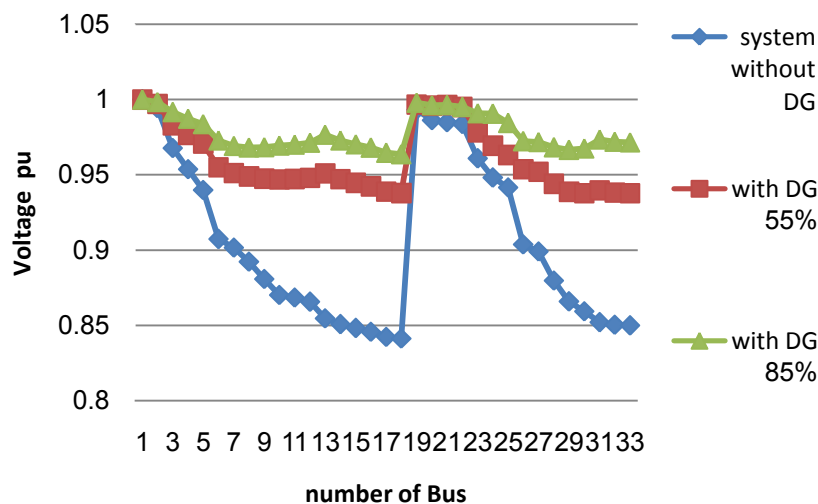


Figure 4. voltage at each bus case 150% from normal load

In third case when using 200% loading (7162KW & 3490 kVar) the harmony search selected the rating for DG as (802,609,772 and 1900) KW around 56% from load. The DGs are at buses (13, 21 24 and 31) which caused increasing in voltage to reach 0.8918 pu and the losses reduction to 3.91% & 5.54% of loading for both active and reactive power losses from 14.58% & 19.95%. When increasing the DG rating to (6170 KW) which present 86% the losses are reduced to 2.7% & 3.99% of loading for both active and reactive power losses

and the minimum voltage reach to 0.9546 pu as appear in Tabel.4 . Fig 5 displayed the voltage at each bus.

TABLE IV. SYSTEM AT 200% LOADING

Case of system	Minimum voltage pu	Maximum voltage pu	Active power losses		Reactive power losses	
Without DG	0.7766	1	1.0446e+3 kW	14.58%	696.5683 kVar	19.95%
With DG (4075 kW) 56% of loading	0.8918	1	280.6055 kW	3.91%	193.4003 kVar	5.54%
With DG (6170 kW) 86% of loading	0.9546	1	198.3354 kW	2.7%	139.4459 kVar	3.99%

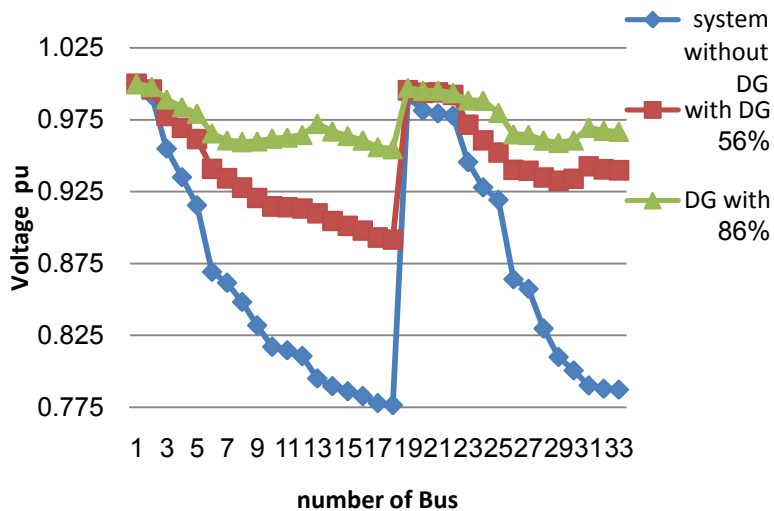


Figure 5. voltages at each bus case 200% from normal load

In last case when using 250% loading (8952KW & 4362KVar) the harmony search select rating for DGs as (1500,709,892 and 2201) KW present around 59% from load. The DGs are installed at buses (13, 21 24 and 31) which caused increasing in voltage to reach 0.8953 pu and the losses are reduced to 4.50% & 6.29% of loading for both active and reactive power losses from 21.10% & 28.9%. last case when increasing the rating of DG units to (7816 KW) which present 87% of the load, the minimum voltage in the system is reached to 0.9505 pu and the losses are reduced to 3.47% and 5.03% of

loading for active and reactive losses. As displayed in Tabel.5. Fig 6 display the voltage at each bus.

TABLE V. SYSTEM AT 250% LOADING

Case of system	Minimum voltage pu	Maximum voltage pu	Active power losses		Reactive power losses	
Without DG	0.7039	1	1.8893e+3 kW	21.10%	1.2632e+3 kVar	28.9%
With DG (5302 kW) 59% of loading	0.8953	1	403.3315 kW	4.50%	274.7843 kVar	6.29%
With DG (7816 kW) 87% of loading	0.9505	1	311.7798 kW	3.47%	219.4653 kVar	5.03%

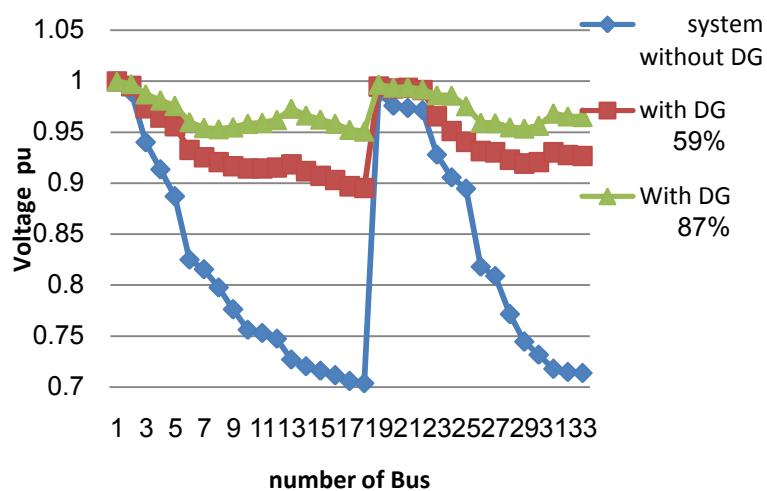


Figure 6. voltages at each bus case 250% from normal load

By looking for Table 7 where Displays the priority in voltage and the losses in system where can see clear advantage on minimum voltage and the total losses in the system in the method used in this paper than others two methods (Improved analytical IA & PSO ) that used in [16] to find optimum sizing and siting. Fig 6 shows the voltage at each bus in those cases.

TABLE VI. COMPARISON BETWEEN IMPROVED ANALYTICAL IA METHOD, PSO METHOD AND(2/3 RULE & HARMONY)

Method	DG Rating kW	Min voltage pu	Max voltage pu	Active Power losses kW	Reactive power losses kVAr
AI method[16]	2560.2300	0.957416	1	110.1537	non
PSO method[16]	1857.5	0.940027	1	92.4365	non
2/3& harmony	1685	0.9526	1	72.2734	47.7134

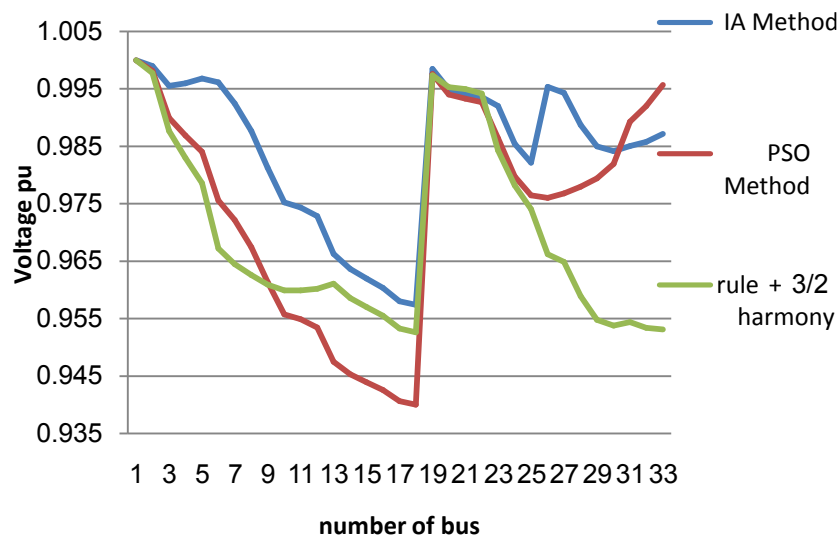


Figure 7. voltage at each Bus 100% loading

## CONCLUSION

In this paper introduced 2/3 rule with harmony method to select the optimum location and sizing for DG units at many several loading conditions. Where in each case the insertion of DGs into the system can reduce the losses in system and improve the voltage profile. Also in case with DGs have high rating; the losses and the voltage profile are better. By looking to the last comparison between the 2/3 rule with harmony showed the priority of this optimization techniques on Improved analytical IA method and PSO where used less rating of DG, improve the voltage profile and reduce the losses better than other cases.

## REFERENCES

- [1] Aquino-Lugo A. A., Klump R., Overbye T. J. A control framework for the smart grid for voltage support using agent-based technologies. *IEEE Transactions on Smart Grid*. 2011;2(1):161-168. doi: 10.1109/TSG.2010.2096238
- [2] Philip P. Barker and Robert W. de Mello, "Determining the Impact of Distributed Generation on Power Systems: Part -I radial DG systems", *Power Engineering Society Summer Meeting*, 2000.
- [3] P. Chiradeja and R. Ramakumar, "An Approach to Quantify the Technical Benefits of Distributed Generation," *IEEE Trans. on Energy Conversion*, Vol. 19, No. 4, pp. 1686- 1693, December 2004.
- [4] H. L. Willis, "Analytical methods and rules of thumb for modelling DG-distribution interaction", *IEEE*, 2000.
- [5] Ambika. R and Rajeswari .R." Optimal Siting and Sizing of Multiple DG Units for the Enhancement of Voltage Profile and Loss Minimization in Transmission Systems Using Nature Inspired Algorithms " *ScientificWorldJournal*. 2016; 2016: 1086579. Published online 2016 Feb 8. doi: 10.1155/2016/1086579 <https://www.ncbi.nlm.nih.gov/pmc/articles/PMC4761755/>
- [6] Zhu, R.P. Broadwater, Tam, K.-S., Seguin, R., As-geirsson, H. "Impact of DG Placement on Reliability and Efficiency with Time-Varying Loads" *IEEE Trans. Power Syst.*, Vol. 21, No. 1, pp. 419-427, Feb .. (2006),
- [7] A.Keane and O'Malley, "Optimal Allocation of Embedded Generation on Distribution Networks", *IEEE Trans. Power Syst.*, Vol. 20, No. 3, pp. 1640-1646, Aug. M. (2005),
- [8] A.M.El-Zonkoly, "Optimal Placement of Multi-distributed Generation Units Including Different Load models using Particle Swarm Optimization", *IETGener., Transm., Distrib.*, Vol. 5, No. 7, pp. 760-771, Jul. (2011)
- [9] Le, A.D.T., Kashem, M.A., Negnevitsky, M. and Ledwich, G. "Optimal Distribution Generation Parameters for Reducing Losses with Economic Consideration" *Power Engineering Society Gener. Meeting IEEE*, pp.I-8. (2007),
- [10] M. Shaaban, and Petinrin, "Sizing and Siting of DG in Distribution System for Voltage Profile Improvement and Loss Reduction," *IJSGCE Gener.*, Vol. 8, No. 1, pp. 1-7. (2013),
- [11] Mohamad Amiri, Mina SheikholeslamiKandelousi, and Mahmood Moghadasian" *Distribution Feeder Reconfiguration Considering Distributed Generators using Cuckoo Optimization Algorithm " 2nd International Conference on Research in Science, Engineering and Technology (ICRSET'2014)*, March 21-22, 2014 Dubai (UAE)
- [12] Kim, IO., Nam, S.W., Park, S.K. and Singh, C. "Dispersed Generation Planning using Improved Hereford Ranch Algorithm", *Elect. Power Syst. Res.*, Vol. 47, No. 1, pp. 47-55, Oct(1998).
- [13] L.Wang, and C. Singh,"Reliability-constrained Optimum Placement of Reclosers and Distributed Generators in Distribution Networks using an ant Colony System Algorithm", *IEEE Trans. Syst., Man, Cybern. C, Appl. Rev.*, Vol. 38, No.6, pp. 757-764, Nov. (2008)
- [14] R.S.Rao, , K.Ravindra, , K.Satish, and S. Narasimham, V.L., "Power Loss minimization in Distribution System using Network Reconfiguration in the Presence of Distributed Generation", *IEEE TRANSACTIONS ON POWER SYSTEMS*, VOL. 28, NO. 1, FEBRUARY 2013
- [15] N.G.A. Hemdan, and Kurrat, M., "Efficient Integration of Distributed Generation for Meeting the Increased Load Demand", *In!. J. Electr. Power EnergySyst.*, Vol. 33, No. 9, pp. 1572-1583, Nov. 2011.
- [16] T. Ravi Kumar and G. Kesava Rao " Analysis of IA and PSO Algorithms for Siting and sizing of DG in Primary Distribution Networks " *International Journal of Control Theory and Applications*
- [17] J. Kilonzi Charles, N. AbunguOdero" Effects of Distributed Generation penetration on system power losses and voltage profiles" *International*

- [18] W. EL-KHATTAM & M. M. A. SALAMA " Impact of Distributed Generation on Voltage Profile in Deregulated Distribution System "
- [19] Sani A. Muhammad<sup>1</sup>, Bello Muhammad<sup>2</sup> and Hamza Abdullahi<sup>3</sup>" THE EFFECT OF DISTRIBUTED GENERATION ON POWER SYSTEM PROTECTION A-REVIEW " International Journal of Electrical and Electronics Engineers , ISSN- 2321-2055 (E) , IJEEE, Vol. No.7, Issue No. 01, Jan-June, 2015
- [20] Philip P. Barker, R. W. "Determining the Impact of Distributed Generation on Power Systems" Part 1 - Radial Distribution Systems. 12. IEEE. Retrieved 02 16, 2011, from IEEE. (2000).
- [21] Angel FernándezSarabia" Impact of distributed generation on distribution system "thesis introduce to Master in Dissertation Submitted to the Faculty of Engineering, Science and Medicine, Aalborg University in Partial Fulfilmen. Aalborg, Denmark. june ,2011
- [22] Philip P. Barker and Robert W. de Mello, "Determinin g the Impact of Distributed Generation on Power Systems: Part -1 radial DG systems", Power Engineering Society Summer Meeting, 2000
- [23] Mohamed Talal Mohamed Elmathana" The Effect of Distributed Generation on Power System Protection" thesis for the degree of Masters by Research, Presented to the University of Exeter, September 2010
- [24] G. W. Chang ; S. Y. Chu ; H. L. Wang "An Improved Backward/Forward Sweep Load Flow Algorithm for Radial Distribution Systems", IEEE Transactions on Power Systems Volume: 22, Issue: 2, May 2007.
- [25] Ibrahim M. Diao, Niveen M. Badra and Mahmoud A. Attia, "Harmony Search Algorithm and Teaching-Learning-Based Optimization Approaches to Enhance Power System Performance"issue 10, vol. 34 , World Applied Sciences Journal (WASJ), 2016.
- [26] Z. Geem, J. Kim, et aI. , "A new heuristic optimization algorithm: harmony search," Simulation 76 (2) (2001) 60-68 .



Abdulsalam Aref Aloukli got his B.Sc Degree in Electrical Power and Machines from omer el-mokhtar University, dernah/ libya and studing in Master of Science - Electrical Engineering Electrical Power & Machines in Ain Shams University, Cairo, Egypt. also he works at

IRASA network as Project Engineer



M. A. El-Sharkawy was born in Daqahliyya, Egypt in 1942. He received the B. Sc. Degree (Honors) and M. Sc. Degree in Electrical Engineering from Ain-Shams University in Cairo, Egypt in 1964 and 1970, respectively. He received the Ph. D. degree from the Polytechnic Institute of Leningrad in the former Soviet Union

in 1974. Currently he is emeritus professor of Electric Power Engineering in Ain Shams University. Dr. Sharkawy had been Professor of Electric Power Engineering in Ain Shams University since 1987. Dr. Sharkawy has supervised a large number of Ph. D. and M. Sc. research works in Electric Power Engineering. He is the author and co-author of many published refereed papers. Dr. Sharkawy is also a Professional Engineer since 1987. He designed and supervised the construction of electrical and electro-mechanical systems of a large number of big projects in Egypt and Saudi Arabia.



Mahmoud Abdallah Attia, He received B.Sc., M.Sc. and Ph.D. in electrical engineering from Ain Shams University (ASU), Egypt in 2005, 2010 and 2015 respectively. He has joined ASU teaching stuff since 2007. He authored many journal and conference papers. He is a reviewer for power component and systems journal, Ain

Shams Engineering Journal Elsevier and International Transactions on Electrical Energy Systems. 2009, He was in Technical committee of ASU international conference ASCEE-3. He is a Member of "Continuous Improvement & Quality Assurance Unit of Faculty of engineering ASU". He is the author of books 'Optimal Allocation of FACTS Devices in Electrical Power Systems: A Genetic Algorithm Based Approach', in April 2013 and 'Enhancing Power System Performance with Growing Wind Power Penetration: optimal Allocation of FACTS', in July 2015 LAP LAMBERT Academic Publishing.

# Static VAR Compensator for Weak Grid Systems

Muhammad Kashif Khan, Dr.AbdulBasit, Faheem Ali

**Abstract**—In our daily routine life majority of electric loads used are inductive in nature. Adequate supply of active power and reactive power must be supplied to these loads to ensure proper operation. If not provided with required active power and reactive power, these inductive loads burden the system unnecessarily. Hence resulting in low power factor. In a local electrical distribution system it is uneconomical to upgrade existing network for improvement of power factor. In weak grid system residential consumers use voltage stabilizers to cope up with poor quality of voltage, while industrial consumers use switched capacitors. But voltage stabilizers regulate the voltage on cost of drawing more current from system. On the other hand switched capacitors technology is not robust enough to handle instant variations in power demand. Low power factor on local grid systems can be addressed using static var compensators. In this paper designing of SVC for local grid system is discussed.

**Keywords**— Static Var Compensator (SVC), Thyristor switched capacitor (TSC), Thyristor controlled reactor (TCR), Gate turn off thyristor (GTO), Flexible alternating current transmission systems (FACTS)

## I. INTRODUCTION

In this modern era stable supply of electricity is need of everyone. [1] Electric power system consists of generation, transmission and distribution. Electricity is generated at power station by means of different sources, that can be either hydal, wind, nuclear or thermal energy. Generated electricity is transmitted to grid stations through transmission system. End consumers are connected to electric power system via distribution system. Grid is unnecessarily loaded if consumers are supplied with poor power quality. As to compensate with poor power quality consumer employ different methods which aren't effective enough. Residential consumers uses voltage stabilizers. If voltage at consumer end is lower than nominal voltage then voltage stabilizer step up the voltage on cost of drawing more current from system. As an accumulative result voltage stabilizers draws more reactive power from system. [2] [4] Industrial consumers uses switched capacitors. However control of switched capacitor is manual and can't be used under varying voltage. Therefore a compensating device is required which can compensate for reactive power support according to system requirement. [3] [5] Static var compensator (SVC) is used for power quality improvement under dynamic conditions. But flexibility of SVC is limited for local grid station. In this paper detailed design for SVC is discussed. Designed model is simulated in MATLAB for different loading conditions & results are obtained for different scenarios.

## II. STATIC VAR COMPENSATOR (SVC)

First static var compensator (SVC) was installed in 1987. They are considered to be first generation of FACTS devices. SVC is a shunt compensating device. [6] SVC is used in electric power system for reactive power compensation and to provide voltage support. SVC has three basic configurations: Thyristor switched capacitor (TSC), Thyristor controlled reactor (TCR) and combination of both TSC & TCR.

### A. Thyristor switched capacitor (TSC)

[7] Thyristor switched capacitor consists of thyristor valves, current limiting reactor and power capacitor. Thyristor valve consists of two inverse parallel thyristors in parallel to each other. As thyristor allows current in one direction, that's why this inverse parallel thyristor symmetry is needed. Thyristor valves are added in series to withstand line voltage. TSC is used to add leading reactive VARs to system. TSC can be switched on or switched off using thyristor valve. But TSC can't be operated in phase control fashion. Blocking / deblocking of TSC can only be varied in steps. However proper care must be taken while deblocking TSC. Optimum time to unblock a TSC is when line voltage is at minimum. Any sudden excitation or misfiring will damage thyristor valve.

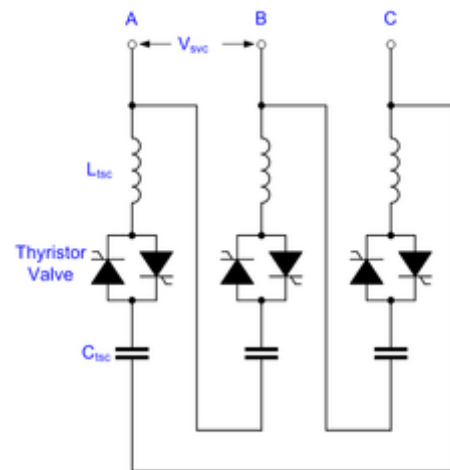


Figure-1: Thyristor Switched Capacitor (TSC)

### B. Thyristor Controlled Reactor (TCR)

Thyristor controlled reactor mainly consists of thyristor valves and inductor (reactor). TCR is used to limit the voltage and improve power factor on lightly loaded transmission lines. For capacitive power factor of system, TCR is used to add reactive (inductive) power to system. TCR can be operated in phase controlled fashion. Reactive power delivered to system



can be adjusted by varying the firing angle for thyristor valve. Unlike TSC, TCR generates high harmonics. [8] TCR is usually connected in delta fashion to filter these harmonics.

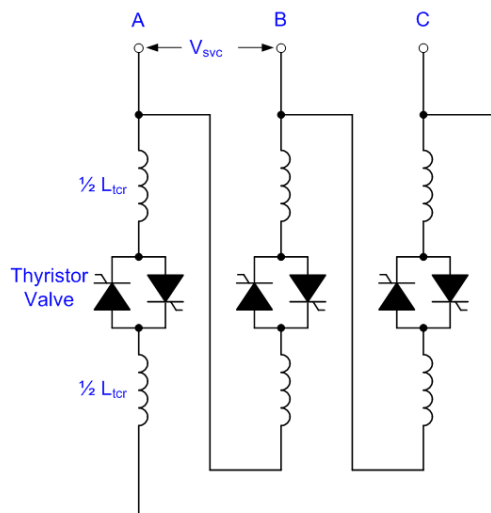


Figure-2: Thyristor Controlled Reactor (TCR)

### C. Combination of TSC and TCR

TSC and TCR are oftenly used in combination to provide more flexibility to compensation of reactive power. Their combination is known as SVC. SVC can be used to provide lagging or leading VARs according to system demand. SVC isn't installed directly on main line, rather its connected through a stepdown transformer. This reduces number of components that are to be used in SVC designing.

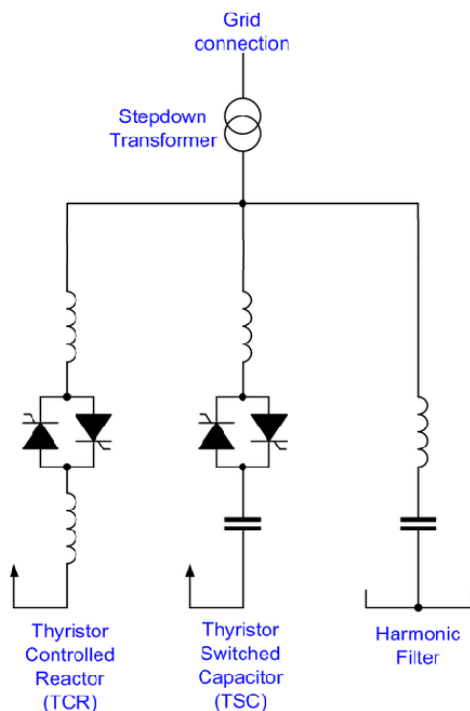


Figure-3: Static VAR Compensator (Combination of TSC & TCR)

### III. DESIGNING OF STATIC VAR COMPENSATOR

Static VAR compensator consists of mainly two components, TSC and TCR. Figure 4 is showing thyristor switched capacitor which is designed in Simulink (MATLAB).

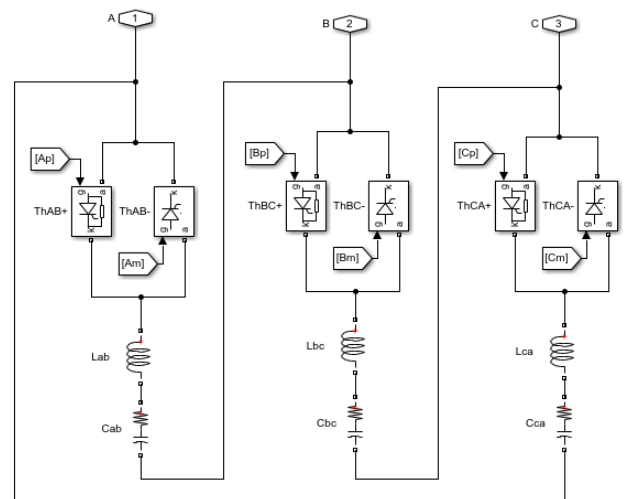


Figure-4: Three Phase Thyristor Switched Capacitor Block (Simulink)

Three branches of TSC are connected in delta fashion. TSC is consisting of capacitor, inductor and thyristor valves. [9] Thyristor valve control the injection of reactive power from TSC to system by means of firing angle. Firing angle is controlled by external circuitry. Firing angle is increase or decreased by control circuit depending on reactive power need. Value of capacitor to be used depends upon system reactive power need. [10] The equation which relates reactive power with capacitance is given by:  $QC = VL-L2 \times 2 \times \pi \times f \times C$  In this model each capacitor has value of 0.2F to provide a reactive power support of 30MVAR (leading). Reactor (Inductor) is used to protect the capacitor from incoming surges of currents. [11] Inductor must have a value of  $LR = (0.67 * C) \times (Vmax/Imax)^2$ . Value of current limiting reactor in this case is set to be 0.3uH. Figure 5 is showing thyristor switched reactor block.

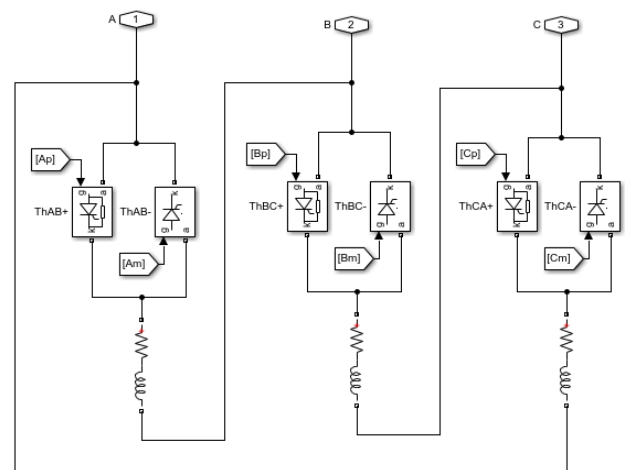


Figure-5: Three Phase Thyristor Controlled Reactor Block (Simulink)

In SVC thyristor controlled reactor (TCR) is used alongside thyristor switched capacitor (TSC). TCR is used to limit the voltage. Also during transient period TCR provides lagging VARs to system whenever needed. Injection of reactive power from TSC and TCR is controlled by switching of thyristor valves with application of gating pulses. These gating pulses control blocking and deblocking of SVC. Control circuit

generates these measurements by instant measurements of system reactive power consumption. Figure 6 is showing control blocks for SVC.

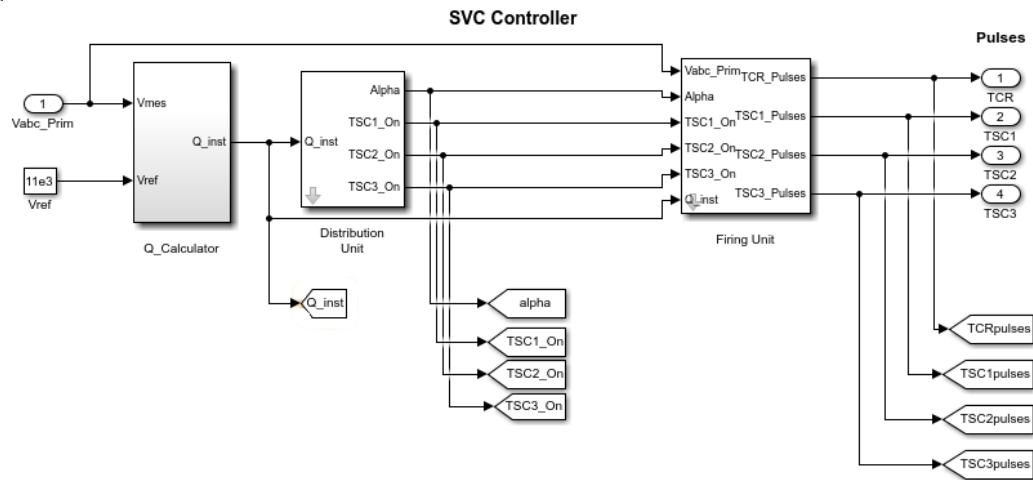


Figure 6: SVC Controller

SVC controller measures  $Q$  of the system. Depending on value of  $Q$ , distribution unit turns on or turns off TSC units. Each TSC unit can provide upto 30MVAR (1d) support. If required reactive power is within range of 30MVAR then only first TSC is switched on. For 31-60 MVAR range both TSC 1 and TSC 2 are switched on. And they both provide equal reactive support. For example, required reactive support is 40 MVAR, then both TSC 1 and TSC 2 will provide 20MVAR each. If required compensation is above 60MVAR then TSC 3 is also switched on. Firing unit generates gating signals for thyristor controlled rectifier and thyristor switched capacitor.

In this simulation gate turn off thyristor was used. Advantage of using gate turn off thyristor is that it can be turned on or turned off at any instant using gate signals. While a simple thyristor can only be turned on using gate signal. It turns off only when the polarity reverses. But in case of gate turn off thyristor it can be brought into conduction state by applying gate signals also it can be switched off by using gate signal of opposite polarity. That's why switching of gate turn off thyristor can be fully controlled by external gating signals. Figure 7 is showing gating signals for thyristor valves.

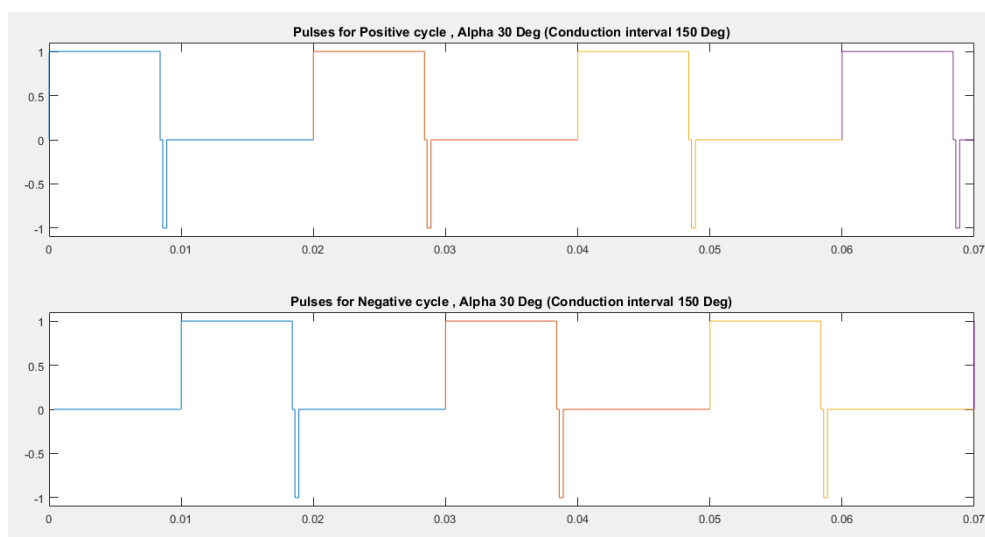


Figure 7: Gating signals for conduction interval of 150 degree

#### IV. SIMULATION & RESULTS

Designed model is simulated for different loading conditions. Voltage and current graphs are plotted for simulated scenarios. For each loading condition system is first simulated without SVC. Power factor of each loading condition is noticed initially. Then system is simulated for same loading condition with SVC. Effect of SVC on power factor improvement is then observed under each loading conditions. It is observed that SVC compensates for consumed reactive power and power factor of system is improved. Following figure is showing results for different loading scenarios.

In above figure column 1 and 2 are specifying the loading conditions. Column 3 is showing power factor of system before compensation by SVC. Column 4 is showing power factor of system after compensation by SVC. In each scenario power factor is greatly improved. Following figures shows voltage and current waveforms for loading condition for 50MW active load and 24MVAR lagging reactive load.

Active Load (MW)	Reactive Load before Simulation (MVAR Lg)	Power Factor before Simulation (Lg)	Power Factor After Simulation (Lg)	Compensated (MVAR)
25	12	0.9	0.94	3
25	15.5	0.85	0.96	8.5
50	24.2	0.9	1	24.2
50	37.5	0.8	0.98	28.8
50	45	0.75	0.96	31.2
100	62	0.85	0.96	34
100	75	0.8	0.94	39.5

Figure 8: Results Table

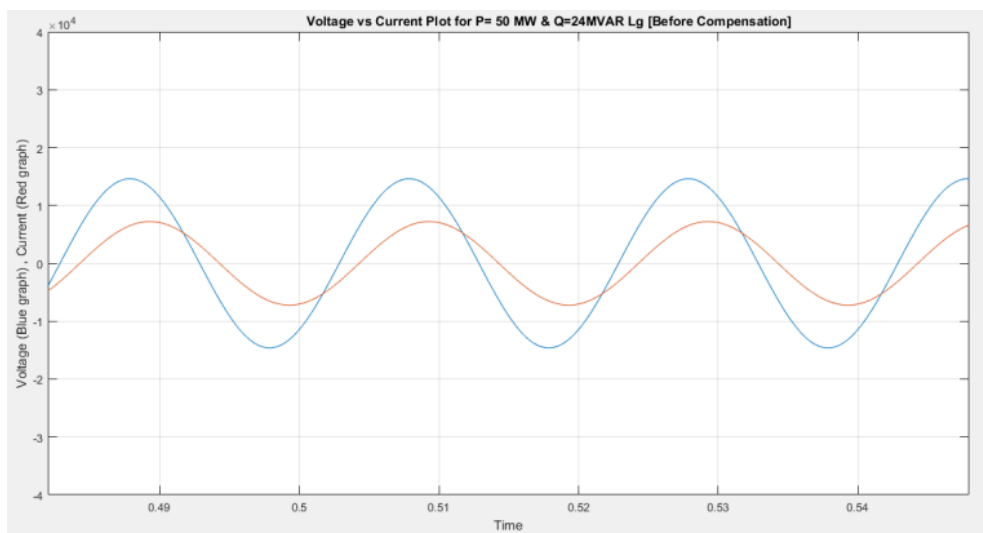


Figure 9: Voltage vs Current Graph (Before Compensation)

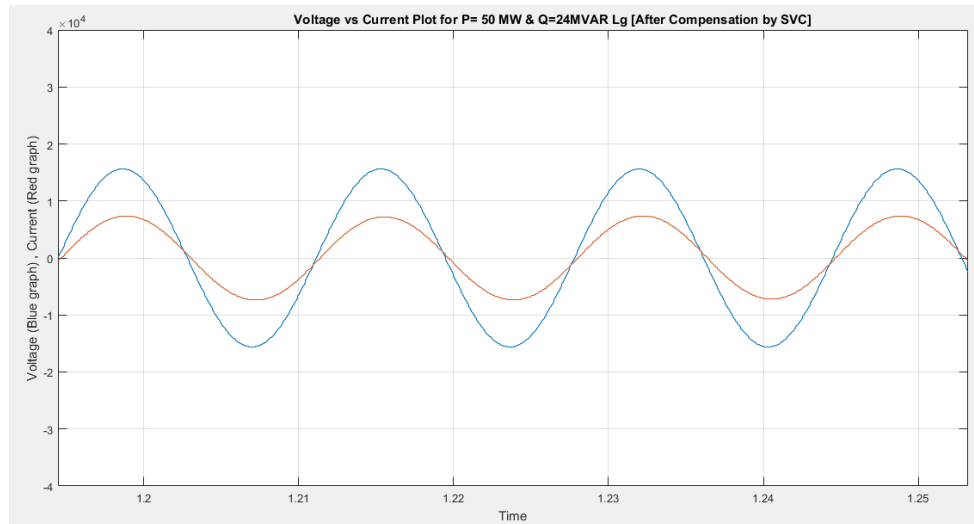


Figure 10: Voltage vs Current Graph (After Compensation)

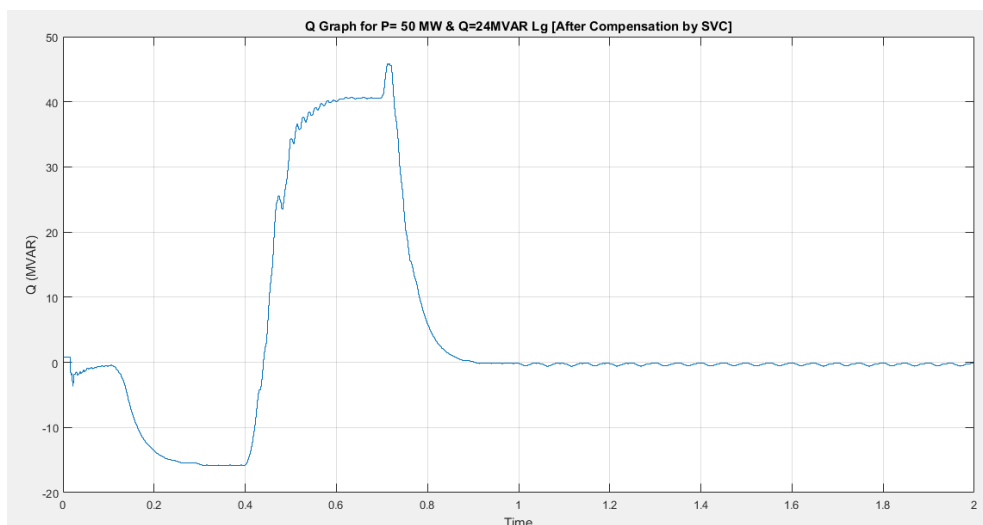


Figure 11: System Q Graph

Results of simulation shows that SVC has compensated for system reactive power within 0.8 secs. After 0.8 sec system response becomes stable, & power factor is improved to unity.

#### CONCLUSION

The work presented in this paper is about use of SVC on weak grid lines for voltage support, compensation of reactive power and improvement of power factor. The model presented in this paper was simulated in MATLAB. From results it can be concluded that with help of phase controlled SVC real time power factor improvement can be done in comparatively short time. Harmonics generated by switching of SVC are nullified if gating signals are provided to SVC at appropriate time. With improvement in power factor, demand of reactive power will

decrease and hence burden from local grid stations will decrease.

#### ACKNOWLEDGMENT

We would like to offer our thanks to Directorate of science and technology (DOST), Khyber Pakhtunkhwa (KPK), Pakistan for providing us funding for this project.

#### REFERENCES

- [1] Schipman, Kurt, and François Delincé. "The importance of good power quality." ABB Power Qual. Prod., Charleroi, Belgium, ABB Review (2010).
- [2] Oo, MarlarThein, and EiEi Cho. "Improvement of power factor for industrial plant with automatic capacitor bank." proceedings of world academy of science, engineering and technology. Vol. 32. 2008.
- [3] Pradhan, P. C., et al. "POWER QUALITY IMPROVEMENT IN A WEAK BUS SYSTEM USING FACTS CONTROLLER."

- [4] Tey, L. H., P. L. So, and Y. C. Chu. "Improvement of power quality using adaptive shunt active filter." IEEE transactions on power delivery 20.2 (2005): 1558-1568.
- [5] Saito, Daisuke, and Shinichi Nomura. "Unity power factor control and harmonic current reduction of thyristor converters using variable series capacitors." Power Electronics and Applications (EPE), 2013 15th European Conference on. IEEE, 2013.
- [6] Das, Sankar, Debashis Chatterjee, and Swapan Kumar Goswami. "SVC Switching Scheme for Load Balancing and Source Power Factor Improvement." IEEE Transactions on Power Delivery 31.5 (2016): 2072-2082.
- [7] Ohtake, Asuka, et al. "Development of 200-Mvar class thyristor switched capacitor supporting fault ride-through." Power Electronics Conference (IPEC-Hiroshima 2014-ECCE-ASIA), 2014 International. IEEE, 2014.
- [8] Reid, W. Edward. "Power quality issues-standards and guidelines." IEEE transactions on industry applications 32.3 (1996): 625-632.
- [9] Zemerick, Scott Alan. Design of a Prototype Personal Static VAR Compensator. Diss. West Virginia University Libraries, 2002.
- [10] Dr BV Sumangala. "Implementation of Thyristor Switched Capacitor for Reactive Power Compensation at Secondary of Distribution Level Feeders for Voltage Stability Improvement." International Journal of Engineering Research & Technology (IJERT) Vol 2 (2013): 322-329.
- [11] Lu, Zhengyu, Daozhuo Jiang, and Zhaolin Wu. "A new topology of fault-current limiter and its parameters optimization." Power Electronics Specialist Conference, 2003. PESC'03. 2003 IEEE 34th Annual. Vol. 1. IEEE, 2003.



**Muhammad Kashif Khan** graduated from University of Engineering and Technology (UET) Peshawar in 2015. He holds B.Sc degree in Electrical Engineering. He is currently enrolled in M.Sc Electrical Energy Systems Engineering at US Pakistan Center for Advanced Studies in Energy (USPCASE) UET Peshawar. His major field of study is Electrical Power Engineering. He worked as trainee engineer with HUAWEI Telecommunication for 3 months. Currently he is working as Lecturer in Department of Electrical Engineering at UET Peshawar.



**Abdul Basit** completed his B.Sc. degree in electrical engineering from University of Engineering & Technology (UET) Peshawar, Pakistan in 2006. He received his M.Sc. degree in electrical power engineering from Chalmers University of Technology, Sweden in 2011 and his PhD from the Department of Wind Energy of the Technical University of Denmark (DTU) in 2015. He is currently working as Assistant professor at U.S. Pakistan Center for Advanced Studies in Energy (USPCAS-E) of the University of Engineering & Technology (UET) Peshawar. His research interests are on protection, power factor improvement, power system operation, renewable power integration and automatic generation control.



**Faheem Ali** completed his B.Sc Electrical Engineering from University of Engineering & Technology (UET) Peshawar, in 2012. He Completed his M.Sc Electrical Power Engineering in 2014. Currently he is pursuing his PhD in field of electrical power engineering. Also he is currently working as Lecturer in department of Electrical Engineering University of Engineering & Technology (UET) Peshawar.



# Grid Integration of Multistring Photovoltaic Plants with Modular Multilevel Converter

Ahmad Kamal, Dr. Abdul Basit

**Abstract**—This paper presents the application of Modular Multilevel Converter (MMC) for connecting multistring photovoltaic generation plant. The proposed approach makes it possible for an increased PV plant capacity to be integrated with the grid, while also improving efficiency of conversion and power quality. To increase the efficiency of individual PV module, a DC-DC boost converter is employed with maximum power point tracking (MPPT). The MPPT is implemented by employing Perturb & Observe (P&O) algorithm. The PV modules with DC-DC boost converters are connected in parallel to form a DC bus which is connected to the utility grid with MMC. The MMC inverts the DC bus voltage for interfacing to the grid while maintaining the DC bus voltage constant. The simulation of the overall system in Simulink/MATLAB verifies the validity of the proposed system.

**Keywords**— Renewable integration, Modular Multilevel Converter, maximum power point tracking, MPPT, photovoltaic system

## I. INTRODUCTION

The continuously growing demand for energy and depletion of fossil fuels has increased the need for efficient integration of renewable resources in the current grid [1]. Solar PV energy has seen a tremendous increase over the past few years. The steady reduction in manufacturing cost of PV modules is the contributing factor towards this growth. This growth is evident from the fact that in 2013 alone, 30 GW of new PV capacity was installed. It is encouraging that the PV integration has increased to more than 100 GW since 2012 [2].

There are basically two main topologies to connect large scale PV systems to the grid: the multistring configuration and the centralized configuration [3, 4]. In the centralized configuration several PV strings are connected in parallel to dc bus. A voltage source converter is used to invert the DC voltage to the grid while also implementing MPPT for all the connected PV strings. The multistring configuration has a similar structure with the centralized configuration with the exception that the PV strings are connected to the DC bus with individual DC-DC boost converters.

The individual DC-DC boost converter perform MPPT for

each PV string exclusively and thus can produce more power than the centralized configuration. The voltage source converter in the centralized configuration also has to tackle the issues of partial shading and panel mismatch increasing its complexity. Owing to these facts the multistring configuration is preferred over the centralized configuration even with the increased initial cost of the DC-DC boost converters.

The increase in PV farms of MW capacity require a significant increase in the power handling capability of the grid tied converter. The traditional voltage source converters with two level topology is incapable of efficiently handling this higher power flow. Also the grid codes applied on such PV farms continue to demand efficient integration [5]. The multilevel converters offer several benefits over the traditional two-level topology such as higher power and voltage ratings, lower switching frequency and total harmonic distortion (THD) [6]. Due to these advantages, multilevel converters are gaining popularity in many applications such as motor drives, traction and even in renewable integration [7].

Most of the literature on using multilevel converters for grid interface of PV farms proposes the use of neutral point clamped (NPC) and cascaded H bridge (CHB) based multilevel converters. The studies of [8] and [9] propose a three level neutral point clamped (3L-NPC) multilevel converter with two PV strings. The PV strings are connected without a DC-DC converter with the two DC-link capacitors, enabling MPPT capability for each string. However, the lack of DC-DC boost converter requires several panels to be connected in series for raising the string voltage to be NPC compatible. This series connection of panels introduces the problems of efficient MPPT implementation, partial shading and panel mismatch. Additionally, as the DC-link capacitors have to operate at different MPPT voltages this can cause dc-link unbalance and thus introducing distortions at the grid side. This imbalance of DC-link may also have negative impacts on AC side control of the converter.

The studies of [10] and [11] propose Cascaded H-bridge (CHB) multilevel converters for this application. The CHB topology is implemented on a single phase system, due to the intrinsic power unbalance of each phase. This is not allowed by the grid codes due to the injection of unbalance currents into the grid. Additionally, this topology also has the disadvantages associated with the NPC multilevel converters discussed above.

This paper presents multistring PV system with three phase modular multilevel converter (MMC). Each PV string is

Ahmad Kamal: Department of Electrical Energy Systems Engineering US-PCAS-E, UET Peshawar, Paksitan. (e-mail: engr.ahmad.kamal@live.com)

Dr. Abdul Basit: Department of Electrical Energy Systems Engineering US-PCAS-E, UET Peshawar, Paksitan. (e-mail: abdul.basit@uetpeshawar.edu)



connected to a common DC bus with individual DC-DC boost converters with MPPT capability. The remainder of the paper is divided into four sections. Section II depicts the overall system structure and describes all the three stages that the overall system is divided into. Section III explains the overall control system which is further subdivided into 4 subsections that is: boost stage control, MMC output current control, MMC circulating current control and MMC submodule voltage balance control. The system parameters, simulation and the results are presented in section IV. Finally, the conclusion of the study is presented in section V.

## II. OVERALL SYSTEM DESCRIPTION

The detailed circuit of the proposed overall system is illustrated in Figure 1. The system has basically three major stages: PV string stage, DC-DC boost converter stage and the grid-tied three phase modular multilevel converter (MMC). It should be noted that only a single phase of the MMC converter is displayed in this illustration. The PV strings are formed by connecting several PV modules in series to raise the voltage level to the desired level. For connecting the PV string to DC bus any topology of the DC-DC boost converter can be used according to specific requirements. In this study, the typical boost converter topology is used due to simplicity and ease of simulation.

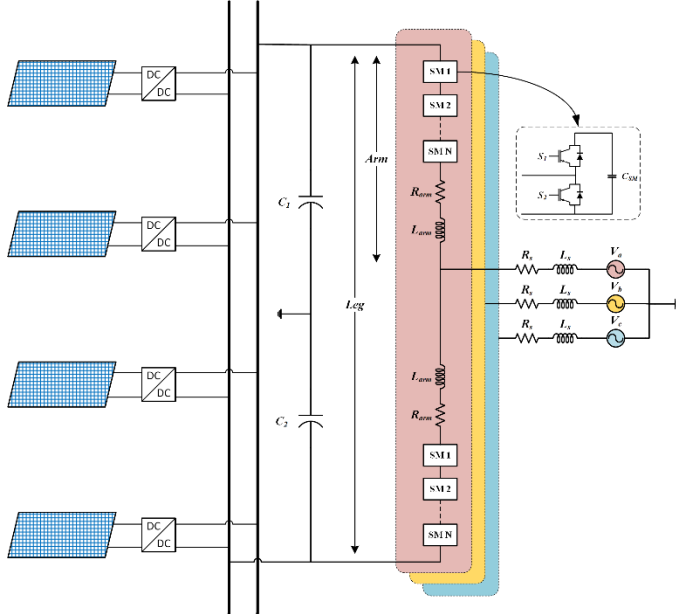


Figure 1. Proposed system configuration

Modular multilevel converter is a relatively newer topology of multilevel converters for medium to high voltage applications. Modular multilevel converter has many advantages compared with the traditional multilevel converters such as: minimizing the total harmonic distortion (THD) on output voltage, operating with lower switching frequency, low dv/dt thus lower stresses on power switches and operating with any voltage level.

The basic building block of the MMC is a submodule. It is essentially a half bridge inverter with capacitor as shown in

Figure 1. The half bridge can be constituted with any power switch such as IGBT, IGCT or MOSFET with antiparallel diode, according to specific requirements. The two switches of the submodule operate in a complimentary fashion. When switch  $S_2$  of the submodule is turned-on the submodule capacitor voltage becomes the output voltage of the submodule. When  $S_1$  is turned-on the submodule is essentially turned-off, or in the case of MMC referred to as being bypassed. When N number of submodules are connected in series it forms an 'arm' of the MMC as shown in Figure 1. Two arms combine together to form the individual phase, called the 'leg' of the MMC.

The number of output voltage levels generated by the MMC can be with either  $N+1$  or  $2N+1$  depending on the modulation strategy used. The three main modulation strategies used for MMC are the pulse width modulation (PWM), space vector modulation and the nearest level modulation. The modulation strategy used in this study is the carrier phase shifted PWM.

The benefit of using the modular multilevel converter is the modularity of the system which means that the system can be scaled from small KW level to large MW level PV systems.

## III. CONTROL SYSTEM

Decoupling MPPT control from the grid converter makes it possible to design and implement control for DC-DC boost converter and MMC independently.

### A. DC-DC Boost Converter Control

The main control objective of the DC-DC boost converter is to implement the MPPT algorithm for the PV string while stepping up the string voltage.

The controllable variable of the DC-DC boost converter is the inductor current. This inductor current can control either the input voltage or the output voltage of the DC-DC boost converter. As the output voltage of the converter, that is the DC bus voltage, is controlled by the grid-tied MMC so the boost converter controls the input voltage. The input voltage of the DC-DC boost converter in continuous conduction mode is given by the following equation.

$$V_{in} = V_{out} (1 - D) \quad (1)$$

As  $V_{out}$  is controlled by the MMC, changing the duty cycle  $D$  of the converter changes the input voltage  $V_{in}$ , which is essentially the PV string voltage. Figure 2 shows the control structure of the DC-DC boost converter.

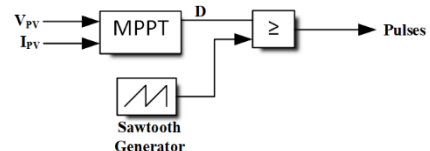


Figure 2. Boost converter control with MPPT

The MPPT algorithm used in this study is the well-known Perturb and Observe (P&O) algorithm. The output of the control structure 'Pulses' are the pulses that drive the power switch of the boost converter. The flowchart for the Perturb and Observe (P&O) MPPT algorithm is depicted in Figure 3.

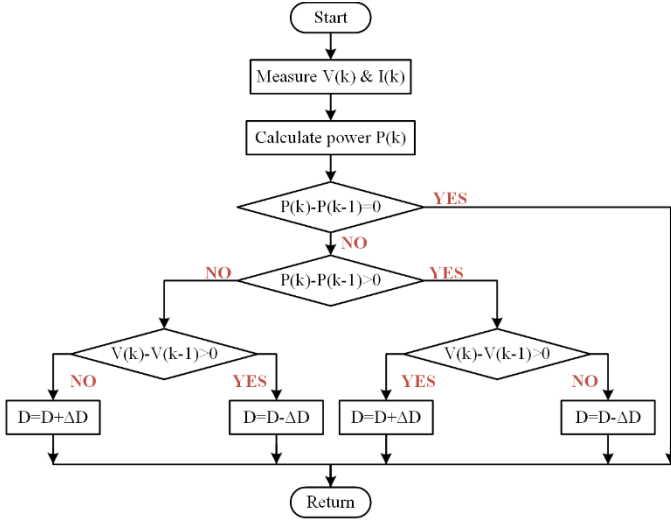


Figure 3. Perturb and Observe (P&O) MPPT flowchart

### B. MMC Output Current Control

The control scheme for output current control of MMC is similar to that of two level converters control in dq rotating reference frame [12]. The control system is divided into two control loops: inner control loop and outer control loop. The outer control loop controls the DC bus voltage by generating reference signal for d-axis current. The relationship between DC bus voltage  $V_{dc}$  and d-axis current  $i_d$  can be derived from AC side and DC side power balance of MMC, given as:

$$P = \frac{3}{2} V_d i_d = V_{dc} i_{dc} \quad (2)$$

$$i_{dc} = C \frac{dV_{dc}}{dt} \quad (3)$$

Transferring to s domain and combining (2) and (3) the system transfer function is given as:

$$\frac{V_{dc}(s)}{i_d(s)} = \frac{3V_d}{2V_{dc,ref}} \cdot \frac{1}{sC} \quad (4)$$

The above system transfer function is used to derive the control system for DC voltage control, shown in Figure 4.

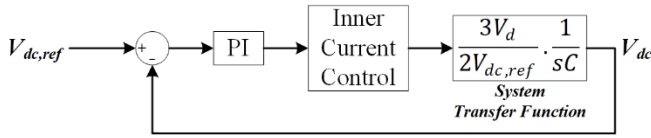


Figure 4. DC voltage control loop

The inner control structure can be deduced from the dynamic equations of the MMC, given as:

$$L_s \frac{di_j}{dt} = -R_s i_g + V_g - V_t \quad (5)$$

The above dynamic equation in the dq-frame is given as:

$$L_s \frac{di_d}{dt} = -R_s i_d + V_{gd} - V_{td} + \omega L i_q \quad (6a)$$

$$L_s \frac{di_q}{dt} = -R_s i_q + V_{gq} - V_{td} - \omega L i_d \quad (6b)$$

In the above equations,  $V_{td}$ ,  $V_{tq}$ ,  $i_d$ ,  $i_q$ ,  $V_{gd}$ ,  $V_{gq}$ ,  $\omega L i_d$ ,  $\omega L i_q$  are d and q axis components of MMC output voltage,

output current, grid voltage and coupling terms respectively. Based on the above equations, the architecture of the inner current control loop is derived as in Figure 5.

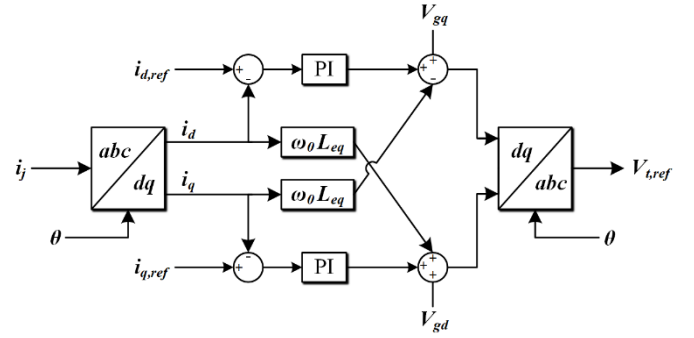


Figure 5. Inner current control loop

### C. MMC Circulating Current Control

The floating nature of the submodule capacitors results in a circulating current that flows from the DC bus to the MMC and between different phases of MMC. The harmonic components of the circulating current does not contribute in power transfer but increases power losses and current rating of electrical components. Therefore, the major component of the harmonic components, the second harmonic component, is controlled to zero. This circulating current can be represented by the following equation:

$$i_{cc,j} = \frac{i_{uj} + i_{lj}}{2} - \frac{I_{dc}}{3} \quad (7)$$

Substituting the above equation in dq-frame in the dynamic equations of the MMC gives the following relationship:

$$V_{cc,d} = R_{arm} i_{cc,d} + L_{arm} \frac{di_{cc,d}}{dt} + 2L_{arm} \omega i_{cc,q} \quad (8a)$$

$$V_{cc,q} = R_{arm} i_{cc,q} + L_{arm} \frac{di_{cc,q}}{dt} - 2L_{arm} \omega i_{cc,d} \quad (8b)$$

Considering the above equations, it is evident that the circulating current can be controlled directly by  $V_{cc,d}$  and  $V_{cc,q}$  as shown in Figure 6. The output of this circulating current controller will be subtracted from both lower and upper arm voltage references generated by inner current loop.

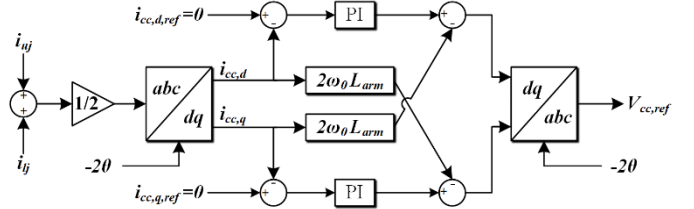


Figure 6. Circulating current control loop

### D. MMC Submodule Voltage Balancing Control

The floating nature of the submodule capacitors has the adverse impact that the capacitor voltages diverge with time. This divergence if not kept small or preferably negligible can collapse the entire system. Therefore, to keep the submodule voltages equal an active balancing algorithm is required.

The most widely used method for this purpose is the sorting method [13]. Generally, the number of submodules to be inserted in each arm is known after modulation. The decision

of which submodules to insert or bypass, to balance the submodule voltages, is taken by the sorting algorithm. The algorithm first measures and sorts all the submodules capacitor voltages. Submodules with the lowest voltages are inserted to be charged if the arm current is positive. Whereas, submodules with the highest voltages are inserted to be discharged if the arm current is negative. However, bypassing the submodule keeps its voltage unchanged.

#### IV. SIMULATION & RESUTLS

The whole system with the control schemes was simulated in Simulink/MATLAB. Since the simulation used detail models of all the converters, and the system was simulated with different temperature and irradiation levels, only four PV string with individual boost converters were used. The panels used in the simulation were SunPower SPR-315E-WHT-D rated at 315W, with output current of 5.76A and 54.7V output voltage at MPP at STC (radiation of  $1000\text{W/m}^2$  and panel temperature of  $25^\circ\text{C}$ ). A single PV array is built with 64 modules in series per string and 5 strings in parallel. The DC-DC boost converter stage steps up the voltage of the PV array to 500V of the DC bus voltage. As the DC bus voltage is 500V the number of submodules per arm are selected to be 6. This is considering the voltage rating of the submodule is to be kept at 100V, which makes it possible to use a wide variety of power switches. The system parameters used for the simulation are summarized in Table 1.

TABLE I  
OVERALL SYSTEM PARAMETERS

Symbol	Quantity	Value
$V_g$	Grid voltage	11KV
$f$	Grid frequency	60Hz
$L_g$	Grid inductance	45 $\mu\text{F}$
$R_g$	Grid resistance	1m $\Omega$
$L_{arm}$	MMC arm inductance	60 $\mu\text{H}$
$R_{arm}$	MMC arm resistance	1m $\Omega$
$C_{SM}$	MMC submodule capacitance	96mF
$V_{dc}$	DC-link voltage	500V
$C_1, C_2$	DC-link voltage capacitance	1mF
$L_b$	Boost converter inductance	5mH
$V_{mp}$	PV array voltage at maximum power	274.5V
$I_{mp}$	PV array current at maximum power	367.2A
$T_s$	Sampling Time	50 $\mu\text{s}$

The MPPT performance is evaluated with different levels of irradiance and ambient temperature as shown in Figure 7. The resulting varying duty ratio, array voltage and power is depicted in the same figure. To validate the performance of the DC bus voltage control of the MMC, the irradiance level of all the converters connected with the DC bus are varied as shown in Figure 8. It can be seen that the varying irradiance level changes the combined power output of all the PV modules but the DC bus voltage stays relatively unchanged.

The performance of the circulating current suppression control of the MMC can be evaluated from Figure 9, which shows the circulating current, upper arm current and submodule capacitor voltages of phase A. The circulating current suppression control is enabled at  $T=0.2\text{s}$ , resulting in a

significant decrease in the circulating current, arm current and submodule capacitor peak-peak voltage.

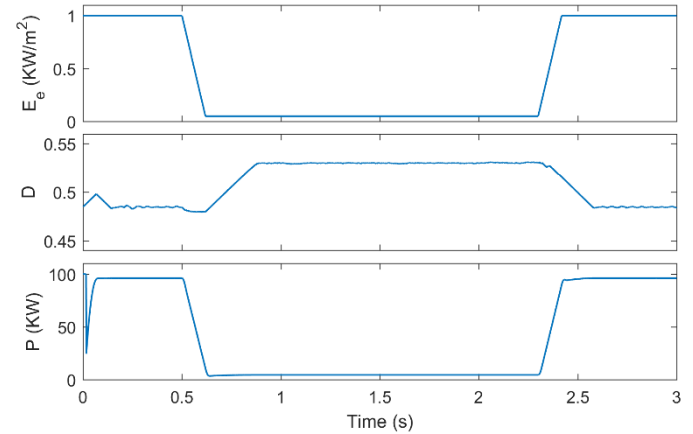


Figure 7. PV array 1 irradiance, duty cycle and power

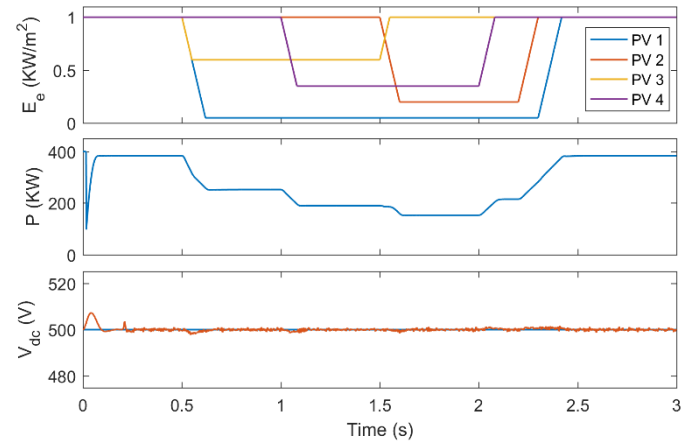


Figure 8. PV farm output power and dc bus voltage with varying irradiance

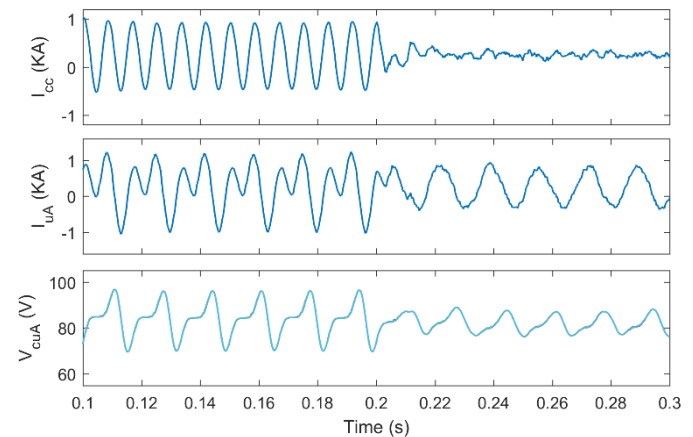


Figure 9. Performance of circulating current control

The effectiveness of the voltage balancing algorithm can be validated from Figure 10, which compares the submodule capacitor voltages of phase A upper arm with and without voltage balancing algorithm.

Finally, the steady state three phase output voltages and currents of the MMC are displayed in Figure 11. The steady

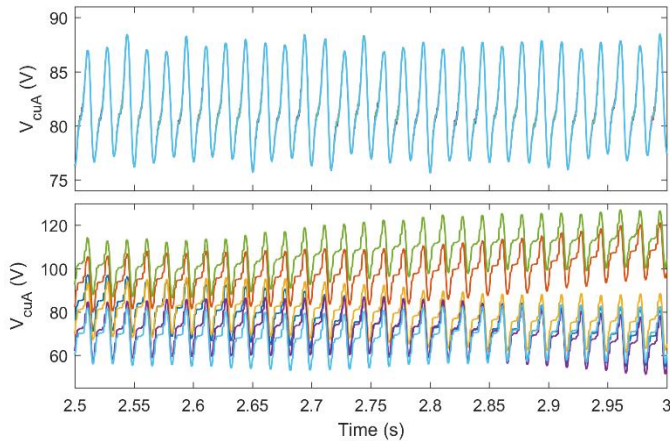


Figure 10. Performance of voltage balancing algorithm

state output shows a satisfactory performance with a 4.5% total harmonic distortion of currents.

## V. CONCLUSION

The proposed multistring photovoltaic DC bus energy conversion system with modular multilevel converter is capable of interfacing a large MW scale PV farm with the grid. Individual DC-DC boost converters for PV arrays increase system efficiency by better implementation of MPPT algorithm. The use of modular multilevel converter improves power quality, overall efficiency and reduces switching frequency compared to the traditional 2L-VSC. The modular multilevel converter also makes it possible to easily scale the system to any power level.

## REFERENCES

- [1] A. M. T. O. A. S. A. P. W. a. M. A. G. Shafiullah, "Meeting energy demand and global warming by integrating renewable energy into the grid," in *2012 22nd Australasian Universities Power Engineering Conference (AUPEC)*, Bali, 2012.
- [2] European Photovoltaic Industry Association, "Global market outlook for photovoltaics 2013–2017," 2013.
- [3] J. K. P. a. F. B. S. B. Kjaer, "A review of single-phase grid-connected inverters for photovoltaic modules," *IEEE Transactions on Industry Applications*, vol. 41, no. 5, pp. 1292–1306, Oct. 2005.
- [4] M. M. a. G. Cramer, "Multi-String-Converter: The next step in Evolution of String-Converter Technology," in *9th European Conference on Power Electronics and Applications*, Graz, Austria, Aug. 2001.
- [5] E. B.-M. M. A.-P. O. G.-B. Ana Cabrera-Tobar, "Review of advanced grid requirements for the integration of large scale photovoltaic power plants in the transmission system," *Renewable and Sustainable Energy Reviews*, vol. 62, pp. 971–987, Sep. 2016.
- [6] J.-S. L. a. F. Z. P. J. Rodriguez, "Multilevel inverters: a survey of topologies, controls, and applications," *IEEE Transactions on Industrial Electronics*, vol. 49, no. 4, pp. 724–738, Aug. 2002.
- [7] M. C. a. V. G. Agelidis, "Multilevel converters for single-phase grid connected photovoltaic systems-an overview," in *Industrial Electronics, 1998. Proceedings. ISIE '98. IEEE International Symposium*, Jul. 1998.
- [8] M. L. R. T. C. K. a. M. S. T. Kerekes, "Evaluation of Three-phase Transformerless Photovoltaic Inverter Topologies," *IEEE Trans. Power Electronics*, vol. 24, no. 9, pp. 2202–2211, Sep. 2009.

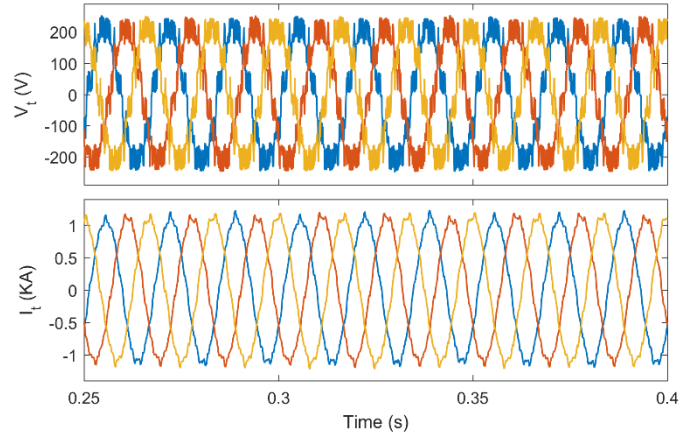


Figure 11. Steady-state output voltage and current of MMC

- [9] S. O. a. L. M. T. E. Ozdemir, "Fundamental-frequency-modulated Six-level Diode-clamped Multilevel Inverter for Three-phase Stand-alone Photovoltaic System," *IEEE Trans. Industrial Electronics*, vol. 56, no. 11, pp. 4407–4415, Nov. 2009.
- [10] P. C. J. R. a. M. P. E. Villanueva, "Control of a Single-phase Cascaded H-bridge Multilevel Inverter for Grid-connected Photovoltaic Systems," *IEEE Trans. Industrial Electronics*, vol. 56, no. 11, pp. 4399–4406, Nov. 2009.
- [11] A. M. E. V. P. C. B. W. a. J. R. S. Kouro, "Control of a cascaded h-bridge multilevel converter for grid connection of photovoltaic systems," in *35th Annual Conference of the IEEE Industrial Electronics Society (IECON09)*, Porto, Portugal, Nov. 2009.
- [12] S. B. J. R. S. K. a. R. L. M. A. Perez, "Circuit Topologies, Modeling, Control Schemes, and Applications of Modular Multilevel Converters," *IEEE Transactions on Power Electronics*, vol. 30, no. 1, pp. 4–17, Jan. 2015.
- [13] J. Q. B. B. M. S. a. P. B. S. Deb Nath, "Operation, Control, and Applications of the Modular Multilevel Converter: A Review," *IEEE Transactions on Power Electronics*, vol. 30, no. 1, pp. 37–53, Jan. 2015.





# Research in Sensorless Vector Control of Induction Motor based on MRAS Technique

Kader Ali Ibrahim, Shen Yan-Xia, Hoch Omar Hoche

**Abstract**—Model Reference Adaptive System (MRAS) represents one of the most attractive and popular solutions for sensorless control of AC drive. According to the principle of asynchronous motor vector control, taking two phase rotating coordinates current model as the adjustable model and improved voltage model as reference model, a speed sensorless vector control system is built. The model reference adaptive system (MRAS) method is used to identify system speed. Model reference adaptive system method is applied to asynchronous motor speed estimation and achieves speed sensorless control of asynchronous motor. The approach is implemented on Matlab /Simulink software. The simulation results show that the system has good control performance and accuracy. It proves the feasibility and practicability of the system.

**Keywords**—motor; speed sensorless, model reference adaptive system, SVPWM, vector control

## I. INTRODUCTION

This With the continuous improvement of power electronics technology and control theory, pay flow motor speed control system increasingly towards high performance. Ac asynchronous power machine speed sensorless speed control system to speed identification algorithm instead of sensing the speed of the detection device, to avoid speed sensor detection errors caused poor and sensor installation and maintenance of the difficulties, and has the price the advantages of the project has an important application of significance, is a modern communication important research direction. In induction motor speed sensorless control technology, the motor turns speed identification method after

another, such as: extended kalman filter [1-4] neural network [5-8], pi adaptive method[9-11] and so on. The model reference is self-adaptive the theory of MRAS (model reference adaptive system)[12-14] is in recent years, speed sensorless induction motor vector control more good application of speed identification technology, which is characterized by guaranteed parameter estimation the gradual stability of the same time, changes in motor parameters and external disturbances has strong robustness. With the microcontroller, digital signal processor such as the continuous improvement of microprocessor performance, MRAS speed identification technology in the field of speed sensorless ac speed has a very good application prospect.

In this paper, the speed sensorless motor control, the introduction of model parameters Self-adaptive speed identification theory, through the rotor speed estimation the system can accurately identify the actual speed, the experimental results verify the propose a strategy of feasibility and effectiveness.

## A. Vector Control System

### a. Control System Program

The system measures the current  $i_A$ ,  $i_B$  from the stator side of the motor And voltage  $u_A$ ,  $u_B$ , Converted to  $is_\alpha$ ,  $is_\beta$  by Clarke And  $us_\alpha$ ,  $us_\beta$ , Into the rotor flux The observer model calculates rotor flux linkage angle and flux linkage values. The actual rotation of the motor The speed  $n$  is obtained by MRAS model estimation, according to the speed command value  $n_{ref}$  And the difference between the feedback value  $n$ , the speed regulator output corresponding electromagnetic torque The current value of the component is  $T_{ref}$ , And then with the system given excitation current component  $i_{mref}$   $U_s T_{ref}$  through the current regulator together And  $us_{mref}$ , through Park inverse transform voltage  $us_\alpha$   $ref$  This scheme can make the torque and flux completely decoupled, very good To estimate the motor speed, speed, current closed-loop control.

Kader Ali Ibrahim: Engineering Research Center of Internet of Things Technology Applications Ministry of Education, Wuxi 214122, China.

Shen Yan-Xia: Engineering Research Center of Internet of Things Technology Applications Ministry of Education, Wuxi 214122, China.

Hoch Omar Hoche: Engineering Research Center of Internet of Things Technology Applications Ministry of Education, Wuxi 214122, China.

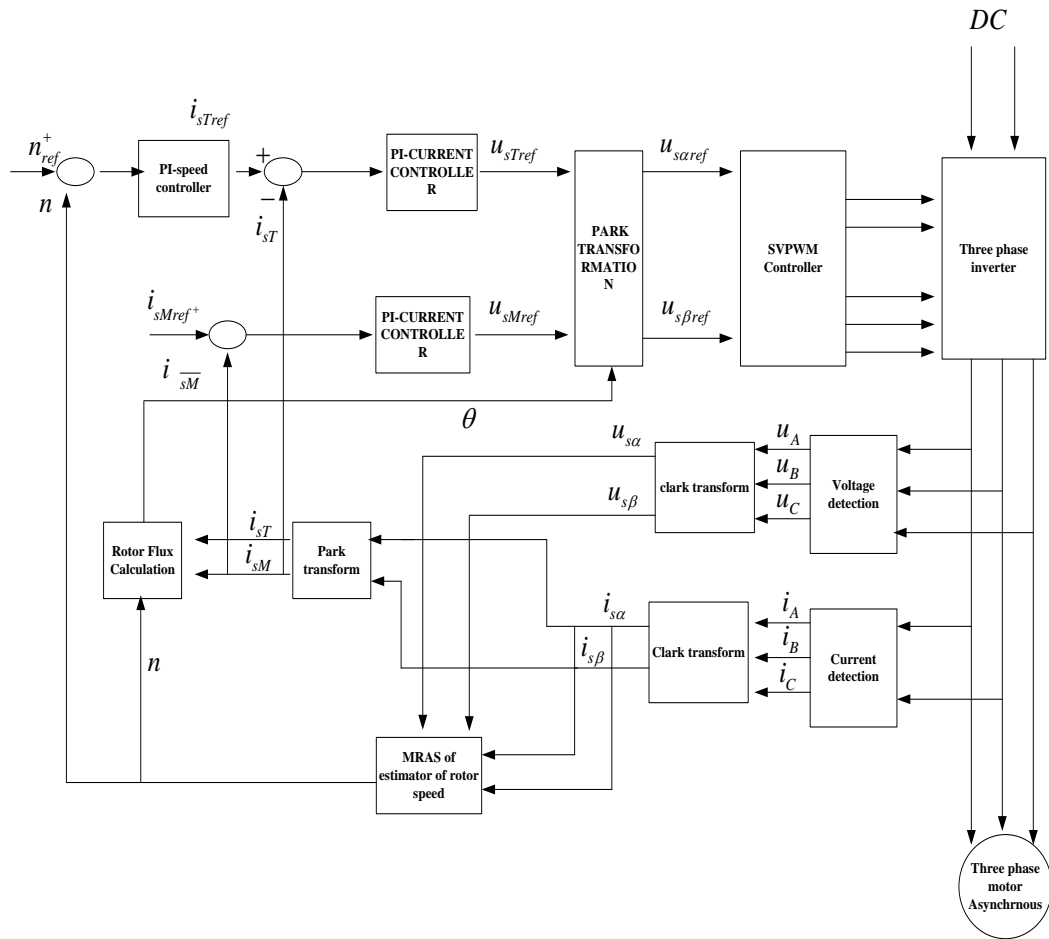


Figure 1. Speed sensorless vector control system block diagram

#### b. Rotor flux Observer

In the sensor less vector control [15], rotor flux linkage observation Sub-important. Using the voltage model as a reference model, the current model can be adjusted Model of the program to calculate the flux linkage.

##### Fluc Linkage Model:

Stator current by 3s / 2r transform excitation componentism And the torque component  $i_{st}$ , the motor vector control equation is

$$T_e = n_p \frac{L_m}{L_r} i_{st} \psi_r \quad (1)$$

$$\omega_s = \frac{L_m i_{st}}{T_r \psi_r} \quad (2)$$

$$\psi_r = \frac{L_m}{T_r p + 1} i_{sm} \quad (3)$$

Where,  $T_e$  For torque;  $L_m$  For mutual inductance;  $L_r$  For the rotor inductance;  $\psi_r$  For the rotor Flux;  $i_{st}$  is the torque current component;  $T_r$  For the time constant. According to formula (1) ~ (3) can calculate the motor slip frequency  $\omega_s$ , the stator current frequency  $\omega_1$  ( $\omega_1 = \omega_s + \omega_r$ ) and  $\psi_r$  [4]. The two-phase rotating coordinate system rotor flux linkage model can be adjusted Model to stator current and speed  $\omega_r$  As an input to calculate the rotor flux, the mathematical model as shown in (4), (5) below.

$$\psi_\alpha = \frac{L_m}{T_r} i_\alpha - \frac{\psi_\alpha}{T_r} - \omega_r \psi_\beta \quad (4)$$

$$\psi_\beta = \frac{L_m}{T_r} i_\beta - \frac{\psi_\beta}{T_r} - \omega_r \psi_\alpha \quad (5)$$

Compared with two-phase stationary coordinate flux model, two-phase rotation coordinate Flux model more suitable for computer real-time computing, easy convergence, more accurate Indeed However, Eqs. (4) and (5) also show that the



current and speed are used as input. The current model relies heavily on the rotor  $T_r$ . If  $T_r$  deviates, it will directly lead to the magnetic field not being allowed to cause rotation between the axis of the system. Strong coupling, so the current model cannot be used alone without speed sensing. Vector control, the need to use together with the voltage model [5].

### B. Fundamentals

Asynchronous motor vector control theory, is to produce the same spin. The stator current  $i_A, i_B, i_C$  in the three-phase coordinate system are the criterion. By 3s / 2s transformation, can be equivalent to two-phase static coordinate system under the electricity flow  $i_\alpha, i_\beta$ . And then through the synchronous rotation transformation, the motor stator current

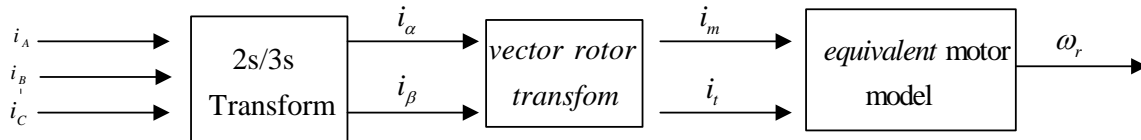


Figure 2. Vector control schematic

### c. Mathematical model of asynchronous motor

From the asynchronous motor in the three-phase coordinate system can be seen in the mathematical model. The motor is multivariable, non-linear, strongly coupled system. To obtain the speed-regulating performance similar to that of DC motor, vector control must be carried out. Mathematics of Asynchronous motor in two-phase synchronous d-q coordinate system model.

Voltage Equation:

Stator Voltage Equation

$$\left. \begin{aligned} u_{ds} &= R_s i_{ds} + \frac{d\varphi_{ds}}{dt} - \varphi_{qs} \frac{d\theta_s}{dt} \\ u_{qs} &= R_s i_{qs} + \frac{d\varphi_{qs}}{dt} + \varphi_{ds} \frac{d\theta_s}{dt} \end{aligned} \right\} \quad (6)$$

Rotor Voltage Equation

$$\left. \begin{aligned} u_{dr} &= R_r i_{dr} + \frac{d\varphi_{dr}}{dt} - \varphi_{qr} \frac{d\theta_r}{dt} \\ u_{qr} &= R_r i_{qr} + \frac{d\varphi_{qr}}{dt} + \varphi_{dr} \frac{d\theta_r}{dt} \end{aligned} \right\} \quad (7)$$

Flux linkage equation:

Stator flux equation

$$\left. \begin{aligned} \varphi_{ds} &= L_s i_{ds} + L_m i_{dr} \\ \varphi_{qs} &= L_s i_{qs} + L_m i_{qr} \end{aligned} \right\} \quad (8)$$

Rotor flux equation

$$\left. \begin{aligned} \varphi_{dr} &= L_r i_{dr} + L_m i_{ds} \\ \varphi_{qr} &= L_r i_{qr} + L_m i_{qs} \end{aligned} \right\} \quad (9)$$

Torque equation

$$T = \rho L_m (i_{qs} i_{ds} - i_{qr} i_{dr}) \quad (10)$$

In the above formula,  $u_{ds}, u_{qs}, u_{dr}, u_{qr}$  Respectively, set, the rotor voltage d - q axis component;  $i_{ds}, i_{qs}, i_{dr}, i_{qr}$  Respectively, the rotor current d - q axis Component;  $\varphi_{qs}, \varphi_{dr}, \varphi_{qr}$  Respectively, fixed, rotor flux d - q axis points Quantity;  $L_r$  For the d - q coordinate system, the rotor is equivalent to the two - phase winding Feeling; For the d - q coordinate system between the stator and the rotor coaxial equivalent winding Mutation;  $p$  is the differential operator;  $\theta$  is the rotor a axis and  $\alpha - \beta$  coordinate system  $\alpha$  The angle between the axes;  $\omega_r$  For the rotor angular velocity,  $\omega_r = d\theta / dt$ ;  $\theta_s$  For the d axis with Two - phase stationary  $\alpha - \beta$  coordinate system  $\alpha$  axis between the angle;  $\omega_s$  Rotate for the stator Magnetic field synchronous angular velocity,  $\omega_s = d\theta_s / dt$ ;  $\theta_r$  For the d axis and the rotor a axis

The angle of  $\theta_r = \theta_s - \theta$ .

## II. MODEL REFERENCE ADAPTIVE SYSTEM DESIGN

The model reference adaptive speed[16,17] is calculated using the rotor flux. The pressure equation and the current equation are respectively calculated for the rotor flux due to the voltage model Does not contain the speed signal, while the

current model contains the speed signal, so the voltage model As the output of the rotor flux, the current model of the output as The calculated value of the rotor flux, to calculate the motor speed. Model Reference adaptive principle shown in Figure 2, Figure 3 shows.

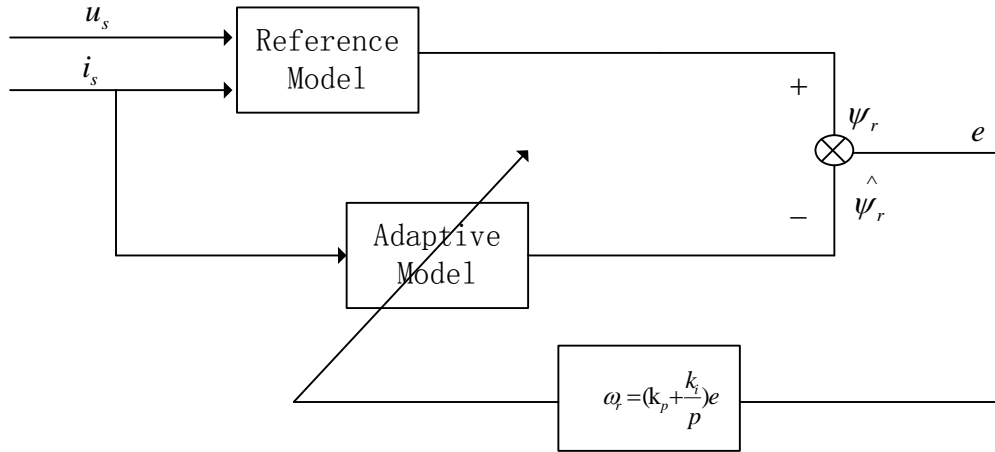


Figure 3. Model reference adaptive angular velocity identification algorithm

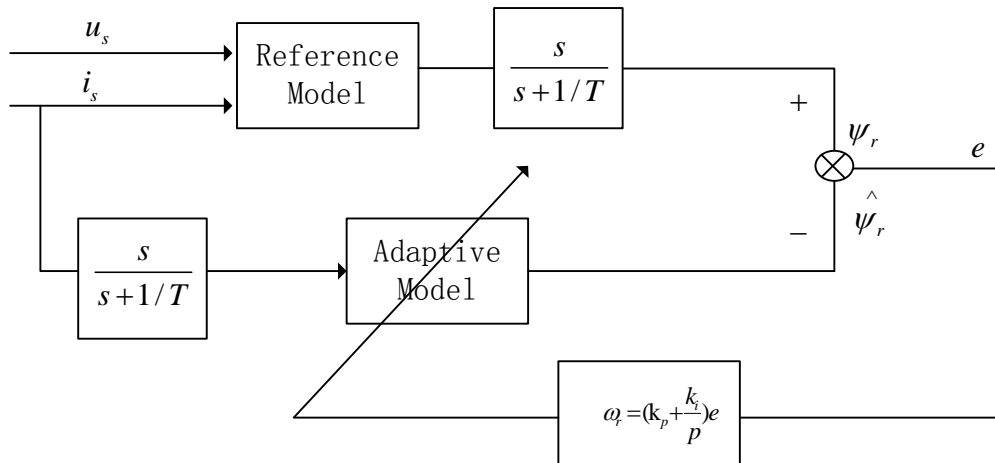


Figure 4. MRAS angular velocity identification algorithm with filter link

As the MRAS shown in Figure 2 is prone to error accumulation and DC Offset problem, so the traditional MRAS to improve, as shown in Figure 3. After the improved algorithm, to a certain extent, can improve the pure integral band To the impact of the choice of adaptive law can make the system gradually stable

## III. SIMULATION SYSTEM

### A. Simulation Model

This paper is based on Matlab/ simulink for Asynchronous motor MRAS the speed calculation system is simulated and simulated induction motor parameters show in table1 .

Parameters	Values
Stator resistance(Rs)	0.435Ω
Rotor resistance(Rr)	0.816Ω

Stator self inductance(Lls)	0.002 mH
Rotor self inductance(Llr)	0.002 mH
Magnetizing inductance(Lm)	0.067 mH
Rotor inertia	0.18 kg · m2
No pole	2
DC voltage	510V
voltage	380V
frequency	50Hz

- 2) Simulation results shown. System given speed of 1 200 r / min, no load start, in the vector
- 3) Under control, the speed rise steadily, after loading, a slight decline but then recovered,

### B. Simulations Results

1) Figure 6 to Figure 9 are simulated according to the simulation model shown in Figure 5

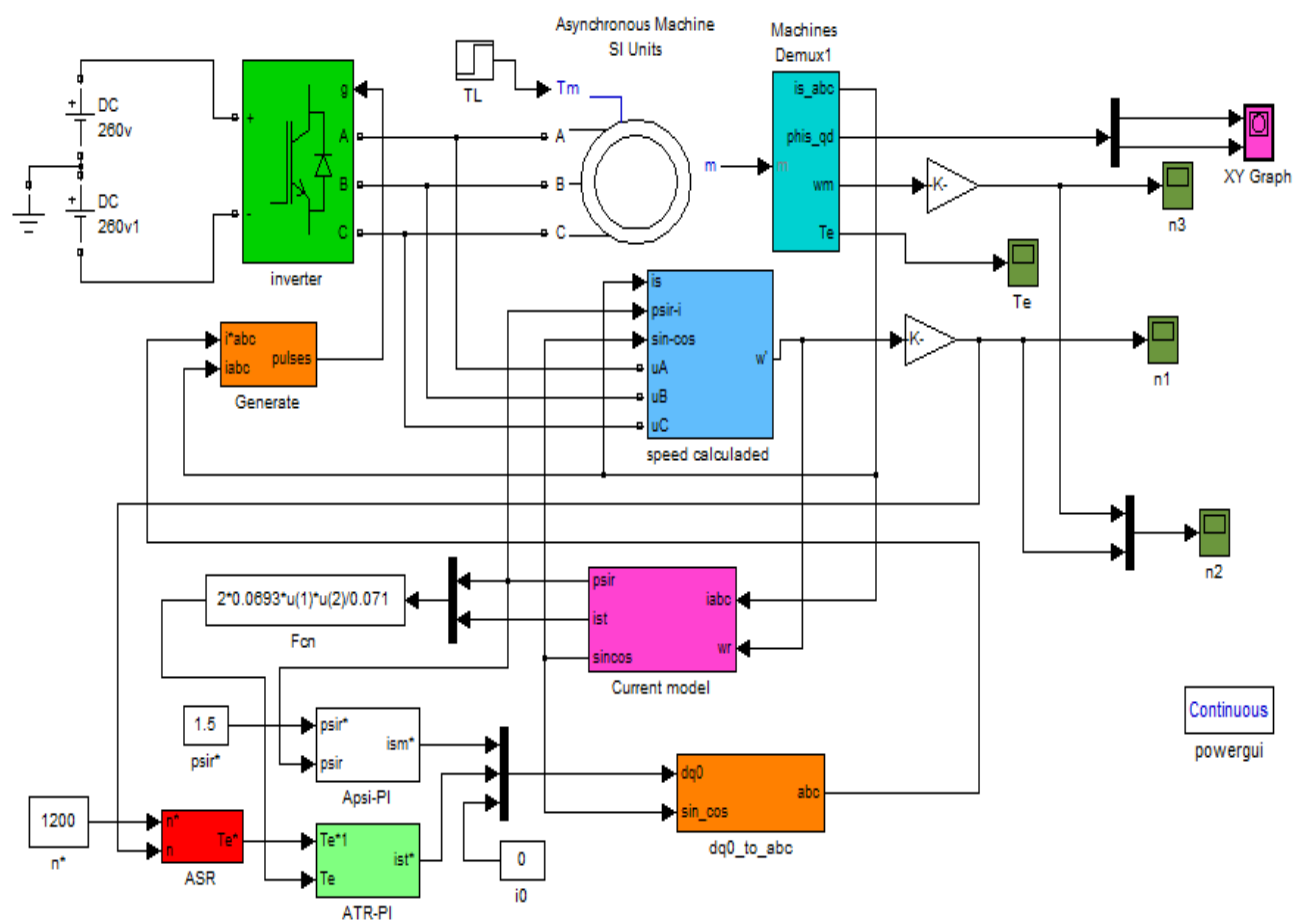


Figure 5. System simulation Model

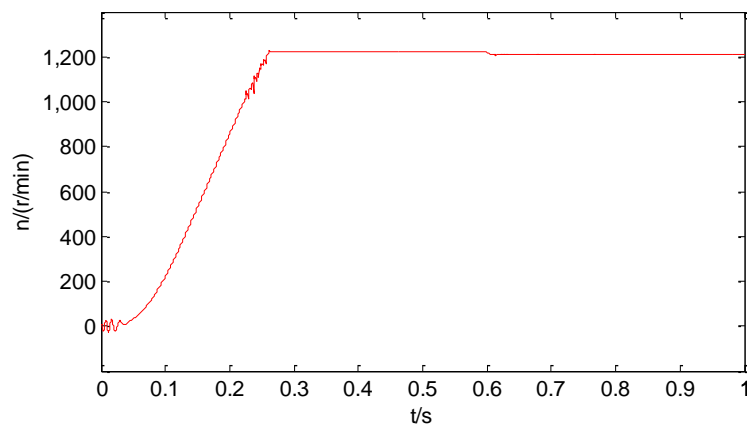


Figure 6. Estimated speed

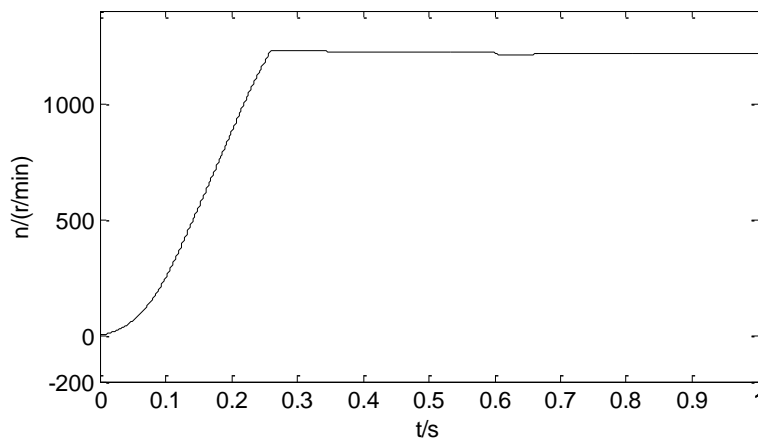


Figure 7. Actual speed

At a given speed of 0.26 s and a load of 0.6 s, the system regulator And the torque has a corresponding response. The rotor speed is at  $t = 0.26$  s at start-up Has stabilized state, the stator flux at the start of a large change, electricity The

magnetic torque has overshoot at the start and the given speed command change, but soon Tends to be stable, the stator flux amplitude gradually becomes constant, the system estimates the

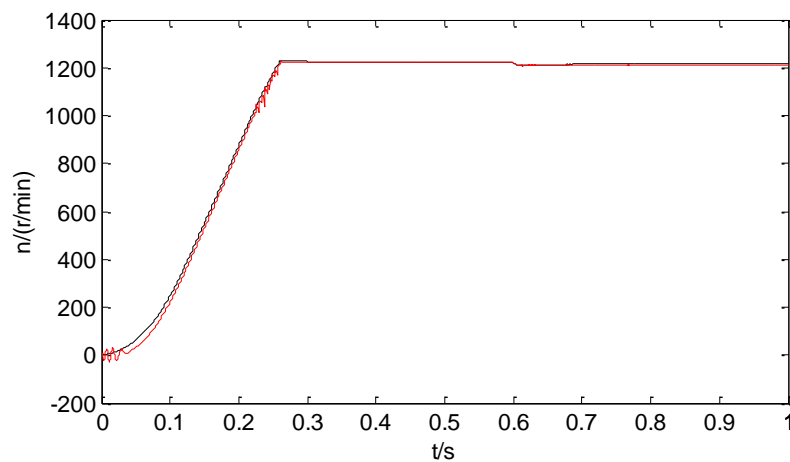


Figure 8. Estimated and actual speed at the same coordinate

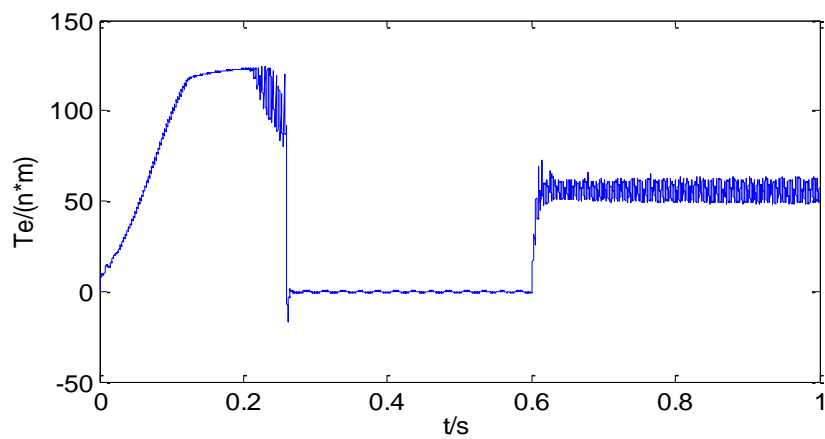


Figure 9. Motor output torque

Figure 11 to Figure 14 are simulated according to the simulation model shown in Figure 10 Simulation results shown. System given speed of 700r / min, no load start, in the

vector Under control, the speed rise steadily, after loading, a slight decline but then recovered,

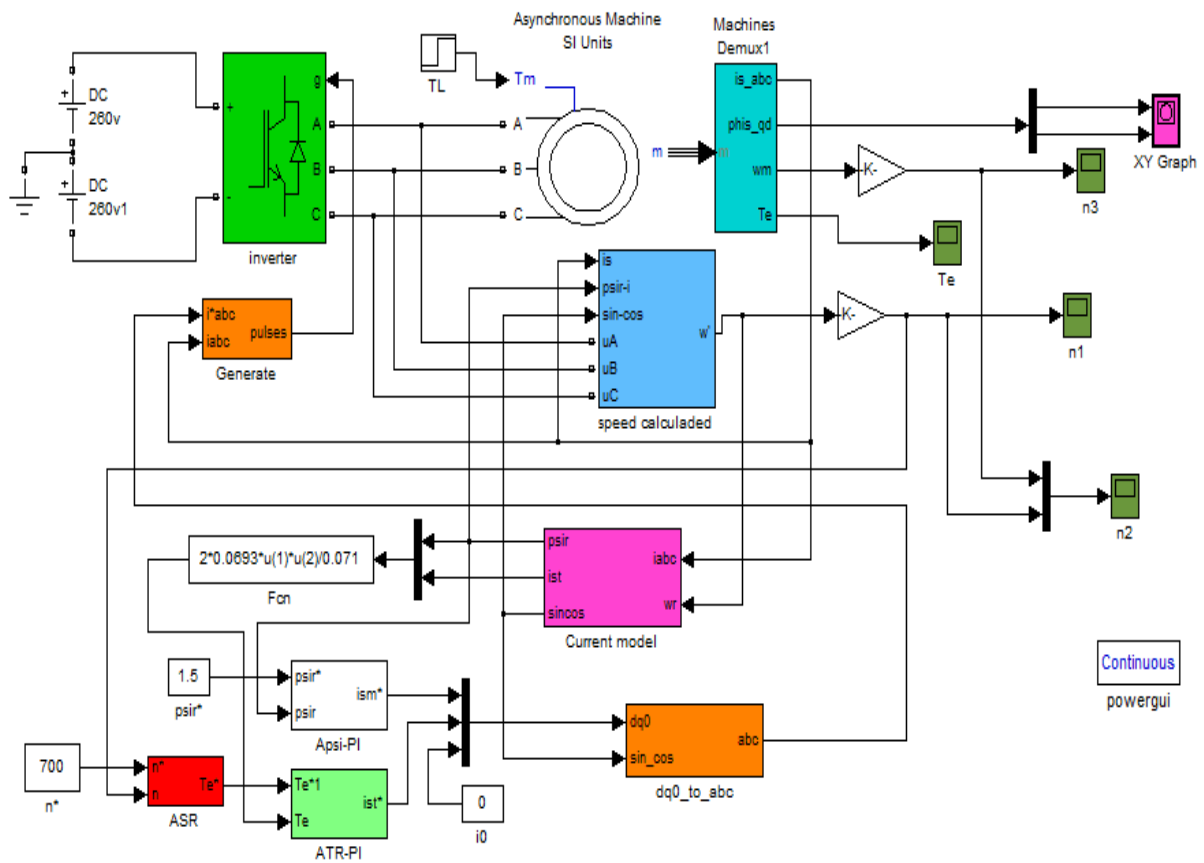


Figure 10. System simulation Model

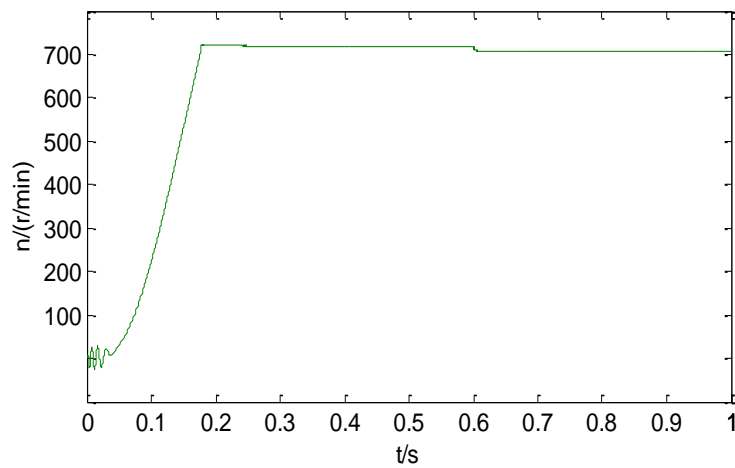


Figure 11. Estimated speed

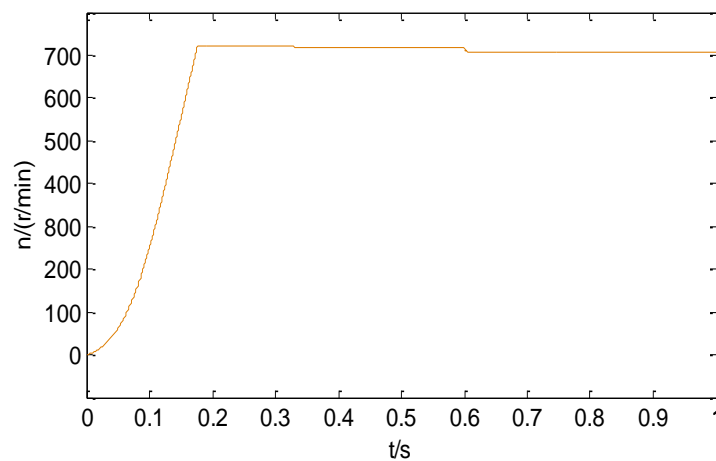


Figure 12. Actual speed

At a given speed of 0.26 s and a load of 0.6 s, the system regulator And the torque has a corresponding response. The rotor speed is at  $t = 0.26$  s at start-up Has stabilized state, the stator flux at the start of a large change, electricity The

magnetic torque has overshoot at the start and the given speed command change, but soon Tends to be stable, the stator flux amplitude gradually becomes constant, the system estimates the

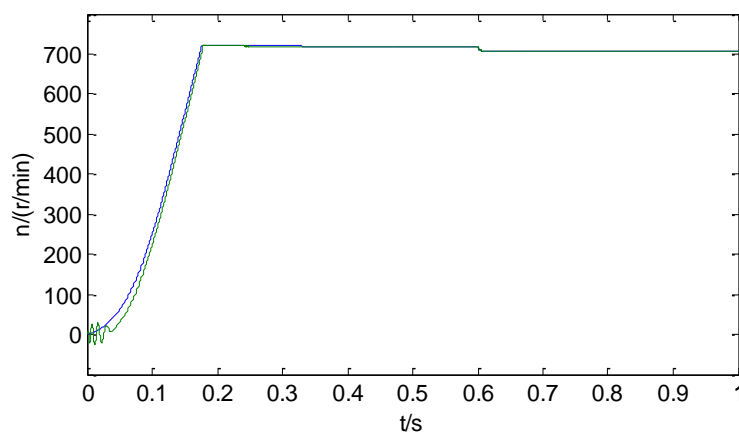




Figure 13. Estimated and actual speed at the same coordinate

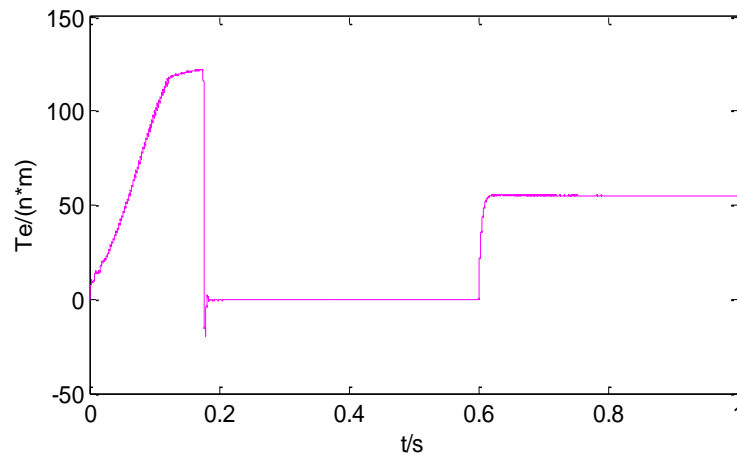


Figure 14. Motor output torque

Figure 16 to Figure 19 are simulated according to the simulation model shown in Figure 15. Simulation results shown. System given speed of 150 r / min, no load start, in the

vector Under control, the speed rise steadily, after loading, a slight decline but then recovered.

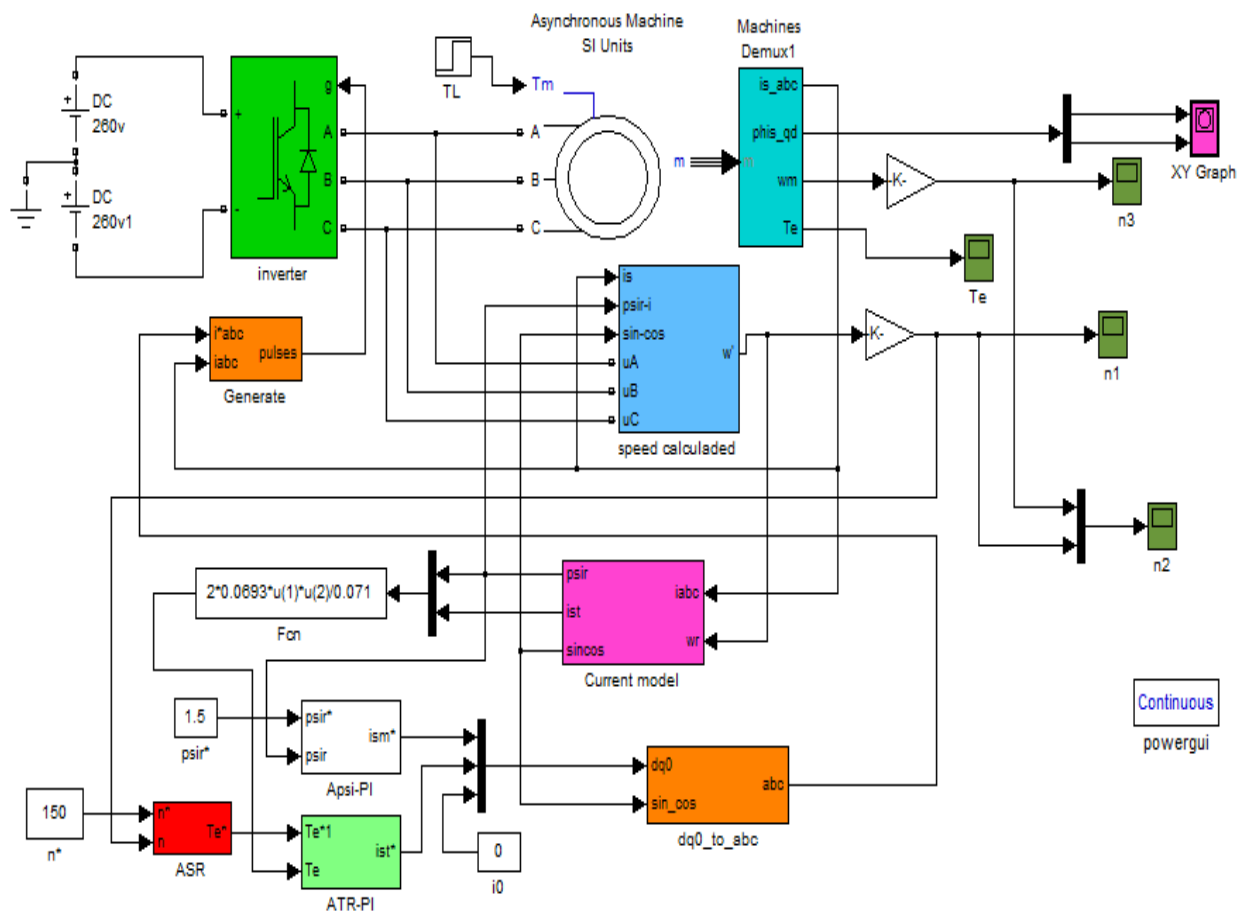


Figure 15. System simulation Model

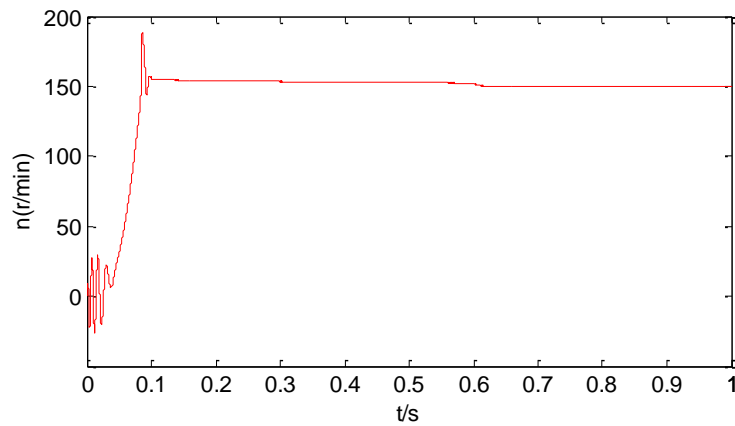


Figure 16. Estimated speed

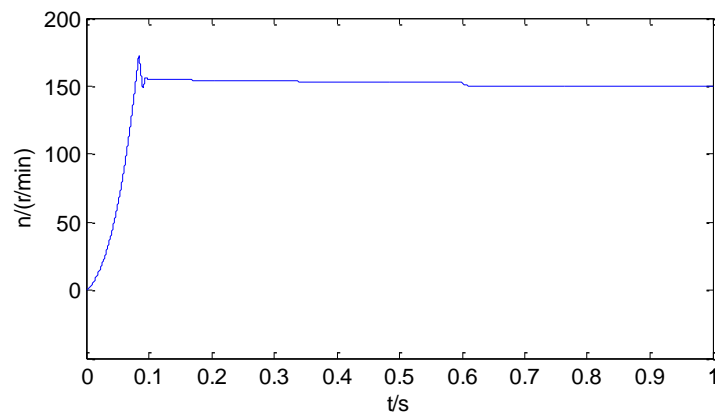


Figure 17. Actual speed

At a given speed of 0.26 s and a load of 0.6 s, the system regulator and the torque has a corresponding response. The rotor speed is at  $t = 0.26$  s at start-up has stabilized state, the stator flux at the start of a large change, electricity The

magnetic torque has overshoot at the start and the given speed command change, but soon Tends to be stable, the stator flux amplitude gradually becomes constant, the system estimates the

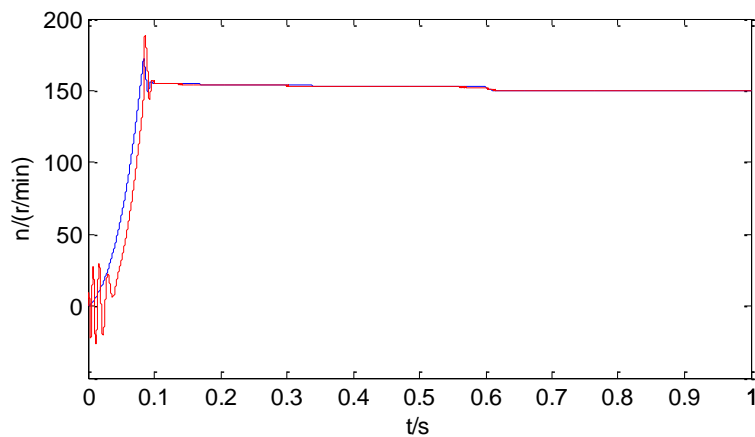


Figure 18. Estimated and actual speed at the same coordinate

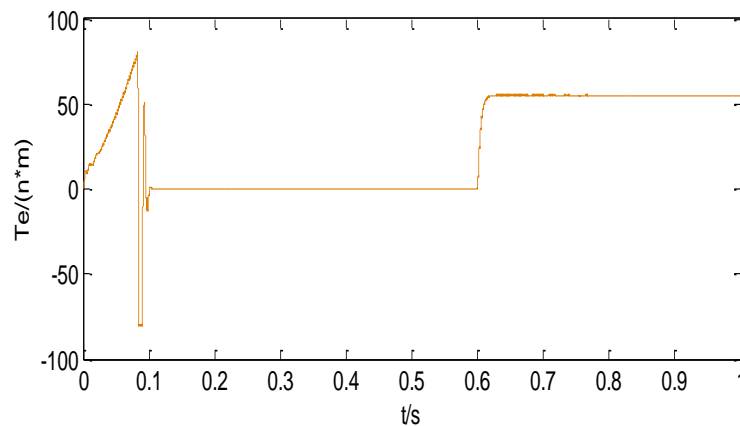


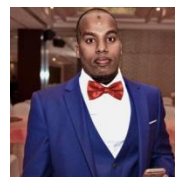
Figure 19. motor output torque

### CONCLUSION

Neural network has a certain degree of ascension, can be considered as a control System strategy applied to the practical application. While the reality of the car temperature in the fine The degree does not need to do very high, mainly taking into account the cost of research and development. This limits the application of neural network control in the car, but according to the future The direction of development, people for the comfort and rapid response requirements are not Improve the control, neural network control will have a great development prospects

### REFERENCES

- [1] Zerdali E, Barut M (2016) Novel version of bi input-extended Kalman filter for speed-sensorless control of induction motors with estimations of rotor and stator resistances, load torque, and inertia. *Turk J Electr Eng Comput Sci* 24 (5):4525-4544. doi:10.3906/elk-1408-136
- [2] Usta MA, Okumus HI, Kahveci H (2017) A simplified three-level SVM-DTC induction motor drive with speed and stator resistance estimation based on extended Kalman filter. *Electr Eng* 99 (2):707-720. doi:10.1007/s00202-016-0442-x
- [3] Kung YS, Thanh NP, Wang MS (2015) Design and simulation of a sensorless permanent magnet synchronous motor drive with microprocessor-based PI controller and dedicated hardware EKF estimator. *Appl Math Model* 39 (19):5816-5827. doi:10.1016/j.apm.2015.02.034
- [4] Inan R, Barut M (2014) Bi input-extended Kalman filter-based speed-sensorless control of an induction machine capable of working in the field-weakening region. *Turk J Electr Eng Comput Sci* 22 (3):588-604. doi:10.3906/elk-1208-31
- [5] Venkadesan A, Himavathi S, Muthuramalingam A (2013) Performance comparison of neural architectures for on-line flux estimation in sensorless vector-controlled IM drives. *Neural Comput Appl* 22 (7-8):1735-1744. doi:10.1007/s00521-012-1107-y
- [6] Gutierrez-Villalobos JM, Rodriguez-Resendiz J, Rivas-Araiza EA, Martinez-Hernandez MA (2015) Sensorless FOC Performance Improved with On-Line Speed and Rotor Resistance Estimator Based on an Artificial Neural Network for an Induction Motor Drive. *Sensors* 15 (7):15311-15325. doi:10.3390/s150715311
- [7] Maiti S, Verma V, Chakraborty C, Hori Y (2012) An Adaptive Speed Sensorless Induction Motor Drive With Artificial Neural Network for Stability Enhancement. *IEEE Trans Ind Inform* 8 (4):757-766. doi:10.1109/tii.2012.2210229
- [8] Mouna B, Aicha A, Lassaad S (2011) Neural Network Speed Sensor less Direct Vector Control of Induction Motor Using Fuzzy Logic in Speed Control Loop. *Int Rev Electr Eng-IREE* 6 (5):2237-2246
- [9] Mishra RN, Mohanty KB (2017) Implementation of feedback-linearization-modelled induction motor drive through an adaptive simplified neuro-fuzzy approach. *Sadhana-Acad Proc Eng Sci* 42 (12):2113-2135. doi:10.1007/s12046-017-0741-6
- [10] Kilic E, Ozcalik HR, Yilmaz S (2016) Efficient speed control of induction motor using RBF based model reference adaptive control method. *Automatika* 57 (3):714-723. doi:10.7305/automatika.2017.02.1330
- [11] Wang SY, Tseng CL, Chiu CJ (2015) Design of a novel adaptive TSK-fuzzy speed controller for use in direct torque control induction motor drives. *Appl Soft Comput* 31:396-404. doi:10.1016/j.asoc.2015.03.008
- [12] Zbede YB, Gadoue SM, Atkinson DJ (2016) Model Predictive MRAS Estimator for Sensorless Induction Motor Drives. *IEEE Trans Ind Electron* 63 (6):3511-3521. doi:10.1109/tie.2016.2521721
- [13] Holakooie MH, Taheri A, Sharifian MBB (2015) MRAS Based Speed Estimator for Sensorless Vector Control of a Linear Induction Motor with Improved Adaptation Mechanisms. *J Power Electron* 15 (5):1274-1285. doi:10.6113/jpe.2015.15.5.1274
- [14] Brandstetter P, Dobrovsky M, Kuchar M, Dong CST, Vo HH (2017) Application of BEMF-MRAS with Kalman filter in sensorless control of induction motor drive. *Electr Eng* 99 (4):1151-1160. doi:10.1007/s00202-017-0613-4
- [15] Kumar R, Das S, Syam P, Chattopadhyay AK (2015) Review on model reference adaptive system for sensorless vector control of induction motor drives. *IET Electr Power Appl* 9 (7):496-511. doi:10.1049/iet-epa.2014.0220
- [16] Dehghan-Azad E, Gadoue S, Atkinson D, Slater H, Barrass P, Blaabjerg F (2018) Sensorless Control of IM Based on Stator-Voltage MRAS for Limp-Home EV Applications. *IEEE Trans Power Electron* 33 (3):1911-1921. doi:10.1109/tpe.2017.2695259
- [17] Kumar R, Das S (2017) MRAS-based speed estimation of grid-connected doubly fed induction machine drive. *IET Power Electron* 10 (7):13. doi:10.1049/iet-pel.2016.0768



My name is kader ali Ibrahim. I'm from djibouti and I born 6 November 1992. I am currently Living in Wuxi and I'm doing master degree in electrical engineering at jiangnan university, China Wuxi. My research interest in Power electronics such as Sensorless Vector Control, Induction Mortor and MARS techniques.



# A Novel Method for Insulation Testing of High Voltage Electrical Equipment

Taimur Khan, Adnan Haleem

**Abstract**—Different equipment's are used to test the insulation of electrical machines and measure the break down voltages of different materials, e.g. Rogowski Profile, Borda Profile and fluke insulation tester. These testing techniques works on a common principle of applying a very high voltage across the insulating material and keep increasing the voltage which increases the electric field until the breakdown voltage is reached where the insulation breaks down. Different materials are tested via insulation testers to determine their breakdown voltages so that the corresponding correct materials are used accordingly in different situations. Devices with higher impurities causes sparks and arcing, so dielectrics having higher breakdowns should be used as their insulation, otherwise, a suitable dielectric should be used. This paper offers a novel method to overcome the above-mentioned problems using an insulation testing device that should be automated, less bulky, less expensive, portable and which shall be easy to use with higher degree of safety.

**Keywords**— A.C., D.C., CT, SA, HTS, HV, FBT, LOPT

## I. INTRODUCTION

The potential benefits of electrical energy supplied to a number of consumers from a common generating system were recognized shortly after the development of the 'dynamo', commonly known as the generator. The first public power station was put into service in 1882 in London (Holborn). Soon several other public supplies for electricity followed in other developed countries. The early systems produced direct current at low-voltage, but their service was limited to highly localized areas and were used mainly readily apparent. By 1890 the art in the development of an A.C. generator and transformer for electric lighting. The limitations of D.C. transmission at low voltage became had been perfected to the point when A.C. supply was becoming common, displacing the earlier D.C. system. The first major A.C. power station was commissioned in 1890 at Deptford, supplying power to central London over 28 miles at 10kV. Although the majority of the world's electric transmission is carried on A.C. systems, high voltage direct current (HVDC) transmission by overhead lines, submarine cables, and back to-back installations provides an attractive alternative for bulk power transfer. HVDC permits a higher power density on a given right-of-way as compared to A.C. transmission and thus helps the electric utilities in meeting the environmental requirements imposed on the transmission of

electric power. HVDC also provides an attractive technical and economic solution for interconnecting asynchronous A.C. systems and for bulk power transfer requiring long cables. [1]

## II. EXISTING TECHNIQUES FOR HIGH VOLTAGE MEASUREMENT

This research paper presents the operating principle, design, and testing of a coaxial D-dot (the time derivative of electric flux density) probe to measure fast-front high voltages, e.g., the residual voltages of surge arresters (SAs). This probe consists of three identical copper toroid's placed around a high-voltage electrode, where all are coaxially assembled in a large earthed cylinder.

The probe was first simulated by a finite-element package to optimize the assembly and reduce the electric field inside it. This was confirmed by an alternating current test to ensure a corona-free design. Simultaneous impulse voltage measurements were done using the designed D-dot probe – two commercial mixed resistive-capacitive (RC) probes and a damped capacitive voltage divider.

The linearity of the D-dot probe was checked under unloaded and loaded conditions. Results reveal that the larger the toroid separation and/or the lower the attenuator capacitance is, the higher the measured voltage from the middle "signal" toroid will be. The residual voltage waveforms for an 11-kV SA, measured by two commercial mixed RC-probes and the damped capacitive voltage divider, showed an initial inductive overshoot superimposed on the waveform and a significant decay, even before the current peak instant [3].

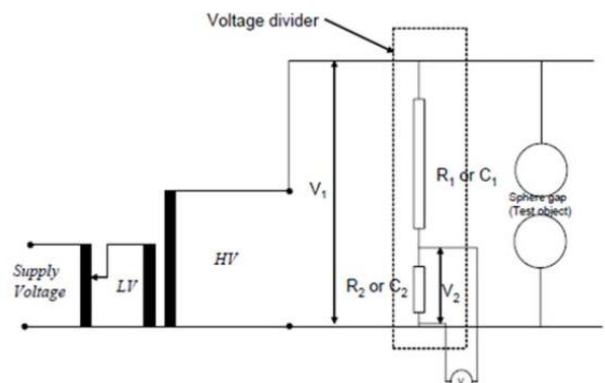


Figure 1. Schematic diagram of a typical A.C test transformer

Taimur Khan: was with Bahria University Islamabad, Pakistan and currently employed as an E/M Engineer at Pakistan Civil Aviation Authority, Peshawar. (email: taimur1358@gmail.com)

On the contrary, the voltage measured by the designed D-dot probe gave a voltage waveform that looked like that of the current and slightly led the latter. For the damped capacitive voltage divider and the two commercial mixed RC probes, neither the peak voltage nor the voltage at peak current gave the correct current-voltage characteristics. This confirms the contradiction of some published SA models in the high-conduction regime because most models were based on measurements done by different and large-impulse capacitive or resistive voltage dividers with improper compensation. Fig.1. shows the schematic diagram of a typical AC test transformer and its connections.

The development of high superconductors (HTS) has now reached the stage where their application in power system equipment is in the process of being implemented. Consequently, there is a need to investigate the properties and applicability of high voltage insulation at cryogenic temperatures. This paper will examine the insulating materials being used at such temperatures and the dielectric properties of such materials. A major factor in the deterioration of electrical insulation at normal operating conditions is the insulation temperature and there is a well-developed understanding of the aging characteristics under such temperature conditions. However, at cryogenic temperatures the properties of insulation under high electric stress may be quite different than the case for conventional operating temperatures and the aging process may be substantially altered. There is thus a need to investigate the insulation properties at cryogenic temperatures. This paper reviews the test methods for condition monitoring of insulation under such conditions and reports the first part of experimental results at ambient condition. The results obtained and further study at cryogenic temperature will provide necessary information for design of new HTS equipment. Fig.1. shows insulation resistance values for HV cable. [4]

TABLE I. INSULATION RESISTANCE VALUES FOR HV CABLES

Cable Rated Voltage	MINIMUM IR @ 1KV DC NEW CABLE	Minimum IR @ 500V Screen-E	Minimum IR @ 1KV DC Existing Cable	Minimum IR @ 500V Screen-E Existing Cable
11 KV	400 MOhm	100 MOhm	100 MOhm	1.0 MOhm
22 KV	400 MOhm	100 MOhm	100 MOhm	1.0 MOhm
33 KV	800 MOhm	100 MOhm	200 MOhm	1.0 MOhm
66 KV	800 MOhm	100 MOhm	200 MOhm	1.0 MOhm
132 KV	800 MOhm	100 MOhm	200 MOhm	1.0 MOhm

The minimum values for IR tests vary depending on the type of equipment and the nominal voltage. They also vary according to international standards. Some standards will define the minimum IR test values for the general electrical installations. In the ANSI/NEC world, the standard provides test procedures and acceptance levels for most types of electrical equipment. [5] Fig.II provides representative

acceptance values for IR test measurements, which should be used in the absence of any other guidance.

TABLE II. IR TEST VOLTAGE FOR ELECTRICAL EQUIPMENT

Maximum Voltage Rating of Experiment	MINIMUM DC TEST VOLTAGE	Insulation Resistance Test Voltage for Electrical Apparatus
250 V	500 V	25 MOhm
600 V	1000 V	100 MOhm
5000 V	2500 V	1000 MOhm
8000 V	2500 V	5000 MOhm
15000 V	2500 V	20000 MOhm

### III. FLOW CHART

A flow chart is developed for the project as shown in Fig.2. The flow chart is initiated using the Remote-Control which will send signals to the Receiver Section using Bluetooth. The microcontroller used at receiver's side will generate the desired frequency, vary the voltage supplied to the primary side of the ferrite core transformer, as a result, the secondary voltage from the ferrite core transformer will be supplied to the electrode that will be used for testing. The secondary voltage available at the electrodes will be monitored using CT and optocoupler circuit and as the spark occurs across the spark gaps breakdown voltage will be displayed on LCD in Receiver Section.

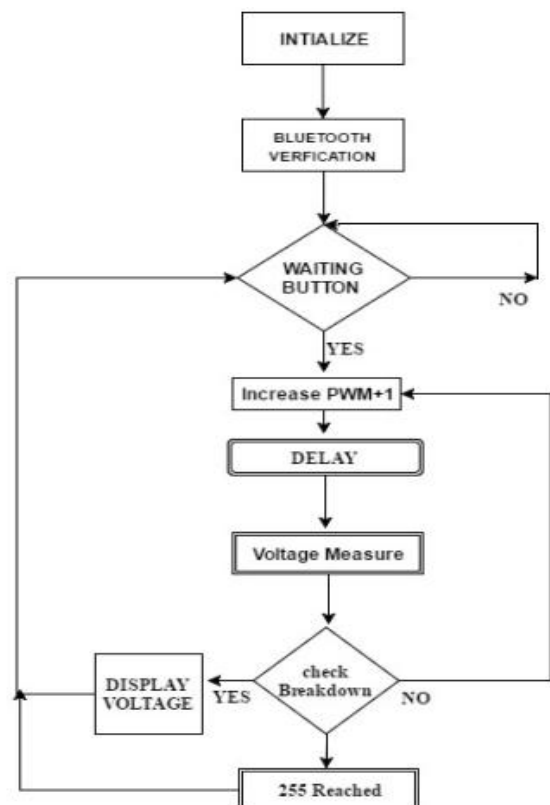


Figure 2. Flow Chart of Insulation Situation Analysis

#### IV. BLOCK DIAGRAM

The block diagram developed for the project is shown in Fig.3

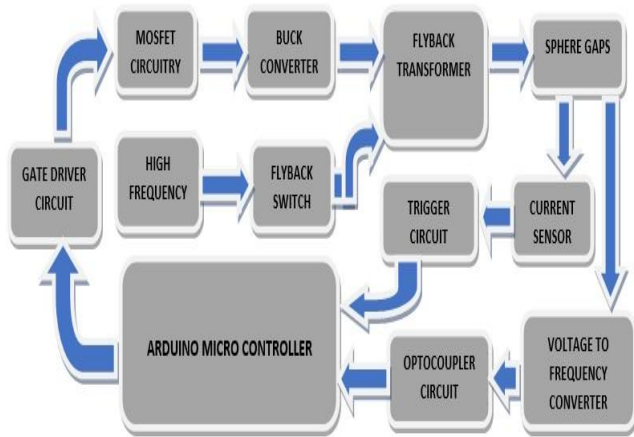


Figure 3. Block Diagram

#### V. MATHEMATICAL MODELLING

A voltage mode PWM controller(SG3525) is used as DC to DC converter for controlling the output voltage as well as for switching ON/OFF MOSFET(80NF70). PWM signals of different duty cycle (0-98%) will be provided to buck converter. As it will be pulsating DC so buck converter will make it a pure DC, that voltage will be supplied to the primary side of the Fly-back transformer, whereas, the secondary voltage will be provided to the spark gaps, with a voltage divider connected in parallel. The output of the voltage divider is provided to the voltage to frequency converter (LM331 IC), the output frequency of which will be interpreted by the Photocoupler (4N25) and read by the Arduino Microcontroller and the corresponding voltages via bluetooth module (HC06) will be displayed on LCD (16x2 Matrix).

##### Selecting Frequency of IC SG3525

A Fly-back transformer typically operates with switched currents at much higher frequencies in the range of 15 kHz to 50 kHz and it is used extensively in switched-mode power supplies for both low (3 V) and high voltage (over 10 kV) supplies. A high frequency driver is required to drive the fly-back transformer, for that, an IC SG3525 is used in the circuitry. Its main function is to either increase or decrease the duty cycle depending on the voltage levels on inverting and non-inverting inputs (Pin 1 and 2). The frequency of PWM is dependent on timing capacitance(CT) and timing resistance(RT). The deadtime resistance(RD) also slightly affects the frequency. The frequency is related to CT, RT and RD as follow,

$$f = \frac{1}{C_T (0.7 R_T + 3 R_D)} \quad \dots[8]$$

Where,

RT is in the range of 2KΩ to 150 KΩ,  
CT must be in the range of 1nF to 0.2μF, and  
RD is in the range between 10Ω to 47Ω.

Taking CT as 1.4x 10<sup>-9</sup>F, RD as 40Ω and RT as 6000Ω, So, frequency (f) comes out to be 17Khz which is supplied to Fly-back transformer.

##### Calculation for Ferrite Core Fly-back Transformer

A flyback transformer (FBT), also called as a line output transformer (LOPT), generate high voltage sawtooth signals at a relatively high frequency. The primary turns for this project are calculated using the formula,

$$N_{pri} = \frac{V_{in(nom)} \cdot 10^8}{4 \cdot f \cdot B_{max} \cdot A_c} \quad \dots[9]$$

Where, Vin(nom) is the nominal input voltage usually taken as 12V, f is the operating switching frequency (Hz) which is taken as 16.5-17 Khz, Bmax is the maximum flux density in Gauss (taken between 1300-2000G) and Ac is the effective cross-sectional area in cm2 (For ETD39 it is 1.25cm2). The primary turns calculated are 9 and are wound on primary end of ferrite core transformer as shown in Fig.4.



Figure 4. Primary turns of the Ferrite Core Transformer

Now the voltage ratio is calculated using formula,

$$V_{ratio} = V_s / V_p = 16.5KV / 12V = 1375V$$

Knowing the Secondary to Primary voltage ratio we can now easily calculate the Secondary turns of the Fly-back transformer,

$$N_{ratio} = N_s / N_p = N_s / 9$$

##### Finding frequency of IC LM331

The LMx31 family of voltage-to-frequency converters are ideally suited for use in simple low-cost circuits for analog-to-digital conversion, precision frequency-to-voltage conversion, long-term integration, linear frequency modulation or demodulation, and many other functions. The output when used as a voltage-to-frequency converter is a pulse train at a frequency precisely proportional to the applied input voltage whose frequency can be calculated using the formula,

$$F_{out} = (V_{in} / 2.09V) \times (R_s / R_I) \times (1 / (R_t \times C_t))$$



To keep the same linearity as before with the frequency to voltage conversion stage,  $R_s = R_1 = 100\text{ K}\Omega$ , hence  $R_s/R_1 = 1$ . The parameter  $V$  is the same as before, which is 12 volts. The timing value of the resistor  $R_t = 4\text{ K}\Omega$ , and capacitor  $C_t = 0.01\text{ }\mu\text{F}$ , Hence, the equation simplifies to that shown below.

$$F_{out} = 996.81 \times V_{in}\text{ Hz}$$

This  $V_{in}$  is provided using a Voltage divider circuit.

*Calculation for Voltage divider circuit*

A typical voltage divider circuit is used, the formula for which is,

$$V_{out} = \frac{R_2}{R_1 + R_2} \cdot V_{in}$$

Where,  $R_1=194\text{M}\Omega$ ,  $R_2=84\text{K}\Omega$  and  $V_{in}=2310.524\text{V}$ , So  $V_{out}$  is equal to 1V.

*Response of Remote Section*

From the above calculation, it can be concluded that as the Voltage( $V_{out}$ )=1V is received by the remote section via Bluetooth, the remote section will display a value of 2310.524V.

*System Model of the Project*

This system model of the project comprises of two sections. A Remote-Control Section and a Receiver Section. The Remote-Control section comprises of an Arduino microcontroller that uses Bluetooth technology to remotely connect to the Receiver connection and thus provide portability and high degree of Safety. The Receiver Section comprises of a Buck converter, Ferrite Core transformer, Gate driver and MOSFET circuitry, two Sphere Gaps, CT and an Optocoupler circuit for voltage sensing and an Arduino microcontroller which controls the Receiver Section and communicates with the Remote-Control section. Both the section was successfully simulated in Proteus Software as shown in Fig.5.

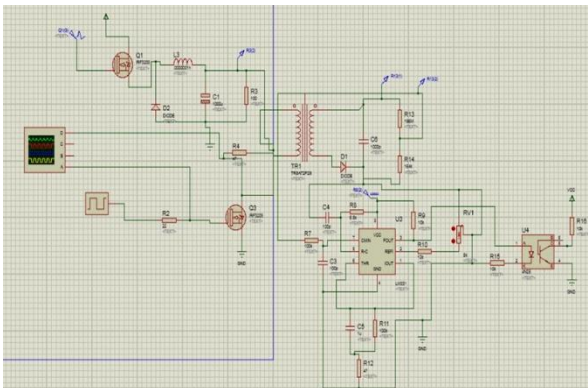


Figure 5. System Model in Proteus Software

## VI. SIMULATION

A PWM signals of different duty cycle from will be given to buck converter. As it will be pulsating DC so that voltage will be given to buck converter to make it pure DC. That

voltage will be supplied to the primary side of the fly back transformer. The voltage at secondary side will be given to spark gaps. Voltage divider is connected in parallel with spark gaps, LM331 IC will change voltage into frequency and then this frequency will be read by Arduino Micro Controller and voltage value will be shown on LCD connected at remote side. When voltage across the spark gaps reaches the breakdown voltage of an insulator placed in between the spark gaps a flash over will happens due to flash over current will increase and that current will be sensed by Current transformer. [6] Current transformer will give signal to Microcontroller to stop the generation of PWM signal LM331 IC will convert the breakdown voltage into frequency, this frequency via Photo coupler will be sent to and interpreted by the Arduino Micro Controller. Fig.6. shows the simulation results as on digital oscilloscope which clearly indicate that the Input wave (Yellow) is much smaller as compared to the output wave (Green) of a fly back transformer.

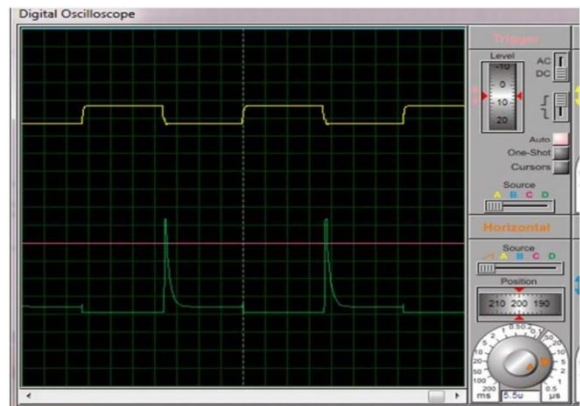


Figure 6. Simulation Results on Digital Oscilloscope

## VII. HARDWARE MODELLING

The hardware model comprises of a fully populated Arduino board which connects the LCD to the Arduino as well as shown in Fig.7. A pair of spark gaps which consists of a two electrodes separated by a gap usually filled with air, fully assembled, All the PCBs are attached to the acrylic sheet through nuts and bolts The two male pin header connectors which are connected to the CT board and Triac switch board through IDE cable, as shown in Fig.6.



Figure 7. Remote Connectivity and Display Module

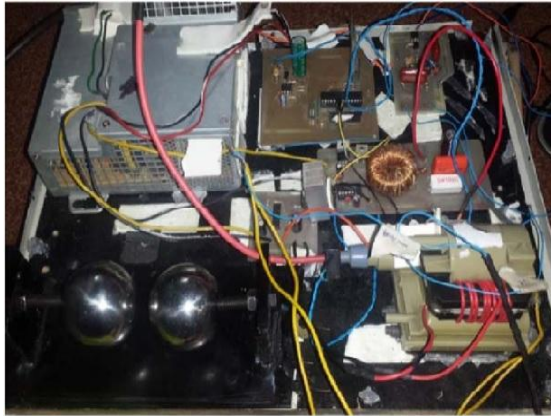


Figure 8. Hardware Model of the Project

## VIII. RESULTS

### Breakdown Voltage for Air

The breakdown voltage of air was tested with different air gaps between the electrodes and it is observed that as the air gap increases, the breakdown voltage increases. [7] Fig. 4 shows air breakdown voltages at different gap distance but after certain gap distance, the device stops measuring the voltage. The reason is that gap length exceeds the device measuring capacity.

TABLE III. BREAKDOWN VOLTAGE OF AIR AT DIFFERENT GAP DISTANCES

BREAKDOWN VOLTAGE (KV)	SPHERE GAP DISTANCE (MM)
5	1
10	2.6
15	4.2
20	5.8

### Breakdown Voltage for Solid Insulators

The Breakdown voltage of other insulations such as paper, rubber, and hardboard breakdown can also be measured with this device Fig. 5 shows the breakdown voltage of solid insulators.

TABLE IV. BREAKDOWN VOLTAGE OF SOLID INSULATORS

INSULATING MATERIAL	BREAKDOWN VOLTAGE (KV)
A4 Paper	0.8
Chart Paper	2
Hard Board	2.6
Rubber	11
Wood	16

## CONCLUSION

In this paper, the breakdown voltage of Air and other solid insulators was investigated. The experimental results confirmed that the impact of the barrier is dependent on the air gap length. Also, the results highlight the effect of physical characteristics of the dielectric barriers in the breakdown voltage enhancement. Finally, we used the experimental results that were carried out in the high voltage laboratory to validate the hardware model. The study shows that the results were in good agreement with the experimental results.

## REFERENCES

- [1] I. A. Metwally, "-Dot Probe for Fast-Front High-Voltage Measurement," in *IEEE Transactions on Instrumentation and Measurement*, vol. 59, no. 8, pp. 2211-2219, Aug. 2010.doi: 10.1109/TIM.2009.2030928
- [2] T. R. Blackburn, C. Grantham, B. T. Phung, Z. Y. Liu, M. F. Rahman and J. X. Jin, "High voltage insulation test for high Tc superconducting types," *Applied Superconductivity and Electromagnetic Devices (ASEMD), 2013 IEEE International Conference on*, Beijing, 2013, pp. 241-244.doi: 10.1109/ASEMD.2013.6780753
- [3] IEEE Standard Techniques for High-Voltage Testing," in *ANSI/IEEE Std 4-1978*, vol., no.,pp.0\_1-,1978doi:10.1109 / IEEESTD.1978.119190
- [4] D. Pan, H. W. Li and B. M. Wilamowski, "A low voltage to high voltage level shifter circuit for MEMS application," *University/Government/Industry Microelectronics Symposium, 2003. Proceedings of the 15th Biennial, 2003*, pp. 128-131. doi: 10.1109/UGIM.2003.1225712
- [5] R. R. M. Pendor, Z. Abas and A. K. Yahya, "Winchester-Banana platform for high temperature and high-voltage reliability testing with voltage monitoring capability," *36th International Electronics Manufacturing Technology Conference, Johor Bahru, 2014*, pp.1-7.doi: 10.1109 /IEMT.2014.7123113
- [6] K. A. O'Connor and R. D. Curry, "High voltage characterization of high dielectric constant composites," *2010 IEEE International Power Modulator and High Voltage Conference*, Atlanta,GA,2010,pp.159-162.doi: 10.1109 /IPMHVC.2010.5958318
- [7] R. Minkner, "Development trends in medium- and high voltage technologies for measuring systems, filters and bushings," *Power Tech, 2005 IEEE Russia*, St. Petersburg, 2005,pp.1-8.doi: 10.1109/PTC.2005.4524818.
- [8] M. S. Naidu and V. Kamaraju, *High Voltage Engineering*, Tata McGraw-Hill 2004.
- [9] E. Kuffel, W. S. Zaengl, and J. Kuffel, *High Voltage Engineering. Fundamentals*, Butterworth-Heinemann, 2nd edition, 2000.



# Effect of Sandstone on Concrete Procedure With Plastic Synthetic Aggregate

UZOH U.E, MBADIKE E.M

**Abstract**—In this research work, the effect of sandstone (SS) on concrete produced with plastic synthetic aggregate (PSA) was investigated. A mix proportion of 1:1.6:3.6 with water cement ratio of 0.50 were used. The percentage replacement of coarse aggregate (CA) with plastic synthetic aggregate and plastic synthetic aggregate/sandstone used were 0%, 5%, 10%, 20%, 30% and 40%. Concrete cubes of 150mmx150mmx150mm of CA/PSA and CA/PSA/SS were cast and cured at 3,7,28,60 and 90 days respectively. At the ends of each hydration period, the concrete cubes were crushed and their compressive strength was determined. The result of compressive strength of 5-40% replacement of coarse aggregate with plastic synthetic aggregate ranges from 8.07-36.71N/mm<sup>2</sup> as against 24.55- 41.21N/mm<sup>2</sup> for the control test. The result of the compressive strength of 5-40% replacement of coarse aggregate with plastic synthetic aggregate and sandstone ranges from 5.05-31.75N/mm<sup>2</sup> as against 24.58- 41.21N/mm<sup>2</sup> for the control test. The workability for 5-40% replacement of coarse aggregate with plastic synthetic aggregate ranges from 15-68mm as against 8mm for the control test (0% replacement).

**Keywords**— plastic synthetic aggregate, coarse aggregate, sandstone, compressive strength, workability

## I. INTRODUCTION

Lightweight concrete can be produced by partially replacing the normal weight coarse aggregate particles with plastic synthetic aggregate and sandstone. In the previous research [1], the effect of plastic synthetic aggregate in the production of lightweight concrete was studied. In that research, plastic synthetic aggregate was used to replace 0-40% of coarse aggregate by weight. In the research presented here, second material sandstone was used together with plastic synthetic aggregate. The plastic synthetic aggregate is commercial available with suitable chemical coating, which is necessary to achieve a uniform dispersion in the fresh concrete mixture and to avoid segregation during mixing and handling of concrete. The plastic synthetic aggregate has negligible water absorption due to the closed cellular structure. [2]

the plastic synthetic aggregate concrete since they are sensitive to the weight of concrete. [3] Made similar observation when working with some materials together with plastic aggregate. The use of plastic synthetic aggregate in concrete manufacture may provide a satisfactory solution to the problem posed by concrete production [4]. The use of plastic synthetic aggregate should not impair concrete durability. Traditional assessment methods must therefore be adopted to evaluate this material [5]. This study contributes to the development of a methodology for assessing concrete manufactured from plastic synthetic aggregate. The methodology is based on the study of concrete containing these materials. The durability and the environmental impact of concrete are closely connected to its transport properties which control the kinetic of the penetration of water and aggressive agents into concrete [6]. The movement of chemical species within the material and the leaching of certain chemicals are also closely linked to concrete diffusivity [7].

Finally, the strength characteristics of concrete containing increasing level and plastic synthetic aggregate and plastic, synthetic aggregate/sandstone were studied to identify the influence of these materials on concrete produced with them.

## II. MATERIALS AND METHOD

Concrete mixture with six levels of PSA and PSA/SS replacement ranging from 5- 40% and control mixtures with no PSA were investigated to determine their effect on compressive strength. The mixtures were labeled MO, M5, M10, M20, M30 and M40 with the different plastic synthetic aggregate (PSA) replacement percentages represented by the final digits in the label. Crushed plastic synthetic aggregate angular in shape with a non toxic chemical coating and having a mean diameter of 2.5mm were used in the concrete mixtures. The sandstone which was also used was obtained from Ezumoha in Isiala Mbano L.G.A of Imo State. The sandstone is reddish in colour and angular in shape. The fine aggregate used was a clean river sand free from deleterious substances with specific gravity of 2.62 and bulk density of 1,533kg/m<sup>3</sup>. The coarse aggregate was obtained from a local supplier with a maximum size of 20mm, specific gravity of 2.65 and bulk density of 1,467kg/m<sup>3</sup>. Both aggregate conforms to [8] and [9] respectively for coarse and fine aggregates.

The cement used was ordinary Portland cement (Dangote) which conforms to [10]. Test to determine compressive strength, workability and density were carried out in this study. For the compressive strength test, PSA and PSA/SS were used to replace 0-40% of coarse aggregate by weight. For the

UZOH U.E: Department Of Civil Engineering, Gregory University, Uturu Abia State Nigeria, E-Mail Address: uzohuzochukwu@gmail.com.

MBADIKE E.M: Department Of Civil Engineering Michael Okpara University Of Agriculture, Umudike, Umuahia, Abia State, Nigeria.

Reported that the standard workability tests are not suitable for

compressive strength test 150mm(6in) cube specimen were used. A total of 180 specimens were cast and cured in water at room temperature in the laboratory for 3,7,28,60 and 90 days. At the end of each hydration period, three specimen for each mixture were tested for compressive strength and the average recorded. For the workability, a standard slump cone measuring 300mmx200mmx 100mm was used. The compaction was also in three layers as carried out in compressive strength, i.e. 1/3, 2/3, 3/3 using tamping rod [11, 12].

### III. RESULTS AND DISCUSSION

Fig 1 and fig 2 shows the result of compression strength obtained when plastic synthetic aggregate was used to replace coarse aggregate at a replacement level of 0%, 5%, 10%, 20%, 30% and 40% respectively. The result of the compressive strength of 5 - 40% replacement of coarse aggregate with plastic synthetic aggregate ranges from 8.07-36.71N/mm<sup>2</sup> as against 24.58-41.21N/mm<sup>2</sup> for the control test. Fig 3 and 5 shows the result of the compressive strength obtained when both plastic synthetic aggregate and sandstone were used at the same percentage replacement level of coarse aggregate. The result of the compressive strength of 5-40% replacement of coarse aggregate with plastic synthetic aggregate and sandstone ranges from 5.05 - 31.75N/mm<sup>2</sup> as against 24.58-41.21N/mm<sup>2</sup> for the control test. The result of this study showed that sandstone decreases the early strength of the plastic synthetic aggregate concrete (5-40% replacement) and that the early age gain of strength due to high process of hydration when plastic synthetic aggregate alone was incorporated has been reduced by replacing half of plastic synthetic aggregate with sandstone. [13] Made the same observation when worked with plastic synthetic aggregate and other materials. Table 12 shows the result of workability of concrete produced when plastic synthetic aggregate was used to replace 0-40% of coarse aggregate. The result of workability for 5-40% replacement of coarse aggregate ranges from 12-61mm as against 8mm for the control test, fig 4 and 6 shows the result of workability for 5-40% replacement of coarse aggregate with plastic synthetic

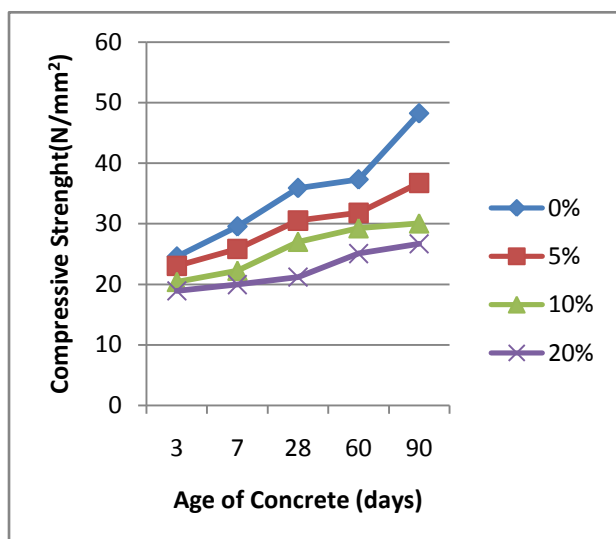


Figure 1. Compressive Strength of PSA concrete vs Age of Concrete 0%-20%

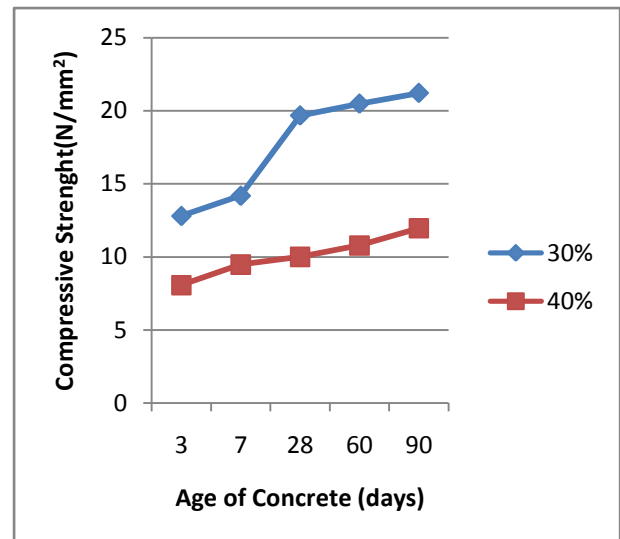


Figure 2. Compressive Strength of PSA concrete vs Age of Concrete for 30%-40%

aggregate and sandstone which ranges from 15-68mm as against 8mm for the control test. The result as shown in fig 6 shows that the workability of concrete produced when both plastic synthetic aggregate and sandstone were used to replace coarse aggregate is greater than the workability concrete produced when plastic synthetic aggregate alone was used to replace coarse aggregate in concrete matrix. The higher the workability of concrete, the lower the strength, the result of workability of the concrete produced justified the result of the compressive strength obtained.

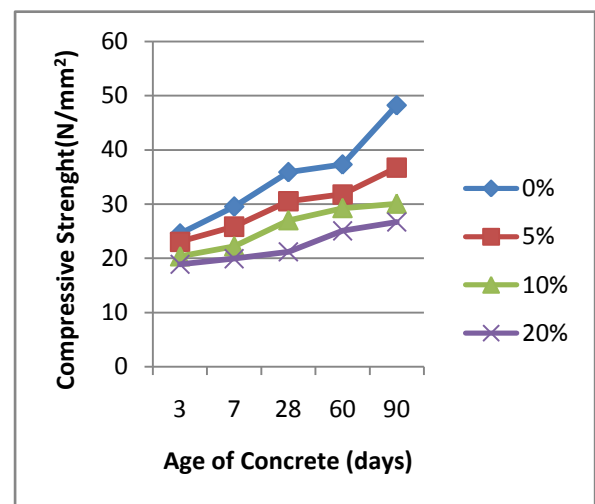


Figure 3. Compressive Strength of PSA/SS concrete vs Age of Concrete 0%-20%



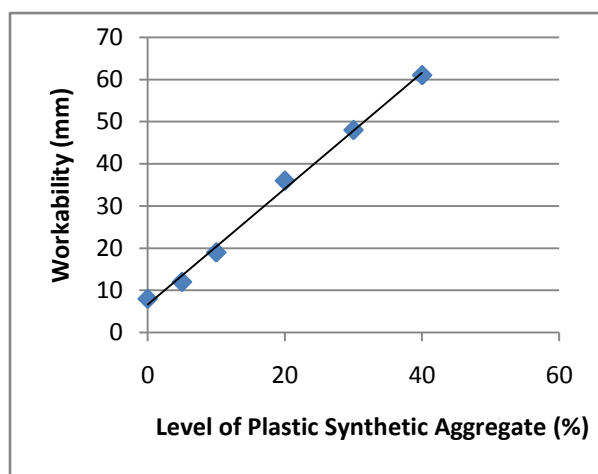


Figure 4. Workbilty of Concrete vs Level of PSA (%)

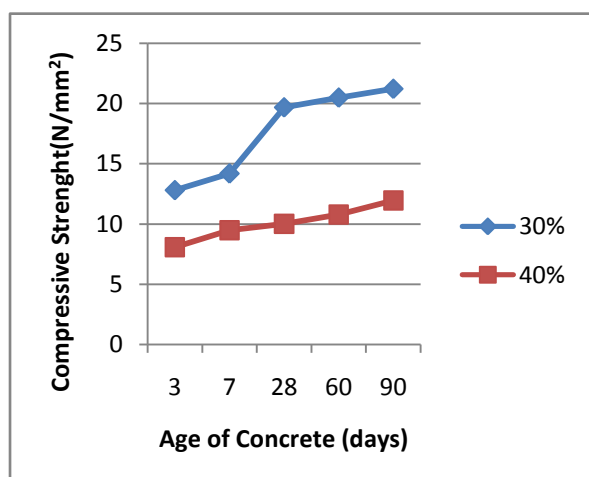


Figure 5. Compresive Strenght of PSA/SS concrete vs Ages if concrete 30%-40%

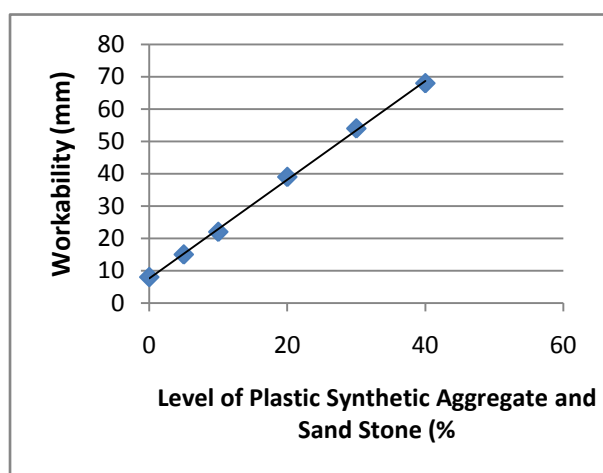


Figure 6. Workability of Concreate vs Level of PSA/SS (%)

## REFERENCES

- [1] Elvis M. Mbadike and Ezeokpube G.C. (2014): Effect of Plastic Synthetic aggregate in the production of Lightweight concrete. *Journal of Advances in Biotechnology, USA*, No 1, Vol 2, pp 83-88.
- [2] Cook, D.J. (2013): Coarse aggregate polystyrene granules mixes for use in masonry unit,,building and environment, pp 150-182.
- [3] Sri Ravindrarajah, R. (2012): Bearing strength of concrete containing polystyrene aggregate, 8th International conference on durability of buildings materials and components, Vancouver, Canada, Vol 1, pp 505-514.
- [4] Basheer P.A.M, McCabe C.C and Long A.E (2014): "The influence of admixture on the properties of fresh and hardened concrete". *Journal of scientific Industrial Research*, Vol 8, pp 199-214.
- [5] Chatterji A.K. (2011): "Adsorption of lime and Pozzolan activity; *Journal of scientific Industrial Research* Vol 20, pp 490-495.
- [6] Pimienta P, Remond S, Rodrigues N. and Boumazel J.P (2011). Assessing the properties of mortar containing municipal solid waste incineration fly ash. *International congress creating with concrete*, University of Dundee, pp 319-326.
- [7] Remond S, Punicnta P, and Bentz, D.P (2010): Effect of Incorporation of municipal solid waste fly ash in concrete. *Journal of cement and Concrete Research*, vol 10, pp 12-14.
- [8] British Standard Institution, BS 877 (1967): Foamed or expanded blast furnace slag lightweight aggregate in concrete ". London, pp8.
- [9] British standard institution BS 3797 (1964): "Lightweight aggregates for concrete", London, pp8.
- [10] British standard institution, BS 12 (1978): "Specification for Ordinary and Rapid Portland cement, London, pp 38.
- [11] Neville A.M. (1981). "properties of concret " 3rd Edition, Pitman, New York.
- [12] Neville A.M. (2000): "Properties of concrete" 4th edition Pearson Education, Asia Pte Ltd, England.
- [13] Khan M.J. Lynadaic C. and Waldron P. (2013): Interaction of plastic synthetic aggregate and silica fume influence on concrete strength, *A vision for the next millennium*, R Swarmy edition, Sheffield Academic Press, pp 300-309.



# Optimizing Computations in Intermittently Powered Wireless Sensor Nodes

Hussain Ahmad, Jawad Ali, Syed Waqar Shah, Durre Nayab

**Abstract**— Communicating man and machine is always beneficial when their linkage is for information exchange. Information Communication Technologies (ICT) thus seek for such technologies and communication schemes where it can eliminate the use of frequent, time to time re-programming as well as charging/ topping up the battery resource. For the same purpose, researchers are always into the development of such Wireless networking based schemes where the battery constrains are minimized. Internet of things (IoT) is one of these emerging technologies. This research focuses on the implementation of IoT based techniques to minimize the battery re-charge time by studying the behavior of motes (Nodes in IoT) with respect to its information exchange, network throughput and power management. The research uses capacitor driven motes that can accept data wirelessly and transmit it directly after its reception or can restart the mote while the data is being preserved in its Read only flash. There different scenarios have been sequentially analyzed for incremental number of nodes from 2 to 15, whereas the capacitance is calculated for nominal data transfer. The results conclude that once the deployment of the network goes from sparse to densely populated network, the charge due to the mode's capacitance exponentially optimizes. The research concludes that lower number of nodes must be greater in order to use higher capacitance values whereas lower network density must follow the strategy of broadcasting its data without writing it on Read only flash memory.

**Keywords**— Internet of Things, Wireless Sensor Networks, Intermittently powered nodes, Power analysis of communication.

## I. INTRODUCTION

This document concentrates on power/energy profiling of wireless sensor nodes in wireless networks. In wireless sensor networks, the wireless nodes energy is restrained resource. Engineers and Scientists worked hard to optimally utilize the

available energy. But on every passing moment; the energy requirement is increase due vast range of newly develop application of WSNs. Internet of Things (IoT), is rising concept of Wireless Sensor Networks. In IoT, the number of wireless sensors nodes ranges from hundreds to tens of thousands are distributed over the desired locations for in demand applications. The wireless sensor nodes are also called motes. These motes must have some energy resource for their essential functions and this energy resource should be utilized efficiently. The number of method use for increasing the energy consumption efficiency of these motes likely CRFIDs [1], Computational RFIDs, reduce power consumption of motes by modulating the reflection of power uttered by an external transmitter instead of transmitting actively. The general purpose battery less sensor devices [2], is micro controller based devices which harvest energy from environmental factors, for example sun light, vibration etc. Energy harvesting system [3] energized itself by harvesting energy of its surroundings. The energy is mostly temporarily available, offering intermittently supply or power resource. As the energy vanish, the processor turn off. The processor start up again as soon power available, but also restart computations. Hence, difficult for motes to complete necessary computations.

As per Internet of Things application requirements, the motes have possible minimum energy storage capability to serve in medical implants [4] and smart dust. Mememtos [5] is relatively recent development which place Watchdogs/checkpoint [6] in pre execution (Compile) time. Momemtos save volatile memory to non-volatile memory just as voltage level drops threshold value (pre-determined value). Herbenus [8]; in this mechanism the device or mote swing between two states: active state and hibernating state. The hardware interrupt for swing between two states is define by threshold voltage. The device store last setup or necessary information on nonvolatile memory prior to shifting hibernating state.

## II. LITERATURE REVIEW

WSN network are employed to optimize industrial processes, autonomous control, vehicular and non-vehicular traffic, health care application and its improvement, and various surveillances system etc. Till date, major industrial manufacturer has deployed more than 30,000 networks across the world to improve safety and process efficiency in different locations. These industries are ranging from beverage and food plants to oil refineries and production facilities [7].

Hussain Ahmad: Department of Electrical Engineering, University of Engineering and Technology, Peshawar, Pakistan 25000, Email: hussain-ahmad@live.co.uk.

Jawad Ali: Department of Electrical Engineering, University of Engineering and Technology, Peshawar, Pakistan 25000, Email: jawad.ali@uetpeshawar.edu.pk.

Syed Waqar Shah: Department of Electrical Engineering, University of Engineering and Technology, Peshawar, Pakistan 25000, Email: waqar.shah@uetpeshawar.edu.pk.

Durre Nayab: Department of Electrical Engineering, University of Engineering and Technology, Peshawar, Pakistan 25000, Email: naayaab.khaan@gmail.com.



### A. Wireless Sensing in IoT

The sensor network is the key to Internet of Things and big data support. Sensor networks require to transmit sensed data to sink or some central processing unit. The mote may send data to central processing unit directly if it is lying within mote wireless transmission range. Else, it may convey its acquired data indirectly via intermediate mote using multi hop transmission. Multiple ad-hoc routing protocols have been proposed in [8]. In all these ad-hoc routing protocols, it is assumed that all motes are active all the time. In IoT, motes are commonly in sleep mode instead of activity. It is employed for saving the scarce energy resource that is equally contrary to the research assumption in [8]. As mote communication modules work only in active state, it is essential for successful multi hop communication in network that all intermittently power motes are in active state. Therefore, intermittently powered motes communication protocols are being dealt further for their proper categorization.

### B. Synchronous and Asynchronous connectivity

The protocols are devised into synchronous and asynchronous communication protocols. Traffic Adaptive Medium Access Protocol (TRAMA) [9] and Lightweight Medium Access Protocol [LMAC] [10] are synchronous protocols. In synchronous protocol all motes communicate the control data signals. In asynchronous Intermittent Receiver-Driven Data Transmission (IRDT) [11] protocol, the mote delay its transmission for the next hop neighbor mote to be active without continuous transmission of control messages [11]. In Low Power Listening (LPL) [12] Protocols, motes wastes a significant amount of energy on communicating control messages. Thus it can be concluded that, in intermittently power mote communication protocols, the throughput and energy consumption are the figure of merits. The superficial sleep mode that is the key feature of a mote, in its advance transmission protocols that includes synchronous, asynchronous and event driven based radio switching protocols needs to be evaluated [10].

## III. EXPERIMENTAL SETUP

Low Power wireless network becoming essential part of our daily life. The figure of merit is power consumption of these devices, but measurement of power consumed by these mote is challenge. In Contiki operating system, Powertrace is network level power profiling module. The powertrace module can be used for both; simulation like cooja, and hardware. According to experimental results, it had been proved that their result is 94% accurate.

### A. Sensing Investigation depth

For in depth investigation of power consumption of wireless sensor mote at network level, powertrace is optimally best tool used in contik-3.0[13]. The skymote telosB module emulator is use in the experimental setup developed in contiki-3.0. The selectivity of telosB module is easy availability in market with low prices. Most of research community is using the above said hardware due to multiple flexibilities, but here its discussion is out of scope.

### a) Power trace

For in depth investigation of power consumption of wireless sensor mote at network level, powertrace is optimally best tool used in contik-3.0.

- ALL\_CPU: the amount of power consume in active mode of CPU.
- ALL\_TX: total number of ticks in transmit state.
- ALL\_RX: total number of ticks in receive state.
- ALL\_LPM: total number of ticks in Low Power mode.

$$E_c = \frac{\text{Energest Value} \times \text{Current} \times \text{Voltage}}{\text{RTIMERSECOND} \times \text{RunTime}} \quad (1)$$

Where  $E_c$  is referred to as the Energy consumed by node. Current & voltage are referred from data sheet solve an example.

$$\text{Duty Cycle} = \frac{\text{Energest\_TX} + \text{Energest\_RX}}{\text{Energest\_CPU} + \text{Energest\_LPM}} \quad (2)$$

Mesh networking and broadcast is most common practice for WSN network and especially for IoT base applications. Numbers of simulation were performed to identify the power profile of the motes in network. The number simulations were performed in cooja (contiki-3.0) by varying the number of motes and their topology.

The simulation time and code model (mote-programming) are kept same for ease in comparisons. The contiki-3.0 includes number of hardware emulators. I opted sky t-mote for simulation in contiki-3.0. T-mote sky [14] is low power sensor module. It can be used for various kind of sensor network application; like monitoring applications or may be for application prototyping. T-mote upgrade industrial standards by addition of USB and seamlessly interoperability with other devices. T-mote sky support multiple application of wireless mesh network and open source software movement in addition.

### b) Features

Dealing the structural and functional characteristics, ST M25P80 40MHz serial flash code memory is part of sky t-mote module as external memory for code storage. The flash memory are 16 segments, each having 64KB in size, shares SPI communication lines with CC2420 transceiver. Flash memory (48KB) is available for data and code storage in sky t-mote module. The flash or microcontroller are programmable when the voltage is at least 2.7volts.

### c) External Flash

ST M25P80 40MHz serial flash code memory is part of sky t-mote module as external memory for code storage. The flash memory are 16 segments, each having 64KB in size, shares SPI communication lines with CC2420 transceiver. Flash memory (48KB) is available for data and code storage in sky t-mote module. The flash or microcontroller are programmable when the voltage is at least 2.7volts. The mote can be used without battery module if it is connected to the computer via USB. The functioning voltage is 3 volts when USB is plugged in to computer. Table I has typical operating

conditions for operation of read/write and erase operation with external flash memory via communication with SPI share with the radio communication.

### B. Setup 01

In this simulation setup, wireless communication of sensor nodes are blocked. Only writing and reading of flash memory (available in T-mote sky module) are performed. The powertrace application is used for calculation of energy consumed by the mote for performing the above said activity. This is for the accurate measurement of energy consumed by flash operation only. In other words, it simplifying calculation by not considering all energy, i.e. energy consume by initialization of mote, consumed by motes except flash memory operation. The energy consumed by mote for writing/reading of flash memory is independent of network setup, number of nodes and communication protocols.

TABLE I. CHARACTERISTICS OF MOTES

Device characteristics	Minimum	Nominal	Maximum
Supply voltage during flash memory programming (v)	2.7	n.a.	3.6
Erase/Programming cycle (CPS)	n.a.	n.a.	100,000
Active Current (READ) (mA)	n.a.	n.a.	4
Active Current (WRITE/ERASE) (mA)	n.a.	n.a.	20
Standby Current (mA)	n.a.	8	50
Deep Power down Current (mA)	n.a.	1	10

### C. Setup 02

The objective of this setup is to analyze the energy consumed by nodes/motes (T-mote sky module) by wirelessly communicating with different nodes/motes. For wireless communication between motes, broadcast protocol is used. The number of nodes are different in different simulations. The position of nodes are random, but multiple nodes are in range with other multiple motes. The network is simulation for fifteen minutes. The simulation result may be analyzed against different parameters discussed in coming sections.

## IV. SIMULATION

The simulations are analyzed for the two setups studied. Each one is explained in detail as under.

### A. Setup 01

Table II collects the result of simulation of the writing & reading of flash memory of T-mote sky module. First column

represents time of call of powertrace application, Second energest and third one is just remarks regarding operations.

### a) Calculated Results

We have calculated the energy consume by sky t-mote by erasing, writing and reading of external flash memory in this section.

TABLE II. SIMULATION RESULTS OF READ/WRITE OPERATIONS

Time of Operation	CPU (Energest)	Remarks
00:05.702	2040	Just Before Operation
00:06.702	5665	Just After Operation

Consumption is 3588.25 m-Joule.

### b) Energy consumed by writing/Erasing

Writing to flash operation memory is accompanied by erasing the flash operation. Both operations withdraw 20-mA current. The calculation is performed at lowest, average and peak/maximum possible voltage level as shown in Table III.

TABLE III. CALCULATED RESULTS FOR ERASE/WRITE OPERATION

Energy parameters for the following Operations	Voltage (V)	Estimated Energy (mJ) @20mA Current
Maximum energy estimated for Writing Process	3.6 (max.)	3240
Average energy estimated for Writing Process	3.15 (avg.)	3240
Minimum energy estimated for Writing Process	2.7 (min.)	3240

### c) Energy consumed by Reading

The reading from flash memory withdraws current of 4-mA. The calculated results are represented in Table IV.

TABLE IV. CALCULATED ENERGY FOR READ OPERATION

Energy parameters for the following Operations	Voltage (V)	Estimated Energy (mJ) @20mA Current
Maximum energy estimated for Reading Process	3.6 (max.)	648
Average energy estimated for Reading Process	3.15 (avg.)	567
Minimum energy estimated for Reading Process	2.7 (min.)	486

## B. Setup 02

These simulations were performed by varying the number of nodes from 2 to 15 nodes. To differentiate between multiple results, the topic name of simulation result is same to the number of node in simulation.

### a) 2 Nodes simulation

This simulation consists of two nodes connecting with radio link. The total, CPU, LPM (Low Power Mode), transmit and receive are represented categorically in Table V.

TABLE V. SIMULATION RESULTS OF 2 NODE SIMULATION

Node Sr. No.	Total	CPU	LPM	Transmit	Recieve
Node ID 1	63.8645	3.618681	0.18556	35.18578	24.87449
Node ID 2	63.4126	3.606071	0.185601	34.82958	24.79135
Average	63.6385	3.612376	0.185581	35.00768	24.83292

### b) 3 Nodes simulation

The total, CPU, LPM (Low Power Mode), transmit and receive are represented for 3 nodes connecting on radio link in broadcast in Table VI.

TABLE VI. SIMULATION RESULTS OF 3 NODE SIMULATION

Node Sr. No.	Total	CPU	LPM	Transmit	Recieve
Node ID 1	63.86259	3.618996	0.185559	35.18992	24.86812
Node ID 2	66.03793	3.661529	0.185416	34.8342	27.35679
Node ID 3	65.42726	3.674218	0.185375	36.59353	24.97414
Average	65.10926	3.651581	0.18545	35.53922	25.73302

### c) 4 Nodes simulation

The total, CPU, LPM (Low Power Mode), transmit and receive are represented for 4 nodes connecting on radio link in broadcast in Table VII.

TABLE VII. SIMULATION RESULTS OF 4 NODE SIMULATION

Node Sr. No.	Total	CPU	LPM	Transmit	Recieve
Node ID 1	65.68992	3.671949	0.185413	35.19359	26.63897
Node ID 2	68.15268	3.701087	0.185316	34.48443	29.78185
Node ID 3	67.46985	3.714494	0.185272	36.24993	27.32016
Node ID 4	68.92565	3.726176	0.185232	35.1971	29.81714
Average	67.55953	3.703427	0.185308	35.28126	28.38953

### d) 5 Nodes simulation

The total, CPU, LPM (Low Power Mode), transmit and receive are represented for 5 nodes connecting on radio link in broadcast in Table VIII.

### e) 10 Nodes simulation

The total, CPU, LPM (Low Power Mode), transmit and receive are represented for 10 nodes connecting on radio link in broadcast in Table IX.

TABLE VIII. SIMULATION RESULTS OF 5-NODES SIMULATION

Node Sr. No.	Total	CPU	LPM	Transmit	Recieve
Node ID 1	66.24095	3.670813	0.185386	35.18769	27.19706
Node ID 2	70.88756	3.749253	0.185123	34.48118	32.472
Node ID 3	70.20857	3.770689	0.185053	36.24386	30.00897
Node ID 4	68.13719	3.721932	0.185215	35.19008	29.03997
Node ID 5	68.28231	3.740555	0.185154	36.94972	27.40688
Average	68.75132	3.730648	0.185186	35.61051	29.22498

TABLE IX. SIMULATION RESULTS OF 10 NODE SIMULATION

Node Sr. No.	Total	CPU	LPM	Transmit	Recieve
Node ID 1	74.73757	3.858749	0.184759	36.24545	34.44861
Node ID 2	83.24769	4.011763	0.184248	34.48246	44.56922
Node ID 3	77.56841	3.907865	0.184596	36.24003	37.23591
Node ID 4	73.50033	3.811742	0.184915	34.83802	34.66566
Node ID 5	71.406	3.802726	0.184946	37.29541	30.12292
Node ID 6	75.63848	3.846006	0.184801	34.46987	37.1378
Node ID 7	77.73977	3.885067	0.184671	34.13805	39.53198
Node ID 8	70.99896	3.766749	0.185065	35.14452	31.90263
Node ID 9	71.249991	3.756918	0.185099	34.831329	32.476644
Node ID 10	74.86302	3.845238	0.184786	35.89642	34.93657
Average	73.38383	3.849282	5.706466	32.0091	31.81899

### f) 15 Nodes simulation

The total, CPU, LPM (Low Power Mode), transmit and receive are represented for 15 nodes connecting on radio link in broadcast in Table X..

TABLE X. SIMULATION RESULTS OF 15 NODE SIMULATION

Node Sr. No.	Total	CPU	LPM	Transmit	Recieve
Node ID 1	79.31705	3.928555	0.184527	35.53688	39.66709
Node ID 2	90.22996	4.166287	0.183733	34.84025	51.03969
Node ID 3	86.88806	4.089647	0.183989	35.50215	47.11228
Node ID 4	79.02398	3.916029	0.184568	35.18864	39.73474
Node ID 5	75.6609	3.883756	0.184676	36.94351	34.64896
Node ID 6	82.34139	3.996052	0.184301	35.87842	42.28262
Node ID 7	87.35558	4.089152	0.18399	34.4815	48.60094
Node ID 8	78.4809	3.896004	0.184635	35.18498	39.21528
Node ID 9	73.12847	3.780901	0.185019	34.83786	34.32469
Node ID 10	85.21528	4.16158	0.193602	37.29382	43.56628
Node ID 11	88.26998	4.118981	0.18385	35.491	48.47615
Node ID 12	79.34961	3.93306	0.184484	35.52573	39.70634
Node ID 13	83.73351	4.001418	0.184251	35.19549	44.35235
Node ID 14	68.83757	3.709518	0.185245	35.18737	29.75544
Node ID 15	70.41201	3.724667	0.185189	34.12706	32.37509
Average	80.54962	3.959707	0.185071	35.41431	40.99053

## V. RESULTS AND ANALYSIS

Results for Setup 01 and setup 02 are tabulated and explained in the coming sections.

### A. Results of Total energy consumed by complete process for Setup 01

As the simulation time is one second, therefore these simulated results and calculated results are comparable. The comparison of calculated and simulated results are available in Table XI. The table also shows the difference in results in last column. The correlation between the calculated and simulation result is more than 94%.

TABLE XI. COMPARITIVE ANALYSIS

Energy Parameter	Voltage (Volts)	Estimated Energy (mJ)	Simulation Results	Difference (%)
Total Maximum Energy Estimated for Process	3.6 (max)	3888	4110	5.4
Total Average Energy Estimated for Process	3.15 (avg)	3402	3425	5.5
Total Minimum Energy Estimated for Process	2.7 (min)	2916	3083	5.4

### B. Results of Total energy consumed by complete process for Setup 02

Energy profile of the nodes that are the part of simulation in setup 02 are given by Table XII. These values are the average of 600 simulations, each with variable data of transmission and reception.

### C. Observations

The observation noted are given underneath.

- As the number of motes increase, the total energy consumption of each motes increase.
- The energy consumption of motes in Low power mode and transmit columns are almost the same. Transmission of packet were define at constant periodic period.
- The energy consumption of motes by receiving packet shows significant increase because the motes are expected to receive more numbers of packets as the network density increases.
- The mote's CPU spend more energy in process of receiving more packet as network population increase.

## VI. DISCUSSION

The research summarizes the fact that IoT and sensory network are indeed a great way to communicate chunks of information without wasting a large amount of energy if such discharge based nodes are used. We have used motes of difference capacitances in order to find out the transmission

rate and modes of communication. Based on the continuation/resuming of data transmission, the transmission schemes have been devised into three kinds that are; resume and restart, reboot and go to sleep mode and resume. The energy calculation of information exchange is calculated in mJ. The undergone application uses a fixed amount of energy for each restart which suggested that, in order to communicate between these low energy communicating motes, one must reduce the number of restarts instead writing different codes for already developed application.

The second option is also unique in which we use a resuming mechanism. The resuming mechanism are then devised into two broader types. The first one comprises of OS sleep methods. The application (tiny OS) that is being run on the mote, goes to a power saving mode and the transmission is intermitted. It reduces the energy consumption in the sense that each restart must use energy besides cutting energy from the same reservoir for information exchange. The second option also uses external flash/ROM in order to keep the present state and upon power up the module, all the data is recovered from the ROM. This facility allows the motes to overcome the reboot energy by saving the state of the OS. Such phenomenon can be seen while an operating system is hibernated.

## CONCLUSION

The research conducted acknowledges the resuming mechanism to be more effective. The resuming the motes in internet of things is more advanced and motes uses it instead of restarting or rebooting the whole processing node. As discussed earlier, the resuming requires a fixed amount of energy just to keep the RAM alive after going to hibernating period. This idle state is used mainly due to two reasons. The first one is, when no information is available for reception and transmission. In that case, saving and accumulating energy is done by this built-in standby option. Secondly, during transmission, when the threshold is reached and no further bits are supported by the mote for both transmission and reception, in such case, the mote must go to its standby state to avoid the restarting and rebooting.

Quantifying the methods of resuming transmission without more delays is the key point of research likewise. In the Table XII, it is clear that reading from flash memory require 2.19 micro Joule and Writing to and reading from flash require 13.1-mJ. The amount of energy 309-nJ and 6-mJ is enough for the mote to keep them alive for one second time (sufficient time for IOT motes) in Low Power (LPM) mode and in CPU (Not LPM, but No wireless communication) respectively. Hence, restarting or rebooting motes, which will read network status after each restart/reboot, consume more energy and causing delay in sending packets.

These emulated research facilitates the user to avoid delays due to waiting for charging pulses. Hence it is of greater usage and will benefit the research community and the user of intermitted nodes based wireless networking platforms.

## FUTURE AND MODIFICATIONS

Such leading edge researches are, as mentioned earlier, of greater value to both researcher community and the end user or network employers. We can extrapolate the research by embedding the ROM internally rather externally connecting it to the transmitter/receptor circuitry. That is actually an advancement with respect to the mote's manufacturing. The research can further be furnished if we compare the

transmission schemes and other options concerning these motes that may include number of motes, protocols for transmission, packet stream arguments, communication channel particulars, reserved energy quantity, node mobility etc.

The future work may comprise of the above point but is not limited to it. Hence there is a great research and development area waiting for us to explore in IoT and intermitted nodal connectivity in scarce environments.

TABLE XII. SUMMARY OF NODE SIMULATION IN CONTIKI-3.0

Node Nos.	Total	CPU	LPM	Transmit	Recieve
2-Nodes	63.63855	3.612376	0.185581	35.00768	24.83292
3-Nodes	65.10926	3.651581	0.18545	35.53922	25.73302
4-Nodes	67.55953	3.703427	0.185308	35.28126	28.38953
5-Nodes	68.75132	3.730648	0.185186	35.61051	29.22498
10-Nodes	75.0950221	3.8492823	0.1847886	35.35815	35.7027944
15-Nodes	80.54962	3.959707	0.185071	35.41431	40.99053

## REFERENCES

- [1] Veen, "BLISP: Enhancing backscatter radio with active radio for computational RFIDs," Master's thesis, TU Delft, 2015.
- [2] Y. Yang, L. Wang, D. K. Noh, H. K. Le, and T. F. Abdelzaher, "Enhancing data reliability in solar-powered storage-centric sensor networks". In Proc. 7th Annual Int'l Conference on Mobile Systems, Applications, and Services (MobiSys-09), pages 333-346, ACM, 2009.
- [3] P. D. Mitcheson et al., "Energy Harvesting From Human and Machine Motion for Wireless Electronic Devices," Proc. IEEE, vol. 96, no. 9, pp.1457-1486, Sept. 2008.
- [4] M. R. Mhetre et al., "Micro energy harvesting for biomedical applications: A review," Proc. ICECT 2011, vol. 3, pp. 1-5, 8-10 April 2011.
- [5] B. Ransford et al., "Mementos: System Support for Long-Running Computation on RFID-Scale Devices," ASPLOS11, Newport Beach, CA, USA, Mar. 5-11, 2011.
- [6] P. A. Bernstein et al., "Concurrency Control and Recovery in Database Systems," Addison-Wesley Longman Publishing, Boston, USA 1987.
- [7] Rose Yu, Thomas Whetteyne "Reliable, Low Power Wireless sensor networks for Internet of Things: Making Wireless Sensor as Accessible as Web Server".
- [8] C. E. Perkins, "Ad Hoc Networking," Addison-Wesley, 2001.
- [9] V. Rajendran, K. Obraczka, and J. J. Garacia-Luna-Aceves, "Energy-Efficient Collision-Free Medium Access Control for Wireless Sensor Networks," Proceedings of the 1st ACM International Conference on Embedded Networked Sensor Systems, 2003, pp. 181-192.
- [10] J. L. F. W. Hoesel and P. J. M. Havinga, "A Lightweight Medium Access Protocol for Wireless Sensor Networks," Proceedings of the 1st International Conference on Networked Sensing Systems, 2004, pp. 205-208.
- [11] T. Hatauchi, Y. Fukuyama, M. Ishii, and T. Shikura, "A Power Efficient Access Method by Polling for Wireless Mesh Network," Transactions of IEEJ, Vol. C-128, No. 12, 2008, pp. 1761-1766.
- [12] R. Jurdak, P. Baldi, and C. V. Lopes, "Adaptive Low Power Listening for Wireless Sensor Networks," IEEE Transaction on Mobile Computing, Vol. 6, No. 8, 2007, pp. 988-1004.
- [13] Anuj Sehgal, "Using the Contiki Cooja Simulator".
- [14] Texas Instrument Inc CC2420 Datasheet. Available on: <http://www.ti.com/>



Ahmad majorly works in the field of ICT.



development of smart cities. Jawad is supervising final year undergrad student projects on power utilization, renewable energy and wireless communications.



Communication Networks, ICT and Algorithm development. Durre Nayab has also developed forecasting model based on plastic Cartesian Genetic Programming.



Engineering, ICT and graph theory. His research work is taken as base for future endeavors.



# Design of Optimal Linear Quadratic Gaussian (LQG) Controller for Load Frequency Control (LFC) using Genetic Algorithm (G.A) in Power System

Muddasar Ali, Syeda Tahreem Zahra, Khadija Jalal, Ayesha Saddiqa, Muhammad Faisal Hayat

**Abstract**—Nowadays power demand is increasing continuously and the biggest challenge for the power system is to provide good quality of power to the consumer under changing load conditions. When real power changes, system frequency gets affected while reactive power is dependent on variation in voltage value. For satisfactory operation the frequency of power system should be kept near constant value. Many techniques have been proposed to obtain constant value of frequency and to overcome any deviations. The Load Frequency Control (LFC) is used to restore the balance between load and generation by means of speed control. The main goal of LFC is to minimize the frequency deviations to zero. LFC incorporates an appropriate control system which is having the capability to bring the frequency of the Power system back to original set point values or very near to set point values effectively after the load change. This can be achieved by using a conventional controller like PID but the conventional controller is very slow in operation. Modern and optimal controllers are much faster and they also give better output response than conventional controllers. Linear Quadratic Regulator (LQR) is an advanced control technique in feedback control systems. It's a control strategy based on minimizing a quadratic performance index. In despite of good results obtained from this method, the control design is not a straight forward task due to the trial and error involved in the selection of weight matrices Q and R. In this case, it may be hard to tune the controller parameters to obtain the optimal behaviour of the system. The difficulty to determine the weight matrices Q and R in LQR controller is solved using Genetic Algorithm (G.A). In this research Paper, G.A based LQG controller which is the combination of LQR and Kalman Filter is feedback in LFC using MATLAB/SIMULINK software

package. Reduction in frequency deviations and settling time was successfully achieved by using LQG Controller with LFC based on G.A.

**Keywords**— Load Frequency Control, Linear Quadratic Regulator, Linear Quadratic Gaussian, Kalman Filter, Genetic Algorithm.

## I. INTRODUCTION

Natural energy is converted into electrical energy using electrical power system. It is necessary to guarantee the quality of electrical power for the optimization of electrical equipment. The active and reactive power balance must be maintained during transmission, generation and utilization. The demand for a good quality electrical power system is to maintain the voltage and frequency at the desired value regardless of the changes in loads that occurs randomly. It is impossible to maintain the active and reactive power at desired values without use of control system, which results in variations of voltage and frequency levels. Active and reactive powers have a combined effect on frequency and voltage. The frequency depends largely on the active power and the voltage on reactive power. To overcome the effects of load variation and maintain frequency and constant voltage level, a control system is required. Frequency deviation can affect the stability of the system so, in order to maintain system stability imbalances between load and generation must be corrected in seconds to avoid frequency deviation. The problem of controlling the frequency in large power systems is by adjusting the production of generating units in response to changes in the load which is called Load Frequency Control (LFC). LFC is a very important issue in power system operation and control for supplying sufficient and reliable electric power with good quality. The electric power system becomes more and more complicated with an increasing demand. The power system is subjected to local variations of load in random magnitude and duration. As the load varies, the frequency related to that area is affected. Frequency transients should be removed as soon as possible. Generators working in that control area always vary their speed (accelerate or decelerate) to maintain the frequency and relative power angle to the predefined values with tolerance limit in static and dynamic conditions [1]. Electrical Power is generated by converting mechanical into electrical energy. The rotor which consists of turbine and generator units stored kinetic energy due to its rotation. This stored kinetic energy accounts for sudden increase in the load. Now consider the

Muddasar Ali: Lecturer & Researcher, Faculty of Electrical Engineering, Wah Engineering College (WEC), University of Wah, Pakistan. Email:muddasar.ali275@gmail.com, Cell: +92-332-5417228

Syeda Tahreem Zahra: Electrical Engineer & Researcher, Department of Electrical Engineering, University of Engineering & Technology (U.E.T), Taxila, Pakistan.

Khadija Jalal: Lecturer & Electrical Engineer, Faculty of Electrical Engineering, Army Public College of Management & Science (APCOMS), Rawalpindi, Pakistan.

Ayesha Saddiqa: Lab Engineer & MSc Scholar, Faculty of Electrical Engineering, Army Public College of Management & Science (APCOMS), Rawalpindi, Pakistan.

Muhammad Faisal Hayat: Lab Engineer & MSc Scholar, Faculty of Electrical Engineering, Wah Engineering College (WEC), University of Wah, Pakistan.



input of mechanical torque by  $T_m$  and the electric output torque by  $T_e$ . Disregarding the rotational losses, a generating unit is operating in steady state at constant speed. The difference between these two elements of torque is zero. In this case we say that the accelerating torque is zero.

$$T_a = T_m - T_e \quad (1)$$

When power demand increases suddenly, the electric torque increases. However,  $T_m$  remains constant without any feedback control mechanism to alter mechanical torque. Therefore, as a result, the accelerating torque becomes negative causing a deceleration of the mass of rotor. As the rotor decelerates kinetic energy is released to supply the increase in load. During this time the frequency of the system, which is proportional to the rotor speed also decreases. The deviations of the frequency from its nominal value of 50 or 60 Hz is indicative of the imbalance between  $T_m$  and  $T_e$ . The frequency decreases when  $T_m < T_e$  and rises when  $T_m > T_e$ . The frequency must remain almost constant for satisfactory operation of the power system. Frequency deviations can directly impact power system performance, system reliability and efficiency [5]. Large frequency deviations can damage equipments and degrade load performance. Overloading can ultimately lead to a system collapse. Variation in frequency adversely affects the operation and speed control of induction and synchronous motors. Several control strategies have been proposed and investigated by several researchers for the design of LFC in power systems. Many classical approaches have been used to provide a supplementary control that will drive the frequency to the normal operating value within a very short time [9]. This extensive research is due to the fact that LFC is an important function of the power system, where the main objective is to maintain frequency fluctuations within preset limits. LFC incorporates an appropriate control system that has the ability to re-adjust the power system frequency to original set point values or very close to set point values effectively after the load change [2].

## II. BRIEF LITERATURE REVIEW

Pradipkumar Prajapati has presented various conventional controllers for Multi-Area LFC in the power system. A comparison was made between PID controller and PI controller with battery storage system in terms of frequency deviations and settling time for 2-area LFC. Simulation results showed that the PID controller with battery outperformed the PI controller in terms of less frequency deviation and settling time [1]. Gajendra Singh Thakur used PI and PID controller to solve the LFC problem of single area power system. The simulation results show that the PID controller performs better than the PI controller because it reduces settling time with less overshoot. PID with a simple focus can provide better performance compared to the conventional PI controller. The results of the simulation show the superior performance of the system using the Z-N tuned PID controller. [2].

Mohinder Pal used the PI controller for LFC in the power system. It is seen that PI Controller results in a stable frequency. With appropriate choice of control parameters, frequency deviations can be effectively controlled. Due to

disturbances in the power system frequency deviates. To overcome this problem PI controller is used [3]. Mohammed Wadi presents the analysis of an optimal LQR controller and the Legendre Wavelet function. A comparison was made between an optimal LQR controller and an optimal controller based on the Legendre Wavelet function in terms of performance in single area power systems. The results of the simulation showed that the optimal controller based on the method of approximation of the Legendre wavelet function surpassed the LQR controller in terms of less frequency deviation and steady state error, while both had the same settling time. A numerical example demonstrated the effectiveness of the optimal control proposed through the Legendre Wavelets Function over the LQR controller [4]. Divya has presented the hydro-power system simulation model. He has taken an assumption of same frequencies of all areas, to overcome the difficulties of extending the traditional approach. His model was obtained by ignoring the difference in frequencies between the control areas [11]. The concept of optimal control for LFC of in power system was first started by Elgerd. [17] R. K. Green discussed a new formulation of the principles of LFC. He has given a concept of LFC, directly controlling the set point frequency of each unit [18]. Fosha and Elgerd [17] were first presented their work on LFC using optimal process. A power system of two areas was considered for investigation. R. K. Cavin has considered the problem of LFC using optimal stochastic system point of view. An algorithm based on control strategy was developed which gives improvised performance of power system. The special attractive feature of the control scheme was that it required the recently used variables [20].

## III. LOAD FREQUENCY CONTROL

In large electrical power systems, nominal frequency depends significantly on the balance of produced and consumed active power. Peak demands do not have any certain time so, they can occur in power system at any random time of the day. When the active power imbalance occurs in any part of the system this will result in changes in the overall system frequency. If there is an abrupt change in load in control area of the power system then there will be a frequency deviation. The generators in a control area always vary their speed together (accelerate or slow) to maintain the frequency at predefined values with a tolerance limit under both static and dynamic conditions. The main LFC is to keep the frequency constant by means of the speed control. The industrial loads connected to the power supply system are very sensitive to the quality of electrical energy mainly the frequency component. Thus, the steady-state frequency error in the system must remain within acceptable values in order to maintain the equilibrium. Possible increase in load reduces the nominal frequency of the system. This frequency alternation is detected by a regulator in the primary control loop. Thereafter, the speed of rotation of the turbine increases, resulting in an increase in the power produced. Frequency deviations can directly impact power system operation, system reliability and efficiency [6]. Large frequency deviations can damage

equipments, overload transmission lines, degrade load performance and adversely affect the performance of system protection schemes.

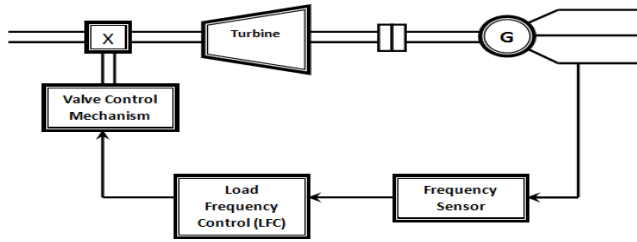


Figure 1. Example Block Diagram of LFC in Power system [8].

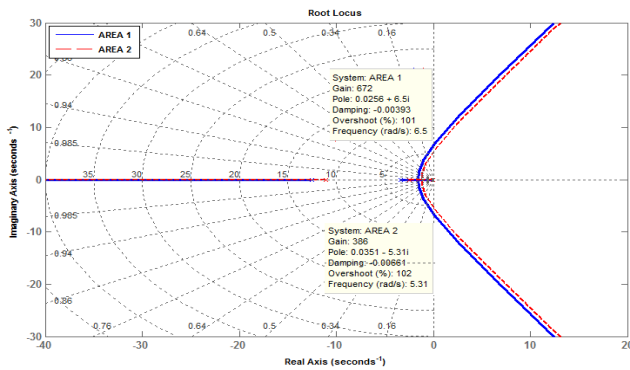


Figure 2. Root Locus of LFC in Power System

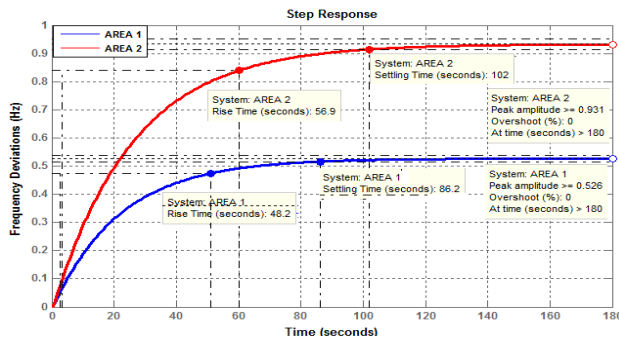


Figure 3. Open Loop Step Response of LFC in Power system

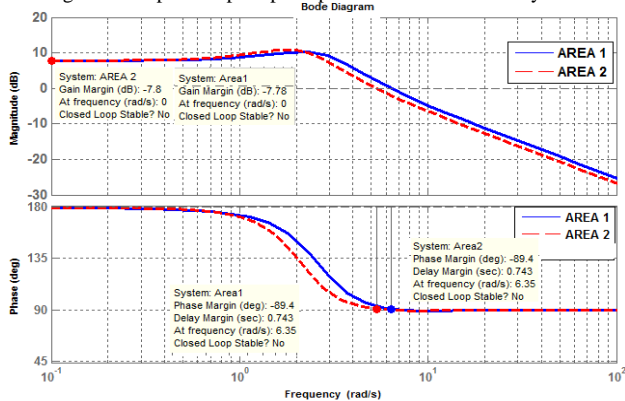


Figure 4. Bode Plot of LFC in Power system

These large-frequency deviation events can ultimately lead to a system collapse. The frequency variation adversely affects the operation and speed control of induction and synchronous

motors. In household appliances refrigerator's efficiency decreases, reactive power consumption of television and air conditioners increases considerably with reduction in power supply frequency. It is very important to keep the frequency within an acceptable range. Due to the dynamic nature of the load, the continuous load change cannot be avoided but the system frequency can be maintained within sufficiently small tolerance levels by continuously adjusting the generation using LFC [4].

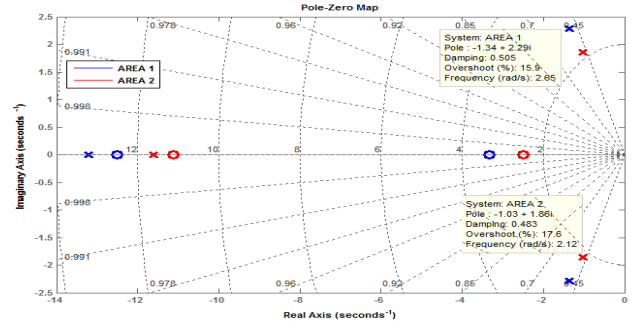


Figure 5. Pole Zero Mapping of LFC in Power system

#### IV. LINEAR QUADRATIC REGULATOR

This is a technique applied in the design of the control system that is implemented by minimizing the performance index of the system variables. Here, we discussed the design of optimal controllers for linear systems with quadratic performance index, also called LQR controller. The aim of the optimal regulator design is to obtain a control law  $u^*(x, t)$  which can move the system from its initial state to the final state by minimizing the Performance Index. The Performance Index is selected to give a best trade-off between performance and cost of control. The Performance Index which is widely used is the Quadratic Performance Index and is based on minimum error and minimum energy criteria [9].

Consider a plant:

$$\dot{X}(t) = Ax(t) + Bu(t) \quad (2)$$

The aim is to find the Vector K of the control law,

$$U(t) = -Kx(t) \quad (3)$$

It minimizes the value of the Quadratic Performance Index J of the form,

$$J = \int_{t_0}^t (x^T Q x + u^T R u) dt \quad (4)$$

Where Q is a positive semi definite matrix and R is real symmetric matrix. The choice of the elements of Q and R allows the relative weighting of individual state variables and individual control inputs.

To obtain the solution we make use of the method of Langrange Multipliers. The problem reduces to the minimization of the following unconstrained equation, [9]

$$L[x, \lambda, u, t] = [x^T Q x + u^T R u] + \lambda^T [Ax + Bu - \dot{X}] \quad (5)$$

The optimal values are found by equating the partial derivative to zero.

$$\frac{dL}{d\lambda} = AX^* + BU^* - \dot{X}^* = 0 \quad , \quad X^* = AX^* + BU^* \quad (6)$$

$$\frac{dL}{du} = 2RU^* + \lambda^T B = 0 \quad , \quad U^* = \frac{-1}{2} R^{-1} \lambda^T B \quad (7)$$

$$\frac{dL}{dx} = 2x^T Q + \lambda^T + \lambda^T A = 0 \quad , \quad \dot{\lambda} = -2Q\dot{X}^* - A^T \lambda \quad (8)$$

Assume that there exists a symmetric, time varying positive definite matrix  $P(t)$  satisfying,

$$\dot{\lambda} = 2P(t) X^* \quad (9)$$

Substituting (3) into (7) gives the optimal closed-loop control law,

$$U^*(t) = -R^{-1}B^T P(t) X^* \quad (10)$$

Where,

$$K = R^{-1}B^T P$$

Obtaining the derivative of (9),

$$\dot{\lambda} = 2(\dot{P} X^* + P\dot{X}^*) \quad (11)$$

From (8) and (11), we obtained

$$P(t) = -P(t)A - A^T P(t) - Q + P(t)B R^{-1}B^T P \quad (12)$$

The above equation is referred to as Matrix Riccati Equation. For linear time invariant systems, since  $\dot{P}=0$ , when the process is of infinite duration  $t_f \rightarrow \infty$  (12) becomes,

$$PA + A^T P + Q - P B R^{-1} B^T P = 0 \quad (13)$$

One approach to find a controller that minimize the LQR cost function is based on finding the solution of above Algebraic Riccati Equation (ARE). The property of LQR controller is that it guarantees nominally stable closed-loop system. The MATLAB can be used for the solution of the Algebraic Riccati Equation. Choosing the weight matrices  $Q$  and  $R$  usually involves some kind of trial and error and they are usually chosen as diagonal matrices. In despite of the good results obtained from this method, the control design is not a straight forward task due to the trial and error method involved in the definition of weight matrices  $Q$  and  $R$  [8].

The solution of LQR results in an asymptotically stable closed-loop system if,

The system  $(A, B)$  is controllable.

$R > 0$

$Q = C^T C$  Where  $(C, A)$  is observable.

The LQR design procedure is in stark contrast to classical control design, where the gain matrix  $K$  is selected directly. To design the optimal LQR, the design engineer first selects the design parameters weight matrices  $Q$  and  $R$ . Then, the loop time response is found by simulation. If this response is unsuitable, new values of  $Q$  and  $R$  are selected and design is repeated [9]

Classically the weight matrices  $Q$  &  $R$  can be written as, [9]

$$Q = C^T C \quad , \quad R = 1 \quad (14)$$

The MATLAB code is written in MATLAB-R2011. The MATLAB command to obtained feedback K-Matrix is given as, [8]

$$[K, P] = \text{lqr2}(A, B, Q, R) \quad (15)$$

The optimal gain vector  $K$  for Area 1 & Area 2 in Power system for LFC is obtained by using (15),

Feedback K-Matrix for Area 1= $K_1 = [-0.0861 \ -0.5078 \ -0.9094]$

Feedback K-Matrix for Area 2= $K_2 = [-0.0771 \ -0.5292 \ -0.9146]$

## V. KALMAN FILTER

To fully implement the advantage of state feedback, all the states should be feedback. Typically the physical state of the system cannot be determined by direct observation. A state observer is a system that provides an estimate of the internal state of a system, from the measurements of the input and output of the system. If a system is observable then it is possible to design the system from its output measurements, using the state observer commonly known as Kalman Filter. It is based upon a measurement of the output given by (16) & (17) and known input  $U$ . This observer is guaranteed to be optimal in the presence of estimated states. The state estimation problem is given by [9].

$$\dot{X}(t) = A x(t) + B u(t) + \omega \quad (16)$$

$$Y(t) = C x(t) + D u(t) + v \quad (17)$$

Where,

$A, B, C$  are the plant's state coefficient matrices.

$\omega$  is the input-process noise vector.

$v$  is the output-measurement noise vector.

The optimal observer (Kalman Filter) is given by,

$$\hat{X}(t) = A \hat{x} + B u + L (Y - C\hat{x}) \quad (18)$$

Where  $\hat{X}$  is the estimate of state  $x$  and  $L$  is the gain of Kalman Filter. The observer gain is computed as,

$$L = S C^T Z^{-1} \quad (19)$$

Kalman filter is an optimal observer, the problem of Kalman filter is solved using Algebraic Riccati Equation as, [5]

$$AS + SA^T - SC^T V^{-1} CS + B \omega B^T = 0 \quad (20)$$

Eq. (20) is very similar to the LQR solution known as Riccati Equation. The  $\omega$  and  $v$  represent the intensity of the process and sensor noise input and it can be selected by the user. These matrices are known as co-variance matrices. Their size is a measure of how strong the noise is; the larger the size, the more random or intense the noise hence it is called the noise intensity. Finally the mathematical condition for the design of Kalman Filter is that the matrices  $\omega$  and  $v$  are positive semi definite and the system must be observable [9].

The Kalman gain matrix  $L$  is calculated with  $\omega$  and  $v$  matrices as follows, [5]

$$\omega = 10 B^T B \quad (21)$$

$$v = 0.01 C C^T \quad (22)$$

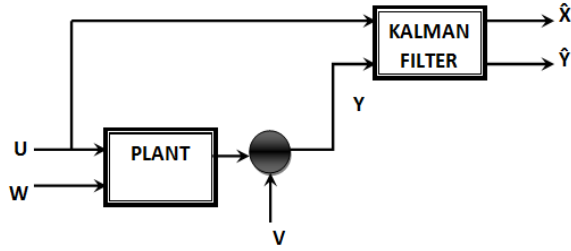


Figure 6. Block Diagram of Kalman Filter for LFC [9].

The MATLAB code is written in MATLAB-R2011. The Algebraic Riccati Equation can be solved using the specialized Kalman Filter MATLAB Command lqe. The MATLAB command to obtain observer gain L of Kalman Filter which is given by [5],

$$[L, S] = lqe(A, B, C, \omega, v) \quad (23)$$

Where,

L is the returned Kalman filter optimal gain.

S is the returned solution to the Algebraic Riccati Equation.

The observer gain L of Kalman Filter for Area 1 & Area 2 in Power system for LFC is obtained by using (23),

$$\text{Observer L-Gain of Kalman Filter for Area}_1=L_1=\begin{bmatrix} -4.9329 \\ -0.0162 \\ 939.230 \end{bmatrix} \quad (24)$$

$$\text{Observer L-Gain of Kalman Filter for Area}_2=L_2=\begin{bmatrix} -4.366 \\ -0.0150 \\ 673.4705 \end{bmatrix} \quad (25)$$

## VI. LINEAR QUADRATIC GAUSSIAN CONTROLLER

LQR controller and Kalman Filter were designed separately for LFC in the power system. First LQR controller is designed which is the cause of minimization of the quadratic objective function. Kalman Filter (State Estimator) is then introduced for LFC with presence of noise process  $\omega$  and measurement noise  $v$ . The combination of LQR with the Kalman Filter forms an optimal compensator which is called as LQG Controller. The optimal compensator design process is the following, [5]

- Design an optimal regulator (LQR) for a linear plant using full-state feedback. The regulator is designed to generate a control input  $U(t)$ , based upon the measured state-vector  $X$ .
- Design Kalman Filter for the plant assuming a known control input  $U(t)$  a measured output  $Y(t)$  including noises  $\omega$  &  $v$ .
- Combine the separately designed LQR controller and Kalman Filter into an optimal compensator that generates the input vector  $U(t)$ , based upon the

estimated state-vector  $\hat{X}$  rather than the actual state vector  $X$ , and the measured output  $Y(t)$ .

The plant equation and the problem solution is now repeated,

$$\dot{X}(t) = A x(t) + B u(t) + \omega \quad (26)$$

$$Y(t) = C x(t) + v \quad (27)$$

The Control-Law of LQR is now given by,

$$U(t) = -K \hat{X}(t) \quad (28)$$

The state-space equation of Kalman Filter is given by,

$$\dot{\hat{X}}(t) = A \hat{X} + Bu + L(Y - C\hat{X}) \quad (29)$$

By putting (28) of LQR controller in (29) of Kalman Filter, the state-space equation of LQG Controller is given by,

$$\dot{\hat{X}}(t) = (A - B K - L C + L D K) \hat{X} + LY \quad (30)$$

Where,

K & L are the optimal regulator and Kalman Filter gain.

$\hat{X}$  Is the estimated state vector.

Fig. 7 shows the block diagram of Eq. (30) of optimal LQG-compensator,

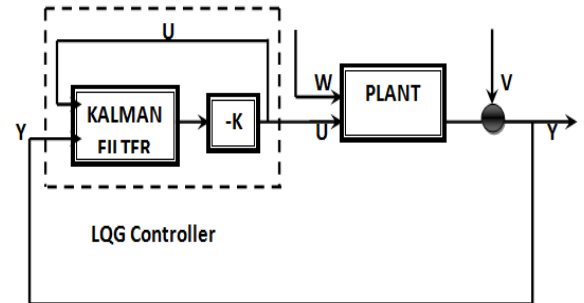


Figure 7. Block Diagram of LQG Controller for LFC [9]

Using MATLAB software, a state-space model of the closed-loop system can be constructed as follows, [5]

$$\text{Sysp} = ss(A, B, C, D); \quad (31)$$

$$\text{Sysc} = ss(A - B * K - L * C + L * D * K, L, K, \text{zeros}(\text{size}(D'))); \quad (32)$$

$$\text{Syscl} = \text{feedback}(\text{syp}, \text{sysc}); \quad (33)$$

Where,

Sysp = State-space model of the plant (LFC).

Sysc = State-space model of the LQG compensator.

Syscl = State-space model of the closed loop (Feedback) system.

## VII. GENETIC ALGORITHM

G.A is a search algorithms based on the mechanics of natural selection and natural genetics. It was invented in 1975 by John Holland at University of Michigan [23]. The G.A starts with no knowledge of the correct solution and depends

on response from its environment and evolution operators to arrive at the best solution. By starting at several independent points and searching in parallel, the algorithm avoids local minima and converging to optimal solutions. In this way, G.A has been shown to be capable of locating high performance areas in complex domains without experiencing the difficulties associated with high dimensionality. G.A is typically initialized with a random population. This population is usually represented by a real valued number or a binary string called a chromosome. The algorithm starts with a random population of individuals (chromosomes) and through genetic processes similar to those occurring in nature, evolve under specified rules in order to minimize a cost function. Since, the population is generated randomly the G.A is able to virtually search the entire solution space and provide simultaneous searches at different points in this space. During the algorithm execution the chromosomes that possess the best fitness (lowest cost) generate offspring and improving the average cost value of the population as a whole [12].

In LQG problem, the weighting matrices Q and R have profound effect on controller performance. On the other hand, finding the best Q and R needs many computer simulation and trial and errors, which are very time-consuming. Thus using intelligent optimization methods for finding Q and R is more effective [13]. The G.A objective here is to determine matrices Q and R so that LFC presents small overshoot and less settling time in the event of a load disturbance. For this, each chromosome is composed by the genetic structure defined in Table 1. The weight matrixes Q and R are generally used in the form of a diagonal matrix. They can be optimize by using the following representation, [21].

$$Q_w^{G.A} = \begin{bmatrix} q_{11} & 0 & 0 \\ 0 & q_{22} & 0 \\ 0 & 0 & q_{33} \end{bmatrix}, \quad R_w^{G.A} = q_{44} \quad (34)$$

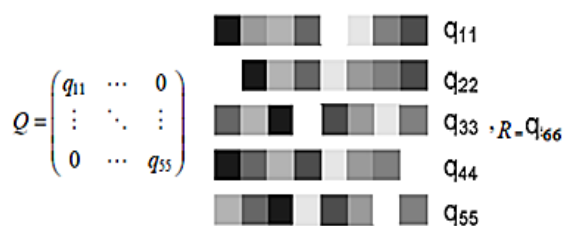


Figure 8. Chromosomal Representation of Q and R Matrices [13].

G.A is universally applicable, because they need only a good fitness function to work which is a requirement for any optimization technique so; objective function is the most important part of G.A [23]. An objective function is created to find a weight matrices Q and R for LQG controller that gives the smallest overshoot and quickest settling time. Each chromosome in the population is passed into the objective function one at a time. The chromosome is then evaluated and assigned a number to represent its fitness, the bigger its number the better its fitness. The G.A uses the chromosome's fitness value to create a new population consisting of the fittest members.

TABLE I. GENETIC STRUCTURE FOR OPTIMAL Q AND R MATICES [21].

Gene	1	2	3	4
Parameters	$q_{11}$	$q_{22}$	$q_{33}$	$r_{11}$

The chromosome is formed by three values that correspond to the three gains of the weight matrix Q and R. The gains  $q_{11}$ ,  $q_{22}$  and  $r_{11}$  are positive numbers and characterize the individual to be evaluated.

The objective fitness function to find the optimal values of weight matrices Q & R is, [12]

$$F(Q, R) = 1 / (q_1 x_1^2 + q_2 x_2^2 + q_3 x_3^2 + q_4 u^3) \quad (35)$$

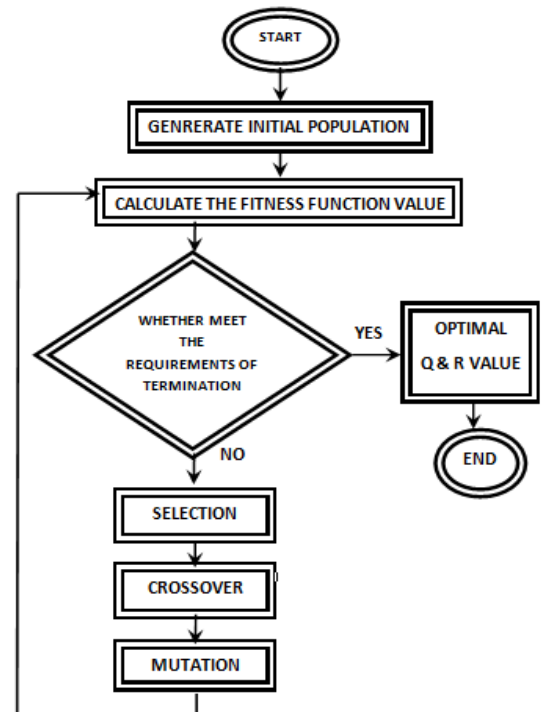


Figure 9. The Flowchart for Optimal Value of Q & R Matrices Using G.A [12].

The MATLAB is used to find the optimal weight matrices Q & R, which is found by using fitness values and current best individual using (35),

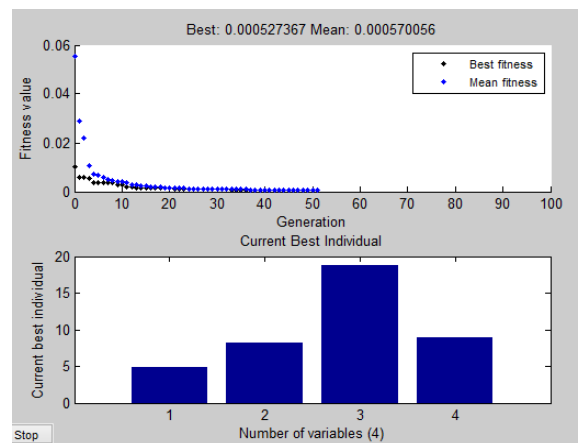


Figure 10. Matlab Simulation of G.A for Optimal Value of Q & R

$$Q_w^{G.A} = \text{diag} (4.821, 8.139, 18.743), R_w^{G.A} = 8.904 \quad (36)$$

The MATLAB code is written in MATLAB-R2011. The MATLAB command to obtain feedback K-Matrix is, [5]

$$[K, P] = \text{lqr2}(A, B, Q, R) \quad (37)$$

The optimal gain  $K$  for Area 1 & Area 2 using G.A for LFC is obtained by using (37),

### Feedback K-Matrix Using G.A for Area 1:

$$K1 = [-0.0430 \quad -0.5592 \quad -1.4152]$$

### Feedback K-Matrix Using G.A for Area 2 :

$$K2 = [-0.0361 \quad -0.5738 \quad -1.4185]$$

## VIII. SIMULATION AND RESULTS

A comparison of LFC consists of six scenarios: the first one contains no controller (uncompensated LFC), the second scenario used PID Controller, the third scenario used LQR Controller, the fourth scenario used LQG Controller, the fifth scenario used LQR controller based on G.A and finally the last scenario used LQG Controller based on G.A has been observed. The comparison is made in terms of performance with respect to frequency deviations and settling time as shown in Table 4. The parameters of the numerical example of LFC are shown in Table 3. The simulation is carried out using MATLAB/SIMULINK software.

### A. LFC without any Controller

In the first scenario, Simulink diagram of LFC is constructed using MATLAB and solved without using any controller. Fig. 11 and Fig. 12 show the Simulink diagram of LFC and the frequency deviations respectively,

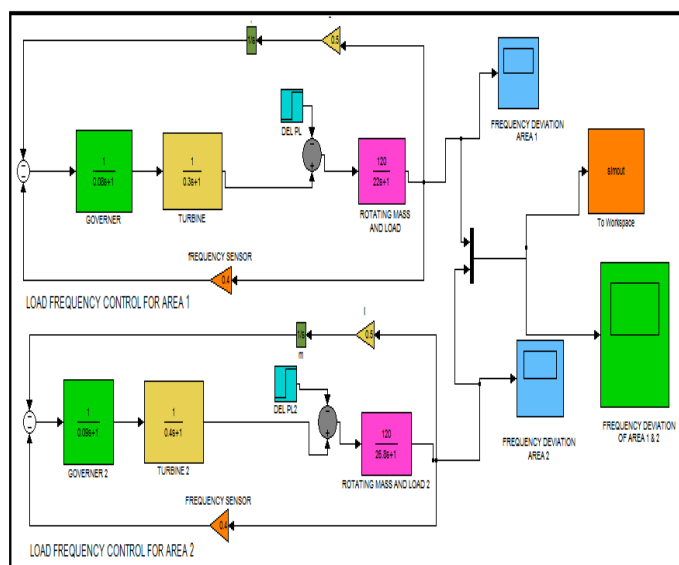


Figure 11. Simulink Model of First Scenario for LFC without any controller (uncompensated LFC)

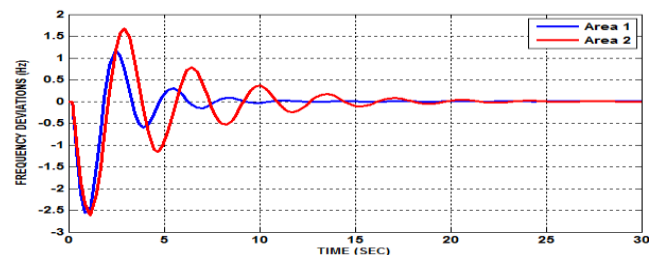


Figure 12. Frequency Deviation of First Scenario for LFC without any controller.

### B. LFC with PID Controller

In the second scenario, MATLAB Simulation of LFC is constructed in which PID controller is designed to reduce the frequency deviations and settling time of the LFC in the power system. Fig. 13 and Fig. 14 show Simulink diagram and the frequency deviations respectively,

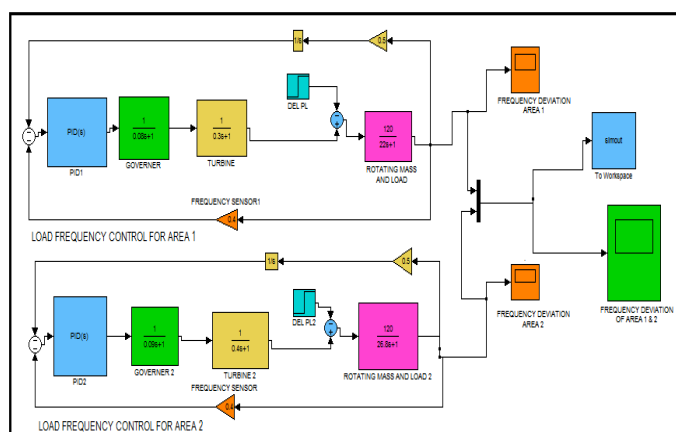


Figure 13. Simulink Model of Second Scenario for LFC using PID controller.

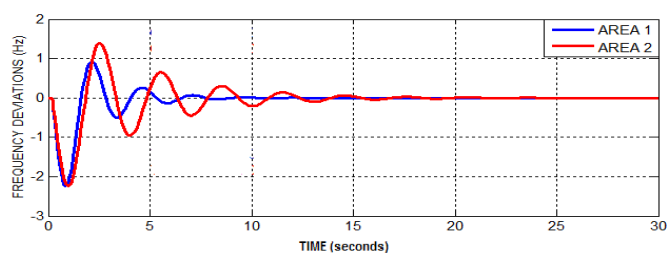


Figure 14. Frequency Deviation of Second Scenario for LFC using PID controller.

### C. LFC with LQR Controller

In the third scenario, LQR controller is designed in which K-gain vector is used as a feedback to reduce the frequency deviations and settling time of the LFC in the power system. The LQR controller is designed using (15) in M-file and MATLAB. The Simulink diagram and the frequency deviations are shown in Figs. 15 & 16 respectively.



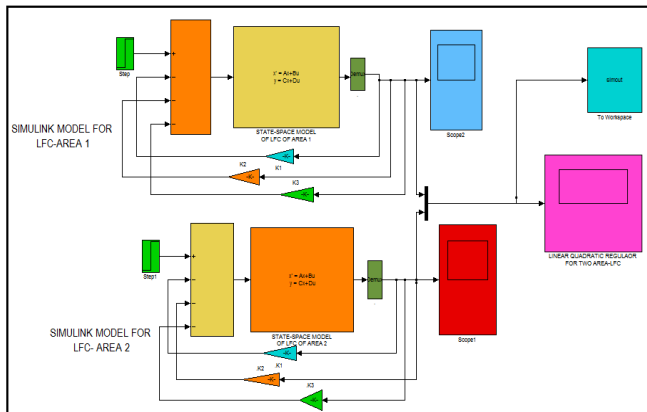


Figure 15. Simulink Model of Third Scenario for LFC with LQR\_Controller.

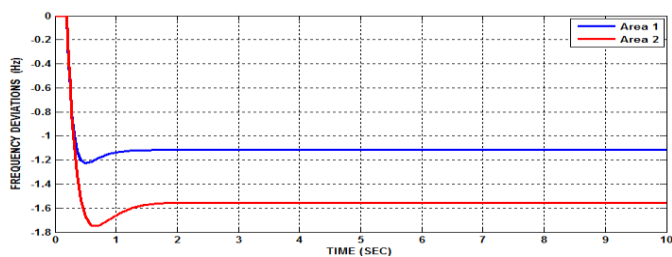


Figure 16. Frequency Deviation of Third Scenario for LFC with LQR\_Controller.

#### D. LFC with LQG Controller

In the fourth scenario, LQR controller is combined with Kalman Filter to form LQG controller, which is then used as feedback in LFC to reduce the frequency deviations and settling time in Power system. The LQG controller is designed using (31) to (35) in M-file using MATLAB. The frequency deviation is shown in Fig. 17,

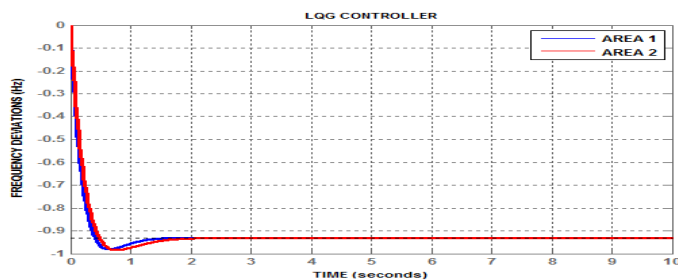


Figure 17. Frequency Deviation of Fourth Scenario for LFC with LQG\_Controller.

#### E. LFC with LQR Controller based on G.A.

In fifth scenario, LQR optimal controller is designed using G.A which is used to search the optimal value of Q & R. The K-gain vector is then used as a feedback to reduce the frequency deviations and settling time of the LFC in the power system. The LQR controller based on G.A is designed using (15) in M-file and MATLAB. The simulink diagram and the frequency deviations are shown in Figs. 18 & 19 respectively

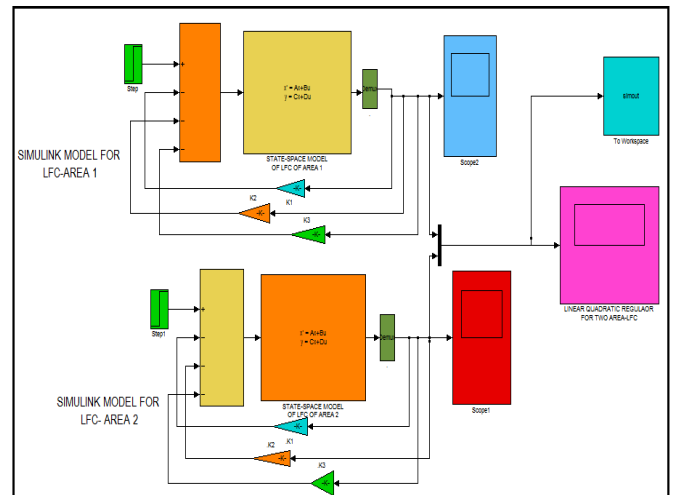


Figure 18. Simulink Model of Fifth Scenario for LFC with LQR\_Controller based on G.A

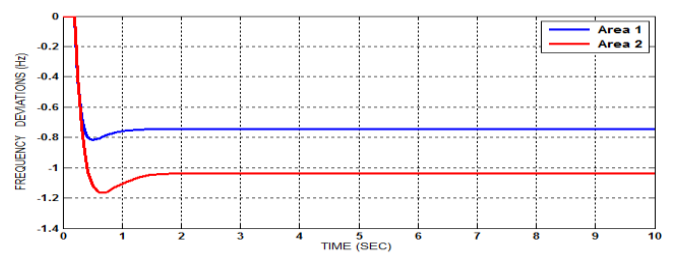


Figure 19. Frequency Deviation of Fifth Scenario for LFC with LQR\_Controller based on G.A

#### F. LFC with LQG Controller based on G.A.

In the final scenario, G.A based LQR controller and Kalman Filter are combined with to form LQG controller, which is used as a feedback in LFC to reduce the frequency deviations and settling time in Power system. The LQG controller is designed using (31) to (35) in M-file using MATLAB. The frequency deviation is shown in Fig. 20,

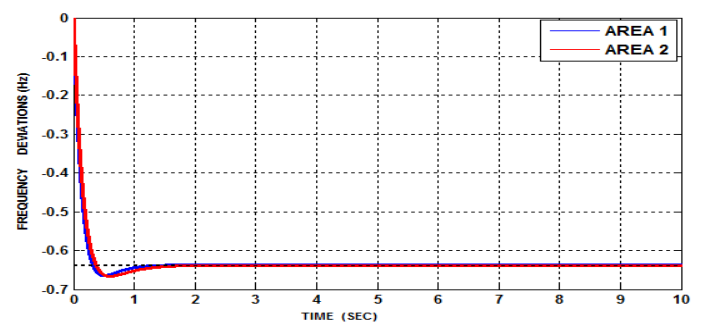


Figure 20. Frequency Deviation of Final Scenario for LFC with LQG\_Controller based on G.A.

#### G. Performance of LFC during different sudden load disturbance ( $\Delta P_L$ )

For Area 1



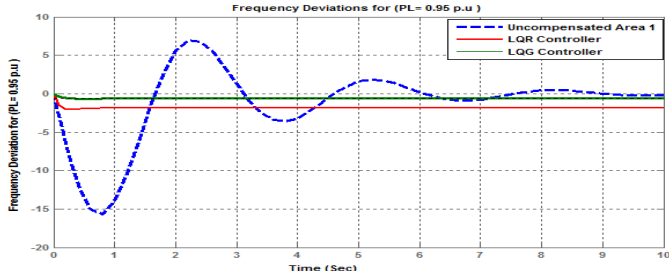


Figure 21. Frequency Deviations due to Load Disturbance with & without LQG & LQR controllers at  $\Delta P_L = 0.95 P.u$

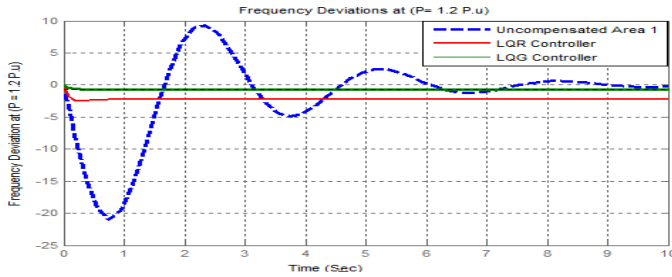


Figure 22. Frequency Deviations due to Load Disturbance with & without LQG & LQR controllers at  $\Delta P_L = 1.2 P.u$

For Area 2

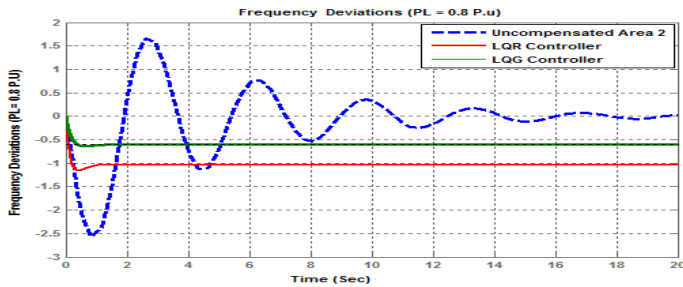


Figure 23. Frequency Deviations due to Load Disturbance with & without LQG & LQR controllers at  $\Delta P_L = 0.8 P.u$

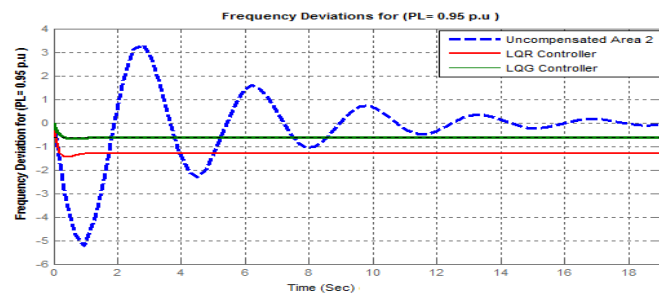


Figure 24. Frequency Deviations due to Load Disturbance with & without LQG & LQR controllers at  $\Delta P_L = 0.95 P.u$

#### H. Comparative Analysis of Different Controllers with LFC

Fig. 25 & Fig. 26 show the performance of LFC for Area 1 & Area 2 by various controllers over frequency deviations and settling time in power system.

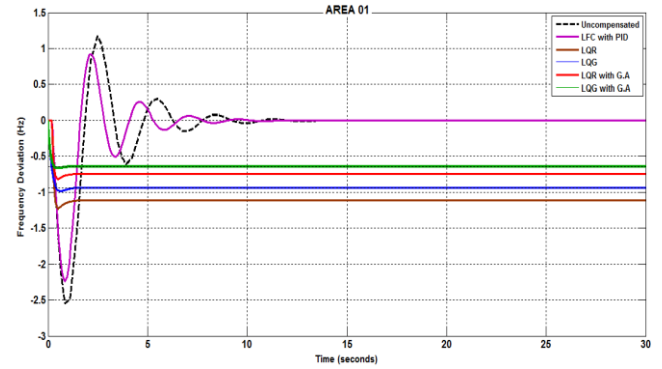


Figure 25. Comparative Analysis of different Controllers with LFC for Area 1

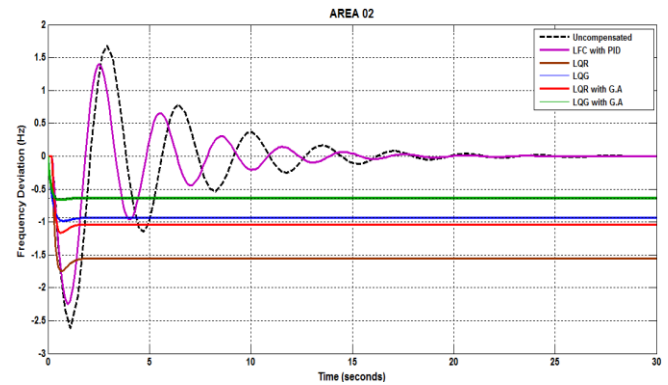


Figure 26. Comparative Analysis of different Controllers with LFC for Area 2

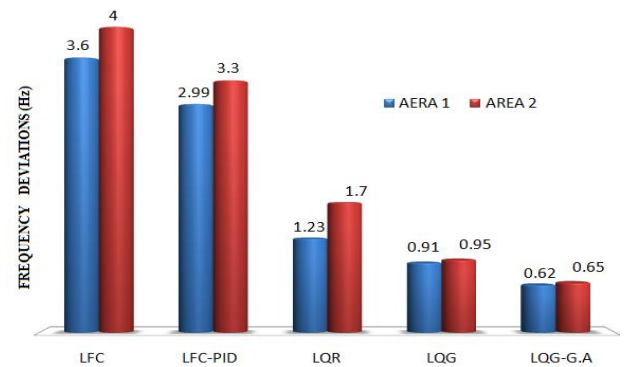


Figure 27. Frequency Deviations of LFC with Different Controllers

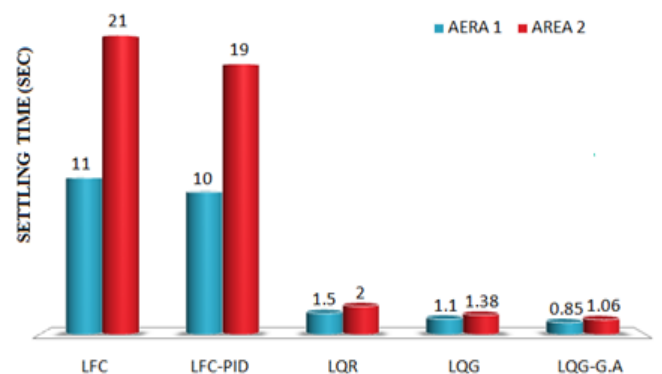


Figure 28. Settling Time of LFC with Different Controller

TABLE II. COMPARATIVE ANALYSIS OF DIFFERENT CONTROLLERS WITH LFC

Parameter	Area	LFC without any Controller	LFC with PID Controller	LFC with LQR Controller	LFC with LQG Controller	LFC with LQR Controller using G.A.	LFC with LQG Controller using G.A.
Overshoot	1	1.1	0.89	0	0	0	0
	2	1.5	1.20	0	0	0	0
Undershoot	1	2.5	2.1	1.23	0.91	0.8	0.62
	2	2.5	2.1	1.7	0.95	1.18	0.65
Settling Time	1	11	10	1.5	1.1	1.0	0.85

## ACKNOWLEDGMENT

All Co-authors are thankful to Mr. Muddasar Ali, Lecturer & Researcher, Faculty of Electrical Engineering, Wah Engineering College (WEC), University of Wah, Pakistan for his valuable suggestions and necessary recommendations.

## REFERENCES

- [1] P. Prajapati, "Multi-Area Load Frequency Control (LFC) by various Conventional Controllers using Battery Energy Storage System (BES)," International Conference on Energy Efficient Technologies for Sustainability (ICEETS), ISSN: 978-1-4673, IEEE, 2016.
- [2] G. S. Thakur, "Load frequency control (LFC) in single area with traditional Ziegler-Nichols PID tuning controller," International Journal of Research in Advent Technology, vol. 2, no. 12, E-ISSN: 2321-9637, December 2014.
- [3] M. Pal, "To Control Load Frequency by using Integral Controller," International Journal of Innovative Research in Science, Engineering and Technology, (An ISO 3297: 2007 Certified Organization), vol. 3, no. 5, May 2014.
- [4] M. Wadi, "Optimal Controller for Load Frequency Control via LQR and Legendre wavelet function," Journal of Automation and Control, vol. 3, no. 2, pp. 43-47, © Science and Education Publishing, DOI: 10.12691/automation-3-2-2, 2015.
- [5] A. M. YOUSEF, "Improved Power System Stabilizer by Applying LQG Controller," Advances in Electrical and Computer Engineering, ISBN: 978-1-61804-279-8.
- [6] P.S. Kumar, "Load Frequency Control Of Multi Area Power System Using Fuzzy And Optimal Control Techniques," International Journal of Recent Trends in Engineering & Research (IJRTER), vol. 2, no. 8, ISSN: 2455-1457, August 2016.
- [7] S. K. Joshi, "Analysis of Load Frequency Control (LFC) using PID Controller," International Journal of Emerging Technology and Advanced Engineering, ISSN 2250-2459, ISO 9001:2008 Certified Journal, vol. 4, no. 11, November 2014.
- [8] Hadi Saadat, "Power System Analysis," PSA Publishing, 2010
- [9] Stefani, "Design of Feedback Control Systems," 4th ed.
- [10] A. Tewari, "Modern control design with Matlab".
- [11] A. H. Khan, "Optimized Reconfigurable Control Design for Aircraft using Genetic Algorithm," Research Journal of Applied Sciences, Engineering and Technology, vol. 6, no. 24, ISSN: 2040-7459; e-ISSN: 2040-7467, Maxwell Scientific Organization, 2013.
- [12] Bingbing Wu, "Design and implementation of the inverted pendulum optimal controller based on hybrid genetic algorithm," International Conference on Automation, Mechanical Control and Computational Engineering, (AMCCE 2015).
- [13] S. A. Ghoreishi, "Optimal Design of LQR Weighting Matrices based on Intelligent Optimization Methods," International Journal of Intelligent Information Processing, vol. 2, no. 1, March 2011.
- [14] K. J. Astrom, and R. M. Murray, "An Introduction to Feedback System," Princeton University Press, April 2010.
- [15] C. Concordia, and L. K. Kirchmayer, "Tie line power and frequency control of electric power systems," Amer. Inst. Elect. Eng. Trans., Pt. II, vol. 72, pp. 562-572, June 1953.
- [16] N. Cohn, "Some Aspects of Tie-line Bias Control on Interconnected Power Systems," Amer. Inst. Elect. Eng. Trans., vol. 75, pp. 1415-1436, February 1957.
- [17] O. I. Elgerd, and C. Fosha, "Optimum Megawatt Frequency Control of Multi-area Electric Energy Systems," IEEE Trans. Power App. Syst., vol. PAS-89, no. 4, pp. 556-563, April 1970.
- [18] R. K. Green, "Transformed Automatic Generation Control," IEEE Trans. Power Syst., vol. 11, no. 4, pp. 1799-1804, November 1996.
- [19] D. Das, J. Nanda, M. L. Kothari, and D. P. Kothari, "Automatic Generation Control of Hydro Thermal system with new area control error considering generation rate constraint," Elect. Mach. Power Syst., vol. 18, no. 6, pp. 461-471, Nov./Dec. 1990
- [20] R. K. Cavin, M. C. Budge Jr., and P. Rosmunsen, "An Optimal Linear System Approach to Load Frequency Control (LFC)," IEEE Trans. On Power Apparatus and System, pp. 2472-2482, PAS-90, Nov./Dec. 1971.
- [21] V. F. Montagner, "A Robust LQR Applied To A Boost Converter With Response Optimized Using A Genetic Algorithm," Power Electronics and Control Research Group, Federal University of Santa Maria, 97105-900, Santa Maria, RS, Brazil.
- [22] M. D. Youns, "Optimization Control of DC Motor with Linear Quadratic Regulator and Genetic Algorithm Approach," Tikrit Journal of Engineering Sciences, vol. 20, no.5, June 2013.
- [23] Q. Wang, "An Overview of Genetic Algorithms Applied to Control Engineering Problems," Proceedings of the Second International Conference on Machine Learning and Cybernetics, Xi'an, pp. 2-5, November 2003.



**Muddasar Ali** has obtained BE Electrical Engineering from Air University, Islamabad in 2015 and MS Electrical Engineering from University of Engineering & Technology (U.E.T) Taxila, Pakistan in 2017. Currently, he is working as a Lecturer & Researcher at the Faculty of Electrical Engineering at Wah Engineering College (WEC), University of Wah, Pakistan. His research interest includes,

Power System Engineering, Electrical Machine Modeling, Power system Stability and controls and Power Transmission system. He is currently doing research on the Controller Selection for better Performances of Load Frequency Control (LFC) in Power Systems.



# Classification Performance of Linear Binary Pattern and Histogram Oriented Features for Arabic Characters Images: A Review

Sungin Behram Khan, Dr. Gulzar Ahmad, Faheem Ali, Farooq Faisal, Irfan Ahmed, Salman Elahi

**Abstract**—There are millions of texts store in both off line and online forms. To utilize these documents properly, there is need of organizing these documents systematically and lots of applications are available for this purpose. Text classification is an important area of image processing deal with how the document belongs to its suitable class or category. Like other languages, Arabic language is also very rich and complex inflectional language which makes Arabic language very complex for ordinary analysis. In this review paper, we focus on the published research, especially in the field of Arabic text classification. Regard these all, three different types of feature extraction techniques are also implemented to extract features from different images of Arabic characters and presents a performance results of these techniques. From the result, it can be concluded that the combination of Linear binary pattern descriptor and Legendre moment, based moments features outperform and increase the accuracy of the LBP classifiers from 91.99 % to 93.12%.

**Keywords**— Text classification, Local Binary Pattern descriptor, Histogram of Gradient Feature descriptor, Legendre Moment, Classification.

## I. INTRODUCTION

Text classification is a technique to extract useful information from the large amount of textual data. In the last few years, there is a dynamically growing of textual data in various fields of daily life, which made the text classification one of the most important research issues. Text classification is an active research area in which different labels are assigned to text documents with different categories from a predefined set known in advance [1]. There are two different terms in text classification, the first term is text categorization which deals with sorting documents by contents, while the term text

classification is used to classify the characters [2]. There are two methods for the classification of text data: rule base and machine learning [3]. In the rule based, a system automatically classifies a textual data with the help of built in knowledge engineer and a domain expert while in the machine learning approaches, a system is fed to a set of data for training a machine and classes are defined for each different character. And new data are classified according to their distant properties [4]. Like other languages, the Arabic language has also very rich morphology and have complex shapes of their character [5]. Due to complex writing styles of Arabic characters, there is a decreased research in the area of Arabic text classification [6]. There are 28 letters in Arabic language [7]. The quality of the data set of data may very affect the classification performance of a machine; the redundant and irrelevant features of data may also reduce the classification performances of any algorithms [3]. For English text, there are seven different standards of text available free for research purposes, but for Arabic text classification unfortunately there is no specific standard data set [8]. Researches in the field of text classification collected their data from the online web sites [9]. The rest of the paper is organized as follows. Section 2 presents a brief summary of the previous work in the field of Arabic text classification follow by section 3 in which different feature extraction techniques are presented. Section 4 presents the classification and types of classifiers used in this research. In section 5 results of different features extraction techniques and classifiers are presented and 7 presents the conclusion.

## II. RELATED WORK

Handwritten character recognition is one of the most challenging research directions (area) in artificial intelligence and pattern recognition [10, 11]. Character recognition helps you to transform different historical books, inscription, newspaper and unrestricted document formats to an intelligible format. It is almost impossible to manually annotate all of these handwritten documents. Therefore, there is a need of automatic system for labeling the words in the handwritten documents. Furthermore, the character recognition systems are related to research areas such as writer identification and verification [10]. Arabic handwriting recognition was first performed by [12] which is based on Fourier transformations. In [12], features are extracted from both isolated characters and cursive characters. The author classifies 175 samples of hand printed letters correctly. [13] introduced a method based on the

---

Sungin Behram Khan: Department of Electrical Engineering, University of Engineering and Technology Peshawar, Pakistan.

Dr. Gulzar Ahmad: Department of Electrical Engineering, University of Engineering and Technology Peshawar, Pakistan.

Faheem Ali: Department of Electrical Engineering, University of Engineering and Technology Peshawar, Pakistan.

Farooq Faisal: Department of IBMS Agriculture University Peshawar.

Irfan Ahmed: Department of Electrical Engineering, University of Engineering and Technology Peshawar, Pakistan.

Salman Elahi: Department of Electrical Engineering, University of Engineering and Technology Peshawar, Pakistan.

statistical approach for the recognition of isolated Arabic characters. Character recognition system is mainly divided into different types according to their techniques of data/image acquisition methods. Arabic recognition system is mainly divided into two types, i.e. Online and offline line systems. Some of these online systems [5] [6] get character data in real time. [19] develop a recognition method which segment the cursive words into different characters. Some recognition systems recognize the text words without segmenting it into words, characters or primitives [1, 7]. Images of separate characters are used in our experiments.

### III. FEATURE EXTRACTION

Feature extraction is the process of extracting information from input image of the character or word and used that information for the recognition of the character. These extracted information is called feature vectors. It is most the important step in developing recognition system. Different types of feature extraction techniques are used to extract feature vector from images of characters. Some of these techniques are pixel-based method [14]. In this research paper, different feature extraction techniques, namely the Linear Binary Pattern descriptor (LPP),

Histogram of Gradient descriptor (HOG) and combined features of Legendre moment, based and local binary pattern are used to classify different Arabic characters. These descriptors are further explained in the coming next sections.

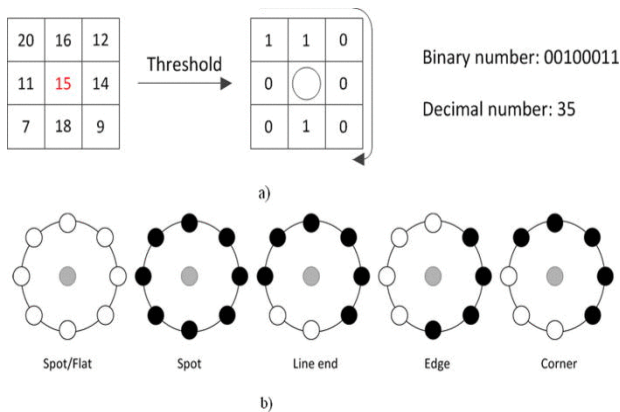


Figure 1. (a) The LBP operator. (b) Examples of texture primitives which can be detected by LBP, where white circles represent ones and black circles zeros. For instance, the rightmost pattern detects corners in an image

#### A. Local Binary Pattern Descriptor

The Local Binary Pattern descriptor introduced by [15], is a regional descriptor-based approach for texture description. It was later introduced into the face recognition area by [16]. The LBP generation approach in [15] is described as follows. A Local Binary Pattern label is a binary number which is created for each pixel of images where each bit is assigned a value based on its difference from one of the pixels at a given radius. Figure 1 (a) shows a simple version that labels each pixel by a number derived from its 3x3 neighborhood. Neighboring pixels are assigned a binary value of 1 if larger than the center pixel and 0 otherwise. Figure 1 (b) shows how different bits can be

clustered to representative's spots, edges, lines, corner and edges. Locations of any pixel having not integer coordinates, these coordinates are calculated by using bilinear interpolation of each neighboring pixels. The feature vectors are from each section is obtained from the histograms of the LBP-operated image sections.

The feature vector assignment algorithm steps consist of different steps.

- Labeling each pixel using the LBP operator
- Dividing the image into  $m \times m$  small equal sized rectangular regions  $R_0, R_1, \dots, R_{(m-1)}$
- Obtaining the histogram from each computed region
- Combining all calculated histograms into one vector

Let  $f(x, y)$  be the LBP label of pixel of images at coordinates  $(x, y)$ . Then the histogram for this region  $j$  can be computed using equation below.

$$H_{i,j} = \sum_{x,y} I[f(x,y) = i] I(x,y) \in R_j \quad (1)$$

where  $i = 0, 1, \dots, n-1, j = 0, 1, \dots, m-1$  and

$$I\{A\} = \begin{cases} 1, & A \text{ is true} \\ 0, & A \text{ is false} \end{cases} \quad (2)$$

Histograms computed by equation 2 are estimates of the density function of the regional data which contains information about the patterns there in each pixel.  $i$  is a histogram domain that corresponds to one of the  $n = 2^P$  binary numbers generated by LBPPR in the neighborhood of  $P$  pixel. The resultant feature vectors are very high even for typical value of  $P$ . For this some clustering techniques can be used to reduce the feature vector size.

#### B. Histogram Of Gradient Features Descriptor

Dalal et al .[17] introduced Histogram Oriented Gradient for the detection of the human body in an image. It has become very successful in diverse domains such as face detection [18], pedestrian detection [19] and road vehicle detection [20]. HOG is defined as the distribution of the local intensity gradients over a small connected region called "cells". Feature vector is computed for each cell using gradient detectors. Each pixel is then convolved by simple convolution kernel as:

$$\begin{aligned} G_x &= I(x+1, y) - I(x-1, y) \\ G_y &= I(x, y+1) - I(x, y-1) \end{aligned} \quad (3)$$

In equation 3,  $I(x, y)$  is the pixel intensity at location  $x, y$ .  $G_x$  are the horizontal component and  $G_y$  are the vertical components of the gradients. Feature are represented by the combination of the histograms from each block. The size of the feature vector in HOG descriptor depends on the selected numbers of bins and blocks. The performance of the HOG descriptor is mostly depending on the number of selected bins and blocks [19]. The feature descriptors can be normalized using Level 2 block normalization [18] as follows:

$$V'_k = \frac{V_k}{\sqrt{\|V\|^2 + \varepsilon}} \quad (4)$$

- In equation 4,  $V_k$  represent the combined histogram from all block regions,  $\varepsilon$  represent small value close to zero and  $V'$
- $k$  is the resultant normalized HOG descriptor feature vector.
- Legendre Moments and Local Binary Pattern based feature extraction
- Legendre moments for image of order  $p + q$  with intensity function  $f(x)$  is defined by the

$$L_{pq}(t) = \frac{(2p+1)(2q+1)}{4} \int_{-1}^1 \int_{-1}^1 P_p(x) P_q(y) f(x, y) dx dy \quad (5)$$

where  $P_p(x)$  is  $p$ th order legendre polynomials defined as.

$$P_p^r(t) = \sum_{k=0}^i \mathfrak{L}_{i,k} t^k, i = 0, 1, 2 \quad (6)$$

Where

$$\mathfrak{L}_{i,k} = \frac{(-1)^{i+k} (i+k)!}{(i-k)! 7^k (k!)^2} \quad (7)$$

Legendre polynomials are orthogonal in nature and orthogonality condition is.

$$\int_0^1 P_i(t) P_j(t) dx = \begin{cases} 0 & \text{if } p \neq q \\ \frac{2}{2p+1} & \text{otherwise} \end{cases} \quad (8)$$

Using equation 8, any function can be written as.

$$f(x) = \sum_{i=0}^m c_i p_i(t) \quad (9)$$

Where

$$c_i = (2l+1) \int_0^1 f(t) P_i(t) dt \quad (10)$$

As  $l \rightarrow \infty$  the sum of these functions is equal to the exact function. Basically, these character images are 2D array of numerical values. So, first will introduce the mechanism for developing 2D Legendre polynomials. 2D Legendre moments can be generated by taking the product of two basic sets. Assume  $Bm(x)$ ,  $Bm(t)$  be the basis set of Legendre polynomials in two different variables. We can define the basis set of 2D images as  $Bm(x, t) = Bm(x) \times Bm(t)$ . The general term of the basis set  $Bm(x, t)$  can be written as

$$f(x) = \sum_{i=0}^m c_i p_i(t) \quad (11)$$

If we are using scale level  $m$ , then there must be  $(m+1)^2$  terms in the basis set. Any images in the space  $C([0, 1] \times [0, 1])$  can be written as in term of Legendre polynomials as:

$$f(x, t) = \sum_{p=0}^n \sum_{q=0}^m c_{pq} P_p(x) P_q(t) \quad (12)$$

and coefficients can be obtained by the following relation as:

$$cpp = (2p+1)(2q+1) \int_0^1 \int_0^1 f(t, x) P_p(t) P_q(x) dt dx. \quad (13)$$

In hybrid method, we have used the combination of features of Linear binary pattern feature descriptor and Legendre moments based extracted features. These features are combined for further classification.

#### IV. CLASSIFICATIONS

After feature extraction phase, a technique is needed for the classification of these characters. Based on these extracted features, the classifier attempt to identify the pattern that represents the input character. There are many classifiers which makes the decision and can be divided into three types: structural, statistical and neural network classifiers. For instance, Support Vector Machines (SVM) [9] and Sequential Minimal Optimization algorithm for training Support Vector Machine are used. The classifiers take the extracted features as inputs. And classify other instances according to their properties. There are a large number of classifiers available for classification purposes, but in this article two widely used classifier i.e., A Sequential Minimal Optimization algorithm for training Support Vector Machine and Support Vector Machine are used in our experiments. A Sequential Minimal Optimization for training Support Vector Machine (SMO(SVM)) Sequential minimal optimization (SMO) is an algorithm for solving the quadratic programming (QP) problem that arises during the training of support vector machines. In binary classification problem, let  $s(x_1, y_1), \dots, (x_n, y_n)$  be a datasets of sample and  $x_i$  is an input vector and  $y_i \in -1, +1$  is a binary label corresponding to each samples. Support vector machine (SVM) is trained by solving a quadratic programming problem, which is expressed in the dual form. Sequential Minimal Optimization (SMO) is an iterative algorithm for solving the optimization problem. SMO breaks a large problem into smallest possible sub-problems, which can be solved easily analytically. Because of the linear equality constraint involving the Lagrange multipliers.

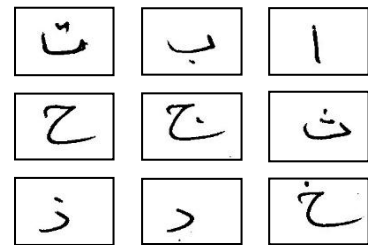


Figure 2. Sample of Arabic Characters in our Experiments the smallest possible problem involves two such multipliers. Then, for any two multipliers  $a_1$  and  $a_2$ , the constraints are reduced to:

$$\begin{aligned} 0 &\leq \alpha_1, \alpha_2 \leq C, \\ y_1 \alpha_1 + y_2 \alpha_2 &= k, \end{aligned} \quad (14)$$



and this reduced problem can be easily solved analytically: we need to find a minimum of a one-dimensional quadratic function. K is the negative of the sum over the rest of the terms in the equality constraint, which is fixed in each iteration.

Support vector machines (SVM) are statistical models that separate two data sets [21]. The classes are divided through an optimal separating hyperplane (OSH). The limits of these classes of data and the OSH are called support vectors. Intuitively, for a set of points divided into two classes, the SVM method finds on one side the hyperplane that separates the highest possible fraction of points that belong to the same class, and on the other side it maximizes the distance between the classes and hyper plane. By using SVM, the user can avoid over-fitting due to its regularization parameter. The real help the SVM comes in is when there is randomly distributed data, taking into account a good training.

### V. EXPERIMENTAL SETUPS AND RESULTS

We will compare the classification performance of three different feature extraction techniques. Our data sets are composed of isolated handwritten Arabic characters. The handwritten images are converted to gray-scale and normalized to a fixed-size image. In these experiments, data sets of each character are manually created. A group of 30 people wrote each character on a plain paper. Every person in the group write each Arabic character 5 times. These words are scanned with the help of a scanner. The scanned documents are treated as single character.

Thus data set of 4004 isolated hand written Arabic characters are obtained. The resolutions of the dataset used in these experiments are 50 x 50 pixels. 63 % of the data are used to for training purpose and 37 % are used to check the classification performance. The sample of these images after segmentation are Shown in Figure 2. The implementation of each feature extraction techniques is designed in using MATLAB 2016.

#### A. Experimental Evaluation of Histogram Of Gradient Descriptor:

The results derived from confusion matrix shows that the classification performance of HOG descriptor in term of accuracy, Sequential Minimal Optimization has performed over the Support Vector Machine. As shown in Table 1, classification accuracy of 88.86% is obtained using Sequential Minimal Optimization technique for training support vector machine. The classifies correctly classify 1207 characters and incorrect classification rate is 154 characters. Other classification parameters are displayed in Table 1. The same extracted features are evaluated on Support Vector Machine. Accuracy of 16.09 % is achieved by using SVM as a classifier. As shown Table 1 total number of correctly classified instances are 219 and incorrectly classified instance are 1134. Detail Accuracy of both the classifiers i.e., SMO and SVM are given in Table 1.

Table 1: Histogram of Gradient Features Descriptor using SMO(SVM) and SVM  
Summary of Histogram of Gradient Descriptor and Classifiers

LBP using SMO(SVM)			BP using (SVM)	
Correctly classified Instance	1252	91.99%	1188	87.88%
Incorrectly classified Instance	109	8.008%	173	12.31%
Kappa Statistic	0.9169		0.8682	
Mean Absolute Error	0.00664		0.0091	
Relative Mean Square Error	96.32%		89.24%	
Relative Absolute Error	96.89%		13.18%	
Total Number of Instances	1361		1361	

Table 2: Local Binary Pattern Descriptor using SMO(SVM) and SVM

HOG using SMO(SVM) HOG using (SVM)			HOG using SMO(SVM) HOG using (SVM)	
Correctly classified Instance	1207	88.68%	219	16.09%
Incorrectly classified Instance	154	11.35%	1134	83.90%
Kappa Statistic	0.8862		0.134	
Mean Absolute Error	0.0664		0.0599	
Relative Mean Square Error	0.1799		0.2448	
Relative Absolute Error	96.34%		87.00%	
Total Number of Instances	1361		1361	

#### B. Experimental Evaluation of Hybrid Method

The results derived from confusion matrix shows that the classification performance of Hybrid methods in term of accuracy, Sequential Minimal Optimization has performed over the Support Vector Machine. As shown in Table 3, classification accuracy of 93.12% is obtained using Sequential Minimal Optimization technique for training support vector machine. The classifies correctly classify 1262 characters and incorrect classify 99 characters. Other classification parameters are displayed in Table 3. The same extracted features are also evaluated on Support Vector Machine. Accuracy of 88.48 % is achieved by using SVM as a classifier. As shown Table 3 total number of correctly classified instances are 1188 and incorrectly classified instance are 173. Detail Accuracy of both the classifiers i.e., SMO and SVM are given in Table 3.



**Tabel 3: Hybrid feature using SMO(SVM) and (SVM)**

Hybrid features using SMO(SVM)			Hybrid features using (SVM)	
Correctly classified Instance	1262	93.12%	1188	88.48%
Incorrectly classified Instance	99	99	173	11.51%
Kappa Statistic	0.9169		0.8682	
Mean Absolute Error	0.0664		0.0089	
Relative Mean Square Error	79.99%		0.0089	
Relative Absolute Error	96.34%		51.64%	
Total Number of Instances	1361		51.64%	

## VI. COMPARISON OF DIFFERENT METHODS

In this section classification performance of three different feature extraction method is presented. In Table 4 the classification performance of these methods are shown. It is clear from Table 4 that for combination of extracted features using Legendre based features and LBP features along with Sequential Minimal Optimization algorithm for training SVM performs better then all other techniques. Classification Accuracy of 93.12% is achieved for SMO(SVM) in this experiment.

**Table 4: Comparison of the all methods**

		Correctly Classified Instances%	Incorrectly Classified Instance%
<b>Hybrid Method</b>	SMO	93.12	11.51
	SVM	88.48	6.88
<b>Histogram of Gradient Descriptor</b>	SMO	88.6	83.90
	SVM	83.90	11.31
<b>Local Binary Feature Descriptor</b>	SMO	12.711	12.711
	SVM	87.28	8.088
<b>Legendre Based Features</b>	SMO	30.34	86.336
	SVM	13.66	30.34

## CONCLUSION

Main objectives of the paper is to find optimal combination of feature extraction methods and classifiers for the Classification of Arabic characters. In this paper we have investigated three different features extraction techniques with two classifiers namely SMO(SVM) and SVM. Result

concluded from Section 6 that, best classification accuracy of 93.13% can be achieved when the combination of hybrid methods and sequential minimal algorithm for training support vector machine is used. Regard these all it can be that SMO(SVM) outperform better then SVM in all cases. In future works, finding the most accurate combination of feature extraction technique and classifier having more classification accuracy i.e, 100%.

## REFERENCES

- [1] Fabrizio Sebastiani, "Machine learning in automated text categorization," *ACM computing surveys (CSUR)*, 34(1):1–47, 2002.
- [2] Peter Jackson and Isabelle Moulinier, "Natural language processing for online applications:Text retrieval, extraction and categorization," volume 5. John Benjamins Publishing, 2007
- [3] AM Mesleh, " Support vector machine text classifier for arabic articles: Ant colony optimization-based feature subset selection, " *The Arab Academy for Banking and Financial Sciences*, 2008.
- [4] Franca Debole and Fabrizio Sebastiani, "An analysis of the relative hardness of reuters-21578 subsets, " *Journal of the Association for Information Science and Technology*, 56(6):584–596, 2005.
- [5] Abdelwaddood Mohd Mesleh, "Support vector machines based arabic language text classification system: feature selection comparative study," In *Advances in Computer and Information Sciences and Engineering*, pages 11–16.Springer, 2008.
- [6] Alaa M El-Halees.Arabic text classification using maximum entropy." *IUG Journa of Natural Studies*, 15(1), 2015.
- [7] Mostafa M Syiam, Zaki T Fayed, and Mena B Habib, "An intelligent system for arabic text Categorization," *International Journal of Intelligent Computing and Information Sciences*, 6(1):1–19, 2006.
- [8] Mohammad S Khorsheed and Abdulmohsen O Al-Thubaity, "Comparative evaluation of text classification techniques using a large diverse arabic dataset, " *Language resources and evaluation*, 47(2):513–538, 2013.
- [9] Bassam Al-Shargabi, Waseem Al-Romimah, and Fekry Olayah, "A comparative study for arabic text classification algorithms based on stop words elimination, " In *Proceedings of the 2011 International Conference on Intelligent Semantic Web-Services and Applications*, page 11. ACM, 2011.
- [10] Lambert Schomaker, Katrin Franke, and Marius Bulacu, "Using codebooks of fragmented. *Pattern Recognition Letters*, " 28(6):719–727, 2007.
- [11] Horst Bunke and Kaspar Riesen, "Recent advances in graph-based pattern recognition with applications in document analysis, " *Pattern Recognition*, 44(5):1057–1067, 2011.
- [12] G'osta H Granlund, "Fourier preprocessing for hand print character recognition," *IEEE transactions on computers*, 100(2):195–201, 1972.
- [13] H Al-Yousefi and SS Udpa, "Recognition of arabic characters," *IEEE Transactions on Pattern Analysis and Machine Intelligence*, 14(8):853–857, 1992.
- [14] K Roy, A Banerjee, and U Pal, "A system for word-wise handwritten script identification for indian postal automation, " In *India Annual Conference, 2004. Proceedings of the IEEE INDICON 2004. First*, pages 266–271. IEEE, 2004.
- [15] Timo Ojala, Matti Pietik'ainen, and David Harwood, "A comparative study of texture measures with classification based on featured distributions," *Pattern recognition*, 29(1):51–59, 1996.
- [16] [16] Timo Ahonen, Abdenour Hadid, and Matti Pietik'ainen, "Face recognition with local binary Patterns," *Computer vision-eccv 2004*, pages 469–481, 2004.
- [17] Navneet Dalal and Bill Triggs, "Histograms of oriented gradients for human detection," In *Computer Vision and Pattern Recognition, 2005. CVPR2005. IEEE Computer Society Conference on*, volume 1, pages 886–893. IEEE, 2005.

- [18] Seung Eun Lee, Kyungwon Min, and Taeweon Suh, "Accelerating histograms of oriented gradients descriptor extraction for pedestrian recognition, " *Computers & Electrical Engineering*, 39(4):1043–1048, 2013.
- [19] Oscar D'eniz, Gloria Bueno, Jes'us Salido, and Fernando De la Torre, " Face recognition using histograms of oriented gradients, " *Pattern Recognition Letters*, 32(12):1598–1603,2011.
- [20] Jon Arr'ospide, Luis Salgado, and Massimo Camplani, " Image-based on-road vehicle detection using cost-effective histograms of oriented gradients, " *Journal of Visual Communication and Image Representation*, 24(7):1182–1190, 2013.
- [21] Samir Al-Emami and Mike Usher, "On-line recognition of handwritten arabic characters,"*IEEE Transactions on Pattern Analysis and Machine Intelligence*, 12(7):704–710, 1990.

**Sungin Behram Khan** belongs to Thana, Malakand, KPK, Pakistan. He has completed his bachelors in Electrical Engineering from UET Peshawar. He is currently the student of MS Electrical Engineering in UET Peshawar, Pakistan. His topic of research is pattern recognition and artificial intelligence.



# Novel Approach to Develop an Efficient Boost Converter by Using Coupled Inductors

Mohsin Saeed, Gong Renxi, Muhammad Aurangzeb, Nadeem Asghar

**Abstract**—This paper focuses on the new approach to develop an efficient Boost Converter by using coupled inductors. In order to eliminate voltage spikes, a buffer circuit is used in the converter. Coupling coils generate leakage flux, and energy in the leakage flux causes voltage spikes. With a high boost ratio, the active switches in the converter can maintain the proper duty cycle, which can significantly reduce voltage and current stress. Since the main switch and the auxiliary switch can be turned on by the zero voltage switching, the switching loss is reduced, and the conversion efficiency is significantly improved. In this paper, an experiment was conducted by building a 200W boost converter model. The results show that the conversion efficiency is greater than 90%, and the surge phenomenon can be effectively suppressed. Finally, the feasibility of low-voltage input systems was verified by photovoltaic and battery system.

**Keywords**— Low-input-voltage, Boost Converter, Coupled Inductor, applications, Photovoltaic Systm.

## I. INTRODUCTION (HEADING 1)

To achieve a high step-up voltage ratio, transformer- and coupled-inductor-based converters are usually the right choices. Compared with an isolation transformer, a coupled inductor has a simpler winding structure, lower conduction loss, and continuous conduction current at the primary winding, resulting in a smaller primary winding current ripple and lower input filtering capacitance. Thus, a coupled-inductor-based converter is relatively attractive because the converter. Present slow current stress and low component count. This paper introduces the new approach to develop an efficient Boost Converter by using coupled inductors [1],[5].

Photovoltaic systems (PV system) use solar panels to convert sunlight into electricity [8]. A system is made up of one or more photovoltaic (PV) panels, a DC/AC power converter (also known as an inverter) [3], a tracking system that holds the solar panels, electrical interconnections, and mounting for other components. Optionally it may include a

maximum power point tracker (MPPT), battery system and charger, solar tracker, energy management software, solar concentrators or other equipment. A small PV system may provide energy to a single consumer, or to an isolated device like a lamp or a weather instrument[7]. Large grid-connected PV systems can provide the energy needed by many customers. The electricity generated can be either stored, used directly (island/standalone plant), or fed into a large electricity grid powered by central generation plants (grid-connected/grid-tied plant).

## II. LITERATURE AND REVIEW

### A. DC-DC Convertors

In many industrial applications, it is required to convert a fixed-voltage dc source into a variable-voltage dc source. A dc-dc converter converts directly from dc to dc and is simply known as a dc converter. A dc converter can be considered as dc equivalent to an ac transformer with continuously variable turn ratio. Like transformer in AC, it can be used to step down or step up a dc voltage source.[1]

Dc converters are widely used for traction motor in electric automobiles, trolley cars, marine hoists, and forklift trucks. They provide smooth acceleration control, high efficiency, and fast dynamic response. Dc converter can be used in regenerative braking of dc motor to return energy back into the supply, and this feature results in energy saving for transportation system with frequent stop; and also are used, in dc voltage regulation[1],[3]. There are many types of DC-DC converter which is buck (step down) converter, boost (step-up) converter, buck-boost (step up- step-down) converter[4].

For low power levels, linear regulators can provide a very high-quality output voltage. For higher power levels, switching regulators are used. Switching regulators use power electronic semiconductor switches in on and off states [2], [4]. Because there is a small power loss in those states (low voltage across a switch in the on state, zero current through a switch in the off state), switching regulators can achieve high efficiency energy conversion.

### B. Functions of DC-DC Converters

The DC-DC converter has some functions. These are:

- Regulate the DC output voltage against line and load variations.
- Convert a DC input voltage into a DC output voltage .

Mohsin Saeed: Guangxi university, China, Email: Mohsin.saeedciit@gmail.com.  
Gong Renxi: Guangxi university, China, Email: rxgong@gxu.edu.cn.  
Muhammad Aurangzeb: Hohai University, Nanjing China, Email: Maurangzaib42@gmail.com  
Nadeem Asghar: Guangxi university, China, Email: engr.nadeem12@gmail.com

- iii. Minimize the DC voltage ripple and DC output voltage below the required level [7].
- iv. Protect the input source and the supplied system from electromagnetic interference.
- v. Provide isolation between the input source and the load (if needed) [9].

The DC-DC converter is often considered as the heart of the power supply. Hence, it affects the total performance of the power supply system. Moreover, the converter accepts DC input voltage and produces a controlled DC output voltage.

Below is an overview of some kinds of DC-DC converters.

### C. Boost dc–dc converters

The development of advance boost dc–dc converters has become urgent for clean-energy vehicle applications, because battery-based energy storage systems are required to cold start and battery recharge. However, back-up power from the battery is supplied using a boost converter, which is employed in many uninterrupted power supplies (UPS) [10], aerospace power systems and industrial applications. The dc back-up energy system normally consists of numerous typical low-voltage-type batteries[9]. Although series strings of storage batteries can provide a high voltage, slight mismatches or temperature differences cause charge imbalance if the series string is charged as a unit. a high-efficiency boost dc–dc converter with high voltage diversity is a key component of batteries connected in parallel. To achieve a high step-up voltage ratio, transformer- and coupled-inductor-based converters are usually the right choices [1],[7].

### D. Operation

As shown in Fig. 1, the proposed converter consists of main switch set M1, boost diode Do, coupled inductors L1 and L2, the clamping circuit, and output filter capacitor Co. The clamping circuit is composed of auxiliary switch set M2, [7]

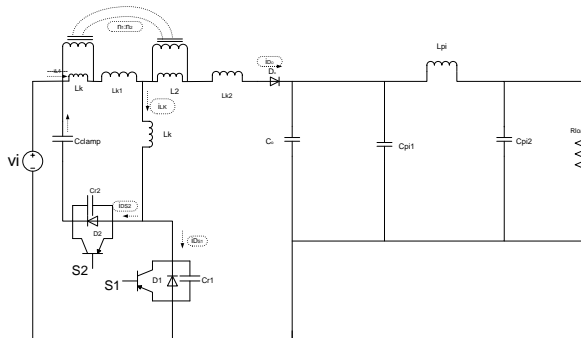
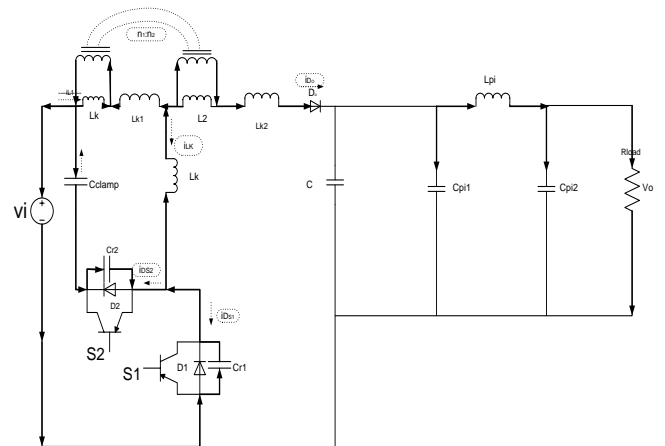


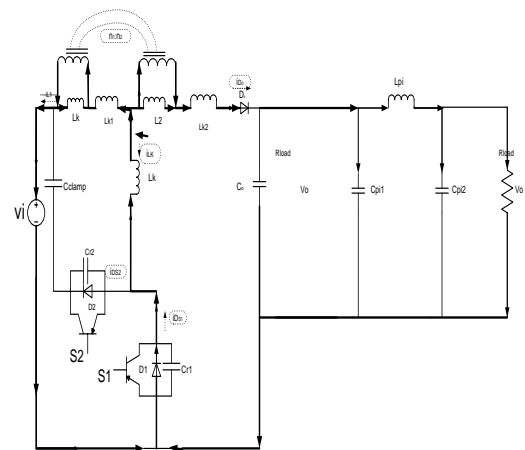
Figure 1. Proposed converter

Resonant inductor and clamping capacitor Cclamp. It should be noted that, since leakage inductor Lk1 is relatively small, inductor Lk is added to the converter to increase the load range with the ZVS condition. Switches S1 and S2 are driven in a complementary manner with a dead time to achieve ZVS. The driving signals and current and voltage waveforms of the key components are shown in Fig.1.1 shows the topological modes of the proposed converter over a switching cycle, which are explained mode by mode as follows;

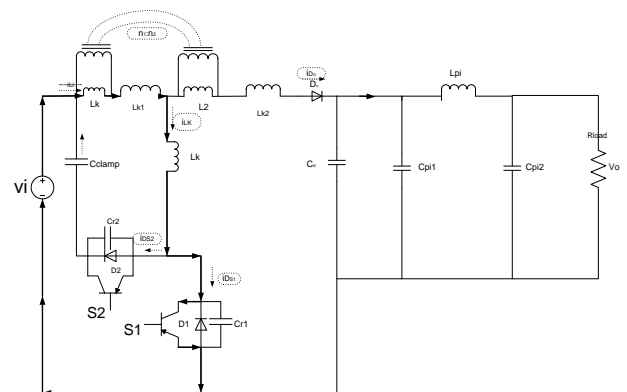
### E. Topological Modes



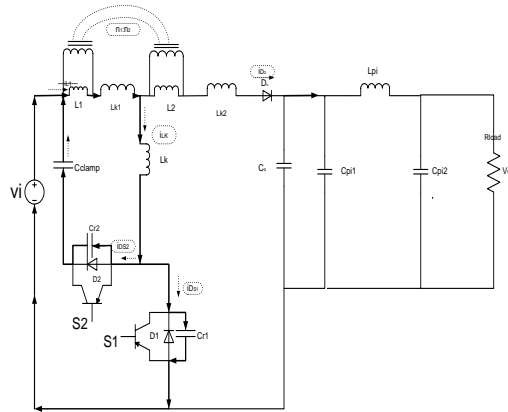
a (Mode 1)



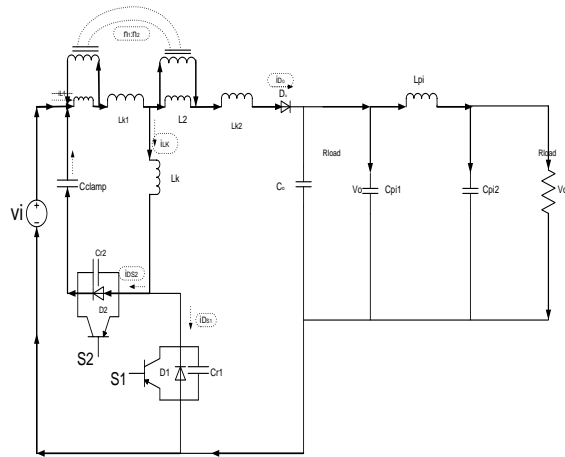
b (Mode2)



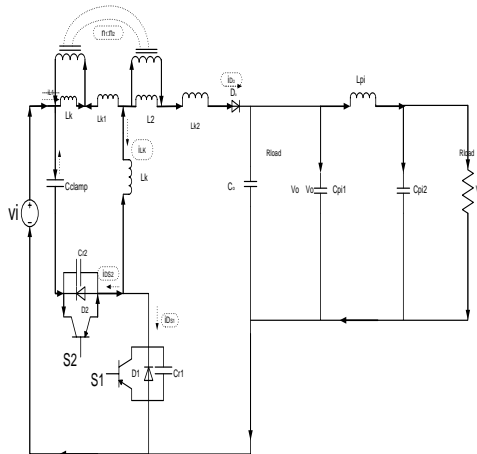
c (Mode 3)



d (Mode 4)



e (Mode 5)



f (Mode 6)

#### Mode 1

$[T_0 < t < T_1]$ : At  $T_0$ , auxiliary switch S2 is turned off, and main switch S1 still stays in the OFF state. In this mode, resonant inductor Lk resonates with Cr1 and Cr2, in which capacitor Cr2 is continuously charged toward  $V_i + V_{clamp}$ , while capacitor Cr1 is discharged down to zero. To achieve a

ZVS feature for switch S1, the energy that is stored in resonant inductor Lk should satisfy the following inequality:

$$0.5 \times [i_{Lk}(T)]^2 L_k \geq 0.5 \times [v_{DS1}(T_O)]^2 (C_{r1} \square C_{r2}) \quad (1)$$

#### Mode 2

$[T_1 < t < T_2]$ : Mode 2 begins when voltage VDS1 drops to zero at  $T_1$ . Inductor current  $i_{Lk}$  forces the body diode D1 of S1 to conduct and create a ZVS condition for S1. The driving signal should be applied to switch S1 when its body diode is conducting, achieving a ZVS feature. Inductor current  $i_{Lk}$  linearly increases, which can be expressed as.

$$i_{Lk}(t) = \frac{(V_i + V_o/n)}{L_k} t + i_{Lk}(T_1) \quad (2)$$

In this mode, resonant inductor current  $i_{Lk}$  increases toward zero, while diode current  $i_{Do}$  drops to zero, with its decreasing rate limited by the resonant inductor, reducing reverse recovery loss.

#### Mode 3

$[T_2 < t < T_3]$ : This mode begins when S1 starts to conduct current at  $T_2$ . In this mode, auxiliary switch S2 and boost diode Do are in the OFF-state, and the input current flows through the path.

Loop: . Inductor current  $i_{L1}$  is linearly increased, which can be expressed as follows:

$$i_{Lk}(t) = \frac{V_i \cdot L_1}{L_1 + L_k} \times t + i_{L1}(T_2) \quad (3)$$

Assuming .

#### Mode 4

$[T_3 < t < T_4]$ : At  $T_3$ , main switch S1 is turned off, while auxiliary switch S2 and boost diode Do still stay in the OFF-state. In this mode, inductors Lk and Lk1 release their energy to capacitors Cr1 and Cr2 in a resonant manner. Capacitor Cr1 is charged toward  $V_i + V_{clamp}$ , while capacitor Cr2 is discharged down to zero. To achieve a ZVS feature for switch S2, the energy that is stored in resonant inductor Lk should also satisfy the following inequality:

$$0.5 \times [i_{Lk}(T_3)]^2 L_k \geq 0.5 \times [v_{DS2}(T_3)]^2 (C_{r1} \square C_{r2}) \quad (4)$$

#### Mode 5

$[T_4 < t < T_5]$ : Mode 5 begins when voltage VDS2 drops to zero at  $T_4$ . Inductor current  $i_{Lk}$  forces the body diode D2 of S2 to conduct and create a ZVS condition for S2. The driving signal should be applied to switch S2 when its body diode is conducting, achieving a ZVS feature. In this mode, voltage VDS1 increases continuously and is clamped to  $V_i + V_{clamp}$ . Meanwhile, boost diode Do begins conducting. Inductor L2 is discharged through diode Do, and inductor L1 is discharged through the coupled inductors to the load. The inductor currents can be expressed as follows:

$$i_{L1}(t) = \frac{(V_o - V_i)/(1+n)}{L_1} \times t + i_{L1}(T_4) \quad (5)$$

And

$$i_{L2}(t) = \frac{(V_o - V_i)[n/(1+n)]}{L_2} \times t + i_{L2}(T_4) \quad (6)$$

Where  $n = n_2/n_1$  is the turns ratio of the coupled inductors. The energy that is stored in resonant inductors  $L_k$  and  $L_{k1}$  is recycled to capacitor  $C_{clamp}$ . Because the capacitance of  $C_{clamp}$  is large enough, voltage  $V_{clamp}$  will remain constant. Thus, inductor current  $i_{Lk}$  is linearly decreased, which can be expressed as

$$i_{Lk}(t) = \frac{V_{clamp} - (V_o - V_i)/(1+n)}{L_k} \times t + i_{Lk}(T_4) \quad (7)$$

Mode 5 ends when inductor current  $i_{Lk}$  drops to zero.

Mode 6

$[T_5 < t < T_6]$ : At  $T_5$ , inductor current  $i_{Lk}$  reverses its direction, and capacitor  $C_{clamp}$  begins to release its stored energy through  $S_2$ ,  $L_k$ ,  $L_{k1}$ , and the coupled inductors. At this interval, diode  $D_o$  is conducting, and inductors  $L_1$  and  $L_2$  are discharged continuously to the load. When switch  $S_2$  is turned off again at the end of mode 6, the converter operation over one switching cycle is complete.

#### F. Analysis

In steady-state operation of the proposed converter, time intervals  $\Delta T_s$  and  $(1-D)T_s$  are very short as compared to one switching period. Thus, they are not considered in the analysis of the DC voltage transfer ratio and the simplified waveforms are shown in Fig.1.1 below, in which the time of main switch is  $\Delta T_s$  and represents the switching period of the converter operation

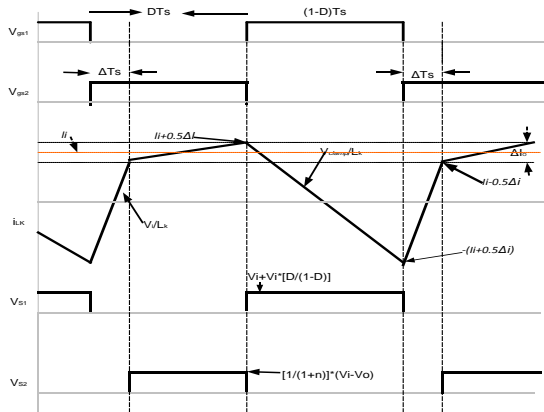


Fig 1.1 Current switching period of operation wrt time

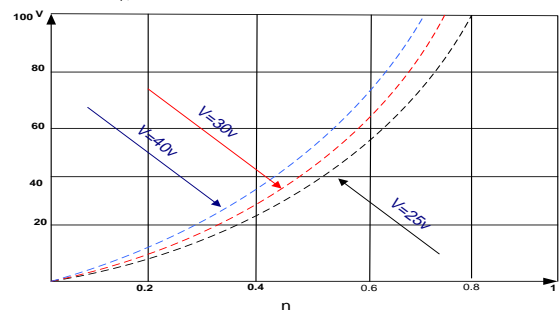


Figure 2. Relationship between voltage  $V_{clamp}$  and duty ratio

According to the plots, voltage will go beyond input voltage when  $D$  is greater than 0.5, which will result in a high voltage stress that is imposed on the components.

Thus, the duty ratio is usually limited to lower than 0.5 in the converter design. The input-to-output transfer ratio can be derived as

$$M_{ideal} = \frac{V_o}{V_i} = \frac{nD+1}{1-D} \quad (8)$$

When ignoring the charging time of resonant inductor. The charging time of the resonant inductor will reduce the effective duty ratio. The lost time interval can be expressed as

$$\Delta T_s = \frac{2I_i \times L_k}{V_i + V_o} \quad (9)$$

$$I_i = \frac{V_o I_o}{nV_i D} \quad (10)$$

And  $\eta$  is the conversion efficiency of the proposed converter. During the charging time, inductor  $L_1$  is continuously discharged, and the effective duty ratio of switch  $S_1$  will be less than that of the control signal that was applied. Thus, the input-to-output transfer ratio that is given in equation (11) should be modified to the following expression:

$$M_{real} = \frac{V_o}{V_i} = \frac{n(D - \frac{\Delta T_s}{T_s}) + 1}{1 - (D - \frac{\Delta T_s}{T_s})} \quad (11)$$

The relationships between  $D$  and for different values of turns ratio  $n$ , as illustrated in Fig 3. Comparing these two sets of curves reveals that the difference between the ideal case and the real is small for small values of  $D$  and  $n$ . From the curves that were shown in Fig. 3.



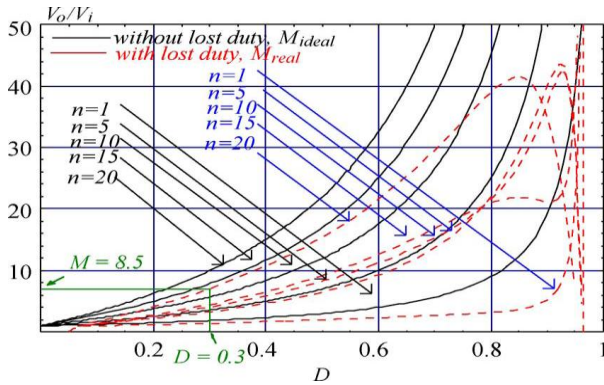


Figure 3. relationships between D and  $M = V_o/V_i$

It is difficult for the converter to achieve a high step-up voltage ratio when it is operated with either a low value of  $n$  or a high value of  $D$ . Additionally the proposed converter operates in a duty ratio that is higher than 0.5, which will induce high voltage stresses on its switches.

Thus, in the design, the duty cycle is usually selected with a value that is lower than 0.5, and the turns ratio  $n$  is higher than five to achieve a high step-up voltage ratio. Analytical expressions of the component stresses are derived in the next section.

#### G. Current Stress and Efficiency:

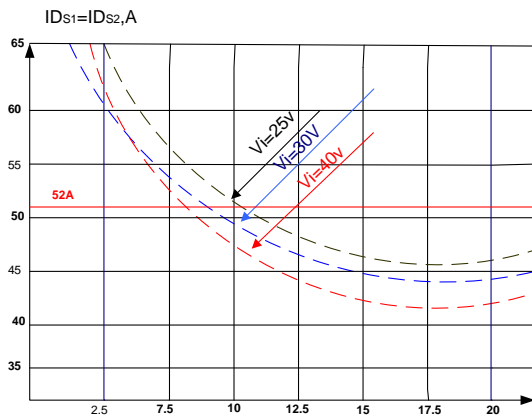


Figure 4. current stress of main switch S1 also decreases with an increase

Fig. 4 shows that the current stress of main switch also decreases with an increase in  $n$ . In the proposed converter, the voltage and current stresses of the active switches can be both reduced. Lower voltage stress implies that switches with lower can be used. Moreover, the energy that is trapped in the leakage inductance and that stored in can be recovered. It is noticeable that the stress results from voltage spike can be eliminated in the proposed converter. However, the voltage stress of the boost diode is increased with the use of coupled inductors, and high-voltage operation of a diode might induce a high reverse recovery loss. In the proposed converter, the leakage inductor of the coupled inductors can limit the decreasing rate of the diode current, resulting in lower reverse-recovery loss. In practice, selection of a high-voltage diode is easier than that of a MOSFET. Thus, it is a good tradeoff with

such a design. The key design step of the converter is to determine turns ratio  $n$  to insure low voltage stress and sufficient operational margin. In practice, the design needs a tradeoff between power losses and turns ration. For a low-input-voltage application and with soft-switching features, conduction loss will be more significant than switching loss. The conduction loss and efficiency of the proposed converter can be estimated as follows:

$$P_{loss} = i_{DS1}^2 r_{ds(on)} D + r_{ds(on)} (1-D) \times [(C_{r1} \square C_{r2}) v_{DS2}^2] / L_k$$

Efficiency of the converter is more than 95% on a low duty ratio. Switching loss also decreases and switching Turn-ON time is decreases to improve the efficiency of this model and decrease the losses.

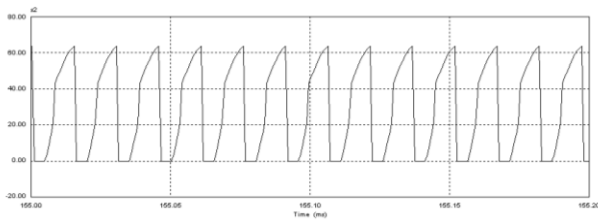
### III. DESIGN & SIMULATION RESULTS

Our topological circuit is advance and efficient and is design for the following rated values which is given in table.

Input voltage ( $V_i$ )	30V
Output voltage ( $V_o$ )	411V
Voltage across switch 1( $V_{s1}$ )	60v
Voltage across switch 2( $V_{s2}$ )	60v
Voltage applied to switch 1( $V_{gs1}$ )	15v
Voltage applied to switch 2( $V_{gs2}$ )	15v
Couple inductor	$L_p=5\text{mh}; L_s=2\text{mh}; N_p=6T; N_s=38T$ EE-55 Core;
Switch	S1=S2: IRFZ44N(150v/0A) $R_{DS(on)}=0.032\Omega$
Buffer	BD140
Diode	Do:Schottky diode (STPS20H100CT,500v/10A)
Capacitor	$C_o=220\mu\text{F}/1000\text{v}$ (Equivalent series resistance $3\Omega$ ) ; $C_{clamp}=12\mu\text{F}/100\text{v}$ (Equivalent series resistance $4\Omega$ )

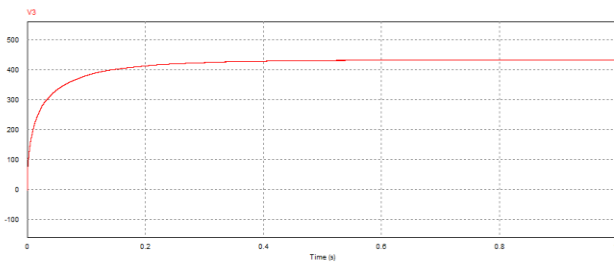


#### Voltage across switch 2:



The above picture shows the voltage waveform measured across switch 2. Above is the measured voltage as compared to the fed voltage

#### Output Voltage :



Measured waveform of the output voltage shows the output voltage is round about 411V.

#### CONCLUSION

This study developed a high-efficiency proposed boost converter with coupled inductors for power sources with large voltage diversity. The proposed converter can yield an excessive step-up voltage ratio and sustain a right duty cycle, resulting in lower electrical stresses. Through adopting the snubber circuit, the power that is trapped in the leakage inductor can be recovered, voltage spike can be suppressed efficiently and ZVS features can be accomplished successfully.

- This topology adopts only two switches to achieve the objectives of power flow.
- The voltage gain and utilization rate of the magnetic core can be substantially increased by using coupled inductors with lower turn ratio and the copper loss in magnetic core can be greatly reduced with lower turn ratio.

- The topology analysis of the converter has been provided in detail, from which layout equations and circuit parameters have also been derived. The proposed converter has an asymmetrical pulse-width-modulation system.
- Experimental results have proven that the proposed converter can gain excessive efficiency over a wide load range. It's far distinctly appropriate for low-input-voltage systems.
- Moreover, the detailed stability analysis on the control issue could be further studied by using dynamic behavior modeling techniques.

#### REFERENCES

- [1] O.K. Marti and H. Wino grad, Mercury Arc Rectifiers, Theory and Practice, McGraw-Hill, 1930, p.419, Fig. 221.
- [2] L. Tang G.-J. Su. An interleaved reduced-component-count multivoltage bus DC/DC converter for fuel cell powered electric vehicle applications[J]. IEEE Transactions on Industry Applications, 2008, 44(5): 1638-1644.
- [3] Irfan Jamil, Zhao Jinquan, Rehan Jamil, "Analysis, Design and Implementation of Zero-Current-Switching Resonant Converter DC-Dc Converter" International Journal of Electrical and Electronics Engineering (IJEET), Vol. 2, Issue 2, May 2013.
- [4] O.K. Marti and H. Wino grad, Mercury Arc Rectifiers, Theory and Practice, McGraw-Hill, 1930, p.419, Fig. 221.
- [5] X. Zhang, L. Jiang, J. Deng, et al. Analysis and design of a new soft-switching boost converter with a coupled inductor[J]. IEEE Transactions on Power Electronics, 2014, 29(8): 4270-4277.
- [6] M. Aurangzeb, Z. Jinquan, I. Jamil, and M. F. Ali, "Case study of development boost converter with coupled inductors for PV system applications," in Ubiquitous Computing, Electronics & Mobile Communication Conference (UEMCON), IEEE Annual, 2016, pp. 1-6.
- [7] Zero-Voltage-Switching Boost Converter Using a Coupled Inductor Hyun-Lark Do Dept of Electronic and Information Eng., Seoul National University of Science and Technology, Seoul, Korea.
- [8] [encon.fke.utm.my/courses/notes/MSc-Chopper.pdf](http://encon.fke.utm.my/courses/notes/MSc-Chopper.pdf)
- [9] G. Chen, Y. S. Lee, S.Y.R. Hui, D. H. Xu, and Y. S. Wang, "Actively clamped bidirectional fly back converter," IEEE Trans. Ind. Electron, vol. 47, no. 4, pp. 770-779, Aug. 2000.
- [10] L. Schuch, C.Rech,H.L. Hey,H.A.Gründling,H.Pinheiro,and J.R.Pinheiro, "Analysis and design of a new high-efficiency bidirectional integrated ZVT PWM converter for DC-bus and battery-bank interface," IEEE Trans. Ind. Appl., vol. 42, no. 5, pp. 1321-1332, Sep./Oct.2006.



# Geomechanical Principles of Hydraulic Fracturing Method in Unconventional Gas Reservoirs

Solomon Anwana Unwana, Patrick Godwin Oyindobra Ossai, Ugochukwu Ilozurike Duru, Princewill Nnaemeka Ohia, Abrakasa Seleggha

**Abstract**—Unconventional gas production from shale formation is not new to oil and gas experts worldwide. But our research work was built around hydraulic fracturing technique with focus on the Perkins Kern-Nordgren (PKN) 1972 hydraulic fracturing model(s). It is a very robust and flexible model that can be used on two major shale reservoirs (with the assumption of a fixed height and fracture fluid pressure). The essence was to compare detailed geo-mechanical parameters extracted from wire-line logs with Perkin-C model to select the right well as candidate for simulation. It aided in the prediction production of shale gas from tight shale formations. These also helped in reviewing safe and economical ways of obtaining clean energy sources. Based on similarities in well and formation properties our research team subjected IDJE-2 well (located in the Agbada shale Formation of Niger Delta, Nigeria) to various conditions, equations and assumptions proposed by the study model while also validating our results with the PENOBSCOT L-30 well, located in Canada (with existing profound results from stimulations). The PENOBSCOT L-30 well (Case 1) and IDJE-2 well (Case 2) were both subjected to same conditions, equations and assumptions as applicable to the study model to enable us compare and evaluate stimulation performances. But both cases tend to react differently. However the fluid behavior at constant injection time increases at about 99.64%. Whereas, the maximum width at wellbore shows that a constant increase of fracture width will yield an increase in proppant permeability, tensile strength and Poisson's ratio for Case 1 & 2. Our research results show how rock properties can affect fracture geometry and expected production rates from stimulated shale

reservoir formations.

**Keywords**— Perkins Kern-Nordgren PKN, Hydraulic fracturing, Niger Delta, Shale gas, Unconventional gas, geo-mechanical principles

## I. INTRODUCTION

Fracturing has been in existence since the 18th century but extracting unconventional gas is relatively new unlike coal-bed methane production that began in the 1980's; Shale gas extraction is even more recent and its technology is widely accepted and applied to improve gas recovery in unconventional reservoirs. Unconventional reservoir to be address here are wells with low permeability, low porosity and complicated geological setting in-situ stress field (as is observed in shale gas). This entire characteristic makes the process challenging. Massaras et al., (2012) stated that fracturing is of four categories namely:

- i. Pneumatic Fracturing; uses gas, pressurized air and fluid
- ii. Dynamic loading which uses cryogenic, thermal/mechanical and,
- iii. Enhanced bacterial methano-genesis.

But for the purpose of this research, hydraulic fracturing method which falls under the pneumatic fracturing category will be considered.

Hydraulic fracturing is a very common and important simulation technique for enhancing unconventional gas reservoirs in the world today, Himanshu, (2011) states. It is basically a process of initiating and subsequently propagating a crack (or fracture) in the surface rock layer by means of a pressurized fluid. It is a process that produces fractures in rock formation which stimulate the flow of natural gas or oil and increasing the volume that can be recovered. Montgomery and Smith, (2010) stated that 2.5 million fracture treatments have been performed worldwide since Stanolind Oil introduced hydraulic fracturing method in 1949. According to them, it is believed that approximately 60% of all wells drilled today are fractured. Fracture stimulation not only increases the production rate, but it is credited with adding to the reserves. Montgomery and Smith, (2006) stated that 9 billion bbl. of oil and more than 700 Tscf of gas were added since 1949 to US

Solomon Anwana Unwana: Petroleum Engineers/Lecturers, Department of Petroleum Engineering, Federal University of Technology, Owerri, Imo State, Nigeria, s.unwana@yahoo.com.

Patrick Godwin Oyindobra Ossai: Petroleum Engineers/Lecturers, Department of Petroleum Engineering, Federal University of Technology, Owerri, Imo State, Nigeria, engrpatrickossai@yahoo.com.

Ugochukwu Ilozurike Duru: Petroleum Engineers/Lecturers, Department of Petroleum Engineering, Federal University of Technology, Owerri, Imo State, Nigeria, ugooduru@yahoo.com.

Princewill Nnaemeka Ohia: Petroleum Engineers/Lecturers, Department of Petroleum Engineering, Federal University of Technology, Owerri, Imo State, Nigeria, princepetra@yahoo.com.

Abrakasa Seleggha: Petroleum Engineer / Lecturer, Department of Geology, University of Port Harcourt, Port-Harcourt, Rivers State, Nigeria, sabrakasa@hotmail.com.

reserves alone—which otherwise would have been uneconomical to develop. Hence accelerating production and net present value of reserves. Wells drilled vertically may now extend hundreds to thousands of feet below the land surface and may include horizontal or directional sections extending thousands of feet. Runar, (2010) stated that the Geo-mechanical assessment of the formation must be viewed and analyze in detail with necessary conversion done to determine the potential of fracturing and faulting caused by initiating the injection process. However, properties to be obtained from well logs such as Poisson's ratio, Young's modulus, stress, strain and shear modulus can be calculated using wireline logs i.e. sonic logs

This research seeks to review existing literature on hydraulic fracturing, its processes, geo-mechanical studies, methods of gathering information, and relevant recommendation.

Nigeria is deeply affected by insufficient power to feed her populace, which has brought slow pace of development in all sectors of its economy. However, the inclusion of unconventional gas to the already existing energy resources cannot be overemphasized as it will go a long way in giving her citizenry energy independence, economic definition and stability. The world's energy demand will increase by 30-40% in the next 20 years making hydraulic fracturing technology vital throughout the world and Nigeria is not exempted.

Oil Producer Trade Section (OPTS) 2016, states that Nigeria is in the position to generate 40,000Mw of power daily for 68 years from the Country's indigenous gas reserve estimated 181Tcf in-turn making her gas super-power- the largest in Africa and ninth largest in the world but it has only 4000kw in full operation which is not up one-tenth of the abundance of its resources.

It has been observed that since inception, Nigeria has always turned a blind eye on her abundant unconventional gas reservoirs which is unfair. Presently, the United States of America, Canada, China and Argentina are beneficiaries of the shale boom which has transformed their economy enormously. However, as a matter of importance and national urgency, gas from shale formation should be considered as a bailout as it will affect Nigerian economy positively, businesses, increase jobs creation and give access to clean and ready gas supply thereby reducing carbon emission by half that of oil making her a net gas exporter. Hence, hydraulic fracturing method in unconventional gas reservoir with the use of geo-mechanical principles is used to develop shale gas deposit. Hydraulic fracturing design models are used as prediction tools for optimizing hydraulic fracturing.

#### A. Shale Reservoir Characteristics

Shale is a sedimentary rock which consists of very fine grained rock of silt and clay particles (basically lithified mud). Sixty percent of the earth's sedimentary crust consists of shale; hence it forms primarily the source rock for conventional hydrocarbon deposit around the world. Despite having reasonable porosity, it has extremely low permeabilities (Nanodarcies to microdarcies). Organic shale are different from other mudstones and clay-stones because they are laminated,

finely layered and fissile mostly characterized by higher level of total organic carbon (TOC) of range 2%- 10% Reservoir, pictorially represented below. Few shale deposits from the abundance are actually okay for development as hydrocarbon resources play. Hence the target for shale gas exploration is characterized by:

- i. High level of Organic matter 2.2wt % ,
- ii. Low level of oxygen,
- iii. Density  $\sim 2500\text{kg/m}^3$ ,
- iv. Porosity up to 30%,
- v. Permeability in nano-darcies to micro-darcies,
- vi. Bulk Modulus  $\sim 10\text{GPa}$ ,
- vii. Young's Modulus 0.2 - 0.4,
- viii. Shear modulus  $\sim 1.6\text{GPa}$ , 5 -100  $\text{MPa}$ ,
- ix. Shear strength 3 - 30  $\text{MPa}$ ,
- x. P-waves velocity 1400 - 3000m/s ,
- xi. S-waves  $\sim 2600\text{m/s}$

As a result of the rock properties, production increases from the onset of hydraulic fracturing, which enables permeable pathway for gas fluid by aiding natural fracture. For emphasis, hydraulic fracturing is the use of the exact formulation of fluid and materials to create or restore small fracture in a formation in order to stimulate production from new and existing gas wells. For proper extraction of natural gas the process stages are:

- i. The acid stage; this consist of the mixture of dilute acid such as hydrochloric acid or muriatic acid and water to clear cement debris on the path of the wellbore thereby opening conduit for frack-fluid to dissolve carbonate minerals near the wellbore.
- ii. A pad stage; consists slick water solution without a propan. This facilitates flow and replacement of propan materials around the wellbore.
- iii. A prop sequence stage; this is done with the intention to keep open or 'prop' the fracture created. The mixture of several hundred-thousand gallons of water combines with propan material (fine mesh sand or ceramics) to use sequentially.
- iv. Finally, the flush stage; this entails the use of fresh water to flush excess propan from the wellbore.

#### B. Stages in Shale Gas Extration

Shale gas extraction consists of three consecutive stages listed below:

- a. Exploration: This is the initial process of the project phase where appraisal wells are drilled (2-3 wells) and fractured to determine the presence of tight gas in the reservoir. Also, to determine the economic viability of the reservoir.
- b. Production: The production stage involves the commercial production of gas. Shale with commercial reserve of gas well typically is greater than hundred meters thick and laterally over a space of over hundred square kilometer down subsurface. They are characterized by shallow dip meaning they

are almost horizontal. Hence horizontal drilling and hydraulic fracturing are likely to increase production.

- c. Abandonment: This happened to every other well. A shale gas well is abandoned once it reaches the end of its producing life- when extraction is no more economic. Section of the well above subsurface is hewed after they are filled with cement to prevent gas from contaminating the water table.

### C. Brief History and Locations (S) of Shale Gas Deposits in Nigeria

Nigeria has no commercial productions of unconventional gas. Nevertheless there is a pointer to the fact of the presence of unconventional gas resources such as the tight sands gas, coal-beds methane (CBM) and shale gas within Nigeria. These resources are located mostly on the inland basins of Benue trough and Maiduguri (i.e. Borno) basin, the study area spans from northeastern to the southeastern parts of Nigeria. The lower Benue (i.e. Anambra basin), the middle Benue and the upper Benue (i.e. Yola sub-basins and Gongola) made up the Benue trough. Facts also have it that Nigeria is not left out in terms of shale deposits. Shale formation are abundantly located in Nigeria most especially the North-east and south-south. Hence there are potentials for shale gas in the Niger Delta basins most especially the Imo shale group with 312m thickness which exists in the Paleocene basin/age and Cross-river basins- south western regions of Nigeria and Benin (Dahomey) basins in the south-south respectively. States such as Benue, Borno, Adamawa, Anambra, and Enugu significantly stands out. also examples of such Basins such as the Agwu shale formation, Eze-Aku Shale, Nsukka formation 233m, Mamu formation, Nkporo shale 1829m, Ajali sandstones 450m, Enugu shale and Afowo shale formation of Dahomey Basins. Ekwueme et al (1995)

Also, the Odukpani formation consists of black calcareous shale which has been assigned. Eze-Aku formation consist black calcareous shale, shelly with boundary thickness towards Aba in Abia state to Owerri. Agwu formation also consist bluish-grey shale a cenomanian age based on the amount of fauna Ehinola et al. (2008)

## II. INTRODUCING THE RESEARCH MODEL (S)

### A. Perkin-Kern-Nordgren (PKN) 1972 Model

We compared and analyzed geo-mechanical parameters from the Niger Delta shale gas reservoir(s) using Perkin-Kern-Nordgren (PKN) 1972 model for possible hydraulic fracturing and validating our result findings using foreign reservoir data(s). We also looked at the applicability of hydraulic fracturing technology history as applied in foreign unconventional reservoir rocks in contrast to Niger Delta. Our research team also extracted foreign reservoir geo-mechanical parameters using Techlog software(s). Defining shale formation geo-mechanical properties and parameters required indirect presentation of hydraulic fracturing from well-log data(s) like sonic, gamma ray, density/porosity log while using conversion equations' methods to calculate the:

- a. Poisson's ratio
- b. Young modulus and
- c. To determine where to fracture the shale formation for maximum flow to the well bore.

#### 1) Perkins-C Model/Method

Perkins and kern (1961) Nordgren (1972) incorporated the carter equation II in the original PKN model which states the engineering procedure for material balance at constant injection rate with fluid leak off. In as much as it is a method, it is more preferred in the oil industry because of its vertical plain strain assumption which is more physically acceptable for proposed height contained fractures where the fracture length becomes considerably greater than the fracture height. Moreover, it predicts fracture length closer than all other 3D models and is widely applicable to unconventional formations.

Fracture in this method requires a constant height H, elliptic vertical cross-section with maximum width Wm at the center, propagated in horizontal x direction given the injection rate (Q0), fluid properties, mechanical properties of the rock formation, in-situ stress  $\sigma_0$ , virgin pore pressure P0, leak-off coefficient, well fracture width and history as well as pressure history in borehole (fracture inlet), fracture direction/ azimuth.

#### 2) General PKN Assumptions

In order to simplify the complex problem the following assumptions were made by the PKN models:

1. The fracture fluid pressure is constant in vertical cross section perpendicular to the direction of propagation.
2. Fracture height  $h_f$  is fixed and independent of fracture length
3. Each plane obtained an elliptical shape with maximum width in the center.
4. Resistance to deformation prevails in vertical plane.

$$w(x, t) = \frac{(1-v)h_f (P-\sigma_h)}{G} \quad (1)$$

5. Flow-rate is a function of growth rate of the fracture width.

$$\frac{\delta q}{dx} = -\frac{\pi h_f}{4} \frac{\partial w}{\partial t} \quad (2)$$

6. Vertical cross-section has an elliptical form
7. Isotropic, homogenous, linear elastic rock mass
8. Fracture is in plain strain in the vertical.

### B. Well Candidacy Selection Criteria

Hydraulic fracturing is a serious and costly business. Hence, the failure or success of a hydraulic fracture treatment depends on the quality of the well(s) selected. Therefore, choosing an excellent well candidate for stimulation is important. However, to select the best candidate for



stimulation, the design engineer must consider the following variables:

- i. Formation permeability: Permeability is either a low-permeability zone or already highly damaged (high skin factor).
- ii. The in-situ stress distribution within the formation
- iii. The reservoir depth: Zones to be fractured are usually thick pay zone with large areal extent.
- iv. Skin factor: this refers to whether the reservoir has been stimulated or is damaged (Note: If it is positive, reservoir is damaged, indicating a good candidate for stimulation)
- v. The reservoir fluid viscosity.
- vi. The condition of the wellbore: Well must possess substantial volume of gas in place (GIP) and the need to increase productivity index should arise.

### C. Data –Set (S) Development

A complete and accurate dataset set is needed by a petroleum engineer for fracture treatment design. Compiling set could be time consuming but rewarding. Fracture design model are often categorized as either ‘controlled’ or ‘Not controlled’ by engineer. Those controlled are the well completion details, treatment volume, injection rate, fracture fluid viscosity, fracture fluid density, proppant agent type and volume, in-situ stress. (Note that all three are primary data) while formation permeability (which is most important), formation modulus, reservoir pressure, reservoir thickness, formation porosity, formation depth, formation compressibility are measured or estimated. In all these, it is important to state in-situ stress profile, permeability of formation to be stimulated above and below target zones which will affect fracture height growth. Meanwhile, data to be design are obtained from various source including the production data, completion records, open-hole log, drilling record and publications. A proper flow chart is given below to illustrate the whole process using these model(s).

### D. Hydraulic Fracturing Principle (S)/ Equations

Firstly, from the starting point at injection time ‘t’, the injection rate entering one wing of the fracture is equal to the sum of the different leak-off rate with the growth rate of the fracture volume. Mathematically, injection rate is given by equation 3.4 below:

$$\frac{q_i}{2} = 2 \int_0^t \frac{c_l}{\sqrt{t-\tau}} \left( \frac{\partial A}{\partial \tau} \right) \partial \tau + (w + 2s_p) \frac{\partial A}{\partial t} + A \frac{\partial w}{\partial t} \quad (3)$$

Where,

$q_i$  = total rate of injection

$C_L$  = Overall Leak-Off Coefficient

$\tau$  = opening time at filtration start

$S_p$  = Spurt Loss

Note:

1. Neglecting width increase during fracture growth
2. Assuming constant injection rate.

Fracture surface area A at a given time ‘t’ is also given by equation (4) below:

$$A(t) = \frac{(w+2s_p)}{4C_L} \frac{q_i}{2} \left[ \exp(\beta^2) \operatorname{erfc}(\beta) + \frac{2\beta}{\sqrt{\pi}} - 1 \right] \quad (4)$$

Where:

$$\text{shape factor, } \beta = \frac{2C_L \sqrt{\pi t}}{w+2s_p}$$

Further recommended because of the inaccuracy of rock properties, fracture width at wellbore  $W_f$  for no leak-off is improved to (5) below as:

$$W_f = 9.15 \wedge \left( \frac{1}{2n+2} \right) 3.98 \frac{n}{2n+2} \left[ \frac{1+2.14n}{n} \right] K \left( \frac{1}{2n+2} \right) \left( \left( \frac{q_1}{2} \right)^n \frac{h_f^{1-n} x_f}{E!} \right) \wedge \frac{1}{2n+2} \quad (5)$$

Where:

$n$  = power law component (dimensionless)

$k$  = consistency index (pas-sec<sup>n</sup>)

Using shape factor ( $\pi/5$ ) for PKN model, the average width ( $\varpi$ ) along fracture length is given by  $W_f = \pi/5$ .

Using carter Equation II with the average fracture width, fracture half-length/ fracture height can therefore be given as:

$$x_f = \frac{(\varpi+2s_p)}{4C_L^2 \pi h_f} \frac{q_i}{2} \left[ \exp(\beta^2) \operatorname{erfc}(\beta) + \frac{2\beta}{\sqrt{\pi}} - 1 \right] \quad (6)$$

The above equation 3.7 serves as the solution to fracture propagation problem knowing values ( $x_f$ ) and ( $q_1$ ). The fracture length or injection time can easily be determined using the numerical root finding method.

Net fracture pressure ( $P_{net}$ ) is calculated:

$$P_{net} = \frac{E'}{2h_f} W_{w,0} \quad (7)$$

Hence, the fracture treatment pressure  $P_{treat}$  at wellbore equals the addition of in-situ stress and net fracture pressure.

At the Wellbore,  $P_{treat} = \sigma + P_{net}$

Nolte et al, (2000) presented an approximate optimum pad volume and proppant schedule which is important to hydraulic fracturing treatment design. He stated that the material balance equation during fracture growth at any time is:

$$v_i = v_f + v_l \quad (8)$$

$$v_i = q_i \times t_i \quad (9)$$

Where:

$V_f$  = fracture volume

$V_l$  = fluid volume leaked.

Economides and Nolte (2000) projected ( $v_f$ ) as:

$$v_f = \frac{\pi}{2} \gamma h_f x_f w_f \quad (10)$$

Final propped width after the closure of fracture is given as:

$$w_p = \frac{W_{pr}}{2x_f h_f (1 - \phi_p) \rho_p} \quad (11)$$

Where:

$W_{pr}$  = Weight of proppant

$Q_p$  = Proppant porosity

$\rho_p$  = proppant density

$2x_f h_f$  = fracture area.

### III. RESEARCHED CASES

#### A. Case 1: PENOBSCOT L-30, Located in Canada

##### Assumptions / Data(s)

Well fracture properties:

Injection rate @ 46 bpm / 0.12189m<sup>3</sup>/s

Leak-off coefficient @ 6×10<sup>-5</sup> m/s

Injection time @ 1000 sec

Young's modulus (E) @ 0.3

Poisons ratio @ 0.40

Fluid viscosity ( $\mu$ ) @ 5.6×10<sup>-7</sup>mPa or 5.6×10<sup>-4</sup>cp

Fracture height ( $h_f$ ) @ 10<sub>ft</sub> / 15.24m

Spurt loss @ 0.65 gal /sq-ft

Fracture length ( $X_f$ ) @ 50 ft.

Fracture half-length ( $L_f$ ) @ 25ft

Porosity ( $\phi$ ) 15% - 25%

Permeability (k) @ 25mD

Maximum fracture width @ the wellbore in terms of power law is given as:

$$W_f = 9.15 \wedge \left( \frac{1}{2n+2} \right) 3.98 \frac{n}{2n+2} \left[ \frac{1+2.14n}{n} \right] K \left( \frac{1}{2n+2} \right) \left( \left( \frac{q_1}{2} \right)^n \frac{h_f^{1-n} x_f}{E!} \right) \wedge \frac{1}{2n+2} \quad (12)$$

Where:

$$E! = \frac{E}{1-v^2}$$

$$n = 0.1756(1000\mu)^{-0.1233} \quad (13)$$

For the fluid behavior as given by Peter P. Valko (2005):

$$k = 47.880(500\mu - 0.0159) \quad (14)$$

Based on our assumptions stated above for Case 1, we have that:

Power law Rheology,  $n' = 0.2$ ,

$k' = 12.6 \text{ lbf/ft}^2 \cdot \text{Sn}$  and  $E! = 0.3$

Substituting these variables into (5), the maximum fracture width gave 94.5m which when converted to inches gave 59.12in respectively.

$$\hat{W}_e = 0.628 W_{w,0} \quad (15)$$

with a shape factor ( $\beta$ ) = 7.04×10<sup>-5</sup>.

More so, the fracture Area 'A' when calculated from (4) at a given time 't' using the complimentary error function table  $erfl$  0.06 – 1.31 A(t), gives a fracture area of 5777m<sup>2</sup>.

The net fracture pressure P(net) from (7) also gave a value of 1.6947psi/ft

#### 1) PROPANT SCHEDULING:

Applying Material balance equation:

$$v_i = v_f + v_l$$

$$\text{Nolte exponent, } \varepsilon = \frac{1 - \eta_e}{1 + \eta_e} = 0.53.$$

$$v_{pad} = \varepsilon v_i = 64.6 \text{ m}^3$$

$$t_{pad} = \varepsilon \times t_e = 530 \text{ sec}$$

$$\text{Fluid efficiency; } \eta_e = \frac{v_{ef}}{v_1} = 0.2798 \text{ or } 28\%$$

The dimensionless fracture gradient (Cf<sub>D</sub>) is given by Cinco-Ley (1978) as:

$$cf_D = 31.4159 k L_f \quad (16)$$

From Case 1 data above, if the formation permeability is 25md and the optimum fracture half-length is 25ft, then the optimum fracture conductivity would be 1964 md-ft. the dimensionless fracture gradient, Cf<sub>D</sub>, at minimum 10 is considered to prevent any clean-up issues hence slick-water is most appropriate to be used as a proppant for hydraulic fracturing this zone. 2.5g/cm<sup>3</sup> was assumed as the density of HPG as well as the weight of proppant as 3.0mmlb.

The injected slurry volume is represented by (17) below and it yielded about 121.89m<sup>3</sup> or 32,199.89 gallons after substituting known values.

$$V_1 = q_1 \times t_e \quad (17)$$

Volume at the end of pumping gives 9.00988m<sup>3</sup> after substituting known values into (18) below:

$$V_{fe} = x_f \times h_f \times \hat{W}_e \quad (18)$$

Final propped width 'W<sub>p</sub>' after closure of fracture as stated in (9) gives approx. 1411.8m

#### B. Case 2: IDJE-2, AGBADA Formation, Nigeria

##### Assumption(s) / Real Data values:

Fracture properties/assumptions for IDJE-2 well, Agbada shale Formation are:

Injection rate @ 46 bpm

Leak-off coefficient @ 6×10<sup>-5</sup> m/s

Injection time @ 1000 sec

Young's modulus (E) @ 2.3×10<sup>10</sup>

Poisons ratio @ 0.33-044

Fluid viscosity ( $\mu$ ) @ 0.15cp

Fracture height ( $h_f$ ) @ 10ft  
 Spurt loss @ 0.65 gal / sq-ft  
 Fracture length ( $X_f$ ) @ 50ft.  
 Fracture half-length ( $L_f$ ) @ 25ft  
 Porosity ( $\phi$ ) @ 30%  
 Permeability ( $k$ ) @ 40mD

Maximum fracture width at wellbore in terms of power law is given as:

$$W_f = 9.15 \left( \frac{1}{2n+2} \right) 3.98^{\frac{n}{2n+2}} \left[ \frac{1+2.14n}{n} \right] K \left( \frac{1}{2n+2} \right) \left( \left( \frac{q_1}{2} \right)^n \frac{h_f^{1-n} x_f}{E!} \right)^{\frac{1}{2n+2}}$$

Where:

$$E! = \frac{E}{1-v^2}$$

$$n = 0.1756(1\mu)^{-0.1233}$$

$$k = 47.880(500\mu - 0.0159) \text{ Peter P. Valko. (2005)}$$

Substituting the values from Case 2 assumptions above gives:

$$\text{Power law Rheology, } n' = 0.1, \text{ and } k' = 3590 \text{ lbft/ft}^2 \text{S}^n \text{ and } E! = 5.84 \times 10^9$$

Therefore, substituting the variables into (5) for the maximum fracture width gives 94.5m which when converted to inches gives 59.12in.

$$\hat{W}_e = 0.628 W_{w,0}$$

Also, with a shape factor ( $\beta$ ) of  $3.08 \times 10^{-3}$

More so, the fracture Area 'A' when calculated from (4) at a given time 't' using the complimentary error function table  $erfl$  0.06 – 1.31 A(t), gives a fracture area of 5777m<sup>2</sup>.

The net fracture pressure P(net) from (7) gave a value of 2.56psi/ft

#### 1) PROPANT SCHEDULING:

Material balance equation as stated by Nolte (1986)

$$v_i = v_f + v_l$$

$$\text{Nolte exponent } (\varepsilon) = \frac{1-\eta_e}{1+\eta_e} = 0.90$$

$$v_{pad} = \varepsilon v_i = 109.8_m^3$$

$$t_{pad} = \varepsilon \times t_e = 900 \text{ sec}$$

Fluid efficiency;

$$\eta_e = \frac{v_{ef}}{v_1} = 0.261 \text{ which is equivalent to 26\%}$$

The required dimensionless fracture conductivity ( $Cf_D$ ) by Cinco-Ley (1978) is:

$$cf_D = 31.4159 k L_f$$

From data above, if the formation permeability is 25md and the optimum fracture half-length is 25ft, then the optimum fracture conductivity would be 1964 md-ft. The dimensionless fracture gradient,  $Cf_D$ , at minimum 10 is considered to prevent any clean-up issues hence slick-water is most appropriate to be used as a propanant for hydraulic fracturing this zone. 2.5g / cm<sup>3</sup> were assumed as the density of HPG as well as the weight of propanant as 3.0mmlb.

The injected slurry volume from equation below gives 121.89.m<sup>3</sup>

$$V_1 = q_1 \times t_e$$

Volume at the end of pumping gives 8.41m<sup>3</sup>

$$V_{fe} = x_f \times h_f \times \hat{W}_e$$

Final propped width 'Wp' after closure of fracture as stated in (9) gives 1411.8m

Having view hydraulic fracturing technology in its entirety in unconventional reservoir rock and tentatively analyzed the geo-mechanical properties using the pern-kern-Nordgren model of different location of interest, I found out the following as answers to my research questions. These are illustrated in figures below.

Also, with basic assumption taken, the model reacted slightly differently in both cases. For the fluid behavior at constant injection time, a noticeable increase of 99.64% in consistency index represents an apparent or effective viscosity as a function of shear rate which describes the behavior of a real non-Newtonian fluid in any flow condition.

## IV. RESULTS, DISCUSSIONS AND INTERPRETATIONS

TABLE 1.1 CALCULATED RESULTS IN SUMMARY FOR CASE 1& 2 APPLYING PKN-PKN-MODEL

P A R A M E T E R ( S )	PENOBSCOT L-30 (WELL1) CASE 1 (CANAI)	I D J E - 2 (WELL 2) CASE 2 (AGBADA, NIGER)
Fluid Efficiency (%)	2 8	2 6
Fracture Area (m2)	5 7 7 7	5 7 7 7
Nolte Exponent	0 . 5 3	0 . 9 0
S h a p e F a c t o r	7.04 X 10-5	3.08 X 10-3
Power Law Rheology (n)	0 . 2	0 . 1
Max.Fracture Width,Wmax (m)	9 4 . 5	9 4 . 5
Net Fracture Pressure (psi/ft)	1 . 6 9 4 7	2 . 5 6 0 0
Optimum Fracture Conductivity (md-ft)	1 9 6 4	1 9 6 4

Injected Slurry Vol.(m3)	1 2 1 . 8 9	1 2 1 . 8 9
Final Propped Width (m)	1 4 1 1 . 8	1 4 1 1 . 8
Final Pumped Vol.(m3)	9 . 0 0 9	8 . 4 1 0

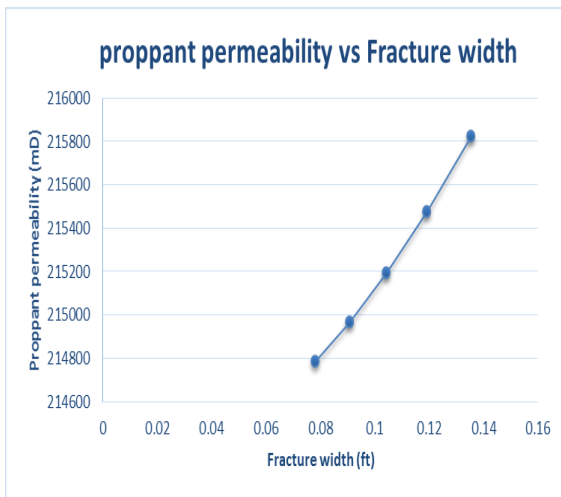


Figure 1. A graph showing the relationship between the power component and the average well fractured width (inch)

#### A. Results Discussions/Interpretations (S):

Fig.1 above shows at a glance the responds of Well 1 and Well 2 properties by the PKN hydraulic fracturing model used. Well 1 showed a higher average well width and Well 2 shows average well width of 0.0552inch. This is considerably low when taking into account the above assumptions which states that before PKN model must be used, its fracture height must be at least twice of the fracture length.

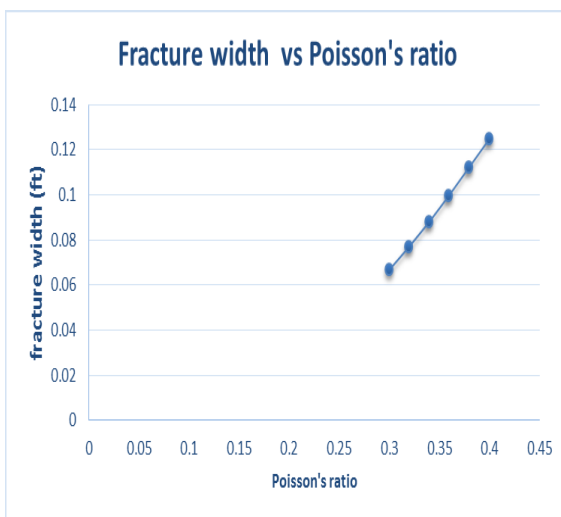


Figure 2. A graph showing the relationship between the fracture width and the Poisson's ratio

#### B. Result Discussions/Interpretations

Rock properties such as permeability, tensile strength and pore pressure affects fracture geometry. Of these, young's modulus, Poisson's ratio stands out as that factor which control

other rock properties, since they affect fracture geometry directly. However, the study of the relationship between the fracture parameters such as Fracture width, height, and half-length was considered closely, also operational parameters such as injection rate was also studied to show their effect on fracture geometry. Young's modulus expresses resistance of material to deform. Therefore, Young's modulus value increases as the expected fracture width decrease. However, the reduction per unit change of Young's modulus is not significant (0.088inches). Shale formation generally has relatively low Young's modulus, meaning that fracture width will be greater than expected width from conventional formation.

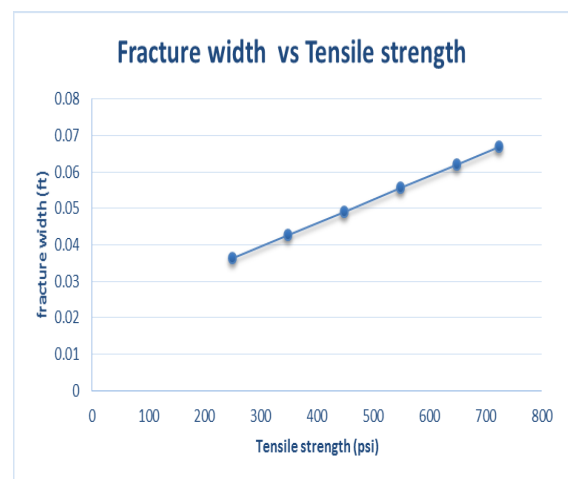


Figure 3. A graph showing the relationship between the fracture width and the Tensile strength

#### C. Result Discussions/Interpretations

Hydraulic fracture increases as width increases which directly increases Poisson's ratio. Also, from analysis has stated that rock with high strength will have less Poisson's ratio since they deform less when compressive force acts on them. To this premise, it is stated that Poisson's ratio will increase as fracture width increases. Since shale formation has low strength compared to conventional formation, expected Poisson's ratio in shale will be higher than any other formation. Tensile strength increases the required break-down pressure which is proportional to the fracture width. Also, proppant permeability is equally proportional to fracture width which will initiate flow. Therefore, the conductivity which is dimensionless increases as permeability increases in a well.

#### CONCLUSION AND RECOMMENDATION

The rock properties, Poisson's ratio and formation tensile strength affects the fracture geometry and expected production rates. As assumed by the PKN model, fracture height should not be fixed and should not be assumed to be larger than the

formation thickness but should be larger, smaller or even equal to the formation thickness depending on the rock properties. Poisson's ratio increases fracture width, increases proppant permeability also as a result of increasing fracture conductivities. The various increase effect on fracture width and fracture conductivity is positive as it also increases the fracture height but inversely affects the half-height whose result causes reduction of fracture width.

#### REFERENCES

- [1] Carl T. Montgomery and Michael B. Smith, NSI Technologies Editor's (2006, December): Hydraulic fracturing; The Fuss, The Facts, The Future. Journal of petroleum technology (JPT) pdf file
- [2] Carl T. Montgomery and Micheal B. Smith, NSI Technologies (2010), hydraulic fracturing: history of enduring technology Journal of petroleum technology (JPT)
- [3] Cinco-Ley, et samaniego- V.F and A.N., D (1978). Behavior for a well with infinite conductivity vertical fracture SPE J 18(4): 253-264.SPE 6014-PA
- [4] Economides, M.J and Nolte G. Kenneth (2000): Reservoir simulation third edition, New York: John Wiley & Sons, ISBN10:047191926 / ISSN 13:9780471491927
- [5] Ekwueme BN, Nyon EE, Petters SW (1995), Geological guide book, South-eastern Calabar, Deeford publishing company, Calabar Nigeria
- [6] Himanshu Yadav M.S.E (2011). Hydraulic fracturing in naturally fractured reservoir and the impact of geo-mechanics on micro-seismicity, <http://hdl.handle.net/2152/ETD-UT-2011-12-4889>
- [7] Massaras L. (2012), Oilpro question and Answer - Type of Fracking GRI, AST and Europe JRC
- [8] Ehinola O.A, Sonibare O.O, Falode O.A and Awofala B.O (2008), Hydrocarbon Potential and Thermal Maturity of Nkporo Shale from Lower Benue Trough, Nigeria
- [9] Oil producer Trade Section OPTS (2016), Nigeria in position to generate 40,000MW through gas reserves, ESI Africa's Power Journal
- [10] Peter P. Valko, Economides (2005), Hydraulic Fracturing short course., Fracture design, Fracture Dimension, Fracturing Modeling. Texas A&M University College station, Texas
- [11] Runar Nygaard (2010), Geo-mechanical Analysis Wabamun Area CO2 Sequestration Project (WASP), University of Calgary, Institute of Energy, environment and Economy (ISEEE), Canada. PDF



# Existence Criteria and Hyers-Ulam Theorem for a Coupled P-Laplacian System of Fractional Differential Equations

Kiran Tabassum, Liu Xiangyang, Syed Furqan Rafique, Irfan Jamil

**Abstract**— Dealing with high order coupled systems of FDEs through nonlinear p-Laplacian operator. We analyze existence, uniqueness & Hyer-Ulam stability (HUS) of the solutions by means of topological degree method. For this purpose, we transform the supposed problem into an integral system via Green's function(s) and assume certain operator equivalent to the integral form of the problem. Then after, the results are proved with some necessary assumptions.

**Keywords**— Fractional differential equations (FDEs), Hyer-Ulam stability (HUS), topological degree theory, existence and uniqueness of solutions (EUS).

## I. INTRODUCTION

The real world physical phenomena described by mathematical models of fractional differential equations (FDEs) are more constructive and practical in memory as compared to the models of integer order differential equations. Due to the application of FDEs, one can learn fractional calculus in diverse fields like metallurgy, signal and image processing, economics, fractal theory, biology and other disciplines [16-26]. Existence of solutions for FDEs is one of the most attracted research areas. For the different classes of FDEs, one can study different methods for existence and uniqueness of solutions. Various nonlinear mathematical models can be found in the scientific fields to study dynamic systems. The classical nonlinear operator  $\phi_p$  is one of the most important and frequently used nonlinear operators, which satisfies

$$\frac{1}{p} + \frac{1}{q} = 1, \quad \phi_p(s) = |s|^{p-2}s, \quad p > 1 \text{ and } \phi_q(\theta) = \phi_p^{-1}(\theta).$$

For details and applications of nonlinear operator  $\phi_p$ , we pass on readers to [27-34].

Here we highlight some related and interested research problems and contribution of scientists. Baleanu et al. [1] proved existence of some super linear FDE solutions and presented some applications of their results. Kuman et al. [2] presented stability and existence results for a class of FDE with help of topological degree theory. Baleanu et al. [3] proved existence solution for a nonlinear FDE on partially ordered Banach spaces. Baleanu et al. [4] studied that under certain assumptions the solutions of FDEs are eventually large and eventually small. Mahmudov and unul [5] studied a FDE with integral conditions involving order  $2 < \alpha \leq 3$ , an impulsive fractional differential equation [6] and FDE with p-Laplacian operator [7], for existence of solutions.

Hu et al. [8] calculated existence of non-linear FDEs using the p-Laplacian operator:

$$\begin{cases} D_{0+}^{\gamma} \left( \phi_p \left( D_{0+}^{\rho} \mu(t) \right) \right) + f(x, \mu(t), D_{0+}^{\rho} \mu(t)) = 0, & t \in (0,1), \\ D_{0+}^{\rho} \mu(0) = 0 = D_{0+}^{\rho} \mu(1), \end{cases}$$

where  $0 < \rho, \gamma < 1, 1 < \rho + \gamma < 2, D_{-(0+)}^{\rho}, D_{-(0+)}^{\gamma}$  are in the sense of Caputo derivatives.

Ali et al. [9] calculated the EUS and HUS for coupled system of FDEs:

$$\begin{aligned} D_{0+}^{\rho} x(t) &= f(t, y(t)), & t \in [0,1], \\ D_{0+}^{\gamma} y(t) &= f(t, x(t)), & t \in [0,1], \\ x(0) &= 0, \quad x(t)|_{t=1} = \frac{1}{\Gamma(\sigma)} \int_0^T (T-s)^{\sigma-1} p(x(s)) ds, \\ y(0) &= 0, \quad y(t)|_{t=1} = \frac{1}{\Gamma(\delta)} \int_0^T (T-s)^{\delta-1} q(y(s)) ds, \end{aligned}$$

where  $\rho, \gamma, \sigma, \delta \in (1,2], D_{0+}^{\rho}, D_{0+}^{\gamma}$  are in the sense of Caputo derivatives,  $p, q \in L[0,1]$ .

Khan et al. [36] recently calculated the existence and uniqueness of positive solutions and HUS for the following system of coupled FDEs:

$$\begin{aligned} D_{0+}^{\gamma_1} \left( \phi_p \left( D_{0+}^{\rho_1} x(t) \right) \right) &= -\Psi_1(t, y(t)), \quad D_{0+}^{\gamma_2} \left( \phi_p \left( D_{0+}^{\rho_2} y(t) \right) \right) \\ &= -\Psi_2(t, x(t)), \\ D_{0+}^{\rho_1} x(0) &= 0 = \left( \phi_p \left( D_{0+}^{\rho_1} x(t) \right) \right)' |_{t=0} = D_{0+}^{\delta_1} x(t)|_{t=\eta_1}, \quad x(1) \\ &= \frac{\Gamma(2-\delta_1)}{\eta_1^{1-\delta_1}} J^{\rho_1-\delta_1} \phi_q \left( J^{\gamma_1} \Psi_1(t, y(t)) \right) |_{t=\eta_1}, \end{aligned}$$

Kiran Tabassum: College of Science, Hohai University, 210098, Nanjing, P. R. China. e-mail: kirantabassam@gmail.com

Liu Xiangyang: College of Science, Hohai University, 210098, Nanjing, P. R. China. e-mail: liuxy@hhu.edu.cn

Syed Furqan Rafique: Department of Electrical Engineering, North China Electric Power University, Beijing, P.R.China. e-mail: syedfurqan@ncepu.edu.cn

Irfan Jamil: College of Energy and Electrical Engineering, Hohai University, 210098, Nanjing, P.R.China. e-mail: I.jamil@hhu.edu.cn



$$D_{0+}^{\rho_2} y(0) = 0 = \left( \phi_p \left( D_{0+}^{\rho_2} y(t) \right) \right)' \Big|_{t=0} = D_{0+}^{\delta_2} y(t) \Big|_{t=\eta_2}, y(1) \\ = \frac{\Gamma(2-\delta_2)}{\eta_2^{1-\delta_2}} \mathcal{I}_{\eta_2}^{\rho_2-\delta_2} \phi_q \left( \mathcal{I}_{\eta_2}^{\gamma_2} \Psi_2(t, x(t)) \right) \Big|_{t=\eta_2}$$

where  $t \in [0,1], \rho_i, \gamma_i \in (1,2], \eta_i, \delta_i \in (0,1]$ , for  $i = 1,2$ , and  $D_{0+}^{\rho_i}, D_{0+}^{\gamma_i}, D_{0+}^{\delta_i}$  for  $i = 1,2$  are denoting Caputo fractional derivatives.

In classical cases the fixed point theorems have some very strong conditions which limit the applications of the results to big extent for the study of many categories of FDEs and their coupled systems. Nowadays, degree theory plays a significant role in relaxing of the necessary conditions required for the study of fixed points of operators and EUS for a large number of FDEs and its coupled systems for their solutions. Different types of degree theorems have been produced including the well-known Brouwer and Leray-Schauder theory which have been considered by a large number of scientists for the

exploration of different aspects of fractional calculus especially dealing with existence of positive solution of differential equations involving integer order as well non-integer. A version of the degree theory acknowledged as topological degree theory which was introduced by Mawhin [10] and further expanded by Isaia [11] was considered for the existence results of linear as well nonlinear FDEs. The proposed technique is also known as prior estimation technique, which does not involve the compactness of operators. For new results on topological degree theory, we suggest the readers for the study of some recently developed results in [12-14].

Enthused from the abovementioned studies, we study the EUS and HUS of a coupled system with initial and boundary conditions and non-linear operator  $\phi_p$  using the topological degree method:

$$\begin{cases} D_{0+}^{\beta_1} \left( \phi_p \left( D_{0+}^{\alpha_1} u(t) \right) \right) = -\psi_1(t, v(t)), & D_{0+}^{\beta_2} \left( \phi_p \left( D_{0+}^{\alpha_2} v(t) \right) \right) = -\psi_2(t, u(t)), \\ \left( \phi_p \left( D_{0+}^{\alpha_1} u(t) \right) \right) \Big|_{t=1} = 0, \left( \phi_p \left( D_{0+}^{\alpha_1} u(t) \right) \right)^{(k)} \Big|_{t=0} = 0, \text{ for } k = 1, 2, 3, \dots, n-1, \\ \left( \phi_p \left( D_{0+}^{\alpha_2} v(t) \right) \right) \Big|_{t=1} = 0, \left( \phi_p \left( D_{0+}^{\alpha_2} v(t) \right) \right)^{(k)} \Big|_{t=0} = 0, \text{ for } k = 1, 2, 3, \dots, n-1, \\ u^{(i)}(0) = 0, \text{ for } i = 0, 1, 2, \dots, m-2, m, \dots, n-1, u^{(m-1)}(1) = 0, \\ v^{(i)}(0) = 0, \text{ for } i = 0, 1, 2, \dots, m-2, m, \dots, n-1, v^{(m-1)}(1) = 0, \end{cases} \quad (1.1)$$

where  $\alpha_i, \beta_i \in (n-1, n], \psi_1, \psi_2 \in L[0,1]$  and  $D_{0+}^{\alpha_i}, D_{0+}^{\beta_i}$  for  $i = 1,2$  stand for Caputo fractional derivative  $\phi_p(\mathcal{N}) = |\mathcal{N}|^{p-2}\mathcal{N}$  is non-linear operator  $\phi_p$  satisfying  $1/p + 1/q = 1, \phi_q$  represents inverse of  $\phi_p$ . Here, we affirm that applying degree method to treat existence, uniqueness also to get the

conditions for the stability of Hyers-Ulam to a coupled system of (FDEs) with  $\phi_p$  (1.1) has not been explored to our loyal awareness and understanding. Therefore, this work may get the attention of researchers to the study of Hyers-Ulam stability for more complex problems. We test enough conditions for the stability of EUS and HUS for system (1.1).

Where  $[\alpha]$  is the integer part of  $\alpha$ .

## II. AUXILIARY RESULTS

**Definition 2.1.** The fractional integral of order  $\alpha > 0$  of  $f: (0, +\infty) \rightarrow \mathbb{R}$  is defined as

$$I_{0+}^{\alpha} \psi(t) = \frac{1}{\Gamma(\alpha)} \int_0^t (t-s)^{\alpha-1} \psi(s) ds,$$

Given that integral on R.H.S is point wise defined on the interval  $(0, +\infty)$ , where

$$\Gamma(\alpha) = \int_0^{+\infty} e^{-s} s^{\alpha-1} ds.$$

**Definition 2.2.** For a function  $\psi(t)$  the fractional Caputo's derivative of  $\alpha$  order is defined by the following integral form (provided it exist)

$$D_{0+}^{\alpha} \psi(t) = \frac{1}{\Gamma([\alpha] + 1 - \alpha)} \int_0^t (t-s)^{[\alpha]-\alpha} \psi^{([\alpha]+1)}(s) ds,$$

**Lemma 2.3.** Let  $\alpha \in (n-1, n], \psi \in AC^{n-1}$ , then

$$I_{0+}^{\alpha} D_{0+}^{\alpha} \psi(t) = \psi(t) + c_0 + c_1 t + c_2 t^2 + \dots + c_{n-1} t^{n-1},$$

For the  $c_i \in \mathbb{R}$  for  $i = 0, 1, 2, \dots, n-1$ .

Consider the space of real valued continuous functions  $V = C([0,1], \mathbb{R})$  with Topological norm  $\|v\| = \sup\{|v(t)|: 0 \leq t \leq 1\}$  for  $v \in V$ . The product space  $\omega = V \times V$  with the norm  $\|(v, z)\| = \|v\| + \|z\|$  is also Banach space. We give a notation  $S$  to the class of all bounded mappings in  $\omega$ .

**Definition 2.4.** For the mapping  $\xi: S \rightarrow (0, \infty)$  Kuratowski measure of non-compactness is:

$$\xi(\mathcal{M}) = \inf_{\{\mathcal{F}\}} \left\{ r > 0: \mathcal{M} \text{ the finite cover for sets of diameter } \leq r \right\}$$

where  $\mathcal{M} \in S$ .

**Definition 2.5.** Let  $T: \vartheta \rightarrow V$  be bounded and continuous mapping with  $\vartheta \subset V$ . Then  $T$  is an  $\xi$ -Lipschitz, where  $\varsigma \geq 0$  if

$$\xi(T(\mathcal{M})) \leq \varsigma \xi(\mathcal{M}) \text{ for all bounded } \mathcal{M} \subset \vartheta.$$

And  $T$  is a strict  $\xi$ -contraction with  $\varsigma < 1$ .

**Definition 2.6.** The function  $T$  is  $\xi$ -condensing if

$$\xi(T(\mathcal{M})) < \xi(\mathcal{M}) \text{ for all bounded } \mathcal{M} \subset \vartheta \text{ such that } \xi(\mathcal{M}) > 0.$$

Therefore  $\xi(T(\mathcal{M})) \geq \xi(\mathcal{M})$  yields  $\xi(\mathcal{M}) = 0$ .

More we have  $T: \vartheta \rightarrow V$  is Lipschitz for  $\varsigma > 0$ , such that

$$\|T(v) - T(\bar{v})\| \leq \varsigma \|v - \bar{v}\| \text{ for all } v, \bar{v} \in \vartheta.$$

The condition  $\varsigma < 1$ , then  $T$  is a strict contraction.

**Proposition 2.7.** The  $T$  is said to be  $\xi$ -Lipschitz with  $\varsigma = 0$  if and only if  $T: \vartheta \rightarrow V$  is said to be compact.

**Proposition 2.8.** The  $T$  is said to be  $\xi$ -Lipschitz for constant value  $\varsigma$  if and only if  $T: \vartheta \rightarrow V$ , is Lipschitz with constant  $\varsigma$ .

$$\begin{cases} D_{0+}^{\beta_1} \left( \phi_p \left( D_{0+}^{\alpha_1} u(t) \right) \right) = -\psi_1(t, v(t)), \\ \left( \phi_p \left( D_{0+}^{\alpha_1} u(t) \right) \right) |_{t=1} = 0, \left( \phi_p \left( D_{0+}^{\alpha_1} u(t) \right) \right)^{(k)} |_{t=0} = 0, \text{ for } k = 1, 2, 3, \dots, n-1 \\ u^{(i)}(0) = 0, \text{ for } i = 0, 1, 2, \dots, m-2, m, \dots, n-1, u^{(m-1)}(1) = 0, \end{cases}$$

is given by the integral equation

$$u(x) = \int_0^1 H^{\alpha_1}(t, s) \phi_q \left( \int_0^1 H^{\beta_1}(s, t) \psi_1(t, v(t)) dt \right) ds, \quad (3.2)$$

where  $H^{\alpha_1}(t, s), H^{\beta_1}(t, s)$  are Green's function(s) defined by

$$H^{\alpha_1}(t, s) = \begin{cases} \frac{(t-s)^{\alpha_1-1}}{\Gamma(\alpha_1)} - t^{m-1} \frac{(1-s)^{\alpha_1-m}}{\Gamma(m)\Gamma(\alpha_1-(m-1))}, & 0 \leq s \leq t \leq 1, \\ -t^{m-1} \frac{(1-s)^{\alpha_1-m}}{\Gamma(m)\Gamma(\alpha_1-(m-1))}, & 0 \leq t \leq s \leq 1, \end{cases} \quad (3.3)$$

$$H^{\beta_1}(t, s) = \begin{cases} -\frac{(t-s)^{\beta_1-1}}{\Gamma(\beta_1)} + \frac{(1-s)^{\beta_1-1}}{\Gamma(\beta_1)}, & 0 \leq s \leq t \leq 1, \\ \frac{(1-s)^{\beta_1-1}}{\Gamma(\beta_1)}, & 0 \leq t \leq s \leq 1. \end{cases} \quad (3.4)$$

*Proof.* Applying operator  $I_{0+}^{\beta_1}$  on (3.1) and with help of Lemma (2.3), we proceed the following

$$\phi_p \left( D_{0+}^{\alpha_1} u(t) \right) = -I_{0+}^{\beta_1} \psi_1(t, v(t)) + c_1 + c_2 t + \dots + c_n t^{n-1} \quad (3.5)$$

Condition  $\left( \phi_p \left( D_{0+}^{\alpha_1} u(t) \right) \right)^{(k)} |_{t=0} = 0$ , for  $k = 1, 2, 3, \dots, n-1$  results  $c_2 = c_3 = \dots = c_n = 0$ . And  $\left( \phi_p \left( D_{0+}^{\alpha_1} u(t) \right) \right) |_{t=1} = 0$ , implies

$$c_1 = I_{0+}^{\beta_1} \psi_1(t, v(t)) |_{t=1} = \frac{1}{\Gamma(\beta_1)} \int_0^1 (1-s)^{\beta_1-1} \psi_1(s, v(s)) ds. \quad (3.6)$$

**Theorem 2.9.** [11] Let  $T: V \rightarrow V$  be an  $\xi$ -condensing and

$$\mathcal{H} = \{z \in V: \text{there exist } 0 \leq \lambda \leq 1 \text{ such that } z = \lambda Tz\}.$$

If  $\mathcal{H}$  is a bounded in  $V$ , there exists  $a > 0$ , and  $\mathcal{H} \subset \mathcal{M}_a(0)$ , with degree

$$\deg(I - \lambda \mathcal{G}, \mathcal{M}_r(0), 0) = 1 \text{ for every } \lambda \in [0, 1].$$

So,  $T$  has atleast one fixed point and collection of all fixed points of  $T$  are contained in  $\mathcal{M}_a(0)$ .

**Lemma 2.10** [15] For the nonlinear operator  $\phi_p$ , we have

1. If  $1 < p \leq 2, \ell_1 \ell_2 > 0$  and  $|\ell_1|, |\ell_2| \geq m > 0$ , then  $|\phi_p(\ell_1) - \phi_p(\ell_2)| \leq (p-1)m^{p-2}|\ell_1 - \ell_2|$ .
2. If  $p > 2$ , and  $|\ell_1|, |\ell_2| \leq F$ , then  $|\phi_p(\ell_1) - \phi_p(\ell_2)| \leq (p-1)F^{p-2}|\ell_1 - \ell_2|$

### III. MAIN RESULTS

**Theorem 3.1.** Let  $\psi_1 \in C[0, 1]$  be an integrable function satisfying (1.1). Then the solution of

By using values of  $c_i$  for  $i = 1, 2, \dots, n$  and (3.5), we have

$$\begin{aligned}\phi_p \left( D_{0+}^{\alpha_1} u(t) \right) &= -I_{0+}^{\beta_1} \psi_1(t, v(t)) + I_{0+}^{\beta_1} \psi_1(t, v(t))|_{t=1} \\ &= -\frac{1}{\Gamma(\beta)} \int_0^t (t-s)^{\beta_1-1} \psi_1(s, v(s)) ds + \frac{1}{\Gamma(\beta_1)} \int_0^1 (1-s)^{\beta_1-1} \psi_1(s, v(s)) ds \\ &= \int_0^1 H^{\beta_1}(t, s) \psi_1(s, v(s)) ds,\end{aligned}\quad (3.7)$$

where  $H^{\beta_1}(t, s)$  is a Green's function given in (3.4).

Applying  $\phi_q = \phi_p^{-1}$  in (3.7), we get

$$D_{0+}^{\alpha_1} u(t) = \phi_q \left( \int_0^1 H^{\beta_1}(t, s) \psi_1(s, v(s)) ds \right). \quad (3.8)$$

Applying operator  $I_{0+}^{\alpha_1}$  on (3.8) and Lemma 2.10, we get

$$\begin{aligned}u(t) &= I_{0+}^{\alpha_1} \left( \phi_q \left( \int_0^1 H^{\beta_1}(t, s) \psi_1(s, v(s)) ds \right) \right) + z_1 + z_2 t + \dots + z_m t^{m-1} + \dots \\ &\quad + z_n t^{n-1}\end{aligned}\quad (3.9)$$

Using condition  $u^{(i)}(0) = 0$ , for  $i = 0, 1, 2, \dots, m-2, m, \dots, n-1$ , we obtain  $z_1 = z_2 = \dots z_{m-1} = z_{m+1} = \dots z_n = 0$ . From condition  $u^{(m-1)}(1) = 0$ , we have

$$z_m = -\frac{1}{(m-1)!} I_{0+}^{\alpha_1-(m-1)} \left( \phi_q \left( \int_0^1 H^{\beta_1}(t, s) \psi_1(s, v(s)) ds \right) \right) |_{t=1} \quad (3.10)$$

Now putting the values of  $z_i$ , for  $i = 1, 2, \dots, m, \dots, n$  in (3.9), we have

$$\begin{aligned}u(t) &= I_{0+}^{\alpha_1} \left( \phi_q \left( \int_0^1 H^{\beta_1}(t, s) \psi_1(s, v(s)) ds \right) \right) - \frac{t^{m-1}}{(m-1)!} I_{0+}^{\alpha_1-(m-1)} \left( \phi_q \left( \int_0^1 H^{\beta_1}(t, s) \psi_1(s, v(s)) ds \right) \right) |_{t=1} \\ &= \left( \frac{1}{\Gamma(\alpha_1)} \int_0^t (t-s)^{\alpha_1-1} - \frac{t^{m-1}}{\Gamma(m)} \int_0^1 \frac{(1-s)^{\alpha_1-m}}{\Gamma(\alpha_1-(m-1))} \right) \phi_q \left( \int_0^1 H^{\beta_1}(s, \wp) \psi_1(\wp, v(\wp)) d\wp ds \right) \\ &= \int_0^1 H^{\alpha_1}(t, s) \phi_q \left( \int_0^1 H^{\beta_1}(s, \wp) \psi_1(\wp, v(\wp)) d\wp \right) ds\end{aligned}\quad (3.11)$$

where  $H^{\alpha_1}(t, s)$ ,  $H^{\beta_1}(s, \wp)$  are defined by (3.3), (3.4), respectively, as Green's function(s).

Following Theorem 3.1, we may write our problem in the following system

$$u(t) = \int_0^1 H^{\alpha_1}(t, s) \phi_q \left( \int_0^1 H^{\beta_1}(s, \wp) \psi_1(\wp, v(\wp)) d\wp \right) ds, \quad (3.12)$$

$$v(t) = \int_0^1 H^{\alpha_2}(t, s) \phi_q \left( \int_0^1 H^{\beta_2}(s, \wp) \psi_2(\wp, u(\wp)) d\wp \right) ds, \quad (3.13)$$

where  $H^{\alpha_2}(t, s)$ ,  $H^{\beta_2}(s, t)$  are Green's function(s) defined by

$$H^{\alpha_2}(t, s) = \begin{cases} \frac{(t-s)^{\alpha_2-1}}{\Gamma(\alpha_2)} - t^{m-1} \frac{(1-s)^{\alpha_2-m}}{\Gamma(m)\Gamma(\alpha_2-(m-1))}, & 0 \leq s \leq t \leq 1, \\ -t^{m-1} \frac{(1-s)^{\alpha_2-m}}{\Gamma(m)\Gamma(\alpha_2-(m-1))}, & 0 \leq t \leq s \leq 1. \end{cases} \quad (3.14)$$

$$H^{\beta_2}(t, s) = \begin{cases} -\frac{(t-s)^{\beta_2-1}}{\Gamma(\beta_2)} + \frac{(1-s)^{\beta_2-1}}{\Gamma(\beta_2)}, & 0 \leq s \leq t \leq 1, \\ \frac{(1-s)^{\beta_2-1}}{\Gamma(\beta_2)}, & 0 \leq t \leq s \leq 1. \end{cases} \quad (3.15)$$

Define  $T_i^*: V \rightarrow V$  for  $(i = 1, 2)$  by

$$T_1^* u(t) = \int_0^1 H^{\alpha_1}(t, s) \phi_q \left( \int_0^1 H^{\beta_1}(s, \wp) \psi_1(\wp, v(\wp)) d\wp \right) ds \quad (3.16)$$

$$T_2^* v(t) = \int_0^1 H^{\alpha_2}(t, s) \phi_q \left( \int_0^1 H^{\beta_2}(s, \wp) \psi_2(\wp, u(\wp)) d\wp \right) ds \quad (3.17)$$

We further define  $F(u, v) = (T_1^*(u), T_2^*(v))$ . Then, with help of Theorem 3.1, the solution of (3.12), (3.13) is equivalent to any fixed point, say  $(x, y)$ , of operator equation

$$(x, y) = F(x, y). \quad (3.18)$$

To proceed further, we need following assumptions in the main results of the paper.

( $Q_1$ ) With positive constant values of  $a_1, b_1, \mathbb{M}_{\psi_1}^*, \mathbb{M}_{\psi_2}^*$  and  $k_1, k_2 \in [0, 1]$ , functions  $\psi_1, \psi_2$  satisfy the following growth conditions

$$|\psi_1(x, v)| \leq \phi_p(a_1 |v|^{k_1} + \mathbb{M}_{\psi_1}^*),$$

$$|\psi_2(x, u)| \leq \phi_p(b_1 |u|^{k_2} + \mathbb{M}_{\psi_2}^*).$$

( $Q_2$ ) There exist real valued constants  $\lambda_{\psi_1}, \lambda_{\psi_2}$  such that for all  $u, v, x, y \in V$ ,

$$|\psi_1(t, v) - \psi_1(t, x)| \leq \lambda_{\psi_1} |v - x|,$$

$$|\psi_2(t, u) - \psi_2(t, y)| \leq \lambda_{\psi_2} |u - y|.$$

For simplicity in calculations, we define the following terms:

$$Y_1 = \left( \frac{1}{\Gamma(\alpha_1 + 1)} + \frac{1}{\Gamma(m)\Gamma(\alpha_1 - m + 2)} \right) \left( \frac{1}{\Gamma(\beta_1 + 1)} + \frac{1}{\Gamma(\beta_1 + 1)} \right)^{q-1},$$

$$Y_2 = \left( \frac{1}{\Gamma(\alpha_2 + 1)} + \frac{1}{\Gamma(m)\Gamma(\alpha_2 - m + 2)} \right) \left( \frac{1}{\Gamma(\beta_2 + 1)} + \frac{1}{\Gamma(\beta_2 + 1)} \right)^{q-1},$$

$$\rho_1^* = (Y_1 + Y_2)(\mathbb{M}_{\psi_1}^* + \mathbb{M}_{\psi_2}^*), \quad \delta^* = (a_1 + b_1)(Y_1 + Y_2),$$

$$\vartheta_1 = (p-1)\sigma^{p-2}\lambda_{\psi_1} \left( \frac{1}{\Gamma(\alpha_1 + 1)} + \frac{1}{\Gamma(m)\Gamma(\alpha_1 - m + 2)} \right) \left( \frac{1}{\Gamma(\beta_1 + 1)} + \frac{1}{\Gamma(\beta_1 + 1)} \right),$$

$$\vartheta_2 = (p-1)\sigma^{p-2}\lambda_{\psi_2} \left( \frac{1}{\Gamma(\alpha_2 + 1)} + \frac{1}{\Gamma(m)\Gamma(\alpha_2 - m + 2)} \right) \left( \frac{1}{\Gamma(\beta_2 + 1)} + \frac{1}{\Gamma(\beta_2 + 1)} \right).$$

**Theorem 3.2.** With assumption ( $Q_1$ ), the operator  $F: \omega^* \rightarrow \omega^*$  is continuous and satisfies following growth condition

$$F(u, v)(t) \leq \delta^* \| (u, v) \| + \rho_1^* \quad (3.19)$$

For each  $(u, v) \in \mathcal{M}_r \subset \omega^*$

*Proof.* Consider a bounded set  $\mathcal{M}_r = \{(u, v) \in \omega: \| (u, v) \| \leq r\}$  with sequence  $\{(u_n, v_n)\}$  converging to  $(u, v)$  in  $\mathcal{M}_r$ . To show that  $\| T^*(u_n, v_n) - T^*(u, v) \| \rightarrow 0$  as  $n \rightarrow \infty$ . Let us consider

$$\begin{aligned} & |T_1^* u_n(t) - T_1^* u(t)| \\ &= \left| \int_0^1 H^{\alpha_1}(t, s) \phi_q \left( \int_0^1 H^{\beta_1}(s, \wp) \psi_1(\wp, v_n(\wp)) d\wp \right) ds - \int_0^1 H^{\alpha_1}(t, s) \phi_q \left( \int_0^1 H^{\beta_1}(s, \wp) \psi_1(\wp, v(\wp)) d\wp \right) ds \right| \\ &\leq \int_0^1 |H^{\alpha_1}(t, s)| \left| \phi_q \left( \int_0^1 H^{\beta_1}(s, \wp) \psi_1(\wp, v_n(\wp)) d\wp \right) - \phi_q \left( \int_0^1 H^{\beta_1}(s, \wp) \psi_1(\wp, v(\wp)) d\wp \right) \right| ds, \end{aligned} \quad (3.20)$$

And

$$\begin{aligned}
|T_2^* v_n(t) - T_2^* v(t)| &= \left| \int_0^1 H^{\alpha_2}(t, s) \phi_q \left( \int_0^1 H^{\beta_2}(s, \wp) \psi_2(\wp, u_n(\wp)) d\wp \right) ds \right. \\
&\quad \left. - \int_0^1 H^{\alpha_2}(t, s) \phi_q \left( \int_0^1 H^{\beta_2}(s, \wp) \psi_2(\wp, u(\wp)) d\wp \right) ds \right| \\
&\leq \int_0^1 |H^{\alpha_2}(t, s)| \phi_q \left( \int_0^1 H^{\beta_2}(s, \wp) \psi_2(\wp, u_n(\wp)) d\wp \right) ds \\
&\quad - \phi_q \left( \int_0^1 H^{\beta_2}(s, \wp) \psi_2(\wp, u(\wp)) d\wp \right) ds.
\end{aligned} \tag{3.21}$$

With the help of (3.20), (3.21) and due to the continuity of the functions  $\psi_1, \psi_2$  we have  $|T_1^* u_n(t) - T_1^* u(t)| \rightarrow 0$  as  $n \rightarrow \infty$ . This implies that  $T_1^*$  is continuous. Similarly,  $|T_2^* v_n(t) - T_2^* v(t)| \rightarrow 0$  as  $n \rightarrow \infty$ , which implies  $T_2^*$  is continuous. The continuity of  $T_1^*$  and  $T_2^*$  implies that operator  $F = (T_1^*, T_2^*)$  is continuous.

Now, for the inequality (3.19), from (3.16), (3.17) and assumption  $(Q_1)$ , we continue as

$$\begin{aligned}
|T_1^* u(t)| &= \left| \int_0^1 H^{\alpha_1}(t, s) \phi_q \left( \int_0^1 H^{\beta_1}(s, \wp) \psi_1(\wp, v(\wp)) d\wp \right) ds \right| \\
&\leq \int_0^1 |H^{\alpha_1}(t, s)| \phi_q \left( \int_0^1 |H^{\beta_1}(s, \wp)| |\psi_1(\wp, v(\wp))| d\wp \right) ds \\
&\leq \int_0^1 |H^{\alpha_1}(t, s)| \phi_q \left( \int_0^1 |H^{\beta_1}(s, \wp)| \phi_p(a_1 \|v\|^{k_1} + \mathbb{M}_{\psi_1}^*) d\wp \right) ds \\
&\leq \left( \frac{1}{\Gamma(\alpha_1 + 1)} + \frac{1}{\Gamma(m)\Gamma(\alpha_1 - m + 2)} \right) \left( \frac{1}{\Gamma(\beta_1 + 1)} + \frac{1}{\Gamma(\beta_1 + 1)} \right)^{q-1} (a_1 \|v\|^{k_1} + \mathbb{M}_{\psi_1}^*) \\
&= Y_1(a_1 \|v\|^{k_1} + \mathbb{M}_{\psi_1}^*).
\end{aligned} \tag{3.22}$$

And

$$\begin{aligned}
|T_2^* v(t)| &= \left| \int_0^1 H^{\alpha_2}(t, s) \phi_q \left( \int_0^1 |H^{\beta_2}(s, \wp)| |\psi_2(\wp, u(\wp))| d\wp \right) ds \right| \\
&\leq \int_0^1 |H^{\alpha_2}(t, s)| \phi_q \left( \int_0^1 |H^{\beta_2}(s, \wp)| |\psi_2(\wp, u(\wp))| d\wp \right) ds \\
&\leq \int_0^1 |H^{\alpha_2}(t, s)| \phi_q \left( \int_0^1 |H^{\beta_2}(s, \wp)| \phi_p(b_1 \|u\|^{k_2} + \mathbb{M}_{\psi_2}^*) d\wp \right) ds \\
&\leq \left( \frac{1}{\Gamma(\alpha_2 + 1)} + \frac{1}{\Gamma(m)\Gamma(\alpha_2 - m + 2)} \right) \left( \frac{1}{\Gamma(\beta_2 + 1)} + \frac{1}{\Gamma(\beta_2 + 1)} \right)^{q-1} (b_1 \|u\|^{k_2} + \mathbb{M}_{\psi_2}^*) \\
&= Y_2(b_1 \|u\|^{k_2} + \mathbb{M}_{\psi_2}^*)
\end{aligned} \tag{3.23}$$

With the help of (3.22), (3.23), we proceed

$$\begin{aligned}
|F^*(u, v)(t)| &\leq Y_1(a_1 \|v\|^{k_1} + \mathbb{M}_{\psi_1}^*) + Y_2(b_1 \|u\|^{k_2} + \mathbb{M}_{\psi_2}^*) \\
&\leq \delta^* \| (u, v) \|^{k^*} + \rho_1^*
\end{aligned} \tag{3.24}$$

This completes the proof.

**Theorem 3.3.** Assume that  $(Q_1)$  holds true. Then  $F^*: \omega^* \rightarrow \omega^*$  is compact and  $\xi$  – Lipschitz with constant zero.

*Proof.* Theorem 3.2 implies that  $F^*: \omega \rightarrow \omega$  is bounded. Next, let  $\mathcal{B} \subset \mathcal{M}_r \subset \omega^*$ . Then, by  $(Q_1)$ , Lemma 3.1, Eq. (3.12), (3.13), then for any  $t_1, t_2 \in [0, 1]$ , we have

$$\begin{aligned}
& |T_1^* u(t_1) - T_1^* u(t_2)| \\
&= \left| \int_0^1 H^{\alpha_1}(t_1, s) \phi_q \left( \int_0^1 H^{\beta_1}(s, \wp) \psi_1(\wp, v(\wp)) d\wp \right) ds \right. \\
&\quad \left. - \int_0^1 H^{\alpha_1}(t_2, s) \phi_q \left( \int_0^1 H^{\beta_1}(s, \wp) \psi_1(\wp, v(\wp)) d\wp \right) ds \right| \\
&\leq \int_0^1 |H^{\alpha_1}(t_1, s) - H^{\alpha_1}(t_2, s)| \phi_q \left( \int_0^1 |H^{\beta_1}(s, \wp)| \phi_p(a_1 \|v\|^{k_1} + \mathbb{M}_{\psi_1}^*) d\wp \right) ds \\
&\leq \left( \frac{|t_1^{\alpha_1} - t_2^{\alpha_1}|}{\Gamma(\alpha_1 + 1)} + \frac{|t_1^{m-1} - t_2^{m-1}|}{\Gamma(m)\Gamma(\alpha_1 - m + 2)} \right) \left( \frac{1}{\Gamma(\beta_1 + 1)} + \frac{1}{\Gamma(\beta_1 + 1)} \right)^{q-1} (a_1 \|v\|^{k_1} + \mathbb{M}_{\psi_1}^*),
\end{aligned} \tag{3.25}$$

$$\begin{aligned}
& |T_2^* v(t_1) - T_2^* v(t_2)| \\
&= \left| \int_0^1 H^{\alpha_2}(t_1, s) \phi_q \left( \int_0^1 H^{\beta_2}(s, \wp) \psi_2(\wp, u(\wp)) d\wp \right) ds \right. \\
&\quad \left. - \int_0^1 H^{\alpha_2}(t_2, s) \phi_q \left( \int_0^1 H^{\beta_2}(s, \wp) \psi_2(\wp, u(\wp)) d\wp \right) ds \right| \\
&\leq \int_0^1 |H^{\alpha_2}(t_1, s) - H^{\alpha_2}(t_2, s)| \phi_q \left( \int_0^1 |H^{\beta_2}(s, \wp)| \phi_p(b_1 |u|^{k_2} + \mathbb{M}_{\psi_2}^*) d\wp \right) ds \\
&\leq \left( \frac{|t_1^{\alpha_2} - t_2^{\alpha_2}|}{\Gamma(\alpha_2 + 1)} + \frac{|t_1^{m-1} - t_2^{m-1}|}{\Gamma(m)\Gamma(\alpha_2 - m + 2)} \right) \left( \frac{1}{\Gamma(\beta_2 + 1)} + \frac{1}{\Gamma(\beta_2 + 1)} \right)^{q-1} b_1 |u|^{k_2} + \mathbb{M}_{\psi_2}^*,
\end{aligned} \tag{3.26}$$

From (3.25), (3.26), we have

$$\begin{aligned}
& |F^*(u, v)(t_1) - F^*(u, v)(t_2)| \\
&\leq \left( \frac{|t_1^{\alpha_1} - t_2^{\alpha_1}|}{\Gamma(\alpha_1 + 1)} + \frac{|t_1^{m-1} - t_2^{m-1}|}{\Gamma(m)\Gamma(\alpha_1 - m + 2)} \right) \left( \frac{1}{\Gamma(\beta_1 + 1)} + \frac{1}{\Gamma(\beta_1 + 1)} \right)^{q-1} (a_1 \|v\|^{k_1} + \mathbb{M}_{\psi_1}^*) \\
&\quad + \left( \frac{|t_1^{\alpha_2} - t_2^{\alpha_2}|}{\Gamma(\alpha_2 + 1)} + \frac{|t_1^{m-1} - t_2^{m-1}|}{\Gamma(m)\Gamma(\alpha_2 - m + 2)} \right) \left( \frac{1}{\Gamma(\beta_2 + 1)} + \frac{1}{\Gamma(\beta_2 + 1)} \right)^{q-1} (b_1 |u|^{k_2} \\
&\quad + \mathbb{M}_{\psi_2}^*)
\end{aligned} \tag{3.27}$$

As  $t_1 \rightarrow t_2$ , (3.27) approaches to zero which may be observe on the right side. Thus, the operator  $F^* = (T_1^*, T_2^*)$  is an equi-continuous on  $\mathcal{B}$ . Arzela-Ascoli theorem implies that  $F^*(\mathcal{B})$  is compact. Ultimately,  $\mathcal{B}$  is  $\xi$  - Lipschitz with constant zero.

**Theorem 3.4.** With assumptions  $Q_1 - Q_2$  and  $\delta^* < 1$ , the system of FDEs with  $\phi_p$  (1.1) has a bounded solution in  $\omega^*$ .

*Proof.* For existence of solution of the coupled differential system of fractional order (1.1), we take help from Theorem 2.9. Let us consider the set

$$S = \{(u, v) \in \omega^*: \text{there exist } \lambda \in [0, 1], \text{ such that } (u, v) = \lambda F(u, v)\},$$

We show that  $S$  is bounded. For this we assume a contrary path. Let for some  $(u, v) \in S$ , such that  $\|(u, v)\| = \mathcal{J} \rightarrow \infty$ . But from Theorem 3.2, we have

$$\begin{aligned}
\|(u, v)\| &= \|\lambda F(u, v)\| \leq \|F(u, v)\| \\
&\leq \delta^* \|(u, v)\|^k + \rho_1^*
\end{aligned} \tag{3.28}$$

Since  $\|(u, v)\| = \mathcal{J}$ , then (3.28) implies

$$\begin{aligned}
\|(u, v)\| &\leq \delta^* \|(u, v)\|^k + \rho_1^* \\
1 &\leq \delta^* \frac{\|(u, v)\|^k}{\|(u, v)\|} + \frac{\rho_1^*}{\|(u, v)\|} \\
1 &\leq \delta^* \frac{1}{\mathcal{J}^{1-k}} + \frac{\rho_1^*}{\mathcal{J}} \rightarrow 0, \text{ as } \mathcal{J} \rightarrow \infty.
\end{aligned}$$



This is a contradiction. Ultimately,  $\| (u, v) \| < \infty$  and hence the set  $S$  is bounded and therefore, by Theorem 2.9, the operator  $F$  has atleast one fixed point which is the solution of the coupled system of FDEs (1.1). And the set of solution of (1.1) is bounded in  $\omega^*$ .

**Theorem 3.5.** Assume that  $Q_1 - Q_2$  hold. Then Eq. (1.1) has a unique solution provided that  $\vartheta_1 + \vartheta_2 < 1$ .

*Proof.* From (3.16), (3.17) and assumptions  $Q_1 - Q_2$  and Lemma (2.10). Then for any  $t_1, t_2 \in [0, 1]$ , we proceed

$$\begin{aligned}
& |T_1^* u(t) - T_1^* \bar{u}(t)| \\
&= \left| \int_0^1 H^{\alpha_1}(t, s) \phi_q \left( \int_0^1 H^{\beta_1}(s, \wp) \psi_1(\wp, v(\wp)) d\wp \right) ds - \int_0^1 H^{\alpha_1}(t, s) \phi_q \left( \int_0^1 H^{\beta_1}(s, \wp) \psi_1(\wp, \bar{v}(\wp)) d\wp \right) ds \right| \\
&= \int_0^1 |H^{\alpha_1}(t, s)| \left| \phi_q \left( \int_0^1 H^{\beta_1}(s, \wp) \psi_1(\wp, v(\wp)) d\wp \right) - \phi_q \left( \int_0^1 H^{\beta_1}(s, \wp) \psi_1(\wp, \bar{v}(\wp)) d\wp \right) \right| ds \\
&= (p-1)\sigma^{p-2} \int_0^1 |H^{\alpha_1}(t, s)| \int_0^1 |H^{\beta_1}(s, \wp)| |\psi_1(\wp, v(\wp)) - \psi_1(\wp, \bar{v}(\wp))| d\wp ds \\
&\leq (p-1)\sigma^{p-2} \lambda_{\psi_1} \left( \frac{1}{\Gamma(\alpha_1 + 1)} + \frac{1}{\Gamma(m)\Gamma(\alpha_1 - m + 2)} \right) \left( \frac{1}{\Gamma(\beta_1 + 1)} + \frac{1}{\Gamma(\beta_1 + 1)} \right) (|v(t) - \bar{v}(t)|), \\
&= \vartheta_1 (|v(t) - \bar{v}(t)|),
\end{aligned} \tag{3.29}$$

And

$$\begin{aligned}
& |T_2^* v(t) - T_2^* \bar{v}(t)| \\
&= \left| \int_0^1 H^{\alpha_2}(t, s) \phi_q \left( \int_0^1 H^{\beta_2}(s, \wp) \psi_2(\wp, u(\wp)) d\wp \right) ds - \int_0^1 H^{\alpha_2}(t, s) \phi_q \left( \int_0^1 H^{\beta_2}(s, \wp) \psi_2(\wp, \bar{u}(\wp)) d\wp \right) ds \right| \\
&= \int_0^1 |H^{\alpha_2}(t, s)| \left| \phi_q \left( \int_0^1 H^{\beta_2}(s, \wp) \psi_2(\wp, u(\wp)) d\wp \right) - \phi_q \left( \int_0^1 H^{\beta_2}(s, \wp) \psi_2(\wp, \bar{u}(\wp)) d\wp \right) \right| ds \\
&= (p-1)\sigma^{p-2} \int_0^1 |H^{\alpha_2}(t, s)| \int_0^1 |H^{\beta_2}(s, \wp)| |\psi_2(\wp, u(\wp)) - \psi_2(\wp, \bar{u}(\wp))| d\wp ds \\
&\leq (p-1)\sigma^{p-2} \lambda_{\psi_2} \left( \frac{1}{\Gamma(\alpha_2 + 1)} + \frac{1}{\Gamma(m)\Gamma(\alpha_2 - m + 2)} \right) \left( \frac{1}{\Gamma(\beta_2 + 1)} + \frac{1}{\Gamma(\beta_2 + 1)} \right) (|u(t) - \bar{u}(t)|) \\
&= \vartheta_2 (|u(t) - \bar{u}(t)|).
\end{aligned} \tag{3.30}$$

From (3.29), (3.30), we have

$$\begin{aligned}
|F^*(u, v)(t) - F^*(\bar{u}, \bar{v})(t)| &\leq \vartheta_1 (|v(t) - \bar{v}(t)|) + \vartheta_2 (|u(t) - \bar{u}(t)|) \\
&\leq (\vartheta_1 + \vartheta_2) (\| (u, v)(t) - (\bar{u}, \bar{v})(t) \|).
\end{aligned} \tag{3.31}$$

With assumption  $\vartheta_1 + \vartheta_2 < 1$ , Banach's contraction principle implies that  $F^*$  has a unique fixed point. As a result, the solution of the system of fractional order with  $\phi_p$  (1.1) is unique.

Recently, Khan *et al.* [35] studied the stability of Hyers-Ulam for the following system of FDEs with  $\phi_p$ :

$$\begin{cases} D_{0+}^{\beta_1} \left( \phi_p \left( D_{0+}^{\alpha_1} u(t) \right) \right) + \psi_1(t, v(t)) = 0, & D_{0+}^{\beta_2} \left( \phi_p \left( D_{0+}^{\alpha_2} v(t) \right) \right) + \psi_2(t, u(t)) = 0, \\ \left( \phi_p \left( D_{0+}^{\alpha_1} u(t) \right) \right) |_{t=1} = I_{0+}^{\beta_1-1} \left( \psi_1(t, v(t)) \right) |_{t=1}, \\ \left( \phi_p \left( D_{0+}^{\alpha_1} u(t) \right) \right)' |_{t=1} = 0 = \left( \phi_p \left( D_{0+}^{\alpha_1} u(t) \right) \right)'' |_{t=0}, \\ \left( \phi_p \left( D_{0+}^{\alpha_2} v(t) \right) \right) |_{t=1} = I_{0+}^{\beta_2-1} \left( \psi_2(t, u(t)) \right) |_{t=1}, \\ \left( \phi_p \left( D_{0+}^{\alpha_2} v(t) \right) \right)' |_{t=1} = 0 = \left( \phi_p \left( D_{0+}^{\alpha_2} v(t) \right) \right)'' |_{t=0}, \\ u(0) = 0 = u''(0), \quad u(1) = 0, \quad v(0) = 0 = v''(0), \quad v(1) = 0, \end{cases} \quad (3.32)$$

Where  $2 < \alpha_i, \beta_i < 3, \psi_1, \psi_2 \in L[0,1]$ , and  $D_{0+}^{\alpha_i}, D_{0+}^{\beta_i}$  for  $i = 1, 2$  are in Caputo sense.

They converted (3.32) system into following coupled system of Hammerstein-type integral equations given below:

$$u(t) = \int_0^1 \mathcal{H}^{\alpha_1}(t, s) \phi_q \left( \int_0^1 \mathcal{H}^{\beta_1}(s, \theta) \psi_1(\theta, v(\theta)) d\theta \right) ds, \quad (3.33)$$

$$v(t) = \int_0^1 \mathcal{H}^{\alpha_2}(t, s) \phi_q \left( \int_0^1 \mathcal{H}^{\beta_2}(s, \theta) \psi_2(\theta, u(\theta)) d\theta \right) ds, \quad (3.34)$$

where the Green's function(s)  $\mathcal{H}^{\alpha_1}(t, s), \mathcal{H}^{\beta_1}(s, \theta), \mathcal{H}^{\alpha_2}(t, s), \mathcal{H}^{\beta_2}(s, \theta)$  are defined in [35].

**Definition 3.6.** [35] The integral (3.33) and (3.34) is HUS if there exist positive constants  $D_1^*, D_2^*$  fulfilling the conditions below:

For every  $\lambda_1, \lambda_2 > 0$ , if

$$\begin{aligned} |u(t) - \int_0^1 \mathcal{G}_{\alpha_1}(t, s) \phi_q \left( \int_0^1 \mathcal{G}_{\beta_1}(s, \theta) \psi_1(\theta, v(\theta)) d\theta \right) ds| &\leq \lambda_1, \\ |v(t) - \int_0^1 \mathcal{G}_{\alpha_2}(t, s) \phi_q \left( \int_0^1 \mathcal{G}_{\beta_2}(s, \theta) \psi_2(\theta, u(\theta)) d\theta \right) ds| &\leq \lambda_2, \end{aligned} \quad (3.35)$$

There exists a pair, say  $(u^*(t), v^*(t))$ , satisfying

$$\begin{aligned} u^*(t) &= \int_0^1 \mathcal{G}_{\alpha_1}(t, s) \phi_q \left( \int_0^1 \mathcal{G}_{\beta_1}(s, \theta) \psi_1(\theta, v^*(\theta)) d\theta \right) ds, \\ v^*(t) &= \int_0^1 \mathcal{G}_{\alpha_2}(t, s) \phi_q \left( \int_0^1 \mathcal{G}_{\beta_2}(s, \theta) \psi_2(\theta, u^*(\theta)) d\theta \right) ds, \end{aligned} \quad (3.36)$$

Such that

$$\begin{aligned} |u(t) - u^*(t)| &\leq D_1^* \lambda_1, \\ |v(t) - v^*(t)| &\leq D_2^* \lambda_2. \end{aligned} \quad (3.37)$$

Khan *et al* also studied HUS for a coupled system of FDEs with initial and boundary conditions [36].

### 1. Hyers-Ulam stability

Here we study Hyers-Ulam stability of nonlinear system of FDEs with  $p$ -Laplacian operator (1.1). By taking help from Definition 3.6 and the work [35], we propose the following definition.

**Definition 4.1.** If there exist positive constants  $D_1^*, D_2^*$ , then coupled systems of integral equations given by (3.12), (3.13) are Hyers-Ulam stable, satisfying:

For every  $\lambda_1, \lambda_2 > 0$ , if

$$\begin{cases} u(t) - \int_0^1 H^{\alpha_1}(t, s) \phi_q \left( \int_0^1 H^{\beta_1}(s, \wp) \psi_1(\wp, v(\wp)) d\wp \right) ds \\ v(t) - \int_0^1 H^{\alpha_2}(t, s) \phi_q \left( \int_0^1 H^{\beta_2}(s, \wp) \psi_2(\wp, u(\wp)) d\wp \right) ds, \end{cases} \quad (4.1)$$

There exist a pair, say  $(u^*(t), v^*(t))$ , satisfying

$$\begin{cases} u^*(t) = \int_0^1 H^{\alpha_1}(t, s) \phi_q \left( \int_0^1 H^{\beta_1}(s, \wp) \psi_1(\wp, v^*(\wp)) d\wp \right) ds, \\ v^*(t) = \int_0^1 H^{\alpha_2}(t, s) \phi_q \left( \int_0^1 H^{\beta_2}(s, \wp) \psi_2(\wp, u^*(\wp)) d\wp \right) ds, \end{cases} \quad (4.2)$$

Such that

$$|u(t) - u^*(t)| \leq D_1^* \lambda_1, \quad (4.3)$$

$$|v(t) - v^*(t)| \leq D_2^* \lambda_2.$$

**Theorem 4.2.** With the assumptions  $(Q_1), (Q_2)$ , solution of couple system of FDEs  $\phi_p$  (1.1), is Hyers-Ulam stable.

*Proof.* From Theorem 3.5 and definition 4.1, let  $(u(t), v(t))$  be a solution of the system (3.12), (3.13). Let  $(u^*(t), v^*(t))$  be any other approximation satisfying (4.2). Then, we have

$$\begin{aligned} |u(t) - u^*(t)| &= \left| \int_0^1 H^{\alpha_1}(t, s) \phi_q \left( \int_0^1 H^{\beta_1}(s, \wp) \psi_1(\wp, v(\wp)) d\wp \right) ds - \int_0^1 H^{\alpha_1}(t, s) \phi_q \left( \int_0^1 H^{\beta_1}(s, \wp) \psi_1(\wp, v^*(\wp)) d\wp \right) ds \right| \\ &\leq (p-1)\sigma^{p-2} \left( \int_0^1 |H^{\alpha_1}(t, s)| \int_0^1 |H^{\beta_1}(s, \wp)| |\psi_1(\wp, v(\wp)) - \psi_1(\wp, v^*(\wp))| d\wp ds \right) \\ &\leq (p-1)\sigma^{p-2} \lambda_{\psi_1} \left( \frac{1}{\Gamma(\alpha_1 + 1)} + \frac{1}{\Gamma(m)\Gamma(\alpha_1 - m + 2)} \right) \left( \frac{1}{\Gamma(\beta_1 + 1)} + \frac{1}{\Gamma(\beta_1 + 1)} \right) \|v(t) - v^*(t)\| \\ &= \vartheta_1 \|v(t) - v^*(t)\|, \end{aligned} \quad (4.4)$$

And

$$\begin{aligned} |v(t) - v^*(t)| &= \left| \int_0^1 H^{\alpha_2}(t, s) \phi_q \left( \int_0^1 H^{\beta_2}(s, \wp) \psi_2(\wp, u(\wp)) d\wp \right) ds - \int_0^1 H^{\alpha_2}(t, s) \phi_q \left( \int_0^1 H^{\beta_2}(s, \wp) \psi_2(\wp, u^*(\wp)) d\wp \right) ds \right| \\ &\leq (p-1)\sigma^{p-2} \left( \int_0^1 |H^{\alpha_2}(t, s)| \int_0^1 |H^{\beta_2}(s, \wp)| |\psi_2(\wp, u(\wp)) - \psi_2(\wp, u^*(\wp))| d\wp ds \right) \\ &\leq (p-1)\sigma^{p-2} \lambda_{\psi_2} \left( \frac{1}{\Gamma(\alpha_2 + 1)} + \frac{1}{\Gamma(m)\Gamma(\alpha_2 - m + 2)} \right) \left( \frac{1}{\Gamma(\beta_2 + 1)} + \frac{1}{\Gamma(\beta_2 + 1)} \right) \|u(t) - u^*(t)\| \\ &= \vartheta_2 \|u(t) - u^*(t)\| \end{aligned} \quad (4.5)$$

Where  $D_1^* = \vartheta_1, D_2^* = \vartheta_2$ . Hence, by the help of (4.4), (4.5) the system (3.12), (3.13), is Hyers-Ulam stable. Therefore, Eq. (1.1) is Hyers-Ulam stable.

## CONCLUSION

We have considered a high order coupled system of FDEs with nonlinear  $p$ -Laplacian operator for the examination of existence, uniqueness of solution and Hyer-Ulam stability by using topological degree theory. For these aims, we transformed the supposed problem into an integral system via Green's function(s) and assumed certain necessary conditions over a Banach space. Our results are more general and useful than the standard case.

## AUTHOR'S CONTRIBUTIONS

All the authors of the paper have equal contribution in the paper. They have read and approved the paper before submission for publication.

## REFERENCES

- [1] D. Baleanua, O.G. Mustafa and R.P. Agarwal, An existence result for a superlinear fractional differential equation, Appl. Math. Lett., Vol. 23(9) (2010), 1129 - 1132.
- [2] P. Kumam, A. Ali, K. Shah, R. A. Khan, Existence results and Hyers-Ulam stability to a class of nonlinear arbitrary order differential equations, J. Nonlinear Sci. Appl., 10 (2017), 29862997.
- [3] D. Baleanu, R. P. Agarwal, H. Mohammadi, S. Rezapour, Some existence results for a nonlinear fractional differential equation on

partially ordered Banach spaces, *Bound. Value Probl.*, 2013 (2013), 8 pages.

- [4] D. Baleanu, O. G. Mustafa, R. P. Agarwal, On the solution set for a class of sequential fractional differential equations, *J. Phys. A*, 43 (2010), 7 pages.
- [5] N. I. Mahmudov, S. Unul, Existence of solutions of  $\alpha \in (2,3]$  order fractional three-point boundary value problems with integral conditions, *Abstr. Appl. Anal.*, 2014 (2014), 12 pages.
- [6] N. I. Mahmudov, S. Unul, Existence of solutions of fractional boundary value problems with p-Laplacian operator, *Bound. Value Probl.*, 2015 (2015), 16 pages. 1.
- [7] N. I. Mahmudov, S. Unul, On existence of BVP's for impulsive fractional differential equations, *Adv. Difference Equ.*, 2017 (2017), 16 pages.
- [8] L. Hu, S. Zhang, On existence results for nonlinear fractional differential equations involving the p-Laplacian at resonance. *Mediterr. J. Math.* 13, 955-966 (2016).
- [9] A. Ali, B. Samet, K. Shah, R. A. Khan, Existence and stability of solution to a toppled systems of differential equations of non-integer order. *Bound. Value Probl.* 2017, 16 (2017).
- [10] J. Mawhin, *Topological Degree Methods in Nonlinear Boundary Value Problems* CMBS Regional Conference Series in Mathematics, vol. 40. Am. Math. Soc., Providence (1979).
- [11] F. Isaia, On a nonlinear integral equation without compactness. *Acta Math. Univ. Comen.* 75, 233-240 (2006).
- [12] J. Wang, Y. Zhou, W. Wei, Study in fractional differential equations by means of topological degree methods. *Numer. Funct. Anal. Optim.* 33(2), 216-238 (2012).
- [13] [13] K. Shah, R. A. Khan, Existence and uniqueness results in a coupled system of fractional order boundary value problems by topological degree theory. *Numer. Funct. Anal. Optim.* 37, 887-899 (2016).
- [14] K. Shah, A. Ali, R. A. Khan, Degree theory and existence of positive solutions to coupled systems of multi-point boundary value problems. *Bound. Value Probl.* 2016(1), 1 (2016).
- [15] T. Shen, W. Liu and X. Shen, Existence and uniqueness of solutions for several BVPs of fractional differential equations with p-Laplacian operator, *Mediterr. J. Math.* (2016) DOI 10.1007/s00009-016-0766-9.
- [16] I. Area, J. Losada, and J. J. Nieto, A note on fractional logistic equation. *Physica A* 444, 182-187 (2016).
- [17] K. S. Miller, B. Ross, *An Introduction to the Fractional Calculus and Fractional Differential Equations*, pp. 209-217. Wiley, New York (1993).
- [18] R. Hilfer, *Application of Fractional Calculus in Physics*. World Scientific, Singapore (2000).
- [19] A. A. Kilbas, H. M. Srivastava, and J. J. Trujillo, *Theory and Applications of Fractional Differential Equations*. North-Holland Mathematics Studies, vol. 24. Amsterdam (2006).
- [20] R. Agarwal, S. Hristova, and D. O'Regan, Stability of solutions to impulsive Caputo fractional differential equations. *Electron. J. Differ. Equ.* 2016, Article ID 58 (2016).
- [21] D. Anderson, R. Avery, Fractional-order boundary value problem with Sturm-Liouville boundary conditions. *Electron. J. Differ. Equ.* 2015, Article ID 29 (2015).
- [22] I. Bachar, H. Maagli, and V. Radulescu, Fractional Navier boundary value problems. *Bound. Value Probl.* 2016, Article ID 79 (2016).
- [23] N. D. Cong, T. S. Doan, S. Siegmund, and H. T. Tuan, Linearized asymptotic stability for fractional differential equations. *Electron. J. Qual. Theory Differ. Equ.* 2016, Article ID 39 (2016).
- [24] M. Ghergu, V. Radulescu, *Nonlinear PDEs. Mathematical Models in Biology, Chemistry and Population Genetics*. Springer Monographs in Mathematics. Springer, Heidelberg (2012).
- [25] S. Kumar, D. Kumar, J. Singh, Fractional modeling arising in unidirectional propagation of long waves in dispersive media. *Adv. Nonlinear Anal.* 5(4), 383-394 (2016).
- [26] S. Peng, J. R. Wang, Existence and Ulam-Hyers stability of ODEs involving two Caputo fractional derivatives. *Electron. J. Qual. Theory Differ. Equ.* 2015, Article ID 52 (2015).
- [27] H. Jafari, D. Baleanu, H. Khan, R. A. Khan, and A. Khan, Existence criterion for the solutions of fractional order p-Laplacian boundary value problems. *Bound. Value Probl.* 2015, 164 (2015).
- [28] L. Diening, P. Lindqvist, B. Kawohl, Mini-Workshop: the p-Laplacian operator and applications. *Oberwolfach Rep.* 10(1), 433-482 (2013).
- [29] X. Han, X. Yang, Existence and multiplicity of positive solutions for a system of fractional differential equation with parameters. *Bound. Value Probl.* 2017, 78 (2017).
- [30] E. Zhi, X. Liu, and F. Li, Non local boundary value problems of fractional differential equations with p-Laplacian. *Math. Methods Appl. Sci.* 37, 2651-2662 (2014).
- [31] L. Zhang, W. Zhang, X. Liu, and M. Jia, Existence of positive solutions for integral boundary value problems of fractional differential equations with p-Laplacian. *Adv. Differ. Equ.* 2017, 36 (2017).
- [32] R. A. Khan, A. Khan, A. Samad, H. Khan, On existence of solutions for fractional differential equations with p-Laplacian operator. *J. Fract. Calc. Appl.* 5(2), 28-37 (2014).
- [33] E. Cetin, F. S. Topal, Existence of solutions for fractional four point boundary value problems with p-Laplacian operator. *J. Comput. Anal. Appl.* 19(1), 892-903 (2015).
- [34] S. Liang, J. Zhang, Existence and uniqueness of positive solutions for integral boundary problems of nonlinear fractional differential equations with p-Laplacian operator. *Rocky Mt. J. Math.* 44(1), 953-974 (2014).
- [35] H. Khan, Y. Li, W. Chen, D. Baleanu, and A. Khan, Existence theorems and Hyers-Ulam stability for a coupled system of fractional differential equations with p-Laplacian operator. *Boundary Value Problems* (2017) 2017:157. DOI 10.1186/s13661-017-0878-6.
- [36] H. Khan, Y. Li, H. Sun, and A. Khan, Existence of solution and Hyers-Ulam stability for a coupled system of fractional differential equations with p-Laplacian operator. *J. Nonlinear Sci. Appl.*, 10 (2017), 5219-5229.



**Kiran Tabassum:** She was born in Pakistan on August 3, 1993. She did her bachelor's degree (2011-2015) in statistics with minor in mathematics and computer science from University of the Punjab, Lahore, Pakistan. She is currently studying her master's degree in mathematics from College of Science, Hohai University, Nanjing, Jiangsu, P.R. China. Her research work interest involves in the existence and uniqueness of solution for complex and difficult fractional differential equations involving p-Laplacian operator. This work is nowadays a hot topic for researchers belonging to engineering and mathematics. In some of complex problems, the question raises whether the system is stable or not. To overwhelm this question I also intend to investigate Hyers-Ulam stability for more complex problems.



# A Case Study of Bio-char Production from Biomass using Microwave Assisted Pyrolysis and its Utilization

Muhammad Zeshan Afzal, Huiyan Zhang, Muhammad Aurangzeb, Wang Bing, Yaping Zhang

**Abstract**—Microwave pyrolysis is a modern technology to produce a good quality biochar. Gives best products, utilization and most important, process is environment friendly. In Microwave, radiation use for pyrolysis and process is: fast, specific heat area. But in conventional pyrolysis heat cannot be controlled for specific area. Microwave pyrolysis depends on the parameters: temperature, reaction time, feedstock type and Microwave Absorbers (MWAs). Production depends on the types of pyrolysis (slow, fast and flash). In the previous work focused on bio-oil and gases. But the biochar is storing source of energy and utilization. This review paper provides information about biochar obtained from microwave-assisted pyrolysis in all aspects and its utilization. It is concluded that microwave-assisted technology is an efficient technique to decrease the reaction time and increases the quality of products. In calculation, this method can overcome the requirements of feedstock destroying and improves the quality of heating.

**Keywords**—Biomass; Biochar; Pyrolysis Parameters; Microwave assisted pyrolysis.

## I. INTRODUCTION

Rise of energy utilization, restricted resources of petroleum, climate problems and global challenges needs more advance methods for the use of biomass in most better ways[1]. Recently most of energy demand is fulfilled by non-renewable energy resources containing nuclear technology and fossil fuel that's also the reason of environment pollution. Now global energy relies on fossil fuels seriously. In 2014 more than 80% of primary energy is provided by fossil fuels[2]. On the other hand, main environmental worries are changing in global environment due to emissions of greenhouse gases. For that reason, renewable energy technologies, such as wind power, bioenergy and solar photovoltaic gained growing interest. In

all these bioenergy is the best option because of its lavish, safe, clean. Moreover, biomass is the only way to produce renewable solid, liquid, and gas fuels. Lignocellulosic biomass, such as wood, crops, and agricultural and forestry residues, is primarily composed of hemicellulose, cellulose, and lignin[3]. Biomass transformation provides three products, biofuel (liquid), biochar (Solid), biogas (Gas). Recently, there has been rising anxieties about the thermochemical exchange of sludge into bio-fuels for energy recovery through pyrolysis and gasification techniques.

As compared to the heat recovery from burning and combustion, through pyrolysis and gasification, specific conditions sludge can be converted into high-quality bio-syngas, flammable tar and char products. Pyrolysis/gasification is an effective technology for a clean conversion[4]. Now biomass is the hot research topic by the researcher because it's not only fulfil the energy demand but also overcome the greenhouse gas emissions[5]. The global prime energy comes from non-renewable fossil fuel resources. Biochar is solid material has pores and generally it looks like charcoal and it is produced by the pyrolysis of biomass under limited oxygen condition. Biochar has high carbon content and also has good surface area[8]. It is thermally stable product and it is the best form of biomass to store for a long time[9]. Biochar can be well-kept for hundreds of years [10]. Biomass is commonly composed of three main groups of natural polymeric materials: cellulose (around 50% on dry basis), hemicellulose (10-30% in woods and 20-40% in herbaceous biomass on dry basis) and lignin (20-40% in woods and 10-40% in herbaceous biomass on dry basis)[11]. Biochar is solid that's mean it is environment friendly that store the CO<sub>2</sub> in it and when it is use for soil abonnement then it gives CO<sub>2</sub> to the plant and that's they need. The production yield depends on the types of process (slow, fast, flash) and pyrolysis conditions (temperature, time, pressure, heating time). Besides fast pyrolysis, microwave pyrolysis (MWP) provides distinct heating method to process diversity of feedstocks and is also right for making liquid, gas and biochar products from coal and biomass. Biochar is basically transparent to microwave (MW) due to its properly low MW absorption capacity. low MW absorption of coal indicates the major uncertain during MWP, although some moisture and mineral contents within coal matrix respond more readily to MW energy. Moreover, the coal sample cannot be paralyzed or achieve sufficient temperature without Microwave Absorber (MWA) even in the presence of high MW power source[6].

Muhammad Zeshan Afzal: National ASIC System Engineering Center, Southeast University, Nanjing, 210096, 3349596259@qq.com

Huiyan Zhang: National ASIC System Engineering Center, Southeast University, Nanjing, 210096, hyzhang@seu.edu.cn

Muhammad Aurangzeb: College of Energy and Electrical Engineering, Hohai University, Nanjing, 210096, maurangzaib42@gmail.com

Wang Bing: National ASIC System Engineering Center, Southeast University, Nanjing, 210096, 767278796@qq.com

Yaping Zhang: National ASIC System Engineering Center, Southeast University, Nanjing, 210096, amflora@seu.edu.cn

Pyrolysis is done by two techniques one is conventional pyrolysis and the second is microwave pyrolysis. The first one is an old method and not well suffices. Nowadays MW pyrolysis is very popular heating method because of its fast heating rate, selective heating, volumetric and uniform heating and that's why its accuracy and efficiency is better. These advantages of MW are attributed to dielectric heating and generated "hot spots"[12, 13]. Many researchers have reported significant reductions in processing times of microwave over conventional sintering[14]. One of other good benefit of MW is that it is easily control by switch buttons and very safe to operate. When it operate, reaction is done in reactor and the emission bad gasses do not come out that's why this technique is environment friendly [15-17]. Hence, MW is an extremely most capable means to accelerate chemical transformations, such as in the pyrolysis of biomass compared to convention pyrolysis (CP), microwave assisted pyrolysis (MAP) is conducive to obtain organic volatiles, chemicals and bio-gas at relatively low temperature with less energy consumption[18]. In microwave a cooling gas is use for immediate quenching of pyrolysis products, which is not possible in conventional pyrolysis systems. Therefore, more benefits arise from the absence of hot gas treatment and energy recovery systems[19]. Recently NASA investigated that the microwave pyrolysis is a practical method for waste recovery of craft in space. Due to this method is a major energy reduction in total energy requirement that is (~70%) compared to conventional heating system[20].

This review paper provides information about biochar obtained from microwave-assisted pyrolysis in all aspects and its utilization. It is concluded that microwave-assisted technology is an efficient technique to decrease the reaction time and increases the quality of products. In calculation, this method can overcome the requirements of feedstock destroying and improves the quality of heating.

## II. MICROWAVE PYROLYSIS

It's a single mode microwave device works at very high frequency 2450 MHz. The magnetron inside the microwave generator can change over electrical power to microwave power which can be balanced from 0 to 2000 W, and after that the microwave vitality can be guided to reaction chamber, as shown in Fig 1 [21]. But all the material cannot absorb the radiation, so the raw material with a high transparency of heat is mixed with that material i.e. carbon is high heat absorber so because of that the material in a microwave reactor get temperature more than 1000°C in a few minutes. If the water exists in the feedstock that will drop the heat rate of CP due to heat absorbed by water and that's why the final pyrolysis temperature will be decreased. But in MW the water in feedstock increase the heart rate, cause to the large MW absorption capacity of water in comparison with dry biomass itself .

The biomass is placed in a glass cubic box and then placed in a reactor and to measure the temperature inside the box a thermocouple is used and N2 or Ar gas is passed to

maintain the temperature and after experiments is cools down. Fig 2 shows microwave pyrolysis process flow diagram[19]. Many researchers worked to know the yield of biochar by changing the different parameter like temperature, heating rate and feedstock in both MWP and CP. Elsa Antunes et al. [22] studied the effect of pyrolysis temperature between 300 °C and 800 °C on the chemical and physical properties of biochar obtained from bio-solids through MWP. Bio-solids were pull out from soil resolving ponds at a sewage treatment facility (Euroa Wastewater Treatment facility in Victoria, Australia), and stored for one month for use in laboratory experiments. To reduce irregularities, a 10 kg lot of bio-solids were mixed to obtain a similar sample. The similar lot was stored in a sealed container in a freezer at 4 °C to reduce bacteriological action. By means of the cone and quarter method, three random samples were taken for categorization. Modified single-mode microwave chamber is used that has power 1.2 kW.

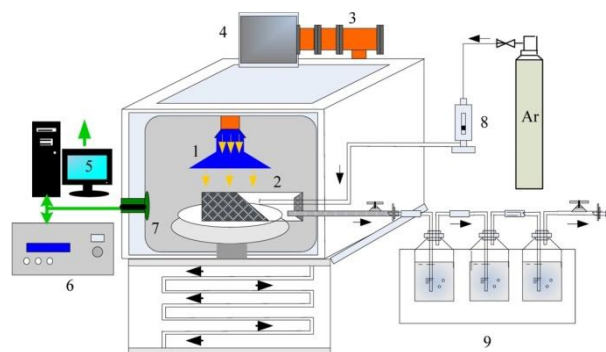


Figure 1. A schematic of the microwave preparation reactor assembly [21]: (1) microwave cavity; (2) quartz reactor; (3) waveguide; (4) magnetron; (5) PC with fuzzy logic algorithm; (6) power governor; (7) infrared radiation thermometer; (8) gas flowmeter; (9) tar products collection unit.

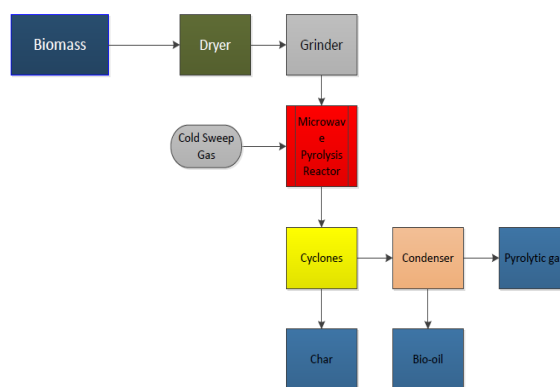


Figure 2. Microwave pyrolysis process flow diagram [19]

The bio-solid was mixed with the activated carbon and then ground after that put into a quartz beaker (volume: 150 ml) inside the MWP chamber. The compartment was eliminated with 11 L/min of nitrogen (99.9% purity) for 40 s before the pointer valve was opened and the pressure lowered to 15 kPa gauge pressure. A nitrogen flow rate of



11 L/min matches at a mean residence time of 6.38 s for the nitrogen in the pyrolysis compartment, so a purge time of 40 s was sufficient. At the start of the pyrolysis, the magnetron output power was set to 600 W to allow for rapid, but controlled heating of the sample and eventual removal of sample moisture. Once the target temperature was reached, the output power of the magnetron was manually adjusted to keep the sample temperature as close as possible to set point ( $\pm 15^\circ\text{C}$ ). The control valve was manually adjusted to maintain the pressure within the chamber around 15 kPa gauge pressure.

Bio-solids samples were paralyzed at different temperatures between  $300^\circ\text{C}$  and  $800^\circ\text{C}$  for approximately 10 min. In testing, a thermocouple was placed in the middle of the sample, in the single-mode chamber, to note the reading of sample temperature. Pyrolysis temperature was checked by a shielded type K thermocouple coupled to an Arduino board, and recorded every 500 ms. The pressure in the microwave chamber was physically measured by an inline needle valve between the cold water tap and the vacuum pump.

#### A. The mechanism of MW for biomass pyrolysis

The mechanism is very simple because everything can be control for example how much heat is required for how long time and which specific area need heat. Microwave furnace is easily operated device. Pyrolysis of biomass such as plants, hardwood raw material, rice straw and forest residue by microwave heating system is a significant biomass learning resource ecological feedstock for the creation of bioenergy and renewable materials. Microwave heating system is better than conventional heating system due of advantages. Hot areas that form by MW radiation could have significance.

It has two steps first one is that energy is absorbed then through conduction process transferred to the biomass. In another step, as the pyrolysis continues, more carbon is created from the raw materials and the microwaves begin to pervade inside the materials, giving surge to reactions unfamiliar in conventional heating system. In the Fig 3 it is explained the nature of microwave heating[23].

Effect on the produce and characteristics of MW handlings products. Use of microwave pyrolysis, almost 50 % of lignocellulosic biomass can be changed into gas product, which is principally made up of  $\text{H}_2$ ,  $\text{CH}_4$ ,  $\text{CO}_2$ , and  $\text{CO}$ , with an increase of bioenergy due to its high  $\text{H}_2$  and  $\text{CO}$  produces[24]. It was discovered that if just the natural wet sludge is heat in the microwave just only drying out of the testis occurs. However, if the sludge is blended with a tiny amount of the right microwave absorber like the char stated in the pyrolysis itself temperature ranges as high as  $900^\circ\text{C}$  so that pyrolysis occurs than drying out the wet biomass[25].

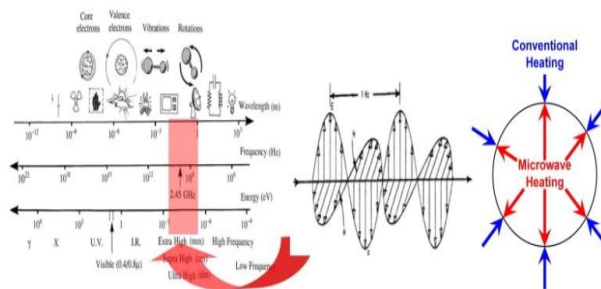


Figure 3. Electromagnetic spectra and microwave heating nature [23]

MWs heating is done my two mechanism that are dipole rotation and ionic conduction. When MWs in contact with polar molecules or iron then heat is induced quickly. In the fast oscillating electric field of the MW polar molecules try to rearrange themselves. Throughout this occurrence, loss of energy is in the form of heat through molecular resistance and dielectric loss. When a MW-absorbing material is placed in an electric field energy is absorbed permanently, because of this technique it gives a fast 'volumetric' heating. In this type of heating, the center of material has clearly been heated to a significantly higher temperature than the outer material, but the conventional pyrolysis is phenomena is opposite the material get heat from the outer side to inner side, the phenomena is shown in Fig 4. MW heating can be defined as a form of energy exchange rather than a form of heating; for example, electromagnetic energy is transformed into heat. Because of this distinctive inverse heating mechanism offers many benefits such as an increase in energy transfer efficiency and decreases in heating time for getting desired temperature for pyrolysis. It is better than conventional pyrolysis. it allows improved controlling of the heating process and removes the threat of the sample surface overheating and possibly degrading an also this technique can be used for drying the wet material.

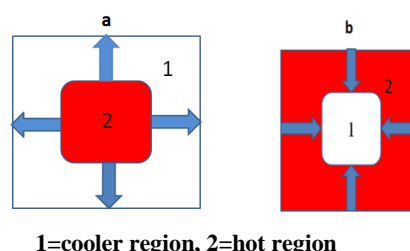


Figure 4. The differences in temperature distribution and direction of heat transfer between conventional and microwave heating.

#### B. Microwave absorber

MWA work is to absorb Microwave heat very efficiently. In an experiment sometime, it is very hard to achieve required temperature or desired peak pyrolysis temperature. So, for that problem material is used as absorber that have high dielectric lost tangent parameter (DLTP). Because of absorber the reaction become faster so its work is like a catalyst too. MWA have been utilized in military applications; such as, antenna design shaping, radar cross reduction and electromagnetic interference (EMI) reduction

for a few decades. Even more recently with the surge of wireless electronics at higher GHz frequency, MWA or noise suppressors are being used to reduce EMI. Magnetic absorbers are slim (0.1-3 mm) polymeric materials filled with permanent magnetic nano/micro sized particles[26-30]. To test the material for a good absorber there are some parameter to test that material. The following points are considered for a good absorber: (I) what frequency bands need to be covered? (II) Is coverage required over the entire range of frequencies or just at specific frequencies? (III) What is the order of importance in coverage? A design can be more easily being finalized if these priorities are met[31].

There is a list of absorber that are char NaOH, Na<sub>2</sub>CO<sub>3</sub>, Na<sub>2</sub>SiO<sub>3</sub>, NaCl, TiO<sub>2</sub>, HZSM-5, H<sub>3</sub>PO<sub>4</sub>, Fe<sub>2</sub>(SO<sub>4</sub>)<sub>3</sub>[23]. These absorbers are used in a microwave pyrolysis. It is calculated that all these absorbers whether they are basic, neutral or acidic, metallic or non-metallic water soluble or insoluble, have increased yield of solid products greatly and decreased yield of gaseous products more or less. Liquid yield undergoes no dramatic change. The absorbers in pyrolysis evolve the gases earlier and for that the absorbers that have sodium play an important role[32].Figure 5 shows the effect the absorbent on heating characteristics using SiC absorbant.

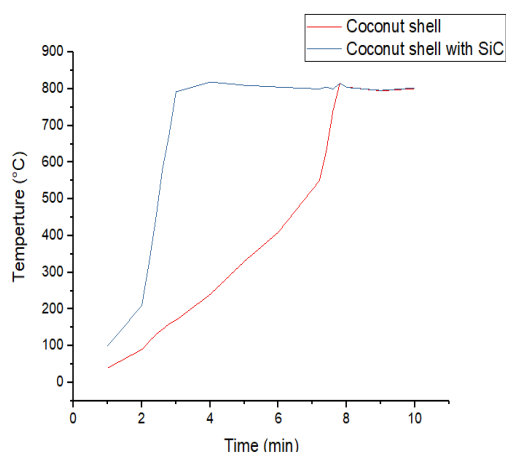


Figure 5. The temperature profiles for coconut shell with and without SiC under microwave heating

### C. Conventional pyrolysis

Conventional heating systems include outward heating by conduction, convection or radiation. In this method a huge amount of energy is wasted and the resulted biochar is not enough capable. Because of this method a huge amount of heat damages the biochar surface and layers. In biomass pyrolysis there are many parameters under consideration like (heating rate, pyrolysis temperature, pressure, particle size). However for the large quantity of biochar to achieve by low temperature and low heating rate is the best condition[33]. It has many drawbacks in which transferring of heat, waste most of the part of heat, no proper heat to the right place, due to high temperature the damage of reactors walls etc. The other flaw is it takes more time to reach the desired temperature and because of long heating time the secondary

reaction take place and because of the secondary reaction the layer of biochar are damage and it effect the overall quality of product[34]. Fig 6 is the design of the CP[35].

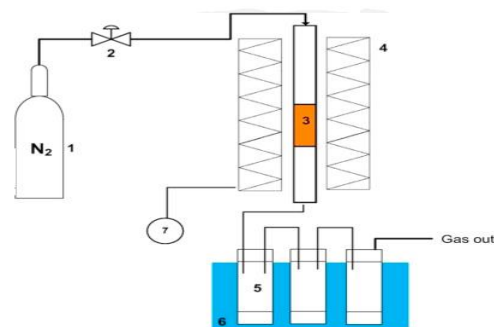


Figure 6. [35] 1 N<sub>2</sub> gas, 2 Mass Flow controller, 3 Biomass sample, 4 Furnace, 5 Bio-oil Condenser, 6 Thermal bath, 7 Temperature controller

### D. Microwave and conventional Pyrolysis

Microwave pyrolysis is one of the many ways of converting biomass into higher value products such as bio-oil, syngas, biochar and chemicals. Table 1 shows the advantages and disadvantages of microwave pyrolysis and conventional pyrolysis [55]. Comparing with conventional pyrolysis, there has a lot of advantages for microwave pyrolysis, such as, no size reduction, wet biomass can be used directly without drying, higher quality of products, and process contingency. All these will not only improve the energy efficiency for the process, but also reduce the capital cost, such as feed storage, size reduction, and feed dryer. Another key advantage of the microwave heating process over conventional heating method is the nature of fast internal heating by microwave irradiation. Microwave energy deposition in the dielectric loss mode of heating can cause spatially uniform heating[56].Biomass fast pyrolysis can be achieved by microwave radiation. Products obtained from MWP and CP at different temperature Table 2 [36,37]. And also the the classification of pyrolysis are listed in Table 3.

TABLE I. ADVANTAGES AND DISADVANTAGES OF MICROWAVE PYROLYSIS VS. CONVENTIONAL PYROLYSIS

	Microwave Pyrolysis		Conventional Pyrolysis	
	Advantage	Disadvantage	Advantage	Disadvantage
1	No size reduction and drying for biomass; Flexibility of feedstocks and products	Temperature measurement	Flexibility of feedstocks and products	Lower quality products (e.g. formation of PAHs)
2	Energy savings at significantly reduced processing temperatures (150-300°C)	Economics of the process scaling-up	Well developed and easy scale-up	Energy consumption due to higher temperature (>600°C)
3	Possibility of	Large scale	Possibility of	Lower quality

	continuous processing with multiple units	inhomogeneities/reproducibility issues in products	continuous processing at large scale	products (e.g. formation of PAHs)
--	---	--	--------------------------------------	-----------------------------------

TABLE II. OBTAINED PRODUCT FROM MWP AND CP AT DIFFERENT TEMPERATURE [36, 37]

	T (°C)	Heating rate (°C/min)	Carrier gas (mL/min)		Product yield (Wt. %)		
			Argon	N <sub>2</sub>	Char	Liquid	Gas
CP	310	20	-		59.7	31.5	8.79
	500	-		60	29.2	13.5	57.2
MP	800	-		60	25.3	11.8	62.9
	200	8	-		43.2	47.1	9.7
	500	-		60	30.2	7.9	61.9

TABLE III. PYROLYSIS CLASSIFICATIONS

Pyrolysis Techniques	Reaction temp./°C	Heating rate/°C s <sup>-1</sup>	Particle size/m	Residence time	Pressure/MPa	Major product Types	References
Slow pyrolysis	300-800	0.1-1.0	5-50	5-30 min	0.1	Biochar, bio-oil and syngas; biochar is dominant	[55-58]
Intermediate pyrolysis	300-450	3-5	1-5	~10 min	0.1	Biochar, bio-oil and syngas	[54,56,58]
Fast Pyrolysis	500-550	10-100	<1	< 2 s	0.1	Bio-oil, syngas and biochar; bio-oil is in high quantity	[59]

### 1) Effect of parameters on MWP yield

TABLE IV. THE YIELD OF BIOCHAR OBTAINED FROM MWP ON DIFFERENT TEMPERATURE

Feedstock	Experiment parameters	MWP	ref
Aspen pellets	T 450-550 °C, MW, catalysts: Al <sub>2</sub> O <sub>3</sub> , MgCl <sub>2</sub> , AlCl <sub>3</sub> , CoCl <sub>2</sub> , and ZnCl <sub>2</sub>	biochar yield: 25-31 wt.%, Bio-oil yield: 35-42 wt.%, (MgCl <sub>2</sub> .6H <sub>2</sub> O: 0.8wt%, dia. 4.8 - 4-8 mm pellets)	[60]
Pine sawdust	T=400-800 °C, MW power =2kW, 4 g sawdust, MW heating time =3 min, N <sub>2</sub> of 30 mL/min; MWA charcoal size 1-2	Char yield: 13-26 wt.%; Syngas composition: CO = 40-48v%, H <sub>2</sub> =16-31v%, CO <sub>2</sub> = 7-30v%,	[61]

	mm		
Wheat straw	T = 400-600°C, MW power = 3 kW, size <90 mm, 5-30 g sample, N <sub>2</sub> of 3L/min, MW heating time = 10min	Char yield: 40-50 wt.%; Gas yield: 17.69 to 22.27 wt.%; Combustible gas ratio=67.21-77.14 vol%;	[62]
Kraft lignin	300 g char and lignin, 623-967 °C, MW power: 1.5-2.7 kW, N <sub>2</sub> of 500 ml/min, 800s heating time	Major products in bio-oil: Guaiacols (135-184mg/g oil)	[63]

### 2) Graphical comparison between MWP and CP

As shown in Fig. 7 a number of researchers observed at MWP in comparison with CP and recognized significant differences between the two technologies emphasizing decomposition temperature, heating rates and requirements [38].

### 3) Energy distribution

The heating values of the oils are the highest, followed by those of the chars, whereas the heating values of the gases are the lowest. The Higher Heating Value (HHV) of the oils and gases are higher when MWP is used to compare to CP, while the char values are similar for both pyrolysis methods (~24 MJ/kg). The effect of temperature on the HHV

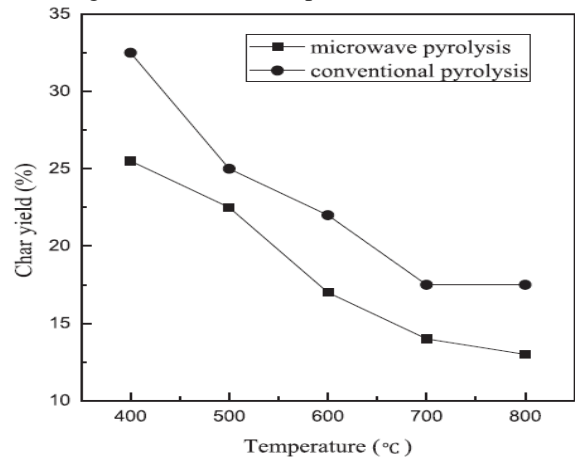


Figure 7. Variation of the char yields from MWP and CP of pine sawdust with temperature [38]

of the oils and chars is practically negligible. However, the HHV of the gases increase with the increase in pyrolysis temperature. The amount of recoverable energy from each pyrolysis product (E<sub>i</sub>) was determined in order to compare it with the energy content of the raw material. E<sub>i</sub> was calculated by the following expression

$$E_i = HHV_i \cdot Y_i; i = \text{char; oil or gas;}$$

where Y is the fraction yield and HHV is the corresponding higher heating value. From these values the energy distribution in each pyrolysis Product (%) was calculated as follows:

$$\text{Energy distribution } i (\%) = 100 \left( \frac{E_i}{HHV \text{ raw material}} \right)$$

Fig.8 give the detail of energy distribution (%) at different temperatures for conventional (CP) and microwave (MWP) pyrolysis. In the microwave, the energy that recovered at all temperatures is almost close to 100 %. Although, it increases with increase in temperature in conventional pyrolysis from 85% to 98% at 500 and 1000 °C, respectively. Production of gas increases by two techniques one is increasing the temperature and other is using microwave. But the error in the recovery of oil and the recoverable energy from the oil is reduced.

In CP at 1000 °C, the percentage of energy distribution in the gas portion is the maximum; contrariwise the oil and biochar portion have minimum energy distribution. Furthermore, the energy accrued by the gas increases as the pyrolysis temperature increases. Inversely, the energy accrued by the char decreases with the temperature. These effects are more prominent in MWP than in CP.

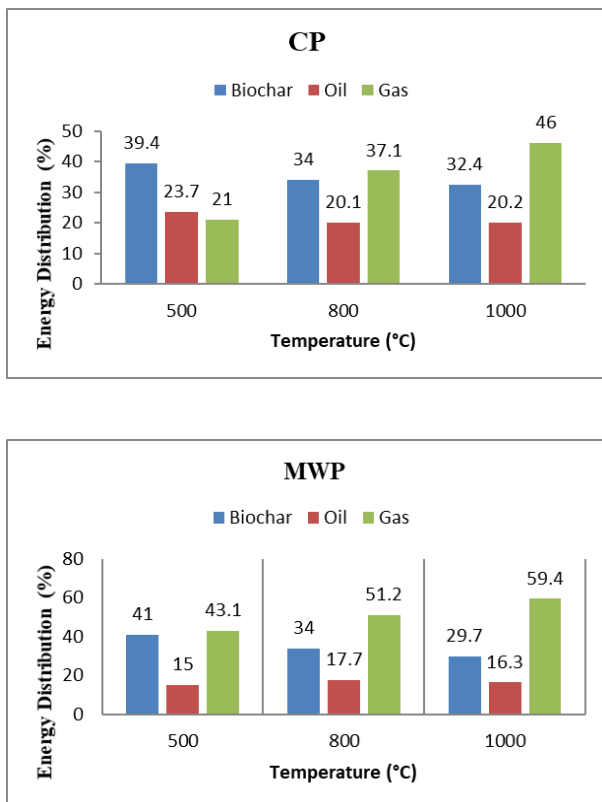


Figure 8. Energy distribution (%) in each fraction from conventional (CP) and microwave (MWP) pyrolysis [37]

### III. UTILIZATION

The biochar has many benefits in environment and agricultural field, including. Decrease from claiming manufactured fertilizers, carbon sequestration, worldwide warming mitigation, water asset protection, soil. Biochar is applied to soil systems for soil improvement, mitigation of climate change, and waste management[39,40]. Furthermore,

improvement in crop production. Biochar for soil is very valuable, effect its chemical and physical properties, reduces greenhouse gas (CO<sub>2</sub>, CH<sub>4</sub> and N<sub>2</sub>O) emissions, and improves the infectious health of soil. It profits agriculture, the budget and the environment a series of benefits. Generally, biochar contains of particles with low density and thus repaying it to soils can decrease soil bulk density, growth soil softness and increase the soil terrene. By addition biochar, the soil is well able to hold moisture and the soil quality improves in terms of several carbon and energy sources as well as mineral nutrition for the development and reproduction of microorganisms[41].

Biochar is mainly used in agriculture where it has many positive aspects related to carbon storage, soil hydrology, soil biota, crop yield, compost improvement, or feed additives[42-45]. Biochar need an incredible possibility will absorb Ecological contaminants because of its totally accessibility of feedstocks, minimal effort Furthermore ideal physical/chemical surface characteristics, for example, an expansive. Particular surface area, microporous structure, Active functional groups, Furthermore high ph. Biochar camwood a chance to be utilized Likewise an impetus straightforwardly alternately Concerning illustration a forerunner to making impetus in the fields for syngas cleaning, change for syngas under fluid hydrocarbons[46]. Biochar produced from microwave catalytic pyrolysis is more efficient in increasing the soil WHC(Water Holding Capacity) due to its high porosity in comparison with the biochar produced from conventional pyrolysis at the same conditions. Strong positive correlations also can be found among soil WHC(Water Holding Capacity) with CEC(Cation Exchange Capacity) and biochar microspore area. Biochar from microwave-assisted catalytic pyrolysis is apparently a novel way for producing biochar with high sorption affinity and high CEC. These catalysts staying in the biochar product would provide essential nutrition for the development of bioenergy and food crops[47]. Biochar and other carbonaceous materials are widely used as treatment materials to remove a range of metals (e.g., As, Cd, Cr, Cu, Ni, Pb, Zn) and organic contaminants from aqueous solutions[48-50].

Elsa Antunes et al. [51] detached silver from an aqueous solution successfully using biochar. The increase in silver concentration and temperature influences positively on silver removal onto biochar. Biochar feedstock plays a main role in silver removal from aqueous solution. Bio-solids almost have 50% moisture content were filtered to get particle size less than 5.2 mm then mixed with activated charcoal, make sure that charcoal particles did not break during the mixing process. Mixture samples (60 g) were used for microwave pyrolysis. The pyrolysis tests were carried out in a modified single-mode microwave at 600 W Temperature was monitored by a type K thermocouple and kept at set-point by adjusting the applied net microwave power.

Huang et al.[52] reported that biochar produced from microwave pyrolysis has a better ability to absorb CO<sub>2</sub>. A

biochar produced by a microwave that has 200W power and maximum temperature 300C can absorb CO<sub>2</sub> with the capacity of up to 80 mg/g at 20 °C, which is higher than the biochar produced by conventional pyrolysis by 14%. The CO<sub>2</sub> adsorption capacity is extremely linked with the specific surface area.

Mohamed et al.[53] showed that the biochar produced from microwave is more efficient than biochar produced by conventional pyrolysis in term of soil water holding capacity and to get a good biochar for soil application the catalytic microwave pyrolysis is best at low temperature 300°C. Biochar's produced from mixing switchgrass with two or more catalysts results greater performance in increasing soil WHC (Water Holding Capacity) and CEC (Cation Exchange Capacity), and improving soil fertility clearly compared with the biochar produced from one catalyst only.

#### CONCLUSION AND FUTURE WORK

Microwave pyrolysis is a modern technology to produce a good quality biochar. And it gives the best byproducts and their best utilization and the most important thing is this process is environment friendly. In Microwave the radiation is used for pyrolysis and this process is very fast, time saving and we can heat the specific area of biomass and also can control the volume of the radiation. And we get a biochar that has a large surface area and very good pores layers. Almost all the reviews explain the characteristics of bio oil and gasses. But in this review Paper it will give the detail about Microwave assisted pyrolysis and the source of biochar, its characteristic, chemical composition, distribution and the amount of Biochar obtained. In Microwave pyrolysis to make the reaction fast and to increase the heat absorption fast for that Microwave absorber and catalyst are use. Because of these the reaction is fast and takes a little time to get our biochar. In reactor the gases are produce so Microwave absorber also react with these gases to maintain the quality of product. Microwave pyrolysis and the obtained biochar is depending on parameters that are very important Temperature, reaction time, feedstock type and to absorb the sufficient heat we use catalyst called Microwave absorbers MWAs. And production depend upon on the types of pyrolysis (slow, fast, flash).

The Conventional and Microwave Pyrolysis are two different techniques. They both are used for different kind of products to obtained. the quality of biochar by microwave pyrolysis is good as compared to Conventional Pyrolysis but quantity is higher in CP. The work is to be done is to increase the more quality and quantity of biochar in MWP by changing the Temperature, reaction time, feedstock type, reactor type and Microwave absorber or catalyst. One more thing need attention that is after getting biochar by Microwave pyrolysis the Microwave absorber remain in the biochar so what will be the effect of absorber on biochar characteristic that need more research.

#### ACKNOWLEDGEMENT

The authors acknowledge the financial support of the National Natural Science Foundation of China (Grant No. 51676045), the Jiangsu Natural Science Foundation (Grant No. BK20170081) and the Excellent Young Teachers Program of Southeast University (Grant No. 2242016R30005).

#### REFERENCES

- [1] AFENG, Z., GENXING, P. & LIANQING, L. 2009. Biochar and the effect on C stock enhancement, emission reduction of greenhouse gases and soil reclamation. *Journal of Agro-Environment Science*, 28, 2459-2463.
- [2] AGBLEVOR, F. & BESLER, S. 1996. Inorganic compounds in biomass feedstocks. 1. Effect on the quality of fast pyrolysis oils. *Energy & Fuels*, 10, 293-298.
- [3] AGBLEVOR, F., BESLER, S. & WISELOGEL, A. 1996. Production of oxygenated fuels from biomass: impact of feedstock storage. *Fuel science & technology international*, 14, 589-612.
- [4] AHMAD, M., RAJAPAKSHA, A. U., LIM, J. E., ZHANG, M., BOLAN, N., MOHAN, D., VITHANAGE, M., LEE, S. S. & OK, Y. S. 2014. Biochar as a sorbent for contaminant management in soil and water: a review. *Chemosphere*, 99, 19-33.
- [5] AHUJA, P., SINGH, P., UPADHYAY, S. & KUMAR, S. 1996. Kinetics of biomass and sewage sludge pyrolysis: Thermogravimetric and sealed reactor studies.
- [6] ANTAL, M. J., VARHEGYI, G. & JAKAB, E. 1998. Cellulose pyrolysis kinetics: revisited. *Industrial & engineering chemistry research*, 37, 1267-1275.
- [7] ANTUNES, E., JACOB, M. V., BRODIE, G. & SCHNEIDER, P. A. 2017a. Silver removal from aqueous solution by biochar produced from biosolids via microwave pyrolysis. *Journal of Environmental Management*, 203, 264-272.
- [8] ANTUNES, E., SCHUMANN, J., BRODIE, G., JACOB, M. V. & SCHNEIDER, P. A. 2017b. Biochar produced from biosolids using a single-mode microwave: Characterisation and its potential for phosphorus removal. *Journal of Environmental Management*, 196, 119-126.
- [9] AZIZI, K., KESHAVERZ MORAVEJI, M. & ABEDINI NAJAFABADI, H. 2017. A review on bio-fuel production from microalgal biomass by using pyrolysis method. *Renewable and Sustainable Energy Reviews*.
- [10] BAHNG, M.-K., MUKARAKATE, C., ROBICHAUD, D. J. & NIMLOS, M. R. 2009. Current technologies for analysis of biomass thermochemical processing: a review. *Analytica Chimica Acta*, 651, 117-138.
- [11] BASSILAKIS, R., CARANGELO, R. & WOJTOWICZ, M. 2001. TG-FTIR analysis of biomass pyrolysis. *Fuel*, 80, 1765-1786.
- [12] BASU, P. 2010. Biomass gasification and pyrolysis: practical design and theory, Academic press.
- [13] BENEROSO, D., MONTI, T., KOSTAS, E. T. & ROBINSON, J. Microwave Pyrolysis of Biomass for Bio-oil Production: Scalable Processing Concepts. *Chemical Engineering Journal*
- [14] BENEROSO, D., MONTI, T., KOSTAS, E. T. & ROBINSON, J. 2017. Microwave pyrolysis of biomass for bio-oil production: Scalable processing concepts. *Chemical Engineering Journal*, 316, 481-498.
- [15] BILBA, K. & OUENSANGA, A. 1996. Fourier transform infrared spectroscopic study of thermal degradation of sugar cane bagasse. *Journal of Analytical and Applied Pyrolysis*, 38, 61-73.
- [16] BJÖRKMANN, E. & STRÖMBERG, B. 1997. Release of chlorine from biomass at pyrolysis and gasification conditions1. *Energy & Fuels*, 11, 1026-1032.



- [17] BRIDGWATER, A. V. 1999. Principles and practice of biomass fast pyrolysis processes for liquids. *Journal of Analytical and Applied Pyrolysis*, 51, 3-22.
- [18] BRIDGWATER, A. V. & EVANS, G. 1993. An assessment of thermochemical conversion systems for processing biomass and refuse, Energy Technology Support Unit Harwell
- [19] BRIDGWATER, A. V. & GRASSI, G. 2012. Biomass pyrolysis liquids upgrading and utilization, Springer Science & Business Media
- [20] CHEN, M.-Q., WANG, J., ZHANG, M.-X., CHEN, M.-G., ZHU, X.-F., MIN, F.-F. & TAN, Z.-C. 2008. Catalytic effects of eight inorganic additives on pyrolysis of pine wood sawdust by microwave heating. *Journal of Analytical and Applied Pyrolysis*, 82, 145-150.
- [21] DI BLASI, C. 1993. Modeling and simulation of combustion processes of charring and non-charring solid fuels. *Progress in Energy and Combustion Science*, 19, 71-104
- [22] DI BLASI, C., BRANCA, C. & D'ERRICO, G. 2000. Degradation characteristics of straw and washed straw. *Thermochimica acta*, 364, 133-142.
- [23] DI BLASI, C., BRANCA, C., SANTORO, A. & HERNANDEZ, E. G. 2001. Pyrolytic behavior and products of some wood varieties. *Combustion and Flame*, 124, 165-177.
- [24] DI BLASI, C., SIGNORELLI, G., DI RUSSO, C. & REA, G. 1999. Product distribution from pyrolysis of wood and agricultural residues. *Industrial & Engineering Chemistry Research*, 38, 2216-2224.
- [25] DOMÍNGUEZ, A., MENÉNDEZ, J. A., FERNÁNDEZ, Y., PIS, J. J., NABAIS, J. M. V., CARROTT, P. J. M. & CARROTT, M. M. L. R. 2007. Conventional and microwave induced pyrolysis of coffee hulls for the production of a hydrogen rich fuel gas. *Journal of Analytical and Applied Pyrolysis*, 79, 128-135.
- [26] DOMÍNGUEZ, A., MENÉNDEZ, J. A., INGUANZO, M. & PÍS, J. J. 2006. Production of bio-fuels by high temperature pyrolysis of sewage sludge using conventional and microwave heating. *Bioresource Technology*, 97, 1185-1193.
- [27] DONG, X., MA, L. Q. & LI, Y. 2011. Characteristics and mechanisms of hexavalent chromium removal by biochar from sugar beet tailing. *Journal of hazardous materials*, 190, 909-915.
- [28] DRUMMOND, A.-R. F. & DRUMMOND, I. W. 1996. Pyrolysis of sugar cane bagasse in a wire-mesh reactor. *Industrial & Engineering Chemistry Research*, 35, 1263-1268.
- [29] FARAG, S., FU, D., JESSOP, P. G. & CHAOUKI, J. 2014. Detailed compositional analysis and structural investigation of a bio-oil from microwave pyrolysis of kraft lignin. *Journal of Analytical and Applied Pyrolysis*, 109, 249-257.
- [30] FOWLES, M. 2007. Black carbon sequestration as an alternative to bioenergy. *Biomass and Bioenergy*, 31, 426-432.
- [31] GARCÍA-PÉREZ, M., CHAALA, A., YANG, J. & ROY, C. 2001. Co-pyrolysis of sugarcane bagasse with petroleum residue. Part I: thermogravimetric analysis. *Fuel*, 80, 1245-1258.
- [32] GARCIA, L., SALVADOR, M., ARAUZO, J. & BILBAO, R. 1999. Catalytic steam gasification of pine sawdust. Effect of catalyst weight/biomass flow rate and steam/biomass ratios on gas production and composition. *Energy & Fuels*, 13, 851-859.
- [33] GLASER, B., LEHMANN, J., STEINER, C., NEHLS, T., YOUSAF, M. & ZECH, W. Potential of pyrolyzed organic matter in soil amelioration. 12th ISCO Conference'. Beijing, 2002. 421-427.
- [34] GOLBER, E. 1985. Black carbon in the environment: properties and distribution. New York, John Wiley.
- [35] GUO, X., ZHENG, Y. & ZHOU, B. Influence of absorption medium on microwave pyrolysis of fir sawdust. *Bioinformatics and Biomedical Engineering*, 2008. ICBBE 2008. The 2nd International Conference on, 2008. IEEE, 798-800.
- [36] GÜTZLOE, A., THUMM, U. & LEWANDOWSKI, I. 2014. Influence of climate parameters and management of permanent grassland on biogas yield and GHG emission substitution potential. *Biomass and Bioenergy*, 64, 175-189.
- [37] HODGSON, E., LEWYS-JAMES, A., RAO RAVELLA, S., THOMAS-JONES, S., PERKINS, W. & GALLAGHER, J. 2016. Optimisation of slow-pyrolysis process conditions to maximise char yield and heavy metal adsorption of biochar produced from different feedstocks. *Bioresource Technology*, 214, 574-581.
- [38] HOMAGAIN, K., SHAHI, C., LUCKAI, N. & SHARMA, M. 2014. Biochar-based bioenergy and its environmental impact in Northwestern Ontario Canada: A review. *Journal of forestry research*, 25, 737-748.
- [39] WANG, C. Catalytic pyrolysis of plant biomass in a powder-particle fluidized bed. *Fuel and Energy Abstracts*, 1996. 31.
- [40] HORNE, P. A., NUGRANAD, N. & WILLIAMS, P. T. 1995. Catalytic coprocessing of biomass-derived pyrolysis vapours and methanol. *Journal of analytical and applied pyrolysis*, 34, 87-108.
- [41] HORNUNG, A. 2014. Transformation of Biomass: Theory to Practice, John Wiley & Sons.
- [42] HUANG, H.-J., YANG, T., LAI, F.-Y. & WU, G.-Q. Co-pyrolysis of sewage sludge and sawdust/rice straw for the production of biochar. *Journal of Analytical and Applied Pyrolysis*.
- [43] HUANG, X., CAO, J.-P., ZHAO, X.-Y., WANG, J.-X., FAN, X., ZHAO, Y.-P. & WEI, X.-Y. 2016a. Pyrolysis kinetics of soybean straw using thermogravimetric analysis. *Fuel*, 169, 93-98.
- [44] HUANG, Y.-F., CHIUEH, P.-T., KUAN, W.-H. & LO, S.-L. 2013a. Microwave pyrolysis of rice straw: Products, mechanism, and kinetics. *Bioresource Technology*, 142, 620-624.
- [45] HUANG, Y. F., KUAN, W. H., LO, S. L. & LIN, C. F. 2008. Total recovery of resources and energy from rice straw using microwave-induced pyrolysis. *Bioresource Technology*, 99, 8252-8258.
- [46] JINYANG, M., GAO, B., PULLAMMANAPPALLIL, P., DING, W. & ZIMMERMAN, A. R. 2010. Biochar from anaerobically digested sugarcane bagasse. *Bioresource Technology*, 101, 8868-8872.
- [47] IOANNIDOU, O., ZABANIOTOU, A., ANTONAKOU, E., PAPAZISI, K., LAPPAS, A. & ATHANASSIOU, C. 2009. Investigating the potential for energy, fuel, materials and chemicals production from corn residues (cobs and stalks) by non-catalytic and catalytic pyrolysis in two reactor configurations. *Renewable and sustainable energy reviews*, 13, 750-762.
- [48] INTANI, K., LATIF, S., KABIR, A. R. & MÜLLER, J. 2016. Effect of self-purging pyrolysis on yield of biochar from maize cobs, husks and leaves. *Bioresource Technology*, 218, 541-551.
- [49] JEFFERY, S., ABALOS, D., SPOKAS, K. A. & VERHEIJEN, F. G. 2015. Biochar effects on crop yield. *Biochar for Environmental Management: Science, Technology and Implementation*, 2.
- [50] JONES, D. A., LELYVELD, T. P., MAVROFIDIS, S. D., KINGMAN, S. W. & MILES, N. J. 2002. Microwave heating applications in environmental engineering—a review. *Resources, Conservation and Recycling*, 34, 75-90.
- [51] KRAMER, C. A., LOLOEE, R., WICHMAN, I. S. & GHOSH, R. N. 2009. Time Resolved Measurements of Pyrolysis Products From Thermoplastic Poly-Methyl-Methacrylate (PMMA). 99-105
- [52] LANZETTA, M. & DI BLASI, C. 1998. Pyrolysis kinetics of wheat and corn straw. *Journal of Analytical and Applied Pyrolysis*, 44, 181-192.
- [53] LEHMANN, J. 2007. A handful of carbon. *Nature*, 447, 143-144.
- [54] LEHMANN, J., GAUNT, J. & RONDON, M. 2006. Bio-char sequestration in terrestrial ecosystems—a review. *Mitigation and adaptation strategies for global change*, 11, 395-419.
- [55] LEHMANN, J., PEREIRA DA SILVA, J., STEINER, C., NEHLS, T., ZECH, W. & GLASER, B. 2003. Nutrient availability and leaching in an archaeological Anthrosol and a Ferralsol of the Central Amazon basin: fertilizer, manure and charcoal amendments. *Plant and soil*, 249, 343-357.
- [56] LI, J., DAI, J., LIU, G., ZHANG, H., GAO, Z., FU, J., HE, Y. & HUANG, Y. 2016a. Biochar from microwave pyrolysis of biomass: A review. *Biomass and Bioenergy*, 94, 228-244.
- [57] LIU, P., PTACEK, C. J., BLOWES, D. W. & LANDIS, R. C. 2016. Mechanisms of mercury removal by biochars produced from different

feedstocks determined using X-ray absorption spectroscopy. *Journal of Hazardous Materials*, 308, 233-242.

- [58] LIU, Y., LIU, X. & WANG, X. 2014. Double-layer microwave absorber based on CoFe<sub>2</sub>O<sub>4</sub> ferrite and carbonyl iron composites. *Journal of Alloys and Compounds*, 584, 249-253.
- [59] LIU, Z., QUEK, A., HOEKMAN, S. K. & BALASUBRAMANIAN, R. 2013a. Production of solid biochar fuel from waste biomass by hydrothermal carbonization. *Fuel*, 103, 943-949.
- [60] MOHAMED, B. A., ELLIS, N., KIM, C. S., BI, X. & EMAM, A. E.-R. 2016a. Engineered biochar from microwave-assisted catalytic pyrolysis of switchgrass for increasing water-holding capacity and

fertility of sandy soil. *Science of The Total Environment*, 566-567, 387-397.

- [61] LO, S.-L., HUANG, Y.-F., CHIUEH, P.-T. & KUAN, W.-H. 2017. Microwave Pyrolysis of Lignocellulosic Biomass. *Energy Procedia*, 105, 41-46.
- [62] LUQUE, R., MENÉNDEZ, J. A., ARENILLAS, A. & COT, J. 2012. Microwave-assisted pyrolysis of biomass feedstocks: the way forward? *Energy & Environmental Science*, 5, 5481-5488.
- [63] Miura M, Kaga H, Tanaka S, Takanashi K, Ando K., 2000. Rapid microwave pyrolysis of wood. *Journal of Chemical Engineering of Japan* 33, 299-302.





# Impact of Solar PV Integration on Short Circuit Current and Protection of Distribution System

Umair Shahzad Khan, Dr. Muhammad Naeem Arbab

**Abstract**— Injection of solar power to current distribution system has provide many benefits such as power quality is improved, reliability is increased and peak demand is full filled. when a solar source is injected despite of it benefits it has some negative impact on protection system that in turn effect reliability and stability of system. injecting solar PV to system cause to increase fault current and severely effect protection system. We use IEEE 13 bus system for simulation with software ETAP. we inject solar PV on different buses and apply fault on different location. we compare the result of short circuit study of normal case and when PV is added. We also increase the penetration of PV and see it impact short circuit current . This comparison enables us to investigate impact of solar PV on short circuit current level and impact of this current on protection scheme and devices in this paper we will investgate the impact of injecting solar power on fault current level of distribution system and study the consequent effect of this fault current on protection system and devices of long transmission line and line losses is also reduced so it encourages to generate electricity in local and supply the near by load rather than constructing a long transmissionline.

**Keywords**—Photovoltaics(PV) ,ETAP,IEEE13 Bus System, Protection System, Distributed Generation (DG)

## I. INTRODUCTION

As we observe electricity demand is increasing day by day and it is task of power engineer to generate electricity from other sources to meet the demand but it same time to generate electricity from such sources which has less effect on environment so renewable energy source has taken greater importance.

However the problem occur when we generate electricity from these sources and integrate it with distribution system .In current distribution system power flow from generating station to load center .The over current protection for current system is based on single direction of power flow .when a distributed energy source such as PV is added the current also flow from DG side .This flow from distributed source effect the protection system by increasing or decreasing the fault current .This increase or decrease in fault current consequently effect the protection system of distribution system.

## II. DISTRIBUTED GENERATION AND ITS TYPES

DG refer to those generations which are very close to the consumer. In DG the distance between the consumer and generating unit is very small. AS the distance between the consumer and generating unit is very small so there is no need. The IEEE defines DG “Those generations whose generating capacity is usually less then the capacity of gentral generating units[3]. The international energy agency defines DG as “Distributed generation are those generation which are feeding the consumer on site[4].

Distributed generation (DG) is usually placing a small power plant near the load center whose capacity is from 5 kw to 25 kw [5]. The distributed generation is of two types .The DG is coupled with grid by two methods .it can be coupled directly with the grid or it can coupled with grid through inverter so we can say DG are of inverter type or rotating machine type .Inverter are used in dc system .The output of DG source is either dc or ac .we need voltages and frequency of certain voltage .in order to achieve the frequency and voltage of desired level we first convert the output of DG source to dc by using specific converter .The dc is then converted to desired value ac .THE rotating machine type DG will be directly connected to grid[5]

The DG technologies are such as photo voltaic system, wind turbines, fuel cells synchronous and induction type generator.

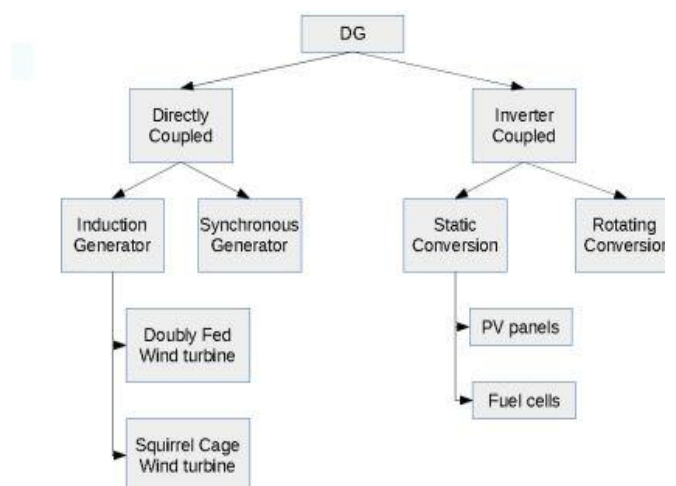


Figure 1. Classification of DG

Umair Shazad Khan: US Pakistan Center for Advanced Studies in Energy (USPCASE) UET Peshawar.

Dr. Muhammad Naeem Arbab: US Pakistan Center for Advanced Studies in Energy (USPCASE) UET Peshawar.

### III. PHOTOVOLTAICS SYSTEM AND ITS CLASSIFICATION

The photovoltaics use the light of the sun and convert the sun light in to usable electrical power. solar cell is used to convert the light of the sun light of the sun in to electrical energy. The Solar cell is made of semi conductor materials . when these semiconductor materials are exposed to sun light it converts the light energy which are present in photon to electrical energy.

When few solar cells combine it form solar array. The solar array is either kept fixed or movable. The array is made movable to track the sun. The reason of tracking trucking sun is to maximize the power that we get from solar panel. we get energy from solar by two techniques either by active solar technique or passive solar technique .in active solar technique we use directly the power of the sun such as in photovoltaics and concentrated solar power. If we orient our building in sun direction it is passive solar technique. As we see the global warming is increasing .it is because of the waste gas and other environment harmful gas in the environment .in diesel power plant lot of the waste goes in to environment. we need to generate energy from the sources that are environment friendly so sun is the biggest sources of renewable energy. This system is environment friendly because there is no emission of the waste which are harmful for the environment. Sun has high potential to generate electricity. the united nation development found that in 2000 that sun has potential of to generate 1575 to 49837 EXA JOULE energy per year .it is several times greater than the world consummation of the energy. Solar system is very easy to design and it require only sun as fuel. The disadvantage of this system is that it has high initial cost and it require large space [8].

PV system are classified in to several categories. The classification is based on the base of function, operational needs and how the components are connected with other power sources.[13] The main classification of solar system is as under

1. Grid connected photovoltaic system
2. Standalone solar system
3. Hybrid photovoltaic system

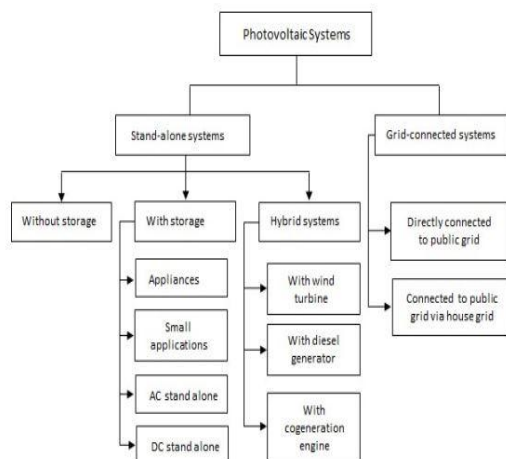


Figure 2. classification of photovoltaicsystem

### IV. IMPACT OF DISTRIBUTED SOLAR PV ON SHORT CIRCUIT CURRENT

The short circuit current value or fault current of the system is changed when a distributed generating source is injected.it is observed that short circuit current level increase as we insert or inject a DG sources when this fault current is compared with fault current of without DG.

The circuit level even also increases if we inject a small generating unit to the system. The increase in fault current with injecting DG depends on many factors.it depends on the size of DG, location of the DG, generating capacity of DG, distance between the generating source and fault and on the type of DG [6]. Let consider a scenario in which we add only one small distributed energy source to the network. The fault current of network increase when fault occur on different location in system. The increase in fault current level due to a small single DG source is not much significant and this increase is very small so DG of very small not cause any problem to the protection system scheme of the network and fuse breaker work in normal way and coordination of the system is remain intact [6]. If we add more the then one small DG it causes increase to fault current level and this increase is very dominant and it has severe effect on the distribution protection scheme. This cause miss co-ordination between the protective device and system not work in normal way. If one large centralized DG is injected to network, it also has more dominant effect on system fault current level. The dg contributes to faults and faults increase and utility contribution in such scenario is reduced [7].

If distance between fault and SOLAR PHOTOVOLTIC source is changed the percentage contribution by DG to fault is also varied however fault current increase in all case. if smaller unit is injected to system whose generating capacity to one large central source, the fault current increase but the increase is smaller as compared to one centralized source. The increase in fault current depends on the type of DG technology we are using. The contribution to fault is very high in case of separately excited synchronous generator.it contribution become more dangerous after few cycle. The inverter type DG contributes less to the fault current level.[14].

### V. IMPACT OF SOLAR DG ON PROTECTION OF DISTRIBUTION FEEDER

The power flow in current traditional power system is in radial direction. The radial flow means power flow in single direction that is from generating station to far away load center. protective devices are placed on the feeder and branches of distribution system to protect the equipment of system from damage and there is continuous flow of electricity to the loads [7]. The protection of the system is not simple or straight forward but we have to take some consideration in to account to protect the whole system. The are several protective devices are placed in network and each has to protect certain area the protection system has to protect this area in very reliable way. however, we solar DG source is added it cause the problem of reduction of reach in same cases. The problem occurs when a solar DG is embedded in a system because there is single

direction of power flow in current system and all device are coordinated for single power flow direction. The case is not true in case of solar DG because current also flow from DG side also. The solar PV has very significant effect on protective device and distribution feeder protection.

### A. False trip or mail trip

it is the condition in which the protection system remove the healthy portion of the system. The system not operate in correct fashion and did the unwanted or unnecessary tripping.[9] Let us see in figure there are two feeders connected to bus and operated in parallel fashion.

The both feeder is feed from grid. A distributed generating source such as PV is connected to one of feeder. if the fault occurs on the feeder which has no PV source connected so it is required the breaker of this feeder to operate and isolate this feeder only. however, PV source contribute to the fault and case the healthy feeder to trip which is not necessary [6][12].

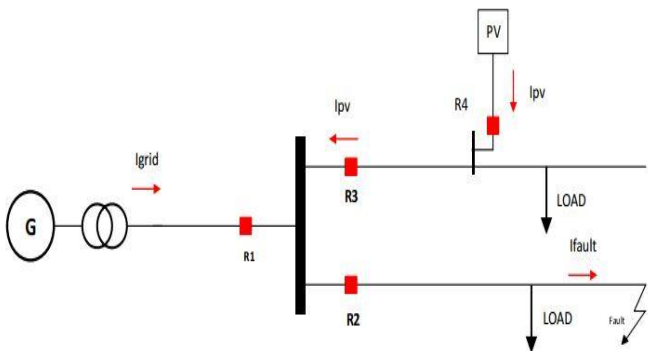


Figure 3. Flase Trip

### B. Blinding or fail to trip

In some cases, when a PV generating source is injected to radial system it can blind the protection system. The protection system is blind and not see the fault and faulted section is still connected with system even fault occur on system. As in figure a radial system is shown and a downstream fault occur. if the contribution from PV source so very less current then flow through R1. the current is very less than the pickup current of relay so relay not sense fault and not operated and faulted section is still connected. [6][2][7]

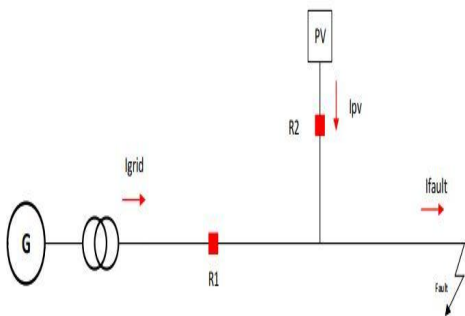


Figure 4. Blinding OR Fail to Trip

### C. Reduction of reach

in power system every protective device has to protect certain area or distance .in some case when a PV power is added, the system is unable to protect its protection zone .it is unable to reach its protective distance [10]. As we see in figure R1 must cover or protect all area from node a to b. when a PV is added and the contribution from PV source so very less current then flow through R1. the current is very less than the pickup current of relay so relay not sense fault and not operated and faulted section is still connected R1 is not able to detect fault in their protective zone [7] [15].

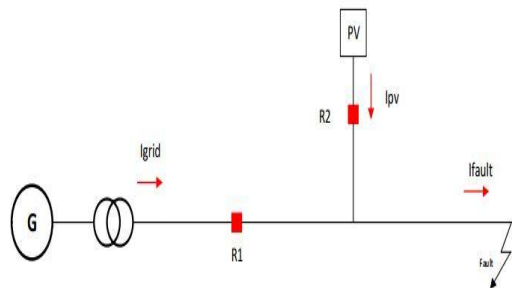


Figure 5. Reduection of Reach

## VI. SIMULATION AND RESULTS

The system used for the simulation is IEEE13 bus system. we run simulation on IEEE 13 bus system by applying fault on different location in the system. First we apply fault on different buses without connecting any PV sources to the system. These values are considered as base values. Then we connect PV sources to the system with different configuration and these results are compared with the result of the base case. The system which is used for simulation is shown below [13].

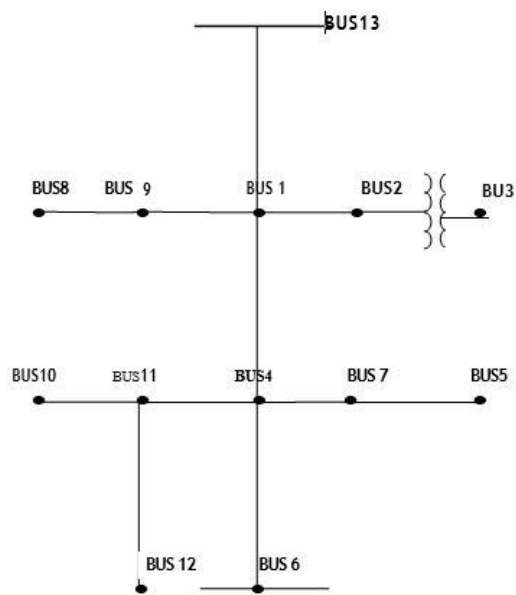


Figure 6. IEEE 13 BUS SYSTEM

We run simulation for different configuration of PV connected to the IEEE 13 BUS SYSTEM .THE FOLLOWING cases is simulated by applying fault on different buses.

*Case 1:Simulation of system with out injecting any pv power*

*Case 2:Simulation of system when pv power of 6MW is injected on the bus 1*

*Case 3:Simulation of system when pv power of 6MW is injected on the bus 3*

*Case 4:Simulation of system when pv power of 6MW is injected on the bus 4*

*Case 5:Simulation of system when pv power of 6MW is injected on the bus 6*

*Case 6:Simulation of system when pv power of 9MW is injected to three different buses in the system*

On running the simulation for above case by applying fault on different buses .THE result which is obtained during simulation is listed below

TABLE I. TABLE 1 FAULT CURRENT OF ALL SCENARIO WHEN FAULT OCCUR ON DIFFERENT BUSES

Faulted bus	Case1	Case2	Case3	Case4	Case 5	Case6
Bus 1	7.12	8.781	7.85	7.84	7.210	8.45
Bus 2	5.12	5.965	6.56	5.57	5.19	5.663
Bus 3	16.99	17.905	30.3	19.5	17.451	17.163
Bus 4	4.214	4.32	4.65	5.78	4.720	4.7
Bus 5	2.946	2.975	3.27	3.35	4.045	4.08
Bus 6	2.510	2.528	3.32	3.94	4.408	3.856
Bus7	4.214	4.23	4.65	5.72	4.371	4.773

The result that is obtained from the simulation is used to investigate impact of PV POWER on short circuit or fault current and it impact on protection scheme .in simulation we get four types of result but we are using one type that occur mostly on power system and that is when single line touch ground known as SLG fault. The above listed table show as the fault current when fault occur in different location in the power system. This table is used to generate comparison chart for each case and then we compare all case with the standard case that is without PV power.

## VII. DISCUSSION

Now we will discuss the impact of this fault current or short circuit current level on protection system of distrinution network. In case1 we run simulation on the IEEE 13 bus system without adding any distributed generation source to the system. From this we get the standard response of the system. the below graph shows the result that are obtained during the simulation. The below chart tells us about the fault current

when we apply fault at different location in the network. These values are considered as the standard or base value and the value that is obtained during the simulation when we add PV source to the system is compared with these standard values. This case result set the value of the all protection equipment that will be used in system.as we see from the result the highest fault current is recorded when fault occur on the bus 3. This is because of the transformer that is connected B/W bus2 and bus 3. The PV are operating on the low-tension side of the transformer that why high fault current is recorded on this bus.

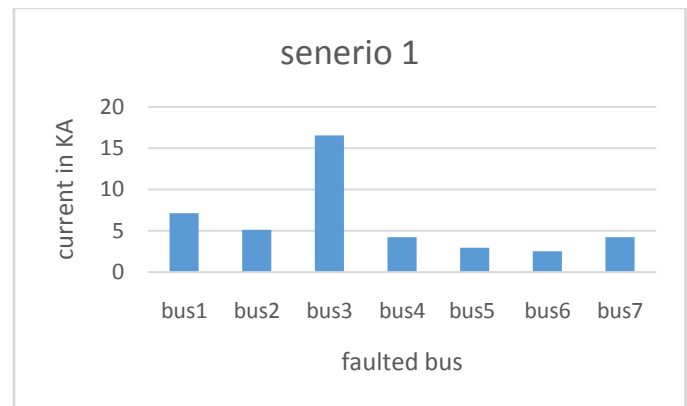


Figure 7. case1

During case 2 we added PV SOURCE to the system whose rating is 6mw.The PV source is connected to the bus 1. when fault occur at different location in the system the fault current value is noted and this fault current value is compared with the value of the case 1. The purpose of doing this to study the impact of the connected PV source. The comparison between the case one and case 2 are shown in below fig.

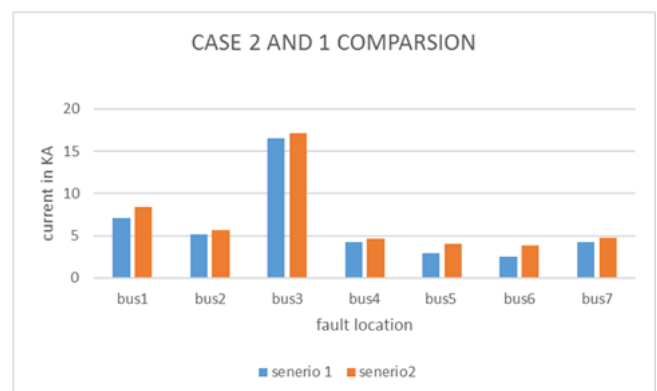


Figure 8. Comparing case 2 and case 1

We see from the comparisons that we add PV source to the bus 1. The level of the short circuit current is increased on all the buses of the system. if we closely see the fig we come to know that maximum increases in the short circuit current level is noticed on the bus 1. This is because of small distance between the faulted bus and PV source so this close location leads to increase the fault current contributions from the PV source. The increase in short circuit level on all the other bus is



very small as compared to BUS 1 because the small distance between PV source and utility and fault location. During case 3 we connect PV source to the bus 3. The PV source used is centralized dg source. We run simulation for different fault location in the system and noted fault current value and these value is then compared with case 1 value. The fig listed below show us the comparison between both the case.

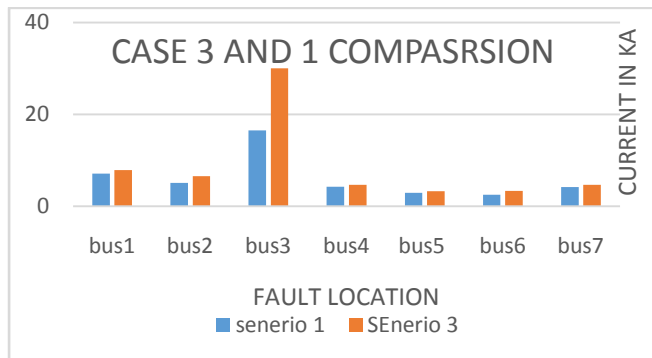


Figure 9. Comparing case 3 and case1

By seeing the above figure, we come to know that when a PV power source is located at bus location on bus 3. There is small increase in all buses short circuit current levels. When fault occur on the bus 3 the PV source contributes a lot to the fault current. We see from figure the fault is increased almost by 90%.the contribution of dg to the fault is very high because faulted bus and photovoltaic source has close distance. Secondly PV operate on low-tension side of transformer so SC current contribution is very high from solar. THE solar and fault both are on low tension side of the transformer so that's why increase in fault current is so high we transform this current to high voltage side of the transformer its value is decreased by apply transformer ratio the current come out 16.3ka on high voltage side of transformer. During case 4 a DG source of 6 mw is connected at BUS 4,the source is centralized DG source which is connected to BUS 4.by applying fault at different bus short circuit current value is noted down. the noted value is compared with the value of the case 1.

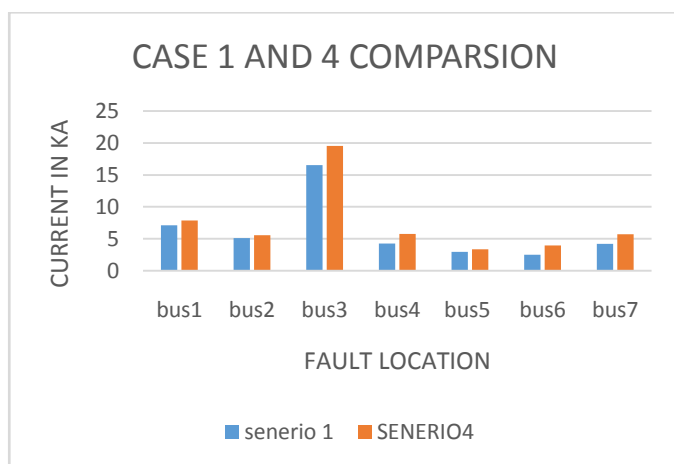


Figure 10. Comparing case 4 and case 1

When solar power source is located on BUS 4 and fault occur on different buses in network the short circuit current level of the system is increased. The largest increased is noted when fault occur on the BUS 4. The fault current is increased by 33%.the increase is due to close location of fault and photovoltaic source.

As we increase distance of fault location and photovoltaics, the solar source contribution to fault current is decreased. We can say the rise in rise in fault current is decreased. in simple word as distance between generating station and fault location is increased the generating station contribute less to fault current.During case 5 we connect photovoltaic source injected to the BUS 6. The photovoltaic source used is centralized source. We run simulation for different fault location in the system and noted fault current value and these value is then compared with case 1 value. The fig listed below show us the comparison between both the case.

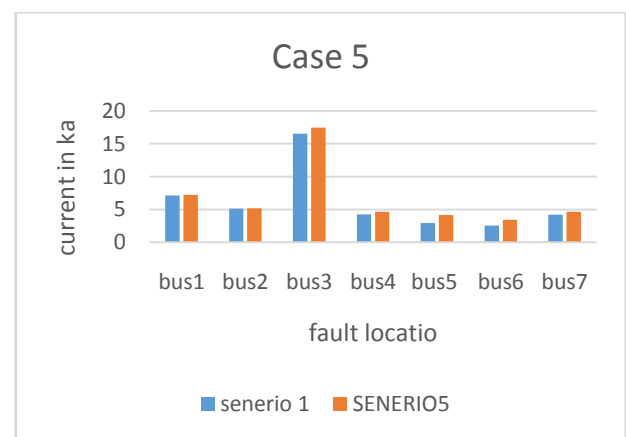


Figure 11. Case 5 and Case 1 Comparing

when we see the figure, it shows us the comparison between the cases. During case 6 the short circuit current level of the network is increased. By placing solar on BUS 6 it has significant effect on the whole system. When fault is applied at BUS 6 the short circuit start to flow in branch BUS 4 to BUS 6. The current that flow from bus 6 to bus 4 is neglected in other scenario. The current flowing in this branch cause lot of the problem to the existing protection scheme because there is no current flowing in this branch in all other cases. The protection system is designed for the case when there is no current flowing in this branch. The protection equipment used for the protection of this part is unable to project the network and cause problems of reduction of reach.

In this case we connect 3 photovoltaic sources each of 3 mw to the network at 3 different buses.in this case we replaced this single centralized solar by multiple decentralized PV sources. We connect the same generating capacity to the network but we divide it in the small PV sources. We connect 3 mw dg at BUS 1, BUS 4 and BUS 5.

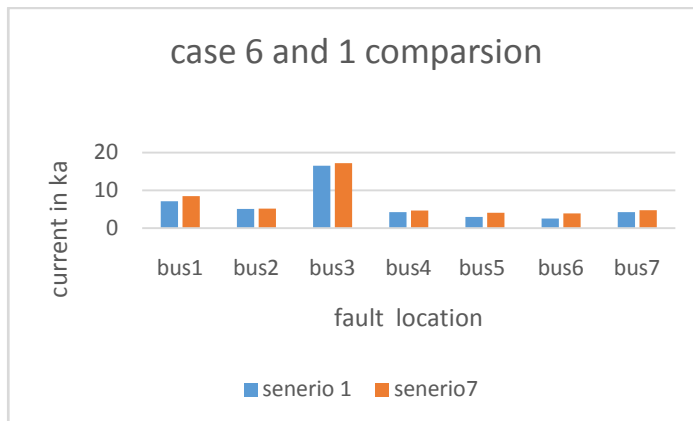


Figure 12. Case 6 and 1 Comparing

This figure is used to study the impact of single centralized and multiple decentralized generation. From figure we see that PV sources increase the fault current level of the network. It increases the fault current of all location at which PV is connected. This increase depends on the configuration at which we connect dg to the system. The difference between single centralized and multiple decentralized dg sources is identified from the percentage contribution to the fault current by dg source and substation. In decentralized generation we see that the percentage contribution to the fault by PV sources is increased. The fault current almost increases for all the location in the network. The percentage contribution by the substation is decreased in decentralized PV sources. The fault current highly increases on bus 1 because of photovoltaic solar located on same bus secondly distance of this bus from Substation is very small.

The current flowing in branch bus 1 to bus 4 is noted from simulation. The below listed graph shows the current flowing in branch bus 1 to 4.

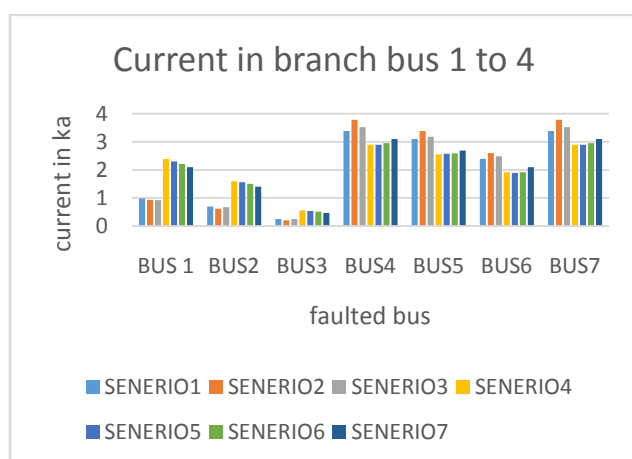


Figure 13. current in branch bus1 to bus4

The branch from bus1 to 4 is considered very important. It is considered as the main branch of the network. The current first passes through this branch and then is delivered to other lateral and load connected. When a photovoltaic source is injected into the network, the current flowing through this branch is increased in all cases but in some cases the increase is so high that it is a very difficult job to

design a protection scheme for this main lateral. The high current can cause a severe damage to the distribution system. If we observe the above-listed comparison, it is concluded that cases 2 and 3 are considered to be the best location for PV solar to be injected in the network because the variation in current is very low for both situations and it is about 9% to 11%, so it is not much high to disturb our current protection scheme. If you inject a photovoltaic source at another bus, the short-circuit current level is very high and it increases up to 200 percent of the normal case fault that is without PV source, so such a scenario makes it very difficult to design a protection scheme for the network.

## CONCLUSION

When a solar photovoltaic is injected, the short-circuit current level of the system is increased. The radial flow of power is lost with the injection of PV because fault current flows from the photovoltaic side also. When the distance between the solar photovoltaic source and the fault occurring location increases, the fault current decreases when we connect the photovoltaic source to bus6. It affects the current protection scheme and causes problems of reduction of reach because in all other scenarios, fault current is zero in this branch from bus6 to bus5, and fault current flows only when photovoltaic is on bus6. In some cases, fault current decreases in certain branches, so relay of the designed protective scheme becomes blind and not able to isolate the faulty section when penetration of PV power increases. The fault current increases more. In simple words, we have to reconfigure our protection scheme when we add a distributed source to the system.

## REFERENCES

- [1] K. Kauhaniemi, L. K. (2004). Impact of Distributed Generation on the Protection of Distribution Networks
- [2] M. C. B. Ravindranath, Power System Protection and Switchgear, New Delhi: New Age International (P) Ltd., 2005
- [3] Kersting WH. Radial Distribution Test Feeders, IEEE Distribution system Analysis Subcommittee Report 2001;908-912
- [4] International Energy association outlook Source: <https://www.iea.org/>
- [5] [https://en.wikipedia.org/wiki/Distributed\\_generation](https://en.wikipedia.org/wiki/Distributed_generation)
- [6] Kersting WH. Radial Distribution Test Feeders, IEEE Distribution System Analysis Subcommittee Report 2001;908-912
- [7] M. T. Doyle, Reviewing the impacts of distributed generation on distribution system protection, IEEE Power Engineering Society Summer Meeting, vol. 1, pp. 109-114, July 2002
- [8] Philip P. Barker, R. W. (2000). Determining the Impact of Distributed Generation on Power Systems: Part 1 - Radial Distribution Systems.
- [9] IEEE. Retrieved 02/16/2011, from IEEE Joint Working Group B5/C6.26/C1RED, "Protection of Distribution Systems with Distributed Energy Resources," March 2015
- [10] P. M. Anderson, Power System Protection, IEEE Press, 1999, pp. 201-240, 249-25
- [11] <http://www.solarfacts.com/panels/>
- [12] J. Holmes, J. M. (2004). Protection of Electricity Distribution Networks. United Kingdom: Power and Energy Series 47
- [13] M. Bollen and F. Hassan, Integration of Distributed Generation in the Power System, 1st ed., John Wiley & Sons, Inc., 2011

- [14] <http://www.electrical4u.com/types-of-electrical-protection-relays-orprotective-relays>
- [15] IEEE, *IEEE 100, The Authoritative Dictionary of IEEE StandardTerms*,Seventhed.,IEEE Press, 2000



**UMAIR SHAHZAD KHAN** who graduated from University of Engineering and Technology (UET) Peshawar in 2014. He holds B.Sc degree in Electrical Engineeirng. He is currently enrolled in M.Sc Electrical Energy Systems Engineering at US Pakistan Center for Advanced Studies in

Energy (USPCASE) UET Peshawar. His major field of study is Electrical Power Engineering. He worked as trainee engineer with PEDO for 3 months.

**Professor Dr. Muhammad Naeem Arbab** is a Professor in University of Engineering and Technology Peshawar in Electrical Department. He got his Ph.D. from UK and author of two engineering books i.e., High Voltage Engineering and Electrical Power Generation and published more than 25 research papers. Email: mnarbab@gmail.com.





# The Behaviour of an Enhanced Earthing System of Transmission Voltage

Noor Hussain, Amjad Khattak, Haseeb Khan

**Abstract**—Lightning strikes pose a major challenge to the safety of high voltage transmission and distribution lines. During a lightning strike a very high voltage is produced which can destroy the insulation and damage power systems. Not only are lightning strikes bad for power systems but also pose a serious threat to human life in the vicinity of electricity tower by increasing potential of the soil. Therefore, an effective lightning protection system is needed to cater those above mentioned problems. The effectiveness of a lightning protection system can be deduced by judging the earth connection of the system. Numerous and national standards are in place to help design a protection system that satisfy conditions necessary for the safety of both system and personnel. In this paper, the performance of a full scale 220kV & 500kV transmission tower base is investigated under DC, AC variable frequency and low and high impulse voltages and some of the values of Enhanced Earthing System are simulated through a MATLAB Program.

**Keywords**— Lightning, insulation, strikes, Simulations

## I. INTRODUCTION

This template, modified in MS Word 2003 and saved as “Word 97-2003 & 6.0/95 – RTF” for the PC, provides authors with most of the formatting specifications needed for preparing electronic versions of their papers. All standard paper components have been specified for three reasons: (1) ease of use when formatting individual papers and (2) automatic compliance to electronic requirements that facilitate the concurrent or later production of electronic products. Margins, column widths, line spacing, and type styles are built-in; examples of the type styles are provided throughout this document and are identified in italic type, within parentheses, following the example. Some components, such as multi-leveled equations, graphics, and tables are not prescribed, although the various table text styles are provided. The formatter will need to create these components, incorporating the applicable criteria that follow.

Lightning strikes pose a major challenge to the safety of high voltage transmission and distribution lines. During a lightning strike a very high voltage is produced which can destroy the insulation and damage power systems [1]. Not only

are lightning strikes bad for power systems but also pose a serious threat to human life in the vicinity of electricity tower by increasing potential of the soil [2].

Therefore, an effective lightning protection system is needed to cater those above mentioned problems [3]. The effectiveness of a lightning protection system can be deduced by judging the earth connection of the system [4]. Numerous standards are in place to help design a protection system that satisfy conditions necessary for the safety of both system and personnel [5].

This paper provides an introduction to role of earthing system and components and also provide summary about various standards.

### A. Earthing Mechanism

Earthing Mechanism in transmission and distribution lines is installed to achieve two objectives [6].

- Protection of personnel in the vicinity.
- Reduce damage to equipment and power system operation

### B. Components

At the transmission level, it consists of the following two main components.

- Earthing grid
- Earth Electrode System's Extension

Earthing grid of a substation is made from horizontal conductor bars varies in size. It can span a large area like 30000 m<sup>2</sup> for outdoor substation while for indoor substation it is quite small [7].

The shield wire which main role is to protect conductors from lightning strikes also plays a vital role in transmission earthing systems. This earthing is connected by the transmission line's shield wire. The same wire is also connected to the transmission lines that are located at the vicinity of the substations [8]. This connection between shield wire and substations earthing grids is called extension of the earth electrode system.

The advantage of the above mentioned connection is that it will reduce the impedances along the way of transmission line thus resulting in decrease of step and touch voltages in transmission tower's surroundings which means increased safety of personnel [9].

---

Noor Hussain: Electrical Engineering UET, Peshawar  
Amjad Khattak: Electrical Engineering UET, Peshawar  
Haseeb Khan: Electrical Engineering UET, Peshawar

In addition to above mentioned advantages, the earth wire greatly reduce overhead outage rate. Data show that changing from no earth wire to one and two earth wires reduces the outage rate from 29.8 per 100 miles to 9.8 and 7 outages per 100 miles respectively.

### C. International Standards

Standards provides us with the mechanism and criteria to follow to ensure efficient completion of a task. Different Standards associated with Lightning Protection include BS EN 50522:2008, BS EN 62305-3:2011 EA TS 41-24 [10]. Analyzing these standards provide some recommend measures that are necessary for safe and sound implementation of earthing systems. These include

- having low inductance path for current,
- Electrodes and conductors are form a network.
- Higher density earthing network in an area having high occurring chance of high transient current.
- Short length earthing connections.
- Low Resistance 10  $\Omega$  for earthing system.

### D. Aims and objectives

The main aim of this thesis is to analyze a 220 KV high voltage transmission tower and its earthing system under different conditions and draw out some conclusion for the improvement of the system. To achieve the purpose of this thesis some objectives are set to effectively carry out the research.

- Investigate Transmission tower under AC conditions and find potential in its surroundings, effect of frequency change on surroundings Potential, Comparison of measured and computed values..
- Comparison analysis of computed and measured DC earthing resistance and examining effects of seasonal variation on the earthing resistance.
- Again investigating surrounding soil potential of the surrounding area of the tower but this time when transmission tower is subjected to low impulse current and comparing it with data from AC analysis.
- Investigating types of impulse currents and analyze transient response of the earthing system.
- Testing of a transmission tower under high voltage and high impulse current and examining the nonlinear behavior.
- Testing the earthing system under high impulse current and investigating different parameters associated with lightning protection system.

### E. Contribution of this research

This research will enable us to better understand the potential of soil in surroundings of high voltage transmission towers at different depths and also in different seasons. Further, we will have an increased knowledge about the effect of earthing systems in reducing damage by lightning strikes and

better understanding towards different parameters of earthing systems. This research will provide a framework to design a testing facility to study transient responses in earthing systems.

### F. Investigation of Characteristics of Earthing

The performance of the earthing system of the transmission system relies on the type of the earthing environment that is employed [11]. The high impulse current characteristic can reflect the robustness of the earthing system of the transmission system [12]. Previously the literature review suggests the common earthing system of the transmission system. The type of the soil detects the resistance that dominates the performance under high impulse current.

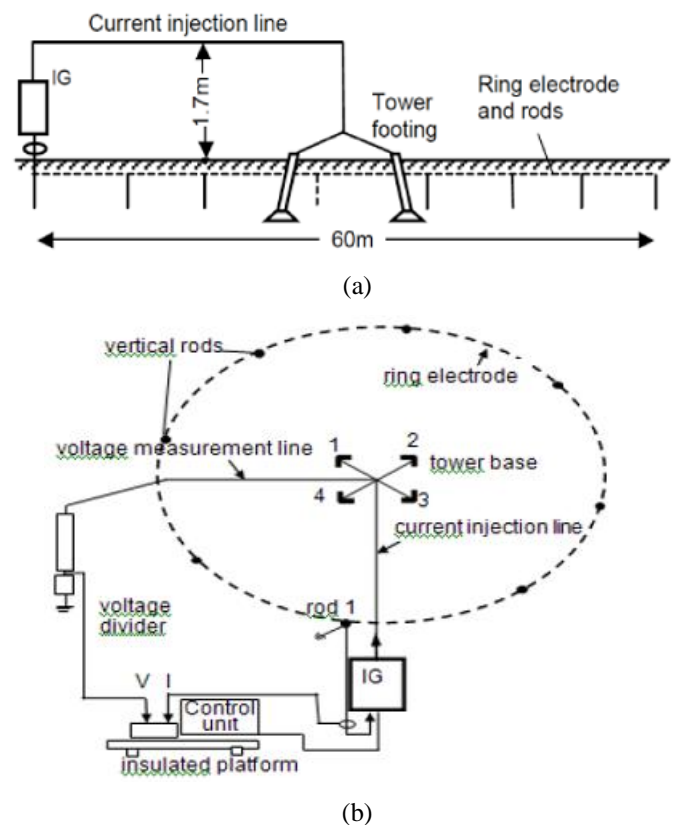
The earth resistance that is dominated by the electrode depends on many factors.

These factors are listed as

- 1) Peak value of impulse current.
- 2) Soil resistivity
- 3) Electrode geometry

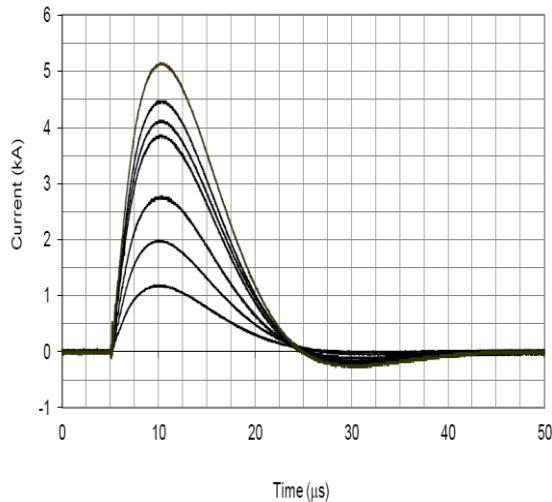
### G. Test setup

The following setup was used to test the characteristics. An impulse generator was used that was capable of generating impulse currents. an overhead transmission line was used that was able to connect the impulse generator with the tower. these are shown in the figures respectively. The impulse generator was connected to the test tower via the wooden poles.



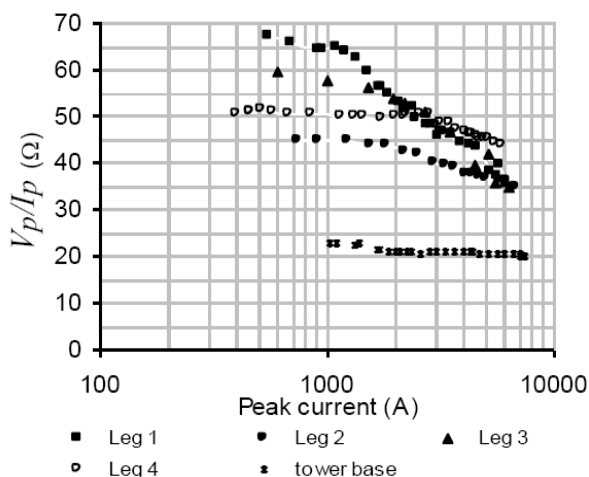
### H. Impulse Resistance of Tower Base

Several impulse tests were carried out having delta rise of the current of 4500 m sec and a tailing time of 1300 m sec. These tests were useful to test the base of the tower with the magnitudes different to the different currents. The currents were ranging from the currents of 900 A to 5000 A. The results are being summarized of the different injected voltages and the currents respectively in the following figure.



Impulse tests at higher current magnitudes

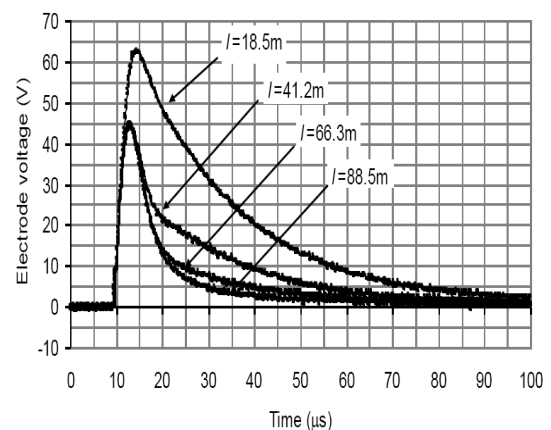
These tests are used to further extend the results of the tests were carried out in the previous sections. The difference between the previous and these tests that the ranges of the current are extended to the values of 4000A and 9000 A respectively. Another change was that the shape of the impulse was also changed. The resistance of the testing electrode was also included and the base of the tower was also included. The following figure shows that the resistance of the impulse is decreasing as the magnitude of the current is increasing for the towers.



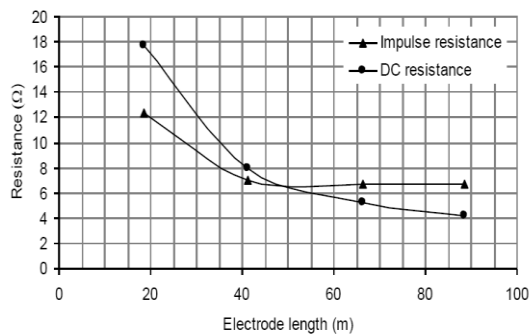
Investigation of Voltage and Current Distribution for the Impulse Conditions

The protection system via earthing system is designated to reroute the fault current which of high magnitude to the ground thus quenching the high current and proving a safety for the persons working as well as for the persons living near the installations of the power systems. Therefore to effectively quenching the high fault currents under the faulty conditions and nominal power frequency, the earthing system should be able to withstand the high fault currents and effectively have a low value of impedance. In order to increase the earthing system of the transmission lines of the steel lines an electrode of the type of ring or may be a single rod may be used. However, in the land having a high resistance of the soil, the type of electrode is changed. For such land a horizontal electrode may be used. This would effectively reduce the impedance at a low frequency of the earth. However, they fail to dissipate the fault current under the lightning conditions. It is due to the fact that the effective length of the electrode may not be effective and it is much lower than the physical length of the electrode. The effective length of the electrode depends upon the resistivity of the soil, the characteristics of the impulse current and the geometry of the electrode. These characteristics have been analyzed in the following section by analyzing the distribution of the current and the voltage taking a horizontal electrode as a case study.

Some additional tests were carried out to further investigate the electrodes in the horizontal position. Both the individual as well as the combined sections were further investigated. There was the step wise increase in the length of the electrode. The first section was injected with the current of 5.0A and all the subsequent sections were then followed by the injection of 5.50 A. The following figure shows the recorded voltage and its shapes when the length of the electrode is increased in the subsequent steps.

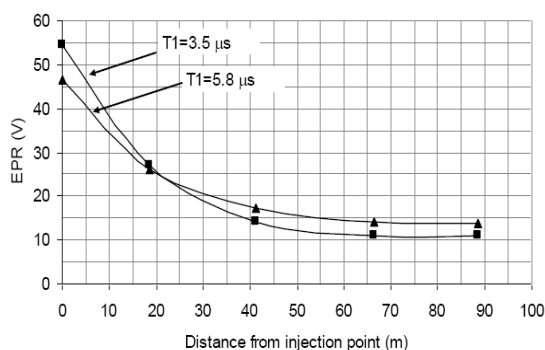
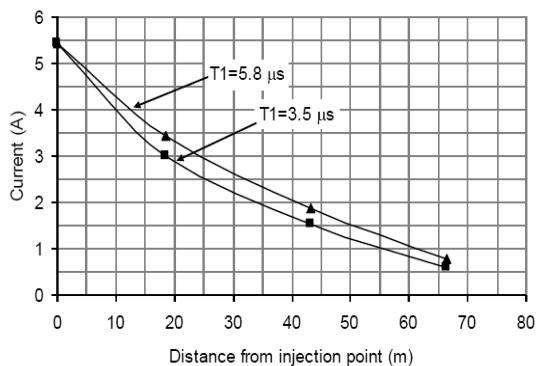


Effect of electrode length



Current Rise Time Effect on current And voltage Distribution

The impulse shape of both the current on the electrode as well as the Earth potential reduction on the electrode was further investigated by using the impulse currents having rise times as 3500 m sec and 5800 m sec. It was concluded that the having the faster increase in the rise and the current reduction in the magnitude the impulse having the lesser rise time showed a slower reduction in the magnitude of the current as shown in the below figure.



## II. CONCLUSIONS

These results show that the impulse current that is quenched depends upon the rise times of the impulse that is applied. It also shows that the length at which the current is injected is also depended on the rise of the earth potential. The

effective length of the electrode is also calculated depending on the resistance of the impulse and is found to be coherent with the formula that is widely used in the literature studies. The results also indicated that the current injection at the mid-point of the electrode has the minimum impulse resistance.

### A. Earthing Enhancement

Earthing frameworks are intended to disseminate high extent blame current to ground additionally to give wellbeing to people working or living near power framework establishments. With a specific end goal to disseminate current successfully under both electric power recurrence and transient blame conditions, the earthing framework ought to have a low impedance esteem. For enhancing or boosting the earthing arrangement of steel transmission lines, singular earth bars or terminals are utilized, in arrive with high soil resistivity, level anodes could likewise be utilized. The expansion of flat ground cathodes will add to the lessening of the low-recurrence earth impedance. All things considered, under lightning conditions, these extra terminals may not precisely be successful in scattering current on the grounds that there is a restricting compelling length of the anode, which is frequently that can be lower than the physical finish cathode. This successful size relies on the span of the cathode edges, soil resistivity and the motivation attributes, and this is the subject of enthusiasm of numerous specialists. The current and voltages appropriations along a side to side terminal have been examined set for a scope of soil resistivity and for low and high current sizes. Estimation models in light of appropriated parameter proportionate circuits have as of late been proposed to decide the drive reaction, the viable length and the impedance of level anodes.

### B. Enhancing Earthing System for a substation of 132KV/220KV

This research uncovers of earthing framework for 132KV/220KV substation and reproduction for calculation of required factors. This exploration is to give data fundamental to safe earthing systems of schedules strategies in AC substation plan likewise for earth to set up the sheltered impediments of potential distinction under ordinary and anomalous conditions. The establishing framework arrangement of is a sensible 220 kV substation is controlled by MATLAB program. The information has been removed from real field examined at the substation. Standard conditions are being utilized as a part of type of earthing framework to get wanted factors, for example, touch and step voltage (conditions benchmarks) for wellbeing, protection, network measure of protection, most extreme matrix current, conductor size and cathode estimate, greatest current level and resistivity of earth soil. By determination even conductor measure, vertical terminal size and soil resistivity, the best decision of the errand for security is led. This examination specifies the calculation required parameters that which can be happen to be recreated by MATLAB program. Some mimicked outcomes are assessed.

In substation earthing framework is basic not only to give the assurance of people working in the region of earthed offices and hardware's against t danger of electric stun yet to keep up proper function of electrical framework. Dependability and security are to be taken in contemplations and in addition

adherence to statutory commitments (IEEE and natural angles). Earthing framework subsequently configuration must be effectively kept up and future extension must be utilized under thought while planning the measurements of earth tangle This paper is giving earthing practices and outline for open air AC substation for control recurrence in the quantity of 50 Hz. DC substation GIS and helping impacts are not shrouded in this paper. With appropriate alert, the technique depicted here is likewise material to indoor level of such substation. By utilizing legitimate conductor and cathode s ize, earthing system might have the capacity to beat helping impacts.

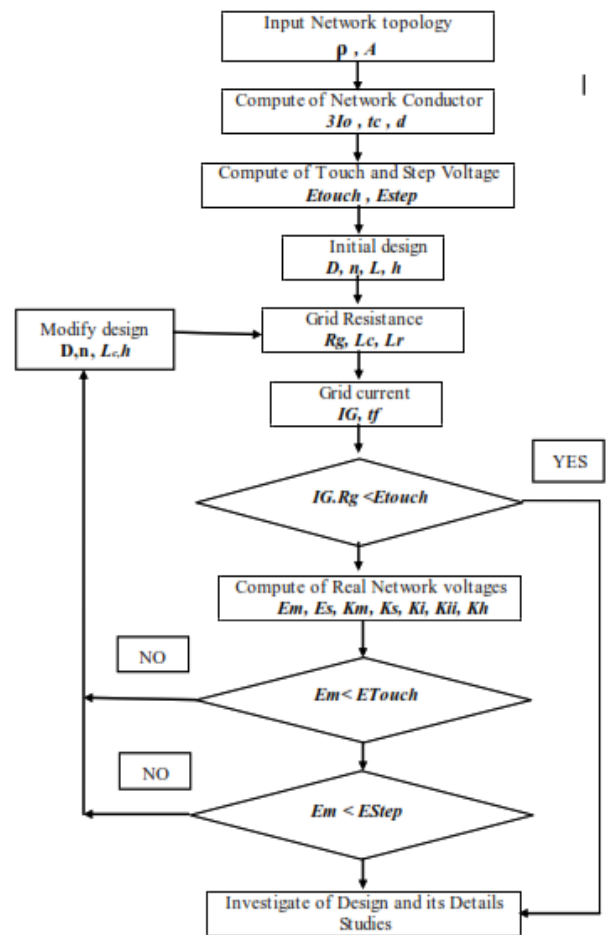
### C. Components required for enhancement earthing system

A productive substation earthing process for the most part comprises of earthing poles, interfacing lines from shrouded earthing lattice to metallic zones of structures and equipment's, contacts to earthed process neutrals, and the planet earthing surface protecting covering material quickly talked about in. Current streaming to the earthing framework from helping arrester operation wish or exchanging s empower flashover of separators and point to surface blame current from the transport or related transmission lines all reason potential varieties between earthed focuses in the substation. Without a sufficiently made earthing process, extensive potential varieties may happen between different focuses inside the substation itself. Beneath normal conditions it's the current constitutes the primary hazard to individual.

Required data for designing of enhance earthing system

- Maximum grid current
- oilresistivityat thesite
- Substationgridarea
- Resistivityofsoilitssurface
- Faultclearingtime

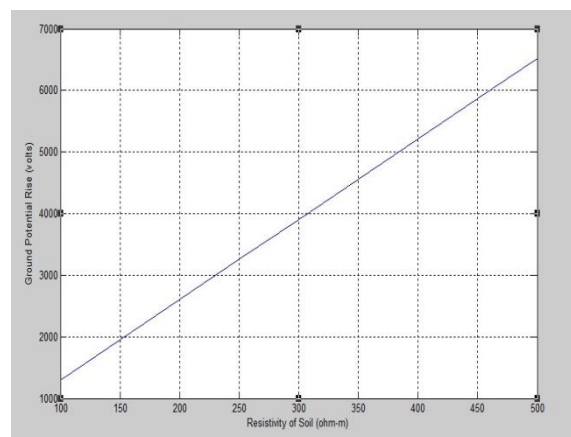
The process can be shown by the following flowchart



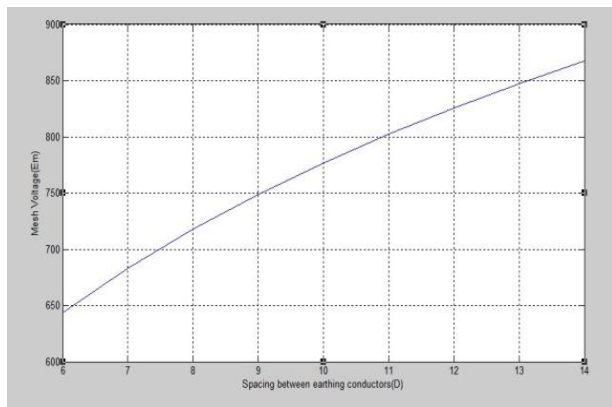
### III. RESULTS

These result are obtained by MATLAB program as given below.

#### A. Voltage and Conductor Spacing







The Fine mesh Voltage relationship with the conductor spacing implies that as we continue to raise the spacing between conductors the fine mesh voltage increases. For a set grid area and all the fixed guidelines as except grid conductor spacing, that upsurge in spacing between adjacent horizontal conductors triggers increase in fine mesh voltage but it'll lowers in step voltage. Nonetheless it can be viewed that reduction in step voltage is more than upsurge in fine mesh voltage. For set grid area, smaller the length between horizontal conductors more the amount of conductors required.

#### B. GPR and Soil Resistivity

From the safeness perspective the resistivity of the land should essentially be kept at the very least so that GPR value is looked after within the permissible limit as is shown by the results in above figure, with the upsurge in soil resistivity the worthiness of GPR boosts as the land resistivity directly influences the part of lightning current diffusing in to the earth when it moves in to the conductor and various soil resistivity will create different results. The productivity results demonstrated that combined with the increase in land resistivity all variables steadily boosts .The increase of garden soil resistivity directly leads to the increase of impulse grounding level of resistance and maximum potential surge of the grounding grid.

#### C. Analysis and Conclusion

In this paper increased earthing system for a substation is talked about, various issues associated with safe practices have been discussed. Standard mathematical formula have been used to compute different parameters associated with enhanced earthing system and several end result have been simulated by using a MATLAB program. From the results obtained from MATLAB programme we concluded that the designer must carefully take decision for conductor parting to keep real fine mesh and step voltage within tolerable limit also should take necessary agreements to keep carefully the ground resistivity within the limit so the ground potential surge is held within the limit.

#### IV. FUTURE WORK

Some important research areas of the future work related to the work mentioned in this thesis could be the following

- 1) Changing the conditions in which impulse current is being applied
- 2) Different Depths of the earthing electrodes having different diameters
- 3) Studying and designing the experiments to further investigate the earthing mechanisms and pitfalls related to the investigated methods

#### REFERENCES

- [1] AIEE Committee Report:Lightning Performance of 110- to 165-Kv Transmission Lines,"AIEE Transactions, vol. 58, pp. 249-306, 1939.
- [2] Dwarka Prasad, H.C.Sharma," Significance of Step and Touch Voltage "International Journal of Soft Computing and Engineering (IJSCE) Volume-1, Issue-5, November 2011, pp.193-197.
- [3] Towne H. M. "Impulse characteristics of driven grounds " General Electric Review, vol. 31, No. 11, pp. 605-609, 1928.
- [4] Bellaschi P. L., Armington R. E. and Snowden A. E."Impulse and 60-cycle characteristics of driven grounds-II" AIEE Transactions, vol. 61, pp. 349-363, 1942.
- [5] A. L. Vainer and V. N. Floru: "Experimental study and method of calculation of the impulse characteristics of deep earthings, Elektrichestvo", vol. 2, No. 5, pp. 18-22, 1971.
- [6] Bewley L. V.: "Theory and tests of the counterpoise "AIEE Transactions, vol. 53, No. 8, pp. 1163-1172, 1934.
- [7] Geri A. and Garbagnati E. "Non-linear behaviour of ground electrode under lightning currents: computer modelling and comparison with experimental results", IEEE Transactions on Magnetics, vol. 28,pp. 1442-1445, March 1992.
- [8] Experimental Investigation of Impulse Characteristics of Transmission Line Tower Footings N. Harid\*, H. Griffiths, N. Ullah, M. Ahmeda and A. Haddad.
- [9] Sonoda Toshio, Hidemi Takesus and Shozo Sekioka, "Measurement on surge characteristics of grounding resistance of counterpoise for impulse currents"International Conference on Lightning Protection (ICLP), September 2000.
- [10] Vanlint V. A. J. and J. W. Erler, "Electric breakdown of earth in coaxial geometry " IEEE Transactions on Nuclear science, vol. NS-29, No. 6, pp. 1891-1896, 1982.
- [11] Srisakot S., H. Griffiths and A. Haddad, "Soil ionisation modelling under fast Impulse" Proceedings of the 36th Universities Power Engineering Conference (UPEC), UK, 2001.
- [12] D. P. Snowden, G. C. Morries, Jr. and V.A.J. Van Lint: "Measurement of the dielectric constant of soil" IEEE Transmissions on Nuclear Science, vol. NS-32, No. 6, pp. 4312-4314, 1985.



# Voltage Profile and Stability Analysis for High Penetration Solar Photovoltaics

Engr. Muhammad Adil Khan, Dr. Naeem Arbab, Engr. Zainab Huma

**Abstract**—The enormous amount of energy from sun has led to a rapid growth of the use of Solar Photovoltaic power. The solar PV power can be used in stand-alone, grid connected, and hybrid configurations. Grid connected solar PV power plants are huge and are increasing rapidly because of the diminishing of conventional fossil fuels' resources for power generation. The solar PV power plants are connected to existing power system at transmission and distribution levels. This solar PV power integration is likely to have impacts on the power system. The steady state impacts of integrating solar PV power were studied on an IEEE 9 Bus test system. Impacts on voltage levels and profile, voltage drop, voltage stability, line losses and loading of the system were studied. A comparative analysis of system without solar PV power, with PV power and different levels of penetration of solar PV power was done with the aid of a power system software namely ETAP. The study revealed that the integration of solar PV power improves the voltage levels and drops and voltage stability. However, the increase in level of penetration beyond a certain point had negative impacts on the power system i.e. worsening of voltage profile, increase of losses which can also lead the system to become unstable. From this the hosting capacity (limit to which maximum power can be penetrated) of the system is determined.

**Keywords**— Solar PV Power, Power Integration, Grid Impacts, Hosting Capacity, IEEE 9 Bus System

## I. INTRODUCTION

Demand of electrical energy is increasing day by day. The depletion of fossil fuels and its high prices had motivated researches and developments in the field of Renewable Energy Systems (RES). The greater use of RES will help reduce the CO<sub>2</sub> emission, a pollutant from burning fossil fuel for energy generation. Several countries are working on electricity generation from renewable sources and have set goals in this regard to meet the ever-increasing demand of electricity.

Among sources of renewable energy, the energy from the sun is an important one. The sun is a huge ball of heat produced from the fusion reaction of hydrogen. Energy from

the sun can be utilized in two different ways; i) heat energy and ii) light energy. Electric power can be produced by exploiting the solar radiations and converting it to electrical energy. Based on how the solar energy is converted in to electrical energy, there are two types of solar power technologies. They are following:

- Concentrated Solar Power (CSP) Systems.
- Photovoltaic (PV) Solar Power Systems.

CSP is some time also known as Concentrated Solar Thermal. Utilization of solar energy by using CSP is like the conventional thermal power generating units. In this technology reflecting mirrors are used which concentrate the solar radiation at single point. This produces enormous amount of heat which can convert a fluid (mainly water) into steam and that steam turbine can be rotated for electric energy generation. By using CSP technology solar energy is indirectly utilized while in the photovoltaic (PV) technology electric energy is directly generated by utilizing solar radiations through semiconductor materials. When radiations from sun strikes the semiconductor material it converts into electrical energy by the photovoltaic property of the material. Operation of the CSP system is pretty much similar to that conventional thermal generating units and its impact on the power system is same as that of a conventional power plant (hydel and thermal). The Photovoltaic (PV) solar power system is of much interest because it operates differently from other conventional generating systems. Hence before integration of such systems in existing grid it is much needed to study the effects solar PV distribution and transmission systems of grid.

Either stand-alone or grid-tied solar PV can operate in both scenarios. At a small level, it can directly be connected to the load and the power be utilized. At a large level, it can be a solar power plant and be connected to a power grid. But in this case, it can alter the grid operating conditions either in a positive or negative way.

## II. IMPACTS OF SOLAR PHOTOVOLTAIC POWER INTEGRATION

During the last decade (2007-2017) solar PV has evolved from a niche market of small scale applications to a mainstream electricity generation source. The enormous potential of solar power and the worldwide energy demand which is calculated to increase by 41% till 2035, [1], has led to

---

Engr. Muhammad Adil Khan: University of Engineering and Technology (UET), Peshawar, Pakistan.

Dr. Muhammad Naeem Arbab: University of Engineering and Technology (UET), Peshawar, Pakistan.

Engr. Zainab Huma: University of Engineering and Technology (UET), Peshawar, Pakistan.



an increased research in the field of solar power systems and its integration to existing power system.

The sun does not shine uniformly throughout the world because of difference in latitude of places. There are several factors such as seasonal variation and cloud cover that affect the amount of sunlight hitting the earth surface. According to [2], the cloud cover affects the generated power of large scale PV power plants to a great extent. This paper states that the variation of clouds mainly impact the output of the PV power plant. To overcome this problem, special modelling of the systems is done for better operations of PV power plants with changing climatic conditions. This implies that it is very crucial to conceive the effects of climatic changes especially cloud cover while studying the impacts of solar PV power integration to a power system.

Today the world is moving towards an increased use of renewable energy sources. The generation of power from solar PVs is increasing day by day and the integration of this power to the network is a challenge for the companies managing the transmission and distribution of power. Therefore, there is a need to fully understand the impacts of integrating a solar PV power plant to the existing power system, both at transmission and distribution level. According to research findings by [3], the integration of solar PV poses a number of challenges from the system's modelling and simulation point of view.

#### A. Impacts on Voltage Stability

Voltage stability is an important parameter of a grid. It shows the ability of the grid to restore initial operating conditions after the occurrence of a fault [4]. At a feeder PV integration delivers locally active power for a unity power factor and also has capability to deliver the support of reactive power needed for less than unity power factor [5], [6]. According to [7] and [8], the steady state voltage stability of a grid improved after PV integration. These studies also suggested methods for determining the steady state voltage stability of a grid.

#### B. Impacts on Voltage Level and Profile

Researches in [7], [9] and [10] suggest that the voltage level and profile of an existing grid varies after the integration of photovoltaic power to the grid. Studies in [9] and [10] has attempted to find the impacts of distributed solar PVs on network voltages and determination and increasing of hosting capacities for photovoltaics in the distribution grids in Sweden. According to these studies, the voltage rise at buses was increased without voltage violations in two of the grids. In one of the grids studied, over voltages at some buses were experienced in the studies. Furthermore, the studies in [10] described that voltage level and profile was not the only factor to be considered in the determination the solar PV power hosting capacity. It also showed that line losses and loading should also be considered for determining the hosting capacities of grids. According to [5], [11], and [12], the voltage level and profile can show an increase because of integration of solar PV power but this increase is dependent on the configuration of the grid to which the power is integrated. Distance from the power source also has an impact on the grid. The feeders which are far from the source get lower voltage

than sending end voltage [13]. The solar PV integration improves the voltage profile along the feeders.

#### C. Impacts on Line Loading and Losses

Solar PV power has the potential to affect the two important parameters i.e. line loading and losses of a grid to which the power is integrated. Every transmission line and distribution feeder have their own capacity up to which they can be loaded. Similarly, losses in a power system can either increase or decrease the operational cost of grid [14]. Work done in [9] and [13] shows the effect of losses in a grid due to PV integration. In these studies, different levels of penetration of solar PV power were applied to grid and its impact on losses was determined. According to [9], the penetration level has a direct impact on grid losses as the losses increased with increase in level of penetration and vice versa. However, work done in [13], shows that the losses increased in grid with rise in penetration levels were attributed to the radial grid's reverse power flow. The reason is the feeder line loading increases with reverse power flow and hence the losses are increased. Also, this can disturb the protection system of the grid. Studies in [6] and [13] describe the variation in line loading with PV power integration. According to these, the increased levels of penetration reduces the line loading in a radial grid as long as no reverse flow of power occur. When reverse flow of power occurs, then with rise in penetration level, increase in line loading occurs.

To summarize, the impacts of solar PV power integration to a power system need broad research because of the speedy growth of use of this renewable energy resource. It is not necessary that the impacts of solar PV integration would be same across the world. There is a need to study and understand particular grids in different countries where there is extensive use of solar PV power and its integration to the power system [6]. The impacts of PV integration are likely to change and affect:

- Line loading, Voltage profile, voltage level and losses, voltage stability (both transient and steady state), power quality fault currents and load mismatch and generation.
- Voltage controlled devices operation, hence can affect the maintenance, life span and reliability of these equipment.
- Changes in power flow direction because of the possibility of reverse power flow which can affect the protection relays.

### III. IEEE 9-BUS SYSTEM – MODELLING IN ETAP

#### A. IEEE 9-Bus System

The IEEE 9-bus test system, which is also known as P.M Anderson 9-bus system, has been modelled in ETAP software. It represents a simple approximation of the Western System Coordinating Council (WSCC) system with 9 buses and 3 generators. Solar PV plant has been integrated into this system. The single-line diagram of the WSCC 9-bus system



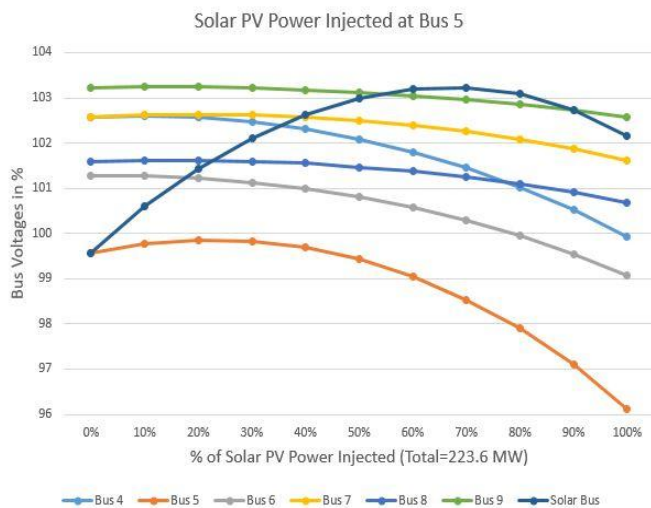


Figure 3. Bus voltages at various PV penetration levels for case 1 (@ Bus-5)

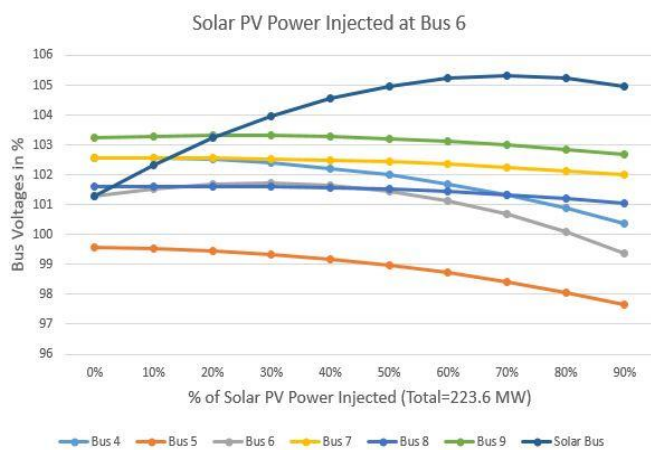


Figure 4. Bus voltages at various PV penetration levels for case 1 (@ Bus-6)

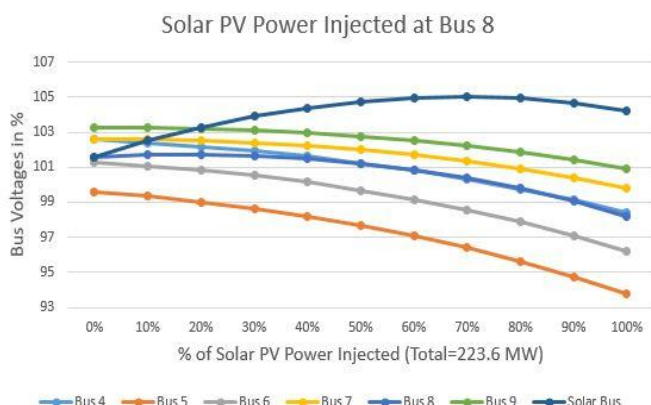


FIG. 5. Bus voltages at various PV penetration levels for case 1 (@ Bus-8)

### B. Impact on System Losses

Fig 5 and 6, shows the plots of the system's real (MW) and reactive (MVAR) power losses respectively. These plots depicts that initially the both the losses (real and reactive)

decreased till a point and started increasing for higher penetration levels. For case 1, the losses decreased till 20% of solar PV power penetration and after that the losses started increasing. For case 2, the losses decreased only for 10% of penetration and increased then. Case 3 i.e. penetration at Bus 8 was the worse one as the losses started increasing right from the beginning of the PV power penetration. Also, the increase in this case was drastic.

From the loss profile as discussed, it can be concluded that the best point for penetration of Solar PV power is at Bus 5.

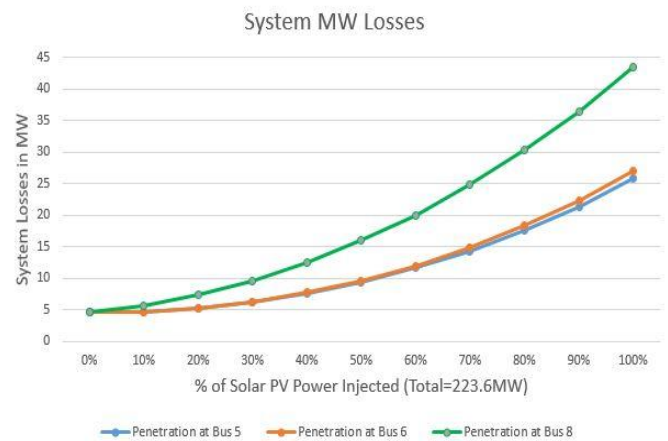


Figure 6. Plot of system losses in MW v/s solar penetration levels for injection at various bus locations

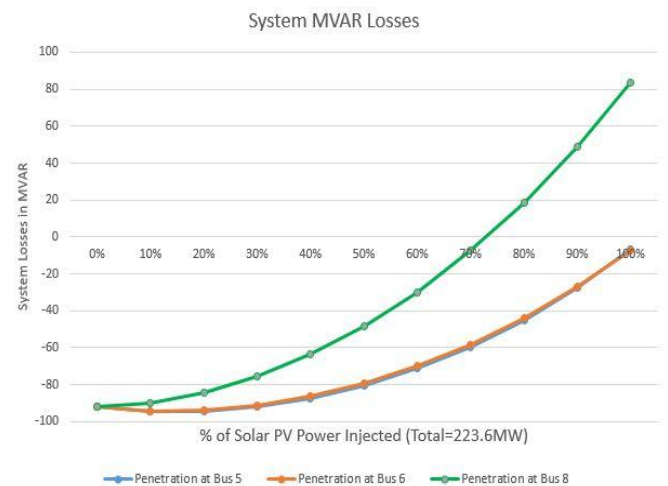


Figure 7. Plot of system losses in MVAR v/s solar penetration levels for injection at various bus locations

### C. Impact on Transmisison Lines Voltage Drop and Power Flow

Fig 8, 9, and 10, shows the plots of %voltage drop, real (MW) power flow and reactive (MVAR) power flow in lines respectively. The plots shows that variations in %voltage drops in lines are mixed. Some lines' (line 1, 5 and 6) %voltage drop decreased initially for certain levels of penetration and voltage drop increased for higher levels of penetration. The variations in voltage drops of these lines were observed to be very slight. Whereas in some lines (lines 2, 3 and 4) the trend was same as

that of other line but the variation observed in these lines was more.

The variations in line loading are also mixed. Lines 3 and 5 experienced an increase in real (MW) power flow with the increase of more PV power whereas lines 1, 4 and 6 experienced a decrease in real (MW) power flow. In line 2, initially, the real (MW) power flow decreased but after some levels of penetration the real (MW) power flow in line 2 increased drastically. Similarly for reactive (MVAR) power flow, the lines showed a different trend. Lines 2, 3 and 4 experienced sign changes for reactive power flow causing the power reversal beyond a certain point.

Hence, it is concluded from the discussion that while integrating a solar PV power plant to a power system, it is very important to consider its impacts on the loading of the transmission lines.

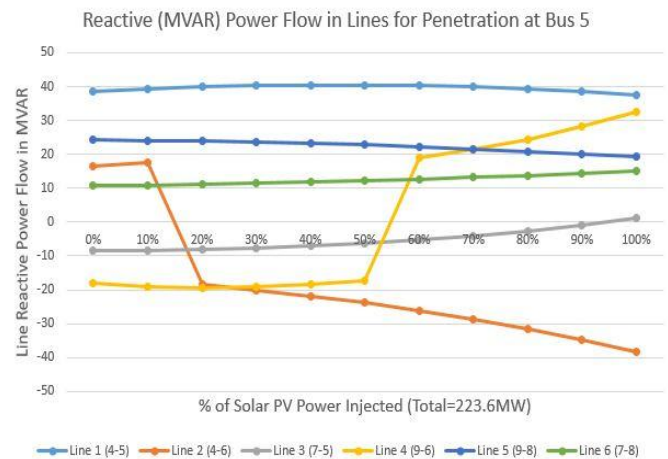


Figure 10. Plot of reactive power flow in transmission lines at various solar penetration levels

#### D. Summary of Steady State Analyses

Table 1 presents the summary of the overall analyses of the IEEE 9 Bus system while integrating a Solar PV power plant to this system. Integrating solar PV power can bring changes in the steady state bus voltages of the system which can affect the voltage stability of the system. The solar PV power integration can also bring variations in others system parameters like steady state real and reactive power flow in the transmission lines and can also affect system losses. Thus it is necessary to perform such studies which will help engineers in planning systems with high penetration levels of solar PV power and in identifying optimal hosting capacities of the system.

Table 1. Summary of Steady State Analyses

Case	Best Location	Maximum Possible Solar PV Power Penetration
Based on Bus Voltage Levels	Bus 5	30% (67MW)
Based on System Losses	Bus 5	20% (45MW)

#### V. CONCLUSION

The solar power industry is growing at an exponential rate. Pakistan's policies and regulatory framework is promoting the renewable energy like never before especially solar PV. Hence the penetration of solar photovoltaics in to Pakistan's power system is set to increase and large scale plants are coming up. It is at this outset that this analysis has been done. The drawbacks of high penetration solar photovoltaics into the power system have been identified. The increased penetration of solar PV into the grid without any specialized controls has been proved to affect both the steady state performance and the transient stability of the grid. The steady state voltages are affected adversely with the location and the level of penetration. The impact on the system loss and slack bus power

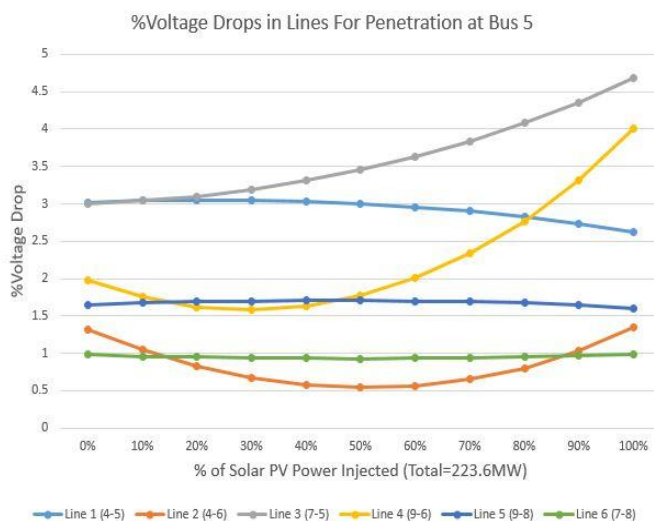


Figure 8. Plot of % Voltage drops in transmission lines vs solar penetration levels for penetration at Bus 5

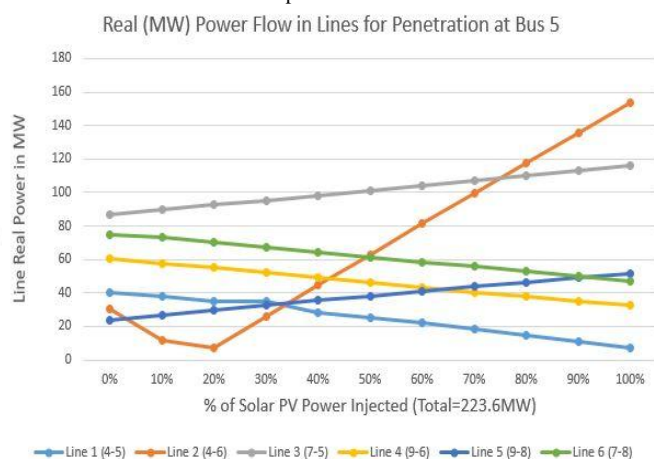


Figure 9. Plot of real power flow in transmission lines at various solar penetration levels



have also been studied. Several cases have been discussed and appropriate location and maximum possible level of penetration for the system under consideration is identified. Thus suitable control mechanisms are required from the upcoming large solar plants to address such issues and to mitigate the stability issues arising out of increased solar PV penetration.

#### REFERENCES

- [1] OGI Editors, BP-statistical review of world energy 2014 63rd Edition BP, London, 2014
- [2] Perez R., Kivalov S., Schlemmer J., Hemker K., Hoff T.E., 2012. Short-term irradiance variability: Preliminary estimation of station pair correlation as a function of distance. *Solar energy*, 2170-2176.
- [3] Joakim Waiden, Ewa Wackelguard, Jukka Pateero and Peter Lond (December 2010) Impacts of distributed PVs on network voltages: Case study of 3 low voltage distribution grids in Sweden.
- [4] Prabha Khundhar (1994), *Power System Stability and Control*, McGraw-Hill, Inc.
- [5] Etherden, N. and Bollen, M. H. (2011), Increasing the hosting capacity of distribution networks by curtailment of renewable energy resources. *IEEE Trondheim PowerTech*.
- [6] Rakebuzzaman Sahaha, N. Mithualananthana, C. R. Bunsulb, V. K. Ramchandara murthy, A review of key power system stability challenges for large scale PV integration, January 2015.
- [7] Fareed Katiraei and Jullio Romiro Agüero (2011), Solar Photovoltaic Integration Challenges, *IEEE Power and Energy Magazine*, vol. 8, no. 2, pages 61 - 70.
- [8] F. Katiraei and J. R. Agüero, "Solar PV Integration Challenges," *IEEE Power & Energy Magazine*, pp. 62-71, May/June 2011.
- [9] H. Lee Willis (2004), *Power Distribution Planning Reference Book 2nd Edition*, Raleigh, North Carolina: CRC Press.
- [10] Math Bollen and Fainan Hassan, *Integration of Distributed Generation in the Power System*.
- [11] R. Tonkoski, D. Turcott, and T. El-Fouly, "Impact of high PV penetration on voltage profiles in residential neighborhoods," *IEEE Trans. Sustainable Energy*, vol. 3, no. 3, pp. 518- 527, Jul, 2012.
- [12] Hadi Saadat (2002) *Power System Analysis*, Published by McGraw-Hill Primis Custom Publishing, Boston, MA.
- [13] C. Rodriguez and A. J. Amaratunga, "Dynamic stability of grid-connected photovoltaic systems", *IEEE Power and Energy Society General Meeting* 2004.
- [14] Heinrich. Habelin (2012), *Photovoltaics System Design and Practice*, Hoboken: John Wiley & Sons.



**Muhammad Adil Khan** graduated from University of Engineering and Technology (UET), Peshawar, Pakistan in 2013. He holds B.Sc degree in Electrical Engineering. Currently, he is enrolled in M.Sc Electrical Energy System Engineering at U.S. Pakistan Center for Advanced Studies in Energy (USPCAS-E), UET Peshawar. His major field of studies is Electrical Power Engineering. He worked as Trainee Engineer at several hydel power station in Khyber Pakhtunkhwa province of Pakistan, including the largest, Tarbela Power Station, hydel power stations of Pakistan. He can be reached at [adilusafzai@gmail.com](mailto:adilusafzai@gmail.com).

**Dr. Muhammad Naeem Arbab**, is the seniormost Professor at the Department of Electrical and Electronics Engineering, UET Peshawar. He got his Ph.D. from University of Manchester, UK and has teaching experience ranging over more than 30 years. He has authored two books of High Voltage Engineering and Electrical

Power Generation. He has also published more than 25 research papers.

**Zainab Huma** graduated from Univeristy of Engineering and Technology (UET), Peshawar in 2015. She holds B.Sc degree in Electrical Engineering. Currently, she is enrolled in M.Sc Electrical Energy System Engineering at U.S. Pakistan Center for Advanced Studies in Energy, UET Peshawar. She has visited Arizona State Univeristy, USA as a Research Scholar during an exchange program of USPCAS-E funded by USAID. Email: [zainab.huma@outlook.com](mailto:zainab.huma@outlook.com).



# Design and Implementation of MPPT for a PV System using Variance Inductance Method

Engr Zainab Huma, Dr Abdul Basit

**Abstract**—Earth receives huge amount of solar energy which is thousands times more than the world's yearly demand. Solar energy is very cheap reliable and pollution free source of energy. Solar energy is converted into electrical energy with the help of solar panels made of solar cells. Various methods have been developed to extract maximum power from these solar panels. Those methods are conventional and they lose huge amount of solar energy causing failure in extracting maximum power. This paper presents very efficient method to extract maximum possible power which a solar panel may deliver. Here MPPT charge controllers are used instead of conventional charge controllers which always keep on tracking maximum possible power. This paper involves designing and implementing Maximum Power Point Tracking System for a Solar Photovoltaic Panel (150 Watt). The efficiency of solar cells is low in general. So the impact of being able to extract maximum possible power out of the PV System is huge. The technique used in this paper to track maximum power point is Variance Inductance Method. This technique compares the actual value of  $\Delta P/\Delta V$  in the circuit with zero on regular intervals to generate a PWM Signal using a microcontroller. This PWM signal then dictates the switching frequency of a buck regulator connected to the solar panel and the load/batteries. Through this switching the values of V and P in the circuit are maintained such that maximum power keeps on getting transferred. This technique is designed and implemented in proteus and output is observed.

**Keywords**— Maximum Power Point Tracking (MPPT), Variance Inductance, Solar Photovoltaic (PV), Efficiency, Pulse Width Modulation (PWM)

## I. INTRODUCTION

Now-a-days, power is being generated using hydro or thermal power plants which use fossil fuels like coal, oil and gas. The ever-increasing depletion of fossil fuels and risk of

climate changes and environmental crisis are a major source of concern for most of the developing countries. Due to this, the modern world is inclining towards the usage of renewable energy sources to produce electricity among which wind and solar are the emerging renewable sources. Renewable energy comes from a source which does not get depleted with usage and time. In our country Pakistan, the energy crisis is severe so solar energy would present itself as a worthy replacement of non-renewable energy resources.

## II. PHOTOVOLTAIC SYSTEM

### A. Solar Energy

Solar energy has found vast use in modern times. Its use is now ever increasing given the long life of solar panels and very low maintenance cost after installation. With recent development in technologies, the efficiency of the solar cells used in panels is increasing. An advantage of using the solar energy is that it can be used to produce electricity and power applications on small to medium scale. Ease of transportation and easy installations (from rooftops to mini-grids) of solar are some added advantages. Low maintenance and longer life of the equipment are also some attractive features. The major disadvantage of using solar or wind energy is the high cost of installations and use of expensive energy-storing technologies. Solar can also be used to provide energy to the areas that still have no access to electricity and it is costly and difficult to connect them to the national grid. It would be a good and feasible solution till the transmission lines are extended to those areas. The use of solar is slowly growing with the increase in general awareness of people about the advantages of renewable energy. Solar panels are being used to generate electricity on very small scales to run solar water heaters, solar lamps, fans, solar pumps etc.

Sun light is a form of energy. This solar energy can be captured and converted into other forms of energies for example electrical energy (to meet our energy demands). Photovoltaic (PV) is the method of converting solar energy into electricity. This is based on photovoltaic effect. The photovoltaic effect is a physical and chemical phenomenon in which voltage or electrical current is produced once a material is exposed to sunlight. The emergence of photovoltaic as possible energy sources came in 1958 yet it was 1980 when they began to commercialize on the basis of high efficiencies and lower costs. Photovoltaic cells are

Engr. Zainab Huma: U.S. Pakistan Center for Advanced Studies in Energy (US PCAS-E) of the University of Engineering & Technology (UET) Peshawar, Pakistan.

Dr. Abdul Basit: U.S. Pakistan Center for Advanced Studies in Energy (US PCAS-E) of the University of Engineering & Technology (UET) Peshawar, Pakistan.



designed that act as devices for this conversion of solar energy to electrical energy.

### B. Photovoltaic Cells

Photovoltaic cells are made up of silicon. These cells are connected in series and parallel combinations to increase the overall voltage and current respectively. A specifically designed arrangement of a number of PV cells forms a PV Module. An orderly grouping of PV Modules forms a PV Array.

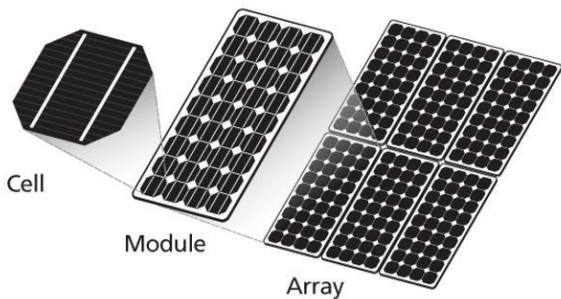


Figure 1. PV cells, modules and Array

### C. Equivalent Circuit

A PV cell can be represented by an equivalent circuit comprising of a current source, a diode in parallel, a shunt resistance and a series resistance.

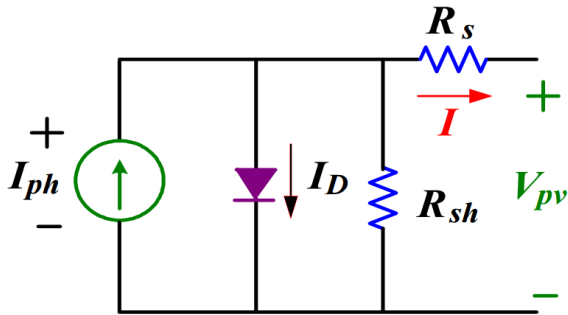


Figure 2. Equivalent circuit of PV Cell

Where,

$I_{ph} = I_{sc}$  is the short circuit current of the PV cell  
Ideally its magnitude is dependent upon the solar irradiation.  
 $I_D$  is the diode current  
 $R_s$  is the series resistance  
 $R_{sh}$  is the shunt resistance  
 $V_{pv}$  is the voltage obtained across the panel

### D. Power & I-V Curves

A graph between terminal voltage and power produced by a solar module is called a PV curve. A graph between terminal current and terminal voltage of a solar module is called an I-V curve. Although different solar panels have

different PV and I-V curves but their curve shape is very similar.

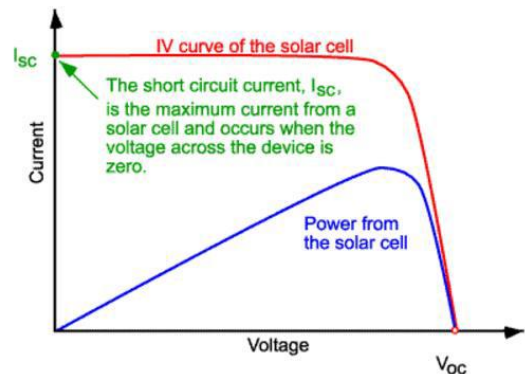


Figure 3. Power & I-V Curve of a Solar Panel

### E. Specifications of PV Module

TABLE I. PARAMETERS OF PV MODULE

Model
Open Circuit Voltage ( $V_{oc}$ )
Short Circuit Current ( $I_{sc}$ )
Optimum Operating Voltage
Optimum Operating Current
Maximum Power at STC
Standard Test Conditions

These specific parameters of PV modules are specified by the manufacturer.

### III. MAXIMUM POWER POINT (MPP)

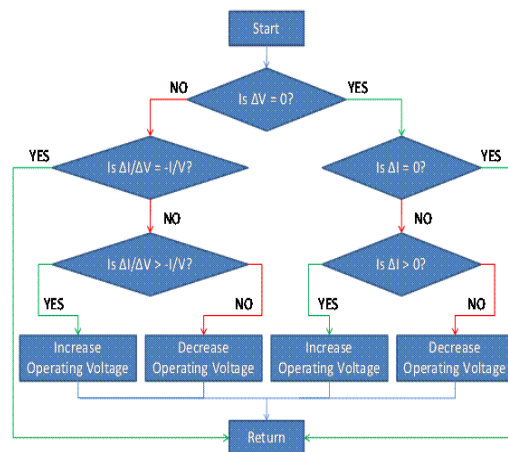
In the PV Curve shown previously, there is observation that the graph has a peak in it. This is the operating point where the solar cell provides maximum power output. The PV module possesses maximum efficiency at this point. It is usually at the knee of I-V curve of a PV panel.

A typical I-V curve with indication of MPP is shown in Figure 4. According to the theory of MPP, Maximum Power Point is the operating point at which:

- Power transfer is maximum
- Output Impedance is equal to input impedance (Maximum Power Transfer Theorem)
- Derivative of Input Power with respect to Input Voltage is zero ( $\frac{\Delta P}{\Delta V} = 0$ )

- 
- The graph shows the relationship between Current (A) and Power (W) versus Voltage (V) for a solar cell. The blue curve represents the Current vs. voltage, starting at the short-circuit current  $I_{sc}$  and ending at the open-circuit voltage  $V_{oc}$ . The orange curve represents the Power vs. voltage, starting at zero, reaching a maximum at the maximum power point (marked with a blue dot at  $V_{mp}$  and  $P_{mp}$ ), and returning to zero at  $V_{oc}$ . The maximum power point is also marked with an orange dot on the current curve at  $V_{mp}$  and  $I_{mp}$ .

Perturb-and-Observe method because it can sense rapid changes. An equation for this method and flow chart is shown Figure 6.



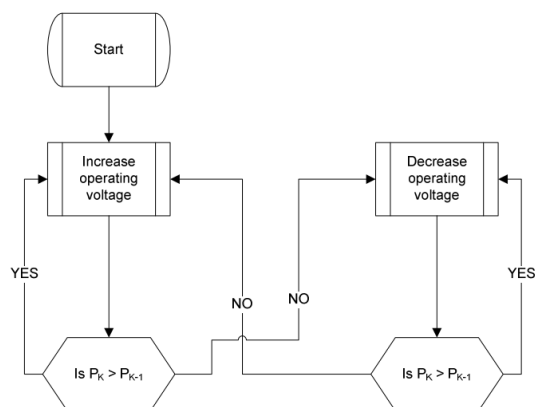
#### IV. DIFFERENT TECHNIQUES OF MPPT

$$\frac{dP_{pv}}{dV_{pv}} = I_{pv} \frac{dV_{pv}}{dV_{pv}} + V_{pv} \frac{dI_{pv}}{dV_{pv}} = I_{pv} + V_{pv} \frac{dI_{pv}}{dV_{pv}} = 0$$

$$\frac{dI}{dV} = -\frac{I}{V}$$

### C. Pilot Cell Method

Open circuit voltage and short circuit current of solar cell are measured and it is assumed that voltage is directly proportional to MPP voltage. It is also assumed that cell exhibits characteristics similar to I-V curve of solar cell model. Hence one cell is modeled and rest of array is calibrated accordingly.



#### D. Variance Inductance Method

This method is an upgraded version of Perturb-and-Observe method. In this method  $\Delta P/\Delta V$  is calculated. This method is better than Perturb and Observe because it involves large number of samples.  $\Delta P/\Delta V$  magnitude and sign is considered. A PWM is generated and a MOSFET is used as switch in Buck converter for variation in duty cycle. The sign of this rate of change of power with respect to voltage, whether positive or negative, dictate the increase or decrease of duty cycle whereas the magnitude of this rate of change determines how much duty cycle will have to vary. A block diagram of the system is shown in the Figure 7. MPPT algorithm is stored inside a microcontroller ATMEGA328 on an “Arduino Platform” which is used because of its good frequency response. The result provided by microcontroller is PWM whose duty cycle is being varied consistently. This duty cycle is provided to MOSFET in Buck Converter which ensures tracking of MPP.

In this method, the derivative of power with respect to voltage is taken into account indirectly.  $\Delta P/\Delta V$  has to be zero for method to work properly. The direction of change is determined and actual MPP is tracked. It is better than

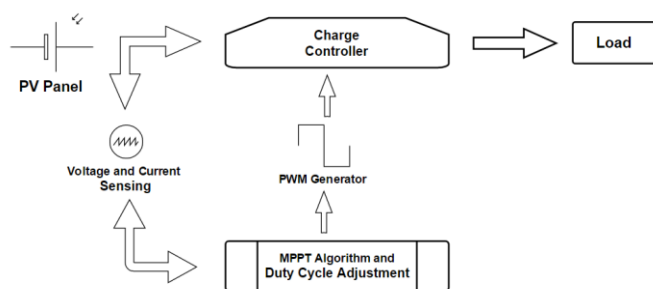


Figure 7. Variance Inductance Method

## V. MICROCONTROLLER – ARDUINO UNO PLATFORM

Arduino platform allows us easy and fast prototyping. Arduino has many printed circuit boards and the one used in this project is Arduino Uno. The board consists of ATMEGA328P microcontroller from ATMEL® studios. It has 16 MHz crystal that can be programmed to generate desired Pulse Width Modulated (PWM) signals. It can be excited by DC power jack or via USB cable. There are female headers with pin numbers displayed alongside them so connections can be made using connecting wires. The LCDs can be used conveniently to display the desired quantities. Moreover, the programming of Arduino is easy to understand as it is in C language. Hundreds of coding libraries can come in handy if any circuit is to be tested.

## VI. DESIGN & SIMULATION

### A. Specifications of Solar Panel

The specifications of the solar panel used in this project are given in the table.

TABLE II. SPECIFICATIONS OF SOLAR PANEL

Model	Solar Land SLP150-12
Open Circuit Voltage ( $V_{OC}$ )	21.6V
Short Circuit Current ( $I_{SC}$ )	9.7A
Optimum Operating Voltage	17.2V
Optimum Operating Current	8.72A
Maximum Power at STC	150W
Standard Test Conditions	1000 $w/m^2$ Air to Mass ratio =1.5at 25°C

### B. Output Requirements

The output requirements are given in the table

TABLE III. OUTPUT PARAMETERS

Output Voltage ( $V_{out}$ )	12V
------------------------------	-----

Maximum Output Current ( $I_o(max)$ )	$I_{sc} = 9.7A$
Output Current Ripple Percentage	30% of $I_o(max)$
Output Voltage Ripple Percentage	2% of $V_{out}$
Output Load Nature	Purely Resistive
Output Load value	4.61 Ohm

### C. Simulation

For simulation purposes MATLAB and Proteus are selected. The choice of simulation software is based on the fact that MATLAB and Proteus both have a user friendly interface. However MATLAB does not have Arduino block. This is where Proteus is used. Proteus software tool is the best Arduino simulator. Another advantage of using Proteus over other simulation environments is that it is fast, reliable and flexible.

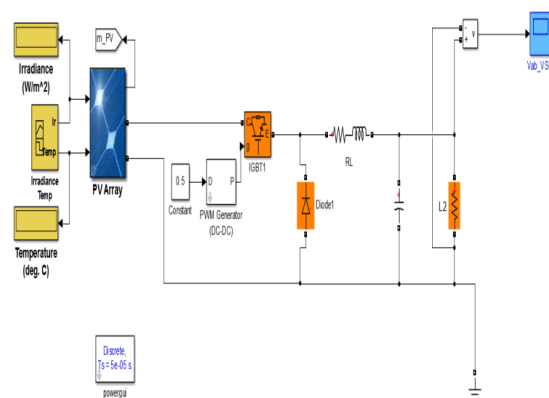


Figure 8. Schematic Circuit Diagram for using MPPT

### D. Overall Project Simulation

The circuit diagram used for the general simulation of this project in SIMULINK and Current, Voltage and Power graphs for the simulation with respect to time are in the figures 9-11

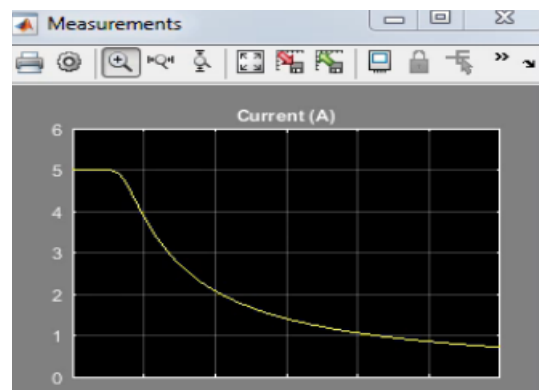


Figure 9. Current Characteristics

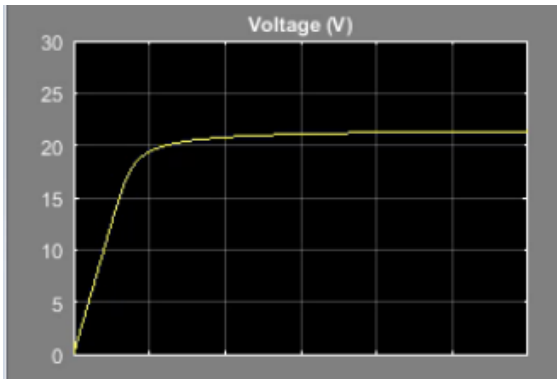


Figure 10. Voltage Characteristics

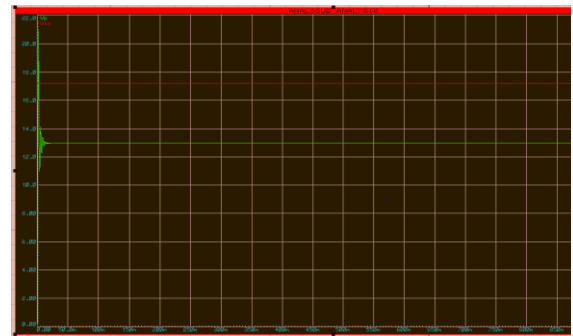


Figure 13. Input and Output Voltage

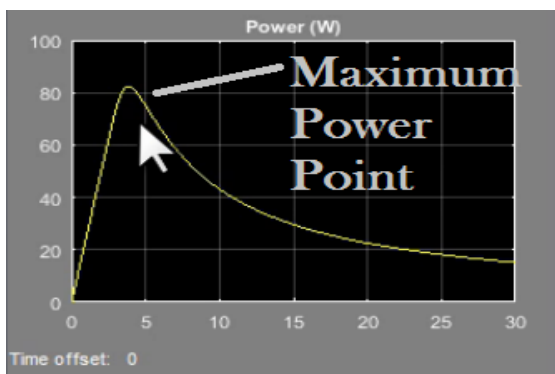


Figure 11. Power Output Characteristics

### E. Buck converter simulation

The following circuit is implemented in Proteus. The values of the components are according to the calculations.

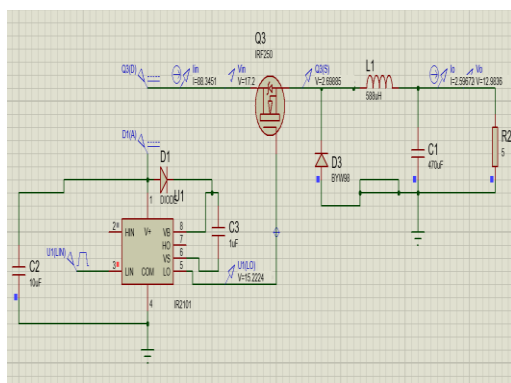


Figure 12. Buck Converter Simulation

#### a. Results:

The red line shown in the figure is input voltage which is 17.2V and the green line showing is output voltage which comes out to be 12.9V. The desired value for the output voltage is 12-13V. The result of the simulation is 12.9V which lie within the required range.

## VII. PROTEUS TESTING OF THE CODE

The Arduino is programmed and the code is developed for implementation of MPPT. The developed code was tried and tested in Proteus 8. The results obtained are shown in the figure. The current sensor IC block is also employed here to check for results. An LCD is interfaced to show results of Power, Voltage and Current on the screen.

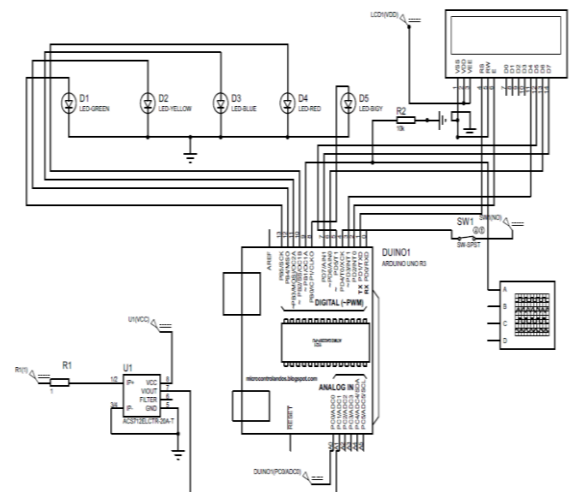


Figure 14. Proteus simulation circuit for MPPT code

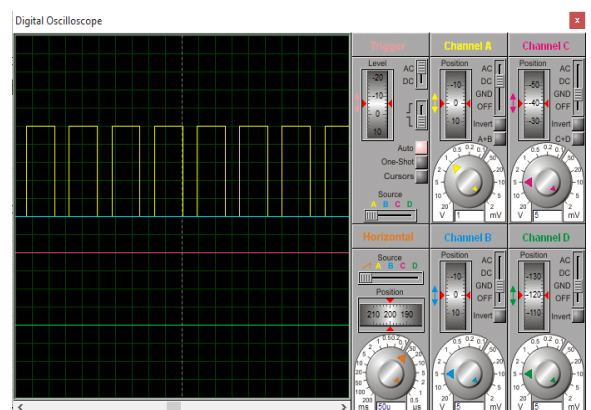


Figure 15. PWM Signal

The main objective is to calculate  $\Delta P / \Delta V$  which is achieved and an increment according to this value is added or subtracted from previous value of duty cycle to calculate new duty cycle. For MPPT to occur,  $\Delta P / \Delta V = 0$ . If this calculated value is greater than 0, we subtract the increment to get it back at 0 and vice versa.

#### CONCLUSION

The several different methods have different algorithms which can be traded for complexity and computational cost. Efficiency and reliability are two features which are extremely important for us to work with. Out of these methods, we have designed and implemented MPPT via variance inductance method. After a series of tests we have come to conclude that the efficiency of the solar panels is very low so there is a need for MPP tracking to harness the maximum available power. To obtain the maximum power, the panel has to be operated at the MPP which was controlled by the duty cycle of the varying PWM generated by the microcontroller. The Variance Inductance method is an upgraded form of Perturb and Observe method and a better methodology to track and obtain the maximum power.

#### REFERENCES

- [1] U. o. C. Scientists, "Union of Concerned Scientists," [Online]. Available: [http://www.ucsusa.org/clean\\_energy/our-energy-choices/renewable-energy/public-benefits-of-renewable.html#.VzrfFZF97IU](http://www.ucsusa.org/clean_energy/our-energy-choices/renewable-energy/public-benefits-of-renewable.html#.VzrfFZF97IU).
- [2] K. Erickson, "NASA," [Online]. Available: <http://science.nasa.gov/science-news/science-at-nasa/2002/solarcells/>.
- [3] "Energy Informative," [Online]. Available: <http://energyinformative.org/best-solar-panel-monocrystalline-polycrystalline-thin-film/>.
- [4] G. R. Energy, [Online]. Available: [http://www.greenrhinoenergy.com/solar/technologies/pv\\_electronics.php](http://www.greenrhinoenergy.com/solar/technologies/pv_electronics.php).
- [5] Academia, "Academia," [Online]. Available: [http://www.academia.edu/4723214/A\\_Comparative\\_Study\\_on\\_Maximum\\_Power\\_Point\\_Tracking\\_Techniques\\_for\\_Photovoltaic\\_Power\\_Systems](http://www.academia.edu/4723214/A_Comparative_Study_on_Maximum_Power_Point_Tracking_Techniques_for_Photovoltaic_Power_Systems).
- [6] M. H. Rashid, "Google Books," 2015. [Online]. Available: [https://books.google.com.pk/books/about/Power\\_Electronics.html?id=-WqvjxMXCIAC](https://books.google.com.pk/books/about/Power_Electronics.html?id=-WqvjxMXCIAC).
- [7] S. Smith, "Academia," [Online]. Available: [http://www.academia.edu/4016409/Microelectronic\\_Circuits\\_by\\_S\\_Smith\\_5th\\_edition](http://www.academia.edu/4016409/Microelectronic_Circuits_by_S_Smith_5th_edition).
- [8] "Arduino," [Online]. Available: <https://www.arduino.cc/en/Main/ArduinoBoardUno>.
- [9] "Henry's Bench," [Online]. Available: <http://henrysbench.capnfatz.com/henrys-bench/arduino-voltage-measurements/arduino-25v-voltage-sensor-module-user-manual/>.
- [10] "Instructables," [Online]. Available: <http://www.instructables.com/id/How-to-Measure-AC-Current-using-Hall-Effect-Sensor/>.



**Engr Zainab Huma** received her Bachelor's degree in Electrical Engineering from University of Engineering and Technology (UET) Peshawar, Pakistan in 2015. She is currently doing her Masters of Science in Electrical Energy Systems Engineering from U.S Pakistan Center for Advanced Studies in Energy (U.S PCAS-E), UET Peshawar. She has also been a research scholar at Arizona State University (ASU), USA. Her area of interest includes solar renewable energy and rechargeable Li-ion batteries.

**Dr Abdul Basit** completed his Bachelor's degree in Electrical Engineering from University of Engineering & Technology (UET) Peshawar, Pakistan in 2006. He received his M.Sc. degree in Electrical Engineering from Chalmers University of Technology, Sweden in 2011 and his PhD from the Department of Wind Energy of the Technical University of Denmark (DTU) in 2015. He is currently working as Assistant Professor at U.S. Pakistan Center for Advanced Studies in Energy (US PCAS-E) of the University of Engineering & Technology (UET) Peshawar, Pakistan.



# A Review on Properties Amelioration of Wearable Antennas

Abid Ahmad, Muhammad Farooq, Gulzar Ahmad, Muhammad Amir, Arbab Masood

**Abstract**—The emergence of Body Area Networks (BAN) in recent times has increased the interest of most researchers in the field of wearable antennas. Due to its widespread popularity most of the research has been done to improve the efficiency and flexibility of the wearable antennas for in-body and on-body applications. This work is the review of the recent development in the area of wearable antennas. Further the use of different textile materials has been studied and their performance has been compared with the ordinary used substrate such as FR-4 for wearable antennas. The results show that use of textile materials have not only increased the efficiency but also they are very flexible and make the antenna suitable for in-body and on-body applications such as medical and military. The properties of antennas inside human body, on human body and finally at some distance from the human body have been studied. It has been noted that as the distance between human body and antenna reduces the properties of antenna such as efficiency, directivity and gain degrade more and more. Also the resonant frequency of antenna shifts from its original position which is a very big issue and need to be rectified. For textile materials the shift in resonant frequency is not too much and also the degradation in other properties of antenna such as efficiency, directivity and gain are insignificant.

**Keywords**— Body Area Network (BAN), Computer Simulation Technology (CST), In-body, On-body, EBG, Textile materials.

## I. INTRODUCTION

This Antenna is an important part of wireless communication; in fact no wireless communication is possible without an antenna [1]. We have to install antennas at both ends i.e. at transmitter side as well as at receiver side as shown in Fig. 1. Transmitter generates the signal and antenna converts this signal into electromagnetic wave and radiates this Electromagnetic wave into air as mentioned in Fig. 1. The antenna which is installed at receiver side will receive this electromagnetic wave and will feed it to the receiver. So antenna can be defined as A device which is used for transmitting and receiving radio waves [2], [3]. The emergence of Body Area Networks (BAN) in recent times has increased the interest of most of the researchers in the field of wearable antennas. Due to its widespread popularity most of the research has been done to improve the efficiency and flexibility of the wearable antennas for in-body and on-body applications. Wearable Antennas are those antennas which operate near the human body, so human body will absorb some of the radiated energy and hence efficiency of antenna will reduce [4]–[7].

The wearable antennas installed on human body may communicate with each other or with an external antenna. This type of network is known as Body Area Network (BAN) [8]. The antennas used in BAN are known as wearable antennas. Fig. 2 shows different examples of wearable antennas.

In-body antennas are those which are inserted inside human body and it is mostly used for medical purpose [9], whereas On-body antennas are those which are installed on the top of human body as shown in Fig. 2. The emergence of BAN shows that in near future almost everyone will be a part of this network, so wearable antenna should be carefully designed in order to achieve all the required properties of antenna even to be in the vicinity of human body or inside the human body. follow.

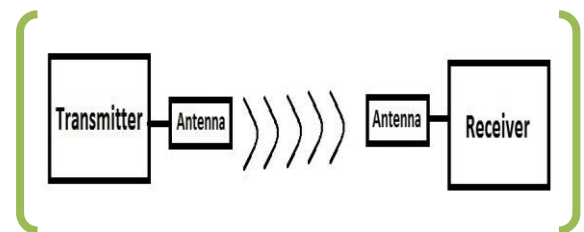


Figure.1



Figure 2.

## II. LITERATURE REVIEW

In [10] a monopole antenna is presented which is basically printed on substrate called Neoprene as shown in fig: 3. this antenna is a dual band antenna covering two bands at the same time. The S-Parameter is obtained both in free spaces as well as



Figure 1 consists of two diagrams, (a) and (b), showing the dimensions of the antenna and ground plane. Diagram (a) is a side view of the antenna, showing a monopole structure with a 50ohm microstrip feed line. The dimensions are: 2.5mm (top width), 1.7mm (top width), 1mm (top width), 36mm (height), 2.8mm (base width), and 50ohm microstrip feed line. Diagram (b) is a top view of the ground plane, showing a rectangular structure with a 2mm wide wing. The dimensions are: 73mm (height), 40mm (width), 1mm (height), 2mm (width), and 38mm (width). Labels include Neoprene, Monopole, Wing, and Ground Plane.




Figure 1 consists of two panels, (a) and (b), enclosed in large green square brackets. Panel (a) is a schematic diagram showing a square sample with a central hole, a blue square frame, and a grid background. Panel (b) is a photograph of the experimental setup, showing a square sample with a central hole, a blue square frame, and a grid background.



---

International Journal of Engineering Works  
ISSN: 2409-2770

---

Vol. 5, Issue 5, PP. 111-115, May 2018

extended the patch due to which return loss is reduced and efficiency has improved. Fig. 9 shows the S-Parameter for 3mm extension in patch. In [17] an E-shaped antenna is proposed as shown and they have used both transmission line feeding as well as coaxial feeding. Three different textile materials have been used as substrate for the antenna. The S-Parameter graphs has shown in Fig. 10. Different measured parameters and their comparison are shown in Table 1. The [18] refer to a wearable antenna for the smart clothing applications which is far better than other conventional antenna in term of radiation efficiency [19]. The failure of radio link occurs due to closeness of human body is problem and is specially addressed by [18]. A conventional fleece fabric is used as substrate of patch antenna whose dielectric constant can be found by the method of cavity perturbation while for the improvement of flexibility the knitted copper is used to design ground plane radiating element as well which improved the bandwidth also. A wearable antenna also contributes in Health Gear Systems doing real time monitoring, collecting data and analyzing the system [20]. Fig. 11 shows the block diagram of health gear system.

Textile materials	Band width (MHz)	Directivity (dBi)	Radiation efficiency (dB)	Gain (dBi)	Impedance bandwidth (%)
Fleece	45.6	8.4	-0.811	7.59	19
Denim	58.6	7.44	-5.74	1.66	25
Velcro	52.1	7.95	-1.39	6.56	22
Fleece (Coaxial probe feed)	84.64	9.12	-0.1375	8.98	36

Table.1

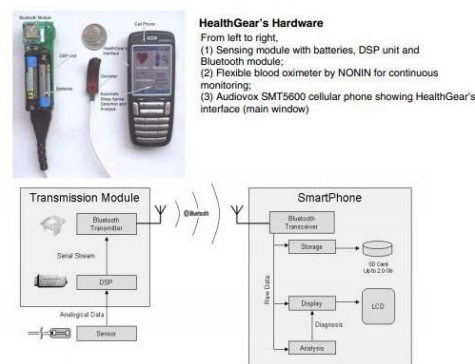


Figure. 11

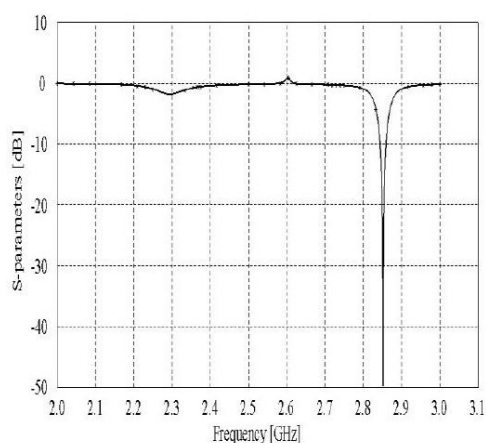


Figure. 9

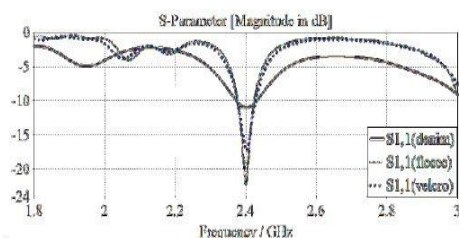


Figure. 10

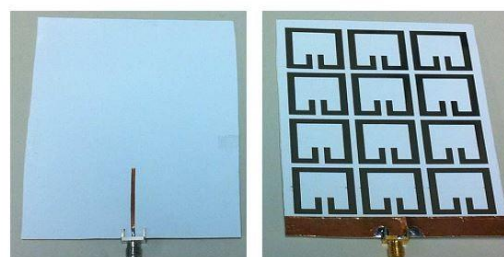


Figure. 12

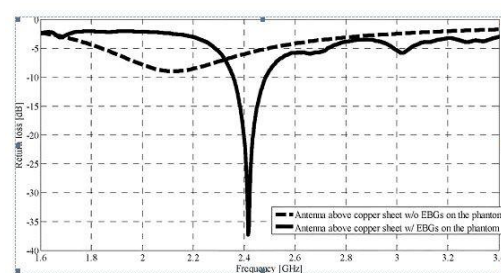


Figure. 13

When the service starts, the client is physiological sensing modules connected to the Media Access Control (MAC) address of the cell phone, number of clients can be accepted by mobile phone from different sensing modules. Its result shows that the health gear system is 100% comfortable and pleasurable in [21] a specific combination of wearable antenna and Electromagnetic Band Gap (EBG) structure is integrated to overcome the losses due to human body. System efficiency has improved by utilization of wearable monopole antenna at Industrial, Scientific & Medical Radio (ISM) band with EBG structure. The closeness to human body reduces the gain of antenna which almost leads to failure of link. The body absorb electromagnetic radiations which also causes some biological effects [22]– [25]. So, all such problems have been avoided by using a specific combination of antenna and EBG structure for safe environment. The Fig 12 and 13 shows the design and result of S-Plot respectively.

The proximity of human body, the overall efficiency of wearable antenna is affected i.e. power absorption, radiation distortion, change in input impedance of antenna and also the operating frequency [26], [27]. As it operates in ISM band which is directly fed by the antenna through via without having extra connecting circuitry. One of the major problems in wearable antenna is parasitic coupling which causes instabilities in circuit [28]. To overcome the effect of parasitic coupling a specific type of flexible form material is used to design an antenna with combination of Low Noise Amplifier (LNA) substrate. The effect of proximity of human body is reduced by this design. But the other aspects are also influenced their effect on the performance of wearable antenna. Such as input match performance and peak Specific Absorption Rate (SAR) value at ISM band [29]. A model to overcome the above mentioned problem a special Wireless Local Area Network (WLAN) textile wearable antenna has been designed using Finite Difference Time Domain (FDTD) method which has developed in University of California, Los Angeles (UCLA). A simple fleece fabric is used as a substrate whose dielectric constant is 1.1 at ISM band. Fabric of 8mm of thickness is used which is optimum for input-match for ISM range. In this design the knitted copper is used to design the patch and ground plane of antenna. A series of simulations have been observed and showed that impedance matching and radiation is almost unaffected by the human body. It has been derived that Printed Circuit Board (PCB) antenna can easily replace the textile antenna [29].

The [30] addressed the problem of patch antenna with low conductivity materials. The revolution of electronics and communication devices made it possible that our near future will have almost wearable devices fabricated in clothing. Wearable antenna is one of the major parts of it. As the conductivity of these material is not enough to treat as perfectly conducting materials and the aim of this research is to design such a compatible wearable antenna with low conductivity material. An antenna with such properties has been designed for all conductors being made of copper with specific dimensions. With the number of simulations the properties of wearable antenna found accordingly. That shows the performance of patch antenna with non-metallic conductors and also defined the limit least conductivity of practical

microstrip patch antenna to implement. The geometry is given in Fig. 14. Its compatibility with low conductive materials made it versatile in nature. Wearable antenna can also be used in multi- band mode [31]. Along with single band uses it has wide use in dual frequency band also which allowing network connection [32], [33]. Here a novel dual band antenna integrated with EBG structure which can be fabricated within clothing. This combination avoids the backward radiations to the maximum level as possible. The ground plane and patch of antenna is made of specific material conducting fabric Zelt.

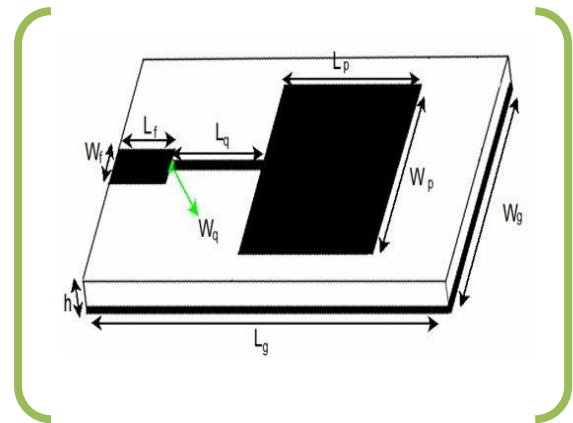


Figure. 14

### III. CONCLUSION AND FUTURE WORK

Recent research presented in these paper shows that textile materials are preferred for wearable antennas as far as efficiency and flexibility is concerned. Also in broad, microstrip patch antennas are suitable for wearing as they have a ground plan appearing in between the patch and human body. So in case of microstrip patch antennas absorption by the human body will be relatively low as compare to other types of antennas. Some more work is still needed in order to increase the range of these antennas applications to improve some parameters which are the major issues concern with wearable antenna. The most common issues the absorptions of radiation by human body due to the proximity of body so the SAR value should be reduce as much as possible and the other issue with such antenna is power consumption. So for better performance these issues should be resolve.

### REFERENCES

- [1] W. L. Stutzman & G. A. Thiele. Antenna theory and design. John Wiley & Sons, 2012.
- [2] J. Carr & G. Hippiusley. Practical Antenna Handbook 5/e. McGraw-Hill/TAB Electronics, 2011.
- [3] P. Nayeri, A. Z. Elsherbeni, & F. Yang. Radiation analysis approaches for reflect array antennas [antenna designer's notebook]. IEEE Antennas and Propagation Magazine, vol. 55, no. 1, pp. 127–134, 2013.
- [4] P. Salonen, Y. Rahmat-Samii, & M. Kivikoski. Wearable antennas in the vicinity of human body. in Antennas and Propagation Society International Symposium, 2004. IEEE, vol. 1, pp. 467–470, IEEE, 2004.
- [5] S. Zhu & R. Langley. Dual-band wearable antennas over ebg substrate. Electronics Letters, vol. 43, no. 3, pp. 141–142, 2007.
- [6] F.-X. Liu, T. Kaufmann, Z. Xu, & C. Fumeaux. Wearable applications of quarter-wave patch and half-mode cavity antennas. IEEE Antennas and Wireless Propagation Letters, vol. 14, pp. 1478–1481, 2015.

- [7] Y. Liu, A. Levitt, C. Kara, C. Sahin, G. Dion, & K. R. Dandekar. An improved design of wearable strain sensor based on knitted rfid technology. in *Antenna Measurements & Applications (CAMA)*, 2016 IEEE Conference on, pp. 1–4, IEEE, 2016.
- [8] M. Seyed, B. Kibret, D. T. Lai, & M. Faulkner. A survey on intrabody communications for body area network applications. *IEEE Transactions on Biomedical Engineering*, vol. 60, no. 8, pp. 2067–2079, 2013.
- [9] D. Wang, M. Ghosh, & D. Smith. Medical body area network (mban) with key-based control of spectrum usage. Mar. 21 2017. US Patent 9,603,024.
- [10] L. Ma, R. Edwards, S. Bashir, & M. Khattak. A wearable flexible multi-band antenna based on a square slotted printed monopole. in *Antennas and Propagation Conference, 2008. LAPC 2008*. Loughborough, pp. 345–348, IEEE, 2008.
- [11] S. Dumanli. Challenges of wearable antenna design. In *microwave conference (FuMC) 2016*, 46th European pp 1350–1352. IEEE 2016.
- [12] I. Gil & R. F. García. Wearable gps patch antenna on jeans fabric. in *Progress in Electromagnetic Research Symposium (PIERS)*, pp. 2019–2022, IEEE, 2016.
- [13] Y. Tawk, A. R. Albrecht, S. Hemmady, G. Balakrishnan, & C. G. Christodoulou. Optically pumped frequency reconfigurable antenna design. *IEEE Antennas and Wireless Propagation Letters*, vol. 9, pp. 280–283, 2010.
- [14] H. Boudaghi, M. Azarmanesh, & M. Mehranpour. A frequency-reconfigurable monopole antenna using switchable slotted ground structure. *IEEE Antennas and Wireless Propagation Letters*, vol. 11, pp. 655–658, 2012.
- [15] Y. Tawk, J. Costantine, & C. Christodoulou. A frequency reconfigurable rotatable microstrip antenna design. In *Antennas and Propagation Society International Symposium (APSURSI)*, IEEE, pp. 1–4, 2010.
- [16] A. J. Agaliya, T. M. Neebha, & M. Nesusudha. Efficient wearable antenna design by patch area extension for body area network applications. In *Communication and Signal Processing (ICCSP)*, 2016 International Conference on, pp. 2130–2134, IEEE, 2016.
- [17] M. S. Ali & K. Ali. Design and optimization of an e-shaped wearable antenna working in ism band. In *Computational Intelligence (IWCI)*, International Workshop on, pp. 26–29, IEEE, 2016.
- [18] P. Salonen & L. Hurme. A novel fabric wlan antenna for wearable applications. In *Antennas and Propagation Society International Symposium, 2003*. IEEE, vol. 2, pp. 700–703, IEEE, 2003.
- [19] K. Fujimoto & J. R. James. *Mobile antenna systems handbook*. Artech House, 2001.
- [20] N. Oliver & F. F. Mangas. Healthgear: a real-time wearable system for monitoring and analyzing physiological signals. In *Wearable and Implantable Body Sensor Networks*, 2006. BSN 2006. International Workshop on, pp. 4–pp, IEEE, 2006.
- [21] S. Kim, Y. J. Ren, H. Lee, A. Rida, S. Nikolaou, & M. M. Tentzeris. Monopole antenna with inkjet-printed ebg array on paper substrate for wearable applications. *IEEE Antennas and wireless propagation letters*, vol. 11, pp. 663–666, 2012.
- [22] H. Nakano, K. Kikkawa, N. Kondo, Y. Itsuka, & J. Yamauchi. Low-profile equiangular spiral antenna backed by an ebg reflector. *IEEE Transactions on Antennas and Propagation*, vol. 57, no. 5, pp. 1309–1318, 2009.
- [23] Y. Huang, A. De, Y. Zhang, T. Sarkar, & J. Carlo. Design of a low profile end-fire antenna using split-ring resonators. In *Antennas and Propagation Society International Symposium, IEEE*, pp. 1–4, IEEE, 2008.
- [24] Y. Liu & X. Zhao. Investigation of anisotropic negative permeability medium cover for patch antenna. *IET microwaves, antennas & propagation*, vol. 2, no. 7, pp. 737–744, 2008.
- [25] E. Y. Kim, J. H. Yoon, Y. J. Yoon, & C. G. Kim. Low profile dual-band reflector antenna with dual resonant amc. In *Antennas and Propagation (APSURSI)*, IEEE International Symposium on, pp. 1800–1803, IEEE, 2011.
- [26] F. Declercq & H. Rogier. Active integrated wearable textile antenna with optimized noise characteristics. *IEEE transactions on antennas and propagation*, vol. 58, no. 9, pp. 3050–3054, 2010.
- [27] A. Sabban. Wearable antenna measurements in vicinity of human body. *Wireless Engineering and Technology*, vol. 7, no. 03, p. 97, 2016.
- [28] B. De Mulder, H. Rogier, J. Vandewege, & D. De Zutter. Highly sensitive, cooptimised active receiver antenna: its use in doppler radar in 2.4 ghz ism band. *Electronics Letters*, vol. 39, no. 18, pp. 1299–1301, 2003.
- [29] P. J. Soh & G. A. Vandenbosch. Textile antennas for body area networks: design strategies and evaluation methods. *Electromagnetics of Body Area Networks: Antennas, Propagation, and RF Systems*, pp. 1–25, 2016.
- [30] E. Yilmaz, D. P. Kasilingam, & B. M. Notaros. Performance analysis of wearable microstrip antennas with low-conductivity materials. In *Antennas and Propagation Society International Symposium, 2008. AP-S 2008*. IEEE, pp. 1–4, IEEE, 2008.
- [31] S. Sankaralingam & B. Gupta. Development of textile antennas for body wearable applications and investigations on their performance under bent conditions. *Progress In Electromagnetics Research B*, vol. 22, pp. 53–71, 2010.
- [32] P. Salonen, Y. Rahmat-Samii, H. Hurme, & M. Kivikoski. Dual-band wearable textile antenna. In *Antennas and Propagation Society International Symposium, 2004*. IEEE, vol. 1, pp. 463–466, IEEE, 2004.
- [33] P. Salonen, J. Kim, & Y. Rahmat-Samii. Dual-band e-shaped patch wearable textile antenna. In *Antennas and propagation society international Symposium, 2005 IEEE*, vol. 1, pp. 466–469, IEEE, 2005.



**Abid Ahmad** was born in Darsamand Hangu 10th March 1992. He has done B.Sc Electrical communication Engineering, University of Engineering and Technology Peshawar, K.P.K Pakistan (2011-2015). He is enrolled in MS Electrical Electronics and Communication Engineering at UET Peshawar (2016-2018).

From 14th June 2013 to 15th Sept 2013 he was an internee engineer at Water and power development authority (WAPDA) Islamabad Pakistan. He was trainee engineer at Pakistan Telecommunication Company Limited (PTCL) from 6th July 2015 to 2nd October 2015. He was appointed as lecturer at CECOS University Peshawar KPK Pakistan from 2nd April 2016 to 2nd October 2016.. Personal hobbies should not be included in the biography.





## To Study the Effects of Heat Treatment on the Welded Joints

Engr. Mujahid, Dr. Saim Saher, Engr. Zainab Huma

**Abstract**— The present research was undertaken to demonstrate the effects of heat treatment on the welded joints. The material used was mild steel and aluminum. Ten flat tensile specimens, ten mounted specimens for micro structure test were prepared for steel and four flat tensile specimens, four mounted specimens for micro structure. This project is an effort to establish better understanding about the heat treatment of the welded joints. The scope of work includes the preparation of test specimens for tensile testing and micro structure analyses.

**Keywords**— Welding, Pre and Post welded joints, Grain size, Heat treatment, Universal testing machine, SEM, Machining.

### I. INTRODUCTION

Fabricated structures often contain a number of welded sub-assemblies and these sub-assemblies generally contain several welded joints. The welded sections may require the Heat Treatment process to enhance the material properties. For tensile testing, from the first sample four set of specimens are prepared. One specimen is the original mild steel, second is “original heat treated” specimen, third sample is welded initially and then heat treated (pre-weld heat treated) and the other set of sample is heat treated initially and then welded (post-weld heat treated). A comparison study is conducted on both types of specimens to evaluate the welding distortion and mechanical strength of the welded joints. Same procedure was repeated in the preparation of samples for the rest of two mild steel specimens and one Aluminum sample preparation.

For micro structure analyses, four set of samples are prepared for the first sample that is “original sample” “original heat treated sample” “pre weld heat treated sample” and “Post weld heat treated sample”. Specimens for all the samples were prepared in the same fashion. After preparing the specimens, images of their micro structure are taken through scanning electron microscope (SEM).

#### A. Major Equipments Used

**Heat Treatment Furnace:** To perform the heat treatment on the selected and prepared specimen one set of samples are “pre-weld heat treated” and other set of samples are “post-weld

heat treated”.

**Scanning electron microscope:** To take images from each of the mounted specimens to study the micro structure and to observe and analyze the effects of heat treatment on the grain size and structures of the specimens. **Universal testing machine (UTM):** To perform the tensile testing on different specimens and to study the effects of heat treatment on the tensile strength of the material selected.

**Lathe machine:** The Lathe machine of workshop section of University of Engineering and Technology Peshawar was used for the conversion of raw material into Dog bone specimens.

#### B. Material selection

We selected our material as “mild steel strip” and “aluminum bar”. As these specimens are manufactured in the local industries of KPK so in order to find their exact composition we performed EDX analysis in CRL Lab University of Peshawar to find out their composition.

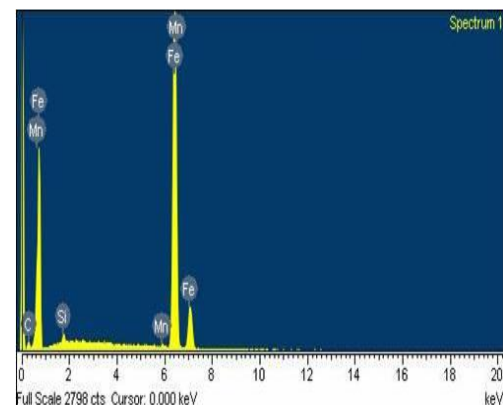


Figure. 1 EDX Analysis of Mild steel

From the results of EDX analysis we come to know about the composition of carbon which is above 0.8%. If the composition of carbon is above 0.8%, it is Hyper-Eutectoid so the metallurgical formulae are not applicable and we will examine its properties from the morphology of the structure i.e. SEM images. Now it becomes the base of our studies. This analysis has been shown in the Figure 1.

### II. PREPARATION OF SPECIMEN

This section includes preparation of specimens for final tests and inspection. Two different sets of specimens were being prepared. They are:

#### A. Specimens for UTM

Engr Mujahid Wasim Durani: U.S Pakistan Center for Advanced Studies In Energy (U.S PCAS-E), UET Peshawar.

Dr. Saim Saher: U.S Pakistan Center for Advanced Studies In Energy (U.S PCAS-E), UET Peshawar.

Engr Zainab Huma: U.S Pakistan Center for Advanced Studies In Energy (U.S PCAS-E), UET Peshawar.

**B. Specimens for microstructure analysis**  
In the following section we are going to describe the overall procedure employed in preparation of the specimens.

#### A. Specimen Preparation for UTM

First of all we take large strips of Mild steel. These large Mild steel strips were then cut into small pieces of strips respectively each having length of 14 inches. Each specimen was then machined in the “Machine shop” of workshop section of University of Engineering and technology Peshawar. Mild steel strips were then machined using Milling machine of workshop section. Where all these specimens were converted into Dog bone specimens. Each Dog bone specimen was having grip length of 3 inches on each side and gauge length of 8 inches. Three different sets of specimens were prepared comprising of 3 Mild steel sets of samples. These sets of samples were prepared for the purpose to have a set of samples for different heat treatment processes.

#### B. Specimen Preparation for Microstructure Analysis

A small part of mild steel strip was cut by using cutting machine of Metallurgy Lab, Department of Mechanical Engineering UET Peshawar. It was then mounted using “Mounting press “ of the same lab and was coated in Bakelite. It was then polished in MRL Lab, Department of Physics, University of Peshawar in three phases.

In the first phase, it was rough polished on polishing wheels of P180, P240, and P320 grain size. In second phase intermediate polishing was done using polishing wheels of P400, P600 and P800 grain size. In third phase we go for fine polishing using P1200 grain size polishing wheel. Finally it was etched using specific etchant (3 parts HCL and one part HN03) and was studied in CRL Lab University of Peshawar for microstructure changes.

Different set of samples were prepared according to our requirement.

We prepared three sets of samples both for microstructure and UTM tests. They are:

- Mild Steel Strip Furnace cooled
- Mild Steel Strip Air cooled:
- Mild Steel Strip water cooled:

### III. RESULTS OBTAINED FROM UTM AND SEM

#### A. Results Obtained From UTM

All the three specimens after preparing them in machine shop were carried to Metallurgy lab Department of Mechanical Engineering UET Peshawar where they were placed in furnace and were heat treated for 800°C & soaking time of one hour and were then furnace, Air and water cooled respectively. After executing all these steps these samples were carried to UTM Lab Department of Civil Engineering UET Peshawar where they were tested for improvement in Mechanical properties i.e. yield strength and ultimate tensile strength. The data obtained

from UTM is tabulated in the below Table 1, 2 and 3 respectively.

TABLE I. MILD STEEL SPECIMEN FURNACE COOLED

Specimen	Yield Strength	Ultimate Strength	$\Delta L$
Original	7.04	10.08	1.5625
Original H.T	5.84	8.94	2.1875
Pre weld H.T	6.8	8.44	0.5625
Post weld H.T	5.34	5.72	0.1875

TABLE II. MILD STEEL STRIP AIR COOLED

Specimen	Yield strength	Ultimate strength	$\Delta L$
Original	6.28	9.09	0.166
Original H.T	No	6.78	0.187
Pre weld H.T	5.94	7.49	0.250
Post H.T	6.45	8.56	0.375

TABLE III. MILD STEEL STRIP WATER COOLED

Specimen	Yield strength	Ultimate strength	$\Delta L$
Original	6.28	9.09	0.375
Original H.T	NO	10	0.125
Pre weld H.T	NO	7.18	0.062
Post H.T	5.63	7.60	0.187

#### B. Results Obtained from SEM Analysis

The results of SEM of all three pre welded specimens are given below.

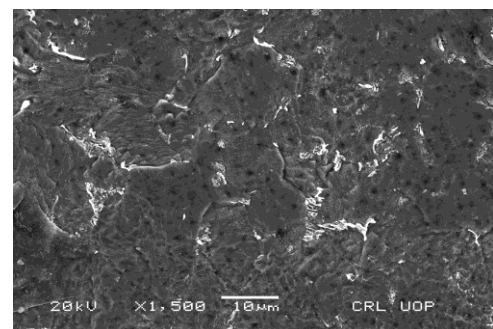


Figure .2 SEM of Pre-weld mild steel strip furnace cooled



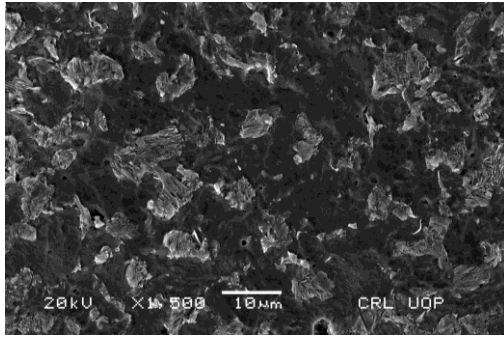


Figure .3 SEM of Pre-weld mild steel strip Air cooled

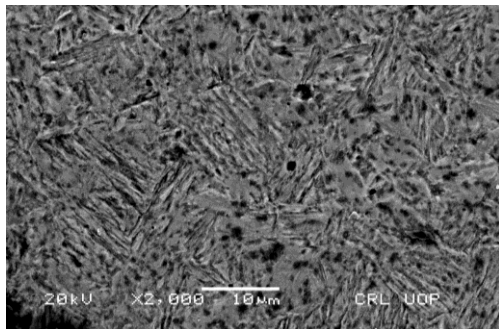


Figure .4 SEM of Pre-weld mild steel strip water cooled

#### IV. CONCLUSION

From the preceding tests and our research studies keeping in view the conditions and the type of heat treatment processes done on the specimen it is clear that if the amount of time provided and available for cooling, the microstructure will be having considerable changes respectively.

In case if we take the original specimen in each case it will be having good mechanical properties But in engineering designs, assembling and fabrication, the use flat part or piece of a material with no welded joints is not possible each and every time. It will definitely contain joints and welded parts, which is the objective of our research work to check for the changes in mechanical properties of welded joints i.e. Pre weld specimens and post weld specimens.

1) If we see the trend of mechanical properties i.e. Yield strength and Ultimate tensile strength in first specimen which is furnace cooled, they are both high in original specimen.

Upon going to the heat treated original sample, value of both of these properties decreases but change in length increases because in furnace cooling a lot of time was available for cooling and upon slow cooling in furnace the size of grain formed was small & fine and the cementite network showing weak zone becomes shallow because of heat treatment process, thus it is having high ductility compared to the original mild steel with no heat treatment. Now coming towards pre weld specimen, recall that it was the specimen that was first welded and then heat treated. Its Yield strength increases but its ductility goes down. It is due to the fact that welded joint can never be as strengthen as the original one and also if we pay attention to its morphology its grains are fine but the welding done on it (producing 10,000°F temperature) distort its properties and thus it is having low ductility. The last one is

Post welded joint in our first group of specimens. It is having decreased tensile strength, ductility and Ultimate tensile strength .It is because of the fact that this specimen was first heat treated at 800°C and after cooling in furnace to room temperature it was then welded. The process of welding as earlier stated increases the temperature of heat affected zone to 10000°F and was then allowed to be cooled in an open air. Hence not a slow cooling and the size of grain formed are large comparatively, thus this specimen is having smaller ductility and other mechanical properties compared to Pre-weld heat treated specimen.

2) If we see the trend of mechanical properties In the second group of specimens that were heat treated and then air cooled, we observe that the mechanical properties goes down up to the extent that no yield point is observed as a result of heat treatment in the original heat treated specimen. It is because of the fact that in the air cooling the heat treated specimen were not having slow cooling as in the air the temperature drops suddenly and the grains thus formed were not fine and the result is the decrease in mechanical properties such as yield strength ,ultimate tensile strength and ductility.

In the case of Pre-weld specimen the mechanical properties are improved as the cementite network is also shallow thus weak zones are small and the grain size formed is considerably small and the cementite network is also shallow thus it has high yield & ultimate tensile strength and ductility compared to original heat treated specimen In the Post weld heat treated specimen the grain formed are much fine and small thus it is having high mechanical properties at the cost of somewhat decreased ductility.

Based upon the findings of this research work it can be deduced that the choice of heat treatment depends upon application and the working condition of welded joints to which it will be exposed .

#### V. ACKNOWLEDGMENT

The Author would like to thanks Dr. Saim Saher, who is also the supervisor of this paper, for his continued support, guiding and supervision throughout the preparation of this manuscript. The author would also like to thanks Engr. Zainab Huma for his untiring efforts and dedication in the testing of specimens and towards preparation of this text. In addition the author would thank staff and management of University of Peshawar, Pakistan where the preparation and testing of specimens actually takes place.

#### REFERENCES

- [1] The effect of post weld heat treatment on the properties of 6061 friction stir welded joints K. N. KRISHNAN CRC for Welded Structures, Department of Mechanical Engineering, The University of Adelaide, Adelaide 5005, Australia
- [2] Mechanical and metallurgical effects of in process cooling during 7075-T6 butt joints AL.Fratini, G.Buffa & R.Shivpuri
- [3] Effect of Post-welded heat treatment on microstructures and properties of friction stir welded joints of 32Mn-7Cr-0.3N steel Y.J.Li, R.D.Fu, L.J.Jing, D.L.Sang & Y.P.Wang
- [4] Effect of pre- and post-weld heat treatment on metallurgical and tensile properties of Inconel 718 alloy butt joints welded using 4 kW Nd:YAG laser Journal of Materials Science, 2009, Volume 44, Number 17, Page 4557 X. Cao, B. Rivaux& M. Jahazi,

- [5] Residual stress modification by post-weld treatment and its beneficial effect on fatigue strength of welded structures Xiaohua Cheng, John W.Fisher, Henry , J.Prask, Thomas Gnäupel-Herold, Ben T.Yenab SougataRoy
- [6] effect of post-weld heat treatment on the interface and microstructure of explosively welded titanium–stainless steel composite
- [7] S.A.A.kbari mussavi, P. Farhadi sartangi Effect of heat treatment on tensile properties of friction stir welded joints of 2219-T6 aluminium alloy H. J. Liu,Y. C. Chen &J. C. Feng



**Engr Mujahid Wasim Durani** completed his Bachelor's degree In Mechanical Engineering from University of Engineering and Technology (UET) Peshawar,Pakistan in 2015. Presently, he is enrolled in Masters in Materials for Energy Storage and Conversion from U.S Pakistan

Center for Advanced Studies In Energy (U.S PCAS-E), UET Peshawar. He has also been a research scholar at Arizona State University(ASU),USA. His area of interest includes heat treatment technologies, mechanical design, Li-ion batteries and SOFC fuel cell. Currently he is working in an aerospace industry in the role of mechanical design engineer and heat treatment specialist of aircraft parts.

**Saim Saher** is Assistant Professor of Materials for Energy Storage and Conversion at USPCAS-E UET Peshawar. He studied characterization and performance enhancement of SOFC materials during PhD research in University of Twente (Netherlands) , RWTH Aachen University (Germany) and University of Montpellier-II (France) funded by EUDIME EACEA-EU. Before, he had studied Aerospace Engineering from Seoul National University (SNU, South Korea) and graduated as M.Sc. Aerospace Engineering in 2010. He has served renown national and international organization such as NESCOM (Pakistan), UET Peshawar, Inorganic Membrane (IM) University of Twente (Netherlands), Samsung Electronics Co. Ltd. (South Korea) and Intelligent Control System Laboratory (SNU, South Korea).

**Engr Zainab Huma** received her Bachelor's degree In Electrical Engineering from University of Engineering and Technology (UET) Peshawar,Pakistan in 2015. She is currently doing her Masters of Science in Electrical Energy Systems Engineering from U.S Pakistan Center for Advanced Studies In Energy (U.S PCAS-E), UET Peshawar. She has also been a research scholar at Arizona State University(ASU),USA. Her area of interest includes electro-mechanical designing, heat treatment technologies rechargeable Li-ion batteries and solar renewable energy.



# An Efficient Plasmonic Back Reflector for Thin-film Silicon Solar Cell Application

Aimal Daud Khan, Javed Iqbal, Salim ur Rehman

**Abstract**—A plasmonic back reflector based on gold nanoparticles were numerically investigated for thin-film solar cell application. A cluster of 21 gold nanoparticles was placed at the bottom layer of the cell with the objective to enhance the absorption of incident solar radiations. Different parameters of the proposed design are changed due to which maximum absorption is obtained. Furthermore, the influence of shape and material are also varied, which also affect and enhance the absorption characteristics of the solar cell.

**Keywords**— Perfect absorber, back reflectors, broadband, polarization-sensitive, solar energy harvesting.

## I. INTRODUCTION

To attain a high broad band absorption of electromagnetic waves from incoming light by a thin film solar cells is one of the most inspiring job, which is not easy for ordinary absorbers. Because the thickness of thin film solar cells are very small compared to traditional solar cells, so some rate of short wavelength light is trap inside the absorbing layer but most high wavelength light penetrate through it which takes no part in absorption. Generally, light trapping falls into two types i.e. one is to reduce the reflection losses from the top surface and allow more low and high wavelength light into the cells. By reducing reflection losses, anti-reflection layers are used. The second type is to increase the optical path length of the photons inside the absorbing layers. In this type, back surface of solar cells are textured in order to permits scattering and diffraction of longer wavelengths back into absorbing layer. The traditional back reflectors are not suitable for thin film solar cells due to its thickness smaller than the back textured surface which increases surface area and give rise to minority recombination losses [1].

By introducing an artificial absorber for thin film solar cells, also called plasmonic perfect absorber, composed of subwavelength size have received great attention [2-4]. These absorbers are based on plasmonic nanoparticles which are being made for different frequencies such as, infrared [5-7] and visible range [8-10]. The plasmonic nanoparticles can

be used for applications, such as solar cells [11-13], slow light [14-17], sensors [18-20], and negative refractive index [21-25]. Plasmonic nanoparticles have been spectrally designed for both narrow and broadband perfect absorptions that can absorb large volume of incident light than old-fashioned absorbers, for both transverse electric and transverse magnetic polarizations [26-29].

Several researches have designed back reflectors to obtained maximum optical path length for solar cells. C. D Hungerford et al., suggested an efficient plasmonic back reflector structure for solar cells. They used a hemispherical nanoparticle at the back surface where they achieved 72% absorption with spectral range 400-600nm but still they didn't cover the entire visible range in solar spectrum [30]. L. J. Crudgington et al., proposed a plasmonic back reflector structure for thin film solar cells, where they used an array of silver nanoparticle at the top surface of back reflector layer. They obtained about 80% absorption with 140nm spectral width. However, their results still lack some requirements, which an ideal solar cell needs [31]. C. Sun et al., suggested a new design for back surface of thin film solar cells, where they used array of silver nanoparticles in the bottom surface of silicon layer. They minimized transmission losses below than 50% from 800-1200nm in solar spectrum. But still half of the visible range suffers from transmission losses [32]. C. Sun proposed another design for back reflectors, where they textured the back surface with blazed grating for thin film solar cells. They minimized the transmission losses at the back surface but this structure is not suitable for thin film solar cells because texturing in thin film solar cells give rise to recombination losses and badly effect the overall efficiency [33].

The earth receives about 48% of visible and 43% of near infrared radiations [34]. Thus, for solar energy harvesting, our focus should be on visible and near infrared region in the solar spectrum. In order to absorb most of the solar radiations, the thin film solar cell can be carefully designed such that the top surface reduces the reflection losses and the bottom layer reduces the transmission losses. Due to small thickness of the thin film solar cells, most of the light penetrate through it without being absorbed and take no part in the formation of current. The existing plasmonic reflectors do not cover completely the visible range of electromagnetic spectrum. Also, some of the structures support single or multiple absorption modes with narrow wavelengths, which is not appropriate for solar energy harvesting applications. To overcome this issue, we designed a back reflector based

Aimal Daud Khan: Sarhad University of Science & Information Technology, Peshawar 25000, Pakistan, aimaldawoodkhan@gmail.com.

Javed Iqbal: Sarhad University of Science & Information Technology, Peshawar 25000, Pakistan.

Salim ur Rehman: Sarhad University of Science & Information Technology, Peshawar 25000, Pakistan.

on plasmonic nanoparticles for thin film solar cells, which increases the absorption of light in large amount.

## II. SIMULATION MODEL

The suggested structure of back reflector is shown in figure 1(a), which is made of three layers: (i) the top layer is an anti-reflection coating (ARC) made of silicon dioxide used to minimize reflection losses and also provide good surface passivation, (ii) a middle layer made of silicon, used to trap light, and (iii) the bottom layer made of silicon dioxide. An array of gold spherical nanoparticles are inserted at the bottom of silicon layer in order to push back maximum light into silicon layer. The unit cell of the structure is shown in figure 1(b), where the period along x is,  $L_x = 420\text{nm}$  and the period along y is,  $L_y = 230\text{nm}$ . Periodic boundary conditions are used for the duplication of unit cell in x and y directions. The geometric parameters of the structure are: radius,  $r = 10\text{nm}$ , and particle separation,  $s = 20\text{nm}$ . The thickness of the bottom layer is,  $t_b = 100\text{nm}$ , thickness of the dielectric layer is,  $t_m = 150\text{nm}$  and thickness of ARC layer is,  $t_a = 80\text{nm}$ . The relative permittivity of silicon and  $\text{SiO}_2$  layer is 11.7 and 3.9, respectively. The electromagnetic waves is incident upon the structure in z-direction. The environment of the entire simulation is chosen air and all the simulations are conducted in COMSOL Multiphysics software.

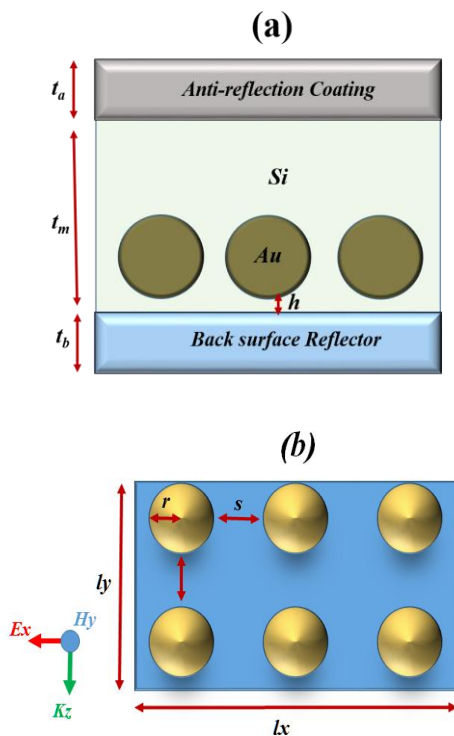


Figure 1. (a) Schematic setup of plasmonic back reflector, (b) top view of the structure

## III. RESULTS AND DISCUSSION

To achieve a best optical absorption of the proposed thin film solar cell structure, we have used an array of 21 nanoparticles at the back surface and analyzed different configurations i.e. influence of particle radius ( $r$ ), influence of particle separation ( $s$ ), influence of space between nanoparticles array and back surface reflectors ( $h$ ), influence of different noble metals, and shapes on efficiency of absorption spectrum. We have first calculated absorption spectra of nanoparticles radius from 5nm to 25nm while keeping constant distance between nanoparticles  $s=20\text{nm}$ , which is plotted in Figure 2(a). Here, several absorption modes are observed for different radii and compared the results with planer gold metal sheet. We have observed that as the particle radius increases the absorption spectrum involving in optical losses and their modes are suppressing. Here, broadband absorption are obtained for  $r=10\text{nm}$ , which have 60% absorption capability and covered the entire visible and near infrared region. This clearly proves that nanoparticles can be implemented at the bottom surface of thin film solar cells to increase the optical path length.

Next we used the same number of particles having radius  $r=10\text{nm}$  and varied inter particle separation from 10nm to 50nm as shown in Fig. 2(b). Here, the absorption efficiency is almost remain unchanged by varying  $s$ . Therefore, it means that the absorption efficiency is independent of  $s$ .

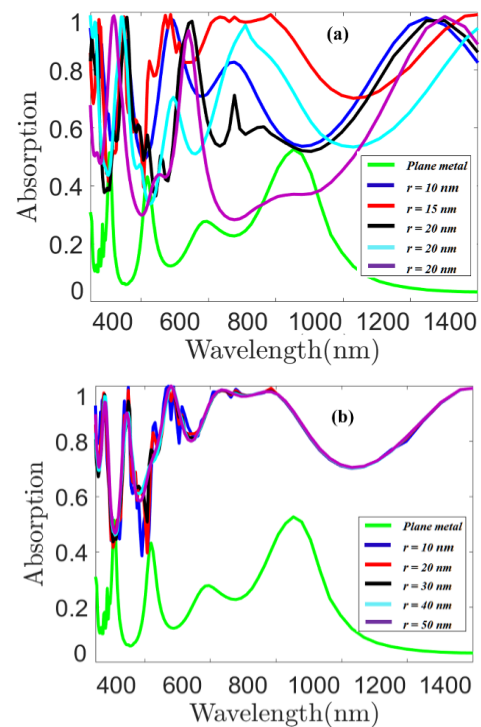


Figure 2. Influence of absorption efficiency on (a) radius and (b) inter particle separation

Next variation in absorption efficiency is investigated by changing space ( $h$ ) between gold nanoparticle array and back reflector. The parameter  $h$  is varied from 20nm to 80nm while keeping the particle separation constant at  $s=20$ nm, radius of nanoparticles at  $r=10$ nm, and used array of 21 nanoparticles, see figure 3. For wavelength higher than 600nm, a slight enhancement in absorption efficiency is experienced but when the array of nanoparticles are moving up i.e. getting close to the surface of silicon substrate then maximum absorption is observed in the wavelength ranges from 400nm to 600nm at  $h=80$ nm. So here we have reached to a point that overall absorption can be improve by inserting array of nanoparticles close to the surface of silicon layer.

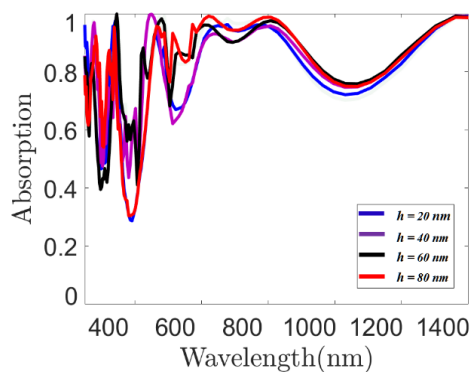


Figure 3. Influence of absorption efficiency on space between nanoparticles array and back surface reflector

Eventually, we investigate the influence of shape of nanoparticles on the absorption efficiency of solar cells. We took some shapes, which includes sphere, pyramid, disk, and square and calculated their influences on the optical absorption. The result is plotted in figure 4(a), where number of particles are same i.e. 21, having radius  $r=10$ nm, particle separation as  $s=20$ nm and inserted array at the bottom of silicon with  $h=0$ nm. We have achieved best absorption spectra for almost all individual shapes and covered the entire spectrum with 70% amplitude. However, the sphere and disk array generates better absorption performance than the other two shapes where improves absorption from 70% to 80% in wavelength from 420nm to 560nm. Now in the final investigation we used different materials for array of nanoparticles and calculated its influence on absorption spectrum, see figure 4(b). In this case, we only considered spherical shape and the radius of nanoparticles were selected as  $r=10$ nm, particle separation,  $s=20$ nm and space between array of nanoparticle and back surface reflectors as  $h=0$ nm. Here, we observed good result for all different materials with 60% absorption capability. The results of this work can be used to optimize other different thin film solar cells with gold nanoparticle arrays.

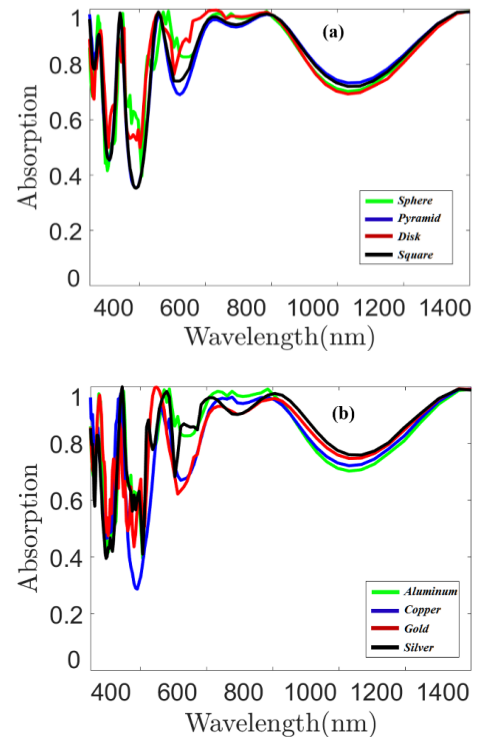


Figure 4. Influence of absorption efficiency on various (a) shapes and (b) materials.

## CONCLUSION

We present a plasmonic back reflector based on gold nanospheres inserted at the bottom surface of silicon layer. The structure is composed of three functional layers i.e. an anti-reflection coating is placed at the top surface and bottom layer is made of  $\text{SiO}_2$  and middle layer is made of dielectric. Different geometric parameters are studied in order to get high absorption efficiency. It is found that nanospheres with 10nm radius, 20nm particle separation can reduce transmission losses with wide spectrum, which also provide best absorption efficiency with spectral bandwidth of 985nm. These results show that the proposed back reflector may be a better choice for thin film and solar energy harvesting applications.

## REFERENCES

- [1] Tang, Z., W. Tress, and O. Inganäs, Light trapping in thin film organic solar cells. *Materials today*, 2014. 17(8): p. 389-396.
- [2] Landy, N.I., et al., Perfect metamaterial absorber. *Physical review letters*, 2008. 100(20): p. 207402.
- [3] Khan, A.D. and M. Amin, Tunable salisbury screen absorber using square lattice of plasmonic nanodisk. *Plasmonics*, 2017. 12(2): p. 257-262.
- [4] Ullah, H., et al., Novel multi-broadband plasmonic absorber based on a metal-dielectric-metal square ring array. *Plasmonics*, 2017: p. 1-7.



- [5] Liu, X., et al., Infrared spatial and frequency selective metamaterial with near-unity absorbance. *Physical review letters*, 2010. 104(20): p. 207403.
- [6] Khan, A.D., et al., Multiple higher-order Fano resonances in plasmonic hollow cylindrical nanodimer. *Applied Physics A*, 2015. 120(2): p. 641-649.
- [7] Muhammad, N. and A.D. Khan, Tunable Fano resonances and electromagnetically induced transparency in all-dielectric holey block. *Plasmonics*, 2015. 10(6): p. 1687-1693.
- [8] Zhang, S., et al., Experimental demonstration of near-infrared negative-index metamaterials. *Physical review letters*, 2005. 95(13): p. 137404.
- [9] Khan, A.D., Multiple Fano resonances in bimetallic layered nanostructures. *International Nano Letters*, 2014. 4(2): p. 110.
- [10] Khan, A.D., et al., Twin dipole Fano resonances in symmetric three-layered plasmonic nanocylinder. *Plasmonics*, 2015. 10(4): p. 963-970.
- [11] Wang, Y., et al., Metamaterial-plasmonic absorber structure for high efficiency amorphous silicon solar cells. *Nano letters*, 2011. 12(1): p. 440-445.
- [12] Wu, C., et al., Metamaterial-based integrated plasmonic absorber/emitter for solar thermo-photovoltaic systems. *Journal of Optics*, 2012. 14(2): p. 024005.
- [13] Rufangura, P. and C. Sabah, Dual-band perfect metamaterial absorber for solar cell applications. *Vacuum*, 2015. 120: p. 68-74.
- [14] Khan, A. and M. Amin, Polarization Selective Multiple Fano Resonances in Coupled T-Shaped Metasurface. *IEEE Photonics Technology Letters*, 2017. 29(19): p. 1611-1614.
- [15] Muhammad, N. and A.D. Khan, Electromagnetically Induced Transparency and Sharp Asymmetric Fano Line Shapes in All-Dielectric Nanodimer. *Plasmonics*, 2017. 12(5): p. 1399-1407.
- [16] Amin, M. and A.D. Khan, Polarization selective electromagnetic-induced transparency in the disordered plasmonic quasicrystal structure. *The Journal of Physical Chemistry C*, 2015. 119(37): p. 21633-21638.
- [17] Khan, A.D. and G. Miano, Investigation of plasmonic resonances in mismatched gold nanocone dimers. *Plasmonics*, 2014. 9(1): p. 35-45.
- [18] Liu, N., et al., Infrared perfect absorber and its application as plasmonic sensor. *Nano letters*, 2010. 10(7): p. 2342-2348.
- [19] Khan, A.D., Refractive index sensing with fano resonant L-shaped metasurface. *Optical Materials*, 2018. 82: p. 168-174.
- [20] Khan, A.D., Enhanced plasmonic Fano-like resonances in multilayered nanoellipsoid. *Applied Physics A*, 2016. 122(4): p. 300.
- [21] Iyer, A.K. and G.V. Eleftheriades. Negative refractive index metamaterials supporting 2-D waves. in *Microwave Symposium Digest, 2002 IEEE MTT-S International*. 2002. IEEE.
- [22] Khan, A.D. and G. Miano, Higher order tunable Fano resonances in multilayer nanocones. *Plasmonics*, 2013. 8(2): p. 1023-1034.
- [23] Khan, A.D. and G. Miano, Plasmonic Fano resonances in single-layer gold conical nanoshells. *Plasmonics*, 2013. 8(3): p. 1429-1437.
- [24] Khan, A.D., et al., Generation of multiple Fano resonances in plasmonic split nanoring dimer. *Plasmonics*, 2014. 9(5): p. 1091-1102.
- [25] Khan, A.D., et al., Excitation of multiple Fano-like resonances induced by higher order plasmon modes in three-layered bimetallic nanoshell dimer. *Plasmonics*, 2014. 9(2): p. 461-475.
- [26] Li, Z., S. Butun, and K. Aydin, Ultranarrow band absorbers based on surface lattice resonances in nanostructured metal surfaces. *ACS nano*, 2014. 8(8): p. 8242-8248.
- [27] Liu, Z., et al., Achieving an ultra-narrow multiband light absorption meta-surface via coupling with an optical cavity. *Nanotechnology*, 2015. 26(23): p. 235702.
- [28] Wang, B.-X., et al., Theoretical investigation of broadband and wide-angle terahertz metamaterial absorber. *IEEE Photonics Technology Letters*, 2014. 26(2): p. 111-114.
- [29] Ullah, H., et al. Plasmonic perfect absorber for solar cell applications. in *Emerging Technologies (ICET)*, 2016 International Conference on. 2016. IEEE.
- [30] Hungerford, C.D. and P.M. Fauchet, Design of a plasmonic back reflector using Ag nanoparticles with a mirror support for an a-Si: H solar cell. *AIP Advances*, 2017. 7(7): p. 075004.
- [31] Crudgington, L., T. Rahman, and S. Boden, Development of amorphous silicon solar cells with plasmonic light scattering. *Vacuum*, 2017. 139: p. 164-172.
- [32] Sun, C., J. Su, and X. Wang, A design of thin film silicon solar cells based on silver nanoparticle arrays. *Plasmonics*, 2015. 10(3): p. 633-641.
- [33] Sun, C., et al., A surface design for enhancement of light trapping efficiencies in thin film silicon solar cells. *Plasmonics*, 2016. 11(4): p. 1003-1010.
- [34] Solanki, C.S., *Solar photovoltaics: fundamentals, technologies and applications*. 2015: PHI Learning Pvt. Ltd.



# Waterflooding: A key Option for Stratified Oil Reservoirs in the Niger Delta

Patrick Godwin Oyindobra Ossai<sup>1</sup>, Princewill Nnaemeka Ohia<sup>2</sup>

Department of Petroleum Engineering, Federal University of Technology,

Owerri, Imo State, Nigeria<sup>1,2</sup>

engrpatrickossai@yahoo.com<sup>1</sup>, princepetra@yahoo.com<sup>2</sup>

Received: 02 July, Revised: 10 August, Accepted: 28 August

**Abstract**—This research work looked at the applicability concept of waterflooding as a key option for enhanced recovery of oil from stratified reservoirs in the Niger Delta, South of Nigeria. Waterflooding is a secondary recovery technique that commences after a homogeneous or multi-layered (stratified) reservoir has reached its economic limit by every possible primary recovery drives (i.e. natural drive mechanisms). The research also covered for Niger Delta the sweep/displacement efficiency deliverability of multi-layered (stratified) reservoirs, reservoir permeability ordering, the effect of waterflooding rates, and effectiveness of waterflooding schemes for multi-layered oil reservoirs, fractional flow of water during waterflooding processes, and the frontal advancement of the water front along the reservoir bed at a given time (t) in days.

**Keywords**—Stratified reservoir, Multi-layered reservoir, Sweep Efficiency, Displacement Efficiency, Niger Delta, Buckley-Leverette theory, Waterflooding, Water Injection, Enhanced Oil Recovery

## I. INTRODUCTION

It is already a known fact that waterflooding is one of the most cost effective and efficient secondary oil recovery technique for mostly offshore oil reservoirs worldwide. Every oil reservoir producing using its natural drive mechanisms must definitely reach its economic limit in no distance time. Hence, there is the need for a secondary recovery technique such as waterflooding. Reservoirs are known to be homogeneous (less complex system) or multi-layered/stratified (complex to very complex reservoir systems). These complex reservoirs that are multi-layered or stratified usually have varying reservoir characteristics horizontally or vertically or both (as the case may be). The important effects of waterflooding as a secondary oil recovery technique are demanding increasing attention in technical enhanced oil recovery (EOR) literatures worldwide. We have two distinguished cases of waterflooding in stratified oil reservoirs. They are:

1. Waterflooding in a stratified reservoir with cross-flow: This means that there is communication between the multi-layers of the oil reservoir
2. Waterflooding in a stratified reservoir without cross-flow: This also means that there is no communication between the multi-layers of the oil reservoir (probably as a result of isolation)

For the first category (with cross-flow), the stratified or multi-layered reservoir is assumed to consist of discrete layers that are uniform (homogeneous) within itself. Only differing from each other in properties such as:

- a. Absolute permeability (k)
- b. Thickness (h) and
- c. Porosity

The performance within each individual layers can be calculated by one dimensional flow theory. The performance of the total stratified reservoir can be gotten by adding up the individual layer performances. It is also expedient to note here also that the capillary and gravity effects are negligible. As for the second category (without cross-flow), things are more relatively complex and difficult since there are capillary and gravity effects that plays a vital role which cannot be neglected. Gravity and capillary effects are responsible for the cross-flow (communication) between layers except in cases of isolation. The differential equations which rigorously describe waterflooding in stratified or multi-layered reservoirs are usually non-linear. Hence, does not facilitate analytical solutions to problems. But, by applying the finite difference approximations one can possibly derive solutions to any degree of accuracy. ADIP (Alternating Direction Implicit Procedure) is one such solution provided by computers. ADIP explores systematically the effects of very important parameters used in waterflooding performance of two-dimensional, two-layered, field scale model of water-wet stratified sandstone reservoir.

## II. PREDICTING WATERFLOODING BEHAVIOUR IN A STRATIFIED RESERVOIR

Predicting waterflooding behavior is very possible using an already existing flexible model that can approximate the cross-flow effects during the process. This model depends on slight changes in the Dietz's theory which create room for adjusting both the permeability and hydrocarbon pore volume. It is also very possible to assume in few cases that the permeability can be characterized by a log-normal distribution. Whereas the hydrocarbons pore volume is characterized by normal distribution. A simple graphical method can help a field engineer to predict the behavior of a stratified waterflooding process. In comparison to other methods we can conclude that:

1. The effects of variations in hydrocarbon pore volume can be neglected under normal conditions.
2. Cross-flow (communication) effects in a stratified/multi-layered reservoir system can be appreciable if the mobility ratios (M) are favorable or unfavorable.
3. Failure to utilize all available permeability data can lead to large avoidable errors when predicting waterflooding behavior for a stratified reservoir.

### a. *The Effects Of Waterflooding Rate And Permeability Ordering In A Stratified Reservoir*

The waterflooding performance of a highly stratified reservoir in which the layers are systematically arranged can be greatly affected by gravity segregation that will also depend on the flooding rate and permeability ordering. Cross-flow is also affected by capillary and gravitational forces to a large degree by flooding rate and permeability ordering in multi-layered reservoir.

Two cases of systematic permeability ordering can be considered as thus:

- i. Layers can be arranged in an ordering form starting from the most permeable layer to the least permeable one. The most permeable strata is considered to be at the top.
- ii. Here layers are arranged in the opposite manner with the least permeable layer/strata is considered to be at the top.

Most importantly, it must be noted that stratified reservoirs can be in any random permeability ordering.

### b. *Predicting Waterflooding Performance In A Stratified Reservoir Systems*

The analytical solutions detailing the cross-flow effects are very possible but only under limiting conditions. These limiting conditions are:

- a. Where vertical equilibrium exist as a result of gravity and capillary displacement dominance.
- b. Where there are highly viscous forces in dominance resulting to no cross-flow.

In most cases a less expensive two-dimensional area x-y model can be employed to solve engineering problems adequately provided the non-uniform distribution of fluid flow in the third or vertical dimension of the areal model is adequately described. Invariably, this implies also that the input data must be varied with respect to the two-dimensional area so that it can account for the vertical effects.

### c. *Predicting Waterflooding Performance By The Graphical Representation Of Porosity And Permeability Distribution In Stratified Reservoirs*

One simple tool that is now available for prediction waterflooding performance from stratified reservoirs has been developed using variations of familiar layer concept. These variations allows for consideration of non-uniform porosity, development and mobility ratio. Such procedure considers predicting cumulative water injected and also the cumulative oil production based on percent water-cut using porosity-permeability system classification. The ease of utilizing the graphical approach to the cumulative oil recovery against the water-cut prediction makes it much easier to evaluate the areal plus the vertical aspect of the flood performance. Most procedures are common to other methods except for the following:

1. It is unnecessary to assume uniform porosity distribution and uniform water saturations
2. It was assumed that in layers of equal permeability capacity, advancement of the water front is not proportional to the mobility of hydrocarbon volume of the layer.
3. Changing the mobility ratio during fill-up periods was assumed.

To evaluate the effect of stratification on vertical sweep efficiency the reservoir permeability data from core analysis must classified based on systems similar to what was proposed by law.

### d. *Waterflooding Performance Of Communicating Stratified Reservoir With A Log-Normal Permeability Distribution*

Analytical answers can be gotten for waterflooding performance of stratified reservoirs with log-normal permeability distribution provided the possibilities of cross-flow exist. The characteristic of the permeability distribution is given by Dykstra-persons variation coefficient which is related to the standard deviation of the log-normal distribution. Its performance is represented as vertical converge as a function of the producing water-oil ratio (WOR). An analogy to the Buckley-Leverette multiple value saturation is found to occur in the law of mobility ratio ( $M < 1$ ) where a multiple valued displacement front is formed. The log-normal permeability is characterized by two permeates and they are:

- a. The standard deviation and
- b. The mean permeability

e. *Combination Method For Predicting Waterflooding Performance In Stratified Reservoir*

A solution that predict waterflooding performance has been created and it combines certain aspects of other published techniques. This approach is based on computer solutions and has eliminated the need for consulting plotted curves. Invariably, it allows for analytical prediction of waterflooding performance for a stratified reservoir. Values predicted are measured in common oil field units rather than in dimensionless terms. The whole calculation process has been programmed into FORTRAN IV and is readily available to users.

f. *Waterflooding Performance Of Stratified Reservoir Systems*

Most published analytical methods as at today that is utilized for the prediction of waterflooding performance of stratified reservoirs does not take into account the actual spatial position of the layers in the reservoir. They commonly assumed a position of layers without existing cross-flow between the strata. Today, further reservoir engineering research has revealed that wide variations of reservoir properties like porosity, permeability, and capillary pressures exist within the individual units in the stratified system.

g. *The Effectiveness Of Waterflooding Scheme For A Multi-Layered Reservoir*

Waterflooding scheme effectiveness for multi-layered reservoirs depends on the following:

- i. The areal extent
- ii. The vertical sweep efficiency and
- iii. The microscopic displacement

These factors are determined by detailed reservoir studies. But, a quick assessment of a waterflooding scheme performance can be done by assigning values (0.0-0.1) for each factor listed above. The overall waterflooding efficiency can be computed by multiplying these three values. For instance, a stratified reservoir that has areal, microscopic and vertical sweep efficiency of 0.5, 0.6 and 0.7 would have an overall waterflooding efficiency of 0.21. This means that only 21% of the oil in place can be recovered using the scheme. Both areal and vertical sweep efficiency depends on large variety of factors. Such as:

1. Perforation placement
2. Well spacing
3. Injection/production rates
4. Reservoir thickness
5. Reservoir fluid properties/characteristics
6. Wettability
7. Anisotropy
8. Distribution of both horizontal and vertical permeability
9. Type of injected fluid (water or gas)

### III. INTRODUCING THE STUDY MODEL/THEORY

The Buckley-Leverette theory/model uses two distinctive equations, namely:

- IV. The frontal advancement equation and
- V. The fractional flow equation

Buckley-Leverette (B-L) made the following theoretically assumptions:

- a. The displacement is incompressible (steady state)
- b. The displacement takes place via vertical equilibrium
- c. Water is displacing oil in a water-wet reservoir
- d. The displacement is considered linear

The generalized fractional flow equation proposed by Buckley-Leverette is given as:

$$F_w = \frac{1 - \left( \frac{dP_c}{dx} + g\Delta\rho\sin\theta \right) \frac{k_o}{q_t \mu_o}}{1 + \frac{k_o}{k_w} X \frac{\mu_w}{\mu_o}} \quad (1)$$

In field or practical units, the fractional flow equation proposed by B-L becomes:

$$F_w = \frac{1 - \frac{1.127 k_o}{q_t \mu_o} (g\Delta\rho\sin\theta + \frac{dP_c}{dx})}{1 + \frac{k_o}{k_w} X \frac{\mu_w}{\mu_o}} \quad (2)$$

Note:

If we neglect capillary effect and consider the reservoir to be horizontal, then the fractional flow equation is given as:

$$F_w = \frac{1}{1 + \frac{k_o}{k_w} X \frac{\mu_w}{\mu_o}} \quad (3)$$

Now, expressing fractional flow equation in terms of reservoir volumes we have:

$$F_w = \frac{1}{1 + \left( \frac{K_o}{K_w} X \frac{B_w}{B_o} X \frac{\mu_w}{\mu_o} \right)} \quad (4)$$

Since  $(K_o/K_w)$  is a function of saturation, then equation (4) above becomes:

$$F_w = \frac{1}{1 + (ae^{-bsw} X \frac{B_w}{B_o} X \frac{\mu_w}{\mu_o})} \quad (5)$$

On the hand, the frontal advance equation proposed by B-L theory is represented as:

$$\text{FRONTAL ADVANCE, } X = \frac{q X t}{A \phi} (DF_w / DS_w) \quad (6)$$

The above equation (6) is valid provided (q) unit is in bbl/day

$$\text{FRONTAL ADVANCE, } X = \frac{5.615 q X t}{A \phi} (DF_w / DS_w) \quad (7)$$

Equation (7) is only valid if (q) unit is in cuft/day

## A Displacement Model For Stratified Reservoir

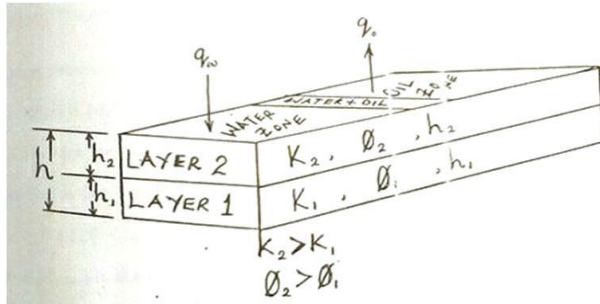


**Fig. 1:** Displacement in a Non-homogeneous reservoir model

<b>LAYER 2</b>
$K_2 = 100 \text{ md}, \phi_2 = 0.17, h_2 = 20 \text{ ft}$
<b>LAYER 1</b>
$K_1 = 50 \text{ md}, \phi_1 = 0.15, h_1 = 10 \text{ ft}$

**Fig. 2:** Reservoir parameters of the Niger Delta stratified reservoir

Note:

The angle of inclination of the Niger Delta stratified reservoir is zero (i.e.  $\theta = 0$ ), water viscosity,  $\mu_w = 0.5 \text{ cp}$ , oil viscosity,  $\mu_o = 5 \text{ cp}$ , specific gravity of the oil,  $\gamma_o = 0.81$  and specific gravity of the water,  $\gamma_w = 1.04$

Now, capillary pressure is related to capillary rise by:

$$dP_c = 0.1 dZ \text{ (PSI)} \quad (8)$$

The phase pressure difference at the center of the reservoir is given by:

$$P_{c|0} = 0.1 (20 - Z_{1-\text{Sor}}) \quad (9)$$

Where:

$Z_{1-\text{Sor}}$  = Elevation of maximum water saturation and

$S_w = 1 - S_{or}$

Mathematically, we have:

1. The average water saturation for the Niger Delta stratified reservoir Layer 1 is given as:

$$\Sigma \overline{S_{w1}} = \Sigma \frac{S_w \times Z_1^2}{h_1} \quad (10)$$

2. The average water saturation for the Niger Delta stratified reservoir Layer 2 is given by:

$$\Sigma \overline{S_{w2}} = \Sigma \frac{S_w \times Z_2^2}{h_2} \quad (11)$$

3. The average water saturation of the Niger Delta stratified reservoir is given as:

$$\overline{S_w} = \frac{h_1 \phi_1 \Sigma S_{w1} + h_2 \phi_2 \Sigma S_{w2}}{h_1 \phi_1 + h_2 \phi_2} \quad (12)$$

$$4. \quad K_{rw}(\overline{S_w}) = \frac{\int_0^h \frac{K(Z) K_{rw}(S_w(Z)) dZ}{\int_0^h K(Z) dZ}}{\frac{h_1 K_1 K_{rw1}(S_{w1}) + h_2 K_2 K_{rw2}(S_{w2})}{\Sigma h_j k_j \quad (j=1)}} = \quad (13)$$

$$5. \quad K_{rw1} S_{w1} = \frac{\int_0^{h_1} K_{rw}(S_w(Z)) dZ}{h_1} \quad (14)$$

$$6. \quad K_{rw2} S_{w2} = \frac{\int_0^{h_2} K_{rw}(S_w(Z)) dZ}{h_2} \quad (15)$$

3.15

## Niger Delta Stratified Reservoir Data And Results In Summary

**Table 1:** Stratification data and Calculated Results for Niger Delta Reservoir Layer 1

STRATIFICATION LAYER 1: $h_1 = 10 \text{ ft}, \phi = 0.15$					
Z (ft)	Pc (psi)	Sw (%)	Krw (mD)	Kro (mD)	$\overline{S_{w1}}$ (%)
10	1.0	0.69	0.18	0.020	3.45
5	0.5	0.78	0.23	0.002	3.90
0	0.0	0.80	0.24	0.000	4.00
					$\Sigma \overline{S_{w1}} = 11.35 \%$

**Table 2:** Stratification data and Calculated Results for Niger Delta Reservoir Layer 2

STRATIFICATION LAYER 2: $h_2 = 20 \text{ ft}, \phi = 0.17$					
Z (ft)	Pc (psi)	Sw (%)	Krw (mD)	Kro (mD)	$\overline{S_{w2}}$ (%)
30	3.0	0.22	0.001	0.55	2.20
25	2.5	0.24	0.003	0.50	2.40
20	2.0	0.29	0.020	0.40	2.90
15	1.5	0.45	0.070	0.18	4.50
10	1.0	0.63	0.170	0.05	6.30
					$\Sigma \overline{S_{w2}} = 18.3 \%$

From the stratification data Table 1 & 2 and applying equation (12), the average water saturation for the Niger Delta stratified reservoir is given as:

$$\bar{S}_w = \frac{h_1 \phi_1 S_{w1} + h_2 \phi_2 S_{w2}}{h_1 \phi_1 + h_2 \phi_2}$$

$$\bar{S}_w = \frac{(10 \times 0.15 \times 11.35) + (20 \times 0.17 \times 18.3)}{(10 \times 0.15) + (20 \times 0.17)} = \frac{(17.025 + 62.22)}{(1.5 + 3.4)} = \frac{79.245}{4.9} = 16.2\%$$

#### *Sweep Efficiency Consideration For The Niger Delta Stratified Reservoir*

Sweep efficiency is the ratio of the volume swept at any given time against the total volume subjected to invasion. Sweep efficiency can be expressed as:

- Pattern Efficiency
- Volumetric Efficiency and
- Invasion Efficiency

For a single linear homogeneous reservoir or bed, we have that:

$$\text{RECOVERY} = \text{SWEEP EFFICIENCY (S.E)} \times \text{DISPLACEMENT EFFICIENCY (D.E)}$$

But, for a stratified or multi-layered reservoir like that of this Niger Delta oil reservoir, we have it as:

$$\text{RECOVERY} = \text{SWEEP EFFICIENCY (S.E)} \times \text{DISPLACEMENT EFFICIENCY (D.E)} \times \text{CONFORMANCE}$$

#### *Sweep Efficiency Calculations For The Niger Delta Stratified Reservoir Considering A 5-Spot Pattern*

**Table 3:** Reservoir data / stratification parameters

Reservoir Parameters	Values
Relative water permeability, ( $K_{rw}$ )	0.24
Relative oil permeability, ( $K_{ro}$ )	0.80
Oil viscosity, ( $\mu_o$ ) cp	5.00
Water viscosity, ( $\mu_w$ ) cp	0.50
Oil formation volume factor, ( $B_o$ )	1.31
Initial oil saturation, ( $S_{oi}$ )	0.65
Residual oil saturation, ( $S_{or}$ )	0.30
Reservoir porosity, ( $\phi$ ) %	0.20
Reservoir area, (A) sq.ft	10.00
Reservoir pay thickness, (H) ft	30.00
Layer 1 thickness, ( $h_1$ ) ft	10.00
Layer 2 thickness, ( $h_2$ ) ft	20.00
Specific oil gravity, ( $\gamma_o$ )	0.81
Specific gravity of water, ( $\gamma_w$ )	1.04

Mathematically:

$$\text{MOBILITY RATION, } M = \frac{Z_w}{Z_o} = \frac{K_{rw}/\mu_w}{K_{ro}/\mu_o} = \frac{0.24/0.5}{0.8/5} = 3.0$$

Taking the reciprocal of the mobility ratio we have:

$$\frac{1}{M} = \frac{1}{3} = 0.33$$

From the sweep efficiency curves/charts,  $1/M = 0.33$  which corresponded to a Sweep Efficiency of 54% at the initial breakthrough. This means that the recoverable oil from the Niger Delta stratified reservoir is only 54%.

$$\begin{aligned} \text{DISPLACED OIL VOLUME} &= 7758 \times A \times H \times \phi (S_{oi} - S_{or}) \quad (16) \\ &= 7758 \times 10 \times 30 (0.65 - 0.3) \\ &= 814,590 \text{ bbls} \end{aligned}$$

The recovery at surface conditions is given by:

$$\text{RECOVERY} = \frac{7758 A h \phi (S_{oi} - S_{or})}{B_o} \quad (17)$$

Hence, if displacement efficiency (D.E) = 1 and sweep efficiency (S.E) = 54%

then:

$$\text{Recovery} = \frac{814,590 \times 0.54}{1.31} = 335,785 \text{ STB}$$

But, if displacement efficiency (D.E) = 68% and sweep efficiency (S.E) = 54%,

then:

$$\text{Recovery} = \frac{814,590 \times 0.54 \times 0.68}{1.31} = 228,334 \text{ STB}$$

#### CONCLUSION /RECOMMENDATIONS

A good waterflooding process has a mobility ratio that is equal to one ( $M = 1$ ). But, if the stratified oil reservoir is much viscous then the mobility ratio could be greater than one ( $M > 1$ ). The displacing fluid (water) sweeps faster in more permeable zones. This means that oil in less permeable zones will be produced over a longer a long period of time. A more favorable displacement (immiscible displacement) for stratified reservoirs occurs when higher permeable layers are uppermost in the reservoir. And for viscous oil having mobility ratio greater than one the displacement water will finger through the reservoir resulting to it bypassing some of the needed oil. Water is usually more efficient than gas in displacing oil from reservoir rocks. This is because the viscosity of water is almost fifty (50) times that of gas. Water is also known to occupy the less conducive portions of the pore spaces whereas gas occupies the more conducive portions. Since there are two sets of relative permeability curves there are also discontinuities in the relative permeability distributions to oil and water at the layers boundaries. The rates of advancement in the separate strata/layers will be proportional to their permeability and the overall effect will be a combination of several separate displacements such as described for a single homogeneous stratum. For best results detailed reservoir studies must be carried out before the implementation of a waterflooding scheme.

## REFERENCES

- [1] Ezeddin S., Gary Z. Waterflooding performance of stratified reservoirs with bottom-water conditions, SPE 77965-MS
- [2] Haq S., Reis J.C. Predicting capillary cross-flow in layered reservoirs, SPE 26651-MS
- [3] James A. Wasson. Combination method for predicting waterflooding performance for 5-spot patterns in a stratified reservoir, SPE-2004, pp1195-1203
- [4] Noaman A.F. El-khatib. The application of Buckley-Leverette Displacement in non-communicating stratified RESERVOIRS, SPE 68976-MS
- [5] Roper W.A, Brown A., Teasdale T.S. Production performance of displacement processes in stratified reservoirs, SPE 194-MS
- [6] Silva L.F, Farouq .A. Waterflooding performance in the presence of stratification, SPE 3556-MS
- [7] Telleria M.S, Vriues C.J.J. Limitations in the use of the frontal advance theory for 2-Dimensional systems, SPE 54004



**Patrick Godwin Oyindobra Ossai**, is currently a post-graduate student at the Post Graduate School of Federal University of Technology Owerri located in Imo State, Nigeria. He holds a bachelors and masters of engineering degree (B.Eng, M.Eng) in Petroleum Engineering from the University of Benin and Federal University of Technology

Owerri respectively. He has to his credit a few seasoned international journal publications in enhanced heavy oil recovery, in-situ combustion applicability, Drilling optimization and well design. Patrick is also a seasoned oil logistics and QHSE expert with NEBOSH certifications. His field expertises are in the areas of Petroleum Engineering (EOR), Oil & Gas logistics and QHSE. He is happily married with kids.

**Ohia Nnaemeka Princewill**, is a Senior Lecturer/Instructor with the Department of Petroleum Engineering, Federal University of Technology, Owerri. After spending over two decades teaching and consulting for both local & international oil and gas companies working on multimillion dollar projects, Nnaemeka knows what truly drives performance, which is how well you connect with the people you're trying to help and communicate your understanding back to them. Nnaemeka's research interests in environmental protection, well engineering and production optimization has landed him with various certifications and awards around the world, including over 45 authored and co-authored journal publications to his credit. Today, Ohia is a member of notable professional bodies such as Council for Registered Engineers of Nigeria (COREN), Nigerian Society of Engineers (NSE) and Society of Petroleum Engineers. In addition to his extensive research, teaching and consulting experience, Nnaemeka is a trained technical coach. Nnaemeka holds a PhD in Petroleum Engineering from the Federal University of Technology, Owerri. (FUTO), Nigeria since 2012.



# In-situ Combustion: Reservoir Candidacy/Project Selection Criteria(s) For Niger Delta Heavy Oil Reservoirs

Patrick Godwin Oyindobra Ossai<sup>1</sup>, Ugochukwu Ilozurike Duru<sup>2</sup>, Boniface Obah<sup>3</sup>, Princewill Nnaemeka Ohia<sup>4</sup>

Department of Petroleum Engineering, Federal University of Technology, Owerri, Imo State, Nigeria<sup>1,2,3,4</sup>

engrpatrickossai@yahoo.com<sup>1</sup>, ugooduru@yahoo.com<sup>2</sup>, bonifaceobah@yahoo.com<sup>3</sup>, princepetra@yahoo.com<sup>4</sup>

Received: 12 April, Revised: 21 April, Accepted: 25 July

**Abstract**—There is a drastic need for the oil companies operating within the onshore(s) and offshore(s) of Nigeria to critically start looking at the various possibilities of heavy oil production from the nation's various fields located in the Niger Delta region using already available Enhanced Oil Recovery techniques/methods such as In-situ combustion (ISC), CHOPS and SAGD. This study focused on In-situ combustion as a means of enhancing likely heavy oil production in the Niger Delta using the Nelson & McNeil 1961 ISC model. The study developed applicable screening criteria(s) for both reservoir candidacy and ISC project selection in the Niger Delta. Corresponding programs and flow-charts that would allow petroleum engineers in the Niger Delta to theoretically evaluate production performances using his/her computer(s) was also developed. It was discovered also during our course of work that all six reservoirs considered in both Case 1 (Venezuela reservoir) and Case 2 (Niger Delta reservoirs) met this study's reservoir candidacy selection criteria(s) for possible applicability of an ISC project performance evaluation(s) with respect to enhancing oil production. These reservoirs were further graded / ranked based on their theoretical ISC project performances as calculated and evaluated using a well known ISC model as documented in the ISC handbook.

**Keywords**— In-situ Combustion ISC, Niger Delta, Reservoir Selection Criteria, Heavy Oil, Enhanced Oil Recovery EOR, Thermal Recovery, Nelson and McNeil ISC model

## I. INTRODUCTION

The importance of crude oil production to Nigeria's economy cannot be overemphasized. However, most will agree that the time of conventional oil, oil that was easy and cheap to find and produce is coming to an end (Nigeria's light oil isn't an exemption to this fact). As conventional oil fields reach maturity and global demand for oil increases, there is a shift to production from unconventional heavy oil reservoirs. They have recently become an important resource as conventional oil reservoirs are in sharp decline. Heavy oil reservoirs are considered to be non-conventional oil reservoirs, and are sometimes ignored as a source of oil because of the difficulties and cost involved in their development, which reduces their

economic viability. The main objective of an EOR method such as in-situ combustion is to achieve higher overall oil recovery and higher production rates. This study was able to demonstrate this theoretically using the Nelson & McNeil (1961) In-situ combustion model as documented in the In-situ Combustion Handbook (Partha, 1999) [10].

It is already a known fact that In-situ Combustion (ISC) is a good EOR technique that has incurred a bad reputation over the years as a result of wrong application and to wrong reservoir prospects. This study findings and development will save the oil industry both time, manpower and most especially money. It will further enhance the participation of both indigenous and multi-national oil and gas companies in boosting Nigeria's energy reserves by venturing into full scale commercial production from its heavy oil reservoirs in the Niger Delta. Applying the right EOR method like ISC to the right heavy oil reservoir prospect remains the key to boosting heavy oil production from the Niger Delta. Hence, this study's reservoir candidacy/ISC project selection and screening criteria (with its corresponding screening Program A and reservoir performance Program B) developed for the Niger Delta heavy oil reservoir will enthusiastically and practically encourage prospective oil companies to critically take steps leading to the eventual commercial production of heavy oil from unconventional reservoirs in the Niger Delta region.

### a. Heavy oil Recovery

Heavy oil recovery can be achieved by injecting steam down a vertical well and into a production zone for a short period. This well is now placed on production for a longer period. This cycle is subsequently repeated provided production is still profitable (Snow et al, 1998) [14]. On the other hand, In-situ combustion (ISC) is a thermal EOR technique that involves a fire-flooding process. Usually, thermal energy is produced in the reservoir by combustion, which is initiated with either an electric heater/gas burner or may occur spontaneously. Air is by far the most common way to introduce oxygen into a reservoir. It is compressed at the surface and continuously injected into the reservoir via the injection well. In the heating and combustion that occur, the lighter parts of the oil are vaporized and moved ahead. Depending on the highest temperature reached, thermal cracking is most likely to happen, and vapor products from this reaction also move downstream. Part of the oil is deposited as a

coke like material on the reservoir rock, and this solid material serves as the fuel in the process. Hence, as oxygen injection is sustained, a burning front slowly progresses through the reservoir, with the reaction components displacing vapor and liquids ahead toward production wells (Green & Willhite, 1998 and Prats, 1982) [4], [12].

As at today we have three types of in-situ combustion methods and they are:

1. Dry in-situ combustion: This occurs where air (oxygen) is the only injectant into the well.
2. Wet in-situ combustion: This takes place when water is injected along with air. Water effectively picks up energy in the burned zone behind the burning front.
3. Reverse in-situ combustion: This type has less application and the burning is carried out in a reverse manner. Combustion is usually initiated at the production wells. Oxygen is still injected at injection wells and so the burning zone tends to move in the direction opposite to the fluid flow (Green & Willhite, 1998) [4].

Injected gases and water, from both the water of combustion and re-condensed formation water, pick up energy as they pass through the burned zone and move toward the combustion front. A hot water-flood usually exists in this region, much in the same manner as in a steam injection process. Ahead of the steam plateau, the temperature decreases to the original reservoir temperature (Green & Willhite, 1998 and Al-Wadhahi et. al., 2005) [2], [4]. One common major problem with in-situ combustion is the difficulty in controlling the progression of the burning front. Sequel to the reservoir properties and fluid distributions the burning front may likely progress non-uniformly throughout the reservoir, but with poor volumetric contact. If proper conditions are not sustained at the burning front, the burning reaction can become weaken and stop completely. The process usefulness is lost if this takes place. Finally, due to the high temperatures produced, major equipment issues can take place at the wells (if such well are poorly designed to withstand thermal stresses). When in-situ combustion is applied in high temperature oxidation mode, the following reactions are expected to take place (Xia et al., 2001) [17]:

- I. Thermal Cracking:  
Crude heavy ends  $\rightarrow$  Crude light ends + Coke
- II. Oxidation of coke:  
Coke + Oxygen  $\rightarrow$  CO + CO<sub>2</sub> + H<sub>2</sub>O
- III. Oxidation of heavy residual:  
Crude heavy ends + Oxygen  $\rightarrow$  CO + CO<sub>2</sub> + H<sub>2</sub>O

#### b. Eor Displacement Mechanisms

Thermal EOR methods depend on various displacement mechanisms to recover heavy oil. The relative significance of each mechanism relies on the type of heavy oil being displaced and the related recovery processes involved. For in-situ combustion processes, the mechanisms are closely related to the thermal and temperature effects of the reservoir rock and

fluid properties. The oil displacement is as a result of the following:

1. Decrease in oil viscosity.
2. Thermal expansion of the reservoir fluids and rocks, thereby decreasing their densities.
3. Thermal cracking and distillation of the oil.
4. A solution gas drive from generated gas that promotes the flow of fluids within the reservoir toward the production wells.
5. Increased pressure gradient caused by the injected air and produced gases.
6. Effect of Gravity drainage: Mechanisms such as distillation drives and thermal expansion of the heated oil add to recovery as crude distillation leads to reduction in residual oil saturation.

Other important parameters to be considered during an EOR process include but not limited to the following:

- I. Reservoir Porosity and Oil Saturation: Economic oil recovery depends on this. This must be high enough to support commercial production. The product of both parameters (i.e.  $\phi \times S_o$ ) should be greater than 0.08 for combustion to be economically successful.
- II. Reservoir Oil Gravity: This parameter is not critical. But, the in-situ viscosity should be low enough to permit air injection that will result in oil production at the desired rate.
- III. Oil Nature of the reservoir: In heavy oil projects the oil has to be readily oxidizable at reservoir and rock matrix conditions. Laboratory experiments can determine the quantity of air required to burn a given reservoir volume (It was determined as 87,120lb/acre-ft. for a 5-acre 5-spot pattern for a heavy oil reservoir located in Venezuela). This is expedient when considering profitability of the process.

Note: The minimum air flux required to maintain higher temperatures at the burning front is projected as 0.125 ft. /day (0.04 m/day) for a successful ISC process. (Partha, 1999)

Table 1: Screening parameters for thermal recovery processes (Green & Willhite, 1998) [4].

Screening Parameters	In-situ Combustion	Steam
Oil Gravity, Deg API	9 - 25	10 - 34
In-situ oil viscosity, $\mu$ (cp)	$\leq 5000$	$\leq 15000$
Depth, D (ft)	$\leq 11500$	$\leq 3000$
Pay-zone thickness, h (ft)	$\geq 20$	$\geq 20$
Reservoir temp, $T_r$ (DegF)	Not Specified	Not Specified
Porosity, $\Phi$ (fraction)	$\geq 0.20$	$\geq 0.20$
Average permeability, k (mD)	$\geq 35$	250
Transmissibility, $kh/\mu$ (mD-ft/cp)	$\geq 5$	$\geq 5$
Reservoir pressure, $P_r$ (psi)	$\leq 2000$	$\leq 1500$
Minimum oil content at start of process, $S_o$ (fraction)	$\geq 0.08$	$\geq 0.10$
Salinity of formation brine (ppm)	Not Specified	Not Specified
Rock type	Sandstone or Carbonate	Sandstone or Carbonate

Many of the criteria(s) in Table 1.0 above do have similar characteristics for steam and in-situ combustion. Consequently, it is not uncommon to find a reservoir that can satisfy these criteria for both processes during an EOR process. Three criteria where there are significant differences include depth, reservoir pressure, and average reservoir permeability. In-situ combustion can be applied in reservoirs that have lower permeability than the permeability limit for steam injection because the air injection rates are sufficient to sustain the combustion front. Table 2.0 below compares recovery efficiency of ISC to other enhanced oil recovery EOR methods.

Table 2: Recovery Efficiency of ISC compared to other EOR methods (Hasiba and Wilson, 1975)[5].

Process	(A) Process Displacement Efficiency (%)	(B) Areal Sweep Efficiency (%)	(C) Vertical Sweep Efficiency (%)	(D) Compound Recovery Efficiency (%)
In-situ Combustion	95	70	85	56
Steam-flood	65	70	85	39
Cyclic Steam	--	--	--	20
Micro-Emulsion flood	90	70	80	50
CO <sub>2</sub> Water-flood	80	50	80	32
NaOH Water-flood	35	70	80	20

Note: (D) = (A) X (B) X (C), and Volumetric Sweep Efficiency = (B) X (C)

#### c. Screening and Reservoir Candidacy Selection Criteria (A)

Thermal EOR processes like any other EOR process involves tremendous planning, man-power, expertise / professionalism, expenditures and high cost of execution. Hence, the need of applying ISC process to the right reservoir

prospect is the key to the success of the whole thermal EOR process. To this end, the importance of screening and selecting the right reservoir candidacy for the applicability of ISC process cannot be overemphasized. Below is a table showing details of program 'A' developed to screen each reservoir properties based on minimum model selection criteria(s). If the reservoir properties pass the screening processes by program 'A' then it will be further considered for ISC applicability using program B. Based on similarities of reservoir properties we subjected Case 1 (Venezuela Heavy oil reservoir) and Case 2 (Five Heavy Oil reservoirs located in a Niger Delta Field that is about 45 miles or 72km East of Port-Harcourt, Rivers State, Nigeria (Kerunwa et al., 2014)) [6] to program A (screening and selection processes) & program B (ISC project performance evaluation using the Nelson and McNeil model) respectively. See the appendix section below for a combined flowchart that shows the processes for both programs. Below Table 3.0 details the minimum screening criteria(s) that can be inputted into our study model's program 'A'.

Table 3: Program A' input data detailing the minimum In-situ combustion screening criteria(s) and Reservoir Candidacy/ Project Selection for Niger Delta heavy oil reservoirs

Input	Input Description with units	Minimum Model Screening Criteria(s)
A	Porosity $\phi$ , (%)	$> 20$
B	Permeability k, (mD)	$> 50$
C	Oil Gravity (deg API)	$> 6 < 25$
D	Oil Viscosity $\mu$ , (cp)	$< 5000$
E	Oil Saturation $S_o$ , (%)	$> 50 < 100$
F	Net Pay Thickness h, (ft.)	$> 10 < 200$
G	Reservoir Depth H, (ft.)	$< 3500$
H	Reservoir Temperature $T_r$ , (deg F)	$> 100 < 135$
I	Air Flux (ft./day)	$> 0.125$
J	Transmissibility "k.h/ $\mu$ ", (mD.ft/cp)	$> 5$
K	Relationship " $\phi$ . $S_o$ " (%)	$> 0.08$
L	Compressor Pattern Sequence	$> 4$
M	Compressor Number of Stages	$> 3$
N	Burning rate (ft./day)	$> 0.125 < 0.5$
O	Frontal Advance Rate (ft./day)	$> 0.125 < 0.5$
P	Reservoir Area Extent (acres)	$> 1 < 5$

## II. PERFORMANCE EVALUATION USING PROGRAM "B"

After a successful reservoir screening and candidacy selection process using program 'A' there is the need to theoretically evaluate the ISC project performances for these reservoirs using a suitable ISC model.

#### a. Introducing the Study Model

Program B was tailored to carry out ISC performance evaluation theoretically using a particular ISC model (see table 4.0 below for program 'B' details). This is done after a particular reservoir has been screened and selected as a potential candidate for ISC project by our study program 'A'. At this point, this study looked at the applicability of Nelson & McNeil ISC model as documented in the ISC handbook for ISC performance evaluation (Partha, 1999) [10]. In 1961, Nelson & McNeil gave engineering details (backed with equations) on how to evaluate the performance of a dry ISC

project. Despite the large number of assumptions made, the model's method and its applicability is centered on considerable field work/expertise. Hence, it can deliver reasonable production estimates as shown in this study results.

Table 4: Program B input data for applicability of the Nelson & McNeil model and its ability to predict ISC performance with respect to enhancing heavy oil production from oil reservoirs

Input	Input Description with Applicable units
A1	Total Air Requirement @ a sweep efficiency of 62.6% (MMscf/acre-ft)
B1	Total Air Volume needed for the 5-spot @ a sweep efficiency of 62.6% (MMscf)
C1	Air Flux needed to sustain the burning front advancement @ 0.125ft/day (scf/ft2day)
D1	Maximum Air Rate (MMscf/day)
E1	Time needed to reach maximum air rate (days)
F1	Volume of injected air during period (MMscf)
G1	Volume of injected air @ constant rate period (MMscf)
H1	Duration/time of the constant rate period (days)
I1	Total time for the entire burning period (years)
J1	Maximum Air injection period (psia)
K1	Compressor Horsepower Requirements for a 4 pattern sequence with 3 stages
L1	Fuel consumption during combustion (lbs/ft3)
M1	Volume of Oil displaced per acre-ft burned (bbl/acre-ft) "Np <sub>1</sub> "
N1	Volume of Oil displaced per acre-ft for unburned portion of the reservoir (bbl/acre-ft) "Np <sub>2</sub> "
O1	Total Volume of Oil Recovery (bbl/acre-ft) "Np <sub>3</sub> "
P1	Overall Recovery Efficiency (%) "ER"
Q1	Oil Recovered per millions scf of injected air (bbl/MMscf)
R1	Maximum Oil Production (bbl/day)
So	Oil Saturation (%)
Φ	Porosity (%)
H	Net pay thickness (ft) (> 30ft)
L	Spacing between injection and production well (> 330ft)

## b. Assumptions

### (i) Model's Assumptions:

- The air injection rate depends on the desired rate of advance of the burning front.
- Satisfactory burning rate ranges from 0.125-0.5 ft. / day.
- Maximum air rate is based on the minimum burning rate of 0.125 ft./ day

**Note:** Details of the formulas and calculations used in achieving the below result tables for this study (considering Case 1 & 2) can be found as documented in the ISC Handbook (Partha, 1999).

Case 1 and 2 tables below details the various reservoir(s) parameters subjected to our study's model and its performance evaluation equations/assumptions.

## Case 1: Venezuela Heavy Oil Reservoir Data (Partha, 1999)

Parameters	Values
Formation thickness	25ft
Formation temperature	146°F
Porosity	22.6%
Specific permeability	1000md
Oil saturation	55%
Water saturation	40%
Production well radius	0.276ft
Oil Gravity	13° API
Oil Viscosity	280cp

## Case 2: Five Niger Delta Heavy Oil Reservoir Data from same Oilfield 45miles/72km East of Port-Harcourt, Nigeria (Kerunwa et al., 2014) [6].

Parameters	Niger Delta Reservoir A	Niger Delta Reservoir B	Niger Delta Reservoir C	Niger Delta Reservoir D	Niger Delta Reservoir E
Pay Thickness (ft)	110	152	69	71	33
Pressure (psia)	2794	3384	1816	2033	2612
Temperature (°F)	128	164	113	122	127
Oil Gravity (° API)	18.08	21.80	19.19	19.03	22.14
Permeability (mD)	600 – 1500				
Oil Saturation, (%)	83.40	82.10	82.60	81.40	22.20
Oil Viscosity(cp)	86.75	4.76	31.81	25.49	29.31
Water Saturation (%) (1-5)	16.40	17.60	16.70	18.30	77.03
Porosity (φ)	20% - 30%				

c. Result(s) in Summary

Table 5: Calculated Maximum Oil Production (M.O.P) and Compressor Horsepower Requirements (C.H.R) (P.G.O OSSAI et al., 2017) [9].

	Venezuela Reservoir	Niger Delta Reservoir A	Niger Delta Reservoir B	Niger Delta Reservoir C	Niger Delta Reservoir D	Niger Delta Reservoir E
<b>M.O.P</b> (bbl/day)	87.6	536.9	728.9	333.4	337.3	268.1
<b>C.H.R</b> (bhp/day)	2017	8868	12249	5565	5724	2661

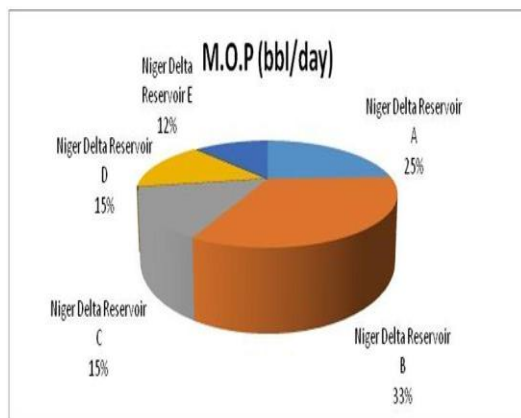


Figure 1: Pie chart showing the percentages of maximum oil productions, M.O.P (bbl/day) for the five Niger Delta reservoirs considered using the ISC model

Table 6: Calculated Max. Oil Production, M.O.P (bbl/day) and Maximum Air Injection Requirement(s), M.A.R ( MMscf/day)

	Venezuela Reservoir	Niger Delta Reservoir A	Niger Delta Reservoir B	Niger Delta Reservoir C	Niger Delta Reservoir D	Niger Delta Reservoir E
<b>M.O.P</b> (bbl/day)	87.6	536.9	728.9	333.4	337.3	268.1
<b>M.A.R</b> (MMscf/day)	1.910	8.398	11.600	5.270	5.420	2.520

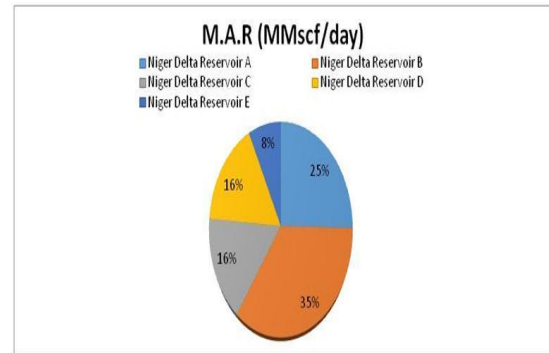


Figure 2: Pie chart showing percentage details of maximum air injection requirements, M.A.R (MMscf/day) for the five Niger Delta reservoirs considered using the ISC model

Table 7: Calculated Oil Displaced (from the burned zone) and Oil Displaced (from the unburned zone)

	Venezuela Reservoir	Niger Delta Reservoir A	Niger Delta Reservoir B	Niger Delta Reservoir C	Niger Delta Reservoir D	Niger Delta Reservoir E
<b>Oil Displaced "burned zone"</b> (bbl/acre-ft)	716	1046	1026	1034	1015	952
<b>Oil Displaced "Unburned zone"</b> (bbl/acre-ft)	386	518	510	513	506	1200

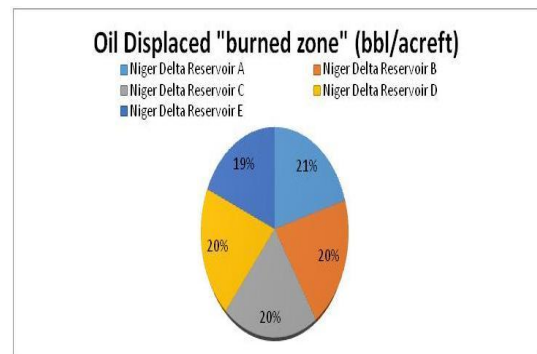


Figure 3: Pie charts showing percentage details of oil displacement from burned zones for the five Niger Delta reservoirs considered using the ISC model

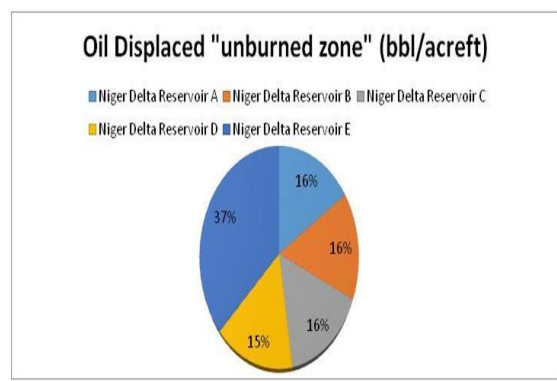


Figure 4: Pie charts showing percentage details of oil displacement from the unburned zones for the five Niger Delta reservoirs considered using the ISC model

Table 8: Calculated Total ISC Period (Time) and Total Oil Recovery

	Venezuela Reservoir	Niger Delta Reservoir A	Niger Delta Reservoir B	Niger Delta Reservoir C	Niger Delta Reservoir D	Niger Delta Reservoir E
Total ISC Period/Time (years)	2.24	2.24	2.24	2.24	2.24	2.24
Total Oil Recovery (bbl/acre-ft)	485	676.4	664.8	669.4	658.4	1125.6

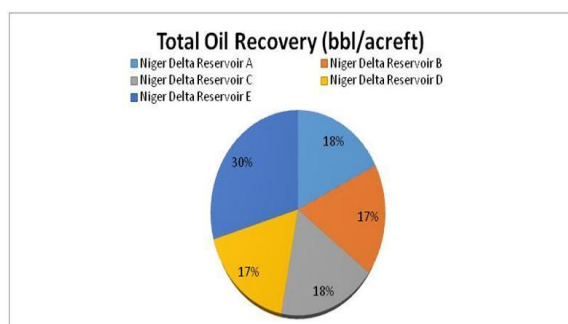


Figure 5: Pie chart showing percentage details of the total oil recovered from the five Niger Delta reservoirs considered using the ISC model

#### d. Reservoir Selection Hierarchy/Ranking based on ISC Performance Evaluation Results

The performance of each reservoir (considering Case 1&2) is depicted in percentages from figure 1 to figure 5 depending on specific evaluation results calculated via the applicability of the ISC model. Below also are Table 9 and Table 10 showing the performance grading/positions for these reservoirs. Figure 6 gives the final ISC project selection rankings for each reservoir considered using the Nelson and McNeil ISC model.

Table 9: Reservoir grading using 1<sup>st</sup> to 6<sup>th</sup> based on ISC performance/evaluated outcomes for Case 1&2 considered respectively

OUTPUT(S)	Venezuela Reservoir	Niger Delta Reservoir A	Niger Delta Reservoir B	Niger Delta Reservoir C	Niger Delta Reservoir D	Niger Delta Reservoir E
Max. Oil Prod.(bbl/day)	6 <sup>th</sup>	2 <sup>nd</sup>	1 <sup>st</sup>	4 <sup>th</sup>	3 <sup>rd</sup>	5 <sup>th</sup>
Max. Air Inj. (MMscf/day)	1 <sup>st</sup>	5 <sup>th</sup>	6 <sup>th</sup>	3 <sup>rd</sup>	4 <sup>th</sup>	2 <sup>nd</sup>
Oil Displaced "burned zone"(bbl/acrefit)	6 <sup>th</sup>	1 <sup>st</sup>	3 <sup>rd</sup>	2 <sup>nd</sup>	4 <sup>th</sup>	5 <sup>th</sup>
Oil Displaced "Unburned zone"(bbl/acrefit)	6 <sup>th</sup>	2 <sup>nd</sup>	4 <sup>th</sup>	3 <sup>rd</sup>	5 <sup>th</sup>	1 <sup>st</sup>
Total Oil Recovery (bbl/acrefit)	6 <sup>th</sup>	2 <sup>nd</sup>	4 <sup>th</sup>	3 <sup>rd</sup>	5 <sup>th</sup>	1 <sup>st</sup>

Table 10: Final Reservoir selection rankings for the ISC project based on grading/position frequencies

	1 <sup>st</sup> (FREQ)	2 <sup>nd</sup> (FREQ)	3 <sup>rd</sup> (FREQ)	4 <sup>th</sup> (FREQ)	5 <sup>th</sup> (FREQ)	6 <sup>th</sup> (FREQ)	Final Reservoir Selection Rankings
Venezuela Reservoir	1	0	0	0	0	4	6 <sup>th</sup>
Niger Delta Reservoir A	1	3	0	0	1	0	1 <sup>st</sup>
Niger Delta Reservoir B	1	0	1	2	0	1	5 <sup>th</sup>
Niger Delta Reservoir C	0	1	3	1	0	0	3 <sup>rd</sup>
Niger Delta Reservoir D	0	0	1	2	2	0	4 <sup>th</sup>
Niger Delta Reservoir E	2	1	0	0	2	0	2 <sup>nd</sup>

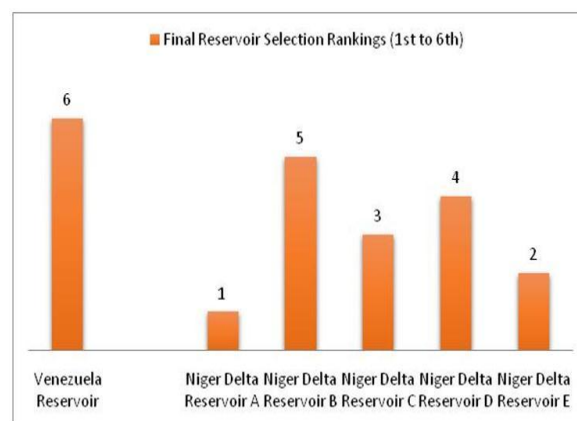


Figure 6: Reservoir Rankings based on ISC performance evaluations for all six reservoirs considered using the Nelson and McNeil ISC model

#### e. General Result Discussion(s) and Interpretation(s)

From result table 5 and Figure 1, the benefits of achieving maximum oil production (bbl/day) using the Nelson & McNeil ISC model came with an increasing cost of compressor horsepower requirements (BHP). Hence, the success, viability and profitability of the ISC project for achieving higher oil



production isn't without paying the price of increasing compressor horsepower demands.

From the result table 6 and Figure 2, it can be seen also that a successful thermal EOR project of achieving profitable maximum oil production rates (bbl/day) from all six reservoirs considered using the Nelson & McNeil ISC model also came with an increasing maximum air injection requirements (MMscf/day) at an additional cost. Theoretically, we can see clearly that maximum oil productions (bbl/day) has direct proportionality with compressor horsepower (BHP) and maximum air injection requirements (MMscf/day) for the thermal EOR process.

From our study's result table 7, Figure 3 and 4, and its corresponding ratio analysis it will be seen that oil displaced from the burned zone of the six reservoirs considered (irrespective of their locations) is almost 50% higher than the oil displaced from the unburned zone of these reservoirs. The drastic reduction in the oil viscosity in the burned zone is due to the high temperature created by the intense in-situ burning process. This accounts for the higher oil displacement from the burned zone over the unburned zone of these six reservoirs considered using the ISC model. Reduction in oil viscosity within the burned zone during the ISC process means increase in its oil flow properties. But, oil displacement from both zones contributes to the overall daily oil production resulting from the thermal EOR process.

From result table 8 and Figure 5, the total oil recovery (bbl/acre-ft) was achieved at the same period of 2.24 years for all six reservoirs considered irrespective of the reservoir locations (Nigeria or Venezuela) using the Nelson & McNeil ISC model.

Furthermore, all six reservoirs (case 1 & 2 respectively) considered by this study was observed to have passed the reservoir candidacy and selection processes for ISC project implementation. Hence, these reservoirs are all viable for subjection to ISC project performance evaluations as documented in this study for possible enhanced oil recovery with heavy oil production at commercial scale. But, ISC project/Investment priorities should first be given to Niger Delta reservoir A because of its highest ISC performance selection ranking, followed by Niger Delta reservoir E and then Niger Delta reservoir C. These three reservoirs have the highest selection rankings and are most likely to yield the fastest return on investments made on the production outcomes resulting from the ISC project(s).

#### CONCLUSION

This study findings and developments will allow oil companies and other relevant stakeholders in the oil industries to subject their heavy oil reservoirs to our reservoir candidacy/ISC project selection processes (Program A), and subsequently to the study's production performance evaluations using program B respectively. It will invariably reduce ISC project/process risks involved in the thermal EOR

process. It will also save the oil industry both time, manpower wastage and most especially in the area of cost reduction. Finally, the Nigeria government as at today despite their diversification drives still depend on internally generated revenue from light/cheap oil produced from conventional reservoirs in the Niger Delta region, south of Nigeria (Ossai PGO et al., 2017) [11]. Hence, we can say invariably that "if in-situ combustion projects and its processes are applicable at commercial scale in Venezuela then why not in Niger Delta region of Nigeria?"

#### RECOMMENDATION(S)

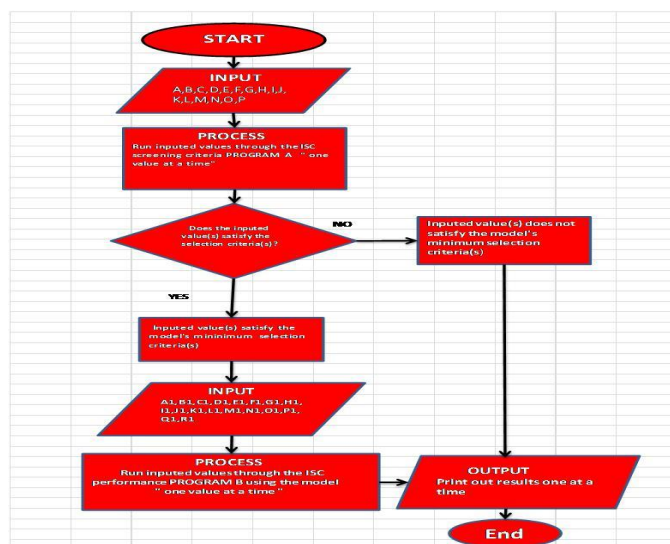
Despite the enormous challenges associated with thermal EOR processes like ISC it is also expedient that heavy oil reservoirs be selected more carefully before embarking on any thermal EOR project. The importance of willingness to do it, the right expertise, adequate funding and the need to subject each reservoir samples to combustion tube test cannot be ignored for ISC projects. Hence, applying the right thermal EOR method like ISC to the right oil reservoir prospect remains the key to boosting oil production from conventional and unconventional oil reservoirs. There are potential heavy oil reservoirs in the Niger Delta and in other regions worldwide that deserves possible thermal EOR attention at commercial scale from all relevant stake holders in the oil industry for future energy sustainability.

#### REFERENCES

- [1] Alizadeh AH et al (2014): Multi-Scale Experimental Study of Carbonated Water Injection: An effective process for mobilization and recovery of trapped oil. *Fuel*, 132 (2014) 219-235
- [2] Al-Wadhahi, M., Boukadi, F., Al-Bemani, A. (2005) .Nimr EOR Identification – Phase 1, Department of Petroleum and Chemical Engineering, Sultan Qaboos University
- [3] Chukwudeme EA, Hamouda AA (2009): Enhanced Oil Recovery (EOR) by miscible CO<sub>2</sub> and water flooding of asphaltenic and non-asphaltenic oil, *Energy journal*, 2, 714-737, DOI: 10.3390/en20300714
- [4] Green, D. W., Willhite, G. P (1998) .Enhanced Oil Recovery", SPE.
- [5] Hasiba, H.H, Wilson, L.A, (1975). The Potential Contribution of Enhanced Oil Recovery Technology to Domestic Crude Oil Reserves
- [6] Kerunwa A, Anyadiegwu C.I.C, Ugwuanyi, A.C (2014). Enhance Recovery of Heavy Crudes in Niger Delta: CHOPS Application A key Option, *The Journal of Applied Sciences Research*, Vol 1, No 3 (2014).
- [7] Muhammad M.R, Mahmoud M (2012): Conventional versus Enhanced Oil Recovery: A review. *Journal of Petroleum Exploration and Production Technology*, DOI: 10.1007/s13202-012-0034-x
- [8] Nelson, T.W, McNeil, J.S (1961). How to Engineer an In-situ Combustion Project, *Oil and Gas Journal*, June 5, 1961, pp58-65
- [9] Ossai, P.G.O, Ohia, P.N, Obah, B, Duru, U.I, Onaiwu, D.O (2017). Enhanced Recovery of Heavy Oil in the Niger Delta: Nelson and McNeil model a key option for in-situ combustion application. *Advances in Petroleum Exploration and Development*. (14) 2, 27-33, DOI:http://dx.doi.org/10.3968/10009
- [10] Partha, S.S (1999). In-Situ Combustion Handbook — Principles and Practices, published 1999 by National Technology Information Services (403 pages)
- [11] Patrick G.O. Ossai, Princewill N. Ohia, Boniface Obah & Ugochukwu I. Duru (2017) In situ combustion: Applicability to heavy oil reservoirs in the Niger Delta, *Petroleum Science and Technology*, 35:1, 51-58, DOI: 10.1080/10916466.2016.1247172
- [12] Prats, M (1982) .Thermal Recovery, SPE, New York

- [13] Sacuta, Aleksy (1980): Enhanced Oil Recovery using Electrical means.  
US Patent No: 4,228,854
- [14] Snow, Dennis M, Tim AO (1998): Method for Enhanced Recovery of  
viscous oil deposits, US Patent No: 5,826,655
- [15] Stevens S, Kuuskraa VA (1998): Enhanced Oil Recovery scoping study,  
Final Report. Palo Alto, Electric Power Research Institute.
- [16] Wang Xinkui (2010): Experimental and Numerical Studies on Multiple  
Well Pairs SAGD Performance: A thesis submitted to the Faculty of  
Graduate Studies and Research, University of Alberta.
- [17] Xia, T. X (2001). Down-hole Upgrading Athabasca Tar Sand,  
SPE69693 presented in the 2001 SPE, International Thermal Operations  
and Heavy Oil Symposium. Porlamar, Margarita Island, Venezuela, 12  
March.

## APPENDIX



A combined flow chart of program A and B to demonstrate the applicability of the whole process (reservoir screening/selection and ISC project performance evaluation).

# An Investigation on the Flow Behavior in the Airfoil of a Flapping Wing

M.Amin Nikbakht<sup>1</sup>, Soheil Mohtaram<sup>2</sup>, Mohammad Hasan Moghadas<sup>3</sup>

Department of Mechanical Engineering, Islamic Azad University, Esfahan, Iran, Amin.nikbakht88@gmail.com<sup>1</sup>

College of Mechanics and Materials, Hohai University, Nanjing 210098, China, Soheil@hhu.edu.cn<sup>2</sup>

Department of Mechanical Engineering, Malek-Ashtar University of Technology, Iran. mhmogh@yahoo.com<sup>3</sup>

Received: 21 July, Revised: 28 August, Accepted: 30 August

**Abstract**—In this investigation, the two-dimensional dynamic analyses of the wing airfoil of a swing-wing micro air vehicle (MAV) were carried out under restrained pitching and flapping oscillations, which varied in the 10-degree oscillation range and the 0.1-10 reduced frequency range. The flow was in a laminar flow with a Reynolds number of 1100. The objective of this simulation was to study the flow behavior in the dynamic motions in a dynamic stall regime. Similar studies on the dynamic stall regime with low Reynolds numbers have not resulted in a particular numerical solution and have separately studied the parameters influencing the numerical solution. The most critical dynamic motions that require utmost precision in numerical analyses were reviewed and validated in this research. The results of the numerical research analyses were compared to the experimental results obtained with a water tunnel.

**Keywords**— micro air vehicle, flapping, pitching, dynamic stall, hysteresis

## I. INTRODUCTION

Unmanned aerial vehicles (UAVs), which use for different purposes such as detection [1], and discovery [2], are among the most military equipment which commonly used by state armies. The lack of need for human pilots in these vehicles along with their size, weight, and low cost has increased the reliability of these vehicles as compared to other alternatives. Recently, UAVs are widely used and are classified into the military and nonmilitary categories by application [3]. Some of the military areas of application of UAVs include espionage and suicidal operations, and the increased reduction in the size of these vehicles is aimed at conducting intelligence operations and attaining military group goals. In addition to the mentioned military uses, these vehicles offer numerous capabilities in the sea, space and on land. Some of these applications include forestry, environmental protection, examination of petroleum and gas lines, etc. Nowadays, unmanned air vehicles are available in different forms and vary by weight and size. These vehicles are grouped into the unmanned air vehicle (UAV) and complex air vehicle (CAV) categories.

The first inclusive research on MAVs was conducted in 1993 by the RAND institute [4]. Later on, extensive research

was carried out on micro air vehicles by various researchers [5]. Today, studies and activities are focused on the construction of MAVs smaller than 15cm for detection and rescue purposes [6]. These air vehicles are small in size and fly slowly [7]. MAVs are grouped into the categories of fixed-wing MAVs, rotary-wing MAVs, VTOL (vertical take-off and landing) micro air vehicles, and the so-called ornithopters. Currently, the design of most ornithopters is inspired by bird and insect anatomies [8]. The first functional ornithopter was built in 1870 in France. The Gustav Tropez flew about 70 meters in an exhibition held by the Académie des Sciences. The wings moved with the activation of the Bourdon tube by gunpowder. In 1871, Jobert et al. [9,10] used rubber bands to enable a small ornithopter to fly. Research on ornithopters has indicated that they are less common than fixed- and rotary-wing MAVs mainly because of their aerodynamic complexity. Hence, fewer studies have been conducted on fixed- and rotary-wing air vehicles [11]. Most micro air vehicle development works are focused on insect models. In spite of the challenges associated with the imitation of the complicated unsteady aerodynamic mechanisms of flapping wings with low Reynolds numbers, insects are considered valuable models in the design of MAVs due to advantages such as their small sizes and power-to-weight ratios. Ornithopter MAVs are generally classified into the NAV, PAV, and MAV groups. The design of MAV, PAV (Pico Air Vehicle), and NAV (Nano Air Vehicle) ornithopters are inspired by birds, insects, and bird-like insects, respectively. In the construction of ornithopter MAVs, shape memory alloys, piezoelectric materials and smart materials are used as flapping stimuli especially in the products of the NAV and PAV categories depending on weight. These materials are also commonly used in PAV micro air vehicles which aren't allow to be used in electric motors. Since bigger birds are unable to move their wings back and forth, they spread their wings downward along the strike direction. They bend their wings along the upward strike to reduce the drag. In general, bending is more highlighted during slow forward flying than rapid forward flying. This state of suspension in the asymmetric space is called the "bird strike" [12,13]. To avoid large drag forces and negative lift forces, these birds bend their wings upward along the strike direction by moving the primary feathers to allow for the inflow of air. Therefore, the dynamic motions of bird wings include simultaneous pitching (rotary movements) and plunging (upward and downward movements)

that together form the flapping function. These motions induce thrusting along the movement direction using the flow properties in the dynamic stall regime. The effects of the unsteadiness of flow were for the first time observed through the rapid variation of the attack angle of an airfoil by Kramer [14]. Following his preliminary research, the dynamic stall phenomenon attracted little attention due to the limited precision of the data collection equipment of the time until extensive research was conducted on the adverse effects of the dynamic stall in 1960 [15,16]. This attention was the result of the abrupt deviation of the pitching moment from the static state, the resulting constraints on the flight coverage of air vehicles, and the need for selection of materials for helicopter propellers. Dynamic stall has also been observed in the propellers of wind turbines [17, 19]. This phenomenon limits the performance of turbines and results in the structural fatigue of the propellers [20]. The result of these consequences is the increase in the overhaul and maintenance costs. In the wind turbine propellers, the dynamic stall is mainly the result of the unsteady inflow, abrupt winds, and rapid wind direction variations [21, 22]. In fixed-wing air vehicles, the flow of a large volume of flow perpendicular to the wing may cause the dynamic stall on the wing during the flight and irritate the occupants. One of the motives for the research on dynamic stall is the interest in omitting or reducing the damaging effects of this phenomenon [23-29]. However, it must be stated that this phenomenon is not always destructive and studies have been carried out on the utilization and control of this phenomenon in increasing the lift. This area of application is mainly considered in studying the flying behavior of insects and birds. Birds, insects, and fish generally move by flapping [30, 31]. Studies of birds suggest that the wing surface and its apparent ratio (AR) [32] are smaller than the body, which accounts for their steady flight [33]. Hence, the insects and birds utilize dynamic stall and increase the unsteady lift to remain suspended during the flight [34]. The need for increasing the maneuverability of aircraft has attracted the attention of researchers to airfoil pitching oscillations at large attack angles [35-37]. Moreover, the use of micro air vehicles for the military purposes and filming hard-to-reach places has been the motive of many researchers for studying and understanding the unsteady aerodynamics of dynamic stall and for increasing the lift force. In spite of all of the recent attempts and progress in understanding the separation of unsteady flows, the dynamic stall phenomenon is one of the major unsolved aerodynamic problems. Hence, a more precise understanding of flow separation is required for utilizing flows. On the other hand, it is impossible to carry out these examinations experimentally in a wind tunnel because of its high expenses and the numerical solution that gives a more precise understanding of flow separation is still unknown. Therefore, this study was an

attempt to assess and validate numerical methods in the fluent commercial software.

In this research, a three-dimensional mesh was created using the square element method. Then, A C-type mesh was made, and the solution range covered a length 20 times the airfoil mid-chord in the flow upstream to a distance 30 times the airfoil mid-chord in the flow downstream. It also covered a diameter 20 times greater than the airfoil mid-chord in the upward and downward directions. The most straightforward and most practical method for the numerical simulation of a viscous flow involves the Navier–Stokes equations. The three-dimensional and incompressible Navier–Stokes equations were used in this research. Moreover, a computation method based on the control volume was used to solve the applicable equations.

## II. THE NATURE UNSTEADY FLOW ON A PITCHING AIRFOIL

For a more precise aerodynamic examination of a pitching model, a pitching airfoil is analyzed in this section. The results of this analysis, which are presented in the following, reflect the aerodynamic complexity of this airfoil. During the pitching of an airfoil (which occurs around one-quarter of its mid-chord), if the pitching occurs at the angles near the static stall, the lift hysteresis ring and pitching moment will be as shown in Figure. 2. Analyses of unsteady flows and phenomenon occurring during oscillations clarify the nature of flow on lambda wings. During pitching, when the attack angle of the oscillation model is larger than the stall attack angle in the static state (point a), first the reversal of flow in the boundary layer occurs and large eddies form in the boundary layer. As the attack angle grows, an eddy forms near the leading edge. The formation of the latter eddy increases the lift slope, which corresponds to point b. Meanwhile, the pitching moment stalls and the leading-edge eddy grows in size with an increase in the attack angle and moves toward the airfoil trailing edge until the dynamic lift factor is maximized and the airfoil stall begins. The result is the most harmful pitching moment. Following the full stall, as the attack angle decreases, the boundary layer is attached from the front of the airfoil to the rear and the surface of the airfoil (part d of the figure). When the flow connects to the surface, it returns to the static state.

The control of the dynamic stall eddy on the upper surface, which is aimed to delay its reattachment to the upper surface, increases the lift and transfers the dynamic stall angle for a long time during the pitching cycle to large attack angles [38]. The increase in the lift and delay of the dynamic stall attack angle depend on numerous parameters such as the oscillation range and frequency, flow regime, and Reynolds number [39, 40].

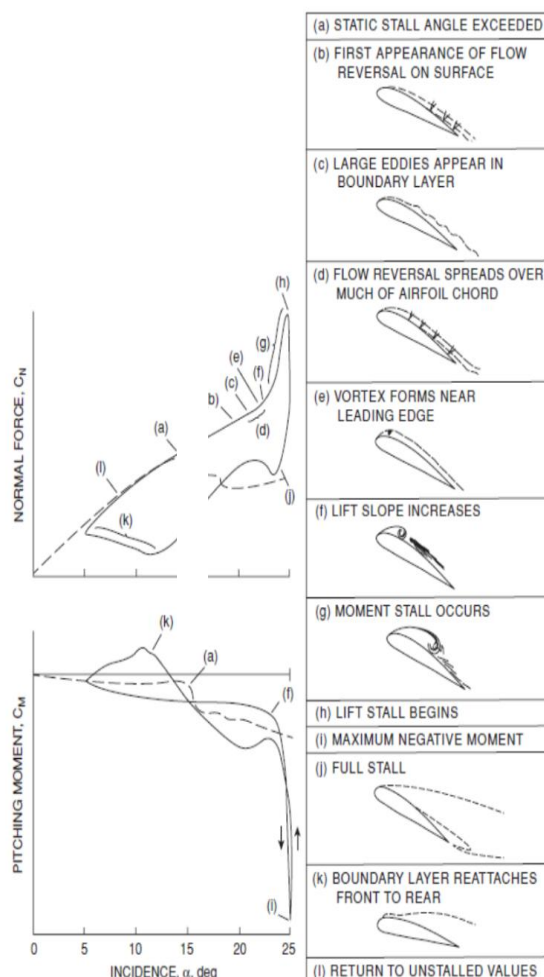


Figure.1. the dynamic stall phenomenon on a pitching airfoil [41]

### I. 3. Mesh Generation and Numerical Solution Range

#### A. 3.1 Mesh Generation

In this research, a three-dimensional mesh was created using the square element method in ANSYS. A C-type mesh was generated, and the solution range covered a length 20 times the airfoil mid-chord in the flow upstream to a length 30 times the airfoil mid-chord in the flow downstream. It also covered a distance 20 times the airfoil mid-chord in the upward and downward directions (Fig. 2). The most straightforward and most practical method for the numerical simulation of a viscous flow involves the Navier–Stokes equations. The three-dimensional and incompressible Navier–Stokes equations were used in this research. Moreover, a computation method based on the control volume was used to solve the applicable equations.

The first step in the numerical simulation of flow in a field (especially in the presence of viscous flows) is meshing the field and converting it from a continuum into a discrete space for the application of numerical methods. It was tried to generate several 18000- to 91000-element meshes before the calculations and to numerically solve the problem under the conditions described in the following to select the optimum mesh for the subsequent analyses. To examine the effect of independence from the mesh, the number of nodes was increased as long as the drag coefficient remained unchanged and with the minimum difference from the experimental drag coefficient. Finally, a 43000-element mesh was used, and 20 rows of boundary layer elements were used on the airfoil. The first element height was 0.5mm. The mesh geometry is depicted in Fig. 4.

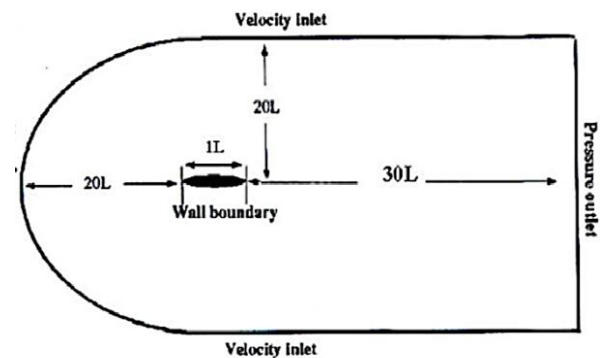


Figure.2. The computation range of the ornithopter airfoil

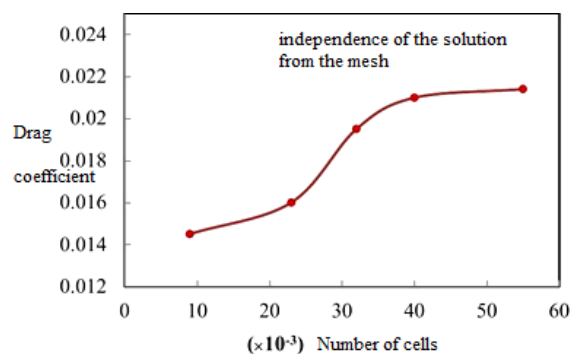


Figure.3. The effect of the independence of the solution from the mesh based on the drag coefficient



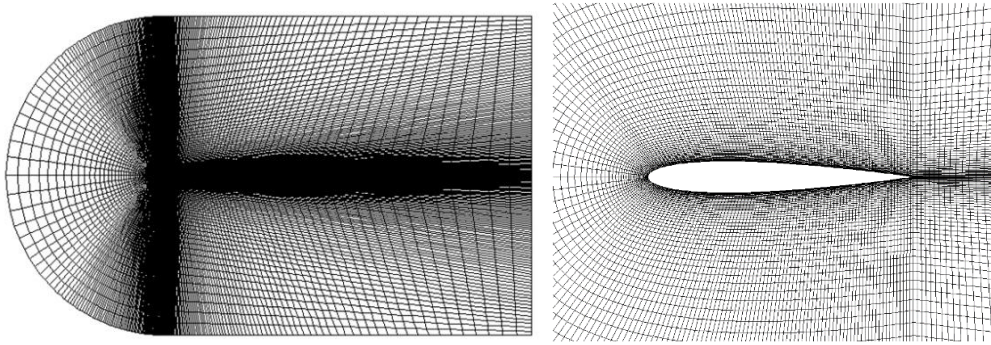


Figure.4. Organized elements around the NACA 0012 airfoil

### B. 3.2 Numerical Simulation Method

The flow around the NACA 0012 airfoil was solved under sea level conditions. The inflow velocity was adjusted to have a Reynolds number of 1100. The pressure-based solver [42, 43] was used in the numerical analysis and the flow was solved as

#### 1) 3.2.1 Main Dynamic Stall Parameters

One of the leading causes of the higher difficulty of the dynamic stall modeling and analysis as compared to static and steady stall modeling and analysis is the dependence of the former on several parameters. In the steady static state, the airfoil geometry, surface roughness, free flow turbulence, the Reynolds number, and Mach number influence the stall behavior [44]. However, during the dynamic oscillation of an airfoil at a constant pitching rate, stall depends on several parameters such as compressibility, Reynolds number, reduced oscillation frequency, oscillation axis position, three-dimensional flow, wind tunnel wall effects, and airfoil geometry. In addition, during sinusoidal airfoil oscillations, the maximum attack angle and the average attack angle are two of the critical parameters [45]. Numerical analyses have been carried out at small attack angles and reduced low frequencies, and given the low complexity of flow, it is possible to carry out these analyses using the most straightforward models and numerical algorithms with relatively high precision.

#### 2) 3.2.2 Reduced Frequency

The reduced frequency is used to express the unsteady nature of flow on airfoils and wings [46]. This parameter is defined as grows considerably [51, 52]. The present research was centered on numerical analyses at high reduced frequencies that may

an unsteady flow. The coupling of velocity and pressure was used along with the second-order spatial discretization. The no-slip wall was used as the boundary condition for the airfoil and the boundary condition around the solution field was far-field pressure. The time step for the unsteady flow solution was 0.001.

the ratio of the connective timescale ( $C/U$ ) to the forced oscillation timescale ( $1/\dot{\alpha}$ ) [47]. For an airfoil with a length of  $C$ , the pitching around one-fourth of the mid-chord at a constant pitching rate,  $\dot{\omega}$  (rad/s), the reduced frequency is defined as follows [48].

$$K = \frac{\omega C}{2U} \quad (1)$$

When  $k=0.1$ , the connective timescale, and oscillation time scale are of the same order, and the flow is unsteady. Even when the reduced frequency is as low as 0.05, there is a considerable difference between the static and dynamic stall characteristics [53]. According to Leishman, reduced frequencies higher than 0.05 are more critical because the unsteady aerodynamics properties can result in significant fluctuations in the pressure acting on the airfoil or wing surface and increase the lift force. At reduced frequencies lower than 0.05, the flow functions as a quasi-steady flow [50].

Numerous studies have been conducted to understand the effects of reduced frequency on the dynamic stall characteristics of different airfoils, and it has been reported that with an increase in the reduced frequency, the dynamic stall is delayed and transferred to larger attack angles. In addition, the lift force generated by the airfoil cause thrusting and forward movements of air vehicles during flapping.

5-degree average attack angle. The results of the aerodynamic coefficients of the problem solution are presented in the following. The parameters required for solving this problem are listed in Table.1. Since the average attack angle (=5 degrees) and the frequency are known the real-time attack angles are obtained using the following relation.

## II. RESULTS AND DISCUSSION

### A. 4.1. Aerodynamic Coefficients in the Static State

In our numerical simulations, the NACA 0012 mid-chord length was 1 meter, the flow density was 1000 kg/m<sup>3</sup>, and the flow Reynolds number was 1100. The numerical analysis of angular airfoil oscillations was carried out in the 3.183-6.3660 frequency range, the 10-20 reduced frequency range, and at the  $\theta = \theta_0 \sin[2\pi f(t - t_0)]$  (2)



After obtaining the time values and drag coefficient from the problem solution, it is possible to produce the attack angle

and thrust coefficient diagrams by time step.

Table.1. The Parameters Required for Solving the Problem in the Angular Oscillation State

Variable	Value
Time step	<b>0.0015</b>
Reynolds number	<b>1100</b>
Density	<b>1000 kg/m<sup>3</sup></b>
Viscosity	<b>0.001</b>
Length	<b>1 m</b>

In any case, the thrust coefficient is obtained from the drag coefficient, and the average thrust is obtained by averaging the thrust coefficients. However, for any K value (i.e., the reduced frequency) one thrust coefficient is obtained. Several examples of the angular oscillation diagrams are depicted in the following. Fig.5, Fig.6, Fig.7, and Fig.8 describe the thrust coefficient variations by time for the k=10, k=14, and k=18 reduced frequencies.

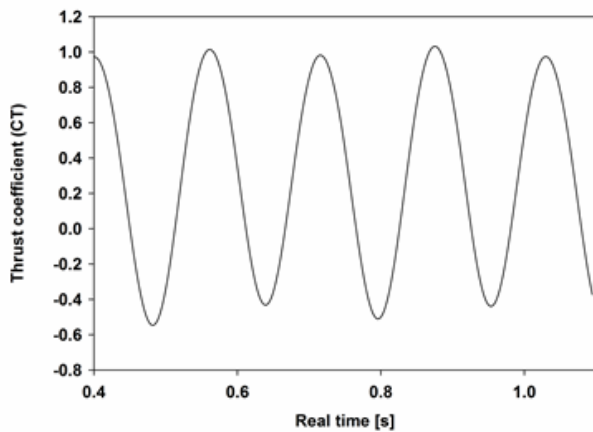


Fig.5. The diagram of thrust coefficient by time in the angular oscillation state for K=10 and f=3.18

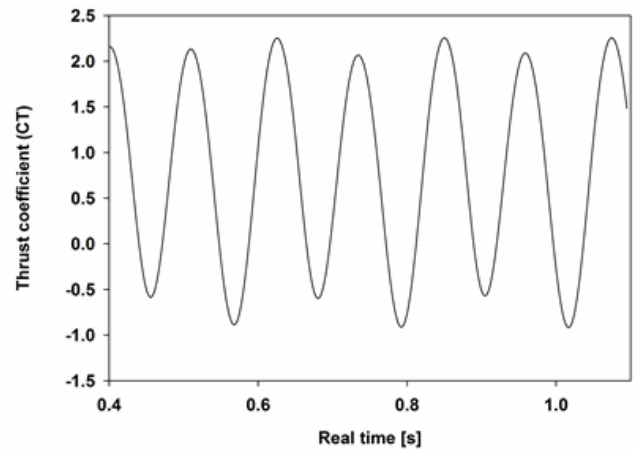


Fig.6. The diagram of thrust coefficient by time in the angular oscillation state for K=14 and f=4.45

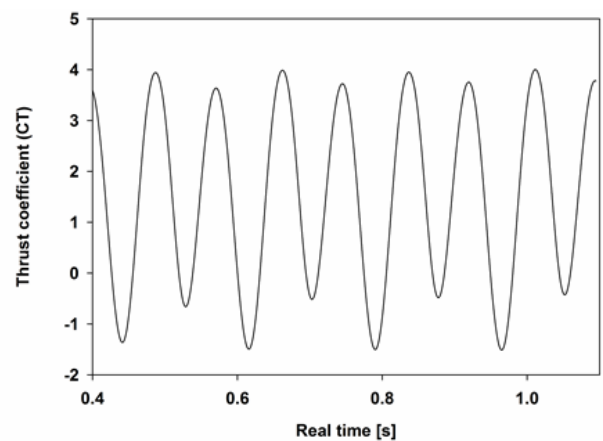


Fig.7. The diagram of thrust coefficient by time in the angular oscillation state for K=18 and f=5.7

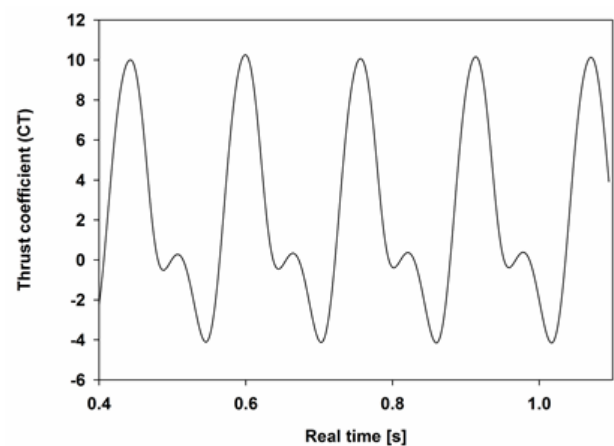


Fig.8. The diagram of thrust coefficient by time in the angular oscillation state for K=20 and f=6.36

As it can be seen in Fig.6, Fig.7 and Fig.8, in the angular oscillation state, if the initial attack angle is invariant and the frequency is variant, with an increase in K the thrust coefficients and the thrust oscillation range increase (i.e., move toward the positive side of the range). The increase in K also results in an increment in the thrust coefficient oscillations. In an oscillation period at the -0-attack angle (an attack angle close to zero), the thrust decreases to the zero-attack angle and as the attack angle grows, the thrust coefficient increases. As soon as the stall occurs and the attack angles reduces to the lowest level (a decrease in the negative direction), the lift escalates and then it decreases following the stall. The non-uniform variations of thrust may be caused by the formation of eddies transferred from the leading edge to the wing. The eddy resulted from the separation bubble and its combination with the trailing edge eddy (that is transferred from beneath the wing to the wing surface can disrupt the uniform thrust variations. Thrust increases with an increase in the strength of this combination. To validate the airfoil thrust coefficient in the angular oscillation state, the thrust coefficient is obtained using the drag coefficient in each state, and after averaging the thrust coefficients, one average thrust is obtained for each reduced frequency. Fig.9 shows the thrust coefficient of the problem numerical solution. The airfoil thrust coefficient curve in the angular oscillation state obtained from Fluent was compared to the thrust coefficient curve presented in [2] to validate the results. As seen, there is a slight difference between the results that reflect the satisfactory consistency of these values. As seen in Fig.10, as the reduced frequency grows, the thrust coefficient escalates. The increase in the thrust coefficient is intensified at reduced frequencies higher than 10.

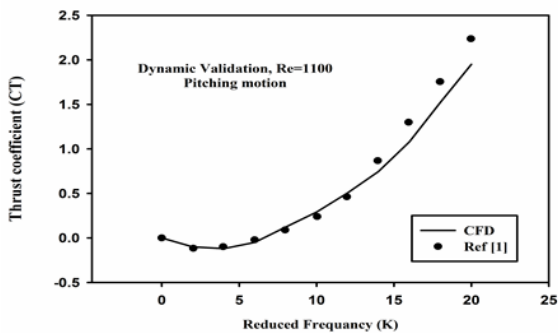


Figure.9. Comparing the variations of the thrust coefficients resulted from our numerical simulation and reference [4]

### B. 4.2. Flapping State Results

This simulation was carried out using an unorganized dynamic mesh in which oscillation was caused by coding in Fluent. The parameters required for solving the problem in simulating the flapping oscillation are listed in Table.2.

Table.2. The Parameters Required for Solving the Problem in the Flapping Oscillation State

Variable	Value
Time step	0.001
Reynolds number	1100
Density	1000 kg/m3

zero angle, the thrust declines and then increases to reach the lowest attack angle (i.e., the attack angle decreases along the negative direction). Following stall point, the thrust decreases again. In an oscillation period at the zero-attack angle, if the lift coefficient is positive, with an increase in the attack angle (an increase in the attack angle along the positive direction) the lift declines.

Viscosity	0.001
Airfoil mid chord length	1 m

In simulating the dynamic flapping motion, the upward and downward motions, which constitute plunging, are modeled using relation (3), and the airfoil pitching motion is simulated using equation.2.

$$h = h_0 \sin[2\pi f(t - t_o) + \Psi] \tag{3}$$

The numerical analysis of the airfoil oscillations in the flapping state was carried out in the 0.05-0.15 frequency range; the 0.1571-0.471 reduced frequency range, and the -12.5-13.30-average attack angle range. The phase difference was 90 degrees and the Strouhal number varied from 0.1 to 3. The aerodynamic coefficients resulted from solving the problem in the flapping oscillation state with the 0.001-time step are shown in Fig.12 and Fig.13. Fig.11 shows the pitching moment coefficient resulted from airfoil flapping in the F1 state, which is a combination of angular oscillation and perpendicular oscillation. The initial time values are omitted (from zero to 1.0) to show the fully periodic oscillations.

Table.3. The Simulation Parameters for Angular and Perpendicular Airfoil Oscillations

f(Hz)	h0/c	Θ0(°)	Ψ0	k	St	α0(°)
0/05	1	30	90	0/157	0/1	-12/56
0/1	1	30	90	0/314	0/2	2/14
0/15	1	30	90	0/471	0/3	13/30
0/2	1	30	90	0/628	0/4	21/49
0/25	1	30	90	0/785	0/5	27/52
0/3	1	30	90	0/942	0/6	32/05
0/35	1	30	90	1/099	0/7	35/55

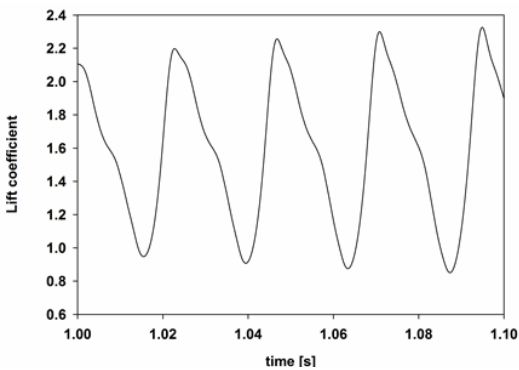


Figure.10. The lift coefficient in the flapping oscillation state

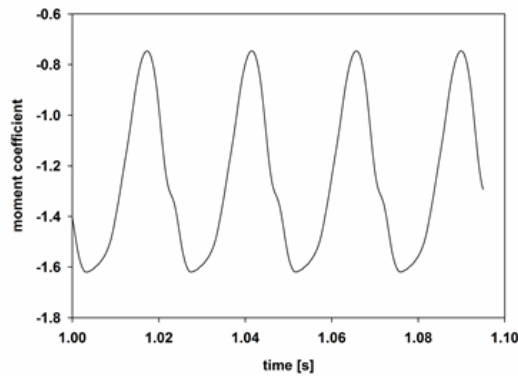


Figure.11. The moment coefficient in the flapping oscillation state

As it can be seen in Fig.12, the thrust coefficient in the flapping oscillation state is varying and the thrust is a forward thrust.

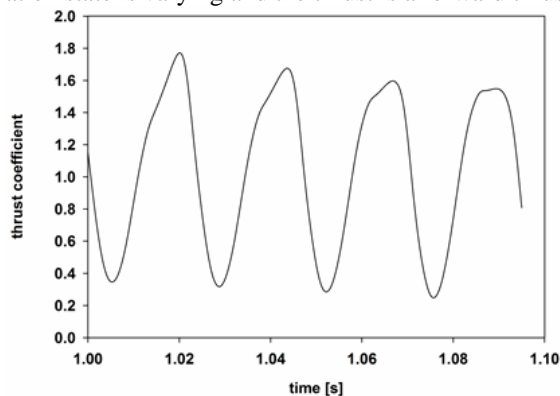


Figure.12. The thrust coefficient in the flapping oscillation state

Fig.13 presents the diagram of the thrust coefficient at the 0.78 reduced coefficient, the 27.5 average attack angle, and the 90-degree phase difference with a Strouhal number of 0.5.

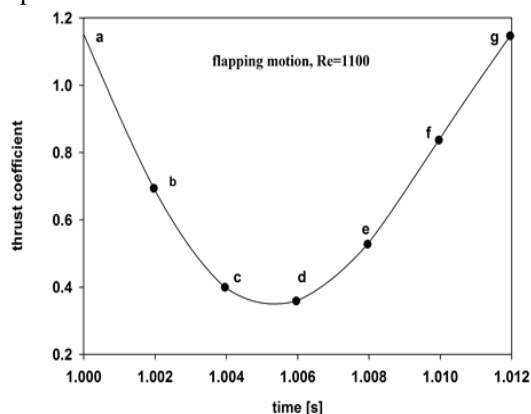


Figure.13. The diagram of thrust coefficient at a single frequency in the flapping state with an attack angle of 27.52 degrees

The contours of the static pressure during airfoil oscillation in the flapping state at the 0.78 reduced frequency are illustrated in Fig.14. In the flapping oscillation, which is a combination of angular and perpendicular oscillations, the increase in the reduced frequency is followed by an increase in the thrust coefficient by the Strouhal number. The highest thrust occurs at the lowest and highest attack angles, and the

thrust at the zero-attack angle is almost zero. As seen, with an increase in the reduced frequency, the thrust coefficient oscillation is unsteady. The static stall occurs at the maximum lift coefficient point. At lower values of reduced frequency, the dynamic stall occurs when the attack angle exceeds the static stall attack angle.

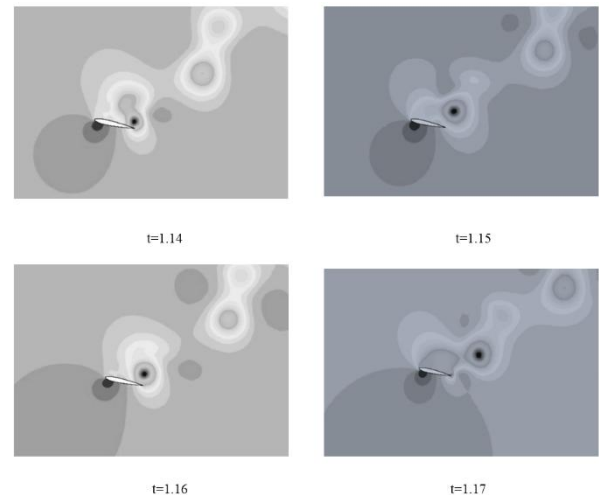


Figure.14. The contours of airfoil oscillation pressure in the flapping state at the 27.52 attack angle

The airfoil aerodynamic coefficients were studied as the reduced frequency remains unchanged and the attack angle changes 0 -12.56, -5, 5, 10, and 15 degrees. Simulation results suggest that the thrust coefficient did not change significantly and in the symmetric attack angle state, the area beneath the diagram of the counter clockwise area of the hysteresis ring becomes symmetrical. Investigation results also indicated that with an increase in the attack angle, the direction of the hysteresis ring of the thrust coefficient changes from the clockwise direction to the counterclockwise direction. However, the clockwise direction of the hysteresis ring of the drag coefficient remains unchanged.

By comparing the airfoil thrust coefficient in the flapping oscillation state in the fluent software to the thrust coefficient in [1], it was found that the result was acceptable and valid.

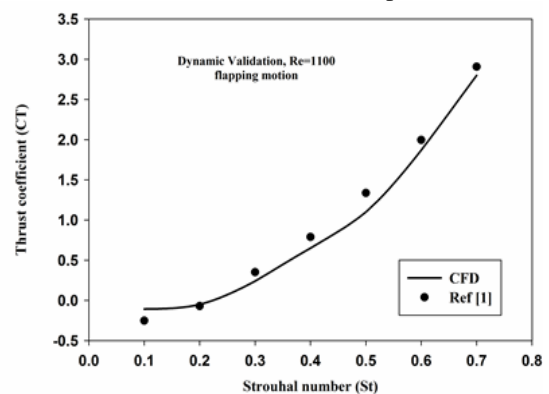


Figure.15. The attack angle by time in the flapping oscillation state

## CONCLUSION

The aerodynamic characteristics of a NACA 0012 two-dimensional symmetric airfoil in the perpendicular and angular oscillation states, and the flapping oscillation state, which is a combination of the angular and perpendicular oscillation states, were analyzed numerically in Fluent at different angles. To study the problem, the flow around the airfoil was assumed to be a viscous unsteady flow, and the aerodynamic coefficients were obtained in the static and dynamic states. Research results revealed that with an increase in the reduced frequency, the average thrust coefficient increases. The slope of the increase in the thrust coefficient exceeds ten at larger

decreasing frequencies. Moreover, if  $k > 10$ , the leading-edge eddy that is transferred to the airfoil surface becomes stronger and increases thrust in the ornithopter full cycle. This increase is depicted as a real-time thrust increase in the diagrams, which shows the unsteadiness of the flow at these frequencies. In the flapping oscillation state, the phase difference between the angular oscillation and the vertical oscillation is highly effective, and by adjusting this difference at any reduced frequency, it is possible to obtain the maximum thrust coefficient.

## REFERENCE

- [1] Soheil Mohtaram, Mohammad Amin Nikbakht, Detect Tool Breakage by Using Combination Neural Decision System & Anfis Tool Wear Predictor, International Journal of Mechanical Engineering and Applications. Vol. 1, No. 2, 2013, pp. 59-63.
- [2] Staelens, Y.D., R.F. Blackwelder, and M.A. Page. Novel Pitch Control Effectors for a Blended Wing Body Airplane in Takeoff and Landing Configuration. in 45th AIAA Aerospace Sciences Meeting and Exhibit 8-11 January 2007, Reno, Nevada. AIAA 2007-68.
- [3] Abas MFB, Rafie ASBM, Yusoff HB, et al. Flapping wing micro-aerial-vehicle: Kinematics, membranes, and flapping mechanisms of ornithopter and insect flight[J]. Chinese Journal of Aeronautics, 2016, 29(5) : 1159-1177.
- [4] McLain, B.K., steady and unsteady aerodynamic flow studies over a 1303 ucv configuration. September 2009, naval postgraduate school.
- [5] A. Gilliot, S.M., et al. Static and Dynamic SACCON PIV tests, Part I: Forward Flowfield. in 28th AIAA Applied Aerodynamics Conference 28 June-1 July 2010, Chicago, Illinois. AIAA 2010-4395.
- [6] Sirohi, Jayant. "Chapter 5 - Bioinspired and Biomimetic Microflyers." Engineered Biomimicry (2013): 107-138.
- [7] Robert, K., et al. Static and Dynamic SACCON PIV Tests, Part II: Aft Flow Field. in 28th AIAA Applied Aerodynamics Conference 28 June-1 July 2010, Chicago, Illinois. AIAA 2010-4396.
- [8] Robert, C.N. and P. Alain, The unsteady aerodynamics of slender wings and aircraft undergoing large amplitude maneuvers. Aerospace Sciences, 2003: p. 185-248.
- [9] Filippone A. Flight Performance of Fixed and Rotary Wing Aircraft[J]. 2006.
- [10] Schutte, A., D. Hummel, and S. M. Hitzel. Numerical and experimental analyses of the vortical flow around the SACCON configuration. in 28th AIAA Applied Aerodynamics Conference 28 June-1 July 2010, Chicago, Illinois. AIAA 2010-4690.
- [11] Jani JM, Leary M, Subic A, et al. A review of shape memory alloy research, applications and opportunities[J]. Materials & Design, 2014, 56(4):1078-1113.
- [12] Gursula, I., R. Gordnierb, and M. Visbal, Unsteady aerodynamics of nonslender delta wings. Aerospace Sciences, 2005. 41: p. 515-557.
- [13] Steven, D.R. and S.A. Andrew, An Inviscid Model for Evaluating Wing Rock Suppression Methodologies, in 32nd Aerospace Sciences Meeting & Exhibit January, Reno. AIAA 94-0808, 1994.
- [14] Kramer, M., Increase in the maximum lift of an airfoil due to a sudden increase in its effective angle of attack resulting from a gust. NASA TM-678, 1932.
- [15] Harris, F.D. and R.R. Pruyn, Blade Stall Half Fact, Half Fiction. J. Am. Helicopter Soc. 13, (1968) 27-48.
- [16] Ham, N.D. and M.S. Garelick, Dynamic stall considerations in helicopter rotors. J. Am. Helicopter Soc. 13, (1968) 49-55.
- [17] Choudhry, A., M. Arjomandi, and R. Kelso, Horizontal axis wind turbine dynamic stall predictions based on wind speed and direction variability. Mech. Eng., Part A: J. Power Energy 227, (2013) 338-351.
- [18] Ferreira, C.S., G.v.B. G. van Kuik, and F. Scarano, Visualization by PIV of dynamic stall on a vertical axis wind turbine. Exp. Fluids 46 (2009) 97-108.
- [19] Schreck, S. and M. Robinson, Blade three-dimensional dynamic stall response to wind turbine operating condition. J. Sol. Energy Eng. 127, (2005) 488.
- [20] Schreck, S., et al., HAWT dynamic stall response asymmetries under yawed flow conditions. Wind Energy 3, (2000) 215-232.
- [21] Shipley, D.E., et al., Evidence that aerodynamic effects, including dynamic stall, dictate HAWT structural loads and power generation in highly transient time frames, in National Renewable Energy Lab., 1994: United States.
- [22] Shipley, D.E., M.S. Miller, and M.C. Robinson, Dynamic stall occurrence on a horizontal axis wind turbine blade, in National Renewable Energy Lab. 1995: United States.
- [23] Carr, L.W., Progress in analysis and prediction of dynamic stall, . J. Aircr. 25, (1988) 6-17.
- [24] Ekaterinaris, J.A. and M.F. Platzer, Computational prediction of airfoil dynamic stall. Aerosp. Sci. 33 (1998) 759-846.
- [25] Kerho, M.F., Adaptive airfoil dynamic stall control. J. Aircr. 44 (2007) p. 1350-1360.
- [26] Krzysiak, A., Improvement of helicopter performance using self-supplying air jet vortex generators. J. KONES Powertrain Transp, (2013) 20.
- [27] Leishman, J. and T. Beddoes, A semi-empirical model for dynamic stall, J. Am. Helicopter Soc. 34, (1989): p. 3-17.
- [28] McCroskey, W., The Phenomenon of Dynamic Stall. DTIC Document, 1981.
- [29] McCroskey, W.J., Unsteady airfoils. (1982) Annu. Rev. Fluid Mech. 14. p. 285-311.
- [30] Liu, H. and K. Kawachi, A numerical study of insect flight. J. Comput. Phys. 146, (1998) 124-156.
- [31] Wang, Z.J., Vortex shedding and frequency selection in flapping flight. J. Fluid Mech. 410 (2000) p. 323-341.
- [32] Gheisari, R., et al. "Experimental studies on the ultra-precision finishing of cylindrical surfaces using magnetorheological finishing process." Production & Manufacturing Research 2.1 (2014): 550-557.
- [33] Shyy, W., et al., Aerodynamics of Low Reynolds Number Flyers. Cambridge University Press, 2007.
- [34] Norberg, U.M.L., Structure, form, and function of flight in engineering and the living world. J. Morphol. 252, (2002) p. 52-81.
- [35] Lang, J.D. and M.S. Francis, Unsteady Aerodynamics and Dynamic Aircraft Maneuverability. DTIC Document, 1985.
- [36] Niu, Y.-Y. and C.-C. Chang, How do aerodynamic forces of the pitching rigid and flexible airfoils evolve? AIAA J, (2013) p. 1-7.
- [37] Visbal, M.R., Dynamic stall of a constant-rate pitching airfoil. J. Aircr. 27 (1990): p. 400-407.
- [38] Karim, M.A. and A. Mukund, Suppression of Dynamic-Stall Vortices over Pitching Airfoils by Leading-Edge Suction. AIAA, August 1994. 32.

- [39] Lars, E.E. and J.P. Reding, Dynamic Stall at High Frequency and Large Amplitude. J. AIRCRAFT. 17: p. 136-142.
- [40] Francis, M.S. and J.E. Keesee, Airfoil Dynamic Stall Performance with Large-Amplitude Motions. AIAA. 23.
- [41] Lawrence, W.C., Progress in Analysis and Prediction of Dynamic Stall. AIRCRAFT, january 1988, 25: p. 6-17
- [42] Mohtaram, Soheil, et al. "Energy-exergy analysis of compressor pressure ratio effects on thermodynamic performance of ammonia water combined cycle." Energy Conversion & Management 134(2017):77-87.
- [43] Mohtaram, Soheil, et al. "Evaluating the effect of ammonia-water dilution pressure and its density on thermodynamic performance of combined cycles by the energy-exergy analysis approach." Mechanics 23.2 (2017): 209-219.
- [44] Anderson, J.D., Fundamentals of Aerodynamics. 2001., New York: McGraw-Hill.
- [45] Leishman, J., Dynamic stall experiments on the NACA 23012 aerofoil. Exp.Fluids 9, 1990: p. 49–58.
- [46] Gupta, S. and J.G. Leishman, Dynamic stall modelling of the S809 aerofoil and comparison with experiments. Wind Energy 9, (2006): p. 521–547.
- [47] Digavalli, S.K., Dynamic Stall of a NACA 0012 Airfoil in Laminar Flow. 1994., Massachusetts Institute of Technology.
- [48] Jumper, E., S. Schreck, and R. Dimmick, Lift-curve characteristics for an airfoil pitching at constant rate. J. Aircr. 24, (1987) p. 680–687.
- [49] Ramsay, R.R., M.J. Hoffmann, and G.M. Gregorek, Effects of Grit Roughness and Pitch Oscillations on the S809 Airfoil. NREL/TP-442-7817, National Renewable Energy Laboratory, 1995.
- [50] Leishman, J.G., Principles of Helicopter Aerodynamics. 2006.: Cambridge University Press.
- [51] Rival, D. and C. Tropea, Characteristics of pitching and plunging airfoils under dynamic-stall conditions. J. Aircr. 47, (2010): p. 80–86.
- [52] S.J. Schreck, Unsteady Vortex Dynamics and Surface Pressure Topologies on a Finite Pitching Wing. 1994., DTIC Document

#### ***Nomenclature:***

L	Length	l	Characteristic length
C <sub>f</sub>	Force coefficient	P	Static pressure
C <sub>D</sub>	Drag coefficient	Re	Reynolds number
C <sub>L</sub>	Lift coefficient	St	Strouhal number
C <sub>m</sub>	Moment coefficient	A	Angle of attack
F	Flapping coefficient	M	Dynamic viscosity coefficient
G	Gravity acceleration	ρ	Fluid density
t	Time	θ	Angle
f	frequency	θ <sub>0</sub>	Initial angle
ω	Angular velocity	h	Displacement height
k	Reduced frequency	h <sub>0</sub>	Initial displacement height
		Ψ	Initial phase

# A Socio-Technical Survey of Micro Hydro Power Projects in District Shangla, Pakistan

Ahmad Amin<sup>1</sup>, Noor Muhammad<sup>2</sup>, Maoz<sup>1</sup>, Saddam Ali<sup>1</sup>, Dr. Abdul Basit<sup>3</sup>, Dr. Tanvir Ahmad<sup>3</sup>

<sup>1</sup>Research Associates, USPCAS-E UET Peshawar, Pakistan, ahmadamin019@gmail.com<sup>1</sup>, maoz.shah@gmail.com, sak2581992@gmail.com

<sup>2</sup>Lab Engineer, USPCAS-E UET Peshawar, Pakistan, nooreng\_wazir@yahoo.com

<sup>3</sup>Assistant Professor, USPCAS-E UET Peshawar, Pakistan, abdul.basit@uetpeshawar.edu.pk, tanvir.ahmad@uetpeshawar.edu.pk

Received: 15 July, Revised: 20 August, Accepted: 30 August

**Abstract**— Rural electrification requires to be designed in a sustainable way to improve the quality of life of rural communities. Pakistan is facing an acute energy crisis for years now. Pakistan's energy mix mainly depends on indigenous natural gas and oil. Due to imports of oil and rapid decrease in gas reserves, there is a significant burden on the economy of Pakistan, which has forced the planners and policy makers to look for renewable energy sources. Micro Hydro Power (MHP) is an example of renewable energy which can be sustainable economically, environmentally and socially as Pakistan is rich in micro-hydro power especially the northern side. This paper analyses the outcomes from a field survey which is conducted in district Shangla, KPK Pakistan, where different agencies have implemented different MHP Projects (MHPPs). The quantitative and qualitative analyses have been used for comparing two MHPPs based on electricity tariff, community involvement, effect on the society and other factors. Quite a few issues were found due to lack of knowledge or unskilful operators in maintenance and operation in these MHPPs which are barriers to sustainable development. This research work concludes that these MHPPs requires proper management, quality work and skilful operators to have a sustainable and reliable system for the community. The MHPPs area already contributing significantly in the development of local communities.

**Keywords**— Sustainable development, Micro hydro power plant, Renewable energy

## I. INTRODUCTION

This Sustainable development is the outcome of increasing awareness of the universal links between growing environmental issues and socio-economic problems much to do with inequality and poverty and worries about a healthy upcoming life for humankind. The concept of sustainable development strongly links to the socio-economic and environmental issues [1]. The world's population comprises of 80% of developing countries but they use only 30% of total world's energy [2]. The world's population is increasing with a very high resulting in increased energy consumption. With the development in information and communication technologies, the common masses are becoming more aware of the environmental hazards as well related to energy. It is becoming

more important to move towards the alternative resources of energy which minimizes these environmental hazards.

Renewable energy is recognized widely to contribute well enough to the sustainable development because of its environmentally friendly nature, lowering the health hazards; mitigating climate change. Thus, renewable energy gradually getting support from government policies, multinational corporations (MNCs), nongovernmental organizations (NGOs) and industry tracking environment, energy and other developmental growth programmes locally and globally too. Renewable energy is also getting considerable importance at commercial market, shifting the investment patterns away from state and international donors to private firms and organizations [2].

Energy is the basic requirement for the development and prosperity of a nation. In fact, nowadays, the progress of a nation could be gauged in terms of how much energy it consumes per person [3]. According to International Energy Agency (IEA), the world energy demand reached to 14050 Million Tonnes of Oil Equivalent (MTOE) in the year 2017, which was 10035 MTOE in the year 2000. The world energy demand has been increased by 2.1% in 2017 as compared to 2016, in which the world energy demand was increased by 0.9% [4].

Electrical Energy is the basic need of modern life due to advancement in technology and inventions day by day. The world electricity generation was 25570 TWh in 2017, which was increased by 3.1% as compared to previous year [4]. Pakistan electrical energy sector is a developing market. For years, the issue of balancing the supply and demand for electricity has remained an unresolved. According to the population census of Pakistan 2017, the total population of the country was 207.7 million, in which the urban population is 75.5 million or 36.4% while the rest live in rural areas.

Pakistan is listed as the 6th most populous country in the world, having the availability of 43-Watt energy per capita, which is almost 1/7th of the world average [5]. The electrical energy demand in Pakistan is increasing day by day. Pakistan's recent energy mix mainly depends on fossil fuels, which is resulting in high prices of energy and also on energy crises and imported at the cost of precious foreign reserves. The total



nominal power generation capacity of Pakistan as on 30th, June 2015 was 24,823 MW; of which 16,814 MW (67.74%) was thermal, 7,116 MW (28.67%) was hydroelectric, 787 MW (3.17%) was nuclear and 106 MW (0.43%) was wind. The installed power generating capacity of Pakistan from 2000 to 2015 [6], is given in figure 1.

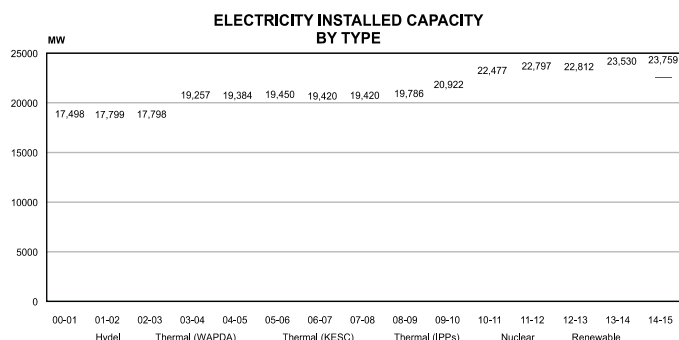


Figure 1. Total Installed Capacity of Pakistan from 2000 to 2015 (NEPRA. State of Industry Report 2015)

The rapidly growing rate of energy demand is 10% per year [5]. The future energy demand in 2030 is predicted at 110 GW as projected in figure 2. For more than a decade now, Pakistan's energy crisis is becoming chronic and the ever growing circular debt is posing major threat to economy of the country. The main causes of the present energy crisis are high cost, poor transmission and distribution system, inappropriate policies, mismanagement and the low level of energy generation compared to demand. The country's increasing population and economic activities necessitates the generation of more energy and all indigenous resources must be used before importing any hydrocarbons. The house hold and industrial level have the issues of energy conservation, overuse and misuse of energy. Other factors such as transmission line losses, pilferage losses, corruption, lack of management and lack of political consensus on the big power projects have significantly contributed to the energy crisis.

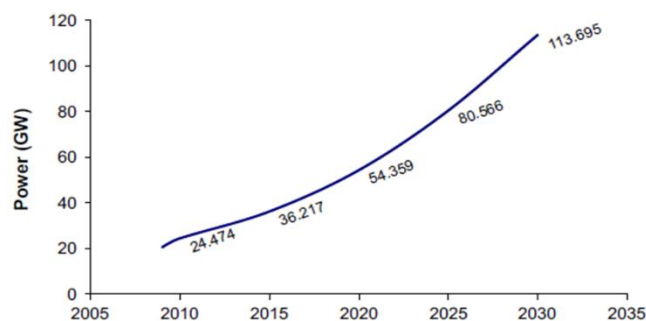
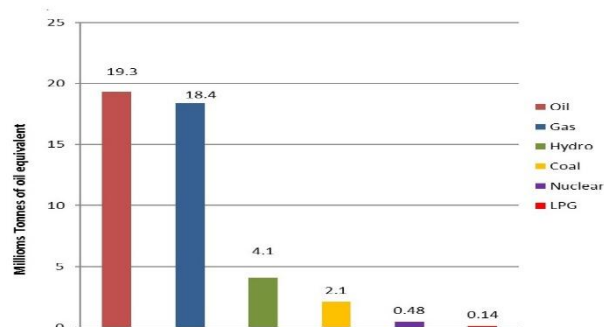


Figure 2. Future Projected Demand of Pakistan (Farooqui, 2014).

The main sources of energy in Pakistan are gas, oil, hydro, nuclear, coal and LPG [7]. The power production in the country from the primary energy resources is shown in figure 3. Due to the issues of climate alteration and environmental deprivation, the significance of renewable energy technologies has been rising. Furthermore, the international environmental agreements make it necessary for Pakistan to concentrate on renewable and clean energy options to meet its growing

demand for energy [8]. The renewable energy sources include hydropower, solar energy, wind, geothermal energy etc. The energy or electricity generated from these sources is clean and environment friendly.



Pakistan Power Sector (Ministry of petroleum and natural resources Pakistan, 2008)

Hydropower is one of the most important renewable energy source providing electric energy world-wide. Small or micro scale hydro mostly "run-of-river", without dam or storage for water, is one of the most cost-effective and environmentally benevolent energy technologies to be considered for rural electrification in developing countries [9]. Small, micro and mini hydel projects have no internationally agreed definition. Different states have different definition as shown in table 1. In India, 2.5 to 25MW is categorized as small hydro [10] whereas European commission categorized hydel project less than 10MW as small hydro [6]. Pakistan renewable energy policy 2006, consider project below 50MW as small hydro [11]. According to world bank, 100kW-1MW is considered as mini hydel projects.

In current pressing energy demand, the low hanging fruits need to be targeted. The case become more viable when the questions of electrifying remote rural communities having low income is raised. Extension of grid is an expensive option and not feasible. Both federal and provincial governments have initiated many projects in small and mini- micro hydro domain. According to Alternative Energy Development Board (AEDB), Pakistan has the potential of 3100 MW power from micro hydro plants in which the operational power is 128 MW, 877 MW is in implementation process while almost 1500 MW is obtainable for the progress. The range of power potential from different regions in the country has shown in the table 2.

TABLE I. DIFFERENT DEFINITIONS OF MICRO HYDRO

Parameter	Description	Reference
Small Hydro	2-25 MW	India Energy Council
Small Hydro	<10 MW	European Commission
Small Hydro	<50 MW	Pakistan Renewable Energy Policy 2006
Micro Hydro	1-100kW	World Bank
Mini Hydro	100kW-1MW	World Bank

In Pakistan, a lot of projects have been implemented in the Kashmir, KP and FATA regions. Pakistan council for

renewable energy (PCRET) has implemented 290 plants in the range of 5-50 kW in KP, FATA and Kashmir accounting for 3.5MW. Similarly, Agha Khan Rural Support Program(AKRSP) has constructed 171 projects in northern Pakistan [12]. However, the country enters a new era, when KP provincial government announced construction of 356 micro hydro projects in KP [14]. 150 projects have been completed and 168 are under construction stage. Four local NGOs have been given the contracts to construct the micro hydro projects namely AKRSP, Sarhad Rural Support Program (SRSP), Fatima Welfare Foundation and Haashar.

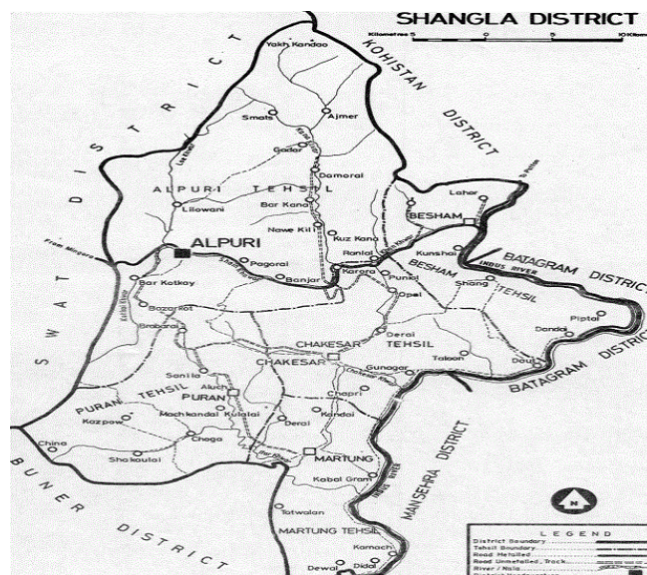
The micro/mini hydropower has the potential to provide electricity to the rural areas in the country, which include the power generation from hilly northern region and power generation through canal fall in the southern region of the country [13]. The country is blessed with hydro power potential especially the province of Khyber-Pakhtunkhwa (KP). Electrifying the rural areas can significantly change the life style and can have a good impact on the sustainable development of the country.

TABLE II. POTENTIAL RANGE FOR MICRO HYDRO POWER

Region	No. of Potential Sites	Potential Range MW	Total Potential (MW)	Remarks
Gilgit Baltistan	200	0.1 to 38	1300	Natural Falls
Khyber Pakhtunkhwa	125	0.2 to 32	750	Small / Micro based on Natural Falls / Flow
Punjab	300	0.2 to 40	560	Canals
Azad Jammu & Kashmir	40	0.2 to 40	280	Natural Falls
Sindh	150	5 to 40	120	Canal Falls
<b>Total</b>			<b>3100</b>	

Alpuri is a hilly place located in district Shangla, KP province of Pakistan and has coordinates of 34° 54' 00" N 72° 39' 00" E. The detailed map of Shangla district is shown in figure 4. The locality has many streams and is suitable for generation from micro-hydro. Several micro-hydro systems have been implemented in the area by different organizations. SRSP, a non-government organization, is implementing 165 community controlled MHPs having an installed capacity of 21 MW with the help of European Union [15]. Alpuri region is selected for this research due to the fact, that in recent years, several MHP's have been implemented with changing factors like funding, processes of design and mechanisms of planning and control. This research is based on investigating the social, technical and environmental impacts of micro-hydro projects implemented by government, non-governmental organizations and local community in the rural regions of KP province, Pakistan.

As mentioned earlier that Pakistan is facing a considerable energy crisis, thus there is a great need to sort out alternatives other than fossil fuels and MHPPs is one of them, for which efficient management is one of the main concerns. In order, to tackle the efficient management of MHPPs, the main objective of this work is to assess the overall performance of two MHPPs in terms of their operations, socio-economic and environmental impacts. The aim is to find out how the community is benefitted from the implementation of these MHP projects and what are the impacts of micro-hydroelectricity on the people of those regions. The research is an attempt to know the factors experienced by the locals after the installation of MHP projects such as education, health, income, economic activities, information etc.



Detailed Map of Shangla District

## II. METHODOLOGY

For this research, data about the impact of these MHPP has been collected through designed questionnaire with the help of individual interviews. The site observation, designed questionnaire and the individual interviews were conducted to collect both quantitative and qualitative data in the survey, see figure 5. Field visit to Shangla district was conducted to observe and find out the households whom are benefited by this micro hydropower. The visit to the field is necessary to know the views and experiences of the local community and to identify the actual impact of MHPP in the community. Questionnaire was designed to collect the correct data from the users of micro-hydro energy in the community. The responders from the local village were obligatory to fill up the questionnaire. The questions were provided to know the views of the local community about the impact of the MHPP's in different sections of the village. Interviews were conducted from villagers, MHPP operators, maintenance staff and other related personnel to give information regarding involvement of community, its social impact, barriers and problems, details of design and technical parameters, funding, plan and policy. The interviews also required to gain the overall perspective of the interviewee for these MHPP's; their benefits, issues and future

prediction. Thus, the primary data was collected from the community households of the research area. Likewise, the secondary data was collected from different reports, publications, feasibility report, internet, journals, experts and organizations related to micro hydroelectricity. The data for the analyses has been organized and tabulated according to the objective of research studies. Simple tools for statistics were used for data analyses like tables, bar graphs etc. With the help of computer programs, like Microsoft excel, SPSS and Matlab data was analyzed. The data analysis is descriptive and analytical.

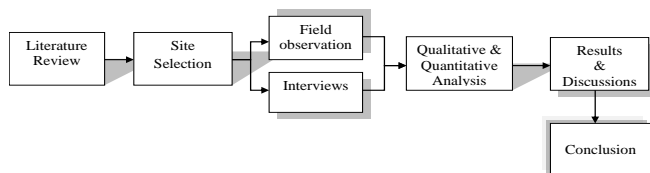


Figure 3. Research process flow chart

### III. RESULTS AND DISCUSSION

The results of the survey are presented to analyze different aspects including the nature of the MHPPs, its funding and the community collaboration. The survey findings also expose the contribution of MHPPs to the sustainable development i.e. its environmental and socio-economic impacts.

#### A. Nature of MHP systems

The MHPPs installed in Alpuri are all run-off-the-river due to the rough location as shown in figure 6, and it is difficult to build dams for storage to gain excess of water for these systems, as the power obtained from the MHPP is determined by the head and flow rate of water to the turbine. Variations in water flow rate have a significant effect on the power produced throughout the year. The annual average flow rates were determined by the qualitative data which were provided by the local community. There was no annual flow rate data available to help the local community for the evaluation of variations in the seasonal flow rate over a long time. The MHPP's are designed with cross flow turbines with no storage system, which means that all the power generated should be either used by the community or the excess of power should be dumped. Some of the technical details are given in table 3.

TABLE III. DETAILS OF MHPP

Parameters	Lilownai MHPP	Kassbela MHPP
Total Capacity (kW)	50	25
Head (ft.)	200	25
Turbine Used	Cross Flow	Cross Flow
Manufacturer	Mukhtiar Energy, Mardan	Chiragh steel company, Mardan
Circuit breakers	Yes	No
Transformer	No	No

In Lilownai MHP system during mid-winter, the canal had minimum level of water. Although complete freezing of the canal never happens, the water-flow rate was the worst case of the year during December. The turbine was producing only 3-5 kW of maximum power under such conditions and was mostly in overloaded situation. In summer, however, turbine was running for 21 hours out of 24 hours a day. The remaining 3-4 hours were used in cleaning of the turbine, penstock and the fore bay tank. The MHP is able to produce 10 – 20 kW power with good to great water flow. Water flow was variable but with enough thrust to keep the reservoir filled always under running condition.

Similarly, for the Kassbela MHP system, the water flow variation is high in summer as compared to winter. The sediments in the channel of water are being filtered in fore bay tank having volume of 960 ft<sup>3</sup>.



Figure 4. Lilownai MHP system

#### B. Funding of MHP systems

The MHP systems installed in the Alpuri region are funded by three different sources: government (PEDO), non-government organization (SRSP) and local community. The Lilownai MHP system is implemented by SRSP with some community collaboration. The MHPP was funded by SRSP and some community shares. A total of 7.78 Million PKR was assigned out of which 3.6% are community shares and the rest was SRSP fund. Technical data collected from Kassbela MHP system shows that this project was implemented in 2016 by SRSP (NGO) and funded by European Union. The land for the project was donated by local community. The total cost of the project was about 2.3 Million PKR in which 10% of amount was paid by the local community organization. The details are shown in table 4.

TABLE IV. FUNDING FOR THE MHP SYSTEM

	Lilownai MHPP	Kassbela MHPP
Funded By	SRSP	SRSP
Total Cost (PKR)	7.78 Million	2.3 Million
Community Shares	3.6%	10%



Total Capacity (kW)	50	25
---------------------	----	----

### C. Community collaboration

During the planning and manufacturing of both of these MHPP's, the communities collaborated and were involved with the SRSP organization. The communities mostly collaborated in the civil works; however, they are also involved in the operation and maintenance of these MHPP's. Mostly in community-based MHPP's, the locals were involved in providing fund, working on the sites and in the maintenance. Both in Kassbela and Lilownai MHP's, the locals helped during the installation stage. The members from both the community backed the SRSP in the constructing and provide their labours to help in completing the projects. The funds provided by the SRSP covered the expenses of the tools and equipment's that is; turbine set, generator, other electrical equipment's and civil materials which is required for the project.

### D. Electric Power Tariffs

The Kassbela village has total of 230 household among which 100 were being electrified by this power house. Average household demand is about 20 to 25 units and has meter based billing system. Schools, shops and other local business were also being electrified. Monthly revenue coming from this project is about 20 thousand PKR and the monthly maintenance is about 10-15 thousand PKR. The details of the households electrified are shown in figure 7.

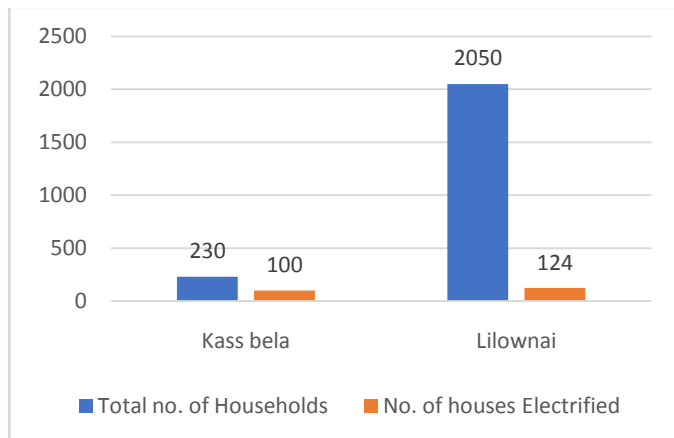


Figure 5. Number of households electrified

The tariff structure for Lilownai village MHPP is different from the Kassbela village. The Lilownai village has more than 2000 houses, out of which 200 households are near to this MHPP and number of household electrified from Lilownai MHPP is 124. Fixed tariff is allocated of 200 PKR per month for households and 300 PKR for Commercial Users. The details are shown in table 5. The bills are being paid by the community in their respective time. They pay the bill on monthly basis to a shopkeeper from where the bill is collected which is the net income of owner of MHP. If they don't pay bill in time they are fined 50 PKR per month. The monthly revenue generated is about 25 thousand PKR while the

monthly maintenance cost is about 6 thousand PKR without any sudden major default. Once the bearing of generator was affected and its maintenance costs were 6800 PKR.

TABLE V. DETAILS OF ELECTRICITY TARIFF

Scheme	Kassbela	Lilownai
Electricity Tariff system	Meter Based	Fixed
Tariff Rate (PKR)	200 Average	200 for houses; 300 for commercial use
Revenue generated/Month (PKR)	20 Thousand	25 Thousand
Maintenance cost/Month (PKR)	10-15 Thousand	6 Thousand

## IV. IMPACT OF MHP SYSTEMS

### A. Socio-economic Impacts

The availability of electricity due to MHPP at low cost in Lilownai village has increased income generation from different sources likeshops, tailoring, hair dressers and carpenter and allows the locals to make savings on expenditures on candles, kerosene and batteries. So, the income enhances as well as the savings of the locals, see figure 8. The possibility to use appliances like freezers has improved the food and diet of the locals and decreased the malnutrition and hunger [16]. Furthermore, the load of work has decreased on women and children as they save their time by spending less time on household works i.e. collection of woods. In general, the safety of the village has increased by the lightning in streets during night time. Moreover, the education and health of the children has improved as they have more productive time to study at night and utilize the evening time by doing healthy activities. Similarly, elders can visit mosques during night time and recite holy books anytime. Lights were now available which promotes studying and reading. The availability of electricity has made it possible for the villagers to use smart phone which can also be considered an educational tool along with its other features. The villagers from the Kassbela village were very pleased with the contribution of MHPP's in their livelihood transformation. The Lilownai MHPP has a great impact on the social communication inside the community as they can arrange meetings conveniently at night and get entertained from electrical appliances i.e. Television and radio. By using these appliances, the telecommunication benefits have been enhanced, the locals are now more aware of the country and world's news which give them more information [17].

On the other hand, almost 40% locals from Kassbela village has reported that they have less communication with neighbours because of MHPP electricity as they use televisions for entertainment purposes. The decreased internal air pollution and use of woods has also positive impact on the community locals due to the implementation of MHPP's. The enhanced electrical appliances used at education institutes and medical centres have attracted more teachers and doctors to these areas which improves the education and health facilities.

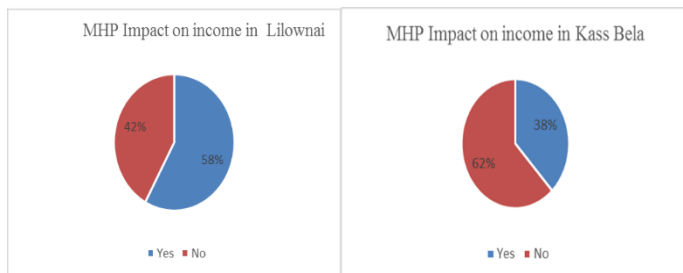


Figure 6. The percentage of respondents who reported that their income has increased after the implementation of MHPP's in lilownai (left) and Kassbela (Right)

## B. Environmental Impacts

The growing population of rural areas has increased the needs for having more wood to be used for lightning and fire purposes, due to which the deforestation rate is increasing day by day. This issue requires instant and effective steps to save the forests from deforestation and keep the forests to optimum level [18]. The MHP projects implemented at Alpuri district has increased the awareness and promotion of suitable watershed management to attain sustainable usage of water resources and has minimized the deforestation.

Lilownai MHPP has a positive impact on the environmental sustainability of the local villagers, as cutting wood for heating and lighting doesn't only affect the environment but also affects the health. Fire produces hazardous smoke. Availability of MHPP has helped in decreasing the use of flammables for light source.

The lighting and cooking has a negative impact on the health as well as on the environment of the region because of burning of kerosene oil, usages of lantern, wood and coal for heating, before MHPP in Kassbela village. But all these have been somehow controlled by the start of this MHPP project. Furthermore, due to controlled wood cutting the forests helps in the protection of the environment. The reduction in the use of kerosene oil and hazardous smoke due to the MHPP helps in the combat with the climate change and increase safety around the community.

The MHP projects installed are run off river which means that there is no storage for water. The water should be directed straight to hydro turbine or the water is lost. The inflow of the water to be utilized depends on the capacity of the MHPP. The regulation of water level is served by the civil works at the intake side of the MHPP. Therefore, the run of river configuration has not same kind of effect on local environment as of large hydro power which has dams or storage for water. The variations in the water flow complicates the power generation from MHPP throughout the year.

## C. Technical Issues

The Lilownai project has faced certain technical challenges during the period. In winter the site becomes overloaded about 6-8 kW due to extra load. During the last 6 months, the failure of turbine was reported 3 times; but the operator of the MHP project, Raham Khan has enough experience in MHPP construction and operation, so the issues and faults has been solved by him but each time it took 2-3 days. The generator

failure has been reported only once. The transmission lines are sometimes touched by trucks which results in short circuiting. In winters, there are also issues of short circuits due to the snowfall and that are solved with the help of the local community. The turbine need frequent maintenance; the minor issues are solved by the operator however the parts and heavy machines of the turbines are not available in the area; they bring it from Mardan/Gujargarh or take the machine to that area for mending. There is also leakage in the penstock and turbine.

The Kassbela MHP project is located at a very safe place, flood resistant and have no issue of land sliding. The maintenance of the power house is under local community having less knowledge of technical studies. Therefore, if there is some major issue at the power house they contact other personnel to solve the issue. Water flow variation is high in summer as compared to winter. There were no issues regarding pipe blocking have been reported. The overloading of the turbine has been observed in summer which results in the turbine failure while in winters, short circuit issues have been observed mostly. The ratio of generator failure is  $\frac{1}{4}$  per month. No power thefts have been reported yet.

## CONCUSLION

The MHPP's installed in district Shangla not only electrified the villages but also developed their social and economic position. Micro hydro power systems are supposed to be a sustainable source for the economic and social growth of isolated communities. Therefore, the micro hydro power systems sustainability is very vital aspect for the alleviation of poverty. From this survey, qualitative and quantitative analyses, it is concluded that the installation of the MHPP has a significantly positive impact on both communities. The young generation who are studying in other cities are happy to return to their homes, as their homes are electrified enough to continue their studies at their own homes. In both Lilownai and Kassbela village, the locals and respondent's incomes have been increased due to the installation of these MHP systems. Most of the locals who told that their incomes have increased significantly as they now make handicrafts in the evening.

Similarly, the local tailors reported that their incomes have increased as they get electricity from the MHPPs which gave them more time to do their job. In the Kassbela MHPP, the low technical knowledge of the operator makes it difficult to have a reliable and sustainable system. There should be high level of training for the operators, to have a comprehensive idea of the MHP systems so that they can solve the issues by themselves. By high level of training, the community locals or operators could mitigate the delays in the maintenance and will not require other technical personnel from other places.

Another problem is the variations in water flow which is based on data analyses of water flow for one season. The data collected is not feasible to capture the water flow throughout the whole year which is not that accurate. In both MHP sites the water flow in winter seasons is low which results in the less electric power generation from these MHPPs. A good structure of hydrology could be achieved by using a better system to

estimate the water flow; its maximum level, average flow and minimum level, for the whole year.

Further studies and research is necessary to examine the successful key factors of establishing the MHPPs for the rural areas. The key findings from the studies could be used for the policies, planning and designing of sustainable MHPP's in the rural areas.

#### ACKNOWLEDGMENT

The research is supported by the joint research program on distributed energy technologies with social science and hydrological research with Arizona State University, USA. I am very much thankful to USAID and USPCASE UET Peshawar for giving us the opportunity to complete our postgraduation. I am grateful to my supervisor Dr. Tanvir Ahmad and respected teacher Dr. Abdul Basit for their help and support throughout my research.

#### REFERENCES

- [1] Hopwood, B., Mellor, M. and O'Brien, G., 2005. Sustainable development: mapping different approaches. *Sustainable development*, 13(1), pp.38-52.
- [2] Martinot, E., Chaurey, A., Lew, D., Moreira, J.R. and Wamukonya, N., 2002. Renewable energy markets in developing countries. *Annual review of energy and the environment*, 27(1), pp.309-348.
- [3] Chaudhry, M.A., Raza, R. and Hayat, S.A., 2009. Renewable energy technologies in Pakistan: prospects and challenges. *Renewable and Sustainable Energy Reviews*, 13(6-7), pp.1657-1662.
- [4] International Energy Agency (IEA), *Global Energy & CO2 Status Report* (2017). Retrieved April 10, 2018 from <https://www.iea.org/publications/freepublications/publication/GECO2017.pdf>
- [5] Farooqui, S.Z., 2014. Prospects of renewables penetration in the energy mix of Pakistan. *Renewable and Sustainable Energy Reviews*, 29, pp.693-700.
- [6] NEPRA. *State of Industry Report 2015*. Retrieved April 10, 2018 from <http://www.nepa.org.pk/Publications/StateofIndustryReports2015.pdf>
- [7] Ministry of petroleum and natural resources, government of Pakistan. Islamabad, Pakistan. (2008). Retrieved March 21, 2018 from <http://www.mpn.gov.pk>.
- [8] Hussain, A. and Gillani, Z.A., 2014. Fulfilling environment related international commitments through implementation of multilateral environmental agreements (MEAs) in Pakistan. *A scientific journal of COMSATS-Science Vision*, 18, pp.1-2.
- [9] Paish, O., 2002. Small hydro power: technology and current status. *Renewable and sustainable energy reviews*, 6(6), pp.537-556.
- [10] Sharma, A.K. and Thakur, N.S., 2016. Analyze the factors effecting the development of hydro power projects in hydro rich regions of India. *Perspectives in Science*, 8, pp.406-408.
- [11] Pakistan Renewable Energy Policy, 2006. Retrieved March 21, 2018 from <https://www.aedb.org/Documents/Policy/REpolicy.pdf>
- [12] Habib, B.I.L.A.L., 2004. Micro hydro electric power in Pakistan. In 19th World Energy Congress. Pakistan.
- [13] Internal Report (2008). Pakistan Council of Renewable Energy Technologies (PCRET), Islamabad, Pakistan. Retrieved March 28, 2018 from [http://apcctt.org/recap/sites/all/themes/recap/pdf/Country\\_Report\\_pakistan.pdf](http://apcctt.org/recap/sites/all/themes/recap/pdf/Country_Report_pakistan.pdf)
- [14] Energy & Power department KPK, Pakistan. (2016). Retrieved April 25, 2018 from <http://www.kpkep.gov.pk/page/hydropowerpolicy/KP%20Hydropower%20Policy%202016.pdf>
- [15] Sarhad Rural Support Program (SRSP), (2017). Retrieved April 25, 2018 from <http://ww3.srsp.org.pk/index.php/pages/about-us/rural-electrification>
- [16] González, A.H., Aristizábal, A.B. and Díaz, R.M., 2009. Micro Hydro Power Plants in Andean Bolivian communities: impacts on development and environment. In *International conference on renewable energies and power quality*, Valencia.
- [17] Korkeakoski, M., 2009. Impact of micro hydropower (MHP) based electrification on rural livelihoods: case study Nam Mong in Luang Prabang province, Lao PDR.
- [18] Akbar, K.F., 2005. SUSTAINABLE SUPPLY OF FUEL-WOOD FOR THE RURAL AREAS OF PAKISTAN: FARM-FORESTRY AS A RENEWABLE-ENERGY SYSTEM. *Technologies and Sustainable Development*, p.55.



**Ahmad Amin:** The author was born in KPK province, District Charsadda, Pakistan in the year of 1993. He did his matriculation from New Islamia Public High school, Charsadda, Pakistan. Afterwards, He pursued his Higher secondary education in Pre-Engineering from Islamia College Peshawar, Pakistan. After that He did his Bachelors Degree in Electrical Power Engineering from Abbottabad, Pakistan. Currently, He is enrolled in MS, Electrical Energy System Engineering from USPCAS-E Uet Peshawar, Pakistan.

The author started his professional career as an Internee at Rawat Laboratories, Islamabad. Later on he joined National Transmission and Dispatch Company, as a Trainee Engineer. Currently working as a Research Associate in a joint research program on distributed energy technologies with social science and hydrological research with Arizona State University, USA.



# An Improvement in Load Forecasting Model using Parametric Tuned Support Vector Machine (SVM) Kernel Based Functions

Engr. Hamad Ullah Khan Bangash<sup>1</sup>, Dr. Amjad Ullah Khattak<sup>2</sup>

<sup>1,2</sup>Department of Electrical Engineering, University of Engineering and Technology, Peshawar, Pakistan  
hamadbangash@yahoo.com<sup>1</sup>, amjad67@gmail.com<sup>2</sup>

**Abstract**— Short term load forecasting (STLF) has gained huge interest among researchers because of its applications in economics, reliability, unit commitment (UC), economic dispatch (ED) and hydro-thermal coordination (HTC) of power systems. The aim of this study is to find an accurate algorithm as it is very important for the prediction of accurate load forecast. Support Vector Machine Regression Model (SVM-R) using different kernels i-e linear, polynomial and gaussian has been used and each kernel function effectiveness and its performance has been examined on real time series using ISO-New England utility data. LibSVM using R language is utilized in this research to employ SVM-R Model. Artificial Neural Network (ANN) is utilized to compare and check the effectiveness of proposed model and its performance by considering least Mean Absolute Percentage Error.

**Keywords**— Short term load forecasting (STLF), Support Vector Machine, kernel function, time series, Artificial Neural Network (ANN).

## I. INTRODUCTION

Forecasting future load has gained importance because power system operation and management of the future will in turn needs decision-making of a character primarily dissimilar than the methods used currently. It needs to be a bit more quicker, decentralized and should have the ability to treat any kind of uncertainty. These dissimilarities as a result will eventually need many different methods of forecasting closely integrated with the decision-making process.

As an important factor in prediction of future loads, power system of the future will need several additional capabilities. Accuracy is another important factor and has drawn a lot of research interest among researchers that an accurate short term load forecasting (STLF) is very useful and the main function of it is to make schedules for generation, transmission and daily operational activities of power grids. Failure in above or poor forecasting of load not only cause increase in operational cost but also misleads the planners involved in planning process. As STLF is extremely helpful for decision makers to make accurate forecasts and make plans regarding maintenance, economic unit allocation, unit commitment, economic

generation allocation, secure analysis of security systems and daily operational activities. There are certain factors which influence the load as it has been noticed that load gives different patterns mainly due to metrological parameters, special events, working or holidays. Usually it has seen statistical approaches give better results on ordinary days and can forecast very well, but the drawback is their capability to examine the load property. In order to overcome these inabilities different machine learning techniques in combination with other models are used these days. In order to handle these issues proposed model has been introduced and the main objective of this model is to overcome these challenges and also helps in reducing the interaction time. The method advised here is a hybrid technique using support vector machine in combination with statistical models.

## II. LITERATURE REVIEW

With the rapid increase in electric load and consumption every year, researchers and economic strategists show keen interest in load forecasting field for accurate load forecasting. In this section a brief literature survey has been presented mainly focussed on STLF and are reviewed according to techniques that are developed during past few years.

There are many techniques/approaches available in the load forecasting field. A.S.Ahmad et.al [1] classified these techniques into three, which are Engineering Method, Statistical Method and Artificial Intelligence (AI) Method. Statistical methods show good results on ordinary days but their inability to examine load properly and lack of accuracy [1][2]. These methods are not widely used these days. Similarly engineering methods [2] show drawback in terms of lack of input information. So, in order to overcome these shortcomings the technique most commonly used these days is Artificial intelligence (AI) which includes Artificial Neural Network (ANN) and Support Vector Machine (SVM) [1][2][3].

Nahi Kandil et. al. introduce ANN model on data set for time series load forecast. The ANN is particularly used as it is simple and robust and because of these attributes it is preferred for forecasting models but the drawback of ANN is its large time consumption in learning stage. The training data has to face several data layers in order to prepare it for forecasting stage. In addition to extra time consumption in learning stage, the neural network model does not provide

specific information about its convergence. Therefore specific count of neurons are not well known in advance due to which over fitting and under fitting problems occur [4].

Srinivasan et. al. presented a combined neural and fuzzy approach in which rapid increase in load was analyzed and load growth effect was incorporated. The need for the development and execution of a hybrid fuzzy based one-day ahead load forecaster was discussed which comprised of three steps. In 1<sup>st</sup> step, the growth trend was analyzed and by making some necessary compensation historical load was updated to the current load demand. In 2<sup>nd</sup> step Kohonen's self-organizing feature mapping (SOFM) was used to map the load profile. Then by using auto associative memory of ANN the current day load prediction was achieved. Metrological parameters has taken into consideration by a fuzzy parallel processor while making daily predictions. The proposed model indicates better results by showing good forecasting accuracy [5]. Ying Chen et.al. presented a modified technique to improve forecasting accuracy through neural network. The data of previous day with 24 hour samples were used to anticipate load of next day. The noisy nature can be improved with the introduction of high frequency and precipitation components. These two components are added to neural network algorithm as inputs for better forecasting results. This technique was also tested on short term and holidays load forecast and gave better results [6]. M. A. Abu El Magd et. al. proposed a hybrid method by combining ANN and time-series model for anticipating hourly heaps of week days. Two strategies were used in this paper, the 1<sup>st</sup> depends on relationship/auto-connection coefficient to choose the input factors and plan a measure to choose training sets and the 2<sup>nd</sup> was creating two calculations for modifying the predictions of occasions, weekends and Mondays. Contrasted with different methodologies, the exactness of the proposed show is incredible [7]. Azzam ul Asar et. al. suggested a hybrid approach by combining the ANN with other intelligent techniques for attaining better accuracy in forecasting problem. ANN and other conventional techniques when used alone didn't give better results due to complexity and non linear nature of load. A multiagent approach by realizing ANN with fuzzy logic was used and results obtained gave better forecasting accuracy and less computational time [8]. Ling et. al. presented a combined model using the addition of improved Genetic algorithm and neural fuzzy logic network. To locate ideal number of fuzzy principles, Genetic algorithm was utilized while fuzzy logic available here was used to manage variable data in stack anticipating and this technique by some ways needs to defeat the regular issues of meeting to nearby minima and affectability to introductory values [9]. Hong-ze li et.al. proposed a new model for estimating future load by using generalized regression neural network (GRNN) in combination with a optimization algorithm called fruit fly (FOA). The spread parameter value for GRNN was automatically selected by FOA. The results attained shows that proposed hybrid technique inspite of small training samples gave smaller MAPE and MSE and better forecasting accuracy as compared to other techniques [10].

Support Vector Machines (SVMs) are the most recent dominant methods used for both non linear and linear data

classification/ regression problems [5]. Support vector machine has become more popular among researchers because it uses non linear mapping by converting a data into high dimension (feature) space and then making decision boundaries also called hyper planes using linear functions in new space.

Amit Jain and B.Satish presented a modified technique to improve forecasting accuracy through SVM by clustering the data at pre-processing stage. The data was clustered by setting a threshold value for testing and training patterns of daily average load. The SVM technique implemented on both clustered and non clustered data inputs gave better forecasting results for clustered data [11]. Jae H.Min and Young-Chan Lee used Support vector machine for Bankruptcy prediction problem. Tuning of parameters were done to get the results with less prediction errors. The results obtained show that RBF kernel gave best results on both training and holdout (testing) data as compared to conventional statistical models [12]. Hwang showed the improvement of STLF master framework called LoFy which comprised of three models i.e. day by day, week after week and uncommon days estimating models. As it is currently a well-established truth that there is no single estimating strategy, which ensures exact outcomes throughout the day. Also, the determining consequences of a specialist are better than that of any hypothetical strategies [13]. Ming-Guang Zhang tested support vector machine on sampled data and found better results in comparison with ANN. The SVM works on the training samples and provide separation of data by introducing higher dimensions. The data is trained with load and temperature inputs. The results of SVM regression techniques gave better accuracy and less computational time [14]. The drawback of ANN for selection of appropriate architecture is replaced in support vector machine by the dilemma of selecting a suitable kernel function [15].

There are certain factors that affect/influence the load and must not be neglected while predicting future load. M.U. Fahad and N.arbab categorized these factors as time factor, economic effect, weather, special events and emphasizes the consideration of these factors while predicting future load. It was observed that "Time of Day" is actually a crucial factor and load curve basically depends on it. Similarly it also depends on day of week, month and season [16]. Another important effect while considering future load is economic effect. Developed and undeveloped countries load curve was compared and observed that highest peak comes from 1100 to 1600 in developed countries while in undeveloped countries it is noticed after 1800 and by adopting "Time of use pricing" load curve peaks can be reduced [17].

Another important factor for load prediction is weather. It has been observed in order to minimize the forecasting error weather must be considered as it is an independent factor in prediction process [18] [19]. In this paper factors affecting the load forecasting has been analysed and SVM-R kernel based model is proposed for short term load forecasting considering these factors which includes metrological parameters, holiday period, real time data, past data etc.

### III. METHODOLOGY

In this paper the technique/method used for predicting future load is Support Vector Machine. Support Vector Machine –SVM (Vapnik, 1979) is used for both nonlinear and linear data classification/regression [5]. The main feature of SVM algorithm is that it uses “nonlinear mapping” which means it converts data used originally in training process into new higher dimension feature space. The data of two different classes is separated from one another in this new dimension using optimal linear hyper-plane (LHP). The SVM decide this LHP using margins and support vectors, this hyper-plane is also called decision boundary. Hyper-plane separates data into two different classes. The goal is to find out best separating hyper plane (SHP) which gives maximum possible margin between two classes and by using Langrangian algorithm we can get optimized separating hyperplane. SVM-R is obtained by

$$R_m = v^T x + a \quad (1)$$

Where  $R_m$  is a forecast variable,  $v$  stands for a vector which represents weight at training sample  $x$  &  $a$  shows bias value. The separating hyper-plane maximum value is given by

$$SHP_{Max} = \frac{2}{\|v\|} \quad (2)$$

Hence, the maximum margin separating hyper plane can be constructed by solving the following Primal optimization problem. After minimizing  $v$  SVM-R sets it's  $v$  and  $a$  which follows with limits as given in equation

$$SHP_{Min}(v, e_d) = \frac{1}{2} \|v\|^2 + \frac{1}{2} \beta \|e_d\|^2 \quad (3)$$

Subject to

$$R_{mi} = v^T x_i + a + e_d, \forall i \quad (4)$$

The two main reasons due to which Langrangian function is applied are

- This allows to easily handle constraints
- The dot product is shown by training data between vectors. This arrangement introduces  $\alpha_i$  (Lagrange multiplier) to form a minimization problem for every constraint. Lagrange function as it deems both the minimizing term and constraint equation is used to find out the solution of the problem in equation (3).

$$LAG = SHP_{Min}(v, e_d) - \sum_{i=1}^n \varphi_i (v^T x_i + a + e_d) \quad (5)$$

Making Lagrange gradient w.r.t  $v$ ,  $a$ ,  $e_d$  and  $\varphi_i$  to zero, following equations can be obtained respectively

$$\frac{\partial LAG}{\partial v} \rightarrow v = \sum_{i=1}^n \varphi_i (x_i) \quad (6)$$

$$\frac{\partial LAG}{\partial a} \rightarrow v \sum_{i=1}^n \varphi_i = 0 \quad (7)$$

$$\frac{\partial LAG}{\partial e_d} \rightarrow v \varphi_i = \beta \quad (8)$$

$$\frac{\partial LAG}{\partial \varphi} \rightarrow v v^T x + a + e_d - R_{mi} = 0 \quad (9)$$

Hence, by solving equations 6-9 we can get appropriate values  $\varphi$  and  $a$  so SVM-R problem can finally be written as,

$$R_m = \sum_{i=1}^n \varphi_i K(L, L_i) + a \quad (10)$$

### IV. PROPOSED SVM-R KERNEL BASED MODEL

Fig.1 shows the steps of proposed model which are discussed one by one. First step; in this step the SVM-R model needs input training vectors which contain system load data as a class variable and the meteorological parameters such as dry bulb, dew point, demand, price sensitive demand and hours of a day are its attributes.

Second step; in this step the data is analysed at pre-processing stage and to make the model effective and for accurate load forecasting the input data used must be in same units. There are number of techniques and methods available for data normalization. In this research the techniques used for normalizing the input data is Min-Max-Scaling [3].

Third step; fine tune the SVM-R model by selecting the best parameters i.e (1) Cost Parameter (C) for linear kernel, (2) Cost parameter (C) and gamma parameter for radial kernel and (3) for polynomial, kernel function parameters  $c$  and  $d$  has investigated.

In fourth and fifth step; the model is trained according to the training input set and its accuracy is tested on testing data set which contains data of 30 days.

Sixth step; using mean absolute percentage error (MAPE) the accuracy is being tested between actual real time data and predicted electric load and in the last seventh step; the comparative accuracy between SVM-R model and ANN has been discussed in terms of MAPE.

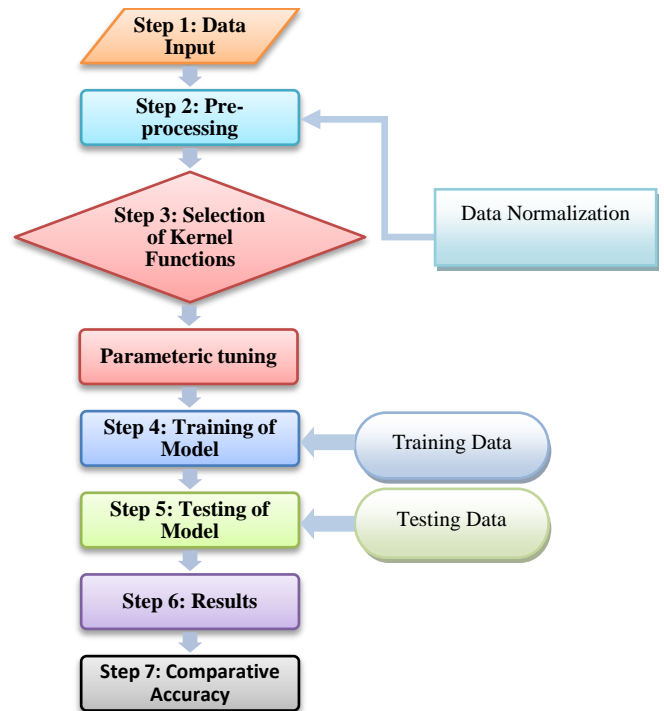


Figure 1. Proposed model

## V. DATA SET

The data of ISO New England for our case study in the time span of (2004-2008) is used in this research and the data set is available online for researchers which can be accessed easily [6].

The data has been analysed at pre-processing stage and divided into two sets. One is Training set and the other is testing set. Training set includes data from (Jan 2004-Nov 2008) and is used for training the proposed model while testing set includes data from (Dec 2008) and is used for monthly ahead forecasting comparison.

The sample size of train set used for training the model is (43105) hrs of data while testing set comprises of (744) hrs of data which is used to evaluate/check the potential of the proposed model by comparing the forecasting load vs system actual load. It has been investigated for the best SVM-R parameter so that the least error in terms of MAPE could be achieved.

As discussed earlier the most important factor in the load forecasting is season variations. To make accurate load forecasting we have split and arranged the data in five scenarios according to seasonal variation and furthermore in working or weekend period that includes

Scenario A: Spring (Mar-May) Data sample for train set is (10296) and test set is (744).

Scenario B: Summer (Jun-Aug) Data sample for train set is (10296) and test set is (744).

Scenario C: Autumn (Sep-Nov) Data sample for train set is (10200) and test set is (720).

Scenario D: Winter (Dec-Feb) Data sample for train set is (10152) and test set is (696).

Scenario E: Working Hours Data sample for train set is (30768) and test set is (552).

Scenario F: Weekends Data sample train set is (12288) and test set is (192).

Each scenario has been investigated to get best SVM-R parameter so least error MAPE could be achieved.

## VI. SIMULATION RESULTS DISCUSSION AND EVALUATION

The results of the experimentation are explained in this section.

### A. Forecasted Results

After data normalization the performance of SVM-R has been investigated by using different kernels i.e linear kernel, polynomial kernel and radial kernel and the effectiveness/accuracy of predicted load is calculated using (MAPE). The predicted load curves are compared with system actual load curve to know the effectiveness of proposed model.

Table 1. MAPE Comparison of Kernel functions

	Linear	Radial	Polynomial
(MAPE)	0.216197	0.5900855	3.987059

Table 1 shows the forecasted load accuracy in terms of mean absolute percentage error of three kernels. It is clear from the above table that Linear SVM-R Kernel outclass the performance of polynomial SVM-R and radial SVM-R kernels and gives better results.

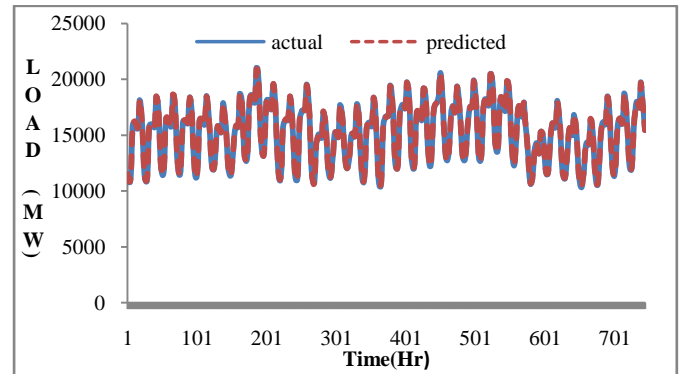


Figure 2. Comparison of Actual vs Predicted Load For Linear Kernel

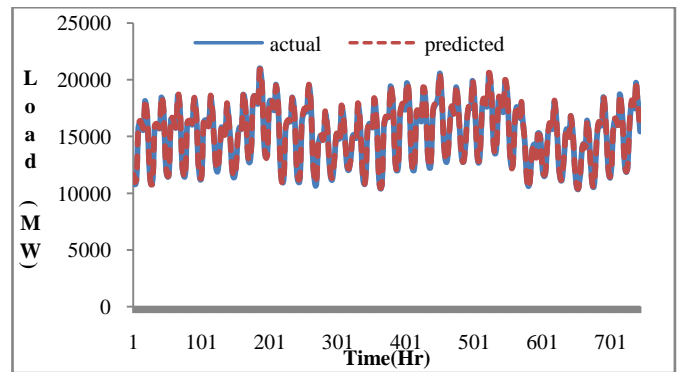


Figure 3. Comparison of Actual vs. Predicted Load For Radial Kernel

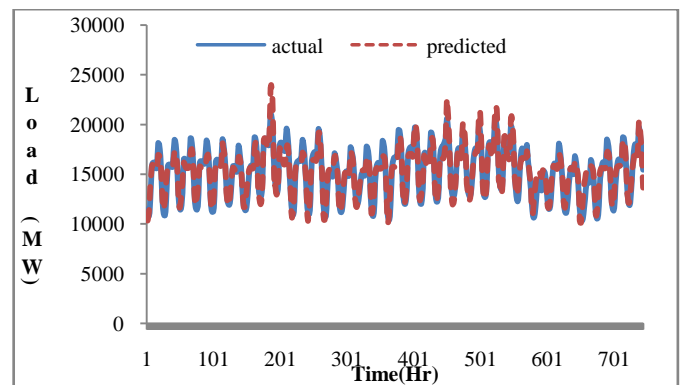


Figure 4. Comparison of Actual vs Predicted Load For Polynomial Kernel

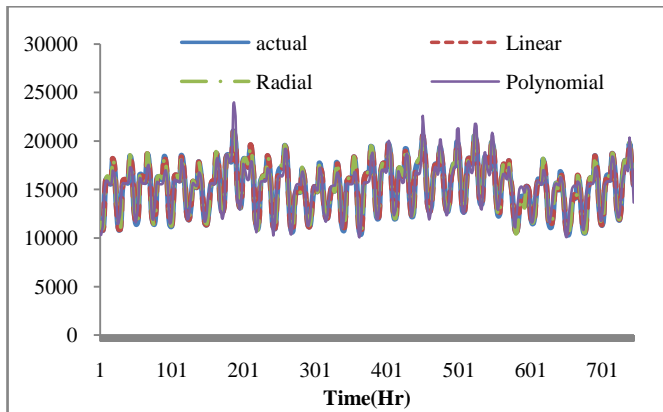


Figure 5. Comparison of Actual vs Linear,Radial,Polynomial Forecasted Loads

Fig .5 shows the actual system laod curve and the predicted load curves using the three kernels. It can be clearly seen from the above figure that linear kernel gives better results then radial and polynomial kernels

#### B. Parametric tuning using Cost parameter (C) for linear kernel.

The parameter used for the linear kernel is cost (C). The best performance can be obtained by fine tuning the linear kernel using several combinations of kernel parameter Cost (C). The best value of C can be obtained by using grid search technique (GS).

Fig 6. shows the best cost value which is **30** on which MAPE is **0.2149602**

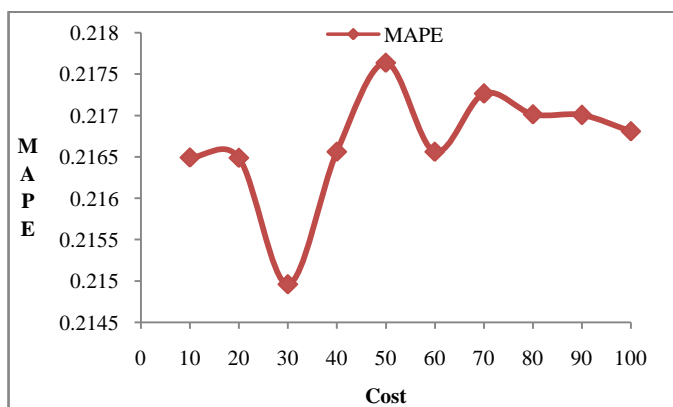


Figure 6. Parametric tuning using cost parameter(c) for Linear kernel

#### C. Parametric tuning using Cost parameter(C) and regularization paramer (gamma) for Radial kernel.

The parameters used for fine tuning the radial kernel are Cost (C) and gamma. The best value can be obtained by using various combinations of cost parameter (C) and regularization parameter gamma. Fig .7 shows the best values of cost (C) and gamma which are **2** and **0.5** using GS technique on which MAPE is **0.5344289**.

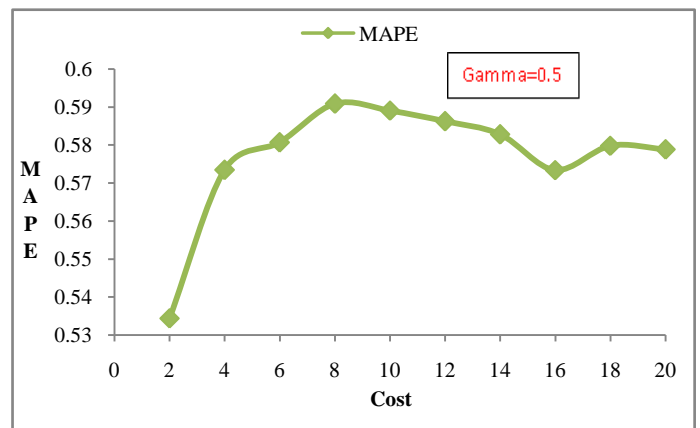


Figure 7. Parametric tuning using cost parameter(c) and regularization parameter (gamma) for Radial kernel

#### D. Parametric tuning using Cost parameter(C), regularization parameter (gamma) and d for Polynomial kernel.

The effect of using parameters for fine tuning the polynomial kernel can be seen in fig.8. It is clear from the fig below that using best optimal values of Cost ,gamma and d which are **15,0.5** and **3** the minimum value of MAPE is **3.965224**.

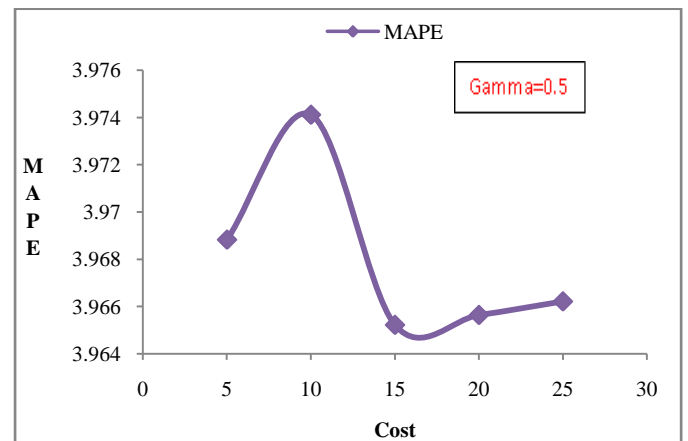


Figure 8. Parametric tuning using cost parameter(c), regularization parameter (gamma) and d for polynomial kernel

Table.2 below shows the optimal combination of parameters used for linear,radial and polynomial kernel.

Table.2.Optimal combination of parameters

	Linear		Radial			Polynomial			
	C	MAPE	C	$\gamma$	MAPE	C	$\gamma$	d	MAPE
Data	30	0.21496	2	0.5	0.5344289	15	0.5	3	3.965224



### E. Forecasted result using ANN

Artificial neural network is widely used in machine languages and has a very good forecasting accuracy. It gives excellent forecasting accuracy in time-series load forecast..In this paper for comparison purpose we use back propagation artificial neural network (BPNN).

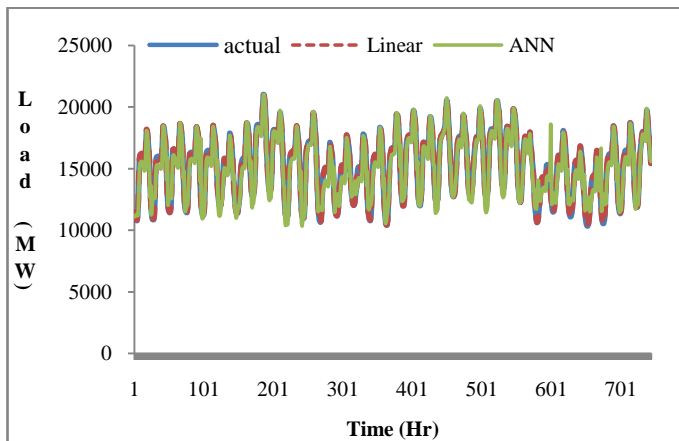


Figure 9. Comparison of Actual vs Proposed SVM-R Linear Vs ANN Forecasted Loads

The comparison of MAPE for load forecast between SVM-R and ANN in table.3 shows extraordinary performance of SVM-R model. Artificial neural network gives some of disadvantages such as over learning, architecture selection ,local minimal point and type over depending.

Table 3. MAPE Comparison of SVM-R vs ANN

	Linear	Radial	Polynomial	ANN
MAPE	0.2149602	0.5344289	3.965224	4.1858331

### F. Comparison of results.

Fig. 10 shows the SVM-R linear kernel gives the better results in terms of mean absolute percentage error (MAPE) i-e 0.2149602 as compared to radial and polynomial having MAPE of 0.5344289 , 3.965224. As it is seen in the figure the results are also compared to BPNN model to compare the effectiveness of proposed SVM-R model and it can be observed that SVM-R model gives better results then BPNN model.

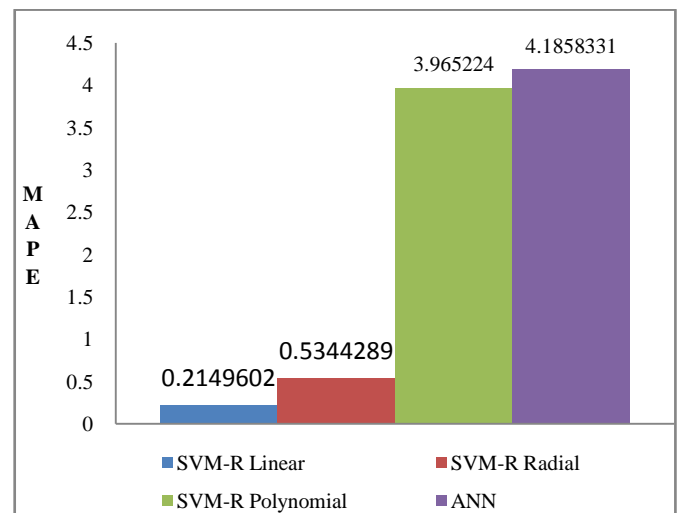


Figure 10. MAPE Comparison (Linear, Radial, Polynomial) and ANN

### G. Scenario result analysis using SVM-R.

The electric load demand varies according to seasons for exmple in summer season electric load demand is higher as compared to other seasons. To make load forecasting more accurate and precise we have divided the data into six scenarios as discussed earlier. Fig.11(a-f) below shows the comaprison of actual vs predicted/forecasted load for scenarios

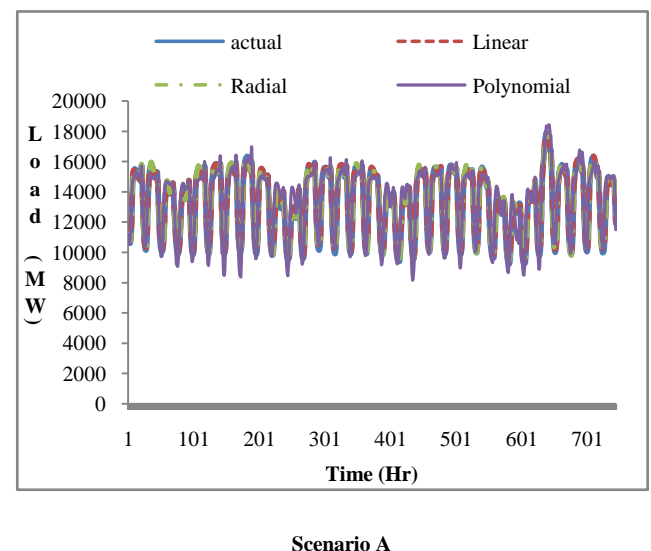
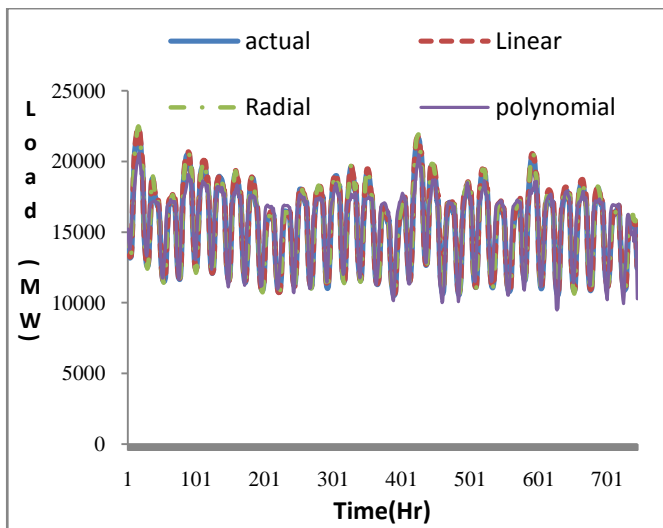


Figure 11(a). Comparison of Actual vs SVM-R Forecasted Loads For Scenario A

Fig.11 (a) shows actual system load data curve and predicted load curves using different kernels of SVM for data set regarding spring season i.e. Mar-May. The input data set used for training samples is 10296 and testing set is 744.

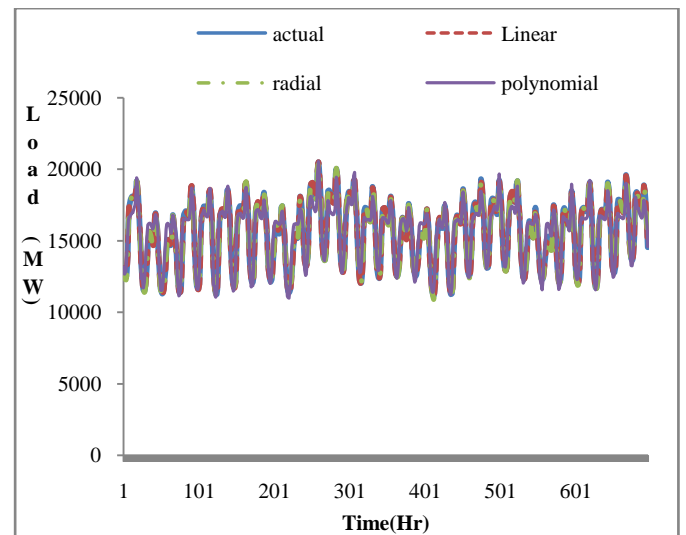




**Scenario B**

Figure 11(b). Comparison of Actual vs SVM-R Forecasted Loads For Scenario B

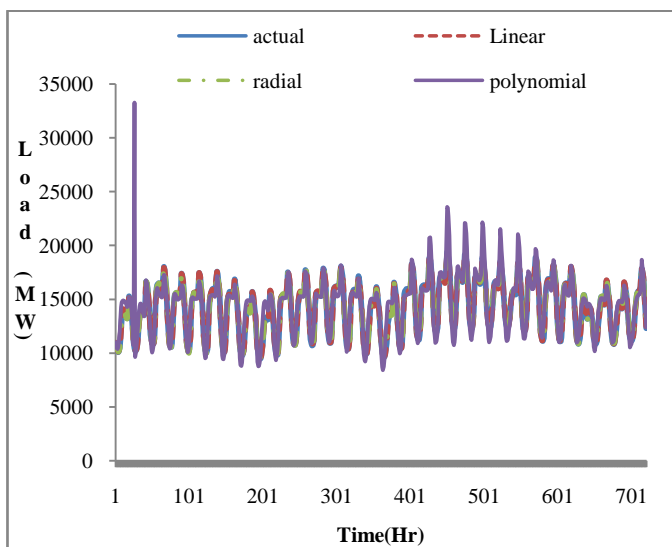
Fig.11 (b) shows actual system load data curve and predicted load curves using different kernels of SVM for data set regarding summer season i.e. Jun-Aug. The input data set used for training samples is 10296 and testing set is 744



**Scenario D**

Figure 11(d). Comparison of Actual vs SVM-R Forecasted Loads For Scenario D

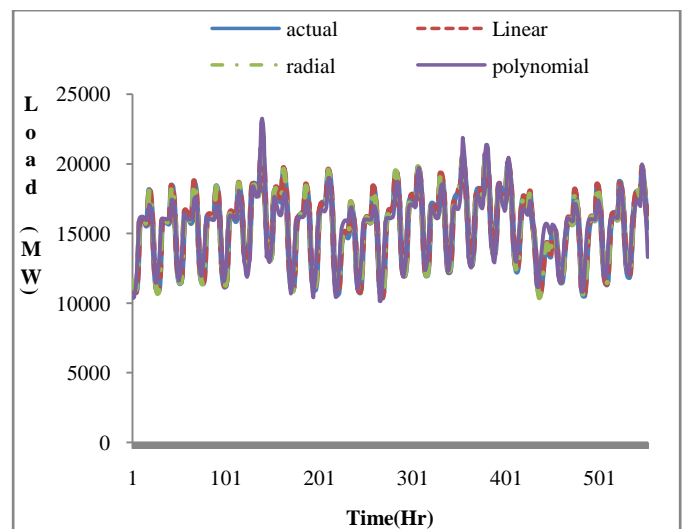
Fig.11 (d) shows actual system load data curve and predicted load curves using different kernels of SVM for data set regarding winter season i.e. Dec-Feb. The input data set used for training samples is 10152 and testing set is 696.



**Scenario C**

Figure 11(c). Comparison of Actual vs SVM-R Forecasted Loads For Scenario C

Fig.11 (c) shows actual system load data curve and predicted load curves using different kernels of SVM for data set regarding autumn season i.e. Sep-Nov. The input data set used for training samples is 10200 and testing set is 720



**Scenario E**

Figure 11(e). Comparison of Actual vs SVM-R Forecasted Loads For Scenario E

Fig.11(e) shows actual system load data curve and predicted load curves using different kernels of SVM for data set regarding working hours. The input data set used for training samples is 30768 and testing set is 552.

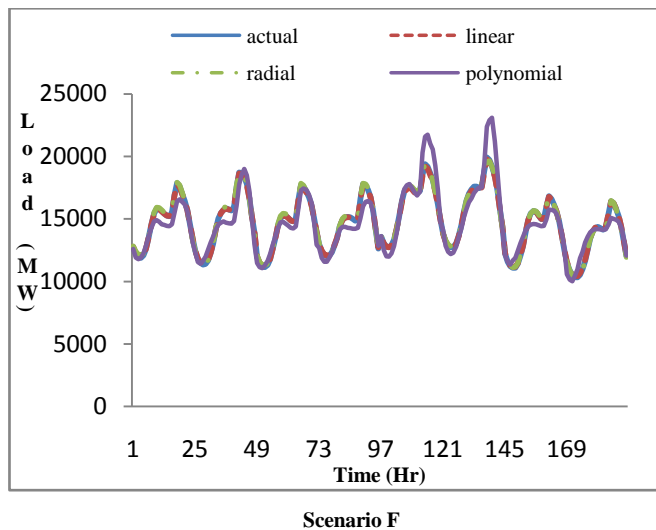


Figure 11(f). Comparison of Actual vs SVM-R Forecasted Loads For Scenario F

Fig.11(f) shows actual system load data curve and predicted load curves using different kernels of SVM for data set regarding weekends. The input data set used for training samples is 12288 and testing set is 192.

The performance accuracy using three kernels is shown in table.4 .It is observed from the table the difference between forecated error is very small between linear and radial kernels. Radial kernel shows extraordinary performance for Scenario A and B while SVM-R Linear kernel gives exemplory performance for Scenario C, D, E and F then radial and polynomial.

Table 4. Scenario Wise MAPE Comparison

	Linear	Radial	Polynomial
<b>Scenario A</b>	0.8855717	0.68289363	4.183518
<b>Scenario B</b>	0.834787	0.8188903	5.080259
<b>Scenario C</b>	0.5324723	0.7122615	4.494134
<b>Scenario D</b>	0.2745534	0.4343161	3.336685
<b>Scenario E</b>	0.4703293	0.4804051	3.933487
<b>Scenario F</b>	0.3126424	0.552294	4.161799

#### H. Scenario result comparison.

The results shown in Fig. 12 gives the comparison between the proposed SVM-R model and ANN model. Both models proves to be good for load forecasting but the comparison between SVM and ANN shows the excellent performance of SVM model and gives better results.

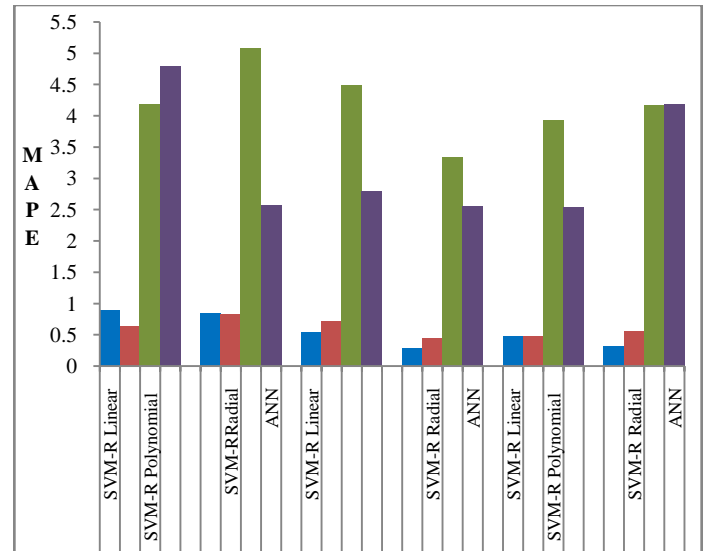


Figure 12. MAPE Comparison (Linear, Radial, Polynomial) and ANN

#### CONCLUSION

In this study, we have concluded that load data is highly complex and non-linear in nature. So we proposed a parametric tuned SVM-R kernel based model.

Proposed SVM-R model is implemented on ISO-New England data set. It is concluded that parametric tuned SVM-R Linear kernel having MAPE of 0.2149602 gives extraordinary performance and gives better results then polynomial and radial kernel having MAPE of 0.5344289 and 3.965224. The proposed model is then compared to BPNN model to compare the effectiveness of proposed model in terms of MAPE and it is concluded that SVM-R outclass the performance of BPNN model having MAPE 4.1858331.

In this research, we have also incorporated some of the factors that influence the load forecasting by dividing our data set in six scenarios according to seasonal variations , working hrs and weekends. Proposed SVM-R model has been implemented to select the suitable kernel for each scenario and it is concluded that SVM-R Radial kernel gives better results for scenario A and B by giving minimum MAPE values of 0.68289363, 0.8188903. Similarly for scenarios C, D, E and F SVM-R Linear kernel gives better results having minimum MAPE of 0.5324723, 0.27455345, 0.4703293, 0.3126424 as compared to radial and polynomial kernel. There is a huge scope of automatic feature selection, optimization of parameters using PSO and other hybrid techniques to further improve efficiency.

## REFERENCES

- [1] A .S. Ahmad, M.Y. Hassan, M.P. Abdullah,H.A. Rahman, F. Hussin, H. Abdullah, R. Saidur , “A review on applications of ANN and SVM for building electrical energy consumption forecasting” Renewable and Sustainable Energy Reviews, vol. 33 , pp. 102 – 109, 2014.
- [2] C. Cortes, V. Vapnik “Support-Vector Networks” Machine Learning, vol. 20, pp. 273-297, 1995.
- [3] V.N. Vapnik “The Nature of Statistical Learning Theory” NewYork, Springer Verlag, 1995.
- [4] Nahi Kandil, Vajay Sood, Maarouf Saad, “Use of ANN for STLF”, IEEE1999.
- [5] Dipti Srinivasan, Swee sien ten, C S.Chang, “Parallel Neural Network – Fuzzy expert system strategy for STLF: System implementation and performance evaluation” IEEE Transactions on Power Systems, Vol. 14, No 3 August 1999.
- [6] Ying Chen, Peter B.Luh, Che Guan, Yige Zhao, Laurnet D.Michel, Matthew A.Coolbeth, Peter B.Friedland, and Stephen J.Rourke. “Short-term load forecasting: similar day-based wavelet neural networks,” IEEE Transactions on Power Systems, Vol. 25, Pages 322-330,2010
- [7] M.A. Abu El Magd, R.D. Findlay, “New approach using ANN and Time Series Models for STLF” Electrical and Computer Engineering, IEEE CCECE , Canadian conference, Vol. 3, Pages 1723-1726,2003.
- [8] A Asar, SR Hassnain, and AU Khattack. "A multi-agent approach to short term load forecasting problem." International journal of intelligent control and systems ,Vol. 10 , pp. 52 – 59, 2005.
- [9] S.H. Ling, H.K. Lam, F.H.F. Leung and P.K.S. Tam, “A neural fuzzy network with optimal number of rules for STLF in an intelligent home” IEEE Fuzzy Systems conference,2001.
- [10] Hong-Ze Li, Sen Guo, Chun-jie Li, Jing-qi Sun. "A hybrid annual power load forecasting model based on generalized regression neural network with fruit fly optimization algorithm." Knowledge-Based Systems, Vol. 37,Pages 378-387,2013
- [11] Amit Jain, and B. Satish. "Clustering based short term load forecasting using support vector machines." PowerTech, 2009 IEEE uchart. IEEE, 2009.
- [12] J. H. Min and Y.-C. Lee, "Bankruptcy prediction using support vector machine with optimal choice of kernel function parameters," Expert systems with applications, vol. 28, pp. 603-614, 2005.
- [13] Kab Ju Hwang, “ STLF Expert System”. IEEE Transactions KOROUS, IEEE, 2001.
- [14] Ming-Guang Zhang. "Short-term load forecasting based on support vector machines regression." International Conference on Machine Learning and Cybernetics, Vol. 7, pp. 4310-4314, 2005.
- [15] Ying LC, Pan MC. “Using adaptive network based fuzzy inference system to forecast regional electricity loads” Energy Conversion and Management , vol.49, pp. 205–11, 2008
- [16] M. U. Fahad and N. Arbab “Factor Affecting Short Term Load Forecasting” Journal of Clean Energy Technologies, Vol. 2, No. 4, pp. 305-309, October 2014.
- [17] “Long-Term Hourly Peak Demand and Energy Forecast, Electric Reliability Council of Texas, Inc., Taylor, TX, 2010, pp. 9.
- [18] M. Altalo and M. Hale,“Turning weather forecasts into business forecasts,” Environmental Finance, May 2004.
- [19] G. Franco and A. Sanstad,“Climate change and electricity demand in California,” Climatic Change, vol. 87, pp. 139-151, 2007.



**Engr. Hamad Ullah Khan Bangash** M.Sc research scholar in Department of Electrical Engineering, University of Engineering and Technology, Peshawar, Pakistan.  
Cell: 0092-3459163680  
E-mail: hamadbangash@yahoo.com

**Dr.Amjadullah Khattak** Professor in Department of Electrical Engineering, University of Engineering and Technology, Peshawar, Pakistan.  
Cell: 0092-321-9158118  
E-mail: amjad67@gmail.com

# Study the Effect of Transient Load on Pipeline Supported by Concrete Blocks

Rafi .M. Qasim<sup>1</sup>, Dr. Abdulameer .Q. Hasan<sup>2</sup>

<sup>1,2</sup>Basra Engineering Technical Collage, Southern Technical University, Basra, Iraq

Received: 18 August, Revised: 30 August, Accepted: 15 September

**Abstract**—A three dimensional analysis of dynamic load-nonlinear soil-concrete blocks - pipeline have been investigated to study the major factors that influencing the response of whole system and which dominate on the interaction between different component of the problem. The present work consider the effect of pipe diameter, distance between applied force and whole system, distance between concrete blocks or span of pipe. Aspects which addressed in this study the effect of the previous factors on deformation which can be express as vertical displacement and bending moment , friction stresses between concrete blocks and soil and Also the behavior of concrete blocks with time and distance. ABAQUS software is used to reveal the effect of these factors on structural behavior of whole system.

**Keywords**—pipeline, concrete blocks, dynamic load, finite element method

## I. INTRODUCTION

Pipes and pipelines are utilized in different engineering application for example used to convey oil or gas in chemical engineering; it is also used to convey potable water, rainfall and sewage in civil engineering so it shows the direct effectiveness on modern life. Piping systems are supported by concrete blocks for pipes above the ground or they are under ground. In both cases because of their natural frequencies they can be affected by ground movement and cyclic load [1]. An earliest study with regard to stresses and deflections that take place in pipelines at the transition from fully restrained to unrestrained situation was achieved by Schnackenberg [2]. The vibration transmission forecast by ground represents a complex problem [3]. In conventional finite element it is assumed that motion and deformation are small and the material behavior as linear elastic. In some cases this situation cannot be convinced leading to include of non-linearity action to the model [4]. Neglecting the ground-structure dynamic interaction will reflect on the response of structure and may give an overestimated or underestimated response [5]. Generally for gravity and operational loads vertical support is sufficient to withstand the vertical seismic forces as compare with other vertical loads [6]. The insufficiency rate of pipeline various significantly depend on the variation in design consideration, construction situation and the environmental condition. Commonly when the period of applied load is short dynamic analysis can be consider more accurate.

## II. METHODOLOGY

The present work concern with three dimensional dynamic load – nonlinear soil – concrete blocks – pipe line interaction model is built by using ABAQUS software to reveal the impact of many factors on structural behavior and stress distribution on whole system. The whole system consist of the following parts:

**Pipeline:** A 30m steel pipeline modeling by a three node beam element (B32: Quadratic beam in space) with linear elastic properties of material.

**Soil:** A solid brick element (C3D20R: Quadratic brick, reduced integration) with 20 nodes is used to model soil with nonlinear properties Mohr-Coulomb model is adopt for modeling nonlinear behavior.

**Concrete blocks:** A solid brick element is used to model support of pipeline with linear elastic properties of material.

For pipeline six different size are considered in the study with constant wall thickness (12.5mm) theses size are (250 ,500 ,750 ,1000 ,1250 and 1500)mm. Table (1) review the elastic properties of steel pipe. A concrete support of dimension (1 x 1 x 1.5)m with 1m embedment depth in soil with elastic properties shown in table(2). Table (3) reviews the nonlinear properties of soil. The size domain of current problem 10 diameter of pipe measured from center line of pipe and with depth equal to 10 diameter of pipe. Fixed boundary condition is considered for all side and bottom of domain except the top is free. Interface element is adopted as linkage element between soil and concrete support (Blocks) with tangential and normal behavior respectively and penalty with coefficient of friction equal to 0.36. Also tie constraint (node to node) linkage element is used between pipe and support and tie constraint (surface to surface) linkage element used between pipe joint. Dynamic load of magnitude (10KN) with amplitude shown in figure (1). The total period of applied load equal to 6 sec with time increase 0.1 sec. For all material damping ratio equal to 5%.

TABLE I. ELASTIC PROPERTIES OF PIPELINE

Modulus of Elasticity (GPa)	Poisson's Ratio	Yield Stress (MPa)
200	0.15	415

TABLE II. ELASTIC PROPERTIES OF CONCRETE BLOCKS (SUPPORT)

Modulus of Elasticity (MPa)	Poisson's Ratio
432000	0.2

TABLE III. SOIL PROPERTIES

Modulus of Elasticity (MPa)	Cohesion (KPa)	Poisson's ratio $\mu$	Angle of internal friction $\phi$
21200	40	0.35	0

It is required to reveal the influence of the following:

- 1-Effect of pipe diameter on vertical displacement and bending moment
- 2-Effect of distance between applied load and system (pipe and concrete blocks) on vertical displacement and bending moment
- 3-Effect of distance between supports on response of pipe on vertical displacement and bending moment
- 4-Effect of pipe diameter on development of friction stresses between soil and support
- 5- Effect of distance between applied load and system (pipe and concrete blocks) on development of friction stresses between soil and support
- 6- Effect of distance between supports on development of friction stresses between soil and support
- 7-Effect of time on vertical displacement of concrete support

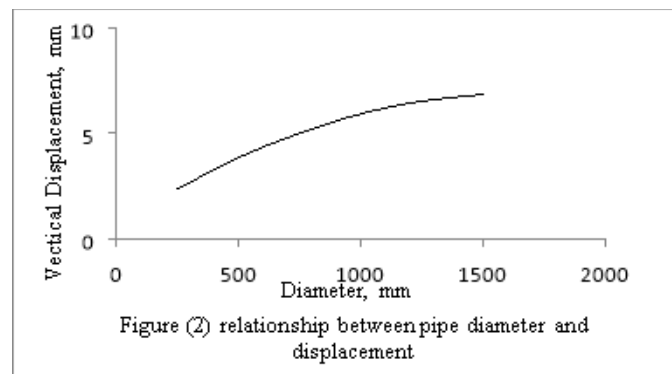


Figure 2. Relationship between pipe diameter and displacement

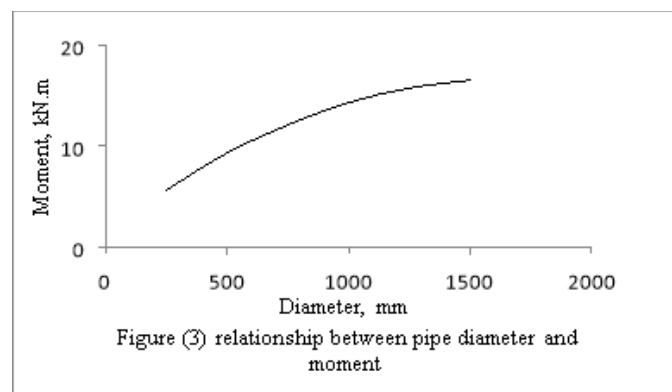


Figure 3. Relationship between pipe diameter and moment

It is difficult to determine the effect of distance on response of whole system but as distance between the applied load and whole system increase the response will decrease because of dissipation in load intensity that transfer by soil to whole system and this will reflect on response which represented by displacement and bending moment so it is appear from figures (4) and (5) as distance between load and whole system increase the displacement and bending moment decrease.

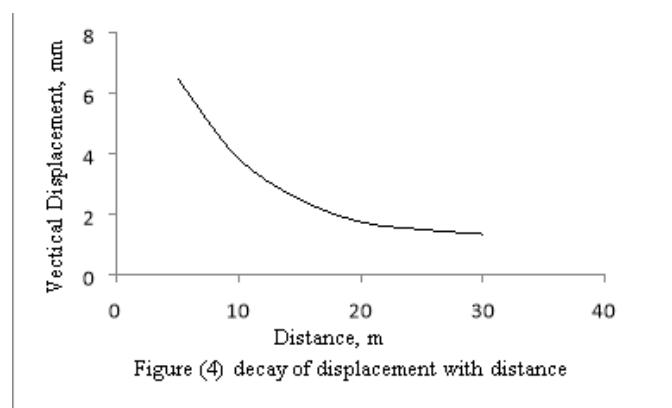


Figure 4. Decay of displacement with distance

Figure (1) relationship between applied load and time

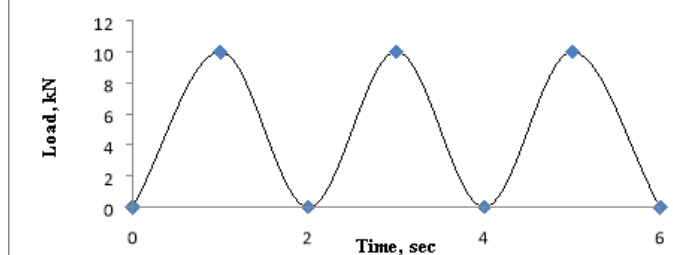


Figure 1. Relationship between applied load and time

### III. RESULT AND DISCUSSION

It is clear from figure (2) as the pipe diameter increase the vertical response increase due to combined effect of applied dynamic load with self-weight of pipe which increase with increasing in pipe diameter in addition to gravity weight of support these load dominate on the vertical response. Also as vertical displacement increase the bending moment will increase due to fact as the displacement or deflection increase the bending moment will increase and this appear clearly in figure (3).

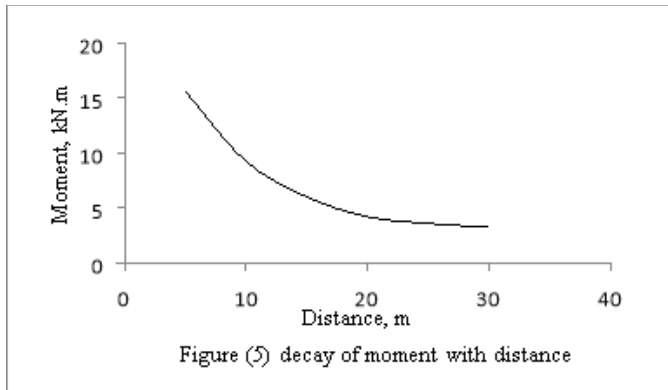


Figure 5. Decay of moment with distance

Figure (6) review as the distance between the supports (increase the pipe span) increase the vertical displacement increase due to increase in the load which represent by the weight of pipe in addition to the effect of applied load. Also figure (7) review as the distance between support increase the bending moment increase take inconsideration as deflection of span increase lead to increase in bending moment.

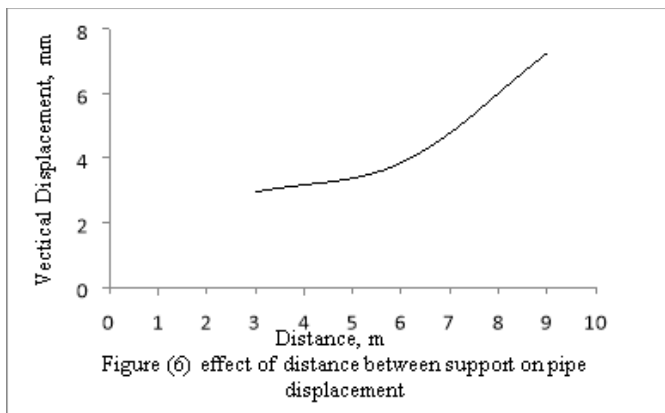


Figure 6. Effect of distance between support on pipe displacement

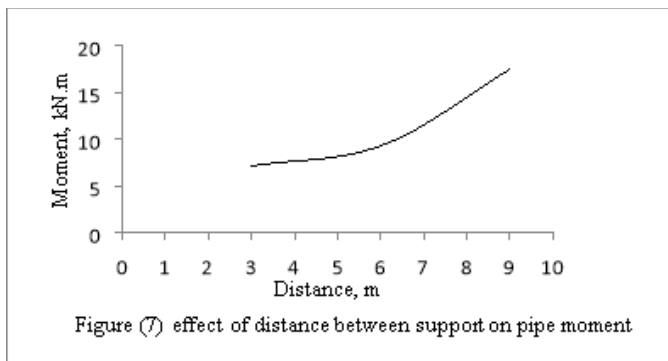


Figure 7. Effect of distance between support on pipe moment

Figure (8) shows as the diameter increase this mean the circumference of pipe increase and the contact area between pipe and concrete blocks support increase so when this area increase the development of friction stresses between pipe and concrete block also concrete block and soil increase

respectively with increase in diameter. Figure (9) shows as distance between the whole system (pipe and concrete blocks) and applied load increase the development of friction stresses between soil and concrete blocks decrease due to dissipated in load transfer by soil to the system so the response will decrease with increase the distance between load and system. Figure (10) shows as distance between neighboring supports increase the friction stresses between soil and concrete blocks increase due to increase in load between the span this load represented by self-weight in addition to applied load which have major effect on response.

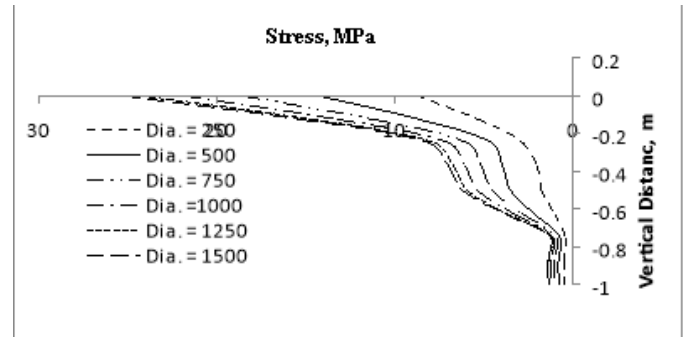


Figure (8) relationship between friction stress between soil and concrete blocks with vertical depth considering various diameter.

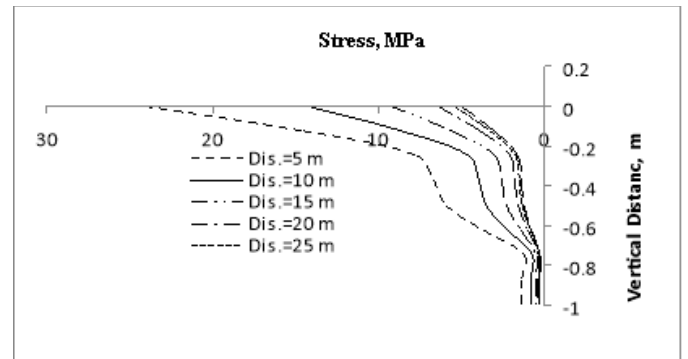


Figure (9) relationship between friction stress between soil and concrete blocks with vertical depth considering various distance between applied load and system.

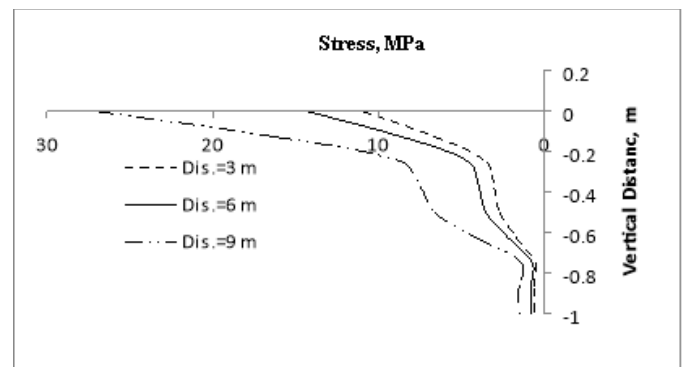


Figure (10) relationship between friction stress between soil and concrete blocks with vertical depth considering various distance between concrete blocks.

It is clear from figure (11) that the vertical response of concrete blocks increases with time and then reduces due to



dissipated in load transmitted by soil with time. Also it is appear from figure (11) the middle support have higher response as compare with the remainder support. Figure (12) shows the deformations occur in concrete support it is obvious that the middle support have higher response as compare with the remainder support. Also figure (13) shows the lateral stresses transmitted by concrete blocks to soil. Take in consideration F1 represent the middle support while F3 represent the third support which located at distance 12m from the first support F2.

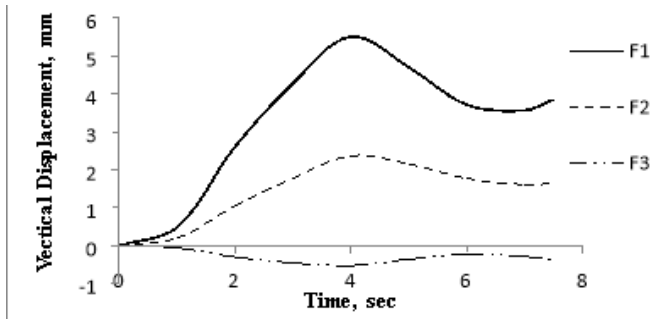


Figure 11. The vertical response of support with time.

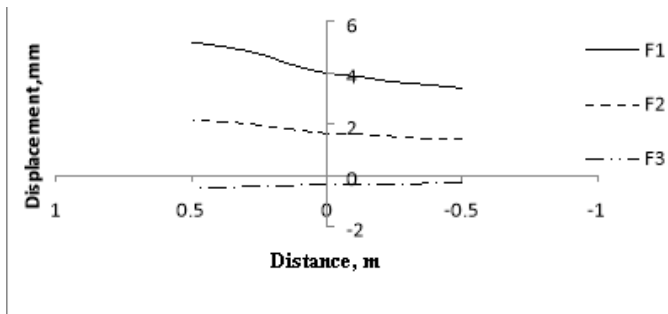


Figure 12. Relationship between vertical deformation and distance

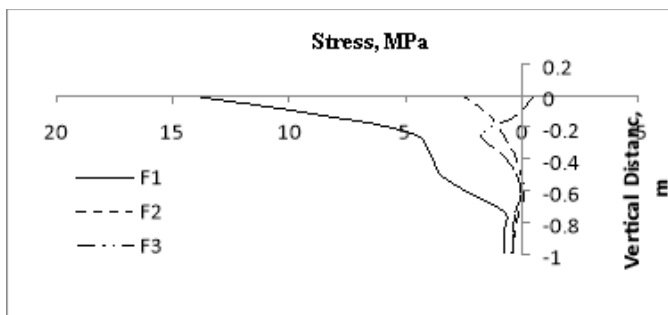


Figure 13. Review the lateral stresses transmitted to soil

## CONCUSLION

1-The vertical displacement and bending moment increase with increasing in pipe diameter

2- The vertical displacement and bending moment decrease with increasing the distance between the applied load and whole system

3- The vertical displacement and bending moment increase with increasing in pipe span

4- The friction stresses between soil and concrete blocks increase with increase in pipe diameter

5- The friction stresses between soil and concrete blocks increase with decrease in distance between applied load and whole system

6- The friction stresses between soil and concrete blocks increase with increase in pipe span

7-The response of concrete support varying with time due to dissipated in load transmitted by soil

## REFERENCES

- [1] Jonsdottir .F. , Jonsson .M.T. " Comparative Study of Seismic Analysis for Piping Systems" 2001 ASME Design Engineering Technical Conferences , September 9-12,2001, Pittsburgh, Pennsylvania , USA.
- [2] Schnackenberg .P.J. "How to Calculate Stress in above/below Ground Transition" Pipe Line Industry, November, 1976, pp. 53-56.
- [3] Barkan. D.D. "Dynamics of Bases and Foundations" 1962. New York: McGraw-Hill Book Company, Inc.
- [4] Lopes. M., Leite. A. "Economic Viability of Seismic Strengthening of Buildings; Ingenium: Greenbelt, MD, USA" 2005
- [5] Warburton. G.B. "The Dynamical Behaviour of Structures" Second Edition 1976.
- [6] Moussou. P. , Potapov. S. , Paulhiac. L. , Tijsseling. A. "Industrial cases of FSI due to internal flows" In Proceeding of the 9<sup>th</sup> International Conference on Pressure Surges, Chester , UK, 24-26 March 2004 ; pp. 167-181.

# Effect of Fly Ash on Mechanical Properties of Aluminum Alloy

Arshad Ali Khan<sup>1</sup>, Afzal Khan<sup>2</sup>

<sup>1,2</sup>Department of Mechanical Engineering , University of Engineering and Technology, Peshawar, Pakistan  
[enr.arshad2012@gmail.com](mailto:enr.arshad2012@gmail.com)<sup>1</sup>

Received: 04 September, Revised: 19 September, Accepted: 25 September

**Abstract**— This paper presents the effect of fly ash as reinforcement on mechanical behavior of aluminum alloy. 5% by weight of untreated fly ash was used as a reinforcement to fabricate the composite samples by sand casting technique. Tensile, Hardness and Fatigue tests were carried out for the samples. It has been observed that by the addition of fly ash to aluminum alloy improves the ultimate tensile strength (UTS) and hardness by 15.87% and 5.64% respectively as compared to sand casted simple aluminum alloy. Similarly fatigue tests reveal that fly ash reinforced aluminum composite has greater fatigue life than the unreinforced aluminum alloy.

**Keywords**— aluminum alloy, sand casting, aluminum composite, mechanical behavior, strength

## I. INTRODUCTION

Composite is the combination of two elements or constituents. The constituents have different composition and they retain their insolubility in each other. There are various types of composites in which they are classified. Most common classes are particulate reinforced composite and fiber reinforced composite. In particulate composite the reinforcement material is in the form of particles and in the fiber reinforced composite the reinforcement is in the form of fiber having some length and width or diameter. It is the need of the day to develop, design and fabricate new type of materials having the desired physical, chemical and mechanical properties for the specific application. Most recent trend in material field is discovering of new materials having low cost, excellent performance and lightweight and good mechanical properties. Combining reinforcement with the suitable matrix metal to achieve excellent properties has become a remarkable area for manufacturing science in MMCs [1]. The family of metal matrix composites (MMCs) has got more attention amongst various categories of composites. This class of composites is most commonly used in automobile and aerospace industries [2]. Pradeep R et.al carried out the study of a composite fabricated from aluminum alloy, silicon carbide and red mud. Al 7075 with different proportion of SiC and red mud were used. Samples were prepared for mechanical characterization having different composition. After performing mechanical tests it was observed that the tensile strength and Hardness enhanced as

compared to the unreinforced aluminum alloy [3]. Ravichandran M et.al synthesized a composite by combining titanium dioxide (TiO<sub>2</sub>) with pure aluminum element. He prepared various samples of the composite. The amount of TiO<sub>2</sub> varied during the fabrication of composite. He performed micro structural analysis for the presence of TiO<sub>2</sub> as reinforcement. He also performed mechanical tests (hardness, tensile) on the samples to compare the hardness and tensile strength of the composite with the pure aluminum. Finally it was concluded that by using 5% of TiO<sub>2</sub> with pure aluminum causes enhancement in the hardness and tensile strength [4]. Keshavamurthy R et. al performed work on the mechanical behavior of Al7075-TiB<sub>2</sub>. For this purpose he took two master alloys having designation as Al -10%Ti and Al-3%Br. Micro structural study of the composite and master alloys carried out. Also mechanical tests were performed for the identification of the mechanical behavior of the composite and the alloys. The results obtained from the tests showed that tensile strength, hardness of the fabricated composite are higher than the alloy [5]. Uvaraja et .al used the concept of hybridization while designing a composite by combining aluminum, silicon carbide and boron tetra carbide. The hybrid material has good fatigue properties, greater strength, dimensional stability at elevated temperatures, high wear resistance and lighter weight [6,7]. Mahendra Boopathi et al investigated the physical/mechanical properties of Aluminum 2024 in the presence of silicon carbide, fly ash and its combinations. The composites fabricated with the SiC (5%) + fly ash (10%) + Al2024 and SiC (10%) + fly ash (10%) + Al2024 compositions were studied. The various tests carried out on these hybrid samples reveal that by the addition of silicon carbide and fly ash the hardness of the hybrid composite increases while the density decreases. Similarly tensile strength of hybrid composite increases while elongation produced in the samples decreases with the addition of reinforcements [8]. A. K. Senapati et al fabricated Aluminum Matrix Composites (AMCs) using waste fly ash obtained from thermal power plant as reinforced material. He used 14.3% by volume of the reinforcement material (untreated fly ash) with aluminum. Also he used 13.2% by volume of fly ash (treated thermally). It was concluded that mechanical properties of treated fly ash reinforced composite are better than the untreated fly ash composite [9]. J. Babu Rao et al took pure aluminum and used five to fifteen (5%- 15%) percent by weight fly ash as reinforcement. Both X-ray Diffraction

(XRD) and Scanning Electron Microscopy (SEM) were used for the identification of the phase presence and for the analysis of microstructure of the fly ash as well as the aluminum-fly ash composite. By the addition of fly ash as reinforcement compression strength and hardness increased while the density of the composite decreased [10].

## II. MATERIALS AND METHODS

Addressing the call of the day for enhanced mechanical properties it is required to use inexpensive and readily available constituents in metal matrix. Various materials that are waste or byproducts can be explored in this regard and their potential to support and develop new combinations may be explored. In the current research aluminum alloy and fly ash were used as a matrix material and reinforcement respectively.

### A. Aluminum Alloy

Aluminum alloy was used as a matrix material. Aluminum alloy composition was checked through elemental analysis technique. The test result for elemental composition has shown in the Table 1 given below.

TABLE 1: ELEMENTAL COMPOSITION OF Al ALLOY

Element	% by weight
Al	82.71
Si	12.54
Cu	2.57
Fe	0.799
Zn	0.65
Mg	0.263
Mn	0.255
Ni	0.078
Sn	0.026

### B. Fly Ash

Fly ash was used as a reinforcement material. Elemental composition analysis was also carried out for it. The chemistry is given in the following Table 2.

TABLE 2: FLY ASH COMPOSITION

Element	% by weight
C	16.65
O	48.75
Mg	1.07
Al	9.11
Si	13.48
P	0.65
S	0.37
K	0.98
Ca	4.62
Ti	0.50
Fe	3.80

### C. Sand Casting of Composite

Once the composition was identified for both the matrix as well as reinforcement material, next step is to mix these two materials in proper way to fabricate a compsite.5% by weight fly ash was used with aluminium alloy to fabricate the aluminium based composite. Sand cating was used as a manufacturing technique for the fabrication of the composite. The steps mentioned in Fig 1 were followed.

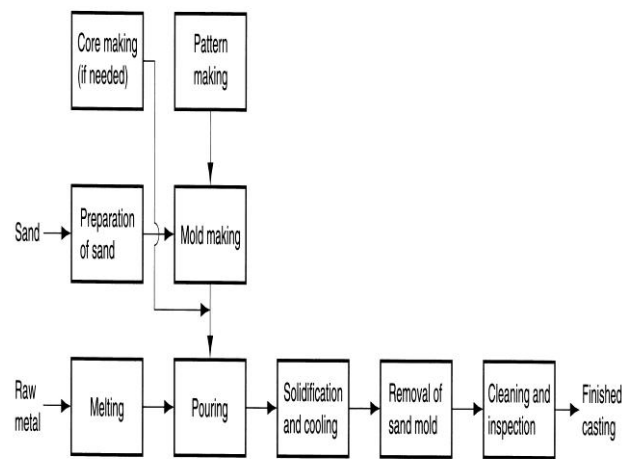


Figure 1: Activities in sand casting



Figure 2: Mould for fabrication of samples



Figure 3: Preparation of composite



Figure 4: Pit Furnace for Alloy melting

#### D. Tensile Test Conduction

The most common test usually used to find the tensile strength/stress of materials. This test is performed on ultimate tensile testing machine shown in Fig 5. Ultimate tensile testing machine has both facilities either to find tensile or compressive strength of the material. Tensile tests were carried out to draw the stress-strain curve on the computer. Standard sample sizes were used during the experiments as per requirement of the machine. Two types of samples were used to predict the tensile behaviour. First samples of unreinforced/ simple aluminium alloy were tested and stress-strain graphs were generated. Similarly keeping the same condition aluminium based matrix composite samples tested also and stress-strain curves were produced.



Figure 5: Ultimate Tensile Testing Machine

#### E. Fatigue Test Conduction

When a mechanical component is subjected to cyclic load it is more unsafe than the situation in which static load is applied. Samples for simple aluminium alloy and aluminium based matrix composite both were tested using fatigue testing machine as shown in Fig 6. During the experiments endurance  $N$  and time were noted.



Figure 6: Machine for Fatigue Test

#### F. Hardness Test conduction

Hardness test is a non-destructive test which is mostly used due to its simplicity. There are four types of hardness machines available to check the hardness value of a material namely, Brinell, Rockwell, Micro Vicker and Vicker hardness testers. We have used Vicker hardness tester as shown in Fig 7 in our experiments. Just like for the tensile and fatigue tests samples were also fabricated for hardness tests. First the hardness value for unreinforced aluminium alloy was found. Secondly the hardness value for the aluminium based composite material was calculated. The test technique is same as Brinell's hardness test but unlike the Brinell's technique, a pyramid-shape diamond is used in the experiment for indentation. The diagonals of the impression are measured and then average of both is taken to find the hardness value of the material.

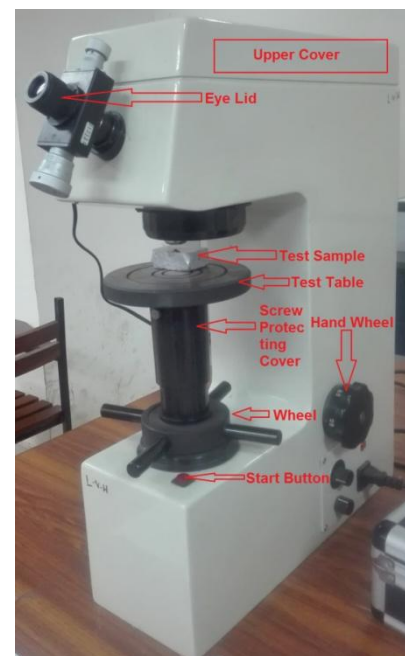


Figure 7: Machine for Hardness Test

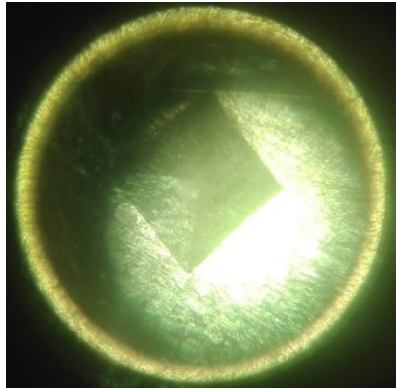
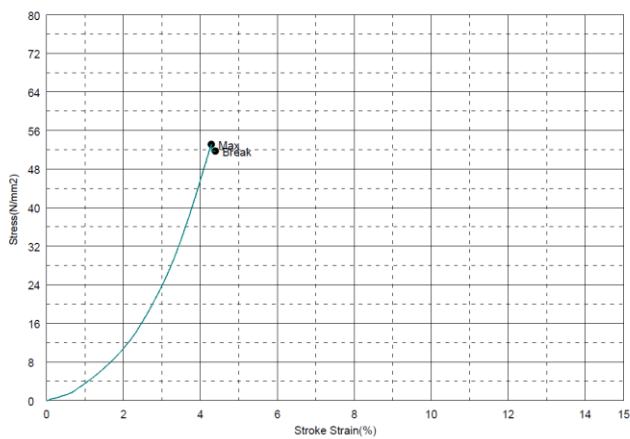


Figure 8: Impression produced during hardness test

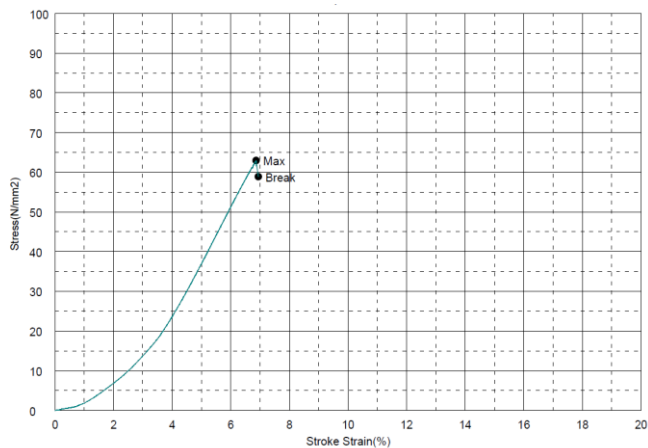
### III. EXPERIMENTAL RESULTS

#### A. Tensile Test Results

The tensile tests results for unreinforced/simple aluminum alloy and aluminum based matrix composite are presented in the Graph 1 and Graph 2 respectively.



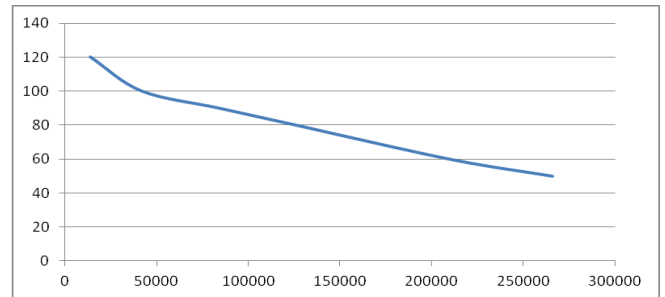
Graph 1: Simple aluminum alloy stress-strain curve



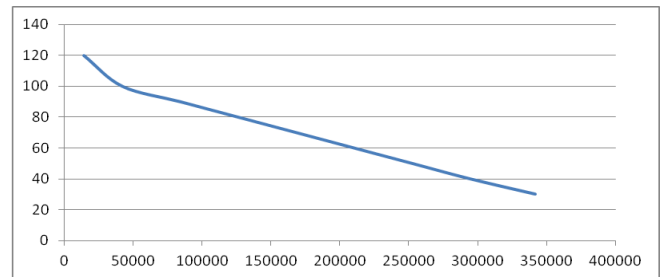
Graph 2: Aluminum based matrix composite stress-strain curve

#### B. Results of Fatigue Test

The fatigue tests results for unreinforced/simple aluminum alloy and aluminum based matrix composite are presented in the Graph 3 and Graph 4 respectively.



Graph 3: S-N curve for sand casted simple aluminum alloy



Graph 4: S-N curve for sand casted aluminum based matrix composite

#### C. Results of Hardness Test

The hardness tests results for unreinforced/simple aluminum alloy and aluminum based matrix composite are presented in the Table 3 and Table 4 respectively.

TABLE 3: TEST FOR UNREINFORCED ALUMINUM ALLOY

Force (Kgf)	Force (N)	Dwell Time (sec)	d <sub>1</sub> (mm)	d <sub>2</sub> (mm)	d = d <sub>1</sub> + d <sub>2</sub> /2 (mm)	VHN
5	49.03	5	0.310	0.314	0.3120	95.3

TABLE 4: TEST FOR 5% FLY ASH REINFORCED ALUMINUM BASED MATRIX COMPOSITE

Force (Kgf)	Force (N)	Dwell Time (sec)	d <sub>1</sub> (mm)	d <sub>2</sub> (mm)	d = d <sub>1</sub> + d <sub>2</sub> /2 (mm)	VHN
5	49.03	5	0.302	0.304	0.303	101



## CONCLUSION

Mechanical behaviour of sand casted simple aluminium alloy and aluminium based composite were presented in this work. By performing various types of tests; tensile, fatigue and hardness it has been observed that mechanical properties are improved. The ultimate tensile strength (UTS) of the sand casted aluminum based composite improves by 15.87% as compared to sand casted simple aluminum alloy. The fatigue strength of the sand casted aluminum based composite increases as compared to simple aluminum alloy. The hardness of the sand casted aluminum based composite increases by 5.64% compared to simple aluminum alloy.

## REFERENCES

- [1] A. K. Senapati, P. C. Mishra, B. C. Routray and R. I. Ganguly "Mechanical Behavior of Aluminium Matrix Composite Reinforced with Untreated and Treated Waste Fly Ash" *Indian Journal of Science and Technology*, Vol 8(S9), 111–118, May 2015
- [2] Hartaj Singh, Sarabjit, Nrip Jit, Anand K Tyagi "An overview of metal matrix composite: processing and SiC Based Mechanical Properties" *Journal of Engineering Research and Studies* Vol. II, Issue IV, 72-78 Oct-Dec, 2011
- [3] Pradeep, R., Praveen Kumar, B.S and Prashanth: "Evaluation of mechanical properties of aluminium alloy 7075 reinforced with silicon carbide and red mud composite" *International Journal of Engineering Research and General Science*, Vol. 2, Issue 6, (1081-88), 2014.
- [4] Ravichandran, M. and Dineshkumar, S.: "Synthesis of Al-TiO<sub>2</sub> Composites through Liquid Powder Metallurgy Route" *International Journal of Mechanical Engineering*, Vol. 1 Issue 1, 2014.
- [5] Keshavamurthy, R., Sadananda Mageri, et.al: "Microstructure and Mechanical Properties of Al7075-TiB<sub>2</sub> in-situ composite" *Research Journal of Material Sciences*, Vol. 1(10), (6-10), 2013.
- [6] Uvaraja, C. and Natarajan, N.: "Comparison on Al6061 and Al7075 with SiC and B<sub>4</sub>C reinforcement hybrid metal matrix composites" *IJART*, Vol.2, pp,1–12, 2012.
- [7] Hartaj Singh, Sarabjit, Nrip Jit et.al: "An overview of metal matrix composite processing and SiC based mechanical properties" *Journal of Engineering Research and Studies*, Vol. II, (72–78), 2011.
- [8] Mahendra Boopathi, M., K.P. Arulshri and N. Iyandurai: "Evaluation of mechanical properties of aluminium alloy 2024 reinforced with silicon carbide and fly ash hybrid metal matrix composites" *American Journal of Applied Sciences*, 10 (3): 219-229, 2013.
- [9] A. K. Senapati, P. C. Mishra, B. C. Routray and R. I. Ganguly: "Mechanical Behavior of Aluminium Matrix Composite Reinforced with Untreated and Treated Waste Fly Ash" *Indian Journal of Science and Technology*, Vol 8(S9), 111–118, May 2015.
- [10] J. Babu Rao, D. Venkata Rao and N.R.M.R. Bhargava: "Development of light weight ALFA composites" *International Journal of Engineering, Science and Technology*, Vol. 2, No. 11, pp. 50-59, 2010.



**Engr. Arshad Ali Khan** born on 07<sup>th</sup> January 1990, is a postgraduate student and Lecturer in the Department of Mechanical Engineering, University of Engineering & Technology (UET), Peshawar, Pakistan. He has completed BSc Mechanical Engineering from UET Peshawar, Pakistan in 2012. His MSc is in the field of Mechanical Engineering Design from UET Peshawar.

After completing his Bachelor degree in Mechanical Engineering, he joined the Department of Mechanical Engineering of CECOS university of IT and Emerging Sciences Pakistan as a LAB Engineer and worked there for a period of one year. He joined University of Engineering and Technology (UET) Peshawar as a

Lecturer. He also worked as a teaching assistant with senior professors. He has supervised laboratory work related to almost all major subject of mechanical engineering. He has administrative experience as well while working on the positions of Hostel Warden and Semester Coordinator in the Department of Mechanical Engineering, Jaloza Campus of UET Peshawar Pakistan.

**Dr. Afzal Khan** is working as a Professor in the Department of Mechanical Engineering UET Peshawar, Pakistan.



# Analysis of Flow Rate and Humidity Effect on Polymer Electrolyte Membrane Fuel Cell Performance using MATLAB/SIMULINK

Muhammad Faisal Khan<sup>1</sup>, M. Naeem Arbab<sup>1</sup>, Haseeb Khan<sup>1</sup>

<sup>1</sup>Electrical Engineering, UET Peshawar

Received: 07 September, Revised: 20 September, Accepted: 28 September

**Abstract**— These days, the world faces glitches like energy crises, global warming and ozone depletion due to the power generation from fossil fuel. Petroleum derivative assets are diminishing with time because of which costs of traditional hydrocarbon fuel ascends in the universal market, along these lines most nations of the world are putting resources into sustainable power sources. Not at all like regular petroleum product run control age framework, is a power source that vitality effective, deliver low pollutions and being provided by boundless minimal effort fuel. The innovation of the fuel cell can handle these difficulties that are the reason as fuel cell is considered as ecological agreeable and effective innovation of future. Among different sorts of fuel cell, Polymer Electrolyte Membrane (PEM) fuel cell is the most diffused and well known kind of market because of its sound highlights, for example, low working temperature, brisk variety as per stack, high proficiency and better power density. In this paper PEM fuel cell stack is outlined and its model is executed in MATLAB/Simulink to dissect the examine the happening in PEM fuel cell stack and the variables that influence the efficiency of the fuel cell stacks. Besides, the properties of fuel cell stack are examined fluctuating flow rate of fuel and oxidants. The attributes curves are broken down with various working temperature, humidification temperatures, and mass (oxygen) exchange proportion.

**Keywords**— Polymer Electrolyte Membrane, Fuel Cell, Exhaust Gas Recession

## I. INTRODUCTION

Energy is vital for the entire humans on globe. Modern time provisions have more enhanced its worth, while a faster life means quicker communication, more rapidly transportation, and faster industrialized processes [1].

In [2], the authors discussed the scaling up of the fuel cell. For this purpose, three types of scaling of fuel cell were done. To achieve 1kW class, PEM a serial scale-up connection with unit cell area of 25cm<sup>2</sup> in a made of four cells was used. In second case, a parallel scale-up of single cell of 100cm<sup>2</sup> was used. In third case, for 1KW class PEM, the parallel series scaling of PEMFC was used with an action area of 150cm<sup>2</sup>. In first case, the maximum power voltage was almost four times of the single cell while in second case that was a bit better than first case. The response characteristic of the three type stacking

was equated and compared for two oxidants i.e. H<sub>2</sub>/air and H<sub>2</sub>/O<sub>2</sub>. The response characteristic of the three types of stacking were reduced. The operational result would help for stacking 20 cells for an energy storage system in smart grid. Aliasger Zaidy, Pooja Pokharkar and Rajesh Krishnan developed a dynamic model of PEMFC and simulated in MATLAB as well as LabView. The suggested model added various operating conditions i.e. variable loading, inverses of input reactant gas and temperature of the cell. The response characteristic of the PEMFC was checked. In order to validate the response an experimental testing was conducted and that the response characteristic of the modeled PEMFC were found valid [3].

The authors discussed the modality of aging mechanism of PEMFC for automobile applications. The modelling and analysis of the PEMFC played a very vital role because age will be reduced due to the transient conditions like load cycle, off cycle, high temperature or low humidification. Some aging models were discussed and the different mathematical models of the PEMFC were also considered [4]. Ahmed Mousa, Salah El-Emam and Mahmud Awad talked about the impact of cell stack introduction angle on the general execution of the energy component with H<sub>2</sub>/air. The authors concluded that they were obviously influenced by working parameters i.e. respond flow rate, oxidizer stream rate and humidity. The execution amid with expanding of the introduction point (orientation angle) of the cell stack frame the diamond cathode air flow rate were additionally considered [5]. Denise A. McKahn and Xinyi Liu discussed certain issues in the implantation of low temperature and polymers electrolyte membrane (PEM) fuel cells. These issues arrived due to thermal and water management. In this work, an experiment on two dissimilar dynamic content-oriental prototypes for open round temperature scrutiny in tiny PEM fuel cell were made under dry condition. After completing experiment, it was absent that cathode inlet relative humidity and resulting injection in a maximum estimation issues of 11% during light condition [6].

In [7], the authors discussed the water flooding and digging of membrane durability and effect of proton exchange membrane fuel cell (PEMFC) are compromised. In this paper a novel method was introduced for water management technique by exhaust gas recession (EGR). In this simulation based system experiment the water content characteristics were captured in pressure and absence of EGR. The MATLAB result demonstrated that the film will probably dry state of lost

stack present and high stack temperature the far reaching EGR technique was confirmed by recreating the genuine test circumstances of PEM power module strategies.

Shubham Chaudary and Yogesh K. Chauhan had discussed different FC technologies, their operating principles and applications. Mathematical modelling and Simulink model of PEMFC and solid oxide FC and operating characteristics was discussed. The effect of permeation, hydrogen and oxygen were analyzed. The V-I and P-V characteristics of the PEMFC and SOFC were analyzed. The outcomes demonstrate the validity of developed MATLAB/Simulink models of FCs [8]. The authors developed a model for understanding the effect of humidification temperature on oxygen mass fraction in the cathode for PEMFC. The model was developed by using times conservation equation and gratuity was considered as source the model was stimulated and can justified that the oxygen carry fraction even affected by either putting cathode upward or anode [9]. Jose David Rojas, Christian Kunusch, Carlos Ocampo-Martinez had discussed the role of flow field designs and current collector dimension next on PEMFC performance. A three dimensional computational mathematical model for the investigation of flow fluid design of current collector were discussed. Three different designs were used with aspect ratio verifying from 0.42 to 9. The good current collector design having aspect ratio was almost 1.5 [10].

In [11], the authors examined the steadiness and phase dynamic of the equilibrium water distribution is PEMFC using first and 2nd order parabolic function based stability was used by physics and mathematics based arrangement. The amount of water inside the fuel cell specifically influenced the execution, effectiveness and solidness. The unsteady states speaking to unbounded development of fluid water mass was discovered adequate for stable fluid dissemination. In [12], the authors studied the upgraded and improved controlled-oriented modelling technique by discussing the thermal dynamics of water-cooled PEMFC. It was examined that they not just advantageous for anticipating for control applications anyway it likewise can be useful for computing the temperature variety for the stack by letting to check the stack. For both the stationary and transient expresses, this method was approved. This methodology was experimented for actual 600W, 20 cells PEMFC system but this could be employed for any number of cells. It was concluded that the system responded for a huge number of operative levels with high precision. The rest paper is organized as: Section II includes Modelling and Simulation of fuel cell. Section III focuses on the results. In Section IV, the conclusions of the research work are discussed.

## II. MODELLING AND SIMULATION OF FUEL CELL

FC Stack block is shown in the figure. It prototypes a 45Vdc, 6kW PEM Fuel Cell Stack coupled to a DC/DC converter rated at 100 Vdc. This DC/DC converter has been loaded by means of a 6kW RL element with a 1 second time constant. For the duration of the 10 seconds, the consumption of the hydrogen gas is kept constant to the nominal value of  $U_{f\_H2} = 99.56\%$  consuming a fuel flow rate controller. After the time equal to 10 seconds, the regulator has been avoided and the fuel proportion will be amplified to 85 litre per minute (Maximum Value) so that the variation in the voltage of stack

is detected and observed, affecting the efficiency of the stack, the air and fuel consumption. In Scope 2, the voltage (V), current (I) of the Fuel cell, the voltage and current signals of DC/DC converter are presented while on the Scope 1, the Fuel flow rate, H<sub>2</sub> / O<sub>2</sub> consumption, air and fuel utilization, and efficiency are presented.

The fuel cell is modelled out in Matlab/Simulink, the model is shown in Figure 1.

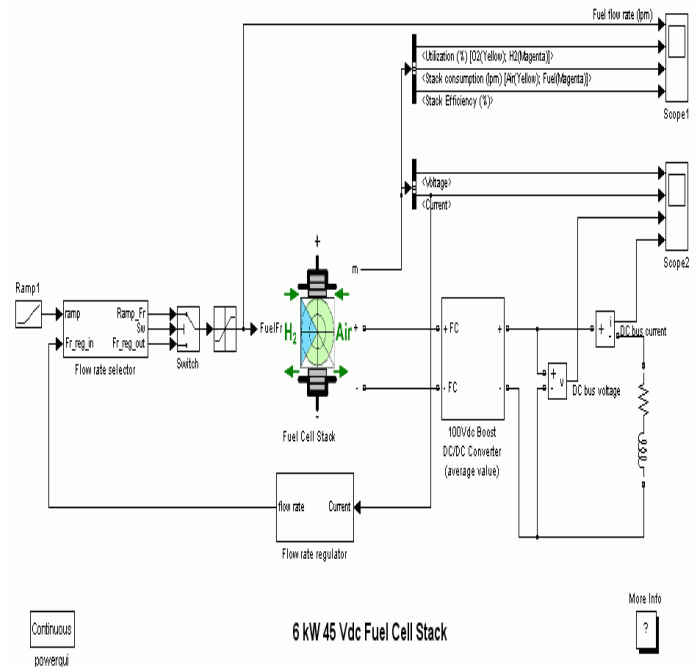


Figure 1. Simulink Model of PEM Fuel Cell

## III. RESULTS

At  $t = 0$  sec, the current of the load is 0 Ampere, and the DC/DC converter does apply 100Vdc near the load (RL). The fuel consumption is established to the nominal rate of 99.5 %. The current escalates and reaches to 133A. The fuel flow rate has been usually fixed so that it can keep the nominal fuel consumption. On Scope 2, we see that the DC bus voltage is controlled through the converter. The voltage regulator transient occurs for the initial state of simulation for the highest voltage value of 122Vdc.

At  $t = 10$  seconds, the flow rate of fuel consumption raises from 50 to 85 litres per minute. For 3.5 second, the hydrogen utilization is reduced, as a result the cell current lessens by increasing Nerst voltage. On Scope 1, a decrease in the efficiency and stack consumption occurs. Simulation is simulated for period of 20 seconds, the system values remain unchanged till 10 seconds of simulation, the value of fuel rate, air flow, humidity and temperature are varied through Ramp Function till rest of the simulation after 10 seconds. The variation in fuel cell stack efficiency in response to the parameters changed above are shown in the Figure 2.

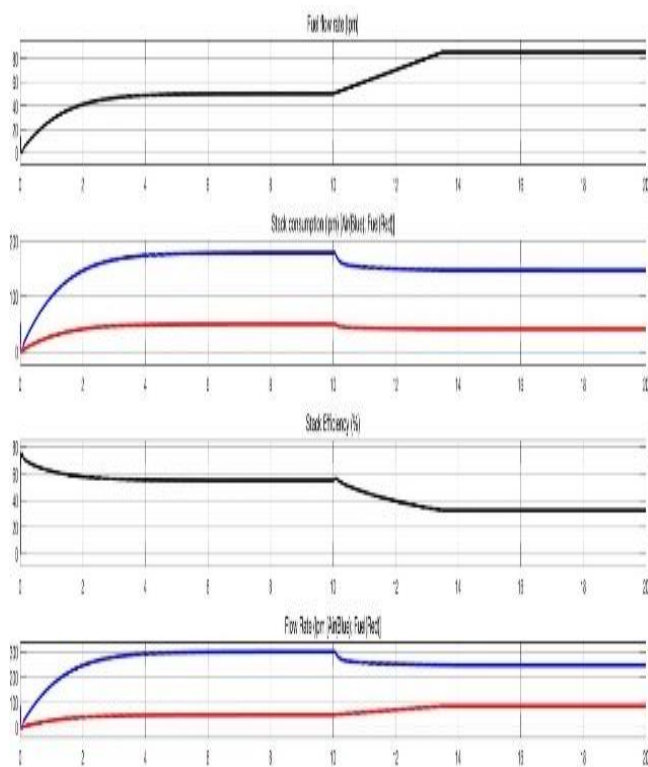


Figure 2. Flow rate, Humidity and Temperature Effect on stack efficiency

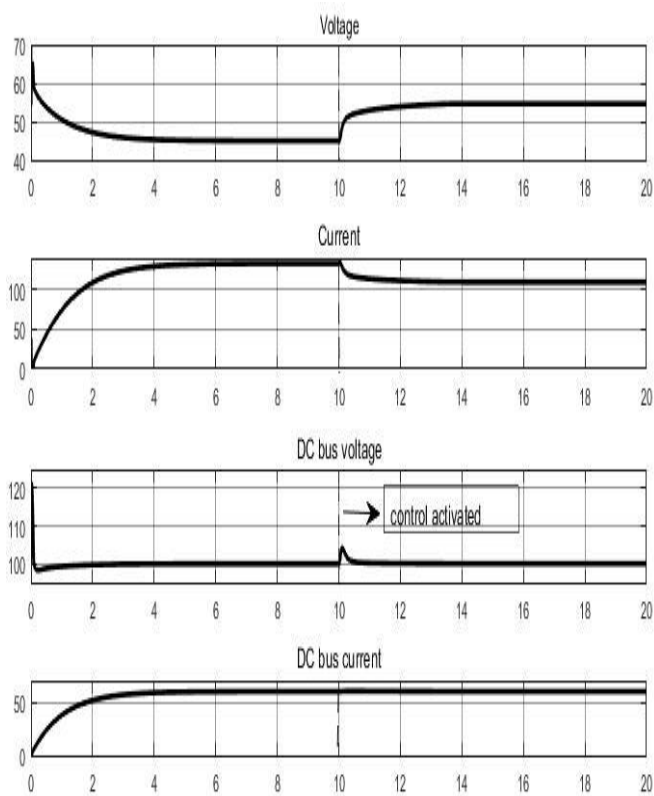


Figure 3. Current/Voltage of PEMFC

The first curve in Figure 3 is showing fuel cell output voltage, if we see the curve at startup we observe a transient behavior the rated output voltage of the stack is 45volts-DC but due to transient behavior we getting about 65volts which decreases and reach rated 45volts after about 1 seconds as shown in curve. After 10seconds when the fuel flow regulator is eluded and fuel rate is the maximum we see an increase in the fuel cell voltage about 5 volts.

The fuel cell current is reacting according to the voltage initially when voltage of stack is maximum the current is minimum but with a decrease in voltage current increases because current is drawn by the load. The DC/DC converter which is linked to the fuel cell stack is 100 volts DC rated. Initially for few milliseconds the bus voltage showing imbalance but later on we observe 100V pure DC from the DC converter.

Similarly, the DC bus current is initially zero which increase when current is drawn by the load and reaches about 60A maximum.

## CONCLUSION

It is evident that increasing fuel flow rate and humidity inversely affect the efficiency of FC stack. The efficiency of FC gets degraded with increase in flow of fuel rate and humidity as well as temperature from their nominal values. The load is interfaced with fc through buck-boost converter. the variation in fuel rate, humidity and temperature also effects the output voltage and current of fc. the output voltage and current should be stabilized for onward supply to load. the fluctuation in fuel cell is regulated through buck-boost converter. The output voltage and current of FC and its regulated DC current and voltage through Buck-Boost converter, it is clear from simulation that after 10 second, due to variation in fuel rate and other associated parameters, the voltage and current of fuel cell also experiences variations. The buck-boost converter driven by PI controller effectively regulates the output voltage and current to it set reference values.

## REFERENCES

- [1] Brain Cook, "An Introduction to fuel cells and hydrogen technology", Canada, Dec 2001
- [2] EG & G Technical Services, Inc, "Fuel Cell Handbook", 7th Edition, Nov 2004
- [3] J. A. J. L. N. D. V. H.-M. K. K. P. G. H. Kap-Seung Choi, "An Experimental Study of Scale-up, Oxidant, and Response Characteristics in PEM Fuel Cells," IEEE TRANSACTIONS ON ENERGY CONVERSION, vol. 29, no. 3, pp. 729-734, SEPTEMBER 2014.
- [4] P. P. R. K. D. S. Aliasger Zaidi, "Dynamic Modeling and Simulation of A PEM Fuel Cell: MATLAB and LabVIEW Modeling Approach," in Proceedings of 2014 1st International Conference on Non Conventional Energy (ICONCE 2014), 2014.
- [5] F. G. A. M. T. Elena Breaz, "A Short review Of Aging Mechanism Modeling Of Proton Exchange Membrane Fuel Cell In Transportation Applications," in IEEE, 2014.
- [6] M. Ahmed, E.-E. Salah and A. & Mahmud, "Effect of Stack Orientation on the Performance of H<sub>2</sub>/Air PEM Fuel Cell," in IEEE, 2010.

- [7] D. A. M. a. X. Liu, "Comparison of Two Models for Temperature Observation of Miniature PEM Fuel Cells Under Dry Conditions," in IEEE TRANSACTIONS ON INDUSTRIAL ELECTRONICS, 2015.
- [8] X. L. L. J. O. M. C. S. a. F. C. Hu Junming, "Water management in a self-humidifying PEM fuel cell system by exhaust gas recirculation," in ITEC Asia-Pacific , 2014.
- [9] S. C. & Y. K. Chauhan, "Studies and Performance Investigations on Fuel Cells," in IEEE International Conference on Advances in Engineering & Technology Research (ICAETR - 2014), India, 2014.
- [10] Y. W. Shizhong Chen, H. Sun and Z. Sun, "Simulation of Humidification Temperature Impact on Oxygen between Anode-upward and Cathode-upward in PEM Fuel Cell," in IEEE, 2010.
- [11] A. B. Y. Z. F. H. A. B. Youcef Kerkoub, "Channels design and dimensions Effect on performance of proton exchange membrane fuel cell (PEMFC)".
- [12] B. M. a. A. S. a. I. Kolmanovsky, "Stability Analysis for Liquid Water Accumulation in Low Temperature Fuel Cells," in Proceedings of the 47th IEEE Conference on Decision and Control, Cancun, Mexico, 2008.

# Modelling A Standalone Hybrid Micro Grid and Analyzing its Voltage Control Capabilities

Imran khan<sup>1</sup>, Dr. Abdul Basit<sup>1</sup>, Muhammad Waseem<sup>1</sup>

<sup>1</sup>US Pakistan Center for Advanced Studies in Energy (USPCASE), UET Peshawar

Received: 12 September, Revised: 24 September, Accepted: 28 September

**Abstract**—Electrical energy is one of the most important component in the development of any society. Electrical energy is primarily generated from fossil fuels, nuclear power or hydro but an increasing gap between demand and generation is leading to find an alternative energy sources that produce clean energy and meet our increasing needs while maintaining the secure and reliable operation of power system. Presently Pakistan is facing extreme energy crisis and the situation is even worse in remote areas that are deprived from basic facility of electrical energy. These areas are normally gifted from natural resources that can play a key role in overcoming this problem. Run on River hydro generating units, solar Photovoltaic cells and Biomass generating units are able to generate clean electrical energy and meet the local demands; however, it is important that the frequency and voltage of that area is maintained within in the specified for the secure operation of power system. The voltage control plays important role in stable and reliable power supply. This research project will model a standalone micro grid where electrical energy will be generated from alternative sources of energy that are renewable i.e. hydro, solar irradiations and biomass resources, and then will employ specific technique for voltage control. This study will analyze the system behavior in different seasons when the load demand varies.

**Keywords**— Micro grid, Micro Hydro power plant, Photovoltaic, Resources, Diesel Generator, Biomass, Super capacitor

## I. INTRODUCTION

In 1880's amongst the most profitable economic business was supply of electrical power to the consumers. As time passed, electrical networks at state level were interconnected with the installation of bigger electricity generating stations and these were connected by long transmission networks, under supervision of the state. The increased demand for the electrical energy by consumers reinforced the idea of improving the centralized power production with bigger hydro electrical, nuclear, thermal generating stations during twentieth century. However, due to shortage of electricity during 1970s, concern about environmental issues rose in eighties, deficiency of fossil fuel reserve and were some of the factors to change the strategy and policy regarding energy.

Electrical network at start were Direct current networks, voltage levels and the distance were limited between generation and load point. The difference between generation and demand was gradually gained because of using some sort of domestic power storage devices, like batteries. As the electrical networks were expanded, the DC grid stations converted into ac. High voltage levels were used for the sake of achieving greater capacity and transmit electrical power overlong distances. However during the last years though, advancement in technology has played an important role in the integration of distributed power systems integrated with the utilization of alternative sources of energy i.e. renewable, due to which grids had became complex, but it has also provided different opportunities in order to avail electricity in most of faraway areas, where till now it was very complicated to supply electricity to them. Standalone hybrid electrical system including diverse electrical resources and storage devices have been manufactured and used in different applications. These appliances improve day by day and fulfilling the requirements.

### A. Goals and Objectives:

This thesis investigates the implementation of a hybrid microgrid to electrify one of the rural village near Mardan district in Pakistan. Several cases have been searched out and these include a PV system, a micro hydro system, biomass system, diesel system and connection of hybrid micro grid with National grid. Energy from renewable resources are very unpredictable and dependent on climatic conditions [15]. The goal of the project is to gain a reliable and efficient operation of the microgrid system and search for the best possible optimized model.

An efficient, reliable, efficient and valid form provides the foundation for assessing system's function like detecting its flaws, implementation of various techniques and making the essential adjustments in order to set up a system contributing a good quality service to the consumer.

### B. What is Micro Grid?

"In Micro grid it is supposed that a cluster of electrical loads and Power generation sources are working as a unity controllable system which supplies electricity to its local consumer." - This idea gives a new prototype for operating distributing generation systems. These small energy generating sources are having much lower expenditure, greater reliability are laid out at consumer side.



### C. Micro Grid Types

Micro grids are basically classified into three types:

Residential Micro grid, Remote Microgrid, Mobile Microgrid.

#### 1) Background

Hybrid Micro Grid technology mainly consist of renewable energy resources. These renewable sources are accessible in abundance and can be utilized up to utmost extent possible. These micro grid technologies earlier comprised of only Batteries, wind turbines and diesel generators in order to deliver power to the load, but there wasn't a better balance between generation and demand as the system was not secure in most of situations. Therefore to solve this issue, controller is used along with PV module. Output of the PV solar arrays depends on the solar irradiation and it varies from place to place depending upon the location. Thus, this thesis defines solar irradiance for Mardan Region located in Khyber Pakhtunkhwa Pakistan to find out the effects on the power flow of system. Biomass is also available in greater amount at the desired site. Along with Biomass we have Micro hydro availability too. Therefore we have multiple renewable energy sources to get benefit from. It is necessary to look out for the best possible combination of these Distributed Energy Resources (DER's). Voltage stability study will facilitate in verifying the stability and reliability of the system through the incident of fault or variation in load in the system. So we have to deal with simulation software to get the best results.

### D. Photovoltaic System

Sun is the greatest source of energy and the energy can be directly extracted via photovoltaic cells. There are many areas in the world which are not connected with grid and there is no electricity but the electricity in these areas can be generated using solar power. Solar energy is clean energy source and is not dangerous for climate change. The energy generated by photovoltaic cell is given by formula.

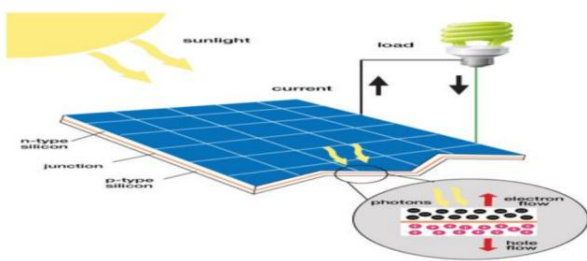


Figure 1. PV Working Principle

### E. Solar Resource for Mardan Region:

Solar radiation potential in Mardan region are estimated having solar radiation of 2.86 KWH/m<sup>2</sup>/day (minimum value) in the month of December and 7.88 KWH/m<sup>2</sup>/day (Peak value) in month of June. Similarly the Clearance index value for the region varies between 0.57 (in month of March) and 0.71 (in month of October).



Figure 2. Solar Resource Available at the Site

#### 1) Inverters:

An inverter is a circuit that converts the direct current (DC) electrical energy generated by sources like batteries, Photovoltaic arrays, or wind turbine system to alternating current electricity. The (AC) electrical energy is then utilized to drive AC appliances similar to the ones those are installed in majority of the household electrical outlets. The resulted AC waveform at the inverter output is a sine wave having frequency of 50Hz or 60Hz depending upon power system at different regions of the world. In Pakistan the required frequency for electrical appliances is 50Hz.

#### 2) Micro Hydro System:

Hydropower is the production of electricity by utilizing kinetic energy of water produced by gravity. The water's kinetic energy in hydro power system dependent on two factors, available head and its flow. Small hydro system converts the potential energy due to head and kinetic energy of flowing water into electrical energy through turbine that drives an electrical generator. Every dissimilar site needs its own estimation in order to conclude the energy that is obtained at the output. This type of system is basically implemented in regions where a lesser stream of water can be utilized for power generation.

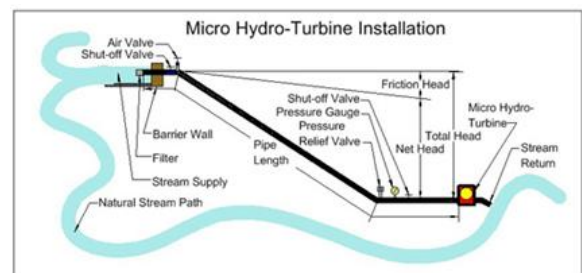


Figure 3. Micro Hydro Schematic

#### 3) Hydro Resources available:

The flow data has been collected for the last six year from 2011 to 2016 on the proposed location from provincial irrigation department Mardan. The total flow of disty katlang at the proposed location has been calculated as 1.89m<sup>3</sup>/sec full supply discharge (FSD) in the peak summer season. Discharge data at Disty Katlang was collected for the last six years (2011-2016) from the office of irrigation department, Government of Khyber Pakhtunkhwa province.



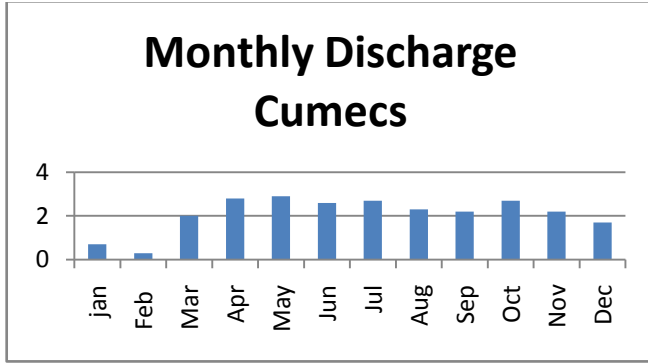


Figure 4. Monthly Stream Flow

#### F. Biomass Energy:

Organic matter is the biggest source of obtaining Biomass energy. This organic matter is derived from plants, animals, humans and marine life. Plants, dry grass, animals waste, garbage, wood pieces and municipal wastes are the examples of biomass. Biomass is another alternative and renewable energy source. Different processes are used to convert biomass to various other forms of energy. Thermo chemical and biochemical conversion are the two main conversion techniques.

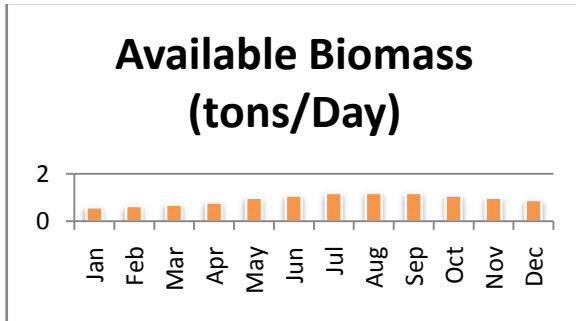


Figure 5. Monthly average biomass available at site

#### G. Diesel Generator:

A diesel generator is comprised of a diesel engine with an electric generator to produce electrical energy. A diesel generator is chosen in simulation software to search out for the best optimized model in a micro grid; as it is of a higher power capacity in order to support the grid in emergency conditions. Emergency stand by diesel generators like those used in hospitals, shopping plazas, are, as a secondary function, widely used in various countries of the world (Short Term Operating Reserve) in order to support the respective national grids at times for a variety of reasons as well as in emergency conditions.

#### H. Area Load Profile

The total electrical load of the area for the listed appliances above was obtained to be supplied by the hybrid system.

##### 1) Types of Loads:

Two types of electrical loads have been used for the selected site. One is the residential load and the other is the commercial load.

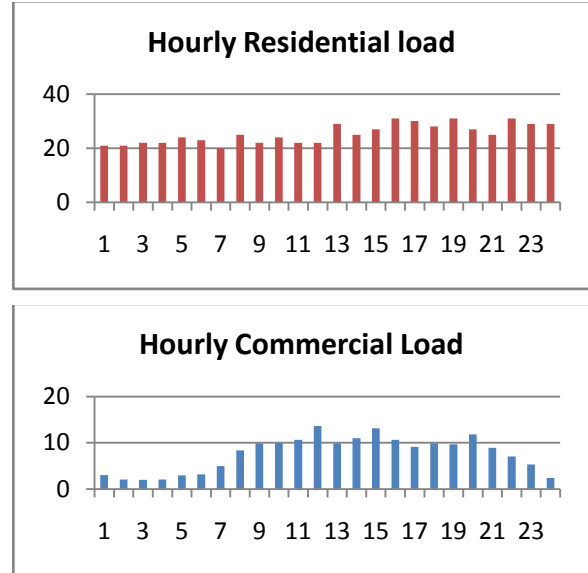


Figure 6. Hourly Commercial and residential load Profile

#### Cost Function For Photovoltaic:

$$PV_{NPC} = PV_{CC} + PV_{ins} + \sum_{t=1}^n PV_{O\&M} * T_{lifeTime} + PV_{rep} * N_{rep} \quad (5.1)$$

#### Biomass Cost Function:

$$BM_{NPC} = BM_{CC} + BM_{ins} + \sum_{n=1}^{8760} BM_{O\&M} * T_{lifetime} + BM_{rep} * N_{rep} + \sum_{n=1}^{8760} BM_{fuel} * T_{lifetime} \quad (5.2)$$

#### Micro-Hydro Cost Functions:

$$MH_{NPC} = MH_{CC} + MH_{ins} + \sum_{t=1}^n MH_{O\&M} * T_{lifeTime} + MH_{rep} * N_{rep}$$

#### Converter Cost Function:

$$CON_{NPC} = CON_{CC} + CON_{ins} + CON_{O\&M} * T_{lifeTime} + CON_{rep} * N_{rep} \quad (5.4)$$

#### System NPC & Objective Function:

$$RES_{NPC} = PV_{NPC} + MH_{NPC} + BM_{NPC} + CON_{NPC} + BB_{NPC} \quad (5.5)$$

## II. SIMULATION & RESULTS

The software used for the simulation of hybrid microgrid project is Homer. All the required data was put in the software. Hydro, Diesel, Biomass, Photovoltaic and Grid connection and isolated system has been optimized. So the following cases have been obtained.

#### Case 1: A Standalone Hydro and Biomass Hybrid Model

The optimized results show that Hydro System has a maximum generated power of 24 kilowatts. Power produced by Biomass resources is 30 kilowatts. So these two generating

systems are the best two in terms of cost of electricity. So no Photovoltaic panels are required because of having greater cost. . The net present cost of complete system is \$476,233 while operating cost is \$29,208. The cost of electricity is \$0.17.

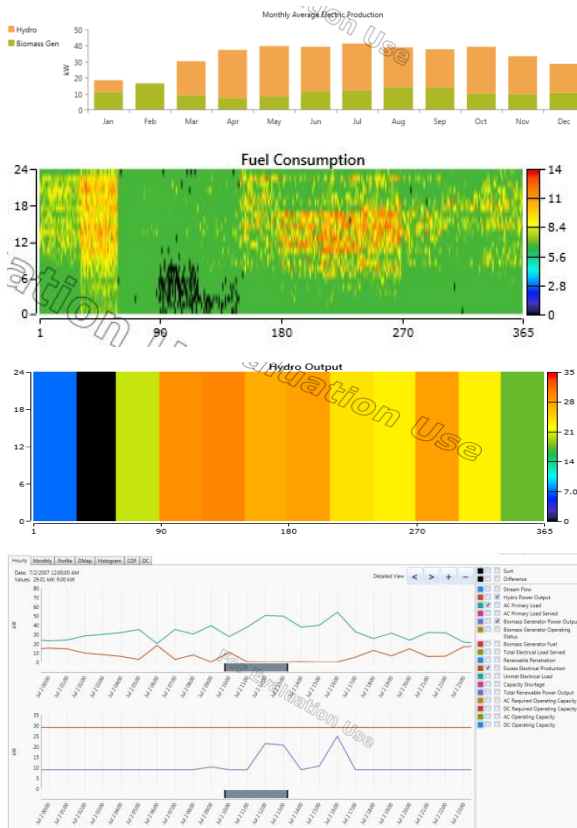


Figure 7. Case 1 System Complete Profile

The results from this model indicates that the cost of electricity and net present cost of Model is very high and secondly that Biomass will not be available for longer time period from area. So this model is not feasible and Biomass Power Generating Unit may be excluded from the model.

#### Case 2: A Standalone Hydro, Diesel Generator and PV Hybrid Model

In this case the generating units considered are Hydro, Photovoltaic and Diesel generator. The biomass resource is not considered in this case because the initial capital cost of Biomass gasifier generating unit is very high so it will be very economical if we use diesel generator set instead of biomass gasifier set.

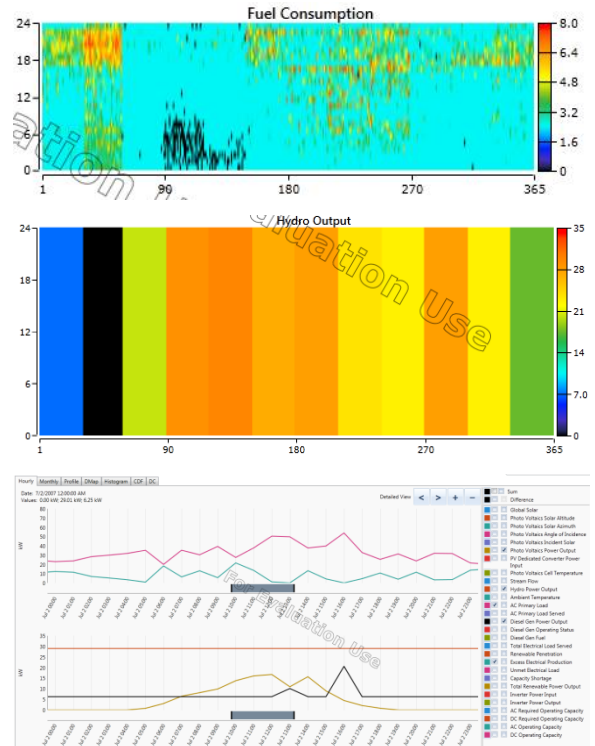
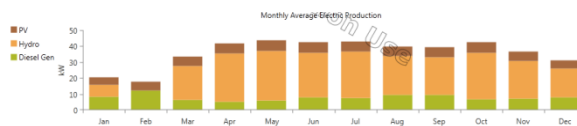
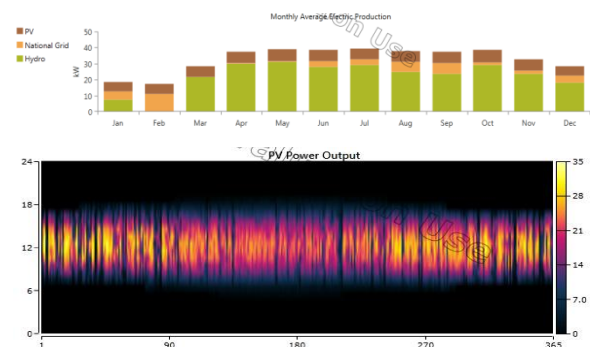


Figure 8. Case 2 System Complete Profile

The results show that we have to install 35 kilowatts of PV, 25 Kilowatts of Diesel Generator and 24 kilowatts of Hydro power generating system. The size of the inverter should be 20 kilowatts. The net present cost of the model is \$344,562 while Operating and maintenance cost is \$27,027. The cost of energy is \$0.127 which is much lower than above case (Biomass and Hydro hybrid i.e \$0.17).

#### Case 3: Hybrid Model with Grid Connected

In this case Hydro, Diesel and PV hybrid model is connected with the national grid. It has been concluded from the results that excess electricity is generated by hybrid model. It will be much economical to sell back this excess electricity to the grid.



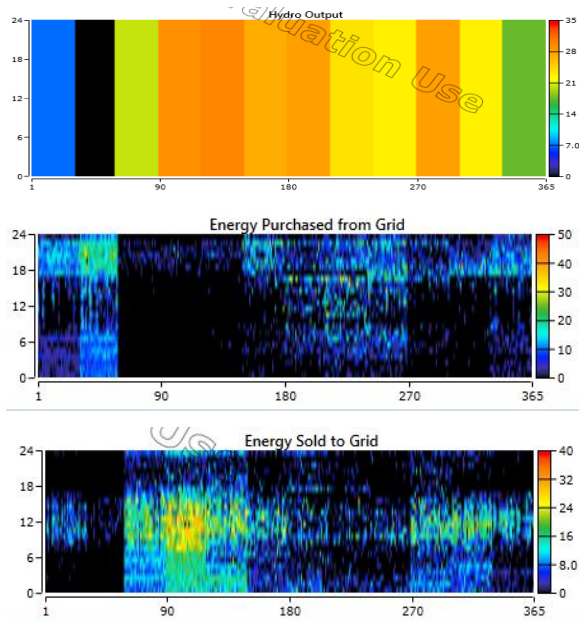


Figure 9. Case 3 System Complete Profile

#### A. Voltage Controlling Micro grid system

The point of common coupling is the point where Micro grid is connected to national grid, which during fault will be disconnected from main grid, after that operation of Micro grid comes under standalone mode. When a micro grid is operated in a grid connected mode a defined voltage value have to be ensured for its successful operation.

#### B. Modeling of the Super Capacitor

The rate of energy density in s Super Capacitors is extremely higher in contrast to ordinary capacitors, because plates are used instead of dielectric material in super capacitors. It has been proved that super capacitors have non linear behavior and its capacitance has invariable value if the parameters such as temperature, voltage and current are not having significant variations.

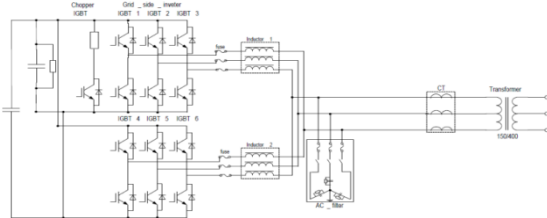


Figure 10. Bi-directional converter topology for SCESS.

#### C. Transient Response of Micro-Grid under Load Increase of 12 KVA:

The transient response of the grid is experimentally calculated with and without the super capacitor. 12KVA of inductive load was further added to already present resistive load at time  $t=80$  ms for the reason to verify the super capacitors on grid.

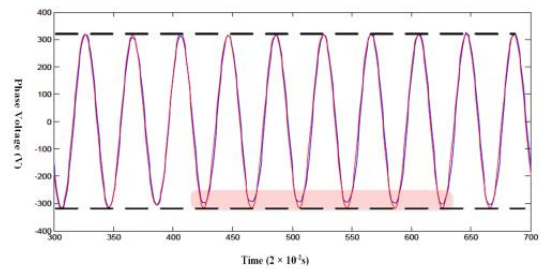


Figure 11. Phase Voltage of system when 12 kVA load is added at  $t = 80$  ms ("Blue" without SCESS and "Red" with SCESS).

It is proved from Figure that as soon as the load varies at  $t = 80$  ms, the system takes round about 50 milliseconds to get better voltage sag without super capacitor whereas the voltage transient response has been improved rapidly with super capacitor has rapidly.

#### D. Transient Response of Micro-Grid under Load Increase of 20 KVA:

In this part of experiment the load is increased twice i.e 20 KVA with the intention to verify system reaction experimentally under the control of super capacitor, and Figure shows the voltage transient response.

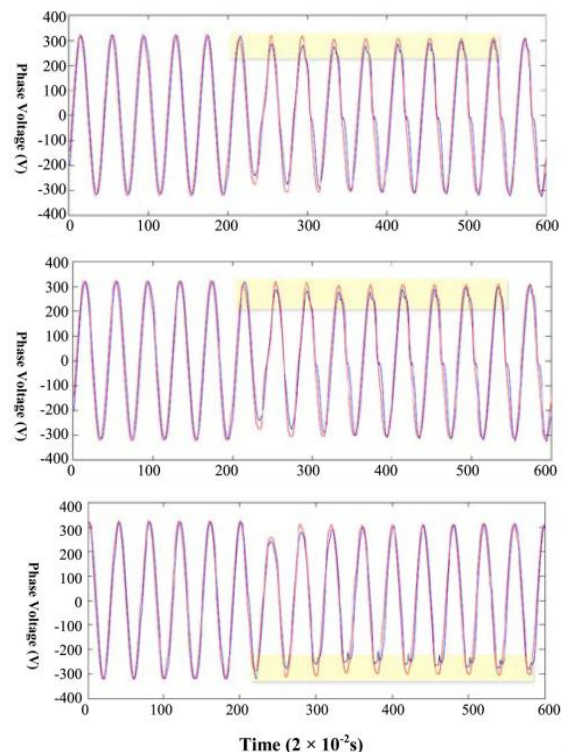


Figure 12. Phase Voltages of the system when load 20 kVA load is added at  $t = 40$  ms ("Blue" without SCESS and "Red" with SCESS) (a) Phase voltage 1; (b) Phase voltage 2; (c) Phase voltage 3.

#### E. Transient Response of Micro-Grid Due to Sudden Start-Up of an Induction Motor

The induction motor draws greater current during starting, so it has regularly a very high initial current value, keeping in



view this point the effect of impulsive start of an induction motor on system with and without super capacitor is studied.

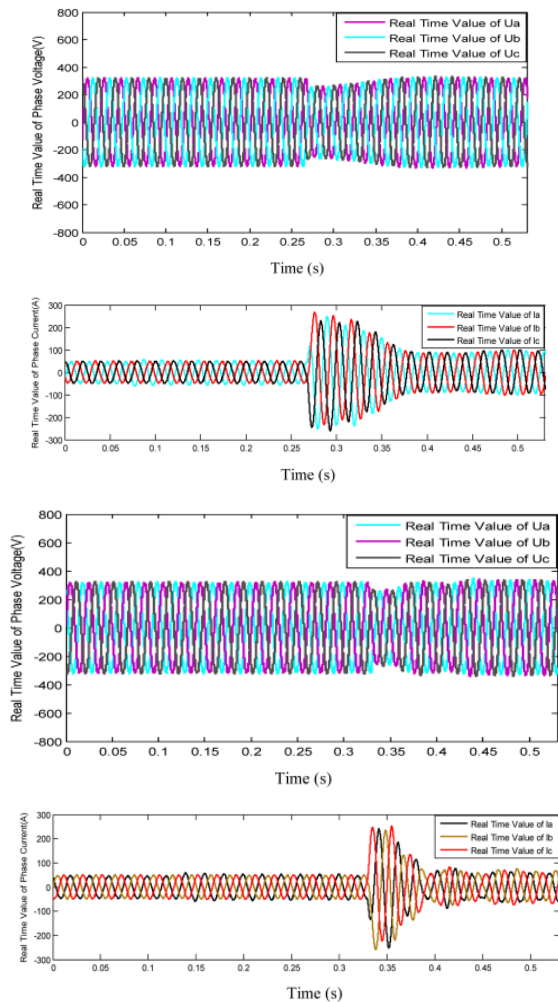


Figure 13. Phase voltages of the system when an induction motor start-ups (a) Three Phase Voltages (without SCESS); (b) Three Phase Currents (without SCESS); (c) Three Phase Voltage (with SCESS); (d) Three Phase Currents (with SCESS).

It can be concluded that when induction motor suddenly starts up at time  $t=0.27s$  approx for the system without super capacitor, voltage sags till  $t = 0.45s$  and then voltage is stabilized in about 180 ms but in case when inductor motor starts up at time  $t=0.33s$  for system with super capacitor, the voltage comes to its normal value and get stabilized in very short period of about 70ms. In the same way, the three phase current's amplitude boosts up when the induction motor is allied and with the help of super capacitors less time is taken by current to get stabilized.

#### ACKNOWLEDGMENT

We would like to offer our thanks to Directorate of science and technology (DOST), Khyber Pakhtunkhwa (KPK), Pakistan for providing us funding for this project.

#### CONCLUSION

This research work provides an optimized solution for standalone and interconnected micro grid systems having different energy resources. The sensitivity analysis displays the intermittent nature of renewable resources. It can be concluded from results that an optimized model with mix energy sources help in making the power system operation reliable by maintaining the voltage and frequency at their normal level. Second Portion of research shows that the Transient study of the system is very significant in this observation for its flourishing and stable process. Some of the important factors like upper and lower limits of voltage of system should be taken into account, and a comprehensive study is required to make sure the system's transient response under different load conditions because the hybrid micro-grid must develop a robust system that can operate stably and reliably both in islanded as well as grid-connected mode. It has been proved from simulations that during particular load variations in micro grid system, the transient voltage response of the system is disturbed for some cycles. Therefore super capacitor will facilitate the system to improve and stabilize three phase voltages rapidly.

#### REFERENCES

- [1] S.G. Jimmy Ehnberg and Math H.J. Bollen, "Reliability of small Power system using solar power and hydro " *journal on electric power systems research*. Volume 74, issue1, april 2005.
- [2] B. Bhandari, S.R. Poudel, K.T. Lee and S.H. Ahn, "Mathematical modeling of hybrid renewable energy system" *international journal of precision engineering and manufacturing green technology*. Volume 1, issue 2, april 2014.
- [3] M. Kalantar and S.M. Mousavi, "Dynamic behavior of standalone hybrid power generation system of wind turbine, microturbine, solar array and battery storage" *journal of applied energy* volume 87, issue 10, October 2010.
- [4] Nabil A. Ahmad, Masafumi Miyatake, A. K Al-Othman, "Power fluctuations suppression of standalone hybrid generation combining solar PV/Wind turbine and fuel cell system" *journal of energy conversion and management*. Volume 49, issue 10, October 2008.
- [5] O.C.Onar, M. Uzunoglu, M.S. Alam "Dynamic Modeling, Design of wind/fuel cell/ultra capacitor based hybrid power generation system" *journal of power sources*. Volume 161, issue 1, 20 October 2006.
- [6] X. Liu, P. Wang, P.C.Loh "A Hybrid AC/DC Microgrid and its coordination control". *IEEE transaction on smart grid*. Volume 2, issue 2, june 2011.
- [7] S.K Kim, J. H Jeon, C.H Cho "Dynamic Modeling and control of grid connected hybrid generation system with versatile power transfer". *IEEE transaction on industrial electronics*. Volume 55, issue 4, April 2008.
- [8] J. M Guerrero, J. C Vasquez, J. Matas "Hierarchical control of droop controlled AC and DC microgrids a general approach towards standardization" *IEEE transaction on industrial Electronics*. Volume 58, issue 1, jan 2011.
- [9] kyoungsoo Ro, S. Rahman "Two loop controller for maximizing performance of grid connected photovoltaic / fuel cell hybrid power plant". *IEEE transaction on Energy conversion* volume 13, issue 3, sep 1998.
- [10] Farzam N, S.D Ali, S.H Hosseini "Modeling and control of new three input DC-DC boost converter for hybrid PV/FC/Battery power system" *IEEE transaction on power electronics*. Volume 27, issue 5, may 2012.
- [11] NASA Surface Meteorology and Solar Energy Database
- [12] (NREL, 2008) National Renewable Energy Laboratories
- [13] PEDO Daily discharge at Disty katlang for the year 2011 (cumecs)

- [14] Biomass Energy Potential and Current Use in Different Parts of World (year2004)
- [15] Yang H, Zhou W, Lu L, Fang Z. Optimal sizing method for stand-alone hybrid solar–wind system with LPSP technology by using genetic algorithm. Solar Energy 2008;82:354–67
- [16] A. Hussain et al. Forecasting electricity consumption in Pakistan: the way forward Energy Policy 90 (2016) 73–80
- [17] Daljeet Kaur, P. S. Cheema, Software tools for analyzing the hybrid renewable energy sources:-A review
- [18] Vinay Shrivastav, MS Thesis Thermal Engineering, Design and development of downdraft gasifier for operating CI engine on dual fuel mode, National Institute of Technology Rurkela, 2012.
- [19] S. Stokler, C. Schillings, B. Krass, Solar Resource assessment study for Pakistan, “Renewable and Sustainable Energy Reviews” Volume 58, May 2016 Pages 1184–1188
- [20] Source: Mardan Station – data from O & M manual, Mardan SCARP, 1985 Measure at 10 m above ground
- [21] R S. kumar ; S. K. Kollimalla ; M. K. Mishra, Dynamic Energy management of Microgrids using battery Super Capacitors Combine Storage 2012 Annual IEEE India Conference (INDICON)
- [22] J.A.P. Lopes ; C.L. Moreira ; A.G. Madureira, Defining Control strategies for Microgrids Islanded Operation, IEEE Transactions on Power Systems ( Volume: 21, Issue: 2, May 2006 ).



**Imran Khan Khan** graduated from University of Engineering and Technology (UET) Peshawar in 2014. He holds B.Sc degree in Electrical Engineering. He is currently enrolled in M.Sc Electrical Energy Systems Engineering at US Pakistan Center for Advanced Studies in Energy (USPCASE) UET Peshawar. His major field of study is Electrical Power Engineering. Currently he is working as Junior Engineer In Mepco.



**Abdul Basit** completed his B.Sc. degree in electrical engineering from University of Engineering & Technology (UET) Peshawar, Pakistan in 2006. He received his M.Sc. degree in electrical power engineering from Chalmers University of Technology, Sweden in 2011 and his PhD from the Department of Wind Energy of the Technical University of Denmark (DTU) in 2015. He is currently working as Assistant professor at U.S. Pakistan Center for Advanced Studies in Energy (USPCAS-E) of the University of Engineering & Technology (UET) Peshawar. His research interests are on protection, power factor improvement, power system operation, renewable power integration and automatic generation control.



**Muhammad Waseem** graduated from Comsats University Islamabad in 2013. He holds B.Sc degree in Electrical (Telecom) Engineering. He is currently enrolled in M.Sc Electrical Energy Systems Engineering at US Pakistan Center for Advanced Studies in Energy (USPCASE) UET Peshawar. His major field of study is Electrical Power Engineering. Currently he is working as Junior Engineer In Mepco.

# Synthesis of Ni Nanotubes for Enhanced Oxygen Reduction Reaction at Cathode Side of PEM Fuel Cell

Abid Ullah<sup>1</sup>, Khalid Khan<sup>2</sup>, Kamran Alam<sup>3</sup>, Izaz Ahsan<sup>4</sup>, Muhammad Humayun<sup>5</sup>

<sup>1,2,3,4</sup>US-PCASE, UET Peshawar, 25000, Pakistan UET Peshawar

<sup>5</sup>Basic Science Deptt. UET Peshawar

adhchem@gmail.com<sup>1</sup>, humayunchemist@uetpeshawar.edu.pk<sup>5</sup>

Received: 15 September, Revised: 25 September, Accepted: 03 October

**Abstract**— Electrochemical activity at cathode side in Polymer Exchange membrane fuel cell (PEMFC) is sluggish and requires an active catalyst. Until now Platinum (Pt) is considered as the most feasible and active catalyst for Oxygen reduction reaction at cathode. It is most expensive and also faces the problem of poisoning due to carbon monoxide, hence a more reactive, durable catalyst is required to meet the demand for commercialization. In this study a novel non platinum group metal (N-PGM) Ni nanotubes were prepared by using Solvothermal technique using transition metal precursor with profound insight. Ni nano tubes were obtained after pyrolyzing Ni Zeolitic Imidazolate Framework (Ni/ZIF) at 800 °C under inert nitrogen atmosphere. Its electro catalytic performance was examined by Linear Sweep Voltammetry (LSV), done with Rotating Disk Electrode (RDE) evaluation showing that Ni nanotubes owns splendid electro catalytic behavior for Oxygen Reduction Reaction (ORR) in basic environment. It depicts a current density of -2.6 mA/cm<sup>2</sup> and an over potential of -0.28V Vs. Saturated Calomel Electrode (SCE), and RDE Results were obtained at 400, 800, 1200 and 1600 rpm in 0.1M KOH solution while the Ni/ZIF shows the minimum current density of -1.4 mA/cm<sup>2</sup>. The Pt/C catalyst was also analyzed in the same environment for comparison purpose having a current density of -4.6 mA / cm<sup>2</sup>. The results reflect that Ni nanotubes is promising catalyst for Proton exchange membrane (PEM) fuel cell.

**Keywords**— Proton Exchange Membrane (PEM) Fuel cell, Zeolitic Imidazolate Frameworks (ZIF-67), Ni nanotubes.

## I. INTRODUCTION

Proton Exchange Membrane Fuel Cell (PEMFC) is a promising technology for conversion of fuel (Hydrogen) to electricity with much higher efficiency than internal combustion Engine. PEMFC is an outstanding device to hamper the Global pollution, it is a credible technology for economical Energy. However, high cost is the main hurdle in its commercialization [1] and the cost mainly comes from the catalyst part of the fuel cell, which uses precious metals (Pt, Ru), another problem is the sluggish oxygen reduction reaction (ORR) at cathode side in PEMFC's.

A number of materials were researched to enhance the ORR activity, among them Platinum (Pt) has shown the highest ORR activity and stability till date. Silver (Ag) was meticulously studied due to its abundance, low cost and high activity, but half wave potential of Ag in Rotating disk electrode (RDE) is lower than Pt [3]. Pt, Ru showed higher ORR activity but it is precious and more prone towards CO poisoning. Alloying of transition metals (Co, Fe, Cu, Ni) impart synergistic effect to Pt. The d band center of Pt goes down with alloying, hence dwindling the bonding energy of Pt with oxygenated species [2]. K. Yang et al discovered a new material Nano particles PtFe Nitrogen doped carbon sheets (np-PtFe/NPCS) having three time higher current density and more positive half wave potential than Pt/C [4]. Y. Haoran et al uses a non Pt catalyst for ORR and found its activity better than the commercial Pt/C catalyst. For alleviating our dependence on the precious metals (Pt, Ru) for ORR, more attention were given to develop Non platinum group metals (NPGM) catalysts. H. Jang et al produced Metal organic framework (MOF) having thermally robust and nonporous structure, enhancing surface area for reaction [5]. Zeolitic imidazolate frameworks (ZIF's) is a subclass of MOF has enormous potential for preparation of nanotube catalyst, rich in carbon and nitrogen [6,7]. Transition metal carbon nanotubes (Pt-Co CNTs, CoCNT) were developed from ZIF precursors to impart porosity and enhance the catalytic effect of transition metals [8,9,10]. H. Zhang et al investigated Ni catalyst activity alloyed with Co and CNTs (NiCo<sub>2</sub>O<sub>4</sub>/CNTs hybrid) which showed higher performance than alone Ni, Co and CNT.

In this study a new material, Ni nanotubes were synthesized and tested in alkaline solution. Linear sweep voltammetry (LSV) with RDE evaluation were performed to study and analyzed the ORR electro catalytic activities of Ni-nanotubes. To the best of our cognition this report may be the 1<sup>st</sup> one on the ORR catalysis by Ni-nanotubes prepared by hydrothermal treatment.

## II. MATERIALS AND SYNTHESIS

### A. Preparation of Ni/ZIF

Ni/ZIF samples were prepared as given in the literature [12]. In the synthesis method, 5.5 g of 2-methylimidazole (2-MIM) was dissolved in 20 ml DI water in one beaker and in



another beaker 0.238 g of Nickel (ii) nitrate hexahydrate was also dissolved in 3ml of DI water, a greenish solution is formed. These two solutions were mixed together and constantly agitated for 6 h at room temperature and atmospheric pressure to complete the reaction as much as possible. Then the mixture is transferred to autoclave and maintained at 140 °C under pressure for 24 hour. The sample after removing from autoclave were transferred to centrifuge and orange precipitate were accumulated and washed with water and ethanol alternatively for many time and dehydrated at 80 °C for 24h. The Ni/ZIF was also prepared by this method but it was not sintered and simple Ni/ZIF sample were collected for comparison purpose.

### B. Synthesis of Ni Catalyst

Ni nanotubes specimen were prepared by the method shown in the literature. The dried ZIF-67 samples were heated up at 350 °C for 1.5 h then the temperature is increased to 800 °C at a ramp rate of 5 °C per minute for 3.5 h at Nitrogen atmosphere reflux (Fig 1) after preparing the black powder, it is cooled down to ambient temperature automatically, then it was treated with 0.5 M H<sub>2</sub>SO<sub>4</sub> solution for 10 h. the catalyst which is prepared were accumulated by high centrifugation, recurrently cleaned with DI water and dehydrated at 100 °C under vacuum atmosphere for 2-3 hour. The Ni nanotubes were collected for experimentation. The method of preparation is described in Fig 1.

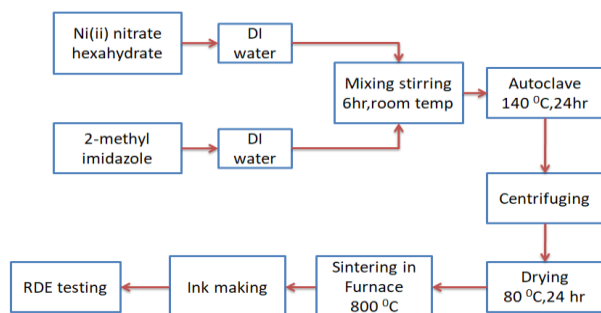


Figure 1. Synthesis steps of Ni nanotubes

### C. Electrode Preparation

The Catalytic sample was synthesize by scattering 7.5mg of Ni nanotubes sintered specimen in 7.6 ml of deionized (DI) water, 2.4 ml Isopropanol alcohol and 40µl of Nafion were dispersed to the ink and sonicated for 20 min in cold water bath of sonicator [13]. In other two vile Ni/ZIF and Pt/C sample were synthesized by same process of scattering the sample in DI water. The thin catalytic layer was generated by dropping a required amount of ink onto the polished glassy carbon disk (4mm in dia, AFE32040GC, Pine Instruments).

For comparison purpose all the catalytic layer were prepared one by one and tested in the same environment in RDE, a homogeneous and stable catalyst layer were prepared by rotation and dehydrated air at room temperature for 20 minute for all the three catalyst [13]. RDE evaluation were done in 0.1 M KOH with oxygen saturated [15]. LSV evaluation were performed Vs SCE at 20 mVs-1 rate having Pt

coil as the opposite electrode and SCE as the reference electrode using a PAR Bistat at different revolution, at room temperature. In order to find the strength and durability of the generated Ni nanotubes catalyst film, LSV were performed for 1000 time revolution to evaluate the degradation of the layer and to analyze the change in the current density.

### D. Characterization

The Fig 2 shows the magnified image of the Ni nanotubes. The image indicates that the nanotubes are formed after the sintering of the Ni/ZIF at high temperature in Nitrogen atmosphere, the width of the nanotubes is of various sizes ranges from 40-70 nm and having larger length than its width. The enhanced reactivity is due to the nanoparticles formation, having increased surface area.

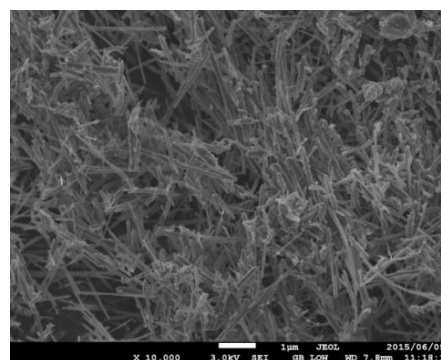


Figure 2. Scanning electron micrograph of Ni nanotubes

## III. RESULTS AND DISCUSSION

In order to evaluate the performance of Ni nanotubes towards ORR performance, kinetic mechanism and durability, the electrode were manufacture and LSV experiment were performed in a three electrode system in 0.1 M KOH electrolyte. For comparison purpose the RDEs with Ni/ZIF and Pt/C commercial catalyst were also conducted at similar environment. Figures 3, 4, 5. shows the ORR activity of Ni nanotubes, non sintered Ni/ZIF and commercial Pt/C catalysts in O<sub>2</sub> saturated electrolyte at different rpm respectively.

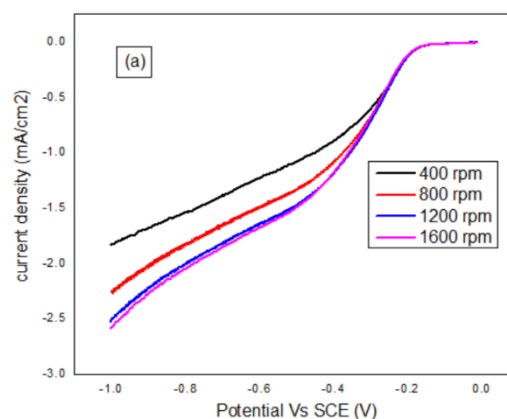


Figure 3. RDE data of Ni nanotubes

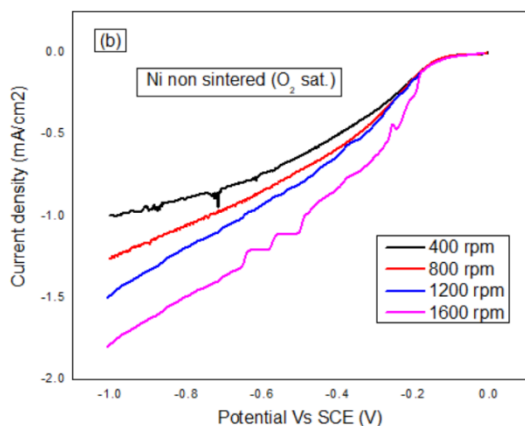


Figure 4. RDE data of Ni/ZIF non sintered

Fig.3 shows the ORR activity of Ni nanotubes at 400, 800, 1200, 1600 rpm in oxygen saturated electrolyte. The current density reaches -2.6 mA/cm<sup>2</sup> at 1600 revolution (rpm).the current density slowly increases from 400 rpm to maximum at 1600 rpm.

While the current density of non sintered Ni/ZIF at same environment reaches to -1.7 mA/cm<sup>2</sup> at 1600 rpm (Fig 4), which reflects that the activity enhances with the heat treatment of the Ni catalyst. This is due to the expected formation of nanotubes, increasing the surface area for catalytic activities.

The Pt/C catalyst has the highest current density of -4.6mA/cm<sup>2</sup> shown in Figure 5. at same environment which is high enough but due to the abundance of Ni and is non-precious it's loading can be increases to acquire the required activity. Fig 6. shows the comparison of all these three catalysts, in which it is indicated that the Pt/C catalyst has the highest current density of all but Ni nanotubes have also greater current density than non sintered Ni/ZIF,clearly indicating the treatment effect on the Ni catalyst. The activity increases, when Ni is sintered.

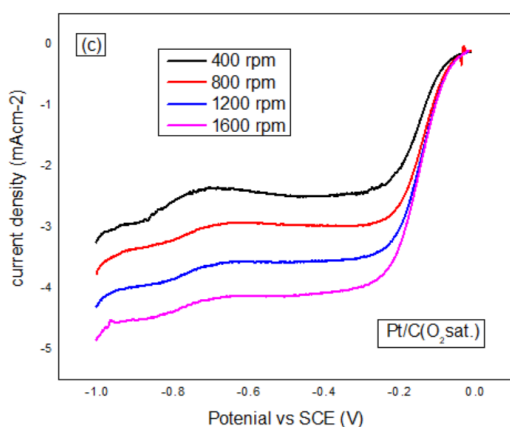


Figure 5. RDE data of Pt/C all at various rpm

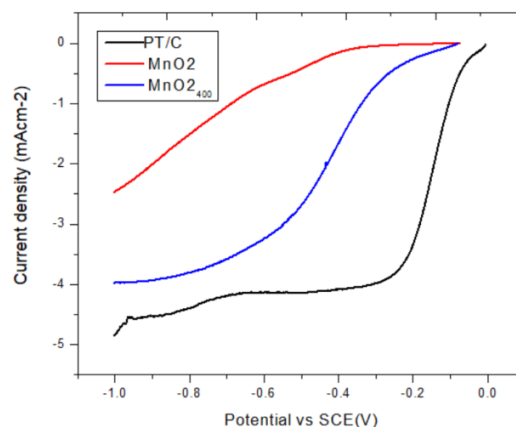


Figure 6. Comparison of Ni nanotubes, Ni ZIF and Pt/C at 1600 rpm

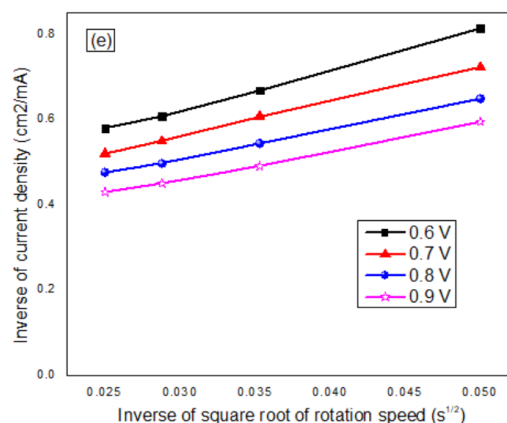


Figure 7. K-L plot for Ni nanotubes at various potentials

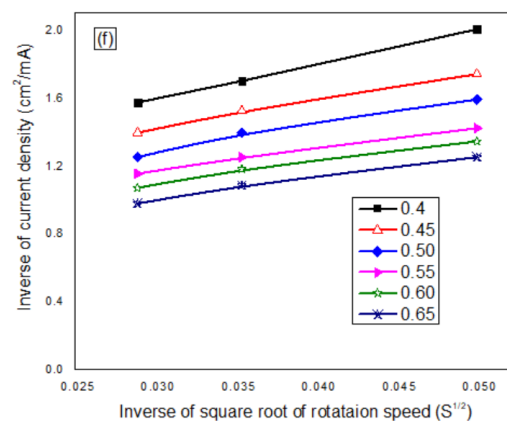


Figure 8. K-L plot for Ni ZIF at various potential

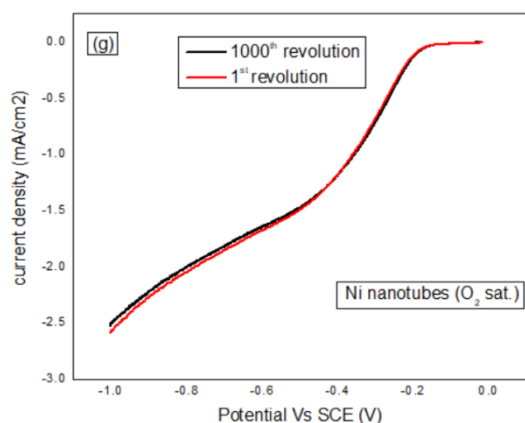


Figure 9. LSV data for Ni nanotubes showing degradation after 1000th cycle

Fig 7. Shows the K-L plot acquired from RDE data on ORR for Ni nanotubes at a number of revolution in oxygen concentrated electrolyte. The extrapolation of the K-L line gives us an intercepts adjacent to zero (0), which demonstrate that the process of oxygen ( $O_2$ ) reduction is totally under the diffusion control, and the slop B can be easily measured.

The electron transfer number is then calculated by the equation 1 to 4. While Fig 8. shows the K-L plot for the Ni ZIF, it clearly shows that the intercept is above zero and also the charge transfer number comes between 2 and 4, which indicate that there is also indirect conversion through hydrogen peroxide. Fig 7. shows that the value for oxygen reduction potential (ORR) for Ni nanotubes approaches to 4 at higher potential, showing direct ORR to water without any peroxide generation in this potential range [14].

To know about the kinetics of electron transfer of Ni nanotubes and Ni ZIF during the ORR, we studied the reaction kinetics by rotating disk voltammetry. The voltammetry profile in  $O_2$  saturated 0.1 M KOH electrolyte shows that the current density is enhanced by an increase in rotation rate from 400 to 1600 (Fig 3.)

The corresponding Koutecky-Levich plots ( $J^{-1}$  Vs  $\omega^{-1/2}$ ) at different electrode potentials (Fig 7) depicts good linearity and parallelism of the plots are considered as example of first order reaction kinetics in regard to the concentration of mixed  $O_2$ . The kinetic parameters can be examined on the basis of Koutecky-Levich equations:

$$1/J = 1/J_L + 1/J_K \quad (1)$$

$$= 1/B \omega^{-1/2} + 1/J_K \quad (2)$$

$$B = 0.62 N F C_0 (D_0)^{2/3} \nu^{-1/6} \quad (3)$$

$$J_K = n F k C_0 \quad (4)$$

In which J is the measured overall current density,  $J_K$  and  $J_L$  are the kinetic and diffusion- Limiting current densities,  $\omega$  is the angular velocity of the disk ( $\omega = 2\pi N$ , N is the linear rotation speed), n is the overall charge transferred number in oxygen reduction, F is the Faraday constant ( $F = 96485 \text{ C}$

$\text{mol}^{-1}$ ),  $C_0$  is the bulk concentration of  $O_2$ ,  $\nu$  is the kinematic viscosity of electrolyte, and k is the electron transfer rate constant. As from the Fig 7. the charge transfer number(n) and  $J_K$  can be calculated from the slop and intercept of the Koutecky-Levich plots. Respectively, and by using parameters  $C_0 = 1.2 \times 10^{-3} \text{ mol L}^{-1}$ ,  $D_0 = 1.9 \times 10^{-5} \text{ cm}^2 \text{ s}^{-1}$  and  $\nu = 0.1 \text{ m}^2 \text{ s}^{-1}$  in 0.1 M KOH. ORR will either occur via the 4 electron reduction pathway where  $O_2$  is reduced to water or the 2-electron reduction pathway where it is reduced to hydrogenperoxide ( $H_2O_2$ ). In fuel cell the 4-electron direct pathway is desirable [11].

## CONCLUSIONS

Ni nanotubes were prepared by hydrothermal treatment and by sintering at 800 °C in Nitrogen neutral environment. As vividly illustrated from RDE analysis, the Ni nanotubes catalyst illustrates extra ordinary catalytic behavior towards ORR compared to the Ni ZIF and also showed good activity if compared to other catalyst although it is lower than Pt/C catalyst but this can be resolved by heavy loading. It is shown from LSV that the degradation is very low even after several hundred cycles and the catalyst is stable in comparison to Ni ZIF under identical condition. The catalyst shows higher ORR and seemed to be good catalyst for oxygen reduction at cathode side.

## ACKNOWLEDGMENT

This research would not have been possible without the facility of FUEL CELL Laboratory provided by Arizona State University. In addition to that the support of US Pakistan Center for Advance Studies (USPCASE) UET Peshawar is highly appreciated to take a firm step for making a way to successful completion of this research.

## REFERENCES

- [1] S. Mukerjee and S. Srinivasan, J. Electroanal. Chem. 357, 201–224, 1993.
- [2] S. Kundu, T. C. Nagaiah, W. Xia, Y. Wang, S. V. Dommele, J. H. Bitter, M. Santa, G. Grundmeier, M. Bron and W. Schuhmann, J. Phys. Chem. C, 113, 14302–14310, 2009.
- [3] B. Su, I. Hatay, A. n. Troj' anek, Z. Samec, T. Khoury, C. P. Gros, J.-M. Barbe, A. Daina, P.-A. Carrupt and H. H. Girault, J. Am. Chem. Soc. , 132, 2655–2662, 2010.
- [4] E. Song, C. Shi and F. C. Anson, Langmuir, 1998, 14, 4315– 4321.
- [5] C. H. Kjaergaard, J. Rossmeisl and J. K. Nørskov, Inorg. Chem, 49, 3567–3572. 2010.
- [6] F. Cheng and J. Chen, Chem. Soc. Rev., 2012, 41, 2172–2192.
- [7] G. He, M. Qiao, W. Li, Y. Lu, T. Zhao, R. Zou, B. Li, J. A. Darr, J. Hu and M. M. Titirici, Adv. Sci., 1600214, 2016.
- [8] J. Yang, H. Sun, H. Liang, H. Ji, L. Song, C. Gao and H. Xu, Adv. Mater, 28, 4606–4613, 2016.
- [9] W. Zhang, A. U. Shaikh, E. Y. Tsui and T. M. Swager, Chem. Mater, 21, 3234–3241, 2009.
- [10] X. Zhang, Y. Chen, J. Wang and Q. Zhong, ChemistrySelect, 1, 696–702, 2016.
- [11] W. Lian, Y. Sun, B. Wang, N. Shan and T. Shi, J. Serb. Chem. Soc., 77, 335–348, 2012.
- [12] Xia Bao Yu, Yan Ya, Li Nan, Wu Hau Bin, Lou Xiong Wen David, Wang Xin, A metal-organic framework-derived bifunctional oxygen catalyst. Nat Energy; 1, 15006, 2016.

- [13] Shinozaki Kazuma,Zack Jason W,Richards Ryan M,Pivovar Bryan S,Kocha Shyam S.Oxygen reduction reaction measurements on platinum electrocatalysts utilizing rotating disk electrode technique 1.impact of impurities,measurements protocols and applied corrections.J electrchem Soc;162(10) :F1144-58, 2015
- [14] Zhou Ruifeng,Zheng Yao,Jaroniec Mietek,Qiao Shi Zhang.Determination of electron transfer number for oxygen reduction reaction; from theory to experiment.ACS Catal:4720-8, 2016.
- [15] Butler Ian B, Schoonen Martin AA, Richard David T. Removal of dissolved oxygen from water:A comparison of four common techniques. Talanta;41(2): 211-5, 1994.



**ABID ULLAH** who graduated from University of Engineering and Technology (UET) Lahore in 2014. He holds B.Sc degree in Chemical Engineering.He is currently postgraduate student in M.Sc Materials for Energy Storage and Conversion (MESc) at US Pakistan Center for Advanced Studies in Energy (USPCASE) UET Peshawar.

# Signal Path Loss Measurement for Future Terahertz Wireless Propagation Links

Sabir Shah<sup>1</sup>, Majid Ashraf<sup>2</sup>

<sup>1,2</sup>Department of Electrical Engineering, University of Engineering & Technology Peshawar, Pakistan  
sabir.shah@gmail.com<sup>1</sup>

Received: 26 September, Revised: 03 October, Accepted: 13 October

**Abstract**—Terahertz Band (100GHz-10THz) offers larger bandwidth and ultra-higher data rates and is visualized as a key technology to alleviate the capacity limitation and spectrum scarcity of the current wireless networks. There are some competent development and design challenges in the realization of wireless terahertz network. Signal high path loss is one of the major constraints for enabling wireless communication networks in the terahertz band. Thus for the consummation of wireless propagation links in the THz band an equivalent signal path loss model is designed incorporating the major peculiarities of the wireless channel that accounts for terahertz wave propagation in LoS propagation. The equivalent path loss model for terahertz LoS propagation is developed and simulated in matlab<sup>R</sup>. The simulation results are compared with the lognormal path loss model results.

**Keywords**— THz, wireless channel, fading, polarizability

## I. INTRODUCTION

High data rates demands in wireless data sharing are extremely grown from the past few years in our society. Customers often demand wide bandwidth and high data rates application with the rapid advancement in Wireless networks and mobile technology [1]. Wireless data rates and capacity has observed increasing every 18 month 2-fold, leads to a distinct decision that 15-Gbps data rate for wireless communication will be required after 10 years. Moreover, wireless migrant data rate capabilities will be impending towards wire-line communication systems [2]. Until now the largest connected spectrum around 60 GHz with 7 GHz available spectrum allocated for current mobile services are challenging to achieve 100 Gbps data rates. To achieve 100 Gbps data rates with realistic and spectral efficiencies of few bit/sec/Hz requires sufficiently larger bandwidth beyond 10 GHz. THz band is one of the most promising band to offer larger unregulated spectrum [3]. The current increasing demand of high data rates and wireless networks can be accomplished with the allocation of higher data rates and large bandwidth waves in terahertz band [4].

Terahertz frequency spectrum or so-called millimeter band ranges between 0.1 THz and 10 THz frequencies waves within electromagnetic spectrum between infrared and microwaves,

with correlating wavelengths between 3 mm and 30  $\mu$ m offer larger bandwidth and high data rates. Terahertz various wireless applications at short range already used in spectroscopy, imaging and remote gas sensing etc, reveals that THz band will be attractive for future larger bandwidth and higher data rates wireless communication [5]. Terahertz band applications used in security equipments at airports and other public places have high selectivity because of molecular resonance frequencies in terahertz spectrum, can penetrate through many dense materials enabling suspicious materials detection. Due to their non-ionizing nature like microwaves, terahertz radiation can be used in close vicinity to a human body [6]. It will support next generation small cells cellular networks in future [7]. Terahertz will enable interconnection of different ultra high speed links like optical fiber wire links to tablets and other wireless links. Large wireless data sharing and HD video conferencing will be enabled through terahertz technologies [8]. Terahertz networks could be used to provide secure communication in military and defense fields. Terahertz equipments could be used in health monitoring systems to gather important information about patient's health [9].

Terahertz networks technologies are swiftly developing and the new advancement in the antennas field and transceiver architectures are bringing wireless communication in THz spectrum closer to the reality [10]. THz frequency spectrum is imagined to overcome the problems related to spectrum scarcity and capacity limitations of the current wireless communication networks. Short-range and wide bandwidth THz communications for indoor wireless communication along THz standardization have been proposed within the WPAN (Wireless Personal Area network) THz band interest group IEEE 802.15 [11], but they are considered terahertz transmission up to several meters. One of the major constraints for the realization of the terahertz wireless communication is the high signal path loss [12]. Atmospheric absorption attenuation because of molecular absorption like oxygen molecules and water vapors in the air and high frequency propagation, terahertz signal experience harsh path loss that restrict the wireless communication to few meters [13]. In an atmospheric medium the molecular absorption influence the terahertz signals propagation [14]. Molecular absorption can be defined as the process in which some part of signal energy is converted to kinetic energy of the charged medium molecules. In addition to some other such factors like fading, spreading loss, molecular absorptions weakened the



propagated signals wireless communications in the THz spectrum [5]. In this paper we proposed a path loss model for THz signal line of sight propagation incorporating the signal spreading in free space and scattering effect from particles in addition to molecular absorption in the atmospheric medium. Besides molecular absorption, molecular noises produced as a result of discharge of absorbed energy are also considered.

## II. PATH LOSS MODEL

Terahertz signal path loss is the main component in the design and interpretation of wireless propagation links. The signal path loss or loss in signal strength may occur due to several effects like free space path loss or signal spreading loss, absorption losses due to signal interactions with atmospheric molecules because of molecular resonances due to oxygen and water vapors in the atmosphere. Molecules present in the atmospheric medium are energized by electromagnetic waves radiation at terahertz band. molecular noise generating when molecules in the medium discharge absorbed energy back to the medium Due to shorter wavelength terahertz signal scattering are also occur from medium molecules having size greater than propagating signal present in LoS propagation of terahertz signal. Terahertz signal path loss is directly proportional propagating signal frequency, distance between transmitter and receiver and the medium composition in free space wireless communication. Terahertz signal total path loss  $PL_{Total}(f,d)$  can be defined as the spreading loss function  $PL_{spr}(f,d)$ , absorption loss function  $PL_{abs}(f,d)$ , scattering loss function  $PL_{scat}(f,d)$  and noise function  $PL_{Noise}(f,d)$  as

$$PL_{Total}(f,d) = PL_{spr}(f,d) \times PL_{abs}(f,d) \times PL_{scat}(f,d) \quad (1)$$

Terahertz signal spreading loss due to signal expansion can be calculated by Friis formula as a function of signal frequency, propagation distance and speed of light as

$$PL_{spr}(f,d) = 20 \log \left( \frac{4\pi \cdot f \cdot d}{c} \right) \quad (2)$$

The atmospheric absorption that a propagating terahertz signal suffers due to molecular absorption over distance  $d$  depends on transmittance of the medium  $\psi$  can be determined with the help of Beer-Lambert law as

$$\psi(f) = \frac{P_i}{P} = e^{-\beta_{mole}(f_s)d} \quad (3)$$

The atmospheric attenuation coefficient  $\beta$  depends upon the composition of mixture of medium gasses. Assuming office air as standard that is mainly composed of nitrogen 78%, oxygen 21% dust particles and water vapors 1% [15], the atmospheric attenuation coefficient  $\beta$  can be determined as

$$\beta(f) = \sum_g \beta^g(f) = \beta^{N_{O_2}}(f) + \beta^{O_2}(f) + \beta^{H_2O}(f) \quad (4)$$

The molecular absorption coefficient of a medium for transmitting signal having frequency  $f$  depends upon temperature, pressure and medium composition of the

molecules. Molecular absorption coefficient can also be represented as

$$\beta(f_s) = N\partial^{abs}(f_s) \quad (5)$$

Where  $\partial^{abs}$  represents the cross sectional area of the absorbing species and  $N$  represents their number. Molecules natural abundances for terahertz signal wireless channel can be predicted in high resolution transmission molecular absorption database HITRAN [16]. Dry air integrants natural abundances should be investigated by using water vapors volume mixing ratio. The water vapors volume mixing ratio is calculated with saturated water vapor partial pressure  $P_w$  as

$$P_w = 6.1121(1.0007 + 3.46 \times 10^{-6}p) \cdot \exp \left( \frac{17.502T}{240.97 + T} \right) \quad (6)$$

So water vapor volume mixing ratio in presence of relative humidity  $\omega$  is given by

$$\epsilon_{water} = \frac{\omega}{100} \cdot \frac{P_w}{p} \quad (7)$$

So the moist air components abundance is given by

$$\epsilon_{moist} = \epsilon_{dry}(1 - \epsilon_{water}) \quad (8)$$

The saturated water air Atmospheric attenuation coefficient because of these gases, dust particles and water vapors in the air can be found in detail in [12]. Also the absorption loss function  $PL_{abs}(f,d)$  for terahertz signal molecular absorption loss in equation (1) can now be written as

$$PL_{abs}(f,d) = \frac{1}{\psi(f)} \quad (9)$$

$$PL_{abs}(f,d) = e^{\beta_{mole}(f)d} \quad (10)$$

The molecular noise generating due to molecular discharge energy [5] can be written as

$$PL_{Noise}(f,d) = K_B \cdot B(N_L(f,d) + N_A(f)) \quad (11)$$

The propagating signal path loss due to molecular and particle scattering in LoS propagation medium can be calculated by using scattering coefficient [17] as inverse Beer-Lambert law as

$$PL_{scat}(f,d) = \alpha_{scat}(f)d \quad (12)$$

The scattering coefficient for number  $N$  of scattering species cross-sectional  $\partial^{scat}$  can be define as

$$\alpha_{scat}(f) = N\partial^{scat}(f) \quad (13)$$

Rayleigh scattered cross sectional areas of particles can be determined from [18] as



$$\partial^{scat}(f) = \frac{128\pi^5\beta^2}{3\lambda^4} \quad (14)$$

The polarizability  $\beta$  of a molecule can be calculated [19] as

$$\beta = \frac{n(f)^2 - 1}{n(f)^2 + 2} \cdot \left(\frac{x_d}{2}\right)^3 \quad (15)$$

From [20] the Rayleigh scatters cross sectional areas becomes

$$\partial^{scat}(f) = \frac{24\pi^3}{\lambda^4 N^2} \left(\frac{n(f)^2 - 1}{n(f)^2 + 2}\right)^2 \frac{6 + 3p}{6 - 7p} \quad (16)$$

Where the depolarization is  $p$  and their ratio  $(6+3p)/(6-7p) \approx G$ , the air molecules depolarization term  $G$  can be calculated from [17]. Terahertz signal scattering from a molecular particle is shown in Figure 1.

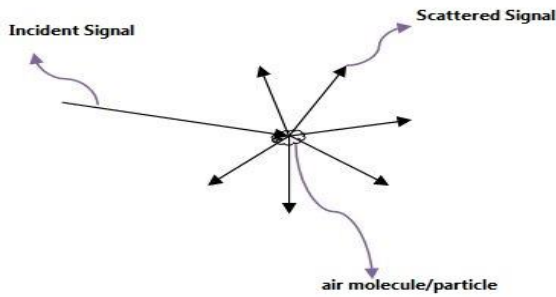


Figure 1. THz Signal Scattering form molecules/particles

The number of scattering particles can be found by log-normal distribution approximated in [21], [22] as

$$N(x_d) = \frac{dN}{dx_d} = \frac{1}{x_d \sqrt{2\pi \ln(\sigma)}} e^{-\frac{((\ln(x_d) - \ln(\bar{x}_d)))^2}{2 \ln \sigma}} \quad (17)$$

The scattering coefficient for scattering particles can be approximated from [21] as

$$\alpha_{scat}(f) = \int_0^\infty \frac{2\pi^5 x_d^5 N}{3\lambda^4 \sqrt{2\pi \ln(\sigma)}} \left(\frac{n(f)^2 - 1}{n(f)^2 + 2}\right)^2 \times e^{-\frac{((\ln(x_d) - \ln(\bar{x}_d)))^2}{2 \ln \sigma}} dx_d \quad (18)$$

Where  $\sigma$  is the standard deviation,  $z$  is the scatter diameter and  $x_d$  is the scattering particle diameter.

The proposed path loss model in equation (1) for terahertz wireless propagation can be summarized as

$$PL_{Total}(f, d) = \left( \left( \frac{4\pi f d}{c} \right) \times e^{\beta_{molec}(f)d} \times e^{\alpha_{scat}(f)d} \right) \quad (19)$$

Where  $B$  is the channel bandwidth,  $K_B$  represents Boltzmann constant  $N_L(f, d)$  and  $N_A(f)$  is the temperature of the molecular noise and other noise. Terahertz signal total attenuation coefficients for line of propagation medium can be approximated as

$$Coeff_{Total} = Coeff_{spr} + Coeff_{molec} + Coeff_{scat} + Coeff_{noise} \quad (20)$$

### III. SIMULATION RESULTS

The proposed path loss model for terahertz signal wireless propagation in LoS channel is demonstrated with the experimental results. The total path loss and attenuation coefficients are simulated for terahertz signal. Signal path loss due spreading of terahertz signal through the medium is simulated as function of THz frequencies and propagation distance in Figure 2.

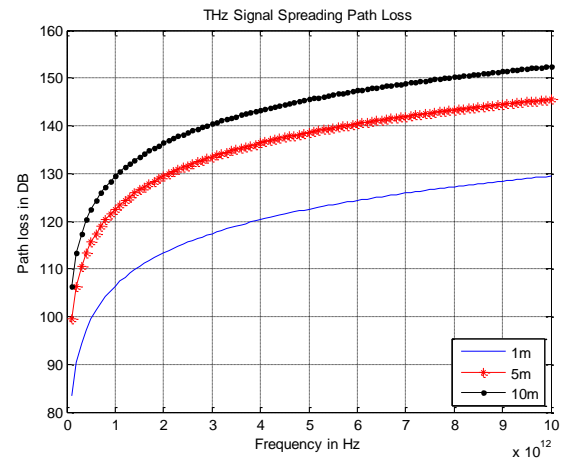


Figure 2. THz Signal Spreading Path Loss Measurement

Molecular absorption losses cause additional attenuation to electromagnetic waves in terahertz band frequencies are approximated in Figure 3. THz signal path losses due to spreading of signals are simulated in Figure 4, shows that molecular absorption loss attenuates the signal strength over distance.

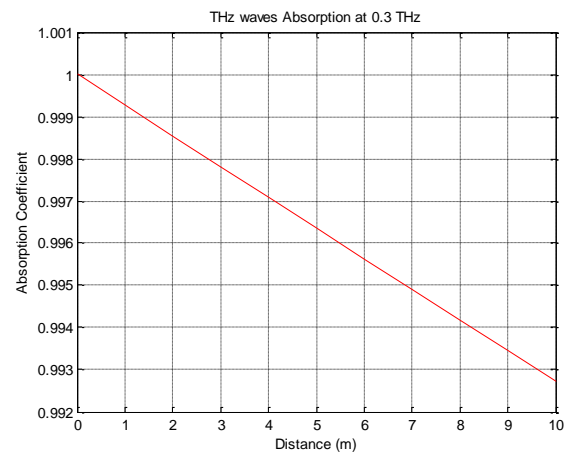


Figure 3. THz Signal molecular Absorption Loss

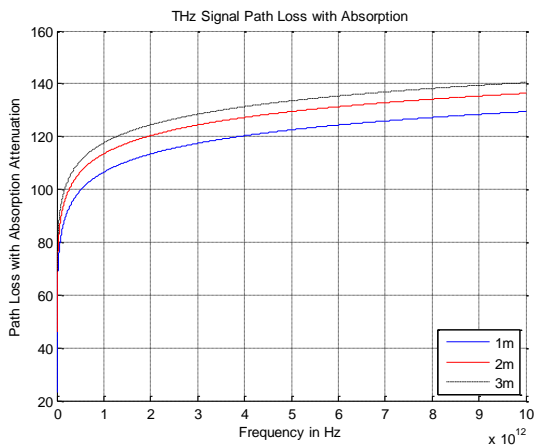


Figure 4. THz Signal Path Loss Considering Absorption

Terahertz signals wireless propagation suffers scattering through medium molecules and particles in wireless propagation. For calculating scattering coefficient the cross section of scattering particle can be calculated from  $s = \frac{\pi x_d^2}{\lambda}$ , the size of particle. Where  $x_d$  is the diameter of the particle and  $\lambda$  is the wavelength [23]. For Rayleigh scattering the average particle size is taken 2.5um [18]. The refractive index of medium and dust  $n(f)$  is taken 1.6 for visible light frequencies [24]. The number of scattering particles per cubic cm3 is considered one million [25]. The scattering coefficient for dry air at 302.5 K temperature, 100.7 Kpa pressure and 70% relative humidity for 2um diameter and 2.7um standard deviation [26] is calculated  $1.3069 \times 10^{-14} \text{cm}^{-1}$ . The average diameter of water droplet is (1-10um) [27]. The scattering coefficient for water vapors calculated  $3.8386 \times 10^{-7} \text{cm}^{-1}$ . A higher frequency signals causes scattering from medium molecules because of their shorter wavelength. The scattering coefficients for high frequencies signal at 100m propagation distance are depicted in Figure 5 below.

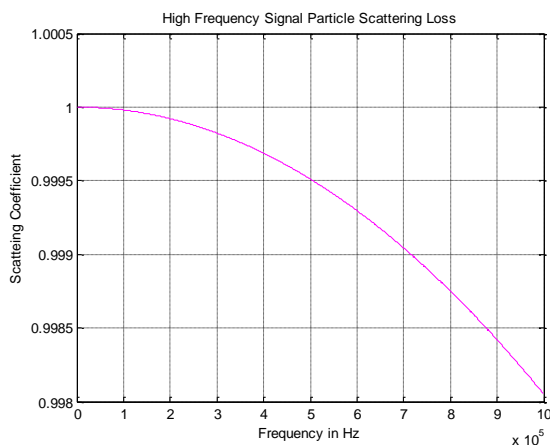


Figure 5. Scattering Coefficient for higher frequencies Signal

THz signal path loss considering free space spreading loss, molecular absorption attenuation and scattering losses due to signal scattering from particles in the medium are simulated over distance in Figure 6.

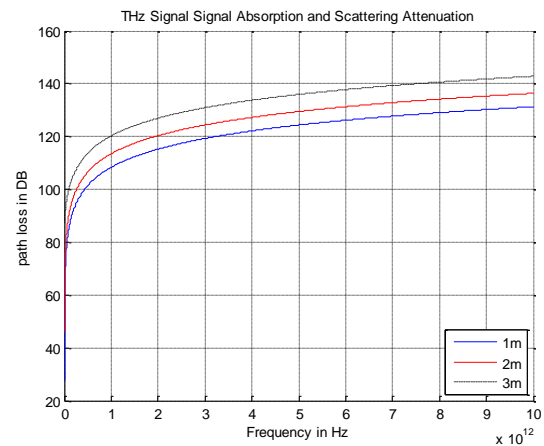


Figure 6. THz Signal Path Loss Considering Scattering

The power spectral density for molecular noise generated when atmospheric molecules re-emit absorb energy in atmospheric medium [5] as shown in Figure 7. When the atmospheric molecules re-emit the absorb energy, temperature of the channel arises causes molecular noise to THz signal wireless propagation in through the channel.

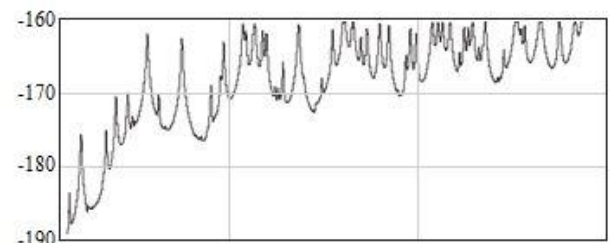


Figure 7. Molecular Noise Power Spectral Density

Finally path loss for a signal in free space wireless propagation at 0.3THz frequency are simulated for a distance of 3m including the effects of spreading loss, molecular absorption and scattering attenuation and molecular noise. The simulation results are compared with the path loss results in [28] shown in Figure 8. The simulation results are very close in value to the lognormal path loss results.

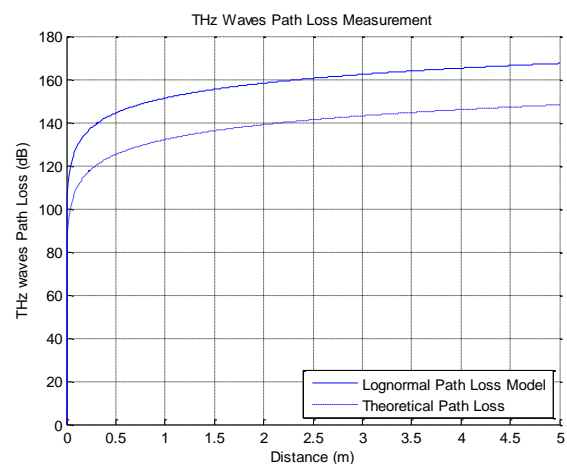


Figure 8. THz Signal Path in Los Propagation

## CONCLUSION

In this paper, the main constraints to wireless communications in the Terahertz spectrum are studied. We examined the line of sight free space signal spreading including molecular absorption losses and signal scattering from medium particles. The effect of molecular noise is also considered in THz signal line of sight propagation. Taking into consideration all these peculiarities of the terahertz wireless communication an equivalent path loss model based is derived. We have validated our proposed path loss model through simulations in Matlab. The simulation results shows that our proposed path loss model is more practical and useful for interference and link budget calculations in the design of future wireless propagation link at terahertz band.

## REFERENCES

- [1] Federici, John, and Lothar Moeller. "Review of terahertz and subterahertz wireless communications." *Journal of Applied Physics* 107, no. 11 (2010): 6.
- [2] Kleine-Ostmann, Thomas, and Tadao Nagatsuma. "A review on terahertz communications research." *Journal of Infrared, Millimeter, and Terahertz Waves* 32, no. 2 (2011): 143-171.
- [3] Kürner, Thomas, and Sebastian Priebe. "Towards THz communications status in research, standardization and regulation." *Journal of Infrared, Millimeter, and Terahertz Waves* 35, no. 1 (2014): 53-62.
- [4] Moldovan, Anamaria, Michael A. Ruder, Ian F. Akyildiz, and Wolfgang H. Gerstacker. "LOS and NLOS channel modeling for terahertz wireless communication with scattered rays." In *Globecom Workshops (GC Wkshps)*, 2014, pp. 388-392 IEEE, 2014.
- [5] Boronin, Pavel, Dmitri Moltchanov, and Yevgeni Koucheryavy. "A molecular noise model for THz channels." In *Communications (ICC), 2015 IEEE International Conference on*, pp. 1286-1291 IEEE, 2015.
- [6] Akyildiz, Ian F., Josep Miquel Jornet, and Chong Han. "Terahertz band: Next frontier for wireless communications." *Physical Communication* (2014)16-32.
- [7] Piesiewicz, R., Kleine-Ostmann, T., Krumbholz, N., Mittleman, D., Koch, M., Schoebel, J., Kürner, "Short-Range Ultra Broadband Terahertz Communications: Concept and Perspectives, accepted" For Publication in *IEEE Antennas and Propagation Magazine Physical Communication*, vol.12 p.16-32, 2014.
- [8] Moldovan, Anamaria, Steven Kisseleff, Ian F. Akyildiz, and Wolfgang H. Gerstacker. "Data rate maximization for terahertz communication systems using finite alphabets in Communications (ICC), 2016 IEEE International Conference on, pp. 1-7, 2016.
- [9] S. Priebe, M. Kannicht, M. Jacob, and T. Kurner "Ultra Broadband Indoor Channel Measurements and Calibrated Ray Tracing Propagation Modeling at THz Frequencies," *IEEE Journal of Communications and Networks*, vol. 15, no. 6, pp. 547-558, 2013.
- [10] Han, Chong, A. Ozan Bicen, and Ian F. Akyildiz. "Multi-ray channel modeling and wideband characterization for wireless communications in the terahertz band." *IEEE Transactions on Wireless Communications* 14, no. 5 (2015): 2402-2412.
- [11] IEEE 802.15 WPAN Terahertz Study Group 100 Gbit/s Wireless (SG100G). Online Available: <http://www.ieee802.org/15/pub/SG100G.html>
- [12] Jornet, Josep Miquel, and Ian F. Akyildiz. "Channel modeling and capacity analysis for electromagnetic wireless nanonetworks in the terahertz band." *IEEE Transactions on Wireless Communications* 10, no. 10 (2011): 3211-3221.
- [13] Kokkonen, Joonas, Janne Lehtomäki, Kenta Umebayashi, and Markku Juntti. "Frequency and time domain channel models for nanonetworks in terahertz band." *IEEE Transactions on Antennas and Propagation* 63, no. 2 (2015): 678-691.
- [14] Priebe, Sebastian, and Thomas Kurner. "Stochastic modeling of THz indoor radio channels." *IEEE Transactions on Wireless Communications* 12, no. 9 (2013): 4445-4455.
- [15] Sheikh, Fawad, Nidal Zarifeh, and Thomas Kaiser. "Terahertz band: Channel modeling for short-range wireless communications in the spectral windows." *IET Microwaves, Antennas & Propagation* 10, no. 13 (2016): 1435-1444.
- [16] Brown, L. R., K. Sung, D. C. Benner, V. M. Devi, V. Boudon, Tony Gabard, Ch Wenger et al. "Methane line parameters in the HITRAN2012 database." *Journal of Quantitative Spectroscopy and Radiative Transfer* 130 (2013): 201-219.
- [17] Bodhaine, Barry A., Norman B. Wood, Ellsworth G. Dutton, and James R. Slusser. "On Rayleigh optical depth calculations." *Journal of Atmospheric and Oceanic Technology* 16, no. 11 (1999): 1854-1861.
- [18] Chandrasekhar, S. and Radiative Transfer. "Dover Publications." New York (1960).
- [19] D. Haubrich, "Instrumentation to Measure Backscattering Coefficient for Arbitrary Phase Functions," Ph.D. dissertation, Texas A&M University, Texas, United States of America, 2010.
- [20] Bodhaine, Barry A., Norman B. Wood, Ellsworth G. Dutton, and James R. Slusser. "On Rayleigh optical depth calculations." *Journal of Atmospheric and Oceanic Technology* 16, no. 11 (1999): 1854-1861.
- [21] [23] C. Zender, "Particle size distributions: Theory and application to aerosols, clouds, and soils," 2010. Online available: <http://dust.ess.uci.edu/facts/psd/psd/pdf>.
- [22] Hussein, Tareq, Arto Puustinen, Pasi P. Aalto, Jyrki M. Mäkelä, Kaarle Hämeri, and Markku Kulmala. "Urban aerosol number size distributions." *Atmospheric Chemistry and Physics* 4, no. 2 (2004): 391-411.
- [23] Moosmüller, Hans, and W. Patrick Arnott. "Particle optics in the Rayleigh regime." *Journal of the Air & Waste Management Association* 59, no. 9 (2009): 1028-1031.
- [24] K. Kandler et al., "Chemical composition and complex refractive index of Saharan mineral dust at Izaña, Tenerife (Spain) derived by electron microscopy," *Atmospheric Environment*, vol. 41, no. 37, pp. 8058-8074, Dec. 2007.
- [25] Schery, Stephen D. Understanding radioactive aerosols and their measurement. Volume 19 Springer Science & Business Media, 2001.
- [26] Bodhaine, Barry A., Norman B. Wood, Ellsworth G. Dutton, and James R. Slusser. "On Rayleigh optical depth calculations." *Journal of Atmospheric and Oceanic Technology* 16, no. 11 (1999): 1854-1861.
- [27] Recommendation ITU-R P.1817-1: Propagation data required for the design of terrestrial free-space optical links, International Telecommunication Union Radio communication Sector (ITU-R) Std.
- [28] Afsharinejad, A. Davy, B. Jennings, and C. Brennan, "An initial path-loss model within vegetation in the thz band," in *Antennas and Propagation (EuCAP), 2015 9th European Conference on*. IEEE, 2015, pp. 1-5.

## Voltage Control for DC-DC Converters

Usman Rahat<sup>1</sup>, Dr. Abdul Basit<sup>1</sup>, Muhammad Salman<sup>1</sup>

<sup>1</sup>University of Engineering & Technology Peshawar, Pakistan

Received: 05 September, Revised: 15 October, Accepted: 04 October

**Abstract**—In this paper, we discussed voltage control method for buck converter operating in continuous conduction mode (CCM) using analog feedback system. The aim of this work is to control the output voltage of a buck converter during the variation in load current. It is obtained by using analog feedback made with operational amplifier (Opamp). However, the same technique can be applied to other DC-DC converters (e.g boost, buck-boost, cuk converter, etc) in CCM mode, but for the purpose of analysis buck converter is chosen as an example.

**Keywords**— Analog feedback, Operational amplifier (Opamp), Buck converter, Continuous conduction mode.

### I. INTRODUCTION

The issue of voltage regulation cannot be neglected in power electronics circuits. The load requires a controlled and regulated output voltage to operate. However, the non-linear and abrupt current drawing nature of the load causes the output voltage of the converter to deviate from the desired level. This could result in failure of the load operation. The main role of a power electronics circuit is to convert one form of electric power to the other form of electric power by changing either voltage, frequency or both. In DC-DC converters the level of voltage is either shifted up or down depending upon the application. In this work the output voltage of a buck converter is controlled. Buck converter converts its input voltage to a lower dc output level. This work is primarily focused on voltage control of DC-DC converter (buck converter as an example). The converter is basically non-linear and time variant in nature. The principles of state space averaging [1]–[6] and circuit averaging [1], [7], [8] can be applied to obtain linear time invariant (LTI) model. Moreover, this paper focuses the continuous conduction mode (CCM) operation. During CCM the inductor current is always positive and never drops to zero. In CCM mode the converter has two states. In general a DC-DC converter can operate in either continuous conduction mode (CCM) or discontinuous conduction mode (DCM). The method discussed in this article can be generalized to other DC-DC power converters as well.

### II. MODELING AND SIMULATION

Modeling is a way to represent a process or phenomenon in a mathematical form. This step can be as simple as setting up some linear equations to as complex as set of non linear differential equations. It is worth mentioning to point out that

mathematical models are not exact but some kind of approximation to the real physical systems. The more accurate a model has more mathematical rigor and thus are more complex. Therefore, we often have to trade off between the level of accuracy we require from our models and the level of complexity we can handle. In fact, what we really tend to do is model the significant components and factors of the system and ignore all the unnecessary details. Moreover, it is better to start with simple model and analyze it, and later on if we find out that the model is inaccurate we can refine it again but in the meanwhile we get some good insights of the system.

The simulation model is setup in LTspice where the buck converter along with its controller is simulated. The simulation model is explained in detail below.

#### A. Load Current Variation

The simulation setup from LTspice in Fig1 is discussed where the main objective is to regulate the output voltage irrespective of output load current. The pulse source is used to model the varying load.

The converter designed has considerably high end specifications which are hard to achieve. The details are given:

- Input Voltage  $v_g=5V$ . The input voltage is 5V.
- Output Voltage  $v=1.5V$ . The objective is to regulate the output voltage at 1.5V.
- Output Current  $i_{load}$  range= 0-10A. The output current can vary between 0 and 10A.
- Power Stage Switching Frequency=2MHz.
- Bandwidth of the feedback loop/Crossover
- Frequency = 200KHz, implies Settling Time = 5 $\mu$ s.
- Phase Margin (P.M) =50 degrees

The PWM block can generate a duty cycle value ranging [ $D_{min} = 0.05$ -  $D_{max} = 0.9$ ]. Some important blocks of the simulation model are:

- **Gate Drivers (U3 and U4)**  
The gate driver block switch on/off the MOSFETs in complimentary fashion.
- **Pulse Width Modular (U1)**

The PWM block generates the switching signal proportional to its input signal.

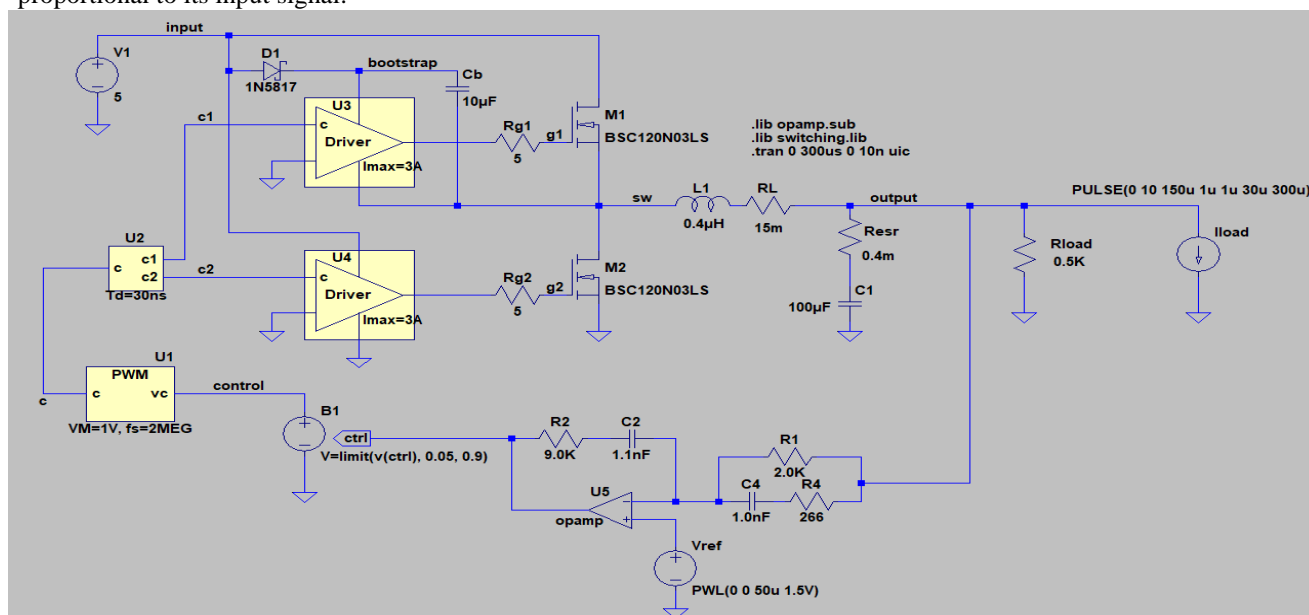


Figure 1 Simulation for Load Variation

- Dead Time (U2)**

The dead time block does not allow both MOSFETs to conduct at the same time.

- Feedback Circuit**

This block has operational amplifier with resistors and capacitors making up the proportional integral derivative (PID) controller.

- Sources**

Input Voltage Source = 5V

Output Current Pulse Source = 0-10A.

achieve the low error state. In doing so the feedback system may damage the power MOSFETs.

The Fig2 shows the output voltage follows a reference value Vref in a linear fashion and the gets stable when reaches to steady state condition.

At 150us there is a step change in the output load current and it jumps from 0 to 10A. The value of output current pulse source remains high for 30us and then at 180us there is another step change but this time from 10 to 0A. It is important to observe that the output voltage in such an enormous step change of load current remains close to 1.5V with good accuracy.

During the rising edge of load current, the inductor current rises, output voltage dips and stabilizes. While during the falling edge of load current, the inductor current drops, output voltage overshoots and stabilizes.

It is important to note that when the load current takes a positive step, there is an output voltage dip. The deviation in the output voltage from its reference value is used as an error signal to drive the opamp. Similarly, during the negative step, the output voltage overshoots the reference value and the error is used to drive the opamp.

TABLE II IMPORTANT BLOCKS IN SIMULATION SETUP

Sr.No.	Component	Value
1.	PWM (U1)	$D_{min} = 0.05; D_{max} = 0.9$
2.	Dead Time (U2)	30ns
3.	Opamp (U5)	$A_{ol} = 100meg; GBW = 10000meg$

### B. Load Current Simulation Overview

In Fig1, for setting the reference level a soft start switching technique is realized. The voltage at reference node increases in a linear fashion from 0 to 1.5V in 50us. The 1.5V is not applied upfront as initially the output voltage will be zero. This will produce high error signal pushing the opamp to its limits to

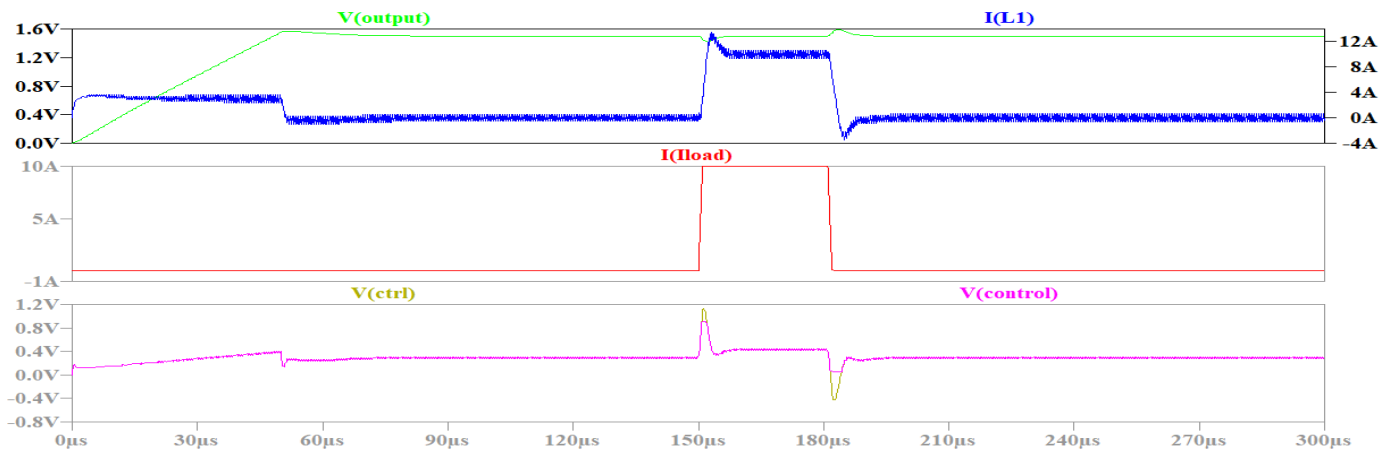


Figure 2. Load Variation Overview

### C. Rising Edge of Load Current and Output Voltage

As mentioned that during the positive step of load current from 0 to 10A, there is a voltage dip in the output voltage. This is verified in Fig3 through LTspice where the voltage dip of -78mV is shown. It should be noted that the control signal in Fig 2 gets saturated for some time, otherwise the dip would have been further lower than -78mV.

### D. Settling Time on Rising Edge

The lower voltage difference of the output voltage from the reference (1.5V in this case) is not the only desired behavior of a good feedback controller. The feedback loop should also have sufficient bandwidth to quickly respond to the variations. The higher the bandwidth of the feedback loop, the lesser the time it would take to reach its steady state condition of reference voltage. In fig4 this is verified that the output voltage with good precision gets very close to 1.5V in the time span of 5μs which is the settling time of the feedback loop.

TABLE II. SOME SIMULATION PARAMETERS

S.No	Parameters	Values
1.	Total Simulation Time	300us
2.	$V_{ref}$	1.5V
3.	Pulse Current Source	Range: 0-10A

### E. Falling Edge of Load Current and Output Voltage

As mentioned that during the negative step of load current from 10 to 0A, there is a voltage overshoot in the output voltage. This is verified in Fig5 through LTspice where the voltage overshoot of 91.92mV is shown. It should be noted that the control signal in Fig2 gets saturated for longer time, otherwise the dip would have been further lower than 91.92mV.

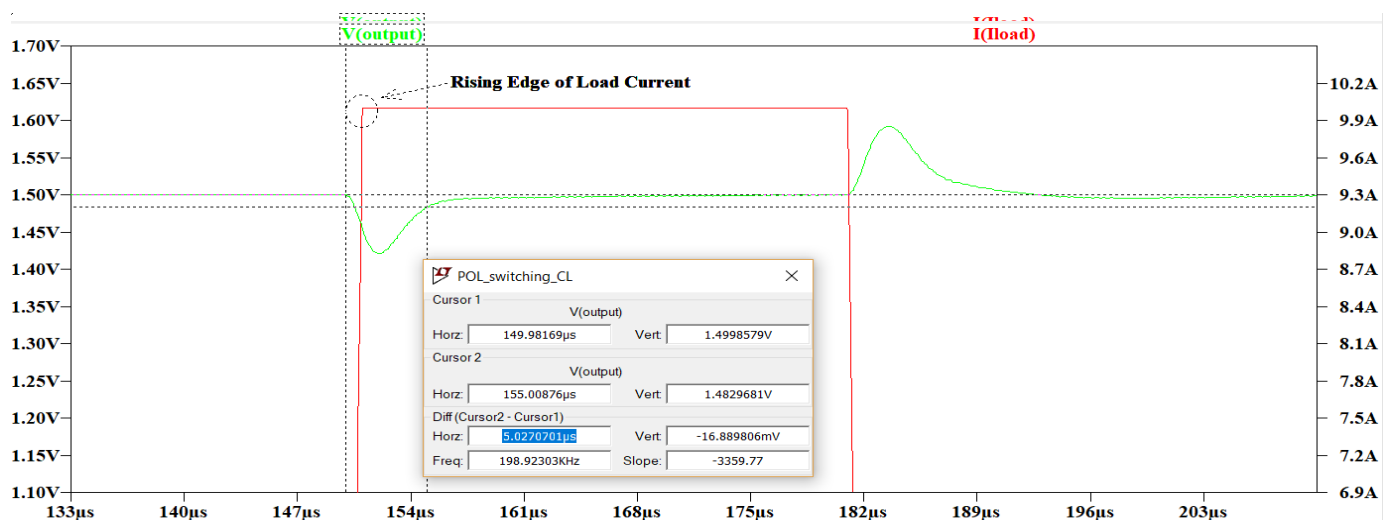


Figure 4. Settling Time on Rising Edge



### F. Settling Time on Falling Edge

The same arguments hold true in this case for the settling time which we can see in Fig6. There is a considerable deviation found in the output voltage after 5 $\mu$ s of the settling time. This is because the control signal in Fig 2 gets saturated for a longer period of time in the case of falling edge.

## III. DISCUSSION AND FUTURE WORK

In this paper the techniques of linear control theory involving circuit averaging are used. However, many other

state of the art and advanced techniques can be applied in the future to solve other issues. These issues include the output voltage deviation in the presence of input voltage deviation or parameters change. In this paper only the output voltage deviation caused by the load current variation is considered. While in reality the voltage deviation due to non regulated input voltage can be crucial to handle. Furthermore, the circuit parameters can change because of temperature variations which could cause the impedance values of the elements to deviate causing the output voltage to deviate dramatically. In this work analog feedback control is used.

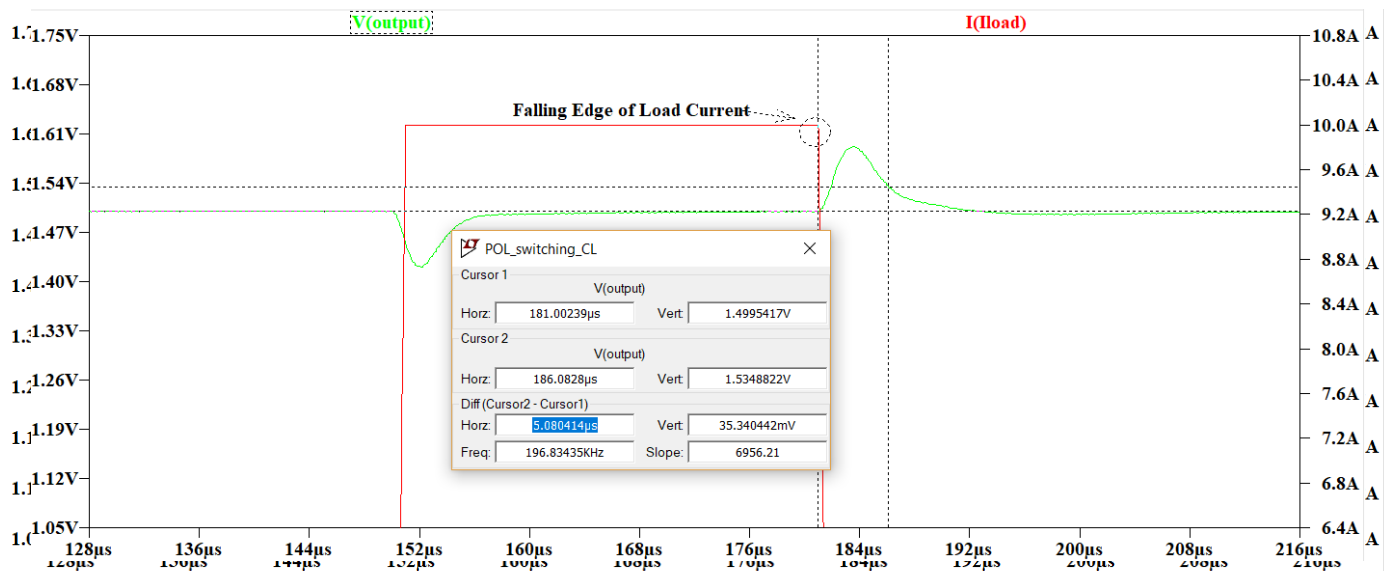


Figure 6. Settling Time of Falling Edge

Digital control can be implemented whose main advantage could be to change the circuit behavior later on according to new requirements. This will reduce the bulk production cost of the system. However, the down side of this approach is that it would cause additional delay due to analog to digital conversion of the signal.

## CONCLUSIONS

In this paper a simulation model was setup in LTspice to regulate the output voltage of the buck converter to 1.5V in the presence of disturbances in the output load current. It was seen that the output current was varied in step change of 10A. The output current was a pulse source which was used to trigger a positive edge of 0 to 10A, and negative edge of 10 to 0A at the load side. In both the cases the output voltage was well regulated near 1.5V. The control signal was saturated for negligible time because the load current variation was very

abrupt and fast, due to which the controller faced some issues to meet the exact settling time requirements.

## REFERENCES

- [1] R. W. Erickson and D. Maksimovic, Fundamentals of power electronics. Springer Science & Business Media, 2007.
- [2] R. Middlebrook and S. Cuk, "A general unified approach to modeling switching-converter power stages," in Power Electronics Specialists Conference, 1976 IEEE. IEEE, 1976, pp. 18–34.
- [3] J. Mahdavi, A. Emaadi, M. Bellar, and M. Ehsani, "Analysis of power electronic converters using the generalized state-space averaging approach," IEEE Transactions on Circuits and Systems I: Fundamental Theory and Applications, vol. 44, no. 8, pp. 767–770, 1997.
- [4] R. Middlebrook, "Small-signal modeling of pulse-width modulated switched-mode power converters," Proceedings of the IEEE, vol. 76, no. 4, pp. 343–354, 1988.
- [5] W. Polivka, P. Chetty, and R. Middlebrook, "State-space average modelling of converters with parasitics and storage-time modulation," in Power Electronics Specialists Conference, 1980. PESC. IEEE. IEEE, 1980, pp. 119–143.
- [6] R. Erickson, "Dc-dc power converters department of electrical and computer engineering university of colorado boulder, co 80309-0425,"

Article in Wiley Encyclopedia of Electrical and Electronics Engineering, 1999.

- [7] E. Van Dijk, J. Spruijt, D. M. O'sullivan, and J. B. Klaassens, "Pwm switch modeling of dc-dc converters," IEEE Transactions on Power Electronics, vol. 10, no. 6, pp. 659–665, 1995.
- [8] A. Ayachit, A. Reatti, and M. K. Kazimierczuk, "Small-signal modeling of pwm dual-sepic dc-dc converter by circuit averaging technique," in Industrial Electronics Society, IECON 2016-42nd Annual Conference of the IEEE. IEEE, 2016, pp. 3606–3611.



**Usman Rahat** received his B.Sc degree in Electrical Engineering from University of Engineering and Technology (UET) Peshawar, Pakistan in 2015. Currently, he is enrolled in M.Sc Electrical Energy Systems Engineering at U.S Pakistan Center for Advanced Studies in Energy (US.PCAS-E) in University of Engineering and Technology (UET) Peshawar. He got his research training in Power Electronics at Arizona State University under the supervision of Dr. Bertan Bakkaloglu. His research interest lies in Power Electronics, Intelligent Systems and Artificial Intelligence.



**Abdul Basit** received his B.Sc degree in Electrical Engineering from University of Engineering and Technology (UET) Peshawar, Pakistan in 2006. He received his M.Sc degree in Electrical Power Engineering from Chalmers University of Technology, Sweden in 2011 and his PhD from the Department of Wind Energy of the Technical University of Denmark (DTU) in 2015. He is currently working as Assistant professor at U.S. Pakistan Center for Advanced Studies in Energy (US.PCAS-E) of the University of Engineering and Technology (UET) Peshawar. His research interests are on power system protection and operations, power factor improvement, renewable power integration and automatic generation control.



**Muhammad Salman** received his B.Sc degree in Electrical Engineering from University of Engineering and Technology (UET) Peshawar, Pakistan in 2016. Currently, he is enrolled in M.Sc Electrical Energy Systems Engineering at U.S Pakistan Center for Advanced Studies in Energy (US.PCAS-E) in University of Engineering and Technology (UET) Peshawar. He got his research training in Power Electronics at Arizona State University under the supervision of Dr. George Karaday. His research interest lies in Power Electronics and Power Converters.

# Heliostats Automation System for a Solar Power Tower Plant's Efficiency Increment

Haseeb Ur Rehman<sup>1</sup>, Muhammad Aurangzeb<sup>2</sup>, Waheed Ur Rehman<sup>3</sup>, Mishkat Ullah Jan<sup>4</sup>, Sheeraz Iqbal<sup>5</sup>

<sup>1,2,4,5</sup>North China Electric Power University, Beijing, China

<sup>3</sup>COMSATS Institute of Information Technology, Pakistan

haseeb@ncepu.edu.cn<sup>1</sup>, maurangzaib42@yahoo.com<sup>2</sup>, rehman@ciit.net.pk<sup>3</sup>, engrmishkat@ncepu.edu.cn<sup>4</sup>, engrsheeraz@ncepu.edu.cn<sup>5</sup>

Received: 15 July, Revised: 10 September, Accepted: 8 October

**Abstract**— In this paper a System for the automatic positioning of the heliostats of the Solar Power Tower plant is presented a cloud detection system and a sun position algorithm will compute the exact position of the Sun, and the clouds will be detected next to the sun in order to preserve the integrity of the power tower's system. The main purpose of this system is to achieve a maximum efficiency by changing the positions of the heliostat to away from the sun, when the clouds are about to cover the sun. In this way we can maintain the integrity of the system and to avoid damaging of the central receiver. The data that are used in the source code for the computation of the outputs from the given input parameters are also discussed. The system is successfully shock free and more efficient.

**Keywords**— Power tower plant, Sun position, Cloud detection, Central receiver, Heliostats

## I. INTRODUCTION

Solar energy is a renewable form of energy and only a onetime cost is required for the life time process of the system, The Power towers are the solar furnaces which are using a central tower to receive the focused sun light on the central receiver at the top of the tower. Molten salts are present in the tower which absorbs the solar heat and thus running the thermal generators to produce a clean and a good amount of power. The molten salts used in the power towers are good heat absorbers and have a high amount of heat capacity, it contain 40% of Potassium nitrate and 60% of Sodium nitrate. The power towers have a capability of generating electricity, even when the sun is not shining and the heliostats are not focusing the sun light on the central receiver, which is at the top of the tower.

We have mainly two issues under this discussion for the power towers, one is that, all the day the sun is not incident directly on the static heliostats and the other one is that, the central receiver has reached the temperature up to about 800 degree centigrade by the continuous focusing of sunlight by heliostats on the central receiver, so when suddenly a cloud covers the sun so the central receiver suffers a thermal stress and when this phenomenon occurs several times so the central receiver gets damage which is a huge loss [1].

We have to make the heliostats mobile so that it should trace the sun automatically all the day by knowing the exact positions of the sun and so that it should change its position away from the incident sunlight when the cloud is near to the sun so that to avoid the thermal shocks of the central receiver, this automatic system will increase the efficiency of the power towers dramatically.

This paper is organized as follows: Section 2 is dedicated to present an algorithm which will show us the exact position and location of the sun at any instance of time. Section 3 is there to present a method to get a super pixel segmented image of the cloud. Section 4 contains conclusions. Below is the positioning system diagram shown which clarify the main idea of our work. We have two inputs to the master control system, one is the result of the digital image processing which gives us the super pixel segmented image as a result and the other one is the sun position algorithmic result which gives us some outputs and those are also inputs to the master control system.that follow.

As shown in the positioning system diagram, first of all we have a method of super pixel segmentation which include some features extraction through digital image processing techniques from the original image of the scene, the image is captured with infrared camera and first image patching features are extracted, then RGB, then image threshold, then grayscale, then edges are detected, then after image segmentation we get the super pixel segmented image which is our output through digital image processing and that super pixel segmented image is given as an input to the master control system. The other inputs to the master control system are the sun position parameters which are showing us the exact position and location of the sun at any particular instant of time.

The outputs which the sun position algorithm will give us are following:

- Azimuth angle
- Zenith angle
- Sun rise time
- Sun set time

Incident angle  
 Julian day  
 Earth heliocentric longitude  
 Earth heliocentric latitude  
 Earth radius vector  
 Observer hour angle  
 Nutation longitude  
 Nutation obliquity  
 Ecliptic true obliquity

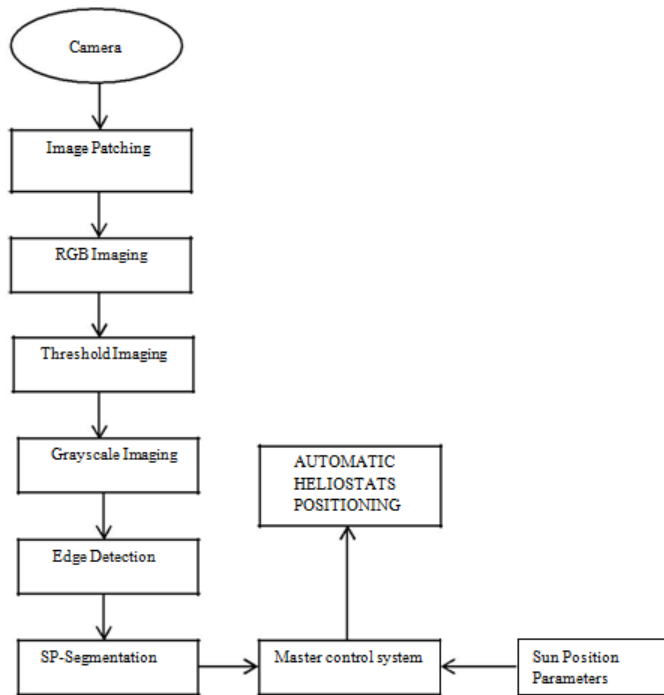


Figure 1. Positioning System Diagram

## II. A METHOD TO LOCATE THE SUN

Actually we are interested in solar tracking system for the solar power tower plant because sun is the basic source for feeding the power towers and thus for the solar generation systems, here we will find the exact location and position of the sun by an algorithm called sun position algorithm. For heliostats positioning toward the sun a solar tracking system is required which will definitely increase the efficiency of the system. The inputs to the master control are also sun position parameters (figure 1).

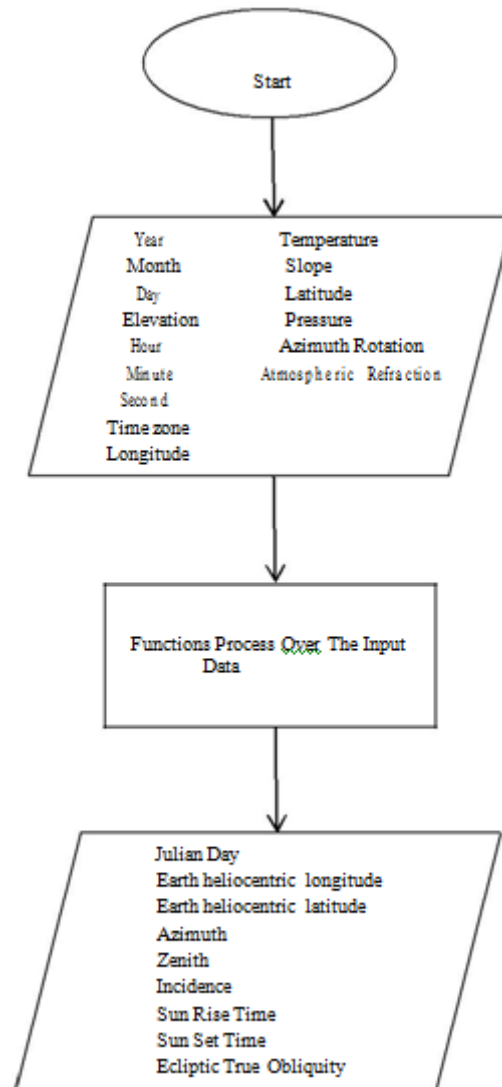


Figure 2. Algorithm Flow Chart

The inputs and outputs of the sun position algorithm are shown in the (figure 2).

The inputs are given to the C language code and functions process over it, and the output is computed which is the actual position of the sun. C language is used for algorithm because it is more nearer to the machine language and hardware interfacing is easy with a little bit modification [2,5].

Actually the C language code has been built in three parts, the header file with .h extension which contains the declaration of the data types of all the inputs and outputs. The second part is the main window which contains the inputs to be defined by the users and the outputs are shown. The source code part is the long part of the algorithm which contains use of functions, arrays, pointers, structures and enumerations. A function is a method or procedure which performs a task, the functions are called by pointers and parameters are passed through it. Array is a kind of data structure which stores elements of same data type[5]. Structure is a user defined data type which combines

data items of Different types under a single name. Pointer is used for addressing a memory location and every variable has an address on memory location, pointer is used with asterisk sign. Enumeration is a data type consisting of a set of data type which is used to make a program clearer to users [3]. In the source code we have included the data of earth periodic terms in arrays which is a fixed data and will be called by the help of pointers in any function where it is needed.

Following are the functions that are used in the source code for the computation of the outputs from the given input parameters:

Radian to degree  
Degree to radian  
Limit\_degrees  
Limit\_degrees 180  
Limit\_zero2one  
Limit\_minutes  
Day\_frac\_to\_local\_hr  
Third\_order\_polynomial  
Julian\_day  
Julain\_century  
Julian\_ephemeris\_day  
Julian\_ephemeris\_century  
Julian\_ephemeris\_millennium  
Earth\_periodic\_term\_summation  
Earth\_heliocentric\_longitude  
Earth\_heliocentric\_latitude  
Earth\_radius\_vector  
Geocentric\_longitude  
Geocentric\_latitude  
Mean\_elongation\_moon\_sun  
Mean\_anomaly\_sun  
Mean\_anomaly\_moon  
Argument\_latitude\_moon  
Ascending\_longitude\_moon  
Xy\_term\_summation  
Ecliptic\_mean\_obliquity  
Ecliptic\_true\_obliquity  
Aberration\_correction  
Apparent\_sun\_longitude  
Greenwich\_mean\_sidereal\_time  
Greenwich\_sidereal\_time

Geocentric\_right\_ascension  
Geocentric\_decination  
Observer\_hour\_angle  
Sun\_equatorial\_horizontal\_parallax  
Topocentric\_right\_ascension  
Topocentric\_local\_hour\_angle  
Topocentric\_elevation\_angle  
Atmospheric\_refraction\_correction  
Topocentric\_elevation\_angle\_correction  
Topocentric\_zenith\_angle  
Topocentric\_azimuth\_angle  
Surface\_incidence\_angle  
Sun\_mean\_longitude  
Approx\_sun\_transit\_time  
Sun\_hour\_angle\_at\_rise\_set  
Approx\_sun\_rise\_and\_set  
Rts\_sun\_altitude  
Rts\_alpha\_delta\_prime  
Sun\_rise\_and\_set

The method for code usage is described below:

```
#in calling the program, include the header file to the top of
the file by generating the line #include "spa.h"
#declare the SPA structure in calling program spa_data spa;
#the required input values are entered into the SPA structure
#then pass the SPA structure from the called SPA calculates
function
```

The output values will be computed and will return to the passed SPA structure, the output is based on function code selected from the enumeration. A non-zero return code from spa\_calculate () indicated that one of the input values did not pass simple bounds tests. The valid input ranges and return error codes are also listed in the header file of the algorithm.

TABLE I. RELATING INPUTS AND OUTPUTS

INPUTS							OUTPUTS						
Year	Month	Day	Time zone	Longitude	Latitude	Elevation	Zenith	Azimuth	Incidence	Sunrise	Sunset	Hour Angle	Julian Day
2001	1	7	+5.0	+106	50	1830.14	147.3	40.15	154.40	05:53:05	14:11:38	202.1	2551917.27
2005	8	7	+6.0	+106	50	1830.14	113.4	7.64	141.39	03:34:37	18:29:23	187.3	2453590.33
2010	2	3	-6.0	+90	40	1230.14	57.11	167.71	27.156	19:06:50	05:21:09	349.2	2455231.55
2015	2	3	-4.0	+80	40	1130.14	73.38	129.16	52.39	21:46:48	08:01:11	309.2	2455231.68
2020	2	3	-4.0	+80	70	1290.13	93.30	131.94	69.93	00:17:48	05:30:50	309.2	2458883.33
2025	4	5	+4.0	+70	70	1290.13	103.5	2.15	132.73	04:03:51	18:44:12	182.1	2460771.35
2030	4	5	+8.0	+70	70	1290.13	94.48	302.33	113.79	04:08:50	22:43:21	122.0	2462597.12
2030	4	5	+3.0	+70	50	1290.13	121.7	20.08	145.44	03:48:27	16:58:02	197.0	2462597.90

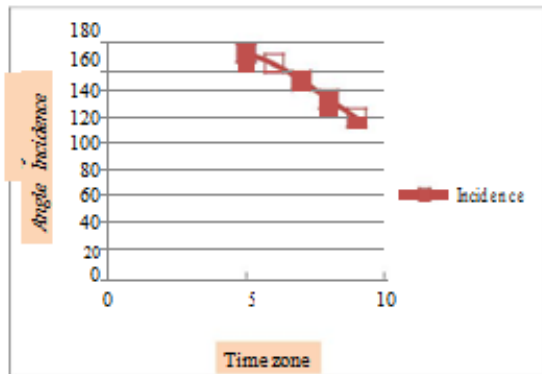


Figure 3. Time Zone vs. Angle of Incidence

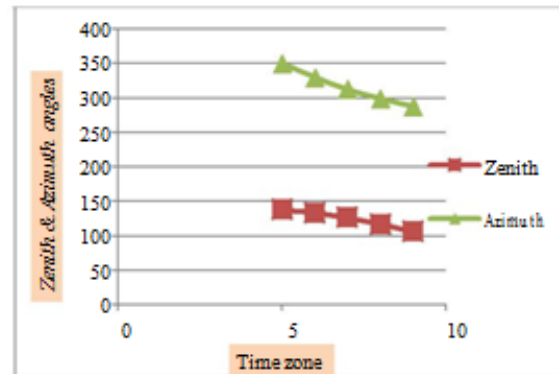


Figure 4. Time Zone vs. Zenith and Azimuth Angles

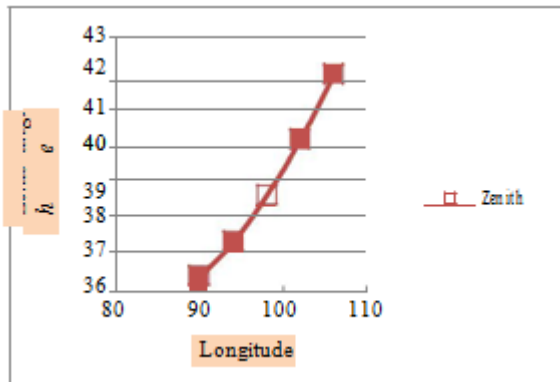


Figure 5. Longitude vs. Zenith Angle

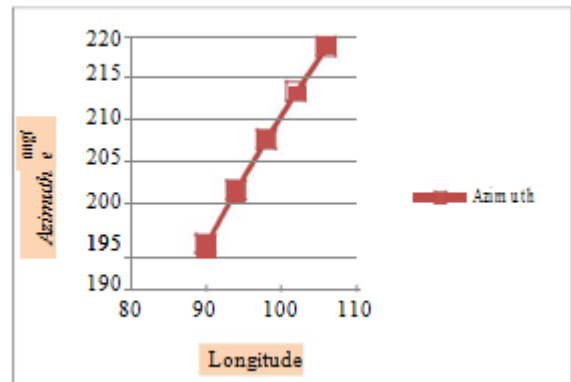


Figure 6. Longitude vs. Azimuth Angle



### III. A METHOD FOR CLOUD DETECTION

Actually a cloud detection system is required for the solar power tower plants because to avoid the damaging of the central receiver due to thermal shocks.

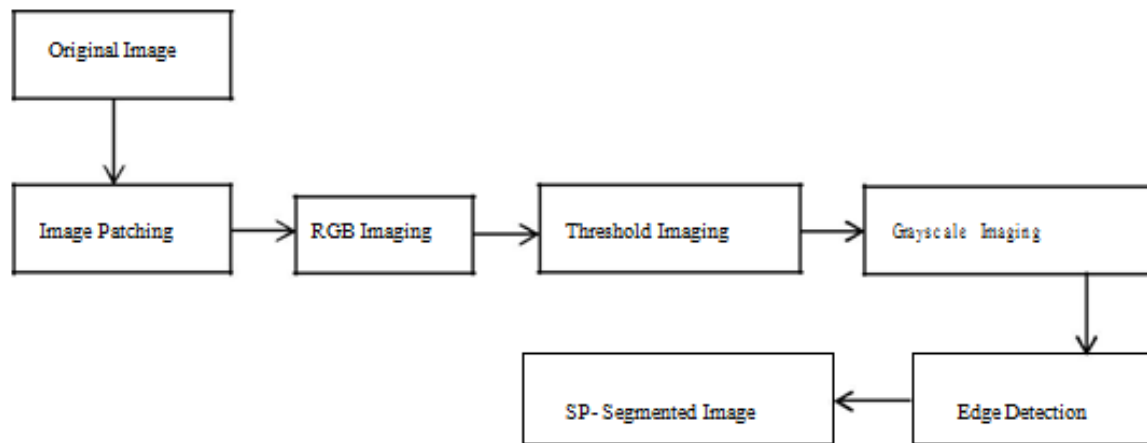


Figure 7. Cloud Dedection System

The clouds will be detected from the original image of the scene by super-pixel segmentation, which is a technique of digital image processing. In image patch ability is provided to select an arbitrary shaped region on the image and replace it with another surface fits to it. Artificial noise is added and unwanted defects are removed in patching. RGB has three channels and each channel can store discrete pixels with conventional brightness, it is used for brightness purpose. Thresholding provides an easy way to perform the segmentation on the basis of different intensities or colours in the background regions of an image.

In threshold each pixel is replaced with a black pixel if the intensity is less than a fixed constant  $T$ , and replaced with a white pixel if the intensity is greater than a fixed constant  $T$ , in threshold a pixel value may be either 0 or 1[5]. Grayscale images are the black & white sort of images and contain shades of gray color only, in this type the colour information is eliminated and only brightness of each pixel is left, the average of three colours is taken at each pixel value. Edge detection is important because edges are significant local changes of intensity in an image. Important features can be extracted from the edges of an image, like, corners, curves and lines. These features are used by higher level computer vision for recognition purposes; actually edge detection preserves the structure of an image [4]. In segmentation an image is partitioned into sets of pixels called Super-pixels, the goal of segmentation is to make the image more clear and easy to

analyse, actually sets of pixels are formed which cover the entire image clearly (figure 7).

### CONCUSLION

A method to locate the sun and to segment the clouds has been shown. The information provided here is basic to operate a solar power tower plant in an efficient manner, and these factors will let the master control system to position the heliostats for purpose of tracking the sun to achieve a good efficiency, and to change positions of heliostats away from the sun when the clouds are about to cover the sun, to maintain the integrity of the system and to avoid damaging of the central receiver.

### REFERENCES

- [1] M. Lopez- Martinez, F.R.Rubio. "Cloud Detection System for a Solar Power Tower Plant". 0-1803-7474-6/021917.00 IEEE (2002).
- [2] Gerro Prinsloo, Robert Dobson, "Solar Tracking Mechanisms and Platforms", in *Solar Tracking, 1<sup>st</sup> ed.* South Africa: Prins-loo, 2014, pp.33-64.
- [3] Brian W. Kernighan, Dennis M. Ritchie, "Control Flow, Pointers and Arrays, Structures, Input and Output", in *The C Programming language*, 2<sup>nd</sup> ed. New Jersey: Prentice Hall, 1988, pp. 55-166.
- [4] Ma, W.Y., Manjunath B.S. "Edge Flow: A Framework of Boundary Detection and Image Segmentation". (1997).
- [5] Grena, Roberto. "An algorithm for the computation of the solar position." *Solar Energy* 82.5 (2008): 462-470.

# Homer based Techno-Economic Comparison of Solar PV, Micro Hydro and Biomass Renewable Energy System with and without Battery Storage

Rizwan Kamal<sup>1</sup>, Muahmmad Younas<sup>2</sup>, Shakeel Ahmed<sup>3</sup>, Muhammad Salman<sup>4</sup>

<sup>1,2,3,4</sup>US Pakistan Center For Advanced Studies in Energy, University of Engineering and Technology, Peshawar  
rkizwan891@gmail.com<sup>1</sup>, aliyounas920@gmail.com<sup>2</sup>, shakeel.engr2014@gmail.com<sup>3</sup>,

12ktele0236@uetpeshawar.edu.pk<sup>4</sup>

Received: 02 October, Revised: 10 October, Accepted: 13 October

**Abstract**—Almost all developing countries are facing severe energy crisis, which is affecting their economy from several years. Most of remote areas have no access or limited access to grid, while grid extension is expensive and time consuming option. Generation from renewable sources at load center is a viable option, but huge investment and intermittency are the main constraints in implementing renewable base projects. By integrating different renewables can minimize cost and enhance reliability of distributed renewable systems. This paper mainly emphasizes on the optimization of hybrid renewable power systems having solar PV, biomass and micro-hydro with and without energy storage for a village in district Mardan, KP, Pakistan using Homer. Solar irradiance data is taken from National Aeronautics and Space Administration (NASA), hydro resource data from local irrigation department and biomass resource data from world bank biomass atlas. We have performed the techno-economic analysis of two different hybrid renewable power systems with unidirectional and bidirectional three phase converters. We have compared net present cost (NPC) and levelized cost of electricity (LCOE) of two models which justifies that system consist of PV, micro-hydro and biomass with battery storage is more economical and reliable.

**Keywords**— Solar PV, Micro Hydro, Biomass, Net Present Cost, Cost of Electricity, Homer

## I. INTRODUCTION

Electrical energy is basic need of modern life. Increase in population in developing countries causes high rise in energy demand which directly or indirectly affect both environment and GDP of countries. In Pakistan electrical energy demand is 85.9bn kWh which was 51.5bn kWh in 2000 while total generation from fossil fuels, hydro, nuclear and renewable resources are 61.8%, 31.8%, 3% and 5.7% respectively [1]. Population of Pakistan touches figure of 200 million in 2017 census report in which 51 million people has no access to electricity which includes 10% of urban areas and 37% of rural areas of country [2]. Using conventional sources for generation of power required imported fuels which would increase the

import prices as import and export are linked with GDP ultimately GDP will shrink while using renewable sources for power generation decreases imports and as a result GDP increases [5]. Global warming and depletion of fossil fuels are some other issues related to use of conventional sources. A healthy solution to tackle the problem of global warming and depletion of fossil fuel is use of renewable resources [6]. Geographically southern part of country is blessed with good wind speed and massive solar energy potential, center being an agriculture part of country has high potential of biomass and solar while northern areas are blessed with tremendous hydro potential. To overcome energy crisis and attract investors to invest in renewable energies different surveys and assessments are done. To assess the technical potential of renewable energies in Pakistan study was carried out in [3] which showed that estimated solar potential was 149GW, energy generation from wind has capacity 13 GW, potential from biomass was 5GW in 2010. Potential of 41.7GW power from hydro resources are available [4]. To electrify rural areas where there is no or limited access to grid, distributed generation using renewable sources is a suitable option if its inconsistent nature and high cost issues are overcome.

Numerous hybrid renewable systems are proposed by researchers to decrease cost of the system and overcome unpredictable nature of renewables using different modelling and optimization tools. Hybrid2, iHOGA, RETScreen, HOMER and sixteen other software tools are discussed in [7] in which Homer is selected as a user friendly and fast processing widely used software for pre-feasibility studies of hybrid renewable energy projects. A study for residential buildings in Saudi Arabia is done in [8] using Homer for modelling a wind-diesel hybrid system for 3512 MWh annual load demand and comparing its cost & carbon emissions with stand-alone diesel generating system. For electrification of remote areas in Ethiopia feasibility study of a hybrid system consist of PV, wind and fuel cell is carried out in [9] using Homer software and its results are compared with previously studied model's (PV, wind and genset) cost and carbon emissions. A control system is designed for PV and battery energy storage system using MATLAB to reduce peak load shaving of underwater tunnel in Canada and further simulated

in Homer to find the economic benefits of this control design

[10]. To electrify a remote village of Karnataka, India, a hybrid

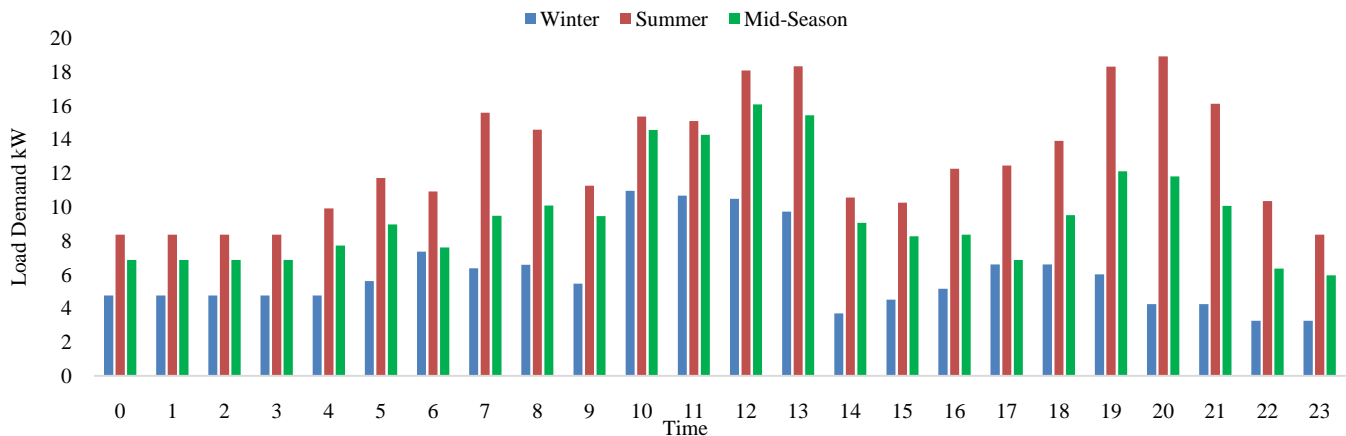


Figure 1. Seasonal Daily Load Profile

power system consists of solar, wind and diesel is simulated in [11] to find the impact of intermittent variables on renewable energy system and propose an optimum design to provide electrical energy at low cost. A hybrid energy system comprising of PV, wind, diesel and battery is simulated in [12] to find optimized models for electrification of commercial, public and residential buildings under diverse climatic environments of Iran. Six different cities of Turkey (Karaman, Kırklareli, Sinop, Konya, Gelibolu and Belen) were selected in [13] to find levelized cost of electricity of grid connected and stand-alone PV system, designed for 2500 kWh annual energy demand, which shows that grid connected PV system is more economical than stand-alone off grid system. A hybrid energy system consist of solar PV, battery and biodiesel was designed in [14] for newly established university in North of Ghana and its price was compared with grid prices using Homer, results in simulation showed that price per unit of electricity from hybrid system is 2% less than grid electricity prices. Socio-economic benefits and potential of hybrid PV, wind, diesel and battery system was designed in [15] for a community of peak demand=51.52kW and daily energy demand=242.56kWh, in northern region of Bangladesh using Homer. An optimized and economical design for electrification of residential community and agriculture farm of small village of district Layyah, Pakistan, using hybrid energy source biomass and PV was proposed in [16], Homer simulated results showed that the combination of 12kW convertor, 32 batteries, 8 kW biogas generator and 10 kW PV modules was optimized solution.

Literature review shows that Homer is recently widely used for modelling and optimization of hybrid renewable energy system. For pre-feasibility studies and economic analysis, it is preferred. Available renewable energy generators in Homer are hydro-turbines, solar PV, wind turbines, fuel cells and biomass generators. Energy storages available in Homer are batteries and hydrogen tanks while loads are primary and deferrable load (AC or DC). This tool is enough smart to recognize the appropriate timings of power supplied to the loads and when the generator should be functioned and when the batteries get charged.

## II. PROPOSED LOCATION

A small remote village of tehsil Dargai, Malakand agency of Khyber Pakhtunkhwa (KP) province is selected for this study. Geography of location is  $71.54^\circ$  east longitudes and  $34.27^\circ$  north latitudes. Locals are farmers by profession as land of this area is agriculture land and sources of irrigation are canals of river Swat. This area being in north of country is blessed with hydro, solar and biomass potential. Majority of rural areas of Pakistan are facing worst load shedding i.e. 18 to 22 hours because of gap between demand and supply, line losses and electricity theft issues. 37% of rural areas of country have no access to national grid. To electrify these areas distributed generations at load center is feasible solution.

## III. METHODOLOGY:

This section describes the procedure implemented throughout this study. An investigation was done to asses the load of diverse consumers of selected area by visiting locals. Resource potential of different renewable energy resources were collected from different sources. HOMER Pro software is used to do the techno-economic comparison of two different models.

### A. Load Assessment:

To model an electrical system for any area, it is recommended to find load demand of that area in first step. For this purpose, a survey was done and load demand of area was found by visiting twenty houses, a mosque and a primary school. Questions asked during survey were about water pumps, lights, fans, PCs and television etc. Questions about fans, water pumps and television usage timings were asked during load survey. One 6kW flour mill machine (industrial load) is also added in load profile which operates daily from 10:00 a.m to 02:00 p.m. Keeping in mind the climatic conditions of the selected area, load profile for three different seasons i.e. summer, mid-season and winter, were made as shown in Fig.1. In winters peak load demand is 11kW which occurs in noon time when industrial load is added to the system. In mid season there are two peaks one in noon time which is 16kW which includes industrial load, mosque and

residential and other peak of 11kW is noted in evening time which is purely residential load. In summer season there are three peaks, two are because of residential load demand, i.e. in morning (15.5kW) and in evening time (18.9kW) while one is in noon time (18.3kW) which includes 6kW industrial load.

### B. Solar Resource Assessment:

Southern and center part of country is blessed with enormous amount of solar potential as Pakistan is in a region with excellent solar insolation. To electrify southern and western deserts and northern hilly areas electrical power can be generated from this solar energy using off-grid and on-grid systems to tackle the crisis of energy in the country. According to NASA surface meteorology and solar energy database, monthly average clearness index is 0.633 and daily average global horizontal radiation is 5.31 kWh/m<sup>2</sup>/day for the proposed site as shown in Fig. 2.

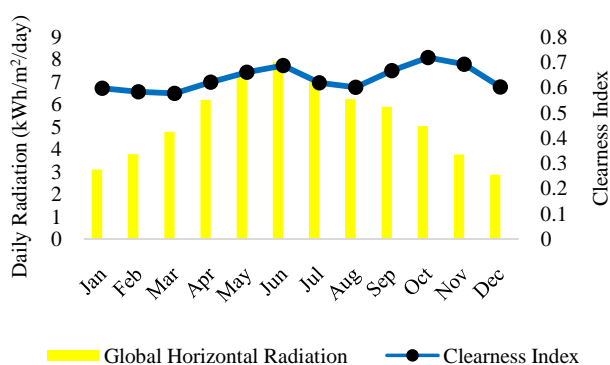


Figure 2. Solar Radiation & Clearness Index Data

The maximum solar radiation is 7.680 kWh/m<sup>2</sup>/day in month of June and minimum GHI is 2.880kWh/m<sup>2</sup>/day in month of December. From April to October GHI is higher than 5 kWh/m<sup>2</sup>/day.

### C. Hydro Resource Assessment:

There is massive hydro power potential present in northern part of Pakistan. To meet the growing energy demand, energy can be produced from these hydro resources which include large network of canals with small heads and high stream flow and natural waterfalls in hilly areas. Electric power generation from mini and micro hydro is one of the feasible and economical option for distributed generation. According to Alternate Energy Development Board (AEDB) 128 sites for small micro hydro on natural falls and flow are identified having potential of 0.2 to 32MW with total potential of 750MW only in KP. The average potential hydro at the planned site i.e. at Jalala Disty canal in Dargai, Malakand agency of KP measured is approximately 89 cusecs and available head is 1.2 m. figure shows flow rate of canal for 2013, 2014 and its average.

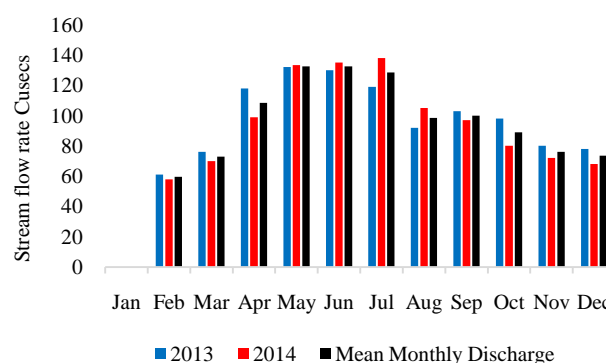


Figure 3. Average Monthly canal flow rate

In month of January every year irrigation department close canals for desilting purpose to improve canals condition and maintain depth of canal. From month of February to June and July canal flow increases when weather changes during winters flow again decreases.

### D. Biomass Resource Assessment:

Being an agricultural country Pakistan is blessed with high biomass fuel stock. Energy crisis can be overcome using latest technology to convert biomass in useful fuel for power generation. To fulfill energy demands of a society most of developing countries are showing interest to bio fuels to tackle problem of variation in fuel prices, energy security and global warming associated with conventional fossil fuels. This is a clean source of renewable energy that has positive impact on energy security, economy and environment. As compared to fossil fuels biomass carbon emission is very less. It can be characterized roughly as animal wastes (animal husbandry), crop residues (bagasse, husks, straw and leaves etc.) and domestic wastes (sewage, rubbish and food). Under Energy Sector Management Assistance Program (ESMAP), World bank and AEDB has developed biomass atlas for Pakistan [17]. As our selected site is located at the boarder of district Mardan and Malakand agency therefore biomass potential of both areas is shown in Fig. 4.

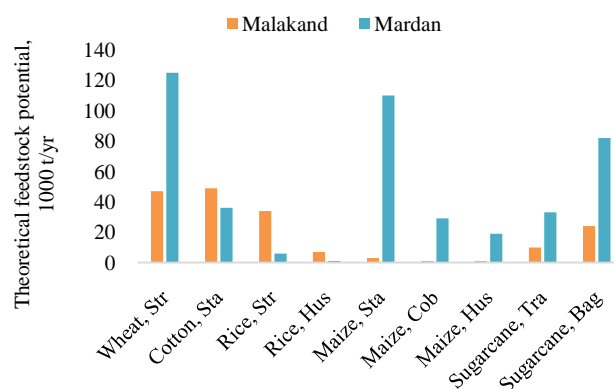


Figure 4. Available Biomass resources

### E. Systems Components and Configuration

Hybrid renewable energy systems are more efficient, stable and reliable which practices various resources to attain an economical system and boost the system lifetime. We configure two systems to compare the technical and economic effect of both systems. Solar PV is the first power generating unit in both systems, we put a derating factor of 80% which means that the generation from PV declines by 20% to take in considerations of soiling effect and temperature. The PV module capital cost is 102,500 PKR/kW and operating & maintenance cost is 6000 PKR/year.

Equation (1) is used by Homer to calculate PV array's output power at each time step.

$$P_{pv} = f_{pv} Y_{pv} \frac{G_T}{G_{T,STC}} [1 + \alpha_p (T_c - T_{STC})] \quad (1)$$

Where,

$Y_{pv}$  = under standard test conditions (STC) output power of PV array i.e. rated capacity (kW)

$f_{pv}$  = derating factor of PV module (%)

$G_T$  = incident solar radiation in current time step over PV array (kW/m<sup>2</sup>)

$G_{T,STC}$  = at STC, incident solar radiation (1kW/m<sup>2</sup>)

$\alpha_p$  = temperature coefficient of power (%/°C)

$T_c$  = in current time step PV cell temperature (°C)

$T_{C,STC}$  = under STC PV cell temperature (25°C)

Next important power source of our hybrid system is micro-hydro in which cross flow turbine and 3 phase synchronous generator with automatic voltage regulator (AVR) is used. As we cannot divert all water towards turbine due some restrictions and rules of irrigation department, turbine is design for 40 cusecs though minimum flow is 60 cusecs. Total initial capital cost of micro-hydro system is 1200,000 PKR and operating & maintenance cost is 80,000 PKR/year. 80% efficiency of complete micro-hydro system is considered.

Equation (2) is used by Homer to calculate output power of micro hydro in each time step

$$P_{hyd} = \frac{\eta_{hyd} \cdot \rho_{water} \cdot Q_{turbine} \cdot g \cdot h_{net}}{1000} \text{ (kW)} \quad (2)$$

Where,

$P_{hyd}$  = hydro turbine output power (kW)

$\eta_{hyd}$  = efficiency of hydro turbine (%)

$\rho_{water}$  = water density (1000 kg/m<sup>3</sup>)

$g$  = gravitational acceleration (9.81 m/s<sup>2</sup>)

$h_{net}$  = effective head (m)

$Q_{turbine}$  = flow rate of hydro turbine (m<sup>3</sup>/s)

3rd source in our hybrid system is biomass system, which consist of gasifier and three phase synchronous generator. Gasifier used in this system is downdraft gasifier while three phase generator has AVR and governor to maintain voltage and frequency stability. Initial capital cost of biomass system is 1.3m PKR, operating & maintenance cost is 80 PKR/hr and biomass fuel cost is 6500 PKR/ton. Biomass output power can

be find using steam flow rate, while steam flow rate depends on temperature and pressure [18] as shown in (3)

$$P = \frac{F}{5} * 1000 \text{ (kWh)} \quad (3)$$

$$F = 1.841 \left( \frac{C}{K} \right) t/h \quad (4)$$

$$K = \frac{0.00471a + 1.286}{0.0102b + 1.032} - (0.0097 - 0.0000132a) \quad (5)$$

Where,

P = output power of biomass system

F = actual steam flow rate of biomass gasifier

C = the output reading of transmitter flow

a = the temperature reading of transmitter output

b = the pressure reading of the transmitter output

4th component used in our systems is converter. As we have designed two different models, in first model we have used 10kW unidirectional converter (SolaX X-10) as shown in Fig. 5(a). Capital cost of this inverter is 380,000 PKR while operating & maintenance cost is 5000 PKR/year. In second model we have used three 4kW bidirectional converters (Schneider) as shown in Fig. 5(b). This converter is both grid following and grid forming battery dedicated converter whose capital cost is 180,000 PKR while operating & maintenance cost is considered as 2000 PKR per converter in second model.

Battery is another important component which we have used in second model to find its economic and technical impact on the system. In this model 12V, 214Ah deep cycle lead acid batteries (Power Sonic) are used whose capital cost is 43000 PKR/battery, replacement cost is 38000 PKR/battery while operating & maintenance cost is 500 PKR/battery/year. Important parameter of battery is state of charge (SoC) of battery which is shown in (6).

$$SoC = \frac{E_{batt}}{C_{batt} \cdot V_{batt}} \quad (6)$$

Where,

SoC = capacity of battery available for further discharging

$E_{batt}$  = Energy capacity of battery (Wh)

$C_{batt}$  = Capacity of battery (Ah)

$V_{batt}$  = rated voltage of a single battery

Other components of the system includes electronic load controller (ELC) which is used to keep the frequency of micro hydro stable, Synch-modules (Deep Sea) for synchronization purpose, energy analyzer (Janitza) to analyze demand and supply of the system, programmable logic control (PLC) unit to take decision about load dispatach and other protection equipments such as breakers and relays etc.



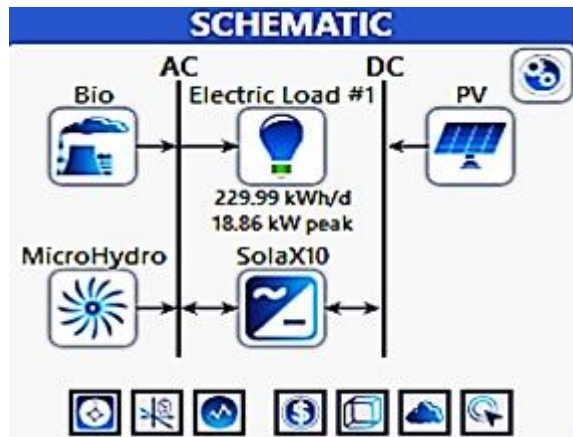
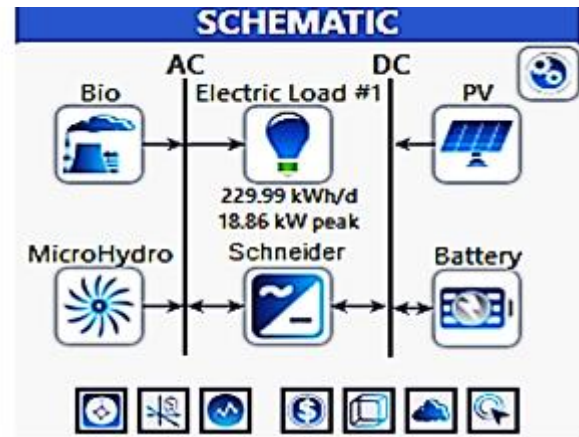


Figure 5. (a) Schematic of First Model



(b) Schematic of Second Model

#### F. Cost Functions

Homer uses different functions to calculate annualized cost, levelized cost of electricity and net present cost.

Equation (7), (8) and (9) shows cost and energy functions which is used to obtain an optimized hybrid renewable energy model.

$$NPC = \sum_{t=1}^T C_{O\&M} + C_C - C_{sal} + (C_{rep} * N) \quad (7)$$

Where

$C_C$  = initial capital cost invested at start of project  
 $C_{O\&M}$  = annual operating and maintenance cost of system  
 $C_{sal}$  = at end of project life salvage value of components  
 $C_{rep}$  = cost required for replacement of components in system  
 $N$  = number of replacements in project lifetime  
 $T$  = Life time of project in years

$$E_{sys} = ((P_{sys} - P_{loss}) * T_{sys}) \quad (8)$$

Where,

$E_{sys}$  = and energy used by the consumer (kWh)  
 $P_{sys}$  = total power generated by system (kW)  
 $P_{loss}$  = Power that is used by system itself or losses (kW)  
 $T_{sys}$  = the time for which system generates power throughout project life (h)

$$COE = \frac{((P_{sys} - P_{loss}) * T_{sys})}{NPC} \quad (8)$$

Where

$COE$  = cost of electricity (PKR/kWh)  
 $NPC$  = total net present cost of the system

To provide electrical energy at low cost to customers the NPC of the system should be reduced to minimize the COE.

#### IV. SIMULATIONS & RESULTS

We simulated two different models, first model is consist of solar PV, micro hydro and biomass with unidirectional

inverter, while in second model there is addition of battery bank and bi-directional converter is used.

##### A. First Model (Unidirectional Converter)

As discussed earlier our first hybrid system is consist of 10kW solar PV, 10.8kW micro hydro and 10kW biomass with unidirectional converter as shown in Fig. 5(a). Solar PV and micro hydro act as primary sources, when load demand rises then biomass start generating power and it continues its generation until load demand falls again to certain level that can be fulfill by solar PV and micro hydro. Monthly average electric production of our first model is shown in Fig. 6.

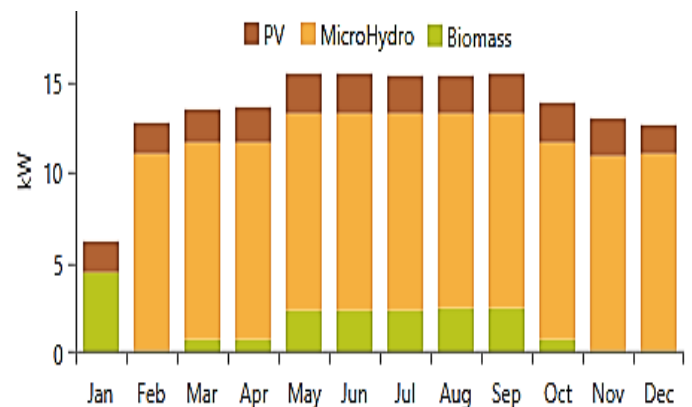


Figure 6. Monthly Average Electric Production

In the absence of micro hydro during month of January maximum power is produced by biomass system. In other three months of winter season, biomass is used for very small time during noon time when industrial load is connected to the system and PV generation is low. While in mid-season biomass operates in noon and evening time to meet peak load demand. While in summer peaks occur during morning noon and evening, in noon PV provide some support to fulfill load demand while in evening time when solar generation is zero biomass operates at its maximum. Micro hydro generation remains same for whole year (except January) because turbine is design for 40 cusecs which less than minimum flow of water in whole year. Daily mean output of solar PV is



47.8kWh and it operates for 4,385hrs/yr. Total share of PV in the system is 14.8%. Micro hydro operates for 8016 hrs/yr and produce 86,815kWh. The micro-hydro contribution is 73.5% of total electric power generation in the system. Biomass operates for 4,106hrs/yr and produce 13,924 kWh/yr which is 11.8% of total power.

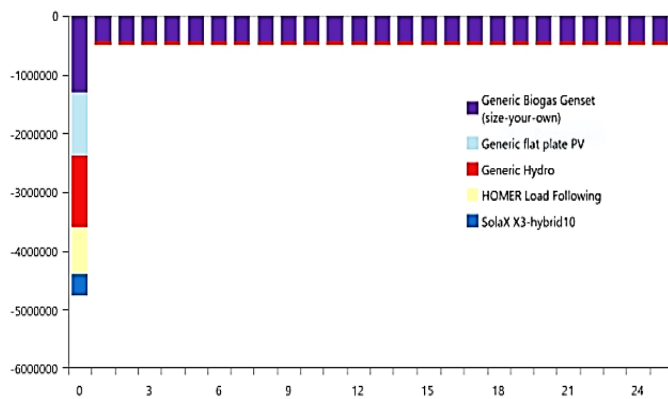


Figure 7. First Model Cash Flow by Components

Cash flow by component of the whole system through out the project lifetime is shown in Fig. 7. First long line shows the capital cost which is invested at the start of the project. Biomass fuel cost is 259,627 PKR/yr, initial capital cost 4.77m PKR while operating and maintenance cost of whole system is 520,867 PKR/yr. Net present cost of system is 11.5m PKR while cost of electricity is 10.6 PKR.

#### B. Second Model (Bidirectional Converter)

Schematic diagram of 2<sup>nd</sup> model which we simulated in Homer is shown in Fig. 5(b), which is consist of 10kW solar PV, 10.8kW micro hydro, 10kW biomass and 8 batteries with bi-directional converter. In this model solar PV and micro hydro act as primary source as discussed in first model but when load demand increase or generation from these two primary sources is not enough then system look at the battery SoC, if SoC of battery is higher than minimum, then battery start discharging and until it reaches its minimum SoC or load demand decreases enough that can be fulfill by primary sources. In other case, when SoC of battery is at its minimum and load demand is high which cannot be satisfy by primary sources then biomass start generation to balance demand and supply.

Monthly average electric production of all three sources is shown in Fig. 8. During month of January there is no micro-hydro that's why biomass operation is shown in month of January where biomass generate most of power to meet load demand. In peak months, i.e. summer season biomass generate electricity at its full capacity during evening time when PV cannot generate power. In morning and noon times (peak load) battery provide support and therefore no need to start biomass system. Micro-hydro generation remains constant throughout the year except January.

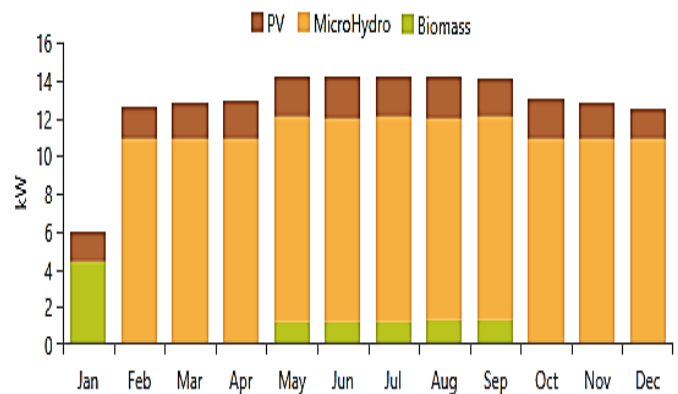


Figure 8. Monthly Average Electric Production

With injection of battery bank in this system biomass operation is reduced. Battery bank get charged mostly during night time when load demand is low and power generation from hydro is still high. Solar PV produces 17,447 kWh/yr and it operates for 4,385hrs/yr. Total share of PV in the system is 15.6%. Micro hydro operates for 8016 hrs/yr and produce 86,815kWh. The micro-hydro contribution is 77.6% of total electric power generation in the system. Biomass operates for 1,279 hrs/yr and produce 7,681 kWh/yr which is 6.86% of total power, while battery bank provides 1,724 kWh/yr. If we compare the biomass operating hours in second model it is reduced by more than 50%.

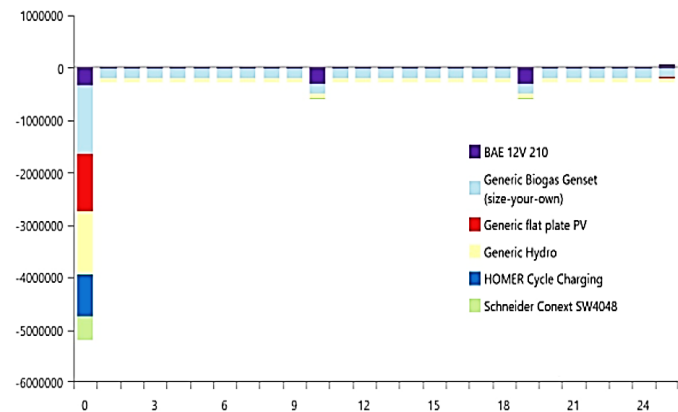


Figure 9. Second Model Cash Flow by Components

Cash flow by component of the of second models for whole project lifetime is shown in Fig. 9. First long bar at left side of image shows the initial investment which is invested at the time of commissioning. Biomass fuel cost is 135,209 PKR/yr, initial capital cost 5.19m PKR while operating and maintenance cost of whole system is 307,549 PKR/yr. Net present cost of system is 9.16m PKR while cost of electricity is 8.44 PKR. Batteries are replaced twice as shown while at the end of project salvage value of batteries is shown. Although initial capital cost is high in this case but operating & maintenance and biomass fuel cost is low, that's the reason of low cost of electricity.

TABLE I. SUMMARY OF BOTH MODEL OF HYBRID RENEWABLE ENERGY SYSTEMS

Model	Biomass				Initial Capital Cost	Annual O&M Cost	Net Present Cost	Cost of Electricity
	Annual Operating Hours	Annual kWh	Total Share	Annual Fuel Cost				
First	4,106	13,924	11.8%	259,627	4.77m	520,867	11.5m	10.60
Second	1,279	7,681	6.86%	135,209	5.19m	307,549	9.16m	8.44

Summary of both models are shown in Table 1. This is clearly shown that operation hours of biomass in first model is more than double as compared to second model. In second model biomass operation is reduced by introducing batteries to the system. Increase in biomass operation causes rise in annual fuel consumption for which extra money is required and ultimately annual fuel cost and operating and maintenance cost rises.

#### CONCLUSION

In this paper we have discussed two different models of solar PV, micro hydro and biomass with and without battery storage. In first model solar PV is connected to AC bus using unidirectional converter that converts DC power generated by solar PV to AC power and feed AC load demand. In second model solar PV and battery bank is connected to AC bus using bidirectional converter. Battery bank get charged from micro hydro during night time when power demand is less and production is more. initial capital cost of first model is less as compared to second model and there is no replacement cost in first model, while in second model initial capital cost is high but NPC and COE of this model is less than 1st model. Second model is more complex because of additional component (battery bank) and bidirectional converter, but if we analyse the system technically, battery bank increases system stability and reliability. In first system when load increases than generation of primary sources, immediate operation of biomass system is required in this scenario, if biomass system doesn't react in given time there will be mismatch in system's demand and supply, as a result system stability and reliability will be at risk. While in second model if load demand increases than primary source's generation, battery is there to provide support to the system. When SoC of battery approaches its minimum limit before touching its minimum SoC, system sends signal to biomass system to start generation, if biomass system takes some time battery is still there to provide because we apply minimum 50% of SoC. Another benefit of battery bank in system is that, when peaks occur in systems, these peak are oftenly for very short intervals, therefore no need of starting biomass system again and again because battery bank can fullfil this demand. Second model is designed in such away that, when demand is less than supply of primary sources then battery bank start charging from these primary sources and when demand increases than primary sources battery bank start discharging. In this manner biomass operation is reduced in second model, which reduces its operation & maintenance and fuel

consumption and ultimately we get electricity at low price as compared to first model.

#### ACKNOWLEDGMENT

We would like to acknowledge Assistant Professor Dr. Muhammad Shoaib Khalid for his valuable knowledge and experience which helped us in achieving this milestone. We are thankful to our fellow students, faculty and all the staff members of United States Pakistan Center for Advanced Studies in Energy at UET Peshawar for their support in this work. We are also thankful to USAID for providing us financial support in our MS studies.

#### REFERENCES

- [1] Energy Consumption in Pakistan. Worlddata.info, Available: <https://www.worlddata.info/asia/pakistan/energy-consumption.php>
- [2] World Energy Outlook 2017, International Energy Agency, Source: [https://www.iea.org/publications/freepublications/publication/WEO2017SpecialReport\\_EnergyAccessOutlook.pdf](https://www.iea.org/publications/freepublications/publication/WEO2017SpecialReport_EnergyAccessOutlook.pdf)
- [3] Farooq, M. K., & Kumar, S. "An assessment of renewable energy potential for electricity generation in Pakistan". *Renewable and Sustainable Energy Reviews* 2013, 20, 240-254.
- [4] Mirza, U. K., Ahmad, N., Majeed, T., & Harijan, K. "Hydropower use in Pakistan: past, present and future". *Renewable and Sustainable Energy Reviews* 2008, 12(6), 1641-1651.
- [5] Zeb, R., Salar, L., Awan, U., Zaman, K., & Shahbaz, M. "Causal links between renewable energy, environmental degradation and economic growth in selected SAARC countries: progress towards green economy". *Renewable Energy* 2014, 71, 123-132.
- [6] Sadorsky, P. "Renewable energy consumption, CO2 emissions and oil prices in the G7 countries". *Energy Economics* 2009, 31(3), 456-462.
- [7] Kaur, Daljeet, and P. S. Cheema. "Software tools for analyzing the hybrid renewable energy sources: -A review." In *Inventive Systems and Control (ICISC)*, International Conference on, pp. 1-4. IEEE, 2017.
- [8] Shaahid, S. M. "Techno-economics of off-grid hybrid wind-diesel power systems for electrification of residential buildings of Yanbu-a potential industrial location of Saudi Arabia". *International Journal of Global Warming* 2018, 16(1), 86-101.
- [9] Hailu Kebede, M., & Bekele Beyene, G. "Feasibility Study of PV-Wind-Fuel Cell Hybrid Power System for Electrification of a Rural Village in Ethiopia". *Journal of Electrical and Computer Engineering*, 2018.
- [10] Omer, M., Ibrahim, M., Pillay, P., & Athienitis, A. "Design and Control of a Peak Load Shaving System for the Louis-Hippolyte-La Fontaine Tunnel" In *IEEE Canadian Conference on Electrical & Computer Engineering (CCECE)* 2018, May (pp. 1-4). IEEE.
- [11] Vendoti, S., Muralidhar, M., & Kiranmayi, R. "HOMER Based Optimization of Solar-Wind-Diesel Hybrid System for Electrification in a Rural Village". In *International Conference on Computer Communication and Informatics (ICCCI)* 2018, January (pp. 1-6). IEEE.
- [12] Farahi, S., & Fazelpour, F. "Techno - economic assessment of employing hybrid power system for residential, public, and commercial buildings in different climatic conditions of Iran". *Environmental Progress & Sustainable Energy* 2018.

- [13] Sekuçoğlu, S. A., & Bali, T. "Design and Economic Analysis of Photovoltaic Systems in Different Cities of Turkey". In Exergy for A Better Environment and Improved Sustainability 2, 2018 (pp. 1101-1109). Springer, Cham.
- [14] Bhandari, R., Gerstner, J., Belhassan, H., Gtz, D., & Hausmann, H. "Autonomous Electricity Supply with Hybrid Renewable Configuration in Ghana". In 7th International Energy and Sustainability Conference (IESC) 2018, May (pp. 1-8). IEEE.
- [15] Mandal, S., Das, B. K., & Hoque, N. "Optimum sizing of a stand-alone hybrid energy system for rural electrification in Bangladesh". Journal of Cleaner Production 2018, 200, 12-27.
- [16] Shahzad, M. K., Zahid, A., ur Rashid, T., Rehan, M. A., Ali, M., & Ahmad, M. "Techno-economic feasibility analysis of a solar-biomass off grid system for the electrification of remote rural areas in Pakistan using HOMER software". Renewable energy 2017, 106, 264-273.
- [17] World Bank Group, Pakistan Biomass GIS Atlas 2016, Available: <https://energydata.info/dataset/pakistan-biomass-gis-atlas>.
- [18] Barsoum, Nader, et al. "Modeling and cost simulation of stand-alone solar and biomass energy." Modeling & Simulation, 2008. AICMS 08. Second Asia International Conference on. IEEE, 2008.



**Rizwan Kamal** has received B.Sc Electrical Engineering degree from department of Electrical Engineering University of Engineering and Technology Peshawar, Pakistan in 2014. He is currently pursuing M.Sc degree in Electrical Energy Systems Engineering from United States Pakistan Center for Advanced Studies in Energy (USPCAS-E) at University of Engineering and Technology Peshawar. He worked on first hybrid renewable energy system of Pakistan which is consist of solar PV, Micro-hydro and Biomass resources installed at Sakhakot, Malakand division KP, Pakistan.



**Muhammad Younas** has received BS degree in Electrical Power Engineering from University of Engineering & Technology Peshawar KP, Pakistan in 2014. Currently pursuing MS degree in Electrical Energy System Engineering from US Pakistan Center for Advanced Studies in Energy, University of Engineering & Technology Peshawar. He has availed exchange program to the partner university of USPCAS-E Arizona State University (ASU), USA in august 2017 as a research scholar. Currently he is working on the first Hybrid Renewable Power System to be deployed at remote site in Malakand division KP, Pakistan.



**Shakeel Ahmed** has received BS degree in Electrical Engineering from University of Engineering & Technology Peshawar KP, Pakistan in 2014. Currently pursuing MS degree in Electrical Energy System Engineering from US Pakistan Center for Advanced Studies in Energy(USPCAS-E), University of Engineering & Technology Peshawar. He has availed exchange program to the partner university of USPCAS-E Arizona State University (ASU), USA in January 2016, as a research scholar. He has good hands on experience in the field of renewable energies especially PV reliability.



**Muhammad Salman** has received BS degree in Electrical Engineering from University of Engineering & Technology Peshawar KP, Pakistan in 2016. He is currently pursuing MS degree in Electrical Energy System Engineering from US Pakistan Center for Advanced Studies in Energy, University of Engineering and Technology Peshawar. He has visited Arizona State University (ASU), USA in exchange program in August 2017 as a research scholar. Currently he is working on multi level inverters.

# Formation Control of Unmanned Vehicles via Extended Feedback Consensus

Irshad Hussain<sup>1\*</sup>, Amir<sup>2</sup>, Waleed Shahjehan<sup>3</sup>, M. Riaz<sup>4</sup>, M. Suleman<sup>5</sup>

<sup>1,2,3,4,5</sup>Department of Electrical Engineering, UET Peshawar, Pakistan

irshad.hussain@uetpeshawar.edu.pk<sup>1\*</sup>, amir@nwfpuet.edu.pk<sup>2</sup>, waleedshahjehan@gmail.com<sup>3</sup>,

m.riaz@uetpeshawar.edu.pk<sup>4</sup>, suleman@gmail.com<sup>5</sup>

Received: 20 June, Revised: 12 October, Accepted: 15 October

**Abstract**—This paper has considered the problem of formation control of multiple quadrotor using a diversified feedback linearization technique. Taking the advantage of double integrator which normally can achieve any unrestrained shape, we have devised a linearization technique that is made possible using extended feedback. The technique has the ability of transmuting the dynamics of a quadrotor's reference point to four double integrators in accordance with yaw angle and position of quadrotor in the space. The traditional exact feedback technique require a jerk (which is the derivative of acceleration) but it is not an issue for the extended feedback method. Ending by the conclusion the section numerical example elucidate formation control of quadrotor by using reference point and center of masses of the quadrotors.

**Keywords**—Cooperative control, Consensus, Formation, Extended Feedback, Multi-agents

## I. INTRODUCTION

Due to large number of researcher attraction to the field of Cooperative or distributed control of multiagent system, the importance of Formation control reached to an undeniable level [1] [2]. And this became possible due to consensus in the formation of multiagent system, which mean that the agents has to coincide on a state or issue. For the formation of arbitrary shaped structure Consensus algorithms are very applicable. Like in homogenous linear systems the agent get-into a formation via the relative distances among multiple agents [3]. However for heterogeneous systems, it could be achieved by using the position of each and every (individual) agent [4].

The linearization over exact feedback [5] technique can be employed to all agents where they have non-linear dynamics like mobile robots on ground and by using this technique the dynamics are linearized to into integrators. In fact the exact feedback linearization could possibly be executed over a quadrotor [6] which leads to such dynamics whose integrators are quadruple. Some time it is very difficult to handle a system, possessing large number of integrators as employability of integrators leads to decrease in gain margin and aggravate the lag (in phase). Additionally jerk is a necessary element of

quadruple integrators whereas the derivative of acceleration is jerk. In general there is no direct method for determining the jerk also it couldn't be computed properly from the estimated value of sensor. Because of these issues we have devised a linearized extended feedback technique which is employed for controlling the formation a network of positive systems. In this technique we have to consider a predetermined point of reference for all quadrotors across which the linearization of model is done. And as a result double integrated model is achieved where no jerk is required. Possibly this linearization technique could be applied to any other formation control framework.

An attempt for controlling the formation of quadrotors via consensus has been done here in this paper. The formation is achieved by using our extended feedback linearization technique. Double integrators are achieved from the natural dynamics of quadrotors by using our diversified technique [7] i.e. extended feedback linearization. As it can be seen in the numerical examples, that the quadrotors' center of mass and reference points achieved a proper shape called formation in the given space.

**Notation:**  $I_n$  represent  $n \times n$  unit matrices while  $\otimes$  signify the Kronecker product's operator.

## II. THE ISSUE OF CONSENSUS

The issue of consensus [3] is considered in this section, as we are going to address formation control of double integrators as agents.

### A. Double Integrator Model

Let assume an agent or vehicle is given by:

$$\begin{bmatrix} \dot{z}_{i,j} \\ \ddot{z}_{i,j} \end{bmatrix} = A_{veh} \begin{bmatrix} z_{i,j} \\ \dot{z}_{i,j} \end{bmatrix} + B_{veh} v_{i,j}, \quad (1)$$

Where,  $\begin{bmatrix} z_{i,j} & \dot{z}_{i,j} \end{bmatrix}^T \in \mathbb{R}^2$  is the state,  $v_{i,j} \in \mathbb{R}$ , is the input

$$A_{veh} = \begin{bmatrix} 0 & 1 \\ 0 & 0 \end{bmatrix}, \quad B_{veh} = \begin{bmatrix} 0 \\ 1 \end{bmatrix}$$

for  $i \in \{1, \dots, N\}$ . The dynamics of all agents are same and the entire system of  $N$  agents could be given for every single agent as given in Eq. (2).

$$\dot{z}_j = A_j z_j + B_j v_j \quad (2)$$

Where  $z_j = [z_{1,j}, z_{1,j}, \dots, z_{n,j}, \dot{z}_{n,j}]^T$  is the state

### B. Designing the Controller

We have taken into account, the controller for the whole system given by (2) has the following controller

$$v_j = F_j L(z_j - r_j) \quad (3)$$

While  $r_j \in \mathbb{R}^{2N}$  is the desired shape of formation which could be given by  $r_j = [r_{1,j}, 0, \dots, r_{N,j}, 0]^T$ . It is obvious from the  $r_j$  matrix that the shape will not be changed as there are Zeroes in the  $r_j$  matrix.  $L = L_G \otimes I_2$  where  $L_G \in \mathbb{R}^N$  represents a network topology of multiple robots that is generally called Graph Laplacian.  $F_j = I_N \otimes F_{veh}$  is perpetual gain where  $F_{veh} = [f_{1j} \ f_{2j}]$ . As a result we acquire a closed loop system using (2) and (3) such as

$$\dot{z} = A_j z_j + B_j F_j L \otimes I_2 (z_j - r_j). \quad (4)$$

The system defined by (2) and  $L_G$  provides base for the Lemma 2.1 given below.

**Lemma 2.1:** [3] The formation  $r_j, z_j \rightarrow r_j$  is achieved by the entire system (2) iff  $L_G$  has a zero eigenvalue having algebraic multiplicity 1 and

$$A_{veh} + \lambda B_{veh} F_{veh} \quad (5)$$

is Hurwitz where each nonzero eigenvalue of  $L$  (that are referred by  $\lambda$ ) and has the value as  $\alpha_j + \beta_j \sqrt{-1}$ .

As the Eq. (5) is Hurwitz, hence the conditions (for achieving the formation) of  $F_i$  could be stated as (below):

$$\begin{aligned} f_{1,j} &< 0, \quad f_{2,j} < 0 \\ \frac{f_{2,j}^2}{f_{1,j}} &< -\frac{\beta_j^2}{\alpha_j(\alpha_j^2 + \beta_j^2)}. \end{aligned}$$

### III. LINEARIZING THE FEEDBACK OF QUADROTOR

Quadrotor dynamics could be given by the following set of equation as in (6)

$$\begin{aligned} \begin{bmatrix} \ddot{x}_i^o \\ \ddot{y}_i^o \\ \ddot{z}_i^o \end{bmatrix} &= \frac{1}{m} R(\psi_i, \theta_i, \phi_i) \begin{bmatrix} 0 \\ 0 \\ U_{i,1} \end{bmatrix} - \begin{bmatrix} 0 \\ 0 \\ g \end{bmatrix}, \\ \dot{\phi}_i &= \dot{\theta}_i \dot{\psi}_i \frac{I_y - I_z}{I_x} - \frac{I_r}{I_x} \dot{\theta}_i \Omega_i + \frac{d}{I_x} U_{i,2}, \\ \dot{\theta}_i &= \dot{\phi}_i \dot{\psi}_i \frac{I_z - I_x}{I_y} - \frac{I_r}{I_y} \dot{\phi}_i \Omega_i + \frac{d}{I_y} U_{i,3}, \\ \dot{\psi}_i &= \dot{\theta}_i \dot{\phi}_i \frac{I_x - I_y}{I_z} + \frac{1}{I_z} U_{i,4} \end{aligned} \quad (6)$$

Where,  $(x_o^i, y_o^i, z_o^i) \in X \times Y \times Z$  is mass center position, while Euler angle is given by  $(\psi_i, \theta_i, \phi_i)$ , i.e. (yaw, pitch, roll). The mass is represented by  $m$ , distance between motor and

mass center is referred by  $d$ , inertia of rotor is  $I_r$ , while the inertia for each axis of whole quadrotor is  $(I_x, I_y, I_z)$ , and finally the rotation of matrix is referred by  $R(\psi_i, \theta_i, \phi_i)$ . The control input for a quadrotor is  $U_i = [U_{i,1}, U_{i,2}, U_{i,3}, U_{i,4}]^T \in \mathbb{R}^4$  where  $U_{i,1}$  is the thrust of rotor and  $U_{i,2}, U_{i,3}$  and  $U_{i,4}$  are the torques in the respective direction given by X, Y, and Z axis. However  $\omega_{i,1}, \omega_{i,2}, \omega_{i,3}$  and  $\omega_{i,4}$  corresponds to the angular velocity of corresponding rotors as is obvious from the following equation.

$$\Omega = -\omega_{i,1} + \omega_{i,2} - \omega_{i,3} + \omega_{i,4}$$

### A. Extended Feedback Linearization

This subsection presents an extended feedback linearization technique [7] for quadrotors. We have introduced a reference point  $(x_i, y_i, z_i) \in \mathbb{R} \times \mathbb{R} \times \mathbb{R}$  which is at a fixed distance  $h$  from the center of mass of quadrotor as given by Fig. 1. By choosing the reference above center of mass will lead to the following equation. i.e. Eq. (7).

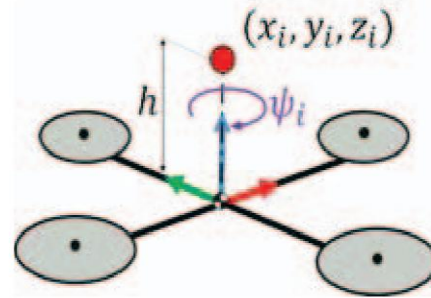


Fig. 1. The reference point above quadrotor

$$\begin{bmatrix} x_i \\ y_i \\ z_i \end{bmatrix} = \begin{bmatrix} x_i^o \\ y_i^o \\ z_i^o \end{bmatrix} + R(\psi_i, \theta_i, \phi_i) \begin{bmatrix} 0 \\ 0 \\ h \end{bmatrix}. \quad (7)$$

By taking the second order derivative of Eq. (7) with respect to time and after substituting the result into Eq. (6) we get Eq. (8) as below.

$$\begin{bmatrix} \ddot{x}_i \\ \ddot{y}_i \\ \ddot{z}_i \\ \ddot{\psi}_i \end{bmatrix} = F(\psi_i, \dot{\psi}_i, \theta_i, \dot{\theta}_i, \phi_i, \dot{\phi}_i) + G(\psi_i, \theta_i, \phi_i) U_i \quad (8)$$

where  $F: \mathbb{R} \times \mathbb{R} \times \mathbb{R} \times \mathbb{R} \times \mathbb{R} \times \mathbb{R} \rightarrow \mathbb{R}^{4 \times 1}$  and  $G: \mathbb{R} \times \mathbb{R} \times \mathbb{R} \rightarrow \mathbb{R}^{4 \times 4}$  are nonlinear complicated matrices. Afterwards a linearization feedback law has been presented such as

$$U_i = G^{-1}(\psi_i, \theta_i, \phi_i) \left( -F(\psi_i, \dot{\psi}_i, \theta_i, \dot{\theta}_i, \phi_i, \dot{\phi}_i) + v_i \right) + q_i \quad (9)$$

$$\forall (\psi_i, \dot{\psi}_i, \theta_i, \dot{\theta}_i, \phi_i, \dot{\phi}_i) \in \mathbb{R} \times \mathbb{R} \times \mathbb{R} \times \mathbb{R} \times \mathbb{R} \times \mathbb{R}$$

where  $v_i = [v_{ix}, v_{iy}, v_{iz}, v_{i\psi}]^T \in \mathbb{R}^4$  and  $q_i = [q_{i1}, q_{i2}, q_{i3}, q_{i4}]^T \in \mathbb{R}^4$



$$q_{i,1} = q_{i,4} = 0, q_{i,2} = k_{\phi_i} \left( \frac{I_x}{d} \right) \dot{\phi}_i, q_{i,3} = k_{\theta_i} \left( \frac{I_y}{d} \right) \dot{\theta}_i$$

Note that  $k_{\phi_i}$  and  $k_{\theta_i}$  are unvaried gains with negative values. The dynamics of quadrotor's reference point (8) are transformed to double integrators by employing feedback law (9), which results in a linearized dynamics for every individual reference point as given by Eq. (10)

$$\ddot{z}_{i,j} = v_{i,j}, \quad j \in \{x, y, z, \psi\}. \quad (10)$$

#### B. Linearization of Exact Feedback

This subsection presents the linearization method [5] of exact feedback scenario which is traditionally being used for quadrotors. As the work [5] generated fully independent result from the results given by [6], then by using Eq. (6), we have an expression of the dynamics of the quadrotor with respect to  $(x_i^0, y_i^0, z_i^0, \psi_i^0)$  that could be given as

$$\begin{bmatrix} \ddot{x}_i^o \\ \ddot{y}_i^o \\ \ddot{z}_i^o \\ \ddot{\psi}_i \end{bmatrix} = A_{i,q,1}(\psi_i, \dot{\psi}_i, \theta_i, \dot{\theta}_i, \phi_i) \begin{bmatrix} U_{i,1} \\ U_{i,2} \\ U_{i,3} \\ U_{i,4} \end{bmatrix} - \begin{bmatrix} 0 \\ 0 \\ \frac{g}{m} \\ 0 \end{bmatrix} \quad (11)$$

where  $A_{i,q,1} \in \mathbb{R} \times \mathbb{R} \times \mathbb{R} \times \mathbb{R} \times \mathbb{R} \rightarrow \mathbb{R}^{4 \times 4}$  is a nonlinear matrix. Taking second order derivative of Eq. (11) while excluding the dynamics of  $\psi_i$  term with respect to time and again considering Eq. (6) we get Eq. (12) as

$$\begin{bmatrix} \ddot{x}_i^o \\ \ddot{y}_i^o \\ \ddot{z}_i^o \\ \ddot{\psi}_i \end{bmatrix} = A_{i,q,2}(U_{i,1}, \dot{U}_{i,1}, \psi_i, \dot{\psi}_i, \theta_i, \dot{\theta}_i, \phi_i, \dot{\phi}_i) \begin{bmatrix} \ddot{U}_{i,1} \\ \ddot{U}_{i,2} \\ \ddot{U}_{i,3} \\ \ddot{U}_{i,4} \end{bmatrix} + F_{i,q}(U_{i,1}, \dot{U}_{i,1}, \psi_i, \dot{\psi}_i, \theta_i, \dot{\theta}_i, \phi_i, \dot{\phi}_i) \quad (12)$$

Where  $A_{i,q,2} \in \mathbb{R} \times \mathbb{R} \times \mathbb{R} \times \mathbb{R} \times \mathbb{R} \times \mathbb{R} \times \mathbb{R} \times \mathbb{R} \rightarrow \mathbb{R}^{4 \times 4}$  and  $F_{i,q} \in \mathbb{R} \times \mathbb{R} \times \mathbb{R} \times \mathbb{R} \times \mathbb{R} \times \mathbb{R} \times \mathbb{R} \times \mathbb{R} \rightarrow \mathbb{R}^{4 \times 1}$  are non-linear complex matrices. Then by commencing a feedback linearization law we have

$$\begin{bmatrix} \ddot{U}_{i,1} \\ \ddot{U}_{i,2} \\ \ddot{U}_{i,3} \\ \ddot{U}_{i,4} \end{bmatrix} = A_{i,q,2}^{-1} (u_i - F_{i,q}) \quad (13)$$

Where  $u_i = [u_{i,x}, u_{i,y}, u_{i,z}, u_{i,\psi}]^T \in \mathbb{R}^4$  is actually the input for  $(x^0, y^0, z^0, \psi)$  while  $A_{i,q,2}$  is nonsingular except  $U_{i,1} = 0$ . And in this manner we acquire dynamics of quadrotor in a linearized form as given by

$$\ddot{z}_{i,j} = v_{i,j}, \quad j \in \{x, y, z, \psi\}.$$

#### IV. NUMERICAL EXAMPLE

The quadrotor has several physical parameters that are enlisted in TABLE I. For the sake of convenience we considered 8 quadrotor i.e.  $N=8$ , whereas the distance  $h$  is taken as  $0.1$  [m]. For the same calculation the values of gain

are  $f_{1,j} = -0.1$ ,  $f_{2,j} = -1$  and  $k_{\theta} = k_{\phi} = -10$ . And the graph Laplacian is

$$L_G = \begin{bmatrix} 2 & -1 & 0 & 0 & 0 & 0 & 0 & -1 \\ -1 & 2 & -1 & 0 & 0 & 0 & 0 & 0 \\ 0 & -1 & 2 & -1 & 0 & 0 & 0 & 0 \\ 0 & 0 & -1 & 2 & 0 & 0 & 0 & 0 \\ 0 & 0 & 0 & -1 & 2 & -1 & 0 & 0 \\ 0 & 0 & 0 & 0 & -1 & 2 & -1 & 0 \\ 0 & 0 & 0 & 0 & 0 & -1 & 2 & -1 \\ -1 & 0 & 0 & 0 & 0 & 0 & -1 & 2 \end{bmatrix}$$

and the topology of multiple quadrotor network is shown in Fig. 2 in the form of undirected graph. Quadrotor is denoted by every circle bearing a number while edge signify the communication between the quadrotors. Lemma 2.1 satisfies the given gains and  $L_G$ . However the desired shape is a  $2 \times 2 \times 2$  cube such as

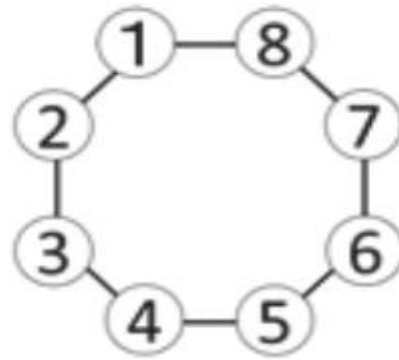


Fig. 2. Quadrotors' Communication Network

$$\begin{aligned} r_x &= [3, 0, 3, 0, 1, 0, 1, 0, 3, 0, 3, 0, 1, 0, 1, 0]^T, \\ r_y &= [1, 0, 3, 0, 3, 0, 1, 0, 1, 0, 3, 0, 3, 0, 1, 0]^T, \\ r_z &= [1, 0, 1, 0, 1, 0, 1, 0, 3, 0, 3, 0, 3, 0, 3, 0]^T, \\ r_p &= [0, 0, 0, 0, 0, 0, 0, 0, 0, 0, 0, 0, 0, 0, 0, 0]^T. \end{aligned}$$

The incipient position are  $x(0) = [0.5, 3, 1, 2, 3, 3.5, 2, 1]^T$ ,  $y(0) = [3, 2, 1, 3, 2, 3.8, 1, 0.2]^T$ ,  $z(0) = [3, 2, 1, 3, 1, 2, 3.5, 0.5]^T$  and  $\psi(0) = [0, \frac{\pi}{2}, 0, \pi, 0, \pi, 0, \frac{\pi}{2}]^T$ . The starting values of Euler's angles can be given as  $\theta(0) = \phi(0) = [0, 0, 0, 0, 0, 0, 0, 0]^T$ , while the initial linear velocities and initial angular velocities are taken zero.

Using the above mentioned parameters and their values we simulated formation control starting from  $t=0$ s till  $t=120$ s using the extended feedback linearization as obvious from Figs. 3-5 and Fig. 6 shows the time responses of mass centers plus yaw angles. After applying the extended feedback linearization



techniques it can be shown that both reference point as well as yaw angles have achieved the formation. In the same way 3D shots of center of masses are shown in Fig. 7-9 and the respective time response are revealed in Fig. 10 from which we can deduce that the formation is achieved by yaw angles and center of masses as well.

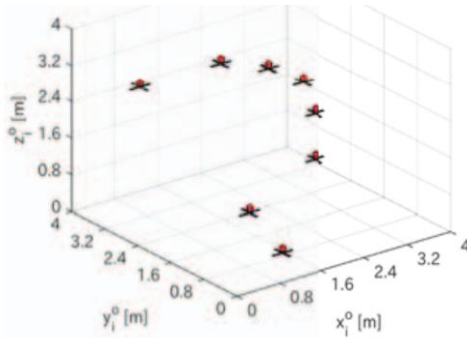


Fig. 3. 3D shot of quadrotors at  $t = 0$  [s] (Extended linearization)

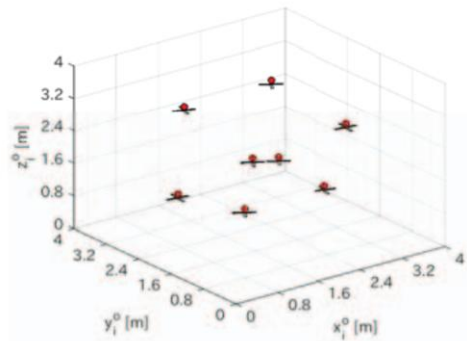


Fig. 4. 3D shot of quadrotors at  $t = 20$  [s] (Extended linearization)

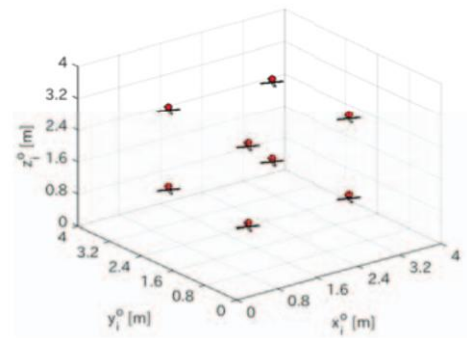


Fig. 5. 3D shot of quadrotors at  $t = 120$  [s] (Extended linearization)

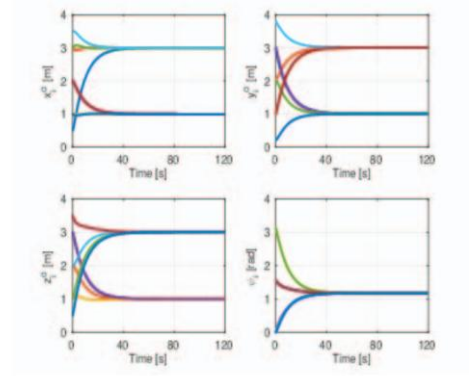


Fig. 6. Time response of positions and yaw angles of each quadrotor (Extended linearization)

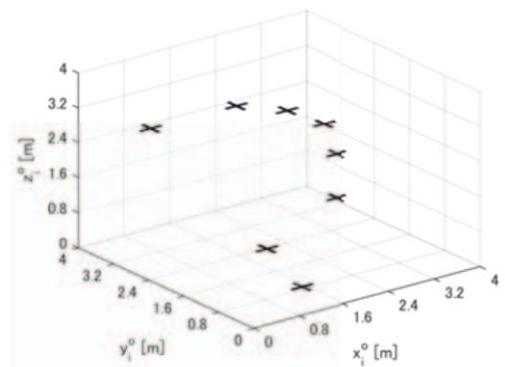


Fig. 7. 3D shot of quadrotors at  $t = 0$  [s] (Exact linearization)

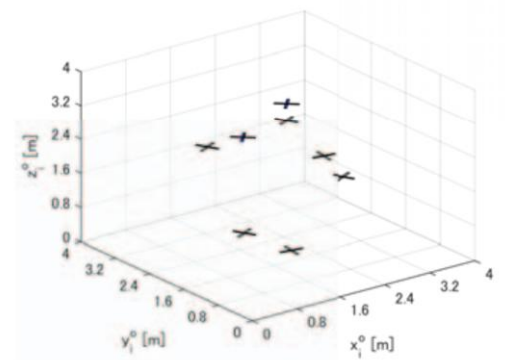


Fig. 8. 3D shot of quadrotors at  $t = 20$  [s] (Exact linearization)

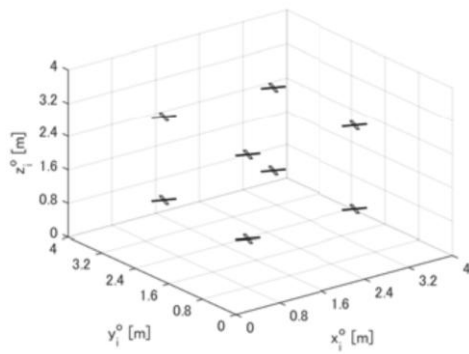


Fig. 9. 3D shot of quadrotors at  $t = 120$  [s] (Exact linearization)

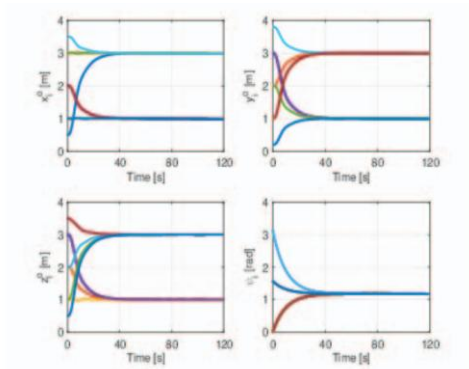


Fig. 10. Time response of positions and yaw angles of each quadrotor (Exact linearization)

## CONCLUSION

To overcome the mentioned problem we developed an additional technique that is obtained from the linearization of nominal dynamics of a quadrotor, which is done to achieve double integrators that are beneficial for achieving the formation of multiple vehicles via consensus. This feedback technique is appropriate for the double integrators (bearing consensus issue), where the UAVs can get their desired shape or formation without going into the space. Unlike the mobile ground robots where such characteristics are not explicitly available in their literature, and where the vehicles can't achieve formation without movement. However the conventional linearization method of exact feedback resolve this issue for quadruple integrator, but the linearized extended feedback method is more attractive in many cases than the exact linearization such as response of the system to frequency.

## REFERENCES

- [1] R. Olfati-Saber and R. M. Murray, "Information flow and cooperative control of vehicle formations," *IEEE Transactions on Automatic Control*, vol. 49, pp. 1465–1476, 2004.
- [2] M. P. K. Oh and H. Ahn, "A survey of multi-agent formation control," *Automatica*, vol. 53, pp. 424–440, 2015.
- [3] G. Lafferriere, A. Williams, J. Caughman, and J. Veerman, "Decentralized control of vehicle formations," *Systems & control letters*, vol. 54, no. 9, pp. 899–910, 2005.
- [4] Y. Ebihara, D. Peaucelle, and D. Arzelier, "Analysis and synthesis of interconnected positive systems," *IEEE Transactions on Automatic Control* (to appear in), 2017.
- [5] A. Isidori, *Nonlinear control systems*. Springer Science & Business Media, 2013.
- [6] A. Mokhtari, A. Benallegue, and Y. Orlov, "Exact linearization and sliding mode observer for a quadrotor unmanned aerial vehicle," *International Journal of Robotics & Automation*, vol. 21, no. 1, pp. 39–49, 2006.
- [7] J. Toji and H. Ichihara, "Formation control of quadrotors based on interconnected positive systems," in *15th European Control Conference*, 2016, pp. 837–842.

# APU Gas Turbine Performance Monitoring and Fault Diagnosis in Aircraft System based on QAR

Zeshan Hassan<sup>1</sup>, Jing Cai<sup>1</sup>, Domenika Sindik<sup>1</sup>, Muhammad Aurangzeb<sup>2</sup>

<sup>1</sup>Nanjing University of Aeronautics and Astronautics, Nanjing, China

<sup>2</sup>Hohai University, Nanjing, China

Received: 02 July, Revised: 15 October, Accepted: 27 October

**Abstract**—The aircraft complex systems (ACS) contains the auxiliary power unit (APU) based gas turbine, the performance assessment is totally cramped to inspection of different kind of parameters. So many other parameters can be observed in Quick Access Recorder (QAR) returns the APU condition from different aspects not having enough attention. The investigation intends to propose incorporated performance indicators by feature extraction many observing parameters. To approve the effectiveness of the strategy by anomaly identification, the clustering analysis is conducted. This technique can possibly effectively evaluate performance of some complex aircraft systems for early cautioning and prevent degradation at early stage. The parameters of Rowen's model for APU based gas turbines in unique studies are assessed by utilization of accessible operational and performance data. Here, the work is planned to make understanding into different parts of the APU model and to present simple and comprehensive strategy to extract the parameters out of basic physical laws, focusing especially on researchers to let their interest in dynamic models and simulations. Gas turbine parameters are approximated by using straightforward thermodynamic assumptions, resulting great performance. In this paper, the step response of the simulation model is also simulated for number of scenarios and is presented here.

**Keyword:** Air-Craft, APU, Gas Turbine, Dynamic simulation, gas turbine, mathematical model, thermodynamic process.

## I. INTRODUCTION

Aircraft systems are complicated system. In the design stage and in the operating process to ensure continued air quality of the aircraft. It is broken down into simpler sub systems that carry out homogeneous functions. There are two types of power supply use in the aircraft system to work, first is main power unit and second is auxiliary power unit. APU works during the phases when the aircraft's main engines are shut down and to support the electrical and air conditioning systems. Auxiliary Power Unit (APU) is one of complex electromechanical systems in aircraft which serves as a small engine. It is mainly used to provide compressed air and electrical power on ground and used as alternative power

supply in air in case of emergency. A typical APU system for commercial aircraft consists of three main sections, the load compressor that provides all pneumatic power, the power section which is a gas generator supplying all power and the gearbox which transfers power. Another two important devices are the inlet guide vanes and the surge control valve, which are used to regulate airflow into the load compressor and maintain turbo machine stable separately. It is typically installed in the aircraft tail cone and the primary function is to provide power to start the main engines and provide energy for functions other than propulsion. APUs can also be used to run accessories like air conditioning system in the cabin while the passengers are boarding before the aircraft engines are started. In normal operation.

A typical APU for commercial transport aircraft is broken up into three main sections –

- (1) the power section,
- (2) the load compressor
- (3) the gearbox.

The power section is the gas generator portion of the engine and produces all the power for the APU. The load compressor is generally a shaft-mounted compressor that provides all pneumatic power for the aircraft. Auxiliary power unit (APU) is standard equipment on today's civil aircraft. It is a small gas turbine engine that makes the aircraft independent of ground power supplies. GAS turbines are one of the fundamental sources for power generation in nations with flammable gas assets and are introduced in various places in globe because of their uncommon qualities. A mathematical representation of gas turbines of power system analyst needs dynamic studies to have a several journals [1]–[3]. A standout amongst the most normally utilized improved models was exhibited by Rowen [1] considering the load-frequency and temperature control and in addition the turbine's thermodynamic reactions as a straight capacity and delta direct vane impacts in a different work [2]. A few models with various degrees of improvement for the representation of gas turbines in dynamic studies were presented, among which the IEEE demonstrate for joined cycle power plants had further sight into internal processes [3]. A review of the models is given in [4].

## II. GAS TURBINE APU

Gas turbines are engines within which the chemical energy of the fuel is converted either into mechanical energy in terms of shaft power or into kinetic energy. Gas turbines that produce shaft power are power generation gas turbines. Gas turbines that convert the fuel energy into kinetic energy are used for generation of thrust to propel an aircraft. The conversion of fuel energy into shaft power or propulsive force, requires interaction of several components of the engine, within each of them a chain of energy conversion takes place.

### Types of gas turbine

- Turboprop engines
- Jet engines
- Aeroderivative gas turbines
- Amateur gas turbines
- Auxiliary power units
- Industrial gas turbines for power generation
- Industrial gas turbines for mechanical drive
- Turboshaft engines
- Radial gas turbines
- Scale jet engines
- Microturbines

### Application Area of gas turbine

- Gas turbine plants are used as standby plants for the hydroelectric power plants.
- **Gas turbine power plants** may be used as peak loads plant and standby plants for smaller power units.
- Gas turbines are used in jet aircraft and ships. Pulverised fuel-fired plants are used in a locomotive.

APU Gas Turbine (APUGT) are exceptionally designed gas turbines for power generation which are determined by their long life and higher accessibility thought about different kinds of gas turbines. AGTs are made out of three major segments: multistage axial stream compressors, can-annular combustors and pivotal stream turbines. Fig. 1 demonstrates an ordinary AGT with its segments. Air with climatic conditions is attracted to the compressor subsequent to passing air channels at the passage. The multi stage compressor expands speed, weight and temperature of the air before it comes to the combustor and bay to the high weight turbine parts. Every compressor arranges contains a row of rotor cutting blades and stator vanes. Of significance is a column of stator vanes at the inlet (variable inlet guide vanes, VIGVs) whose angle might be changed by the control system during activity. As shown in Fig. 1, the packed compressed air with high pressure and temperature will pursue its way to the combustor. The

combustor is fundamentally a heater in which fuel is scorched to increase the temperature at constant pressure.

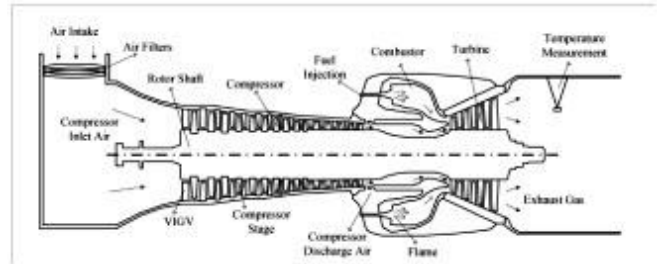


Figure 1. Schematic view of a typical AGT and its major components.

Roughly one third of the compressor discharge air is mixed with the fuel to be burnt, while the remaining air is mixed with combustion products to become the turbine inlet flow which is now at turbine inlet temperature (TIT) [7]. The flow is then expanded in 2–4 turbine stages which drive compressor and generator. Finally, the flow is guided through the exhaust duct to a second environment which can be surrounding ambient conditions or a heat recovery steam generator (HRSG) in combined cycle plants (CCP). In addition to air/gas dynamics passing through major components of the gas turbine, there are other equipments which are of interest in the gas turbine model like exhaust gas thermocouple and its radiation shield and the fuel valve system and valve positioner. An estimation of these equipment parameters is done as well. The gas turbines work with the Brayton cycle. Fig. 2 shows a typical standard Brayton cycle in temperature-entropy frame.

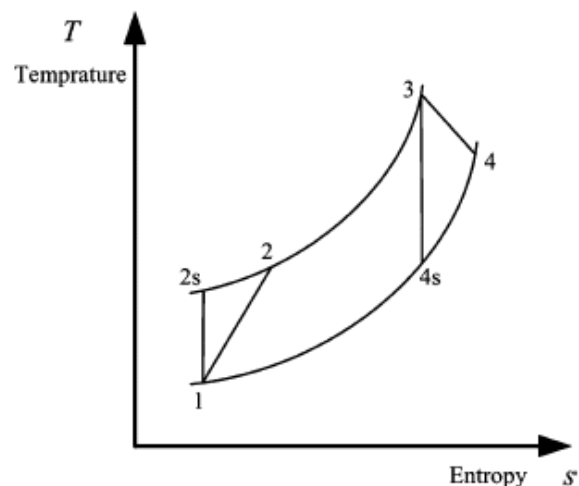


Figure 2. Typical Brayton cycle in temperature-entropy frame.

Air is drawn from point 1 in surrounding condition and is compressed by the compressor in an irreversible procedure to point 2. Input value of heat in the combustor will build the

temperature to point 3 where the combustion product and compressor release air will enter the turbine and grow to point 4. In this figure, the pressure loss in the air filters and the combustion chamber is ignored, i.e., the procedures 2-3 and 4-1 are thought to be isobar.

The procedures in the compressors and turbines are irreversible and non-isentropic; be that as it may, in Fig. 2 the expected isentropic procedures are shown as well. These perfect procedures would be utilized to characterize the compressor and turbine irreversible adiabatic efficiency as pursues:

$$\eta_c = \frac{h_{2s}-h_1}{h_2-h_1} \approx \frac{T_{2s}-T_1}{T_2-T_1} \quad (1)$$

$$\eta_t = \frac{h_3-h_4}{h_3-h_{4s}} \approx \frac{T_3-T_4}{T_3-T_{4s}} \quad (2)$$

Where  $h$  stands for the fluid mixture enthalpy (kJ/kg) and is the absolute temperature in K. The subscript  $s$  indicates the isentropic process. In operation, the turbine's efficiency  $\eta_t$  is more affected by changes in load and speed than compressor efficiency  $\eta_c$  is [7]. This is mainly because the compressor is operated in relatively constant thermodynamic conditions but the turbine condition greatly varies. In deriving the gas turbine model parameters, the above efficiencies are used and assumed constant in a limited range of operational conditions where the turbine response can be approximated to be linear [1], [3]. Therefore, in the next sections operational data are first used to derive the above efficiencies to extract turbine parameters.

### III. APUGT MODEL FOR STABILITY ANALYSIS

The mathematical representation of an APUGT in dynamic studies by Rowen's model is shown in Fig. 3. There are two major controls which are shown in this figure. These are load frequency and temperature control (originally, in [1] acceleration control have been shown and in [2] inlet guide vanes (IGVs) have been modeled which are not included here). Variable IGV (VIGV) are to regulate the air mass flow drawn into the compressor. Actually the VIGV are in operation in CCP applications where they regulate the air flow to maintain the efficiency of gas turbine during operation at partial load. The VIGV control is mainly affected by exhaust gas temperature. If this temperature is below the reference (near to rated temperature) then VIGV will open and, in fact, it will become fully opened in normal operation of around nominal power. Nevertheless, in partial load and start up, the exhaust temperature is not that high and the VIGV are partly closed. In simple cycle operation, VIGV control is only active during start up. In this paper, we do not consider the VIGV and acceleration control as the model is to be tuned around nominal operation and VIGV are considered fully open. The fuel demand signal is the minimum value of temperature and load-frequency control. The sequence of model blocks is: fuel demand limitation, no load consumption, valve positioned and fuel system dynamic, volume discharge delays, turbine model (for output torque and temperature), temperature measurement system [1]. Apart from the control set-points, other parameters of the models are based on physical behavior of the HD GT's components.

(for output torque and temperature), temperature measurement system [1]. Apart from the control set-points, other parameters of the models are based on physical behavior of the HDGT's components.

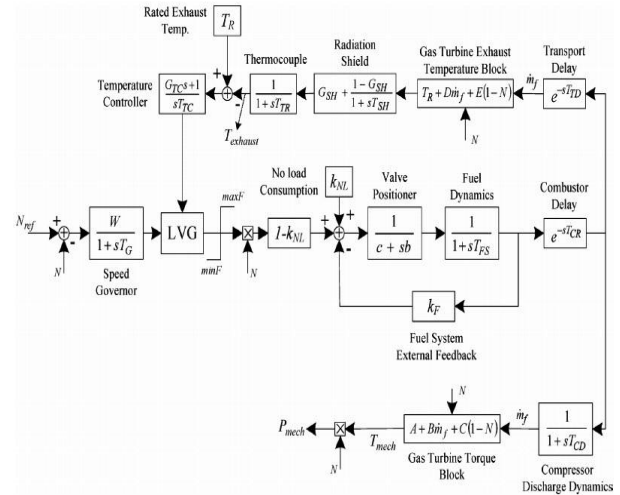


Figure 3. Rowen's model for APUGTs for dynamic studies [1].

The model is to be tuned around nominal operation and VIGV are considered fully open. The fuel demand signal is the minimum value of temperature and load-frequency control. The sequence of model blocks is: fuel demand limitation, no load consumption, valve positioned and fuel system dynamic, volume discharge delays, turbine model (for output torque and temperature), temperature measurement system [1]. Apart from the control set-points, other parameters of the models are based on physical behavior of the HD GT's components.

#### A. Turbine Parameters

In the APUGT model of Fig. 3, the turbine behavior is reflected by two quantities. First, the output torque and second the exhaust gas temperature. To see the turbine parameters in more details, let us start with Fig. 2 and efficiencies of compressor and turbine. In the isentropic process of 1–2s, we have [9]

$$\frac{T_{2s}}{T_1} = \left(\frac{P_2}{P_1}\right)^{\frac{\gamma_c-1}{\gamma_h}} = PR^{\frac{\gamma_c-1}{\gamma_c}} = x_c \quad (3)$$

$$\frac{T_3}{T_{4s}} = \left(\frac{P_3}{P_4}\right)^{\frac{\gamma_c-1}{\gamma_h}} = PR^{\frac{\gamma_c-1}{\gamma_c}} = x_h \quad (4)$$

where  $P_2/P_1 = P_3/P_4 = PR$  (pressure drop in combustor is neglected) is the cycle pressure ratio.  $\gamma_c$  and  $\gamma_h$  are the cold end (compressor) and hot end (combustor, turbine) ratio of specific heats, respectively. The variable  $x$  is defined to make referencing simpler in the next equations. Generally  $\gamma =$

$C_p/C_v$  where  $C_p$  is the specific heat of air at constant pressure

and is the specific heat at constant volume.

It is important to know that  $C_v$  the specific heats and ratio vary with temperature. One common approach is to use the hot end and cold end air properties as follows [10]:

$$\begin{aligned} C_{ph} &= 1.1569 \text{ kJ/kgK} & \text{and} & & \gamma_h &= 1.33 & (5) \\ C_{pc} &= 1.0047 \text{ kJ/kgK} & \text{and} & & \gamma_c &= 1.4 & (6) \end{aligned}$$

Using (1) and (3), temperature after the compressor is computed as follows:

$$T_2 = T_1 \left( \frac{x_c - 1}{\eta_c} + 1 \right) \quad (7)$$

and with (2) and (4), we get

$$T_4 = T_3 \left[ 1 - \left( 1 - \frac{1}{x_h} \right) \eta_t \right] \quad (7)$$

Another process which affects the APUGT's behavior is the process which takes place in the combustor, i.e., 2–3 in Fig. 2. A constant pressure process in the combustor will lead to the following expressions:

$$\dot{q}_H = \dot{m} \cdot c_{ph} \cdot (T_3 - T_2) \quad (9)$$

where  $\dot{m}$  (kg/s) is the air flow rate. The heat is produced by extracting energy from the fuel as follows:

$$\dot{q}_H = \eta_{comb} \cdot \dot{m}_f \cdot H \quad (10)$$

where  $\dot{q}_H$  (kJ/s) is the heat absorption rate in the combustor, is the combustor efficiency,  $\dot{m}_f$  (kg/s) is the fuel flow rate and (kJ/kg) is the lower calorific or lower heating value of fuel in use. The combustor efficiency stands for the portion of fuel that is injected into the combustor but is not burnt. For state of the art designs, combustor efficiency is very high and near to unity. Using (9) and (10) the temperature rise in the combustor can be computed as follows:

$$T_3 = T_2 + \eta_{comb} \frac{\dot{m}_f}{\dot{m}} \frac{H}{c_{ph}} T_2 + \Delta T_0 \frac{\dot{m}_f}{\dot{m}} \quad (11)$$

$\Delta T_0$  is a simplifying symbol of a temperature rise coefficient. Actually, the internal temperatures and pressure ratio and overall response of APUGT vary with speed. These responses are nonlinear and further complicate the models. However, in Rowen's model, a linear model is assumed with respect to speed by applying the speed constraint of 95% to 107% of nominal speed; see Fig. 3. We also will assume a linear response with respect to speed deviations, but first let us assume our APUGT at nominal speed. In this point, the per unit output torque and mechanical power would be the same. Then

$$P_G = \dot{m} \cdot [C_{ph} (T_3 - T_4) - C_{pc} (T_2 - T_1)] \quad (12)$$

By simple mathematics, the above equation is written in the form of the power block in Fig. 3 using (7), (8), and (11), i.e.

$$P_{Gpu} = A + B \cdot \dot{m}_{fpu} \text{ at nominal speed} \quad (13)$$

$$A = \frac{\dot{m}_n \cdot T_1}{P_{Gn}} \left\{ C_{ph} \cdot \eta_t \cdot \left( 1 - \frac{1}{x_h} \right) - \frac{x_c - 1}{\eta_c} \right. \\ \left. \times \left[ C_{pc} - C_{ph} \cdot \eta_t \cdot \left( 1 - \frac{1}{x_h} \right) \right] \right\} \quad (14)$$

$$B = \frac{\eta_{comb} \cdot \eta_t \cdot H \cdot \dot{m}_{fn}}{P_{Gn}} \left( 1 - \frac{1}{x_h} \right) \quad (15)$$

where A and B are the coefficients of output torque in Fig. 3;  $\dot{m}_m$  and  $\dot{m}_{fn}$  are the air and fuel nominal flow rates; and  $P_{Gpu}$  is the per unit output power which is equal to the p.u. torque. It should be stated here that the turbine nominal power is the base of p.u. for [13]–[15]. At nominal speed, the exhaust temperature can be computed by substituting (11) and (7) in (8). Therefore

$$T_4 = T_R - D \cdot (1 - \dot{m}_{fpu}) \text{ at nominal speed} \quad (16)$$

$$D = \eta_{comb} \frac{H}{c_{ph}} \frac{\dot{m}_{fn}}{\dot{m}_n} \left[ 1 - \left( 1 - \frac{1}{x_h} \right) \eta_t \right] \quad (17)$$

Where D is the coefficient of the exhaust temperature block in Fig. 3 and  $T_R$  is the nominal exhaust temperature of the APUGT. To extract the parameters, a typical operational condition is selected to derive the turbine and compressor efficiencies and then all above parameters are computed with available data out of unit operation

$$T_{Gpu} = \frac{k+1}{k} - \frac{1}{k} N_{pu} \quad (18)$$

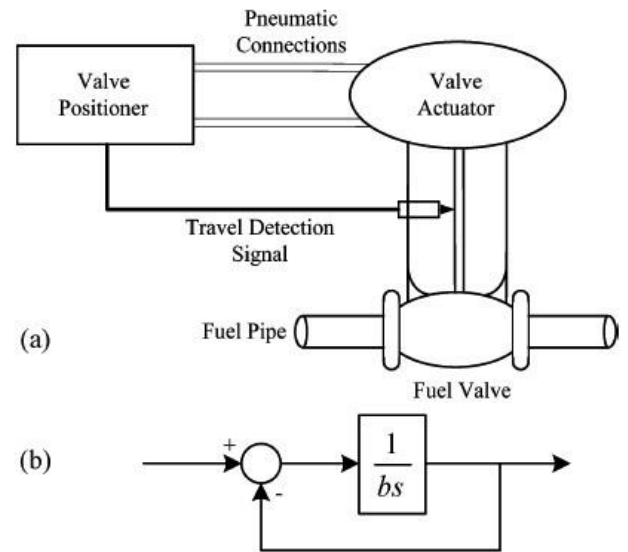


Figure 4. Pneumatic valve positioner and valve actuator.  
(a) Schematic view.  
(b) Internal feedback mathematical model.



where  $k$  is a constant and depends mainly on the thermodynamic cycle design and frictions. It is a tedious job to go through the details of this parameter [9]. Fortunately, the design constraints for APUGTs do not allow high variations in and values of 1.5 to 2 are common. Therefore,  $C'=1/k$  in power block of Fig. 3 varies between 0.5 and 0.67. Note that all above concepts are only valid when we are in the linear area of the turbine response with respect to speed deviations. The same approach regarding temperature changes versus speed will make the coefficient  $E$  in exhaust temperature block of Fig. 3 to vary in the range of 0.55 to 0.65 of rated exhaust temperature. The fact that HDGTs need relatively high fuel consumption to operate even in no load conditions is reflected in Rowen's model by dividing the fuel demand signal to positioner system into a constant part (constant  $k_{NL}$  in Fig. 3) and the reducing gain multiplied by the demand signal (block 1-  $k_{NL}$  in Fig. 3).  $k_{NL}$  can be extracted from available operational data.

There is also a fuel demand signal limiter in the APUGT model of Fig. 3. The maximum extent of the limiter is not reached in normal operation and may act as a backup to temperature control where any increase in turbine exhaust temperature will lead to activation of temperature control and decreasing fuel flow [1]. Anyway, the minimum extent is a negative value which shows the gas turbine ability of transient power absorption. Its value depends on minimum fuel flow required to maintain the flame in combustor. A value of 1.5 p.u. is commonly used for maximum extent while minimum value can be determined by available fuel system data.

#### B. Valve Positioner and Fuel System Lag

The valve positioner moves the actuator to a valve position corresponding to the set point. In Fig. 4, the valve positioned and its connection to the valve actuator and valve system is presented. Due to the fact that APUGTs are able to operate with liquid and gas fuel, the fuel system models are essentially two different systems with similar blocks. In larger APUGTs both fuel systems are supplied with inner loop feedback which senses the current position of the valve and eliminates the error between set point and position signal, see Fig. 4. Therefore, only one time constant will appear, which is in the valve positioner block of Fig. 3. The positioner time constant can be found in the manufacturer data or similar available data for older units. Moreover, in liquid fuel systems, there is a bypass way from the fuel pump output to the pump section. Bypass path is presented in Rowen's model by the feedback loop gain. The value of is explicitly calculated to force the overall valve positioner-fuel system loop gain to unity [1].

As a result, the product of and (valve positioner block in Fig. 3) should become zero, i.e., the value is zero for our large APUGTs if is not. Note that this is not always the case, especially when inner loop feedback does not exist, see [1] for more details. Assuming linear response actuators and valves,

the fuel flow will change directly with the output signal of the valve positioner. However, there is a lag associated with gas/oil flow in the pipes and fuel system manifold. This lag can be approximated by the following expression[8]:

$$T_V = \frac{P_0}{Q_0} V \frac{\partial}{\partial P} \left( \frac{1}{v} \right)_{T_0} \quad (19)$$

where in  $s$  is the time constant of the lag associated with the container of volume in , is the average pressure in Pa (kg/m.sec<sup>2</sup>), is the steady state mass flow out of the container in kg/sec and  $\partial(1/v) \partial P$ (sec<sup>2</sup>/m<sup>2</sup>) is the density change due to pressure changes at constant temperature where is the specific volume. For gas fuels, the lag constant is considerably higher due to higher changes in the specific volume. Knowing the rough estimates of parameters in [17] makes it possible to obtain rough values for the lag time constant; see Section IV.

#### C. Time Delays and Discharge Lag

The gas turbine behavior forces its dynamic model to have small delays and lag time constants. Actually there is a small time delay between the fuel injection and heat release in the combustor which is called combustion reaction delay. In modern systems it is on the order of some ms [10]. This time delay is implemented in Rowen's model as a time delay after the valve systems. There is also a time delay between the fuel combustion and exhaust temperature measuring system. This delay is caused by the exhaust system and turbine to transport the fluid to the measuring point; see Fig. 1, and is in the order of some 10 ms depending mainly on the size of the APUGT and the average fluid speed. A relatively higher time lag exists in the compressor discharge path to the turbine inlet. It can also be approximated by [17].

#### D. Temperature Measurement

Temperature control in APUGTs requires measurement of the exhaust temperatures which may be composed of thermocouple and radiation shield [1]. Generally, there are three ways of heat transfer between materials: conduction, convection and radiation. Here, we are only interested in the exhaust gas temperature out of the turbine (a convective source) to control the temperature and avoid excessive heating. Nevertheless, the radiation source, i.e., the turbine itself, will cause errors in the temperature measurement. The radiation shield is therefore used to overcome the problem. The radiation shield is a polished, highly reflective metal shield that is placed around the thermocouple and reflects most of the radiation away from the thermocouple and itself;

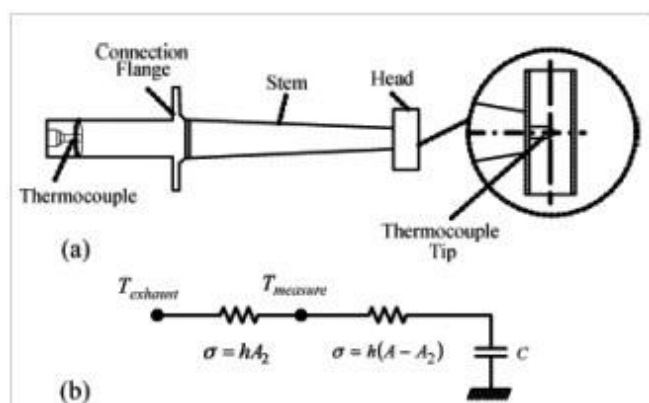


Figure 5. Radiation shield and thermocouple.

(a) Schematic of radiation shield and mounted thermocouple. (b) Simplified equivalent electric circuit for calculating the temperature at thermocouple position. see Fig. 5. This equipment will cause a lag based on its heat transfer behavior to be presented in the model. Let us assume a simple model of the heat transfer paths of Fig. 5. The temperature at the thermocouple tip will then be approximated by

$$\frac{T_{measure}}{T_{exhaust}} \approx \frac{A_2}{A_1} + \frac{1 - \frac{A_2}{A_1}}{\frac{C}{hA_1}s + 1} \quad (20)$$

where  $A_1$  is the total active area for convection heat transfer to the shield head,  $A_2$  is the area effective for convection heat transfer to the thermocouple tip,  $C$  (J/K) is the heat capacity of the shield head and  $h$  (W/m<sup>2</sup>K) is the convection heat transfer coefficient [11]. Temperature measurement device is the thermocouple which has a typical lag with a time constant based on its type and design. Time constant of thermocouple can be easily extracted from its time response documents.

#### IV. RESULT AND DISCUSSION

The complete system is designed and simulated in Matlab/Simulink. The Simulation is done for 50 seconds as shown in the figure 6.

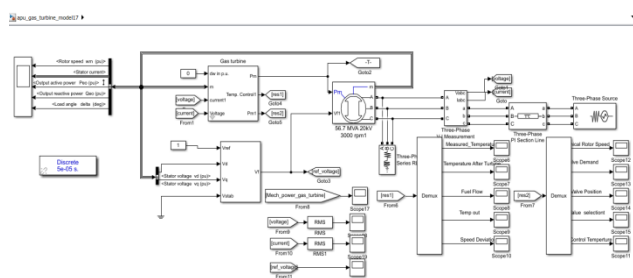


Figure 6. Simulation mode



Figure 7. Mechanical Rotor Speed

In figure 7, the variation of mechanical rotor speed w.r.t time is shown. It varies initially and becomes stable at 8 sec.



Figure 8. Valve Demand

In figure 8, the variation of valve demand w.r.t. time is shown. It varies initially and becomes stable at 8 sec.



Figure 9. Valve Position

In figure 9, the variation of valve position w.r.t. time is shown. It varies initially and becomes stable at 8 sec.

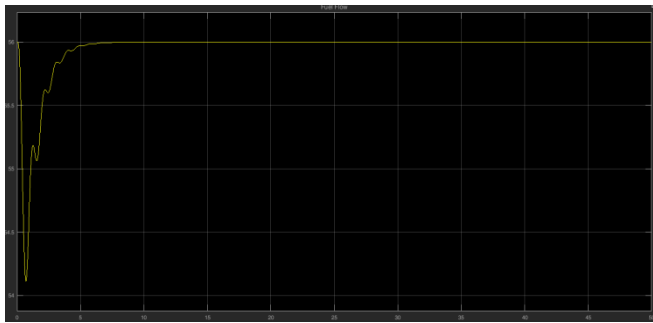


Figure 10. Fuel Flow

In figure 10, the variation of fuel flow w.r.t time is shown. It varies initially and becomes stable to 56 at 8 sec.



Figure 11. Temperature Output

In figure 11, the variation of temperature output w.r.t time is shown. It varies initially and becomes stable to 56.7 at 8 sec.



Figure 12. Speed Deviation

In figure 12, the variation of Speed Deviation w.r.t time is shown. It varies initially and becomes to 0 at 8 sec.



Figure 13. Mechanical Power Gas Turbine

In figure 13, the variation of mechanical power gas turbine w.r.t. time is shown. It varies initially and becomes stable at 8 sec.

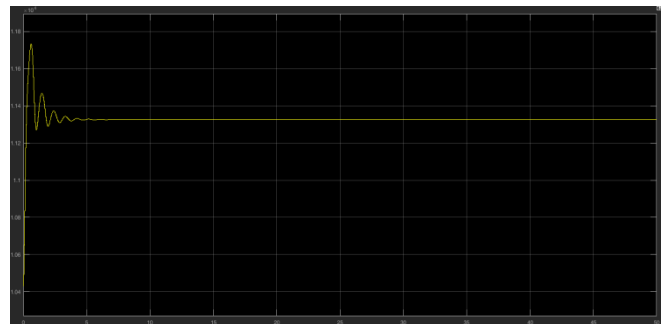


Figure 14. RMS Voltage

In figure 14, the variation of RMS voltage w.r.t. time is shown. It varies initially and becomes stable at 8 sec.

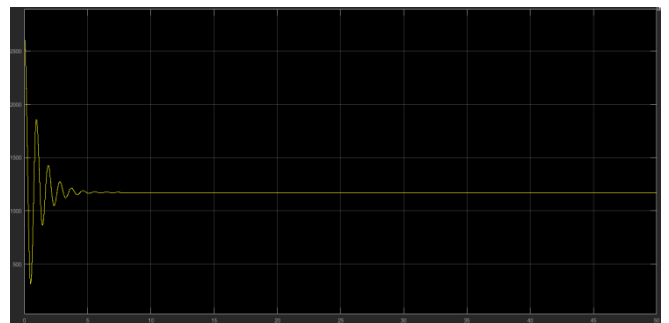


Figure 15. RMS Current

In figure 15, the variation of RMS current w.r.t. time is shown. It varies initially and becomes stable at 8 sec.



Figure 16. Multiple Value Comparison

In figure 16, the variation of rotor speed (p.u.), stator current, active power (p.u.), reactive power (p.u.), load angle w.r.t. time is shown. Initially all values varies and becomes stable at 8 sec.

### CONCLUSION

The research paper is described three progressively propelled techniques to demonstrate the diagnostics of aircraft auxiliary power units (APU). The increasing multifaceted of the methodologies corresponds to the increasing trouble handling them with the legacy engines. It has been shown that a reliable diagnostics of faults is possible even by rarely data collected on such engines. This is accomplished with the use of high fidelity models of the available engine. In view of dependability analysis & forecast, high danger of APU gas turbine's can be scheduled off. The unused APU gas turbine can be set up in advance. Shop repair, investigating and maintenance activities can be better arranged. APU based gas turbine safety & accessibility can be essentially improved, so that operating & maintenance cost can be minimized. The risk of APU based gas turbine APU failures can be observed an aircraft fleet and not for single system. The investigative result can be used by unwavering quality experts and the people managing system. In this paper, a basic technique is shown for evaluating the parameters of Rowen's model. It is described in detail how to extract the model parameters by operational datasets.

### REFERENCES

- [1] W. I. Rowen, "Simplified mathematical representations of heavy-duty gas turbines," *Trans. ASME, J. Eng. Power*, vol. 105, no. 1, pp. 865–869, 1983.
- [2] W. I. Rowen, "Simplified mathematical representations of single shaft gas turbines in mechanical drive service," presented at the Int. Gas Turbine and Aeroengine Congr. and Expo., Cologne, Germany, 1992, unpublished.
- [3] IEEE Working Group Report, "Dynamic models for combined cycle plants in power system studies," *IEEE Trans. Power Syst.*, vol. 9, no. 3, pp. 1698–1707, Aug. 1994.
- [4] S. K. Yee, J. V. Milanovic, and F. M. Hughes, "Overview and comparative analysis of gas turbine models for system stability studies," *IEEE Trans. Power Syst.*, vol. 23, no. 1, pp. 108–118, Feb. 2008.
- [5] P. Kundur, *Power System Stability and Control*. New York: McGraw-Hill, 1994.
- [6] R. K. Turton, *Principals of Turbomachinery*. London, U.K.: Chapman & Hall, 1995.
- [7] M. P. Boyce, *Gas Turbine Engineering Handbook*, 3rd ed. Oxford, U.K.: Gulf Professional, 2006.
- [8] B. Vahidi, M. R. Bank Tavakoli, and W. Gawlik, "Determining parameters of turbine's model using heat balance data of steam power unit for educational purposes," *IEEE Trans. Power Syst.*, vol. 22, no. 4, pp. 1547–1553, Nov. 2007.
- [9] G. J. Van Wylen, R. E. Sonntag, and C. Borgnakke, *Fundamentals of Classical Thermodynamics*, 4th ed. New York: Wiley, 1998.
- [10] P. P. Walsh and P. Fletcher, *Gas Turbine Performance*, 2nd ed. Oxford, U.K.: Blackwell Science, 2004.
- [11] J. V. Nicholas and D. R. White, *Traceable Temperatures*, 2nd ed. New York: Wiley, 2001.
- [12] W. C. Reynolds, *Thermodynamic Properties in SI*. Palo Alto, CA: Stanford Univ., 1979.
- [13] D. Gorinevsky, K. Dittmar, D. Mylaraswamy, and E. Nwadiogbu, "Model-based diagnostics for an aircraft auxiliary power unit," in *IEEE Conference on Control Applications Glasgow, Scotland*, 2002.
- [14] L. Yongjian, Z. Jianying and X. Hongshan, "Fault diagnosis for civil aviation aircraft based on rough-neural network," *Journal of Beijing University of Aeronautics and Astronautics*, vol. 35, pp. 1005-1008, 2009.
- [15] H. Ding, B. Wang and L. Huang, "Modeling and Implementation of Aircraft APU System Performance for CBM Strategy," in *2011 Aviation Maintenance Theory and Technology Develop Nanjing, China*, 2011, pp. 111-115.
- [16] M. Tang, "Modeling and Implementation of the APU Starter Monitoring Model under CBM Strategy," *Aviation Maintenance & Engineering*, pp. 73-75, 2014.
- [17] A. Radun, J. Rulison, and P. Sanza, "Switched Reluctance Starter/Generator," *SAE Technical Papers*, 1995, Paper No. 921974.

# Control of Optimal Operation with Hybrid Energy System

Muhammad Waseem<sup>1</sup> Dr. Abdul Basit<sup>1</sup>, Imran Khan<sup>1</sup>

<sup>1</sup>US Pakistan Center for Advanced Studies in Energy, UET Peshawar

Received: 14 October, Revised: 28 October, Accepted: 01 November

**Abstract**—Fossil fuels is the main energy resource now a day with the advantage of generating gigantic electricity at a given location. Fossil resources, however, are subject to exhaustion rendering energy resources risks. The process of electricity generation from fossils fuels may be less costly compared to other schemes however this advantage comes at the expense of increased pollution, greenhouse gases emission contributing to overall global warming. Sustainable energy production requires reusable energy resources. Each renewable energy resource is characterized by a unique characteristic set and advantages, making it suitable for application of specific nature and location. In a hybrid system, the cumulative sum of the powers generated by the constituent systems should match the load demand rendering its implementation complex mainly due to the non linear behavior of the renewable energy resources and the non linearity of the fuel consumption curve. The dissimilar load demand pattern and the limit on the operation of the battery also poses a constraint. Controlling the process of any compound power source system in an optimal manner is essential and challenging to achieve low overall system cost.

**Keywords**— Renewable Energy Resources, Hybrid System, System Cost.

## I. INTRODUCTION

A hybrid energy system has many renewable energy sources, back-up, battery systems, that is designed to provide power to a given load. The fact that renewable energy resources are variable, whose variation is dictated by factors such as changes in weather, seasons etc.; and the fact that load demand is also variable; optimally controlling all the constituent renewable resources to provide energy to a fluctuating load is one of the fundamental challenge of such a hybrid system. An optimal central control system is thus required to manage each renewable resource in a manner such that the overall system is able to deliver energy efficiently to a fluctuating loads with renewable energy resources, battery back-up and energy storage mechanism. Current research in the hybrid system optimization mainly aims at the sizing aspect of the renewable hybrid system. This section highlights challenges and possible developments that will have an impact on the enhanced performance and optimized control of the hybrid energy system. This section also summarizes the hybrid systems optimization module available in the literature.

Hybrid system designing and controlling often employ conventional methods such as Rule of thumb methods [1] and

Paper-based methods [2]. These approaches are based on reformist experience and trials, characterized by errors. They are, however, limited as they only provide a broader picture that may still very likely be open to improvements [3]. Many research works have assumed numerical approaches for the sizing and optimal cost calculations of the hybrid system, based on the load and resources of energy at a given location [4]. These techniques, however, are time-consuming and complex in implementation, and their complexity is an exponential function of the variables (number of constituents etc) in the hybrid system [5]. Using these approaches, the sizing and optimal initial cost could be determined but the running cost of the average optimized control could not be determined with accuracy. Researchers have coined techniques such as "Graphic method", "Probability based models" which are derivative-based and have shown promising results and efficiency towards improved optimal solutions of optimization problems, however they lack application when applied to advance optimization problems (joint sizing and optimal control) [6].

These techniques employ pure analytical methods, but they may not be best suited for practical problems with high non-linearity. The gradient and Newton methods are limited as they can't handle inequality constraints. Linear programming techniques have oscillatory problems and their convergence is slow for an improper iteration step when optimizing both objective function and constraints [7]. Non-linear programming methods have complex implementation, stability problems, and bad convergence. Mixed integer programming are highly complex and their computation time is poor [8].

A number of software platforms are available that are used to optimize given hybrid renewable energy system. These softwares are designed taking the analytical models of the components systems. Simple linear or complex models are employed in these tools and their design varies within a predetermined interval in a random fashion; still producing sub-optimal results due to the inherent complexity in the system [9].

As hybrid systems are complex and highly non-linear, artificial/computational intelligence based techniques are coined to cope with the high degree of complexity in hybrid systems [10]. To use these modern optimization techniques in an efficient manner, comprehensive and precise models of the hybrid renewable energy system is mandatory [11]. Also the complex interaction between constituent systems sizing and optimal operation control is required follow.

## II. RELATED WORK

The template is used to format your paper and style the text. All margins, column widths, line spaces, and text fonts are prescribed; please do not alter them. You may note peculiarities. For example, the head margin in this template measures proportionately more than is customary. This measurement and others are deliberate, using specifications that anticipate your paper as one part of the entire proceedings, and not as an independent document. Please do not revise any of the current designations.

Many researchers have conducted surveys on optimal control operation of hybrid renewable energy systems. We briefly summarize them in the following paragraphs. A review of the state of the design, functioning, and control for the stand-alone PV solar-wind hybrid energy systems was conducted by [12] using conventional back-up sources such as Diesel Generator (DG). State-of-art control mechanism (like artificial intelligence) was suggested for future use to optimize hybrid renewable energy system and for managing energy efficiently. A summary of techniques for renewable energy systems setup, optimal control, management, and sizing was proposed by [13]. The author also highlighted future developments of how renewable resources can be used to generate energy and challenges due to mass scale growth in future renewable energy systems. Optimization algorithm for renewable energy system designs, planning, and controlling were reviewed by [14]. The authors concluded that there is an increased surge for traditional and heuristic algorithms to solve the optimum control problems in hybrid renewable energy generation and control systems.

A number of optimization techniques were investigated by ranging from software based to sophisticated optimization algorithms [15]. The modeling of Solar and wind renewable energy system models were discussed by [16]. These authors describe the models of the constituent of the hybrid system. They further review the contributions from many other authors and concludes that most publications are not discussing control. A detailed review in core areas of constituent unit sizing, optimization, management of the energy flow, and modeling of the components hybrid system for the last 10 years was presented by [17]. Their work provides a summary of the important parameters and factors which helps in deciding an optimized energy management mechanism. A comprehensive description of the optimal operation control is not presented in this work. A stand-alone hybrid solar-wind energy system in conjunction with battery system was reviewed for simulations, control, and optimization by [18]. They concluded that there is still space for enhancement of the system performance; algorithm establishment for enhancement of accurate prediction of their outputs, and their integration with other conventional or renewable energy generation systems.

## III. MOTIVATION

In a hybrid system, the cumulative sum of the powers generated by the constituent systems should match the load demand rendering its implementation complex mainly due to the following problems.

### A. Sub-Problem 1: Non-linear renewable resources

Since renewable energy resources at a given location are function of season and time, the corresponding power provided by such sources to loads is variable. In a hybrid system, the fraction of energy generated by constituent renewable sources have a high impact on the fuel consumption of DG, which further depends on the alternate resources and fluctuating load demand. The problem of calculating approximate operation cost has been considered in the literature and mostly average monthly renewable resources are used to calculate it. In most cases, however, the interaction between load and non-linear renewable powers on comparatively lesser scale have not yet been considered. This work assumes comprehensive time series data and uses realistic non-linear resource profiles.

### B. Sub-Problem 2: The non-linearity of the DG fuel consumption curve.

The efficiency of DG is optimal when they operate either at 80% or above their measured capacities and show very poor performance when operate at 30% or below the rated capacity. The DG fuel consumption while operating thus is a function of the instantaneous output power and the span of time for which it is running. Many established models related to fuel consumption (the model adopted in HOMER software etc.) assumes a linear behavior between the fuel usage and the corresponding output power of the DG according to:

$$fc = FoYgen + F1.Pgen \quad (1)$$

Equations above represent linear behavior but when the true response of generator is considered, the expressions given above for the fuel usage response become exceedingly non-linear.

### C. Sub-Problem 3: The Load demand pattern is dissimilar

The work in the literature assumes load demand and operational cost to be fixed, from which monthly and yearly costs can be inferred. This assumption however is not valid when the consumer behavior is dependent on days, months and seasons which ask for a more accurate, precise and practical cost model that explains consumer behavior on daily basis.

### D. Sub-Problem 4: Limitation on Battery Operation

The extent when the load demand is fulfilled the surplus energy is stored in battery system. The battery system is callibrated having a paramount charge limit, and can be discharged to a minimum allowed limit in the event of energy deficit at which point the DG is turned on. The following battery operation settings however are conflicting:

- If a battery discharges in longer time, DG run-time and fuel consumption are reduced at the cost of reduced battery life and frequent battery replacement.
- If a battery discharges in short time, DG run-time and fuel consumptions are maximized, though the battery life span is increased.



The impact of battery operation and maximum and minimum discharge rating is necessary to be inspected and checked.

#### IV. MODEL FORMULATION

A hybrid power system is characterized by multiple sources, with multiple variables, exhibiting high non-linearity, and constraints where the objective is minimal cost and enhanced system performance. The operation cost is also highly non-linear and is a function of the constituent sizing, load, re-sources, and dispatch strategy.

We suggest a hybrid system with components; DG system, Photo Voltaic (PV) system, wind turbine, Hydro Kinetic (HK) system, and battery system as depicted in Fig. 1. The operation model is a representation of how the components of the hybrid power system interact, how energy flows between the components, the losses that occur in the transformation of energy, and control of the overall system [19].

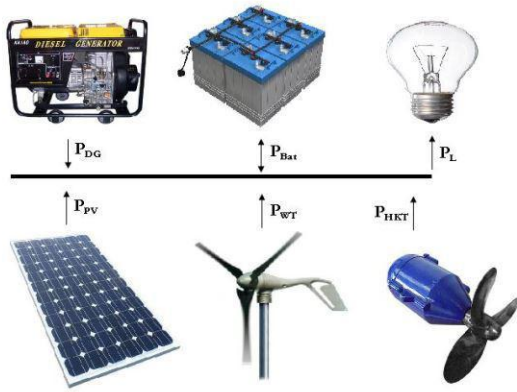


Figure 1. Components of the Proposed Hybrid System

The battery charging is only from HK turbines, the wind turbines, or from PV cells, and DG if used will only be supplying to the load and battery charging will not occur from DG. This configuration has the significance of effectively using renewable resources and the energy is optimally used when the DG is switched on since it satisfies the load demand. For economical usage of the hybrid system and available resources, a plan is required such that the DG fuel usage is minimized, meeting the satisfaction of the load and constraints of the hybrid system. The long span cost of the system includes maintenance, fuel, lubricant, components replace, supply, and repairs. For a short span, however, the only significant cost is the fuel usage cost of the DG.

##### A. Objective Function

We wish to reduce the fuel cost of the DG in the hybrid power system. We wish to minimize the following:

$$\min \int (uP_{DG}(t) + vP_{DG}(t) + w)dt \quad (2)$$

where u, v, and w comes from the consumption plot of the DG and  $P_{DG}(t)$  is the power at the output of the DG.

##### B. Constraints

A list of the constraints is given below with a brief description where necessary:

- The power supplied by the hybrid system must meet the load demand.

$$\sum (P_{DGt} + P_{HKT} + P_{Pvt} + P_{BSt} + P_{WTt} = P_{Lt} \quad (3)$$

where the symbols are mostly self representative, showing powers from different components are the control variables which must sum to the load demand at any instant of time "t".

- All the components of the hybrid system may be subjected to their maximum output as limiting constraints, as no source is able to deliver power beyond its capacity.

$$0 \leq P_{HKT} \leq P_{HKT}^{max} \quad (4)$$

$$-P_{BSt}^{max} \leq P_{BSt} \leq P_{BSt}^{max} \quad (5)$$

$$0 \leq P_{Pvt} \leq P_{Pvt}^{max} \quad (6)$$

$$0 \leq P_{DGt} \leq P_{DGt}^{max} \quad (7)$$

$$0 \leq P_{WTt} \leq P_{WTt}^{max} \quad (8)$$

- State Variable Limits: Battery SOC At any instant of time "t", the battery SOC should be between the minimum and maximum limits as:

$$SOC_{bat}^{min} \leq SOC_{bat\ t} \leq SOC_{bat}^{max} \quad (9)$$

#### V. PROPOSED OPTIMIZATION ALGORITHM

Almost all optimization techniques use the local minima which is effective for linear problem, but in hybrid optimal control, the problem is highly non-linear in terms of resources output, load demand, and component interaction, which makes the solution to the problem rather complicated, with multiples local minima asking for algorithms to search for global minima instead of local one.

"fmincon" solver from MATLAB is used to solve this problem.

$$\min_x [g(x)] \quad (10)$$

Fmincon uses the following strategy while solving the under the restriction that one or more of the following must be true:

$$C(x) \leq 0 \quad (11)$$

and Or

$$C_{equ} = 0 \quad (12)$$

and Or

$$a_x \leq b \quad (13)$$

and Or

$$C_{equ} \leq 0 \quad (14)$$

and Or

$$a_{eqx} = b_{eqx} \quad (15)$$

and or

$$u \leq x \leq v \quad (16)$$

Fmincon is one of the most sophisticated optimization algorithm with ability to solve "Interior Point" problems, with high constraints, provides Hessian information, and robustness.

## VI. SIMULATION

We present the simulations results of optimal operation control of hybrid power system. We use the fmincon library of MATLAB for our simulations. The simulations results will confirm that, using the proposed optimal control algorithm, the system is optimized for low cost, in a fluctuating load environment. Data sets from different locations with different load profiles are used and sensible cost is computed under varying load conditions.

### A. Data Set

We provide a description of the data set used in simulations, extracted from two different sites. We extract data in the form of environment of the site, the load vs energy data, and the size of the constituent of the hybrid power system. The following two case studies are made.

### B. Case 1: Rural Household

We collect daily load data from a household usage located at a certain height. The hybrid power system design is to provide electricity to loads in the form of laptop, stove, charging, ironing, freezer, and electric kettle etc. The load profile is a function of the user requirement and behavior and also vastly depend upon the seasonal changes and time of the year. The velocities of the water, the radiations from solar system, and speeds of the wind is recorded. The least velocity of the water is recorded and is noted in the month of September. The size of the HK generator is chosen such that it provides 1 kW when the velocity of the water is 1.4 m/s.

### C. Case 2: Base Transmit-Receiver (Transceiver) Station

We chose a base station that use to transmit and receive data. The transceiver needs electrical power for its operation

(for heat removal etc). The load profile is a function the daily usage of the power as required for transmission, reception, lighting, antennas, amplifiers, water needs etc. Some of the appliances have specific time usage during the day, say air conditioning, whereas the rest of the transceiver is functioning 24 hours a day. The air conditioning is shut down during winter and is no longer needed. There are two sites at which BTSs are located, making their environment different. The HK system should supply the necessary power to the overall system during a month.

TABLE I. SPECIFICATION FOR SIMULATION

Item	Figure
Sampling Time	30 min
Battery Maximum SOC	95%
Battery Minimum SOC	40%
Battery Charging Efficiency	85%
Battery Discharging Efficiency	100%
Diesel Fuel Price	1.4\$/l
a	0.247
b	0.1
c	0.4200

### D. Component Sizing and Simulation Parameters

As stated earlier, the main focus is cost optimization of the hybrid power system. The optimal sizing of the constituents is done using HOMER. These results serve as inputs to the optimization model. For Case 1 (household load in rural area), the following hybrid system is used.

- Hydrokinetic Turbine of 3kW
- Wind Turbine of 1kW
- Photo-Voltaic system of 1kW
- Diesel Generators system of 1kW
- Battery system of 13 batteries

For Case 2 (Transceiver setup), the following hybrid system is used.

- Hydrokinetic Turbine of 2kW
- Wind Turbine of 1kW
- Photo-Voltaic system of 1kW
- Diesel Generators system of 1kW
- Battery system of 7 batteries

Tab. 1 shows the parameters of DG and battery used for simulations.

The case in which the DG alone is supplying the load is also considered for purposes of comparison.

### E. Simulation Results for Case 1 (Rural Household)

To see the impact of climatic changes on the results of the simulations, we consider two different scenarios. Two scenarios are considered in which the hybrid system is operat-

ing in different climatic conditions to supply the load. These scenarios are simulated to investigate how the climatic changes of loads and resources can influence the optimal operation of the hybrid system. Fig. 2 to fig. 5 highlight the load demand,”  $P_L$ ”, and the power at the output of the components of the hybrid power system (HK, PV, Wind, Battery, DG). The major portion of the power supply comes from the HK system, which significantly reduces the DG fuel consumption and consequent cost of the overall hybrid power system. The results are shown in Fig. 6 to fig. 8.

We conclude from the observation of the results that: The load demand in the morning and night is small, and is mostly met by the HK system. The wind turbine and PV cells are not operational in these hours as the renewable energy resources are not available at those times. We write the power balance as

$$P_{bal} = \sum(\text{Renewable Outputs}) - \text{Load}_{\text{instantaneous}} \quad (17)$$

TABLE II. DAILY FUEL COST SAVINGS

	Winter		Summer	
	Consumption (L)	Cost ( \$ )	Consumption (L)	Cost ( \$ )
DG Only	122 L	171.03\$	40.5 L	56.7\$
Hybrid System	1.84 L	2.58\$	0 L	0\$
Savings	120.16 L	168.45\$	40.5 L	56.7\$

If  $P_{bal} > 0$ , batteries are charged as we are generating more power than that required by the load, however, if  $P_{bal} < 0$ , we use the battery system for the compensation. If the demand cannot be met by both renewable resources and battery system, then DG is used to fulfill the demand.

During day time, however, due to the availability of renewable resources, major portion of power is contributed by HK, PV, wind and battery system.

The demand is at its peak, in the morning between 8 am and 10 am, and HK, PV are used at their rated capacities, whereas DG is used for compensation when needed. The time for which the DG operates, and the fuel consumption and associated cost, are all functions of the load demand, battery state of charge, and the contributions from the renewable power resources. The batteries are not charged with DG; it only compensates for the surplus demand from the load.

Once the peak demand hours are passed, the batteries get charged upto about 40%, and the power from the renewable resources exceeds the demand from the load. The batteries are charged using this extra power upto 95%.

In evening, the demand raises again, between 5pm and 10pm. A combination of HK, PV at their rated capacities with contribution from DG is used to provide for the load demand. After 6pm, however, the PV system is unable to provide any

further significant power, so the contribution from batteries and DG increases.

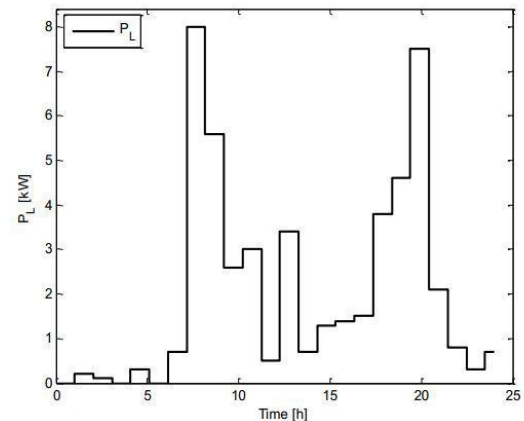


Figure 2. Sketch of Everyday Load in Winter Season

When DG is the only source, the results are shown in the Fig. 9. The DG sizing for this case should be such as it will be able to provide for the entire load alone, in the absence of renewable hybrid model.

The model proposed here is helpful in differentiating the

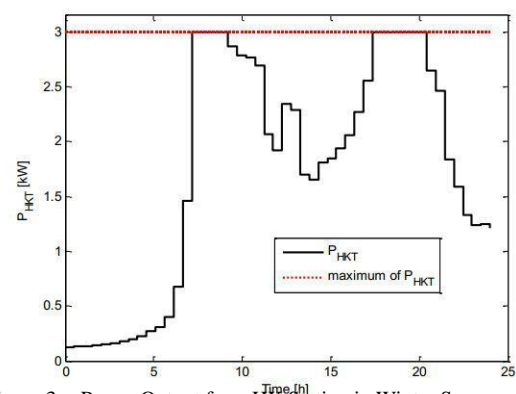


Figure 3. Power Output from HK Station in Winter Season

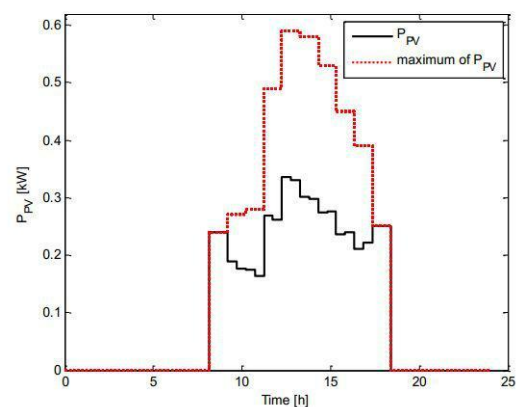


Figure 4. Power Output from PV Setup in Winter Season

behavior of the optimal operation control of the hybrid system under different weather conditions (say summer and winter) which greatly effect the DG fuel consumption and operation hours. The load demand is generally low during summer, and the renewable resources are in high availability, compared to winter. Consequently, DGs operation hours and cost are high during winter compared to summer. During summer, HK, PV, battery SOC all are high, which results in less DG usage and consequently less fuel consumption and cost. The fuel consumption cost can be computed as,

$$Cost_{day} = Price_{diesel} \left[ \frac{dollars}{L} \right] x Fuel_{used} \left[ \frac{L}{day} \right] \tag{18}$$

where the daily fuel consumption is a function of the sizing and type of the DG. Tab. 2 indicates the fuel saving by using a hybrid power system instead of a stand-alone DG system for both winter and summer day.

### F. Simulation Results for Case II (BTS)

We again assume two scenarios. The BTS load demand is a function of the BTS transceiver functions and lighting in addition with air conditioning demand, which reduces to 0 during winter, so the load demand is small during winter on the contrary to the Case I.

We make the observations below.

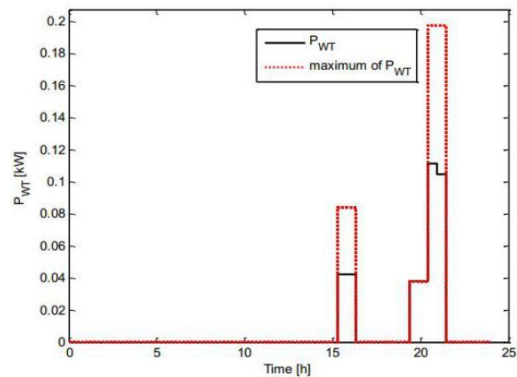


Figure 5. Power Output from Wind Power Station in Winter Season

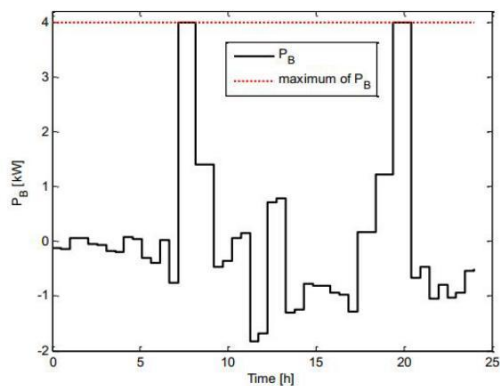


Figure 7. Power Output from battery Source in Winter Season

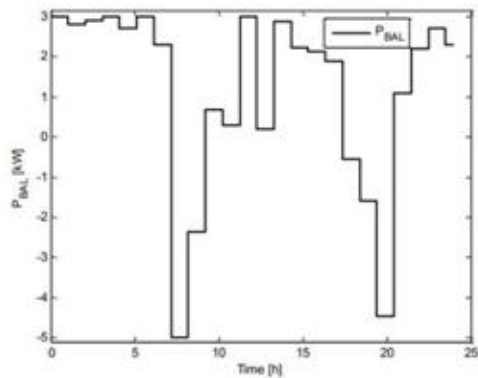


Figure 6. Crosspondenc between Load and Reneable Season during Winter

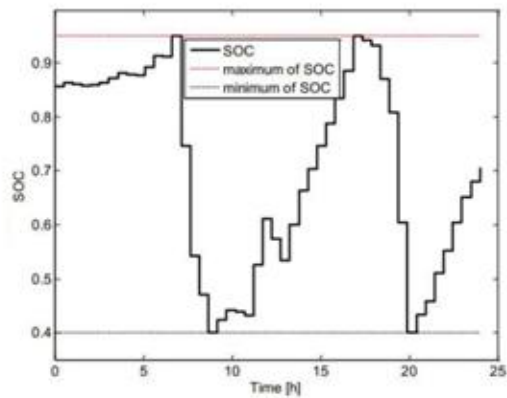


Figure 8. Changing Behaviour of Battery Charging during Winter Season

For most of the time, except when air conditioning turns on, the load demand is constant, and is supplied by the HK and battery systems. When wind, and PV are also supplying power, the surplus energy is used to charge the battery system.

When the demand is at its peak, all the components of the hybrid system, and the better system contributes towards power supply. The DG system is used in the case if there is surplus demand to compensate for the extra power needed. Once the peak demand hours are passed, the SOC reduces to the minimum of 40% and the load demand must be met by the hybrid system renewable resources.

The demand for transceiver is high during summer compared to winter for which a comparison is made on the daily basis. The results show that DG are highly used in summer compared to winter for providing additional air conditioning. The non-linear behaviour of both the loads as well as the renewable resources is evident from the results shown for daily operation cost minimization. Compared to the household Case I, Case II (BTS) uses more diesel fuel in summer day than winter day. We analyse how different DG and battery control settings effect the performance of the simulation results, Even if we have DGs with same kilowatt ratings, their fuel consumption plots will differ if they are coming from different manufacturers.

We can customize the limits for battery operation which will have a significant impact on the simulation results of the hybrid power systems operation cost. We use Case 1 which uses data from the household appliances to illustrate the purpose. If the battery can last for longer, the fuel consumption of DG can be reduced and its life span can be enhanced significantly. This, however, may reduce the life of the battery and may need frequent replace. So a trade off has to be made between battery life span, and the fuel consumption and life span of the DG.

We conclude that:

- Compared the operation cost of different DGs from different manufacturers to see which cost is the lowest.
- The impact of battery setting is analyzed on the results of simulations and it is seen that deep charged batteries can enhance DGs performance at the cost of reduced battery life span.
- The impact of load variations due to seasonal changes and the fluctuating behaviour of the renewable resources is considered.
- Highlight the significance of HK module for cost mini-mization of the hybrid system.

The algorithm, and model used in this study is not complex and easy to implement with fast computations and results generation.

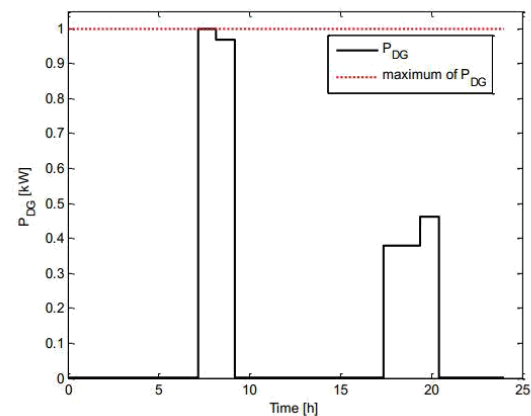


Figure 9. Output Power Vs Optimal Scheduling of DG in Winter Season

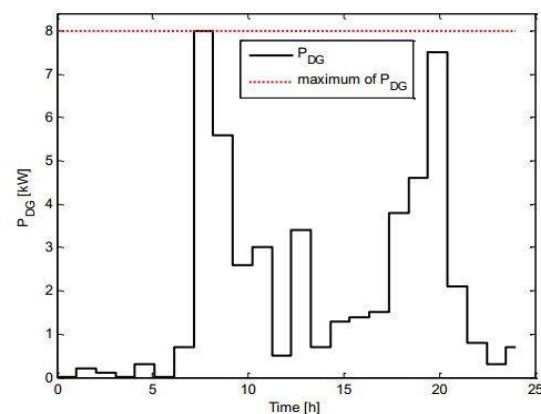


Figure 10. Output Power Vs Optimal Scheduling in Winter Season when Only DG is Considered

## CONCLUSION

This section pivots around the results drawn from the optimal and advantageous operation and simulations of a system consisting of many energy sources. The sources includes PV module, wind turbine, HK and DG. Battery bank also makes part of the system. In a compound system consisting of many sources, the variation between weather conditions and load is a main entanglement in the operation of the system. The cost of the system mainly depends on the aforementioned concern. The study was based to find an optimal way to operate either a single unit of power or a combination of different to reduce the cost factor to a minimum value. As a return the cost of daily operation of the standalone system is significantly reduced. The main aim is to reduce the duration of the operation of DG while prolonging the operation of renewable sources. The idea is to use the renewable sources for maximum possible time. The algorithm selected for optimized operation is fmincon solver with Interior Point. Focus is made on the different non linearities involved in the process. Due to the intermittent behavior of renewable sources the solar irradiation, velocity of water at each hour and wind speed date have been used in the simulation. The simulation also includes the load demand and the fuel consumption of the DG system. The introduction of the



non linear and intermittent behavior of the renewable sources gives accurate results of the operational cost.

#### ACKNOWLEDGMENT

The authors would like to thank US Pakistan Center for Advanced Studies in Energy, UET Peshawar. We are grateful to Dr. Abdul Basit for his sincerity and devotion towards us.

#### REFERENCE

- [1] Ardakani, Fatemeh Jahanbani, Gholamhossein Riahy, and Mehrdad Abedi. "Design of an optimum hybrid renewable energy system considering reliability indices." *Electrical Engineering (ICEE)*, 2010 18th Iranian Conference on. IEEE, 2010.
- [2] Ardakani, Fatemeh Jahanbani, Gholamhossein Riahy, and Mehrdad Abedi. "Optimal sizing of a grid-connected hybrid system for north-west of Iran-case study." *Environment and Electrical Engineering (EEEIC)*, 2010 9th International Conference on. IEEE, 2010.
- [3] Ashari, Mochamad, and C. V. Nayar. "An optimum dispatch strategy using set points for a photovoltaic (PV)CdieselCbattery hybrid power system." *Solar Energy* 66.1 (1999): 1-9.
- [4] Bajpai, Prabodh, and Vaishalee Dash. "Hybrid renewable energy systems for power generation in stand-alone applications: a review." *Renewable and Sustainable Energy Reviews* 16.5 (2012): 2926-2939.
- [5] Bakare, G. A., et al. "Differential evolution approach for reactive power optimization of Nigerian grid system." *Power Engineering Society General Meeting*, 2007. IEEE. IEEE, 2007.
- [6] Banos, Raul, et al. "Optimization methods applied to renewable and sustainable energy: A review." *Renewable and Sustainable Energy Reviews* 15.4 (2011): 1753-1766.
- [7] Barley, C. Dennis, et al. Optimal control of remote hybrid power systems. Part 1: Simplified model. No. NREL/TP-441-7806; CONF-950309-3. National Renewable Energy Lab., Golden, CO (United States), 1995.
- [8] Bashir, Mohsen, and Javad Sadeh. "Optimal sizing of hybrid wind/photovoltaic/battery considering the uncertainty of wind and photo-voltaic power using Monte Carlo." *Environment and Electrical Engineering (EEEIC)*, 2012 11th International Conference on. IEEE, 2012.
- [9] Bashir, Mohsen, and Javad Sadeh. "Size optimization of new hybrid stand-alone renewable energy system considering a reliability index." *Environment and Electrical Engineering (EEEIC)*, 2012 11th International Conference on. IEEE, 2012.
- [10] Bernal-Agustín, Jos L., and Rodolfo Dufo-Lopez. "Simulation and optimization of stand-alone hybrid renewable energy systems." *Renewable and Sustainable Energy Reviews* 13.8 (2009): 2111-2118.
- [11] Borowy, Bogdan S., and Ziyad M. Salameh. "Methodology for optimally sizing the combination of a battery bank and PV array in a wind/PV hybrid system." *IEEE Transactions on energy conversion* 11.2 (1996): 367-375.
- [12] Chen, Fengzhen, et al. "Renewable energy solutions for islands." *Renewable and Sustainable Energy Reviews* 11.8 (2007): 1888-1902.
- [13] Connolly, David, et al. "A review of computer tools for analysing the integration of renewable energy into various energy systems." *Applied energy* 87.4 (2010): 1059-1082.
- [14] Dagdougui, Hanane, et al. "A dynamic decision model for the real-time control of hybrid renewable energy production systems." *IEEE Systems Journal* 4.3 (2010): 323-333.
- [15] Maniaci, David C., and Ye Li. Investigating the influence of the added mass effect to marine hydrokinetic horizontal-axis turbines using a General Dynamic Wake wind turbine code. IEEE, 2011.
- [16] Dagdougui, Hanane, et al. "Modelling and control of a hybrid renewable energy system to supply demand of a green-building." 5th Biennial

Conference of the International Environmental Modelling and Software Society: Modelling for Environment's Sake, iEMSs 2010. Vol. 2. iEMSs Secretariat c/-IDSIA, Galleria 2, Manno, 6928, Switzerland, 2010.

- [17] Dehghan, S., et al. "Optimal sizing of a hybrid wind/PV plant considering reliability indices." *World Academy of Science, Engineering and Technology* 56.32 (2009): 527-535.
- [18] Afzal, Anis, Mohibullah Mohibullah, and Virendra Kumar Sharma. "Optimal hybrid renewable energy systems for energy security: a comparative study." *International Journal of Sustainable Energy* 29.1 (2010): 48-58.
- [19] Diaf, Said, et al. "A methodology for optimal sizing of autonomous hybrid PV/wind system." *Energy Policy* 35.11 (2007): 5708-5718.



Engineer In MEPCO.

**Muhammad Waseem** graduated from COMSATS University Islamabad in 2013. He holds B.Sc degree in Electrical Engineering. He is currently enrolled in M.Sc Electrical Energy Systems Engineering at US Pakistan Center for Advanced Studies in Energy (USPCASE) UET Peshawar. His major field of study is Electrical Power Engineering. Currently he is working as Junior



**Abdul Basit** completed his B.Sc. degree in electrical engineering from University of Engineering & Technology (UET) Peshawar, Pakistan in 2006. He received his M.Sc. degree in electrical power engineering from Chalmers University of Technology, Sweden in 2011 and his PhD from the Department of Wind Energy of the Technical University of Denmark (DTU) in 2015. He is currently working as Assistant professor at U.S. Pakistan Center for Advanced Studies in Energy (USPCASE) of the University of Engineering & Technology (UET) Peshawar. His research interests are on protection, power factor improvement, power system operation, renewable power integration and automatic generation control.



Currently he is working as Junior Engineer In MEPCO.

**Imran Khan Khan** graduated from University of Engineering and Technology (UET) Peshawar in 2014. He holds B.Sc degree in Electrical Engineering. He is currently enrolled in M.Sc. Electrical Energy Systems Engineering at US Pakistan Center for Advanced Studies in Energy (USPCASE) UET Peshawar. His major field of study is Electrical Power Engineering.



# A Qualitative Overview of Fuzzy Logic in ECG Arrhythmia Classification

Ahmed Farhan<sup>1</sup>, Chen Li Wei<sup>2</sup>, Md Toukir Ahmed<sup>3</sup>

<sup>1,2,3</sup>College of Information and Communication Engineering, Harbin Engineering University, China  
ahmedfarhanzisan77@yahoo.com<sup>1</sup>

Received: 24 October, Revised: 30 October, Accepted: 05 November

**Abstract-** Achieving elevated efficiency for the classification of the ECG signal is a noteworthy issue in the present world. Electrocardiogram (ECG) is a technique to identify heart diseases. However, the detection of the actual type of heart diseases is indispensable for further treatment. Various techniques have been invented and explored to categorize the heart diseases which are recognized as arrhythmias. This paper aims to investigate the development of various techniques of arrhythmia classification on the basis of fuzzy logic along with an elaborative discussion on accepted techniques. Moreover, a comparative study on their efficiency has been analyzed to emphasize the scope of novel research areas.

**Keywords** — Arrhythmias, Electrocardiogram, Fuzzy logic, Fuzzy Classifier, Fuzzy Inference System.

## I. INTRODUCTION

Preceding researches and studies over decades have resulted in radical development and advancement of many ECG arrhythmia classification techniques for heart disease. Heart is one of the basic organs of the human body which is like a pump made up of muscle tissue. Heart conducts the blood circulation in the human body. Among many heart diseases, some can become severe at times which is why an appropriate diagnosis, detection, and treatment of heart diseases are essential. Electrocardiogram or ECG is a well-recognized technique to detect heart diseases.

### A. ECG Signal

According to some researchers, four essential processes are required to perform an accurate diagnosis of heart disease and arrive at a quick decision [1]. These include data compression, de-noising, feature extraction, and classification. The heart is monitored by placing sensors at the limb extremities of the subject; Electrocardiogram (ECG) is a documentation of the foundation and the dissemination of the electrical potential in the course of cardiac muscles [2].

Two kinds of information can be extracted from an ECG signal. Firstly it can be determined whether the electrical activity is normal or slow, fast or irregular by measuring the time interval (duration of electrical wave crossing the heart). Secondly, by determining the amount of electrical activity

passing through the heart muscle, a cardiologist can find out if parts of the heart are too large or overworked. The frequency range of an ECG signal is 0.05 – 100 Hz and its dynamic range is 1-10 mV [2]. One cardiac cycle in an ECG consists of the P, Q, R, S and T waves [3]. An excellent performance of an ECG investigating scheme depends greatly upon the exact and dependable detection of the QRS complex, along with the T and P waves [2].

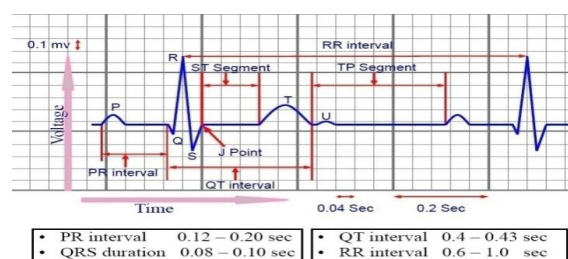


Figure 1 The normal ECG waveform

The P wave lasts about 0.08 seconds and denotes the pumping out of the blood through atrial contraction [3]. The PR interval is calculated from the beginning of the P wave up to the beginning of the Q wave. It symbolizes the length of atrial depolarization. The following portion of the signal is the 'QRS complex' which denotes the interval of ventricle depolarization. This part represents the time duration of the contraction to pump out blood to the entire body via the ventricles. Its standard period is from 0.08 – 0.12 seconds. The next rising section is recognized as 'ST segment', which points out the time interval from the ending of the contraction of the ventricles to the starting of the remaining period. This segment is crucial in order to identify myocardial infarctions and ischemia [4]. The inactive period of the ventricles is denoted by the T wave which exists for 0.16 seconds [3].

### B. Arrhythmias

The unusual or unbalanced rhythm of the heart is recognized as an arrhythmia. Sometimes, the heart pumps very promptly and at times it pumps at a snail's pace. Low blood pressure, dizziness, weakness, exhaustion, fainting and palpitations are several signs of arrhythmia. The cause of arrhythmia is because of the deviations or irregularities in the heart rate. Undeniably Arrhythmias are characterized by ECG Signal [5]. The outline of ECG is changed by reason of arrhythmias. The pattern of ECG signals varies differently for a

variety of arrhythmias. The early analysis of arrhythmia is indispensable for its treatment. If arrhythmia lasts for a long time, then the heart has a high risk to be damaged eternally [4]. Some notorious kinds of arrhythmias are sinus tachycardia, sinus arrhythmias, sick sinus syndrome, premature atrial contractions, paroxysmal atrial tachycardia, atrial flutter, atrial fibrillation are some of the regular atrial arrhythmias and premature ventricular contractions, ventricular tachycardia, and ventricular fibrillation are some familiar ventricular arrhythmias [4].

## II. LITERATURE REVIEW

Appropriate classification of ECG arrhythmias is obligatory to ensure apposite treatment to the patients. Researchers and scientists have explored and invented different types of processes and models to investigate and categorize ECG arrhythmias with the course of time.

### A. Classifier

A classifier is a structure where a rule-based algorithm is used as the foundation. The classifiers apply training algorithms as well as training data sets. If the training data set is unavailable, it can be planned from preceding knowledge. Training is required to make the classifier geared up for operation [6]. The classifier follows some rules and they are represented in the shape of 'If condition Then action' [7].

### B. Various methods for classification of Arrhythmias

Researchers and scientists have anticipated many procedures to classify ECG arrhythmias. For instance, fuzzy classifier [1], wavelet neural network [8], improved classification performance of Linear Feature Extraction [9], correlation dimension and largest Lyapunov exponent [10], wavelet transform and time intervals methodology [11], multiple signal classification algorithm [12], and efficient formation of morphological wavelet transform features along with the temporal features of the ECG signal [13]. Many investigations have developed numerous methodologies for classifying ECG signals like supporting vector machines for cardiac beat detection [14, 15, 16], Artificial Neural Network (ANN) [17, 18], Fisher Linear Discriminate Analysis (FLDA) technique [19], Hermite functions and self-organized map [20, 21], Heartbeat interval combined with the shape and morphological properties of the ECG parameters [22], multi-lead based on random projection feature [23], analysis by Hilbert transform [24, 25], extreme learning machine [26], logistic model tree [27], Gaussian mixture model [28] etc. There are also some models which are based on the combination and correlation of the methods mentioned above. In some cases, the hybrid and combined methods proved superior result to the individual techniques. In this paper, we have talked elaborately about fuzzy logic and involvement of modern research in ECG arrhythmias detection based on fuzzy logic.

### C. Fuzzy Logic

Zadeh was the pioneer of Fuzzy logic. It has multiple values and is parallel to human thoughts. Conventional Boolean and Aristotelian logic handle just absolute values of 0

and 1 along with true or false. On the other hand, fuzzy logic does not work like that. It does not follow a linear function always and deals with the phenomena not having absolute value.

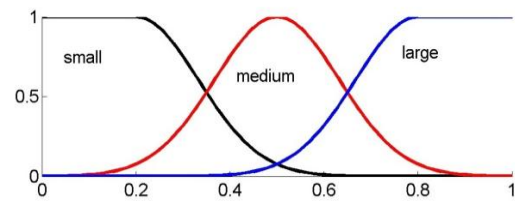


Figure 2 Fuzzy Logic

A conventional set of binary logic considers crisp values while fuzzy sets have fuzzy values with only linguistic variables and can be defined as low, medium and high. The values having fuzzy boundaries can overlap each other [29].

### D. Fuzzy Inference System(FIS)

FIS is an outline where fuzzy sets, fuzzy rules, and fuzzy reasoning are the foundations. Fuzzy reasoning is an estimated reasoning. It illustrates the endings from the fuzzy sets and fuzzy rules.

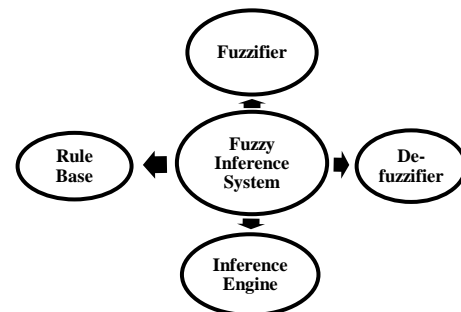


Figure 3 Fuzzy Interface System

It consists of the following four apparatus: fuzzifier, rule base, inference engine, and defuzzifier. Fuzzy sets are formed from the crisp value in fuzzifier along with the formation of fuzzy rules. The inference engine relates the fuzzy rules with the fuzzy sets. The fuzzy output is determined by it and the output is a fuzzy value. In addition to this, the crisp value is found as output by defuzzification process [29].

Fuzzy logic is to some extent beneficial because it is adaptable and cost-effective and it does not require specific and noise-free input. The structure can be designed easily with numerous inputs and outputs because it conducts a rule-based operation. It can model non-linear functions of random complexity and manage those types of non-linear structures whose mathematical models would be complicated [30]. Nevertheless, Fuzzy logic poses exigent difficulties as the membership functions are complicated to a certain extent in nature as well as a collection of too many data for this process becomes a topic of being concerned [29].

### E. Applications of fuzzy logic

The purposes of Fuzzy logic to categorize ECG arrhythmias are highlighted in this review paper. This scheme

can also be utilized in modulation classifier for non-ideal atmosphere. On the other hand, it becomes quite convoluted when a specific probabilistic process is implied according to the suggestion of researchers [31]. Additionally, Fuzzy ‘if-then’ rules already have been applied in different image processing applications [32]. In recent days, researchers estimated the performance of a fusion system using Artificial Neural Network (ANN), Gaussian Mixture Model and Fuzzy Rule-based Classifier to make the detection of H1N1 possible [33]. Fuzzy rule-based classification coordination has been executed in case of pattern classification concern. Due to this case, the learning procedure based on error correction and additional learning procedure is obligatory [34]. In order to execute pattern recognition, a small number of schemes have been employed by researchers over years. For instance, Type-2 Fuzzy sets were used for the pattern recognition procedure [35]. Subsequently, Genetic Fuzzy and Neuro-fuzzy classifier were comprehensively investigated and implemented for credit scoring. The Genetic Fuzzy classifier has given a better accuracy in this case [36].

Furthermore, fuzzy classified data and fuzzy classifier were implemented in medical proteomics which is an elementary apparatus for learning the peptide and protein level in medicine and health care [37]. Fuzzy rules have also been implemented in high-resolution multispectral satellite images which are needed to classify urban and suburban regions [38].

### III. FUZZY CLASSIFIER FOR ECG ARRHYTHMIAS DETECTION

The fuzzy method is very effectual for clinical analysis. Indeed there are several methods on the basis of fuzzy logic and the combination of fuzzy logic with other logics. Fuzzy classifier implements fuzzy logic or sets in order to classify training data.

#### A. Simple Fuzzy Classifier

There are basically two foremost function blocks in this classifier. The first one is ECG parameterizer and the next one is Fuzzy Classifier. ECG Parameterizer is comprised of initialization, pre-processing, fuzzification and defuzzification. After these processes, data is sent to the fuzzy classifier for classification purpose where the fuzzy logic and if-then rule is applied [1]:

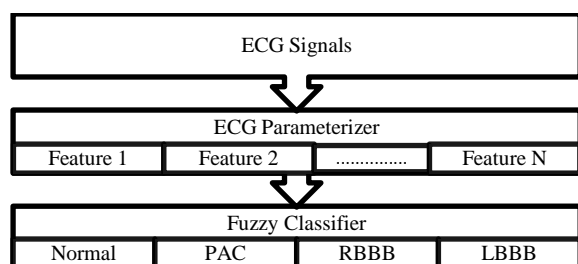


Figure 4 Structure of Fuzzy Classifier [40]

For the classification of ECG arrhythmias using the fuzzy classifier, some ECG patterns and linguistic variables are required, which are tabulated below.

TABLE I. ECG PATTERNS AND LINGUISTIC VARIABLES [40]

ECG features	Medical linguistic variables
Prior-Heart Rate (RR0)	{Short; Normal; Long}
Post-Heart Rate (RR1)	{Short; Normal; Long}
P Wave	{Early; Normal; Disappear}
QRS Complex	{Upward; Downward}
R Wave Amplitude	{High; Normal; Low}
T Wave	{Upward; Downward; Disappear}

It is already mentioned that whole classification begins with the initialization step, where ECG data is read from the database which has already been used. ECG features are revealed in the pre-processing step. Then the crisp values are altered into linguistic or fuzzy variables and after that membership functions are designed in the fuzzification step. The output comes as fuzzy value. Afterward, fuzzy values are defuzzified in order to receive crisp values as output in the defuzzification step [1].

TABLE II. DEFINITION OF THE MEMBERSHIP FUNCTION FOR NORMAL BEAT [40]

Characteristic	Feature	Function Type	Parameter (a)	Parameter (b)
P up-ward	P peak value	S	0.10 mV	0.15 mV
QRS up-ward	R peak Value	S	0.70 mV	0.80 mV
T up-ward	T peak Value	S	0.10 mV	0.15 mV
RR0	Prior-HR	Gaussian	80 bpm	20 bpm
RR1	Post-HR	Gaussian	80 bpm	20 bpm

The tabulated characterization is only relevant to the normal beat. After the completion of the fuzzification step, the incoming aspects are expressed by a membership value [0, 1]. The inference method uses if-then rule. For instance:

IF (“Feature 1” is “Linguistic Variable 1”) AND  
 (“Feature 2” is “Linguistic Variable 2”) AND  
 ...  
 (“Feature N” is “Linguistic Variable N”)  
 THEN (Name of the Class)

Now, in the case of LBBB, the statements are-  
 The direction of T wave and the QRS complex is opposite to each other.  
 Prior Heart Rate RR0 is small.  
 P wave is disappeared.

So, the LBBB classification can be described as

IF (“T wave is upward”) AND  
 (“QRS wave is downward”) AND  
 (“P wave is disappeared”) AND  
 (“RR0 is small”)  
 THEN (Left Bundle Branch Block)

In this rule, the linguistic values are upward, downward, disappeared and small. The product of the membership grades [0, 1] is considered as the hypothesis. If the product goes beyond the limit, then the beat is considered as LBBB.

### B. Adaptive Fuzzy Classifier

Investigations have revealed that an adaptive fuzzy ECG classifier can be used for superior accuracy. This system is in a need of a learning stage in order to optimize the system parameters like threshold values and membership boundaries. The margin values in the membership function are fixed roughly during the learning stage. A predefined rule set is used to categorize a precise beat appropriately. The margin values in the membership function are customized using the noteworthy values of these pre-classified beats. For each record, pre-classification, and self-adaptation take the first 10 minutes in the learning and testing purpose in total time of 30 minutes. The rest 20 minutes is allocated in order to test the updated AFC-ECG [39].

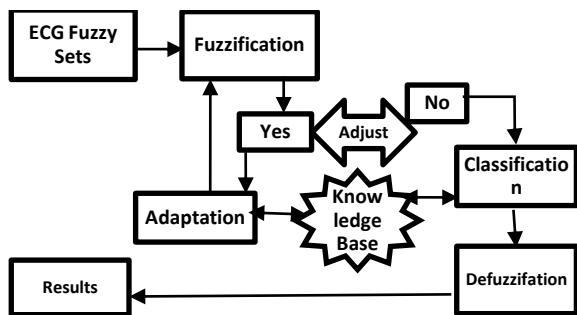


Figure 5 Adaptive Fuzzy ECG Classifier [39]

This process showed excellent performance for classifying ECG signals.

TABLE III. PERFORMANCE COMPARISON OF FUZZY CLASSIFIER AND ADAPTIVE FUZZY ECG CLASSIFIER [39]

Rec ord	MIT-BIH Annotation		Fuzzy Classifier		Adaptive Fuzzy Classifier	
			Result	Accur acy	Result	Accur acy
Sig 106	Normal	1507	1208	80.2%	1258	83.5%
	PAC	0	7	-	1	-
	RBBB	0	30	-	27	-
	LBBB	0	0	-	1	-
	Unclass ified	0	262	-	220	-

The accuracy of adaptive fuzzy ECG classifier is approximately 88.2% on an average [39], which is about 77.0% in case of usual fuzzy ECG classifier [40].

### C. Fuzzy C-means Clustering method (FCM)

Data clustering is used to locate the similarities in data and puts similar data into analogous groups. FCM is a method which deals with data clustering algorithm. In this process, each data point belongs to a cluster to a degree which is specified by a membership grade. The FCM algorithm has four steps. In the beginning, the membership matrix is originated with arbitrary values between 0 and 1. Then c-fuzzy cluster centers are determined and then cost function is computed. The computation should be stopped if it is lower than a certain tolerance value. Also, if its enhancement over the preceding iteration is lower than a certain threshold, then the computation should be brought to an end. In this manner, a new membership matrix is required to be computed and ultimately c-fuzzy cluster centers are calculated once more [41].

TABLE IV. RESULT OF FUZZY CLASSIFIER BASED ON THE FCM CLUSTERING [41]

Type	Sensitivity	Positive Prediction	Accuracy
Normal	99.66%	96.76%	97.41%
LBBB	96.33%	98.29%	
RBBB	98.66%	95.79%	
PB	95.00%	98.95%	

This proposed technique demonstrated an accuracy of 97.41%, which can be considered as an outstanding performance for ECG arrhythmia classification.

R. R. Gharieb, M. Massoud, S. Nady, and M. Moness have established a novel scheme for ECG categorization by adopting linear discriminate analysis (LDA) and minimum distance (MD) in a projected feature space [42]. Continuous wavelet transform of the ECG signal has been applied for the purpose of feature extraction that was followed by Teager-Kiaser Energy (TKE) operator. TKEs were picked appreciably. They were changed to [0, 1] range and were exploited as a feature vector. FCM clustering algorithm was used with the purpose of producing the samples of different categories in the feature space. This method has endowed with 100% accuracy so as to classify PVC and normal beats with MD classifier.

### D. Combination of Wavelet Transform and Fuzzy Neural Network for VPC Detection

Another research paper (Shyu et al., 2004) has focused on the combination of Wavelet Transform and Fuzzy Neural Network with the purpose of detecting the ventricular premature contraction (VPC). The information that is used during the detection of QRS duration is reused in this technique as a positive aspect. The QRS duration is taken in scale three and the area under the QRS complex is taken in scale four. These are regarded as the characteristic features. The R wave amplitude also influences the calculation of the characteristic

features. The LBBB beats are eradicated here. The accuracy for VPC classification using FNN has been demonstrated to be 99.79% [43].

#### E. Fuzzy Support Vector Machine

The method FSVM assigns a range of fuzzy membership values which are necessitated to delineate membership functions. For the computation of membership degree, traditional membership functions are employed. The data specific membership functions can also be exploited. In order to allocate the degree of membership, four functions are used which incorporate one class weighing (OCW), Distance to Class Mean (DTCM), Distance to One Class Mean (DTCOM), Cardinality (CAR) and Fuzzy C-Means (FCM). The projected method is applied to the UCI Arrhythmia Database. To facilitate the dimension reduction, four techniques are brought into play which included Principal Component Analysis (PCA), Factor Analysis (FA), Recursive Feature Elimination with Support Vector Machine (RFE-SVM) and Correlation-based Feature Selection (CFS). Researchers have found different accuracies using these membership functions which are tabularized below [44].

TABLE V. ACCURACY COMPARISON [44]

	PCA	FA	RFE-SVM	CFS
MLP	72.86	79.52	79.05	80.48
SVM	78.57	82.62	82.14	81.43
FSVM-DTCM	78.09	80.71	80.48	83.33
FSVM-DTCOM	78.33	80.95	80.71	82.86
FSVM-CAR	77.62	82.14	80.48	81.67
FSVM-FCM	78.33	82.14	81.19	81.90

#### F. Fuzzy-Genetic Based PCA and ICA

The research paper (Murugan et al, 2010) has highlighted Principal Component Analysis (PCA) and Independent Component Analysis (ICA) techniques for the detection of a different category of arrhythmias. Fuzzy-Genetic based PCA (FGPCA) and Fuzzy-Genetic based ICA (FGICA) are the combination of Fuzzy C-Means (FCM) and Genetic Algorithm (GA) along with PCA and ICA [45]. An accuracy assessment between Fuzzy-Genetic Based PCA and ICA is tabulated in the following:

TABLE VI. COMPARISON OF ACCURACY BETWEEN FUZZY-GENETIC BASED PCA AND ICA [45]

Methods	Accuracy
PCA	86.7%
GPCA	90%
ICA	91%
GICA	93.3%
FGPCA	94.4%
FGICA	94.7%

So, the accuracy of FGPCA is 94.4% and FGICA is 94.7%.

#### G. Hybrid System by Fuzzy KNN, Multi-layer Perceptron

Another research paper (Ramírez et al., 2010) has recommended an innovative technique where Multi-Layer Perceptron with Gradient Descent, fuzzy K-nearest neighbor and momentum Backpropagation and Multi-Layer Perceptron with Scaled Conjugate Gradient Backpropagation classifiers have been used. At the outset, outputs of these classifiers are figured and then they are merged with Mamdani type fuzzy inference system which established enhanced accuracy. In this paper researchers classified LBBB, RBBB, PVC and Fusion Paced and Normal arrhythmias using this method [46].

TABLE VII. COMPARISON OF ACCURACY BETWEEN THREE CLASSIFIERS WITH THE HYBRID METHOD OF THEIR COMBINATION [46]

Method	Accuracy
First Classifier	95.33%
Second Classifier	96.67%
Third Classifier	97.33%
Hybrid Classifier	98%

#### H. Pruned fuzzy K-nearest neighbor classifier

Researchers have developed a simple system namely Pruned Fuzzy K-nearest neighbor which is proficient to classify six types of ECG beats of MIT-BIH Arrhythmia database. The accuracy of this technique is quite analogous as typical FKNN although it lessens the computational complication. The calculation time is found near to the ground compared to FKNN. 11 features have been applied in PFKNN. However, through the use of PCA, these features can be diminished to 6 features. The accuracy of FKNN is found to be 97.63% whereas the accuracy of PFKNN is found to be 97.32% with 11 features and 97.31% with 6 features [47].

#### I. Adaptive neural fuzzy filter method

Another research paper by Golpayegani et al. [48], 2009 has pioneered an Adaptive Neural Fuzzy Filter (ANFF) method for early diagnosis of ECG arrhythmia. ANFF can learn itself according to numerical training data or through proficient knowledge which is extended by the fuzzy if-then rules. This procedure is configured in five layers. Layer-1 nodes are input nodes which represent input variables. Layer-2 and layer-4 nodes are term nodes which act as the membership functions and represent the terms of respective input and output variables.

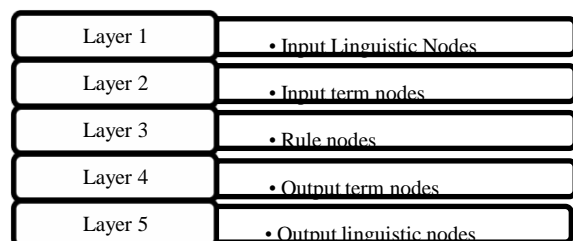


Figure 6 Structure of Adaptive Neural Fuzzy Filter (ANFF) [48].

The layer-3 node is a rule node which specifies the fuzzy logic rule. The linkage between layer-3 and layer-4 function proceed as a connectionist inference engine. Layer-5 nodes act as output nodes which characterize the output variables. In

accordance with the research paper, the structure learning step is comprised of three learning processes which include input fuzzy clustering process, output fuzzy clustering process and mapping process [48]. The accuracy of this process has been revealed to be about 97.6%. This method can be considered satisfactorily for classifying ECG beat.

#### J. Adaptive Neuro-Fuzzy Inference System

Adaptive Neuro-Fuzzy Inference System (ANFIS) was developed with a view of classifying Electrocardiogram (ECG) signals. ICA has been implied to extract features. The feature extraction and Power spectrum with the RR interval serve as the input feature vector and is used as input in the ANFIS classifier. Researchers were capable to classify six types of ECG signals such as normal sinus rhythm (NSR), atrial premature contraction (APC), Ventricular Tachycardia (VT), premature ventricular contraction (PVC), Ventricular Fibrillation (VF) and Supraventricular Tachycardia (SVT) implementing this method. It is indeed the combination of Neural Network Adaptive Capabilities and the Fuzzy Inference System has provided an accuracy of more than 97% [49] and 96% [50].

#### K. Combination of fuzzy c-means clustering (FCMC) algorithm and neural networks

Another research work introduced FCMCNN which is the combination of fuzzy c-means clustering (FCMC) algorithm and neural networks (NN).

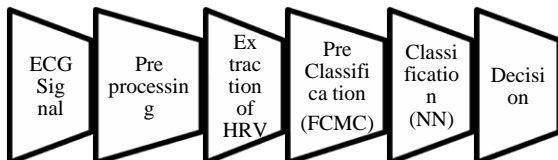


Figure 7 Block diagram of FCMCNN [51]

This combined technique showed the correct classification rate as 99.99% [51].

#### L. Multi-class MLP ECG classifier using FCM

MLP system has an intrinsic formation. This system is time-consuming and bulky. Researchers have shown the progress of MLP system due to the proficient use of FCM. According to the research findings, the total system proved to be faster and more efficient [52].

#### M. Type-2 fuzzy clustering neural network

Type-2 fuzzy c-means clustering is applied in order to enhance the performance of neural network. Different types of arrhythmias for instance normal sinus rhythm (N), ventricular tachycardia (VT), sinus arrhythmia (SA), sinus bradycardia (Br), atrial pre-mature contraction (APC), atrial fibrillation (A.Fib), atrial flutter (A.Fl.), paced beat (P), right bundle branch block (RBBB) and left bundle branch block (LBBB) are considered for this technique [53].

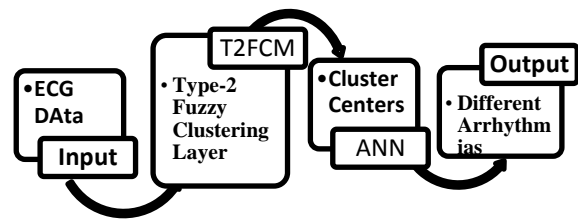


Figure 8 Optimum T2FCNN architecture [53].

The precision of this method is 99.99%. So, this technique is more efficient than other methods [53].

#### N. Fuzzy Gaussian Neural Network (FGNN)

Some research works have shown FGNN as another technique for heart disease diagnosis. The main stages of this technique include Feature extraction from the QRST zone of ECG signals and Pattern classification for IHD diagnosis using the FGNN. This process has four layer structures. They are layer 1, layer 2, layer 3 and layer 4 [54].

#### O. Fuzzy Logic Classification (FLCL) method for VT, OVF and DVF detection

In order to classify ECG arrhythmias into ventricular tachycardia (VT), organized ventricular fibrillation (OVF) and disorganized ventricular fibrillation (DVF), FLCL method has been proved as a proficient method [55]. This technique aims to combine ten ECG detectors which have been calculated in both time and frequency domain. With a two-leveled classification, VT has been detected at first with 92.6% accuracy. The inequity between DVF and OVF was perceived with 84.5% accuracy [55].

#### P. Hybrid model of Wavelet Packet tree and Neuro Fuzzy Network

The research paper [56] has proposed a hybrid model of ANN and Neuro-fuzzy network. This hybrid method has used an algorithm on the basis of wavelet packet tree (WPT) classifier in order to detect QRS complex. By using WPT technique, a set of linear (frequency and time domain) characteristic features have been taken out. A set of non-linear characteristics from the real-time ECG signal have been extracted by exploiting Neuro-fuzzy technique. The hybrid network presents a superior and highly trustworthy error minimization as the result compared with the ANN process.

### IV. RESULT COMPARISON OF DIFFERENT METHODS USING FUZZY LOGIC

In this review paper, different methods, their methodologies, and outcomes are compared and analyzed. Some of the methods are very efficient for classifying ECG data. The comparison between the percentages of the accuracy of the methods discussed above is given below in a tabular form.

TABLE VIII. COMPARISON OF ACCURACY BETWEEN DIFFERENT FUZZY LOGIC METHODS

Method	Reference	Accuracy
Simple Fuzzy Classifier	[40]	77%



Adaptive Fuzzy ECG Classifier	[39]	88.2%
Fuzzy c-means clustering method	[41]	97.41%
Fuzzy Genetic based PCA method	[45]	94.4%
Fuzzy Genetic based ICA method	[45]	94.7%
Hybrid Fuzzy KNN, Multi Layer Perceptron	[46]	98%
Standard FKNN	[47]	97.63%
PFKNN (With 11 Features)	[47]	97.32%
PFKNN (With 6 Features)	[47]	97.31%
Adaptive Neural Fuzzy Filter	[48]	97.6%
Adaptive Neuro-Fuzzy Inference System	[49]	More than 97%,
	[50]	More than 96%
FCMCNN	[51]	99.99%
T2FCM	[53]	99.99%
FLCL	[55]	92.6%

#### ACKNOWLEDGMENT

For the accomplishment of this review paper, we would like to acknowledge the efforts of Rumana Tasnim, the respected faculty member of 'World University of Bangladesh' with appreciation whose support in reviewing the quality of the paper was very significant.

#### CONCLUSION

This paper has aimed to focus on the succeeding development and historical advancement review on different methods based on fuzzy logic and their accuracy in classifying ECG arrhythmias. Also, efficiency and accuracy evaluation, as well as theoretical basics of these techniques, has been presented in this paper. Many methods have not been combined with fuzzy logic whereas the combination of them with fuzzy logic have been proposed and implemented by researchers as well. Research findings agree that the intelligibly combined fuzzy logic with other methods performed significantly better than the uncombined techniques for classifying ECG arrhythmias. It can be projected that the crucial review and thorough investigation will extend the research scope to an advanced level.

#### REFERENCE

- [1] Channappa Bhyri, Satish T. Hamde, Laxman M. Waghmare, "ECG Acquisition and Analysis System for Diagnosis of Heart Diseases", *Sensors & Transducers Journal*, Vol. 133, Issue 10, October 2011, pp. 18-29.
- [2] B. Anuradha and V.C. Veera Reddy, "Cardiac arrhythmia classification using fuzzy classifiers", *Journal of Theoretical and Applied Information Technology*, 2008, pp. 353-359.
- [3] Introductory Guide to Identifying ECG Irregularities, DailyCareBioMedical Inc.
- [4] Miad Faezipour, Adnan Saeed, Suma Chandrika Bulusu, Mehrdad Nourani, Hlaing Minn & Lakshman Tamil, "A Patient-Adaptive Profiling Scheme for ECG Beat Classification," *IEEE Transactions On Information Technology In Biomedicine*, Vol. 14, No. 5, September 2010, pp. 1153-1165.

- [5] Ludmila I. Kuncheva (2008), *Scholarpedia*, 3(1):2925.
- [6] Ryan J. Urbanowicz and Jason H. Moore, "Learning Classifier Systems: A Complete Introduction, Review, and Roadmap", *Journal of Artificial Evolution and Applications*, Volume 2009, Article ID 736398, 25 pages.
- [7] Rahime Ceylan, Yüksel Özbay, "Wavelet Neural Network for Classification of Bundle Branch Blocks", *Proceedings of the World Congress on Engineering 2011, Vol. II, WCE 2011, London, U.K., July 6 - 8, 2011*, pp. 1003-1007.
- [8] R. Acharya, J. S. Suri, J. A. E. Spaan and S. M. Krishnan, "Advances in Cardiac Signal Processing", ISBN-13 978-3-540-36674-4, Springer Berlin Heidelberg New York, 2007, pp. 327-338.
- [9] M. Owis, A. Abou-Zied, A. B. Youssef and Y. Kadam, "Robust feature extraction from ECG signals based on nonlinear dynamical modeling", *23rd Annual International Conference IEEE Engineering in Medicine and Biology Society*, Vol. 2, 2001, pp. 1585-1588.
- [10] O. T. Inan, L. Giovangrandi and G. T. A. Kovacs, "Robust neural network- based classification of premature ventricular contractions using wavelet transform and timing interval features", *IEEE Transaction on Biomedical Engineering*, Vol. 53, No. 12, 2006, pp. 2507-2515.
- [11] A. R. Naghsh-Nilchi and A. R. K. Mohammadi, "Cardiac Arrhythmias Classification Method Based on MUSIC, Morphological Descriptors, and Neural Network", *EURASIP Journal on Advances in Signal Processing*, Vol. 2008, Article no. 202, 2008.
- [12] T. Ince, S. Kiranyaz and M. Gabbouj, "A Generic and Robust System for Automated Patient-specific Classification of Electrocardiogram Signals", *IEEE Transactions on Biomedical Engineering*, Vol. 56, No. 5, May 2009, pp- 1415-1426
- [13] S. S. Mehta and N. S. Lingayat, "Support Vector Machine for Cardiac Beat Detection in Single Lead Electrocardiogram", *IAENG, International Journal of Applied Mathematics*, 2007, pp. 1630-1635.
- [14] Jalal A. Nasiri, Mahmoud Naghibzadeh, H. Sadoghi Yazdi, Bahram Naghibzadeh, "ECG Arrhythmia Classification with Support Vector Machines and Genetic Algorithm", *Third UKSim European Symposium on Computer Modeling and Simulation*, 2009, pp. 187-192.
- [15] Narendra Kohli, Nishchal K. Verma, Abhishek Roy, "SVM Based Methods for Arrhythmia Classification in ECG" *International Conference on Computer & Communication Technology*, 2010, pp. 486-490.
- [16] MiHy Song, Jeon Lee, Sung Pil Cho, KyoungJoung Lee, and Sun Kook Yoo, "Support Vector Machine Based Arrhythmia Classification Using Reduced Features", *International Journal of Control, Automation, and Systems*, vol. 3, no. 4, December 2005, pp. 571-579.
- [17] B. M. Z. Asl and S. K. Setarehdan, "Neural Network Based Arrhythmia Classification Using Heart Rate Variability Signal", *Proceedings of the 2nd International Symposium on Biomedical Engineering*, Bangkok, Thailand, November 2006, pp.149-162.
- [18] B. Anuradha and V. C. V. Reddy, "ANN for classification of cardiac arrhythmias", *ARPN Journal of Engineering and Applied Sciences*, Vol. 3, No. 3, June 2008.
- [19] R. P. W. Duin and M. Loog, "Linear dimensionality reduction via a heteroscedastic extension of lda: the chernoff criterion", *IEEE Trans. PAMI*, vol. 26, no. 6, June 2004, pp. 732-739.
- [20] M. Lagerholm, C. Peterson, G. Braccini, L. Edenbrandt and L. Sörnmo, "Clustering ECG Complexes Using Hermite Functions and Selforganizing Maps", *IEEE Transaction on Biomedical Engineering*, vol. 47, no. 7, July 2000, pp. 838-848.
- [21] Martin Lagerholm, Carsten Peterson, Guido Braccini, Lars Edenbrandt, and Leif Sörnmo, "Clustering ECG Complexes Using Hermite Functions and Self-Organizing Maps", *IEEE Transactions On Biomedical Engineering*, Vol. 47, NO. 7, JULY 2000, pp. 838-848.
- [22] P. de Chazal, M. O'Dwyer and R. B. Reilly, "Automatic Classification of Heartbeats Using ECG Morphology and Heartbeat Interval Features", *IEEE Transaction on Biomedical Engineering*, Vol. 51, No. 7, July2004, pp. 1196- 1206.
- [23] Iva Bogdanova, Francisco Rinc'onand David Atienza, "A Multi-lead ECG Classification Based On Random Projection Features", *IEEE, ICASSP 2012*, pp. 625-628.

- [24] D. Benitez, P. A. Gaydecki, A. Zaidib and A. P. Fitzpatrick, 'The use of the Hilbert transform in ECG signal analysis', *Computers in Biology and Medicine*, 2001, 31, pp. 399-406.
- [25] J.C. Nunes, and A. Nait-Ali, 'Hilbert transform-based ECG modeling'. *Biomedical Engineering*, 2005, Vol.39, No. 3, pp. 133-137.
- [26] S. Karpagachelvi, Dr. M. Arthanari, M. Sivakumar, "Classification of ECG Signals Using Extreme Learning Machine", *Computer and Information Science* Vol. 4, No. 1, January 2011, pp. 42-52.
- [27] V. Mahesh, A. Kandaswamy, C. Vimal, B. Sathish, "ECG arrhythmia classification based on logistic model tree", *J. Biomedical Science and Engineering* 2, 2009, pp. 405-411.
- [28] Roshan Joy Martis, Chandan Chakraborty, Ajoy K. Ray, "A two-stage mechanism for registration and classification of ECG using Gaussian mixture model", *Pattern Recognition* 42, 2009, pp. 2979 – 2988.
- [29] Saniya Siraj Godil, Muhammad Shahzad Shamim, Syed Ather Enam, Uvais Qidwai, "Fuzzy logic: A 'simple' solution for complexities in neurosciences?" *Surgical Neurology International* 2011, Vol-2, Issue-1, page 24.
- [30] Raj Kumar Bansal, Ashok Kumar Goel, Manoj Kumar Sharma, "MATLAB and Its Application in Engineering", Pearson Publication, Fifth Impression, 2012.
- [31] Wen Wei and Jerry M. Mendel, "A Fuzzy Logic Method for Modulation Classification in Nonideal Environments", *IEEE Transactions on Fuzzy Systems*, Vol. 7, No. 3, June 1999, pp. 333-344.
- [32] Tomoharu Nakashima, Gerald Schaefer, Yasuyuki Yokota, Hisao Ishibuchi, "A weighted fuzzy classifier and its application to image processing tasks", *Fuzzy Sets and Systems* 158, 2007, pp. 284 – 294.
- [33] Reza Boostani, Mojtaba Rismanchib, Abbas Khosravani, Lida Rashidi, Samaneh Kouchaki, Payam Peymani, Seyed Taghi Heydari, B. Sabayan, K. B. Lankarani, "Presenting a hybrid method in order to predict the 2009 pandemic influenza A (H1N1)", *Advanced Computing: An International Journal (ACIJ)*, Vol.3, No.1, January 2012, pp. 31-43.
- [34] Ken Nozaki, Hisao Ishibuchi and Hideo Tanaka, "Adaptive Fuzzy Rule-Based Classification Systems", *IEEE Transactions on Fuzzy Systems*, Vol. 4, No. 3, 1996, pp. 238-250.
- [35] Jia Zeng and Zhi-Qiang Liu, "Type-2 Fuzzy Sets for Pattern Recognition: The State-of-the-Art", *Journal of Uncertain Systems*, Vol.1, No.3, 2007, pp.163-177.
- [36] F. Hoffmann, B. Baesens, J. Martens, F. Put and J. Vanthienen, "Comparing a genetic fuzzy and a Neuro-fuzzy classifier for credit scoring", presented at *Int. J. Intell. Syst.*, 2002, pp.1067-1083.
- [37] F. M. Schleif, T. Villmann, B. Hammer, "Prototype based Fuzzy Classification in Clinical Proteomics", *International Journal of Approximate Reasoning*, 2008, 47(1), pp. 4-16.
- [38] Aaron K. Shackelford and Curt H. Davis, "A Hierarchical Fuzzy Classification Approach for High-Resolution Multispectral Data Over Urban Areas", *IEEE Transactions on Geo-science And Remote Sensing*, Vol. 41, No. 9, SEPTEMBER 2003, pp. 1920-1932.
- [39] Wai Kei Lei, Bing Nan LI, Ming Chui Dong, Mang I. Vai, "AFC-ECG: An Intelligent Fuzzy ECG Classifier", A. Saad et al. (Eds.): *Soft Computing in Industrial Applications*, ASC 39, 2007, pp. 189–199.
- [40] Yun-Chi Yeh, Wen-June Wang, and Che Wun Chiou, "Heartbeat Case Determination Using Fuzzy Logic Method on ECG Signals", *International Journal of Fuzzy Systems*, Vol. 11, No. 4, December 2009, pp. 250-261.
- [41] Mohammad Reza Homaeinezhad, Ehsan Tavakkoli, Ali Ghaffari, "Discrete Wavelet-based Fuzzy Network Architecture for ECG Rhythm-Type Recognition: Feature Extraction and Clustering-Oriented Tuning of Fuzzy Inference System", *International Journal of Signal Processing, Image Processing and Pattern Recognition* Vol. 4, No. 3, September, 2011, pp. 107-130.
- [42] R. R. Gharieb, M. Massoud, S. Nady, M. Moness, "Fuzzy C-Means in Features Space of Teager-Kaiser Energy of Continuous Wavelet Coefficients for Detection of PVC Beats in ECG", 8<sup>th</sup> Cairo International Biomedical Engineering Conference (CIBEC) (IEEE Conferences), 2016, pp. 72-75.
- [43] Liang-Yu Shyu, Ying-Hsuan Wu, Weichih Hu, "Using Wavelet Transform and Fuzzy Neural Network for VPC Detection From the Holter ECG", *IEEE Transactions on Biomedical Engineering*, Vol. 51, No. 7, July 2004, pp. 1269-1273.
- [44] N. Özlem Özcan, Fikret Gurgun, "Fuzzy Support Vector Machines for ECG Arrhythmia Detection", *International Conference on Pattern Recognition*, 2010, pp. 2973-2976.
- [45] S. Murugan & Dr. S. Radhakrishnan, "Improving Ischemic Beat Classification Using Fuzzy-Genetic Based PCA and ICA", *International Journal on Computer Science and Engineering (IJCSSE)*, Vol. 02, No. 05, 2010, pp. 1532-1538.
- [46] Eduardo Ramírez, Oscar Castillo, and José Soria, "Hybrid System for Cardiac Arrhythmia Classification with Fuzzy K-Nearest Neighbors and Neural Networks Combined by a Fuzzy Inference System", P. Melin et al. (Eds.): *Soft Comp. for Recogn. Based on Biometrics*, SCI 312, 2010, pp. 37–55.
- [47] Muhammad Arif, Muhammad Usman Akram, Fayyaz-ul-Afsar Amir Minhas, "Pruned fuzzy K-nearest neighbor classifier for beat classification", *J. Biomedical Science and Engineering*, 2010, 3, pp-380-389.
- [48] Glayol Nazari Golpayegani & Amir Homayoun Jafari, "A novel approach in ECG beat recognition using adaptive neural fuzzy filter", *J. Biomedical Science and Engineering*, 2009, 2, pp. 80-85.
- [49] T.M. Nazmy, H. El-Messiry, B. Al-Bokhity, "Adaptive Neuro-Fuzzy Inference System for classification of ECG signals", *The 7th International Conference on Informatics and Systems (INFOS)*, Date of Conference: 28-30, March 2010, pp. 1-6.
- [50] Prarthana B. Sakhare, Rajesh Ghongade, "An Approach for ECG Beats Classification using Adaptive Neuro Fuzzy Inference System", *Annual IEEE India Conference (INDICON)*, 2015, pp. 1-6.
- [51] A. Dallali, A. Kachouri and M. Samet, "Fuzzy C-Means Clustering, Neural Network, WT and HRV For Classification of Cardiac Arrhythmia", *ARPN Journal of Engineering and Applied Sciences*, Vol. 6, No. 10, October 2011, pp. 112-118.
- [52] R. B. Ghongade and A. A. Ghatol, "Optimization of a multi-class MLP ECG classifier using FCM", *Indian Journal of Science and Technology* Vol. 3, No. 9, Sep 2010, pp. 1102-1105.
- [53] Rahime Ceylan, Yuksel Ozbay, Bekir Karlik, "A novel approach for classification of ECG arrhythmias: Type-2 fuzzy clustering neural network", *Expert Systems with Applications*, 30 August 2008, pp. 1-6.
- [54] Victor-Emil Neagoe, Iuliana-Florentina Iatan and Sorin Grunwald, "A Neuro-Fuzzy Approach to Classification of ECG Signals for Ischemic Heart Disease Diagnosis", *AMIA Annu Symp Proc.* 2003; pp. 494–498.
- [55] Nong Weixin, "A novel algorithm for ventricular arrhythmia classification using a fuzzy logic approach," *Australian Physical & Engineering Sciences in Medicine*, Vol. 39, No. 4, Dec 2016, pp. 903-912.
- [56] S. Mahapatra, D. Mohanta, P. Mohanty, S. K. Nayak, and P. K. Behari, "A Neuro-fuzzy Based Model for Analysis of an ECG Signal Using Wavelet Packet Tree," *Procedia Comput. Sci.*, vol. 92, pp. 175–180, 2016.



**Ahmed Farhan** was born in Comilla, Bangladesh on 1st December, 1992. He has received his Bachelor degree in Electrical and Electronic Engineering from Islamic University of Technology, Bangladesh on 2013. At present, he is doing his master in Information and Communication Engineering in Harbin Engineering University, China. He has worked as a Lecturer in the Department of Mechatronics Engineering at World University of Bangladesh, Bangladesh for about 3 years. His research interests are Biomedical Engineering, Image Processing.  
E-mail:ahmedfarhanzisan77@yahoo.com

# Innovative Automation of Production Processes in the Automotive Industry

Isak Karabegović<sup>1</sup>, Edina Karabegović<sup>2</sup>, Mehmed Mahmić<sup>3</sup>, Ermin Husak<sup>4</sup>

<sup>1,2,3,4</sup>University of Bihać, Pape Ivana Pavla II 2, 77000 Bihać, Bosnia and Herzegovina,

<sup>1</sup>E-mail:isak1910@hotmail.com,<sup>1</sup>Tel:+38737226273<sup>1</sup><https://orcid.org/000-0001-9440-4441>,

Received:11 October, Revised: 27 October, Accepted: 01 November

**Abstract**— The world is currently in the process of the fourth industrial revolution due to the development of digital technologies. Developed countries in the world, such as Germany, USA, Japan and those that want to reach developed countries like China, are rapidly developing and implementing innovative technologies with the goal of achieving "intelligent manufacturing processes" or "intelligent factories". Germany is developing and implementing digital technologies through strategy called "Industry 4.0". With their policy named "Advanced Manufacturing Partnership 2.0", the United States want to create high-quality manufacturing jobs, initiate renaissance of the production processes and connect industry with the internet. In May 2015, the Government of China, inspired by the German "Industry 4.0", has announced a ten-year development strategy or a reform called "Made in China 2025", which aims to promote China into a leading technological force by 2025, improve global competitiveness through innovations, explore and apply new jobs through adapting production, or in other words to progressively restructure and innovate the production sector like other industrial countries in the world. The best example of innovation is the automotive industry, for two reasons. The paper presents the representation of industrial robots in production processes, with particular reference to the application of industrial robots in the automotive industry, as well as innovative solutions for the future in relation to industrial robots. The paper also provides a review of innovative solutions in regard to the automotive industry.

**Keywords**— industrial robot, automotive industry, industry 4.0, automation, production process, vehicle production

## I. INTRODUCTION

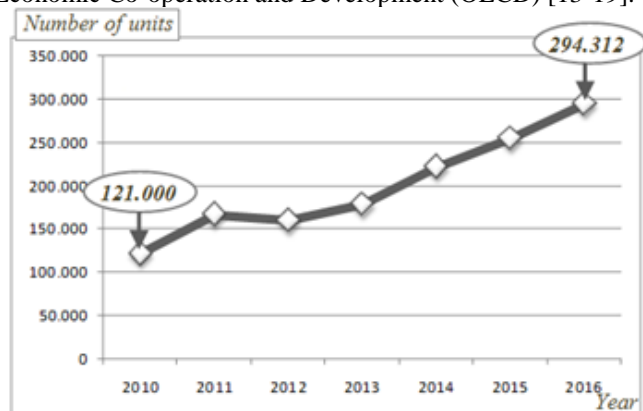
Ever since the third industrial revolution in 1969, when automation in production processes started with the introduction of first industrial robots and computers, there has been a rapid development of digital technologies, as well as new methods and new technologies in the world. Companies worldwide that want to remain competitive in the market are forced to follow this development and implement its application with the purpose of modernization and automation

of production processes. Digital technology brings fundamental changes, because the related industry becomes more flexible and more efficient. One of the reasons why these technologies are already available is due to the low price that is constantly decreasing and it is expected that in the near future they will be fully represented in production processes. Another reason why companies need to follow the development and implementation of these technologies is that customers are rapidly getting new information through ICT technology, thus expanding their requirements, which results in more complex products [1-7]. Companies around the world (including the governments) are working hard to implement adequate new technologies, primarily digital technologies, in the production processes of the industry, in order to use new information and communication technologies (ICT) to produce more efficiently, more productively and more effectively. German government has labeled its strategy of digitization of production processes as "Industry 4.0", and wants to maintain a leading position in the production and development of technology and standards, and export of solutions. Working Group on Industry 4.0 presented a set of Industry 4.0 recommendations for implementing the strategic initiative to the German federal government. At the Hannover Fair 2013, the final report of the Working Group Industry 4.0 was presented [8]. The response to "Industry 4.0" in the United States is named "Advanced Manufacturing Partnership 2.0", which aims to create high-quality marketing jobs, initiate renaissance of the production processes and connect industry with the internet [9]. Japanese government initiated a strategy called "Revitalization and Robots Strategy", with the purpose of increasing productivity in the industry by promoting the development and implementation of the robotic industry, as well as the revitalization of the digital society and the industrial sector [10]. In May 2015 the government of China, inspired by the German "Industry 4.0", has announced a ten-year development strategy or a reform called "Made in China 2025", which aims to promote China into a leading technological force by 2025, improve global competitiveness through innovations, explore and apply new jobs through adapting production, or in other words to progressively restructure and innovate the production sector like other industrial countries in the world[11]. The above-mentioned reform in China will rely on institutions that will strengthen

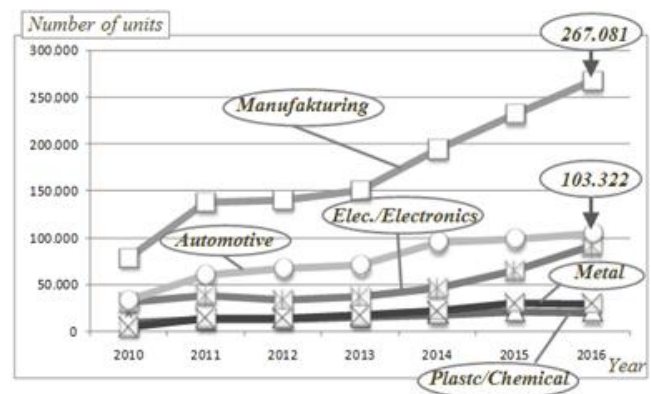
the protection of intellectual property rights for small and medium-sized companies, by enabling them to independently build the technology standards, develop digital technologies, ICT technology and sensor technology and their applications in all industries, especially in the automotive industry. Report Prepared on Behalf of the U.S.-China Economic and Security Review Commission in October 2016 say that in 2013, China surpassed Japan to become the world's largest market for industrial robots, and by 2018 will account for over a third of the industrial robots installed worldwide[12]. Given that robotic technology is mostly used in the automotive industry, its development leads to the development of new generation industrial robots that can cooperate with workers. The companies are trying to introduce "intelligent automation" in production processes, using "intelligent machines" that will be the product of the fourth industrial revolution "Industry 4.0", which will eventually lead to "intelligent factories" in the future. In order to have a view of how this process is structured in the automotive industry, we need to make an analysis of the representation of robots in all industrial branches, with special emphasis on the automotive industry.

## II. THE APPLICATION OF INDUSTRIAL ROBOTS IN THE AUTOMATION OF PRODUCTION PROCESSES

Industrial robots are most important components in the process of automation and modernization of production processes. The actual state of automation in manufacturing processes in all industrial branches, especially in the automotive industry, will be shown in the analysis of the representation of industrial robots in production processes during automation and modernization of production processes. The analysis of the application of industrial robots in production processes worldwide was based on data from the International Federation of Robotics (IFR), the UN Economic Commission for Europe (UNECE) and the Organization for Economic Co-operation and Development (OECD) [13-19].



a – annual application of industrial robots



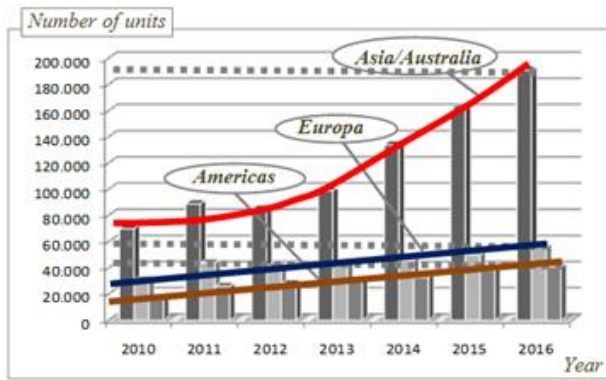
b – application per industrial branches

Figure 1. Annual application of industrial robots in the automation of production processes worldwide, as well as application in production: automotive, electric, metal and chemical (plastic) industry for the period 2010-2016

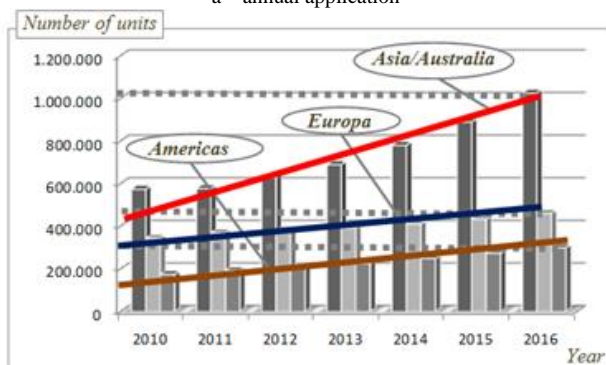
Based on Figure 1.a) we come to the conclusion that in the period 2010-2016 the annual tendency of application of industrial robots in the world was constantly increasing, changing from about 121.000 units of industrial robots used in 2010 to doubled application in 2016, when approximately 294.000 industrial robot units were applied. Charts in Figure 1.b) provide an insight in the representation of industrial robots in the industry worldwide. The largest number of industrial robots, around 90%, is used in production processes in the industry. The first place in the automation of production processes is held by the automotive industry with the highest number of installed industrial robot units and a growing tendency of the application of robots in the automotive industry. The second place is held by electrics/electronic industry that is experiencing a growing tendency, with an increase in the past three years compared to the previous four years. The third place in representation of industrial robots is occupied by metal industry with a slight increasing tendency on annual basis. There is somewhat lower representation of industrial robots in plastics and chemical industry than in metal industry. If we compare the representation of industrial robots in these two industries (metal, plastics/chemical) with automotive and electrical industry, we can see that they are far behind these two industries. It is evident that automotive and electrical industries are the leading industries in the application of industrial robots worldwide. In order to form a true image of the representation of industrial robots we need to conduct an analysis of the representation of industrial robots by continents (without Africa because their representation is very low and not worth the analysis), as shown in Figure 2.

The annual and total application of industrial robots on the continents of Asia/Australia, Europe and the Americas for the period 2010-2016 is shown in Figure 2. The annual industrial robot application on the above mentioned continents is shown in Figure 2.a), based on which we conclude that Asia/Australia is in the first place with increasing tendency that reached its highest value in 2016 with around 191.000 units of industrial robots.





a – annual application



b – total application

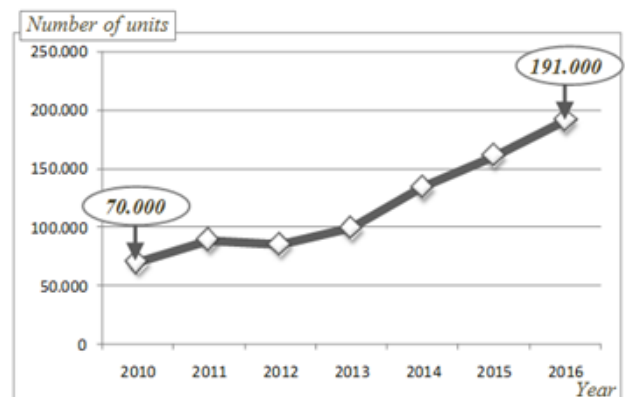
Figure 2. Application of industrial robots in the automation of production processes by continents (Asia/Australia, Europe and Americas) [13-19]

The second place, according to the industrial robots application, is held by Europe, whose increasing tendency is linear function that in 2016 reached 56.000 units, which is far less than the application in Asia. The third place is occupied by the Americas that has identical tendency as Europe, with lower annual application. The overview of the total representation of industrial robots on the continents is given in Figure 2.b), based on which we conclude that the first place is again held by Asia/Australia with linear growing tendency that in 2016 reached about one million industrial robot units. The second and third place is held by Europe and America whose linear growth of the total representation of industrial robots has a lower tendency than the representation of robots in Asia. The analysis of the application of industrial robots was conducted based on continents in different industrial branches, as shown in Figure 3.

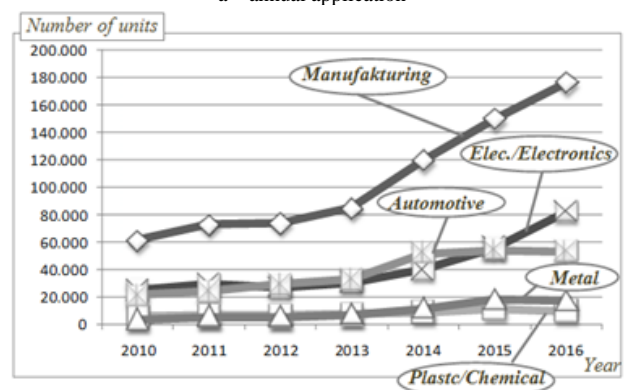
The analysis of application of industrial robots in Asia/Australia for the period 2010-2016 (Figure 3.I) indicates that the largest part of industrial robots is located in the production processes, so that the tendency of application in 2016 reached the highest value of around 180.000 robots, of total 191.000 robot units used. The representation of robot units is the largest in the electrical and automotive industries, which demonstrate growing tendency on annual basis, as shown in Figure 3.I-b). The implementation of robots in these two industries was almost identical until the end of 2015. However, situation changed in 2016 when greater representation of the industrial robots in the electrical industry

compared to the automotive was recorded, indicating an increase of about 30.000 industrial robot units.

Following these two industries, the metal industry and the plastics/chemical industry are somewhat less represented, with a slight increase and almost identical application on the annual level, which in 2016 reached about 17.000 robot units in the metal industry and about 10.000 robot units in the plastics/chemical industry. It can be concluded that the continent of Asia/Australia implements the higher number of industrial robots in the automation of production processed in the electric/electronic industry. The application of industrial robots in the automation process in Europe is shown in Figure 3.I).

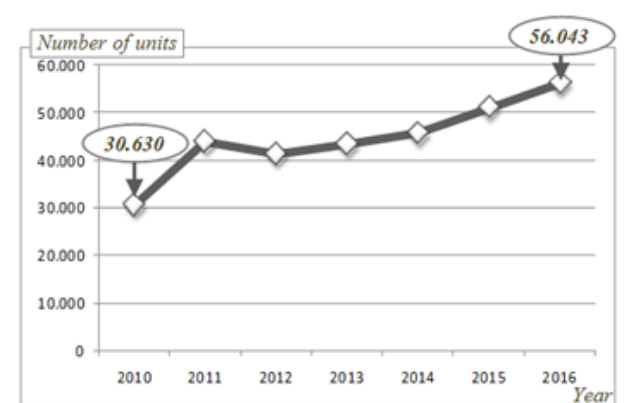


a – annual application

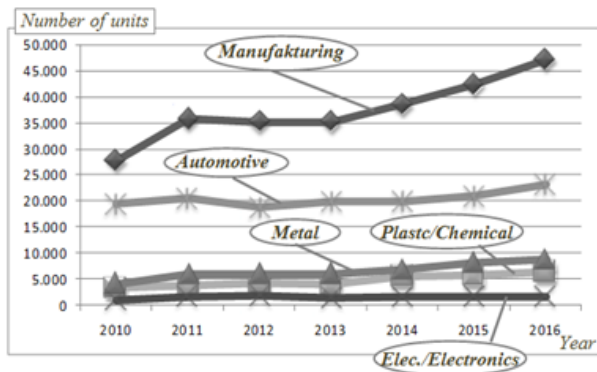


b – application per industrial branch

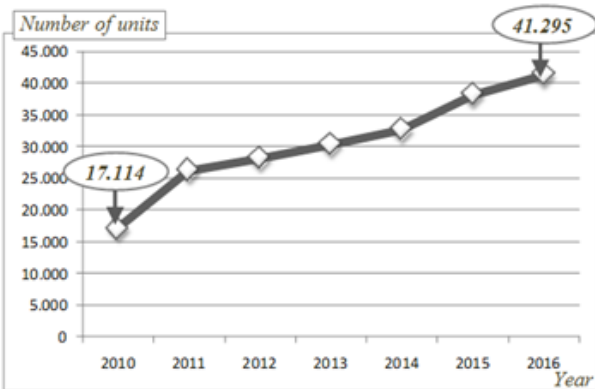
I- application of industrial robots in Asia/Australia



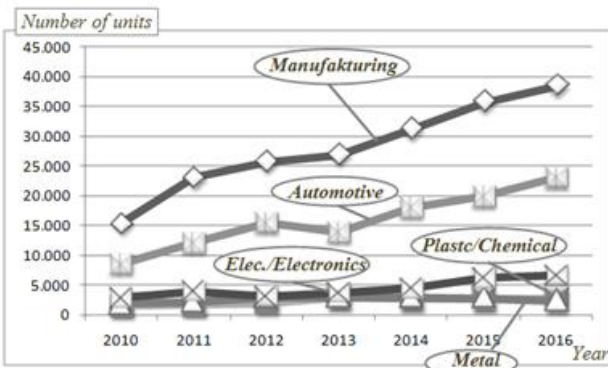
a – annual application



b – application per industrial branch  
II - application of industrial robots in Europe



a – annual application

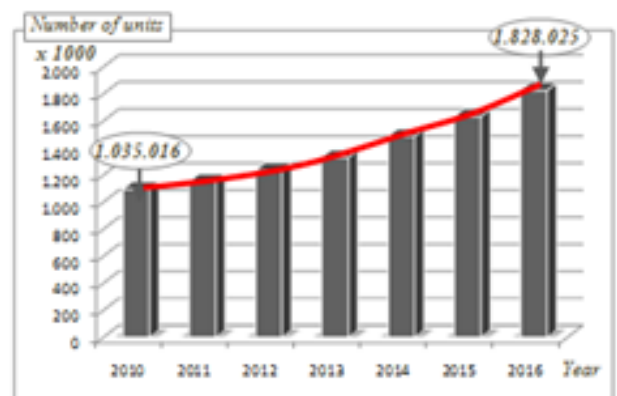


b – application per industrial branch

Figure 3. Application of industrial robots in the automation of production processes by continents, as well as application in production processes in automotive, electrical, metal and chemical (plastics) industry for the period 2010-2016 [13-19]

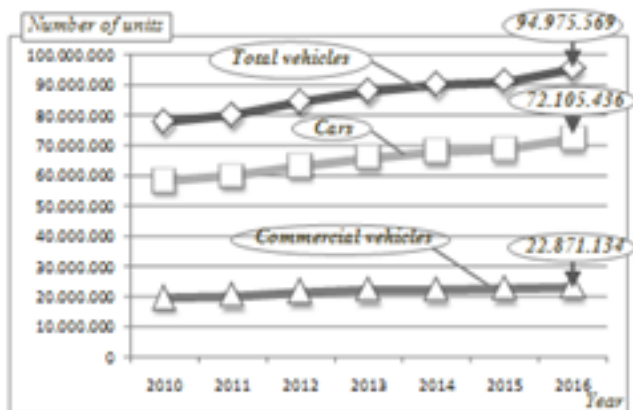
It proves that the industrial robot representation is lower than in Asia/Australia for almost 60%. Trends in the representation of industrial robots by industry in Europe are different from the trends in Asia/Australia. According to the industrial robot application in the process of automation, the first place in Europe is held by the automotive industry, as indicated by Figure 3.I-b). We see that of total representation of industrial robots, automotive industry occupies almost 50% robotic units, with slightly increasing annual tendency for the period 2010-2016. The second place by the representation of

industrial robots in Europe is held by metal industry, followed by plastics/chemical industry and lastly electric/electronics industry. By examining the industrial robots' application on these two continents, we come to the conclusion that Asia/Australia is focused on the automation of the electric/electronics industry, whereas Europe relies on the automation of the automotive and metal industry, which is mostly represented in Europe. The third continent by the industrial robot application in automation processes is America. If we compare the representation of industrial robots in America to Europe in 2016, we can see that America has applied 27% industrial robot units less than Europe. However, in relation to Asia, the representation of industrial robots in production processes is lower by 79% robot units. The tendency of representation of industrial robots is growing every year, as shown in Figure 3, III. The first place in automation of production process is held by automotive industry, as in Europe. The second place in application of industrial robots in America is held by metal industry, which is behind the automotive industry for about 90% of robot units. The third place, with slight increasing tendency, is held by plastics/chemical industry, followed by electric/electronics industry. The analysis of application of industrial robots in the automation of production processes in the world by continents (except Africa where representation is extremely low) provides the conclusion that the largest application of industrial robots is in Asia, followed by Europe and America. Similarly, automotive and metal industries occupy the first place in Europe and America, whereas electric/electronics industry and automotive industry have a leading position in Asia in the period 2010-2016. The answer to questions why application of industrial robots by industrial branches is growing and why the automotive industry holds the first place are provided in the comparative analysis of application of industrial robots and vehicle production in the automotive industry worldwide, as given in Figure 4. The total number of industrial robot units applied in the automation of production processes in industry in period 2010-2016 is given in Figure 4.a). As can be seen, it has an increasing tendency with slight exponential function and in six years it reached 1.8 million units.



a – total application of robot units

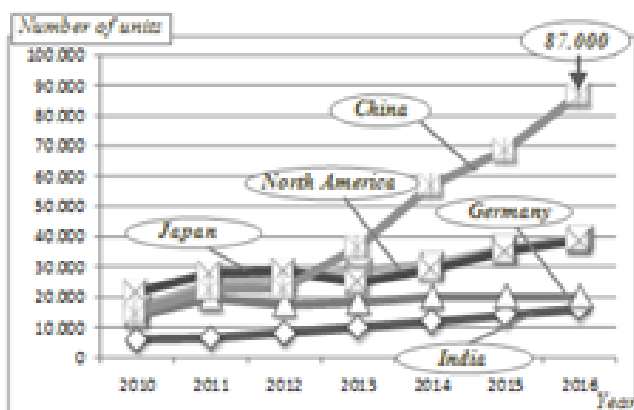




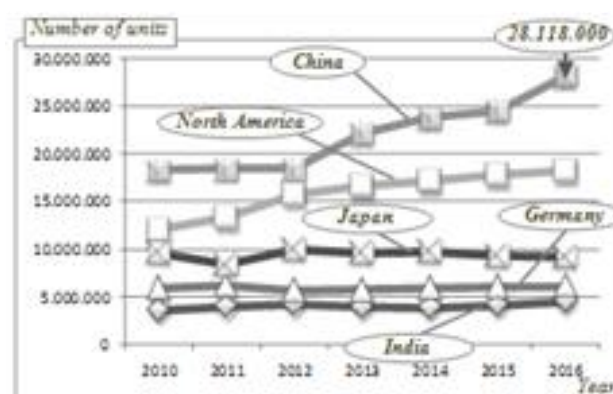
b – total production of vehicles

Figure 4. Total application of industrial robots in the automation of production processes, as well as total production of vehicles worldwide for the period 2010-2016 [20-22]

The tendency of application of industrial robots in production processes is the highest in automotive production processes, and it reflected the vehicle production worldwide, as indicated in Figure 4.b). The trend of vehicle production in the world for the same period is also growing, so that 78 million vehicles produced in 2010 increased to about 95 million in 2016. We see that far more cars are produced compared to commercial vehicles. In 2016 about 72 million car units were produced or about 76% of the total number of vehicles produced, whereas only 23 million units of commercial vehicles were produced which takes only 24% of the total percentage of produced vehicles in the world in the same year. More detailed analysis of the dependence of vehicle production on the presence of industrial robots in automation of production processes can be provided if we analyze the representation of industrial robots and vehicle production in the countries with developed automotive industry, Figure 5. As shown in Figure 5, the following countries have been taken into account for the analysis: India, Germany, Japan, China and North America (USA, Canada, Mexico) for the period 2010-2016.



a – application of industrial robots

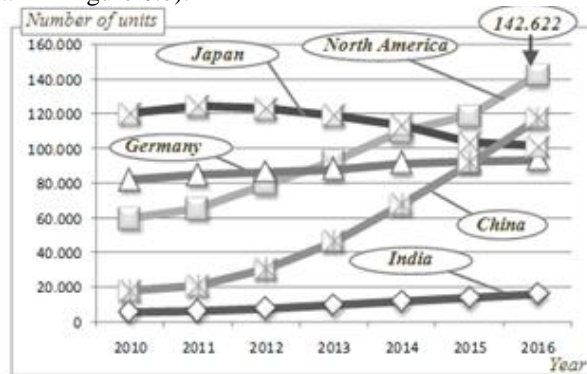


b – vehicle production

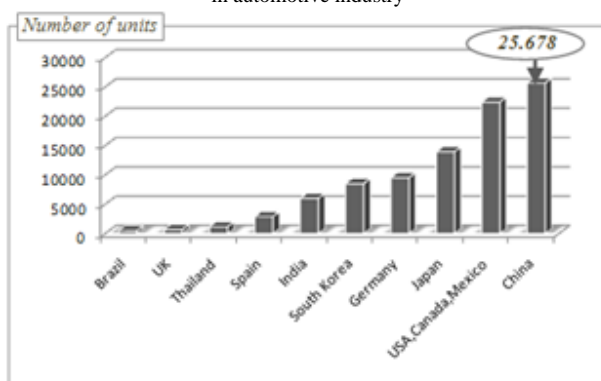
Figure 5. Application of industrial robots and vehicle production in India, North America (USA, Canada, Mexico), Germany, Japan and China [13-23]

Figure 5.a) shows the trend of application of industrial robots in production processes based on which we have concluded that China holds the first place in the past four years, and in 2016 it has reached its maximum in relation to all other countries. In addition, China is also the world's leader in vehicle production (Figure 5.b)) in the period 2010-2016. A sudden increase in robot application has led to rapid vehicle production in the last four years in this period. Japan and North America (USA, Canada, Mexico) are in the second and third place in the past couple of years with nearly identical application of industrial robots in production processes. In regard to vehicle production, North America (USA, Canada, Mexico) stands out compared to Japan, which is expected as there are three countries included. This was also confirmed by the fact that Japan dislocated the production of vehicles to other countries in the world, thus providing the difference in the tendency of vehicle production compared to North America (USA, Canada, Mexico). The world's fourth country in application of robots in production processes is Germany, which is also fourth in the vehicle production, Figure 5.b). India is ranked as the fifth in the application of industrial robots in production processes, and is also the fifth in vehicle production worldwide. In order to obtain clearer presentation, an analysis was conducted of application of industrial robots into automotive industry for the period 2010-2016, as well as application of industrial robots in the top ten countries in the automotive industry in 2016, as shown in Figure 6. The analysis of the trends of application of industrial robots in automotive industry for the period 2010-2016, (Figure 6.a), indicates that China and North America (USA, Canada, Mexico) mark a sudden growing tendency. For example, in 2010 China installed about 18,000 industrial robot units in the automotive industry, and in only six years this number increased to about 118,000 units of industrial robots, which is six-fold increase. In 2016, China, (Figure 6.b) installed about 25,678 industrial robot units in the automotive industry processes. Similarly, the total number of installed industrial robots in North America (USA, Canada, Mexico) in 2016 was 142,000 units, whereas it holds the second place in the annual

application of industrial robots in the automotive industry, as shown in Figure 6.b).



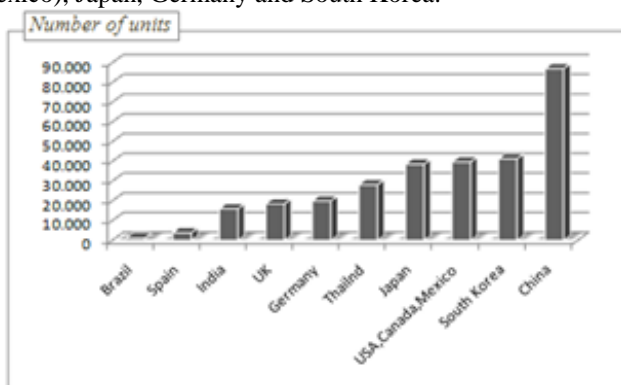
a – application of industrial robots in automotive industry



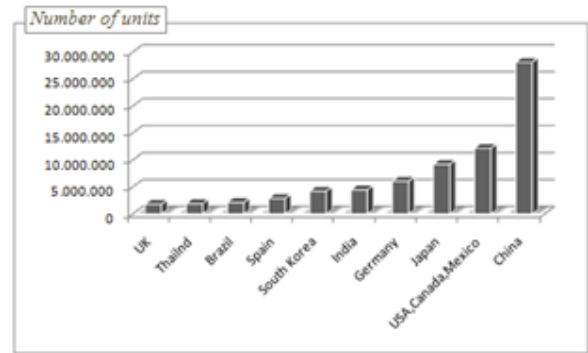
b – annual application of industrial robots in 2016

Figure 6. Application of industrial robots in automotive industry in India, North America (USA, Canada, Mexico), Germany, Japan and China in 2016 [13-23]

It is interesting to note that the tendency of total number of installed industrial robots in the period 2010-2016 in Japan is decreasing (Figure 6.a), even though in 2016 Japan held the third place by installed robots in the automotive industry. On the other hand, there was a slight growing trend in the total number of industrial robots in the automotive industry in Germany and India. In regard to representation of industrial robots in automotive industry, the following five countries are leaders in the world: China, North America (USA, Canada, Mexico), Japan, Germany and South Korea.



a – application of industrial robots



b – vehicle production

Figure 7. Application of industrial robots and vehicle production in 2016 [13-22]

The analysis of chart given in Figure 7.a), which depicts the application of industrial robots in industrial production processes in 2016 in ten top countries, reveals that China holds the first place. It is noted that China applies the largest number of installed robots in the automotive industry, as well as certain number of industrial robot units in the metal processing industry that produces different parts for the automotive industry. This is one of the important factors for vehicle production and it justifies the conclusion that China is the world's leader in vehicle production, as shown in Figure 7.b). The second place by application of industrial robots in 2016 is held by South Korea. However, in the same year South Korea was positioned as sixth in vehicle production (Figure 7.b)), which indicates that the number of installed robots is not directed at the automotive industry. South Korea is applying the largest number of industrial robots in the electronics/electronics industry, which is confirmed by the fact that South Korea is not among five top countries in application of industrial robots in automotive industry, as shown in Figure 6.a). The third position by application of industrial robots in 2016 is held by North America (USA, Canada, Mexico), whereas it occupied the second place in vehicle production in the same year. The reason is that North America is the first in the world in total representation of industrial robots in automotive industry, as given in Figure 6.a). The fourth place in the application of industrial robots in industrial production process is held by Japan (Figure 7.a), while in the same year it occupied the third place in vehicle production, which can be justified by the fact that Japan was the first in the world until 2014. The application of industrial robots in 2016 was the highest in the following ten countries: China, South Korea, North America, Japan, Thailand, Germany, United Kingdom, India, Spain and Brazil, as given in Figure 7.a). Vehicle production in 2016 was the highest in the following ten countries in the world: China, North America, Japan, Germany, India, South Korea, Spain, Brazil, Thailand and United Kingdom. Based on the above analysis it can be concluded that this order is justified, and the predictions are that it will continue in the years to come [14-22].

The desire of the China to invest in technological development and the desire to implement the adopted technological reform

is shown in the Figure 8, which show the growth of innovations and patents in production processes for the period 2006-2015.

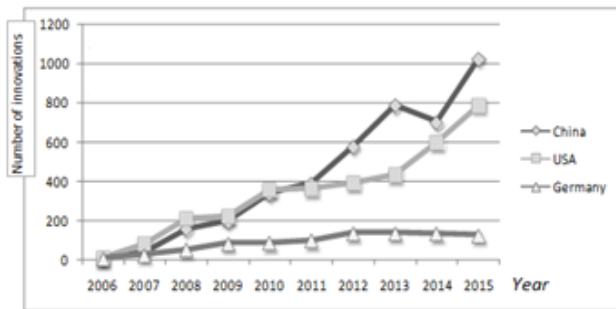


Figure 8. The tendency of innovation growth in the fourth industrial revolution [30]

Based on Figure 8, we can conclude that China, Germany and the USA had almost identical number of innovations and patents in regard to the fourth industrial revolution. However, these trends have changed in ten years and in 2015 China was the first in the world by number patents with about 1000 patents. The second place was held by USA with about 800 patents, whereas Germany was in the third place with about 180 patents. We can conclude that China has experienced the growth of its own patents for "Industry 4.0" each year, thus positioning itself ahead of the developed countries such as the USA and Germany since 2011. China is putting an emphasis on the innovation in advanced technologies. Chinese innovative activities are focused on industry robots, intelligent sensors and wireless sensor networks [23-31]. The predictions are that the fourth industrial revolution "Industry 4.0" will lead to "smart automation" or "smart factories" that could become reality in 10 to 20 years. This process would not be possible unless new generation robots are placed in the center of automation of production processes in all industries.

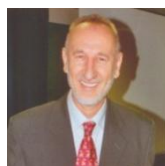
### III. CONCLUSION

The application of industrial robots is increasing on the annual basis. It is estimated that this tendency will continue in the future. The analysis of the application of industrial robots in countries with highly developed automotive industry has shown that China holds the first place (Figure 5a) followed by North America, Japan, Germany and India. The identical order is evident in terms of vehicle production in aforementioned countries. This brings us to the conclusion that important aspect of vehicle production is the application of industrial robots in the production processes. The use of innovative technologies such as digital technology, IC technology, robotic technology enables the automation in the automotive industry to be more flexible and adaptable to any type of vehicle. Constant innovation, development of new methods and technologies enables the development of robotic technology or robots of new generation that have much greater application possibilities compared to existing industrial robots, which will reflect and increase their use in the automotive industry.

### REFERENCES

- [1] Kalpakjian S.; Schmid S.; 2007. *Manufacturing Processes for Engineering Materials*. Amazon, (in USA)
- [2] Sulavik C.; Portnoy M.; Waller T.; 2014. *How a new generation of robots is transforming manufacturing*. Manufacturing Institute USA, Gaithersburg, (in USA)
- [3] Doleček V.; Karabegović I.; 2002. *Robotika*, Tehnički fakultet Bihać, Bihać, (in Bosnia)
- [4] Karabegović I.; 2016. *Role of Industrial Robots in the Development of Automotive Industry in China*. International Journal of Engineering Works, Vol.3., Iss.12., Kambohwell Publisher Enterprises, Multan, Pakistan, pp.92-97. <https://www.kwpublisher.com/?paper=1-114-The-Role-of-Industrial-Robots-in-the-Development-of-Automotive-Industry-in-China#Author>
- [5] Karabegović I.; Karabegović E.; Mahmić M.; Husak E.; 2015. The application of service robots for logistics in manufacturing processes, *Advances in Production Engineering & Management*, Vol. 10. No. 4. Maribor, Slovenia, pp:185-194. <http://dx.doi.org/10.14743/apem2015.4.201>
- [6] Karabegović I.; Husak E.; 2014. Significance of industrial robots in development of automobile industry in Europe and the World. *Journal Mobility and Vehicle*, Vol.40., No.1., 2014., University of Kragujevac, Faculty of Engineering, Kragujevac, Serbia, pp:7-16. [http://www.mvm.fink.rs/Journal/Archive/2016/2016V42N3/volume\\_42\\_number\\_3\\_2016.pdf](http://www.mvm.fink.rs/Journal/Archive/2016/2016V42N3/volume_42_number_3_2016.pdf)
- [7] Mannan B.; Khurana S.; 2012. Enablers and Barriers for Introduction of Robotics as an AMT in the Indian Industrie. *International Journal of Computer Applications*, Januar 2012, New York, USA, pp:19-24. <https://www.researchgate.net/publication/267450380>; DOI:10.13140/2.1.2625.5368
- [8] Recommendations for implementing the strategic initiative INDUSTRIE 4.0, Final report of the Industrie 4.0 Working Group, ACATECH-National Academy of Science and Engineering, April 2013.
- [9] <https://obamawhitehouse.archives.gov/the-press-office/2013/09/26/president-obama-launches-advanced-manufacturing-partnership-steering-com> (15.09.2019)
- [10] New Robot Strategy, Japan's Robot Strategy - Vision, Strategy, Action Plan, The Headquarters for Japan's Economic Revitalization, 2015, [http://www.meti.go.jp/english/press/2015/pdf/0123\\_01b.pdf](http://www.meti.go.jp/english/press/2015/pdf/0123_01b.pdf)
- [11] <https://www.csis.org/analysis/made-china-2025> (10.08.2018)
- [12] Ray J.; Atha K.; Francis E.; Dependahl C.; Mulvenon J.; Alderman D.; Ann Ragland-Luce L.; 2016. *China's Industrial and Military Robotics Development*. Research Report Prepared on Behalf of the U.S.-China Economic and Security Review Commission, Center for Intelligence Research and Analysis (CIRA), Vienna, (in Austria)
- [13] World Robotics 2016, 2016. IFR Statistical Department, hosted by VDMA Robotics+ Automation, Germany. <https://ifr.org/>
- [14] World Robotics 2015, 2015. IFR Statistical Department, hosted by VDMA Robotics+ Automation, Germany. <https://ifr.org/>
- [15] World Robotics 2014, 2014. IFR Statistical Department, hosted by VDMA Robotics+ Automation, Germany. <https://ifr.org/>
- [16] World Robotics 2013, 2013. IFR Statistical Department, hosted by VDMA Robotics+ Automation, Germany. <https://ifr.org/>
- [17] World Robotics 2012, 2012. IFR Statistical Department, hosted by VDMA Robotics+ Automation, Germany. <https://ifr.org/>
- [18] World Robotics 2011, 2011. IFR Statistical Department, hosted by VDMA Robotics+ Automation, Germany. <https://ifr.org/>
- [19] World Robotics 2010, 2010. IFR Statistical Department, hosted by VDMA Robotics+ Automation, Germany. <https://ifr.org/>
- [20] Jahresbericht 2010, 2010. Verband der Automobilindustrie e.v. (VDA), Berlin, Deutschland. <https://www.vda.de/de/services/Publikationen/jahresbericht-2010.html>

- [21] Jahresbericht 2014, 2014. Verband der Automobilindustrie e.v.(VDA), Berlin, Deutschland.  
<https://www.vda.de/de/services/Publikationen/jahresbericht-2014.html>
- [22] Jahresbericht 2016, 2016. Verband der Automobilindustrie e.v.(VDA), Berlin, Deutschland.  
<https://www.vda.de/de/services/Publikationen/jahresbericht-2016.html>
- [23] Makowieckaja O.; 2015. Industrial Robots on the Market of Means of Production Automation. Biuletyn Instytutu Spawalnictwa, No.2. Gliwice, Czechoslovak, : pp:22-27.  
file:///C:/Users/isak/Downloads/03\_makowieckaja\_industrial\_robots\_on\_the\_market\_of\_means\_of\_production\_automation.pdf
- [24] Karabegović I (2017) The Role of Industrial and Service Robots in Fourth Industrial Revolution with Focus on China., Journal of Engineering and Architecture, 5(2), pp:110-117. DOI: 10.15640/jea.v5n2a9 URL: <http://dx.doi.org/10.15640/jea.v5n2a9>
- [25] Robotics 2020 Strategic Research Agenda for Robotics in Europe (2013) Produced by euRobotics aisbl Robotics 2020, Draft 0v42 11/10/2013, euRobotics aisbl, pp:25-43.  
[https://ec.europa.eu/research/industrial\\_technologies/pdf/robotics-ppp-roadmap\\_en.pdf](https://ec.europa.eu/research/industrial_technologies/pdf/robotics-ppp-roadmap_en.pdf)
- [26] The UK Landscape for Robotics and Autonomous Systems (2015) Contact Info Robotics and Autonomous Systems Special Interest Group, Barttelot Road Horsham, UK.  
file:///C:/Users/isak/Downloads/PUB3InnovateUKRASreview2015.pdf
- [27] Anderson J, Smith A (2014) AI, Robotics, and the Future of Jobs <http://www.pewinternet.org/2014/08/06/future-of-jobs/>
- [28] Daniel F.; 2016. Cobots Expand Automation Opportunities, [https://ifr.org/downloads/press/02\\_2016/Editorial\\_WR\\_Industrial\\_Robots\\_2016.pdf](https://ifr.org/downloads/press/02_2016/Editorial_WR_Industrial_Robots_2016.pdf)
- [29] Annual Review 2015/2016, (2016) EDINBURGH CENTRE FOR ROBOTICS Innovation Ready, Edinburgh, Deutschland.  
[https://www.edinburghrobotics.org/sites/default/files/Website%20version%20of%202015-16%20annual%20review\\_0.pdf](https://www.edinburghrobotics.org/sites/default/files/Website%20version%20of%202015-16%20annual%20review_0.pdf)
- [30] Wübbecke J, Meissner M, Zenglein M, Ives J, Conrad B (2016) Made in China 2025. The Marking of a High-Tech Superpower and Consequences for Industrial Countries, Mercator Institute for China Studies, No.2. December 2016:4-41. [www.merics.org](http://www.merics.org)
- [31] Presher A (2014) Automation & Motion Control, Automotive <https://www.designnews.com/automation-motion-control/evolution-industrial-robots/139281170134199>



### ***Isak Karabegović***

Qualification: Doctor of Technical Sciences

Professional and academic career: Full professor at University of Bihać

Competitive research or professional awards received: Author and coauthor of more than 26 books, 80 scientific papers published in international journals, 300 papers published in international conferences. Editor and coeditor of significant number of conference proceedings. Member in editorial board of 21 international journals. Sketch biography (200 words): Prof. Isak Karabegović is a Full professor at University of Bihać, Technical Faculty in Department of Mechanical engineering. He received doctoral degree from Faculty of Mechanical Engineering, University of Sarajevo in 1989, his Master of Science degree from Faculty of Mechanical engineering and naval architecture Zagreb, University of Zagreb in 1982, and bachelor degree of mechanical engineering from Faculty of Mechanical engineering Sarajevo, University of Sarajevo in 1978. His career as professor started on Technical College and later become Full professor at University of Bihać. In this period of time he was Dean of Technical faculty in several occasions and also rector of University of Bihać in several occasions. His research interest includes domains of Mechanics and Robotics. He also works as reviewer, editorial and technical board member in many reputed national, international journal and conferences. He publishes more than 400 papers of different type in international journals, conference proceedings and book chapters.

Full name : Isak Karabegović

Date of birth : 19.10.1955

Nationality : Bosnian

Department : University of Bihać, Technical faculty

Area of teaching : Mechanics, Robotics

Email : [isak1910@hotmail.com](mailto:isak1910@hotmail.com)

Tel : ++38737226273

Bosnia and Herzegovina



# Reducing Energy Consumption of Light Rail Train by using CO<sub>2</sub>-Controlled Ventilation for Air Condition

Radwan Ahmed Bouh<sup>1</sup>, Kader Ali Ibrahim<sup>2</sup>

<sup>1</sup>Djibouti-Ethiopia Railway Company

<sup>2</sup>Control Science and Engineering, School of Internet Things, Jiangnan University

ramkove.rami@gmail.com<sup>1</sup>, kader-ali@vip.jiangnan.edu.cn<sup>2</sup>

Received: 15 November, Revised: 22 November, Accepted: 05 December

**Abstract**—This paper present reducing the energy consumption of light rail train by using co<sub>2</sub>-operated ventilation for air-conditioning. To achieve this precious goal, this paper proposes the use of co<sub>2</sub>-operated ventilation in order to reduce the energy used for air-conditioning purpose. The energy of co<sub>2</sub>-operated air-conditions and CAV (convention system) was simulated and analyzed by HAP software. The result of train simulation report has shown clearly that co<sub>2</sub>-operated air condition consume less energy and is cost energy effective as compared to CAV( conventional system).

**Keywords**— CO<sub>2</sub>, HAP, CAV, Air-Condition

## I. INTRODUCTION

Rail train has been recognized as the most energy sufficient and compatible transportation made. In fact, reducing the energy consumption of rail vehicle is a key issue. The rail train consumes in addition to the energy needed for train motion, a share of electricity for comfort purpose. About 20% to 40% of the energy consumed by the vehicle is used for ventilation and air-conditioning. Nowadays, optimizing the energy used for comfort purpose is a key issue because the air-conditioning accounts the biggest share of comfort energy[1,2].

To satisfy the antagonistic needs of passengers' comfort and low-cost energy by rail-way companies, The passengers care always their comfort and air quality while the operating company needs to conserve the operating energy. It is always difficult to satisfy both at same time , but there is made balancing between these antagonistic to reduce energy consumption and to satisfy the passenger . in train, ventilation is considered to be one of the most important factors for maintaining acceptable indoor air quality in any space . many types of ventilation systems encounter problems to control minimum supply air and thus to consume minimum amount of energy. But a ventilation system based on registration of increasing co<sub>2</sub> concentration can facilitate in solving the given problem. Such a technology is called co<sub>2</sub>-based demand controlled ventilation (DCV)[2,3,4].

The experience and field studies have shown that the level of carbon can be a reliable indicator and quite a cheap instrument of the air quality and ventilation rate. Co<sub>2</sub>-based

demand controlled ventilation system controls the amount of supply outdoor fresh air in a train depending on a number of people. People are the main source of co<sub>2</sub> in a train. If a number of people in coach is doubled, the co<sub>2</sub> level will accordingly double. If one or few people leave at the coach or the saloon, the level of co<sub>2</sub> will proportionally decrease. Thus DCV saves energy solely by not heating or cooling unnecessary amount of outdoor air [3,4]. The benefits of such ventilation are maximal when a number of people continuously changes in train, in extreme climate condition or when the electricity cost is quite high. Co<sub>2</sub> concentration in the coach is a good indication of the number of passenger actually present. Installation of co<sub>2</sub>-sensor and a control circuit for ventilation therefor allows a demand-oriented energy efficient ventilation of passenger coaches[1,3].

HAP( Hourly Analysis Program) software will analyze the energy of co<sub>2</sub>-controlled air-condition and CAV (conventional system) in order to show clearly that co<sub>2</sub>-operated air condition consume less energy comparing to the conventional system. HAP estimates annual energy use and energy cost for HVAC and non-HVAC energy consuming system in a building or train by simulating its operation for each of 8.760 hours in a year[2,4].

There are steps using HAP to energy analysis:

- Defining the problem
- Data gathering
- Data entry into HAP
- Generation of simulation Report
- Evaluation of result

## II. DEFINITION OF THE SCOPE

Normally an energy analysis compares energy use for two or more scenarios . this paper is estimating and comparing the energy use of two design scenarios:

- CAV which is deliver comfort to spaces with similar load
- VAV which is designed with the supply a quantity of fresh air flow. This case describes accurately the quantity of occupant in train[1,3,5].

Based on this, equipment like supply fan, space( door, window, wall and roof of train) and the coach interior data will be sized[4,5,6].

### III. DATA GATHERING

This involves gathering data for Addis Ababa Light Rail Train, its environment and its air system data.

#### A. Train location

The light rail train considered in this study is situated in Addis Ababa, capital of Ethiopia, located at 39° longitude, 9° latitudeand at an elevation 2450.0 meter[7,8,9].

Figure 1. Space input data

#### B. Weather data

The weather data includes monthly maximum and minimum dry bulb and wet bulb temperature, design DB temperature for both summer and winter, summer coincident WB, winter coincident WB, region, location, city, latitude, longitude, elevation , and sunshine hour, for the area of interest, which are collected from the National Metrology Agency(NME)[10,11,12].

Month	Dry Bulb		Wet Bulb	
	Max	Min	Max	Min
Jan	26.7	4.9	19.0	3.7
Feb	28.0	6.3	20.5	4.8
Mar	28.6	7.5	21.0	6.4
Apr	28.4	9.6	20.1	7.0
May	28.5	10.0	21.2	9.2
Jun	27.1	9.6	21.2	8.7
Jul	24.4	9.5	21.2	9.2
Aug	23.6	9.5	21.2	9.2
Sep	24.2	8.3	20.6	8.1
Oct	25.8	6.9	20.1	4.5
Nov	25.2	5.5	19.5	4.0
Dec	25.7	5.4	18.4	4.0

Hour	Jan DB	Jan WB	Feb DB	Feb WB
0000	8.8	7.2	10.2	8.4
0100	7.7	6.3	9.1	7.5
0200	6.6	5.3	8.0	6.5
0300	5.8	4.5	7.2	5.6
0400	5.1	3.9	6.5	5.0
0500	4.9	3.7	6.3	4.8
0600	5.3	4.1	6.7	5.2
0700	6.4	5.1	7.8	6.3
0800	8.4	6.8	9.8	8.0
0900	11.2	9.1	12.6	10.4
1000	14.5	11.8	15.8	12.9
1100	18.2	14.1	19.5	15.5
1200	21.7	16.2	23.0	17.7
1300	24.3	17.7	25.6	19.2

Figure 2. Weather Input Data

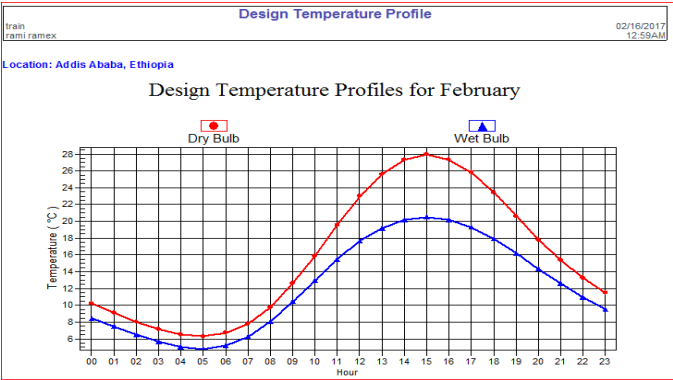


Figure 3. Design Temperature Profile

#### C. Train Structure

The dimension of the passenger compartment in LRT which is to be air conditioned is 23.6x2.65 m in size. It has one floor. It has one floor. The exterior wall of the train is made of stainless steel and the roof of the passenger compartment is low concrete roof. The floor in passenger saloon is structured with polyurethane rubber and covering by PVC floor covering and its length is 23600 mm. the doors are made of aluminum alloy materials. The doors and windows use glass[13,14].

Figure 4. Space Input Data for Train

#### D. Passenger Flow

The rated passenger is 286 person in one tramcar( width 64 seat and 6 standing person per m2)[15]. The HAP software needs an input data the numbers of occupants or passenger in the train per hour. Passenger flow is not same for work days and holidays[16,17] . Based on observation, estimation and interviews, the number of passenger per hour is as follows:



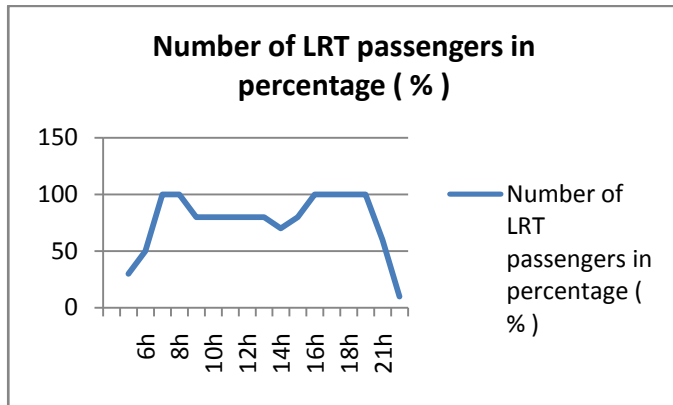


Figure 5. Number of passenger at workdays

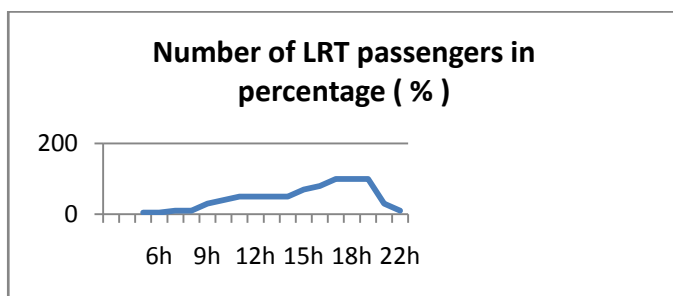


Figure 6. Number of passenger at holidays

#### IV. RESULT

##### A. Conventional system simulation Report

After running the simulation with the HAP software, the Annual energy consumption is summarized in the above table. CAV system which is the conventional system consumes 38,013 kWh annually. This amount of energy consumption concluded from CAV scenarios will be compared with VAV system one.

TABLE I. ANNUAL ENERGY CONSUMPTION

Component	train locomotive
<b>HVAC Components</b>	
Electric (kWh)	33,322
<b>Non-HVAC Components</b>	
Electric (kWh)	4,691
<b>Totals</b>	
Electric (kWh)	38,013

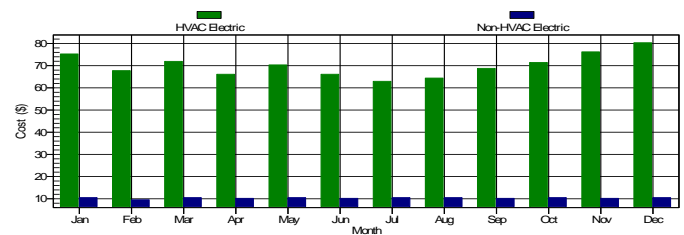


Figure 7. Monthly Energy Cos

##### B. VAV (controlled by co2) system simulation report

TABLE II. ANNUAL ENERGY CONSUMPTION

Component	Train locomotive
<b>HVAC Components</b>	
Electric (kWh)	25,535
<b>Non-HVAC Components</b>	
Electric (kWh)	4,691
<b>Totals</b>	
Electric (kWh)	30,226

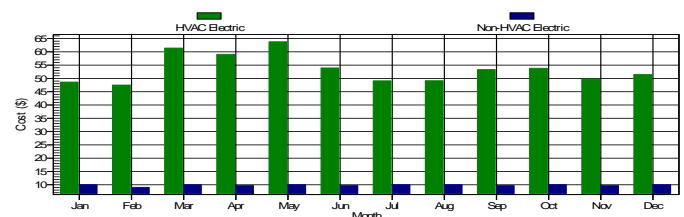


Figure 8. Monthly Cost

#### CONCLUSION

This paper showed that air-condition controlled by co2 system has benefit for both the train operator and passengers. HAP programme produced by Carrier for simulating energy use and calculating energy costs was used to analyse the energy consumption of CAV( conventional system) and VAV( which is controlled by co2) system. The air-conditioned controlled by co2 which has a variable speed fan controls outdoor fresh based on number of passenger. Such system is energy cost effective and consumes less energy in terms of electric. It reduces electricity requirements when an actual occupancy level is below than the design occupancy level during the demanded periods. It creates also improved indoor air quality by increasing ventilation when co2 level rises to unacceptable level.

## REFERENCES

- [1] Guidance on U-Values from Domestic Heating Design Guide, Retrieved from [www.heattrain.ltd.uk](http://www.heattrain.ltd.uk)
- [2] Panagiotis Gkortzas, "Study on optimal train movement for minimum energy consumption" The research paper of Malardalen University of Sweden.
- [3] Kitae Kim, M.ASCE; and M.ASCE, Steven I-Jy Chien (2011) "Optimal Train Operation for Minimum Energy Consumption Considering Track Alignment, Speed Limit, and Schedule Adherence" Journal of Transportation Engineering © ASCE / 665 American Society of Civil Engineers
- [4] Farrington, R., Cuddy, M., Keyser, M., and Rugh, J., "Opportunities to Reduce Air-Conditioning Loads Through Lower Cabin Soak Temperatures," Presented at the 16th Electric Vehicle Symposium, China, October 13-16, 1999.
- [5] Johnson, V., "Fuel Used for Vehicle Air Conditioning: A State-by-State Thermal Comfort-Based Approach," SAE Technical Paper 2002-01-1957, 2002, doi:10.4271/2002-01-1957.
- [6] CISBAT 2015 - September 9-11, 2015 - Lausanne, Switzerland
- [7] ASHRAE 2003 HVAC Applications, Chapter 9 Surface Transportation
- [8] Chan, G.Y., C.Y. Chao, D.C. Lee, S.W. Chan, and H. Lau. 1999. Development of a Demand Control Strategy in Buildings using Radon and Carbon Dioxide Levels. Proceedings of Indoor Air 99 1:48-53.
- [9] Davidge, B. 1991. Demand Controlled Ventilation Systems in Office Buildings. Proceedings of the 12th AIVC Conference Air Movement & Ventilation Control within Buildings: 157-171. Coventry, Great Britain: Air Infiltration and Ventilation Centre.
- [10] Elovitz, D.M. 1995. Minimum Outside Air Control Methods for VAV Systems. ASHRAE Transactions 101 (2): 613-618.
- [11] Emmerich, S.J., J.W. Mitchell, and W.A. Beckman. 1994. Demand-Controlled Ventilation in a Multi-Zone Office Building. Indoor Environment 3: 331-340.
- [12] Emmerich, S.J. and A.K. Persily. 1997. Literature Review on CO2-Based Demand-Controlled Ventilation. ASHRAE Transactions 103 (2): 229-243
- [13] Donnini, G., F. Haghighat, and V.H. Hguyen. 1991. Ventilation Control of Indoor Air Quality.
- [14] Thermal Comfort, and Energy Conservation by CO2 Measurement. Proceedings of the 12th AIVC Conference Air Movement & Ventilation Control within Building: 311-331
- [15] Gabel, S. D., J.E. Janssen, J. O. Christoffel, and S. E. Scarborough. 1986. Carbon Dioxide-Based Ventilation Control System Demonstration. U. S. Department of Energy, DE-AC79-84BP15102.
- [16] Haghighat, F. and G. Donnini. 1992. IAQ and Energy-Management by Demand Controlled Ventilation. Environmental Technology. 13: 351-359.
- [17] Knoespel P, J. Mitchell, and W. Beckman. 1991. Macroscopic Model of Indoor Air Quality and Automatic Control of Ventilation Airflow. ASHRAE Transactions 97 (2): 1020-1030



Radwan Ahmed Bouh , mechanical Engineer of railway. Currently, working at Djibouti-Ethiopia Railway Company.

# Intelligent Control Algorithm for Distributed Battery Energy Storage Systems

Asfand Yar Ali<sup>1</sup>, Juveria Anwar<sup>1</sup>, Rabia bibi<sup>1</sup>, Muhammad Raheel Khattak<sup>1</sup>, Abdul Basit<sup>1</sup>

<sup>1</sup>US Pakistan center for Advance Studies in energy, University of Engineering and Technology Peshawar

Received: 01 December, Revised: 08 December, Accepted: 15 December

**Abstract**— Recent trends towards bulk renewable energy penetration in the power grid have made it essential to have reserve power in the system to overcome variability and intermittent nature of renewable energy sources. Battery energy storage systems (BESS) are vastly utilized for this purpose but the cost and limited life of batteries limits its use. In this paper a control strategy for battery energy storage systems is proposed in which batteries are discharged based on state of charge and state of health. Simulations are performed in MATLAB. By implementing this algorithm load can be shifted small batteries to batteries with better health and capacity. The results show the working of algorithm and the selection of batteries based on set input variable. In this way battery energy storage systems will have longer lifetime, better efficiency and economical operation.

**Keywords**— Battery energy storage systems, State of charge, Control algorithm, Renewable energy

## I. INTRODUCTION

21st century along with its technological advancement also brought some challenges and climate change is one of those critical challenges which is drawing a lot of concern for a sustainable future [1]. Average temperature of earth is increasing gradually due to increased carbon emissions from burning of fossil fuels [2]. Also, natural resources of fossil fuels are depleting with time. To mitigate this problem,

efforts at global level were needed and so an agreement was signed between 195 United Nations Framework Convention in Climate Change (UNFCCC) members. According to this agreement the parties will play active role to minimize usage of fossil fuels to keep the rise of earth temperature within 2°C [3]. This made it essential to seek other energy sources such as wind and solar energy. Current share of Renewable energy is less than 20% and to achieve this target of reducing global warming this has to increase to 65% [4].

Wind and solar energy sources provide a reliable non exhaustive substitute for fossil fuels. But there some challenges associated with it. These energy sources are variable and do not have constant energy output [5]. Wind energy is intermittent by nature while solar energy is available for a limited number of hours per day [6]. Also, these sources are immediately available and have to be utilized instantly otherwise the power will waste. To overcome this challenge reserve power is required and battery energy storage systems are vastly used for this purpose [7]. Excess power is storage in the batteries when the generation is greater than load and is used during peak load hours.

Although, batteries are very reliable way to store excess energy but the cost of battery and limited life makes it difficult to use on large scale [8]. In recent years cost of batteries is reduced drastically due to research and development in this sector because of electric vehicles [9]. Large scale implementation of battery energy storage systems is vastly adapted to increase penetration of renewable energy is the electric grid [10].

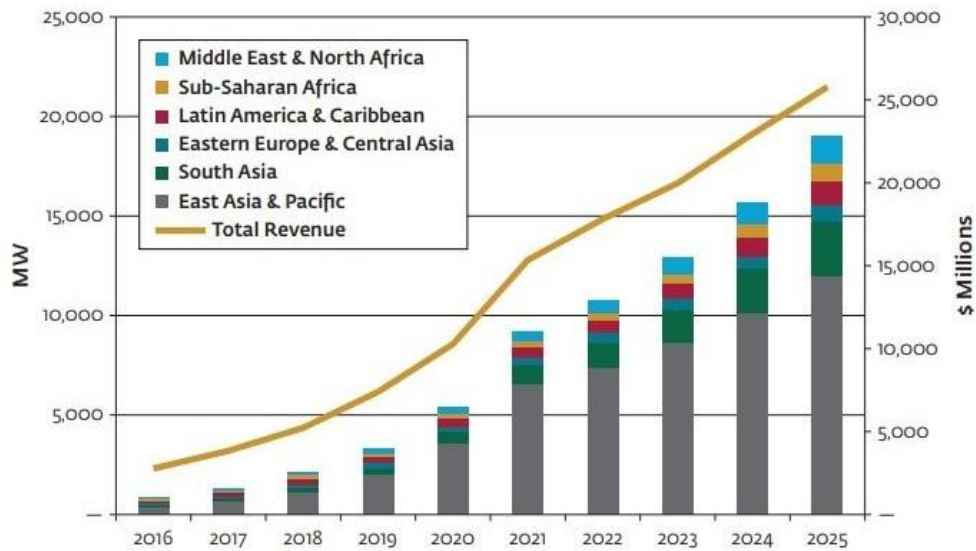


Figure 1: Trends in utilization of Stationary storage systems and future forecast by region

Figure 1 shows the trends in use of battery storage systems. It also forecasts that the utilization of battery technologies may exceed 25000 MW by 2025.

Batteries have limited life cycles and calendar life. Battery capacity fades with each cycle depending on the depth of discharge [11]. For same operation DOD for smaller batteries will be higher than DOD for batteries with higher capacity. Coordinated control systems can be used to control this function which transfers the load to BESS with higher capacity and BESS with lower capacity has lower priority of operation.

## II. CONTROL VARIABLES

### A. Power Generation and Load

For stable operation of system a balance between power generated by power plants and the power utilized by the load should be equal. BESS are added in the system to mitigate variable output of solar. The sum of power produced by PV, power utilized by load and power provided or absorbed by batteries should be equal to zero.

$$P_{gen} + P_{bat} + P_{load} = 0 \quad (1)$$

### B. Stored Energy

Stored energy (SE) is the total energy that is available in battery. It is the product of battery state of charge (SOC), voltage ( $V_{bat}$ ) and the maximum charge storage capacity of the battery (MC).

$$SE = V_{bat} \cdot SOC \cdot MC \quad (2)$$

Where: SE is the stored energy in the battery at any instance. MC is the maximum capacity of the battery.

## III. CONTROL ALGORITHM

Two sets of algorithm are running for coordinated control of BESS.

### A. BESS Operation Mode Control:

BESS operation mode is decided in the central control.

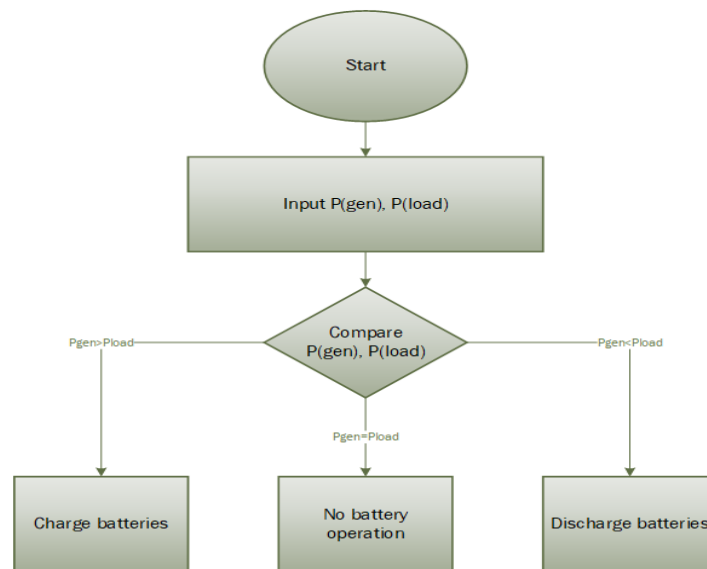


Figure 2: Operation mode control algorithm

The system takes the generation and load demand in real time. This algorithm has three cases given below:

- 1- If the real time generation is higher than load demand then a signal to turn on charging of BESS is generated.
- 2- If the real time generation is equal to load demand then BESS are not operational.

- 3- If the real time generation is less than load demand then a signal to turn on discharging mode of BESS is generated.

#### B. Discharge Control:

Discharge function in the algorithm is called when the central control detects that power deficit between generation and load.

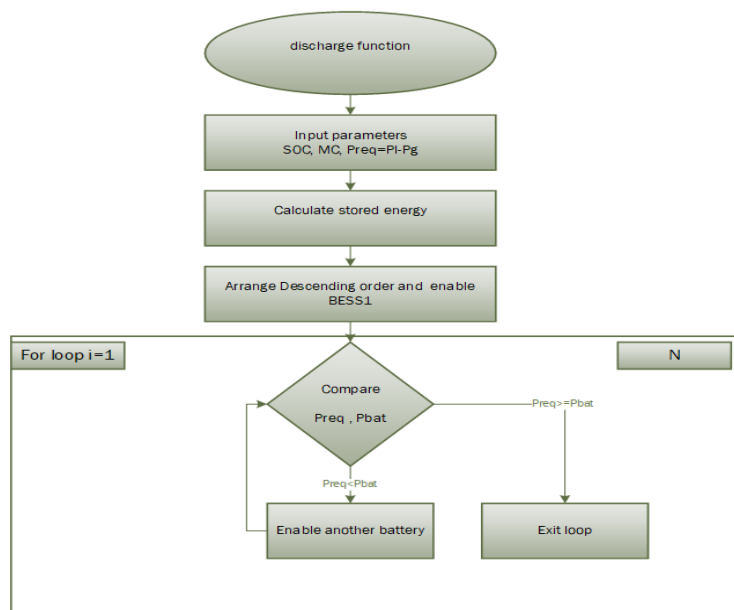


Figure 3: Discharge function flow diagram



Discharge function takes the battery parameters as input, calculates the energy stored in each battery and turns on BESS one by one based on priority of their stored energy.

#### IV. SYSTEM DESIGN FOR SIMULATION

A test system is designed in SIMULINK to implement the proposed algorithm. Fig. 4 shows the Simulink model of test system and Fig. 6 shows the block diagram of test system. It consists of a solar power plant, three battery energy storage systems, dynamic load and a control center to monitor and control the system.

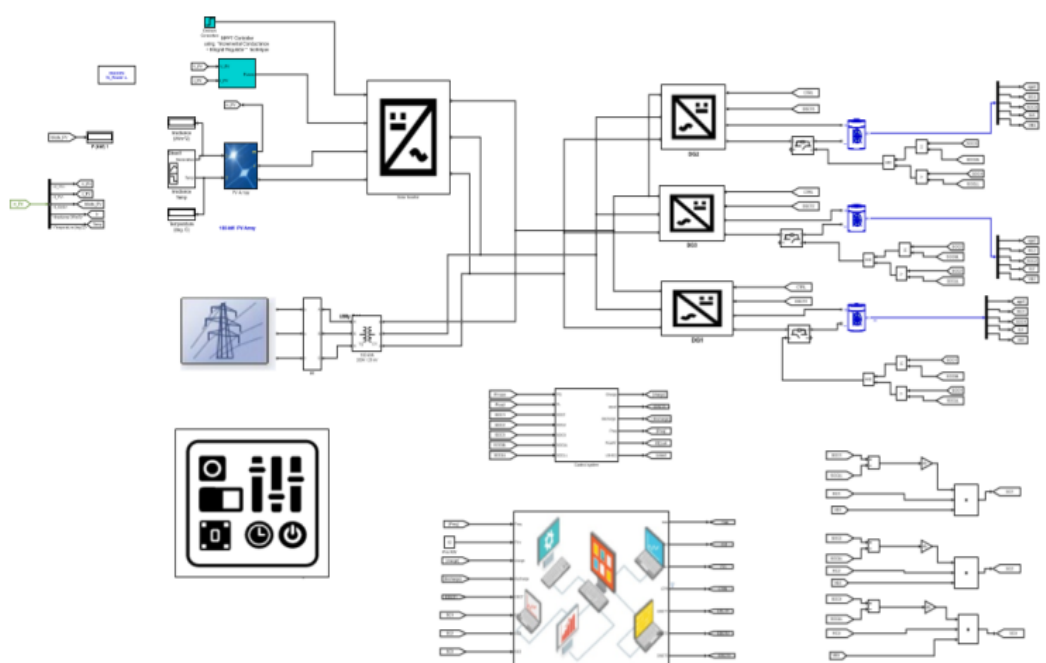


Figure 4: Simulink model of test system

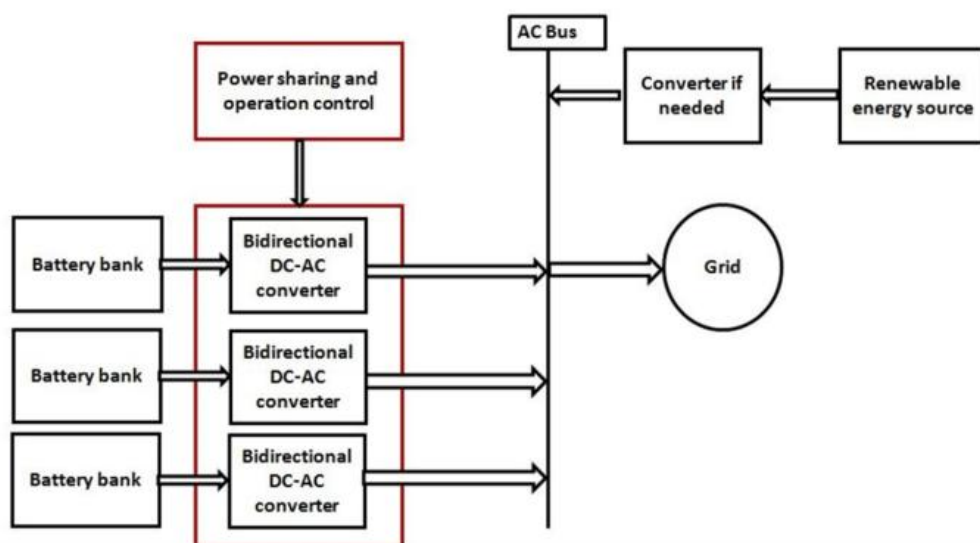


Figure 5: Block diagram of test system

### A. Solar Power Plant

Solar power plant modeled in the test system is 100 KW. Input temperature and irradiance can be controlled by using

sample data curves. Incremental conductance MPPT technique is used with integral regulator for reliable operation. A solar inverter is connected to the output to PV panels which converts the DC voltage to three phase AC voltage.

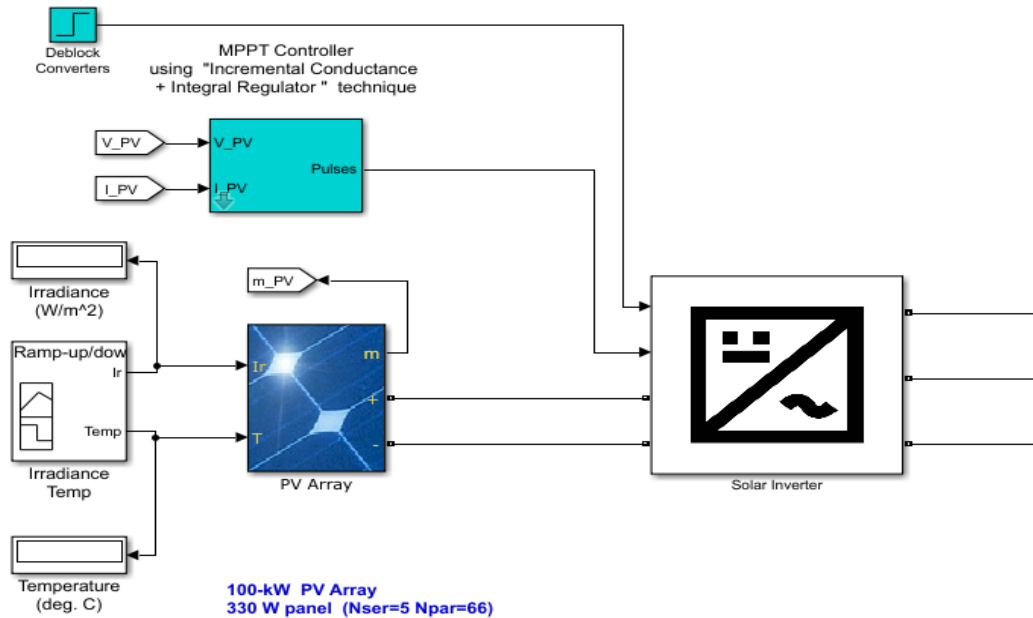


Figure 6: 100KW PV plant simulink model

Fig. 6 shows the simulink model of PV plant developed in the test system. MPPT controller controls the pulses for boost controller at the output of solar panel to regulate DC voltage.

### B. Battery Energy Storage System

Battery energy storage system as shown in Fig. 7 a battery is connected to an ideal switch which controls the SOC limits of the battery. It is then connected to a bidirectional controller which is controlled centrally by coordinated control.

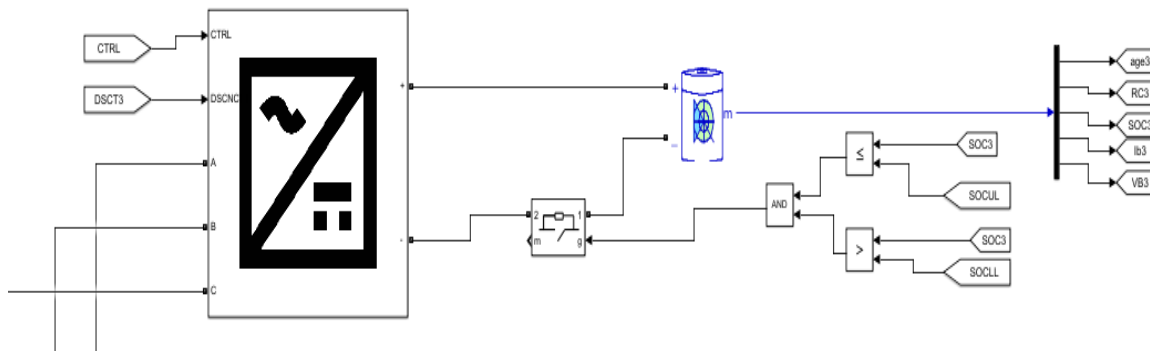


Figure 7: Battery energy storage system Simulink model

### C. Dynamic Load Module

Fig. 8 represents the simulink model of dynamic load in the test system. Active and reactive power of load can be controlled by input load curves.

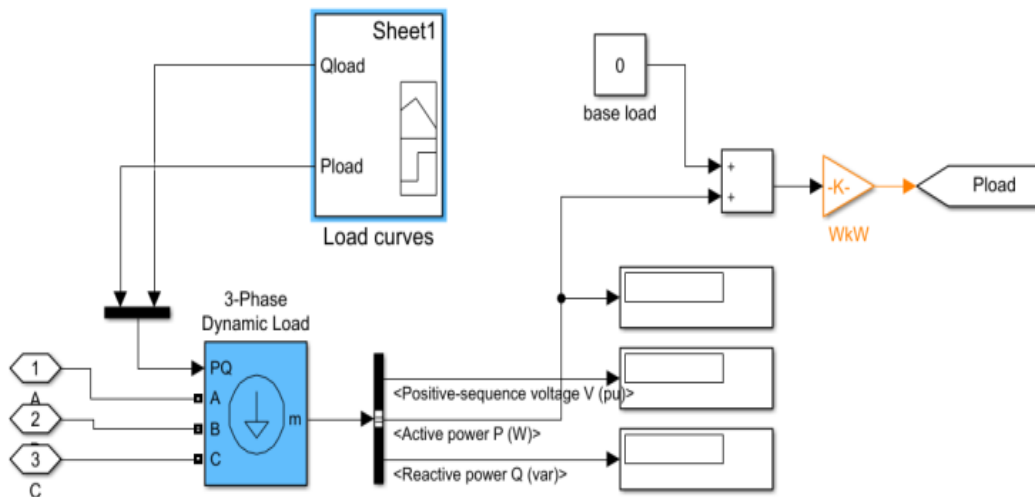


Figure 8: Load representation in Simulink

## V. RESULTS:

Simulations are performed for different cases with initial parameters such as SOC and battery capacity in AH are given below:

- SOC 1 = SOC 2 = SOC 3 = 80%
- BESS 1= 10 AH BESS 2= 20 AH BESS 3= 8 AH
- Inverter rating: 15 KVA

Under different load and generation conditions different results are obtained. Output consists of 4 curves. Operation mode is “1” when discharge operation is required and is “0” when charging operation is required. BESS 1 to BESS 3 represent if that specific BESS is operation or not. “1” represents it is operational and “0” represents it is idle.

### A. Case 1: Charging

In this case PV generation is 50KW and load is 20KW, thus there is excess power in the system. Fig. 9 shows the the output of the system. Here operation mode is “0” indicating charging mode of bidirectional converters. All three of BESS are at level “1” indicating that these are operational and absorbing excess power from the system.

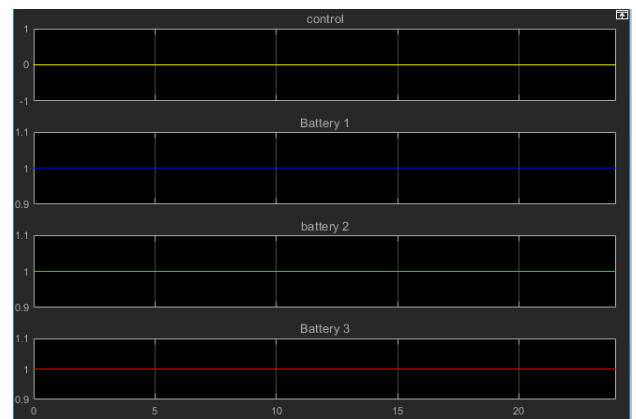


Figure 9: Simulation output for case 1

### B. Case 2: No BESS operation

In this case PV generation is 20KW and load is 20KW thus no battery operation is required. Fig. 10 shows the output of the system. Here operation mode is “0” indicating charging mode of bidirectional converters. All three of BESS are at level “0” indicating that these are disconnected from the system.

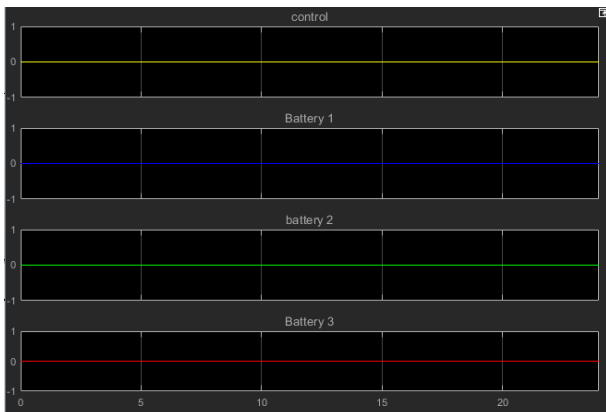


Figure 10: Simulation output for case 2

### C. Case 3: Discharging operation

In this case PV generation is 20KW and load is 30KW, thus power is required from BESS. Fig. 11 shows the output of the system. Here operation mode is “1” indicating discharging mode of bidirectional converters. Only BESS 1 is operational because it has more stored charge due to higher capacity and same SOC level as other BESS. In this case only one inverter is enough to supply power to the load i.e. 10 KW.

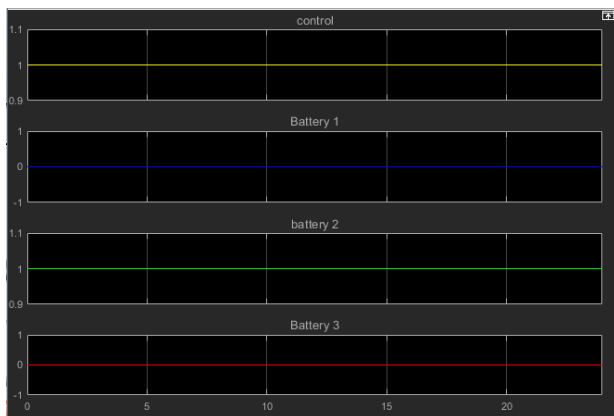


Figure 11: Simulation output for discharging one BESS

Similarly, when the generation is set to 10KW and load is 30 KW. Two inverters will be operational to supply power to load. BESS 1 and 2 have higher capacity then BESS 3 so they are turned on in discharging mode as shown in Fig. 12.



Figure 12: Simulation output for discharging two BESS

When load is further increased to 40KW and generation is kept at 10KW then all three inverters will turn on in discharging mode as shown in Fig 13.



Figure 13: Simulation output for discharging three BESS

### CONCUSLION

Battery energy storage systems provide an effective way to mitigate the variability of renewable energy. By using intelligent control algorithms battery lifetime and efficiency of the system can be achieved. In this paper the proposed algorithm for the selection of battery operation based on stored energy and maximum capacity. This algorithm can be implemented in systems with distributed battery energy storage systems. It has been shown that the proposed algorithm is effectively selecting the batteries operation mode based on system parameters and discharging batteries with higher stored energy on priority. By doing so depth of discharge for batteries can be controlled thus utilizes the limited lifecycles more efficiently.

## REFERENCES

- [1] Trenberth, K., et al., Observations: surface and atmospheric climate change. Chapter 3. Climate change, 2007: p. 235-336.
- [2] Cline, W.R., The economics of global warming. 1992: Institute for International Economics.
- [3] Rogelj, J., et al., Paris Agreement climate proposals need a boost to keep warming well below 2 C. *Nature*, 2016. 534(7609): p. 631.
- [4] Pittock, A.B., Climate change: turning up the heat. 2017: Routledge.
- [5] Painuly, J.P., Barriers to renewable energy penetration; a framework for analysis. *Renewable energy*, 2001. 24(1): p. 73-89.
- [6] Singh, M., et al., Grid interconnection of renewable energy sources at the distribution level with power-quality improvement features. *IEEE transactions on power delivery*, 2011. 26(1): p. 307-315.
- [7] Divya, K. and J. Østergaard, Battery energy storage technology for power systems—An overview. *Electric power systems research*, 2009. 79(4): p. 511-520.
- [8] Oudalov, A., R. Cherkaoui, and A. Beguin. Sizing and optimal operation of battery energy storage system for peak shaving application. in *Power Tech, 2007 IEEE Lausanne*. 2007. IEEE.
- [9] Nykvist, B. and M. Nilsson, Rapidly falling costs of battery packs for electric vehicles. *nature climate change*, 2015. 5(4): p. 329.
- [10] Vrettos, E.I. and S.A. Papathanassiou, Operating policy and optimal sizing of a high penetration RES-BESS system for small isolated grids. *IEEE Transactions on Energy Conversion*, 2011. 26(3): p. 744-756.
- [11] Ning, G., B. Haran, and B.N. Popov, Capacity fade study of lithium-ion batteries cycled at high discharge rates. *Journal of Power Sources*, 2003. 117(1-2): p. 160-169.